Flexibility in Coordination Polymers:
Structure, Topology, Porosity, and Addressability

A thesis submitted to the University of Dublin for the degree of Doctor of Philosophy

Debobroto Sensharma

School of Chemistry

University of Dublin

2019

Declaration

I declare that this thesis has not been submitted as an exercise for a degree at this or any other university and that it is entirely my own work, except where otherwise cited, referenced, acknowledged or accredited.

I agree to deposit this thesis in the University's open access institutional repository or allow the Library to do so on my behalf, subject to Irish Copyright Legislation and Trinity College Library conditions of use and acknowledgement.

Debobroto Sensharma

Summary

Metal-Organic Frameworks (MOFs) are a research area approaching maturity and the industrial application of MOFs to a number of pressing challenges is imminent. These materials are exciting for their porosity and chemical tunability, as well as the applicability of rational principles in their design. MOFs are applied in fields as diverse as gas storage and separation, drug delivery, catalysis, and sensing. The design of MOFs is guided by a few powerful general principles that form the basis of the approach known as reticular chemistry. The reticular approach emphasises symmetric structures obtained by the use of rigid organic components.

In this thesis, a variety of non-rigid behaviours are examined, such as the accommodation of torsional strain in one- and two-dimensional coordination polymer motifs, the diversity of conformations accessible to ligands due to free rotations in alkyl-chain backbones or ethynyl spacers, rotational flexibility about metal-ligand bonds in assembled MOFs, and conformational variability about *p*-phenylene spacers in extended ligands. In the absence of perfectly rigid organic linkers, or in frameworks that allow a degree of internal motion, new and unusual topologies are obtained due to lower-symmetry conformations. These effects are combined with chemical functionality resulting in MOFs that respond to stimuli, such as light or moisture, with changes in structure that reversibly affect porosity.

In chapter 1, chemical and historical contexts for the strategies adopted and results presented in this work are described. A brief history and description of the concepts used is provided, followed by a survey of the current literature in the field and the progress made in the various applied branches of MOF chemistry. The aims of the thesis are delineated.

In chapter 2 mixed-ligand one- and two-dimensional coordination polymers based on various M^{2+} metal ions are described. Both ligands used are tripodal. The accommodation of varying M^{2+} ion radii takes place in **1-4** due to the ability of the ligands used to adopt increasingly strained conformations. This effect permits the recurrent formation of the same one-dimensional coordination polymer motif, and the same packing arrangement in two dimensions. However, supramolecular packing in the third dimension, mediated by aromatic interactions between distorted ligands, varies as a result of increasing ionic radius.

The chelating ligand used in **1**-**4** is replaced with an isomeric capping ligand, and a two-dimensional sheet motif is obtained.

This mixed ligand strategy is applied to ditopic N-donor ligands used in combination with ditopic organic and inorganic charged moieties in Chapter 3. Functionalised ligands are used as pillars in 3D structures which contain accessible 1D channels in **6** and **7**. Prolonged and delicate crystallisations allowed the isolation of compounds based on N-donor ligands with highly flexible alkyl-chain backbones – **8** and **9**, which were both found to be two-dimensional, rather than the three-dimensional structures shown by homologues. **8**, was shown to be intrinsically porous, and showed excellent CO_2 uptake characteristics and selectivity, bringing the most valuable qualities of many 3D MOFs into two dimensions. The ditopic, bridging monodentate coordination mode adopted by the aromatic 4,4'-azopyridine ligand in **10** allows it to pivot about its axis in response to its surroundings. This led to the occurrence of a sharp transition upon the adsorption of 1.5 molecules of CO_2 molecules per unit cell, after which the uptake of CO_2 increased dramatically. **10** was shown to be selective for CO_2 over N_2, and the stimulus-responsive behaviour was shown to result in the highest room temperature CO_2 working capacity between 0.1 bar and 1 bar recorded till date. A reversible transition also occurs between **10** and a hydrated phase **10′**, which is utilised for the instantaneous release of adsorbed CO_2 from **10**.

In Chapter 4, an elegant synthetic strategy is described, by which neutral, ditopic, N-donor ligands of appropriate length were incorporated into frameworks with the **pto** topology. This may be considered a mixed ditopic+tritopic ligand strategy. **11** and **12** were built by the incorporation of the photoresponsive 4,4'-azopyridine ligand into **pto** scaffolds built with highly extended, flexible ligands. As a result, the photoresponsivity of the 4,4'-azopyridine ligand is expressed through static and dynamic changes in the CO_2 uptake of **11** and **12**. Strong responses to irradiation – changes of 40% of the magnitude of uptake under dynamic irradiation conditions – are observed. **11** and **12** are the first reported MOFs with photoresponsive gas uptake in which photoswitching ligands are not the sole organic component. This synthetic strategy was also used to incorporate functionalised ditopic ligands into **pto** scaffolds in **13**-**16**.

Chapter 5 contains a description of novel MOFs based on the highly extended $bteb^{3-}$ and bbc^{3-} ligands and analyses of their structures. Conformational flexibility due to the acetylene and *p*-phenylene spacers allows the adoption of otherwise inaccessible dihedral angles, and lower symmetry conformations. As a result, the frameworks in **17**-**23** form 'non-default' networks. In **19** and **23**, 4,4'-azopyridine is used as an auxiliary ligand, and novel topologies are obtained.

In Chapter 6, a number of MOFs (**24**-**28**) are described which were targeted for specific attributes using the $bteb^{3-}$ and bbc^{3-} ligands. Simulations are carried out to show the potential porosities of these frameworks, and some exceptional attributes are observed.

Chapter 7 describes the experimental details of the work carried out.

Chapter 8 concludes the thesis and offers an outline of the research questions emerging from the results presented which may be addressed in future studies.

Acknowledgements

My foremost thanks are due to my supervisor, Prof. Wolfgang Schmitt. I am grateful for the opportunity to carry out this research under him, and for the steady guidance I have received from him in my time here. I have also had valuable support from the School of Chemistry, TCD, and many senior academics leading up to and during this work - Prof. Govindasamy Mugesh, Prof. Clive Williams, Prof. S.V. Eswaran, Prof. Rashmi Sachdeva, Prof. Shabnam Johri, Prof. Santanu Bhattacharya, Prof. Robert J. Baker, Prof. Aidan McDonald and others - that I acknowledge with thanks.

The work presented in this thesis is collaborative in many respects. Many key chemical ideas used in this thesis are due to the work of Dr. Nianyong Zhu during his time in the Schmitt group. The single crystal X-ray studies presented here, and some of the more delicate powder X-ray measurements were carried out by Dr. Zhu, Dr. Amal Cherian Kathalikkattil, Dr. Lauren Macreadie, Paul Wix, and Friedrich Steuber, with assistance from Dr. Brendan Twamley. Dr. Sebastien Vaesen helped with gas sorption experiments, SEM, and provided selectivity and heats of adsorption data, and Dr. Colm Healy helped to conceive and execute moisture-triggered release experiments. Swetanshu Tandon and Prof. Graeme Watson made DFT calculations available. Prof. Tina Düren and Dr. Matthew J. Lennox performed an important simulation of nitrogen adsorption. I thank Paul and Colm in particular for some key analytical insights. Dr. Guanghua Jin and Dr. Joaquín Soriano López are working on ongoing catalysis experiments. Jens Hartmann and Almudena Sánchez Torres worked under my supervision as project students and made significant contributions to this work.

I also thank Dr. Manuel Rüther for training in numerous instrumental techniques, and for NMR measurements with Dr. John O'Brien. I thank Ann Connolly and Rónán Crowley at UCD for quantitative analysis, Dr. Martin Feeney and Dr. Gary Hessman for mass spectrometry, and Dr. Peter Brien, Patsy Greene, and Margaret Brehon for access to their labs. I would like to acknowledge help received from Frederick Cowzer and Maura Boland in stores, Kieron Galvin for custom-made glass fibres and a chromatography column, and Dr. Sinead Boyce and Anne Marie Farrell for administrative help. Special thanks are due to Dr. Niamh McGoldrick for being as reliable and optimistic as she has been in complicated situations.

A large number of personal acknowledgements are also due. Kevin Byrne, Luana Martins, Paul, Friedrich, Amal, Seb, and Colm have been like elder siblings to me over my time here, and I am grateful to everyone in the Schmitt group for welcoming me and treating me like family. I also owe a huge debt of gratitude to Chris Roche, Ian Morris, and everyone at Bohemian F.C., where I felt at home. I thank the staff at TCD for their effort in making sure our workplaces have been safe and clean.

I owe gratitude to my family, in particular Ma, Baba, and Ira, who have always been a source of every kind of support, and of cheer and good humour. I thank Sthira for her patience and care, despite her own demanding days. I have many friends and elders to thank as well, in Bangalore, Delhi, and elsewhere, for their good wishes, and for keeping my feet on the ground. I have been very fortunate in the opportunities I have had.

Table of Contents

Abbreviations

1D	One-Dimensional
2D	Two-Dimensional
2-tpt	2,4,6-Tris(2-pyridyl)-1,3,5-triazine
3D	Three-Dimensional
4-tpt	2,4,6-Tris(4-pyridyl)-1,3,5-triazine
abtc	Azobenzenetetracarboxylate
ATR	Attenuated Total Reflection
azpy	4,4'-Azopyridine
bbc	4,4',4''-(Benzene-1,3,5-triyl-tris(benzene-4,1-diyl))tribenzoate
bdc	Benzene-1,4-dicarboxylate
BET	Brunauer-Emmett-Teller
bpdc	Biphenyl-4,4'-dicarboxylate
bpet	1,2-Bis(4-pyridyl)ethane
bpy	4,4'-Bipyridine
btb	4,4',4''-Benzene-1,3,5-triyl-tribenzoate
btc	1,3,5-Benzenetricarboxylate
bteb	4,4',4''-(Benzene-1,3,5-triyltris(ethyne-2,1-diyl)tribenzoate
ca.	*circa*
CCDC	Cambridge Crystallographic Data Centre
CCS	Carbon Capture and Sequestration
COF	Covalent Organic Framework
CP	Coordination Polymer
dabpy	3,3'-Diamino-4,4'-bipyridine
DEF	*N,N*-Diethylformamide
DFT	Density Functional Theory
DMF	*N,N*-Dimethylformamide
DMSO	Dimethyl sulfoxide
dnbpy	3,3'-Dinitro-4,4'-bipyridine
DUT	Dresden University of Technology
e.g.	for example
ESI	Electrospray Ionisation

et al.	and others
Fig.	Figure
FTIR	Fourier Transform
HAr	Aryl proton
H-bonding	Hydrogen bonding
HKUST	Hong Kong University of Science and Technology
i.e.	that is
IRMOF	Isoreticular Metal-Organic Framework
IUPAC	International Union of Pure and Applied Chemistry
mea	Monoethanolamine
MIL	Matériaux de l′Institut Lavoisier
mmen	*N*,*N*′-dimethylethylenediamine
MO	Molecular Orbital
MOF	Metal-Organic Framework
MS	Mass Spectrometry
NMR	Nuclear Magnetic Resonance
NOTT	University of Nottingham Metal-Organic Frameworks
NU	Northwestern University
PCN	Porous Coordination Network
PCP	Porous Coordination Polymer
PIM	Polymer of Intrinsic Microporosity
PSA	Pressure Swing Adsorption
PSD	Pore Size Distribution
PXRD	Powder X-ray Diffraction
RCSR	Reticular Chemistry Structural Resource
Ref.	Reference
RPM	Recyclable Rutgers Porous Material
SBU	Secondary Building Unit
$scCO_2$	Supercritical CO_2
SCXRD	Single Crystal X-ray Diffraction
SEM	Scanning Electron Microscopy
SMT	Single Molecule Trap
SUMOF	Stockholm University Metal-Organic Framework

tapb	4,4',4''-(Triazine-2,4,6-triyl-tris(benzene-4,1-diyl))tribenzoate
TCM	Trinity College Material
tdp	Trimethylenedipyridine/1,2-Bis(4-pyridyl)propane
TGA	Thermogravimetric Analysis
TTD	Topos Topological Database
UiO	Universitetet i Oslo
UMC	Unsaturated Metal Centres
UMCM	University of Michigan Crystalline Material
UTSA	University of Texas San Antonio
UV	Ultraviolet
VOC	Volatile Organic Compounds
vs.	*versus*
ZIF	Zeolitic Imidazolate Framework

Chapter 1
Introduction

1.1 - Early History

1.1.1: Coordination Polymers

After Werner's revolutionary investigations describing metal complexes as consisting of metal atoms surrounded by ligands, the modern definition of coordination compounds has changed very little.[1–4] As per the current IUPAC definition, a coordination compound consists of a central atom or ion, usually a metal, to which groups of atoms, called ligands, are attached by coordinate bonding through a donor atom.[5] A suitable arrangement of multiple donor sites on a single ligand can easily be imagined by which this ligand might act as a bridge between multiple metal sites, leading to a one-, two-, or three-dimensional network structure in which the repeating units are coordination entities based on the metal ions and ligand fragments. These extended ordered structures are known as coordination polymers.

The concept of polymerism was first invoked by Berzelius in 1833, in order to describe compounds with similar empirical composition but different properties, originating from a difference in the total number of atoms present.[6] Thus, polymers were materials composed of multiple units of a basic building block, such as ethene and butene. This meaning has changed somewhat over time.[7] The word was first applied in its present sense to organic polymers by Staudinger in 1922, when he theorised that plastic organic materials, such as Bakelite, were composed of repeating patterns of covalently linked organic monomers.[8]

The term 'coordination polymer' surprisingly predates this usage, and was coined in 1916, by Shibata, in reference to oligomeric cobalt(II) ammine complexes.[9] Although coordination polymers such as Prussian Blue have been known, synthesised and used since at least the early 1700s, their structures remained unclear until the advent of suitable X-ray techniques in the 1970s.[10–12] Similarly, the first Hofmann complex, synthesised in 1897, was shown to be a coordination polymer only in 1952.[13,14] The term 'coordination polymer' made sporadic appearances in the literature until the analogy between organic and coordination polymers as infinitely extended structures was explicitly made by Bailar Jr. in 1964, and consolidated by Carraher in 1981.[15–22] The possibility of design and control over structure and dimensionality in coordination polymers is clearly articulated in these studies. Mathey (1977) and Iwamoto (1980-1985) published examples of the coordination of

various linear diamine ligands into extended Hofmann complexes, which were important early steps towards a general theory of design in coordination polymers (Fig.1.1.1).[23–27] However, publications remained relatively rare in the area.

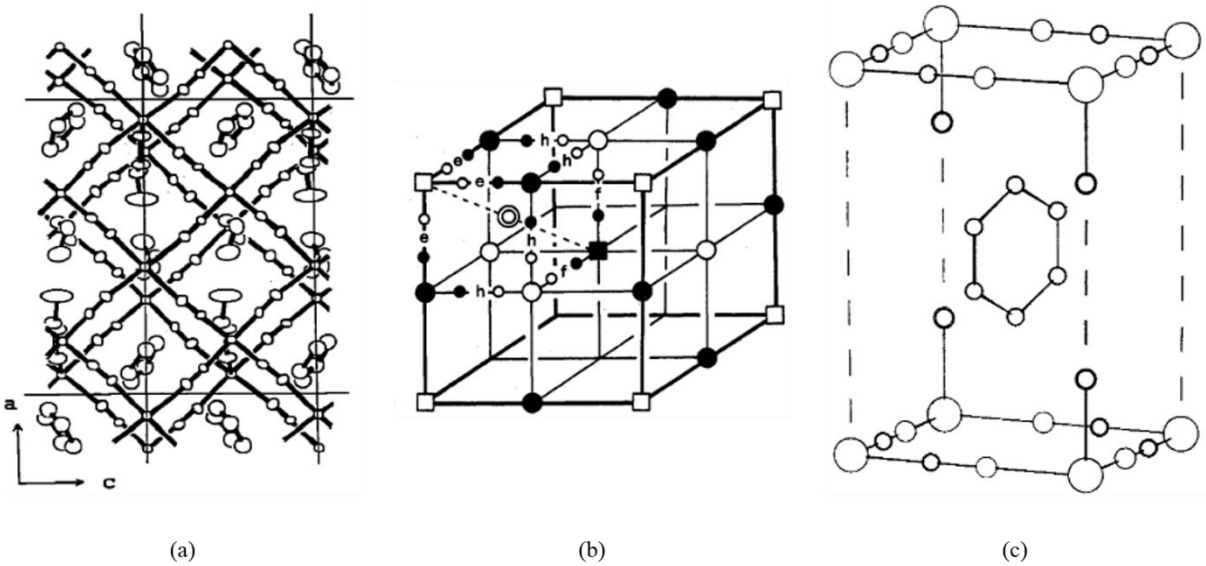

Fig. 1.1.1 – Representations of the crystal structures obtained for (a) the Hoffman complex $[Cd(mea)Ni(CN)_4]\cdot C_4H_5N$ (mea: monoethanolamine), taken from Ref. 27. (b) Prussian Blue, $Fe_4[Fe(CN)_6]_3\cdot xH_2O$, in which large open and closed symbols represent Fe(II), Fe(III) centres, small open and closed symbols represent C and N centres from CN^-, and the double circle represents interstitial oxygen centres from H_2O. Taken from Ref. 12. (c) the Hoffmann complex $[Ni(CN)_2(NH_3)]\cdot C_6H_6$, taken from Ref. 14.

1.1.2: Towards Porosity and Rational Synthesis

In the 1990s, developments in a number of modern chemical fields such as supramolecular chemistry, crystal engineering, and structural inorganic chemistry, as well as paradigm shifts in crystallography and computing, converged to create a conducive environment in which to imagine and realise coordination polymer structures.[28,29] Crystal engineering originated with the work of Schmidt and Kitaigorodsky, who both pioneered general theorisation of crystal structures based on the molecular components of the crystal.[30,31] Despite an important early paper by Leiserowitz in 1976 on the crystallisation of carboxylic acids, relating molecular identity to crystal structure remained a significant challenge for decades.[32] In 1988, an editorial by Maddox was published in Nature, which stated, "*One of the continuing scandals in the physical sciences is that it remains in general impossible to predict the structure of even the simplest crystalline solids from a knowledge of their chemical composition… Solids such as crystalline water (ice) are still thought to lie beyond mortals' ken. Yet we would have thought that, by now, it should be possible to equip a*

sufficiently large computer with a sufficiently large program, type in the formula of the chemical and obtain, as output, the atomic coordinates of the atoms in a unit cell."[33] This appears to have been a crucial intervention in the field, and the editorial has been cited over 300 times (as per Web of Science, June 2018).

At almost exactly this time, the area of crystal engineering experienced a revitalisation. Importantly, over the preceding years, sophisticated direct methods for crystal structure solution had been developed, and a searchable database of crystal structures – the Cambridge Crystallographic Data Centre - was established, and with advances in computing both became more accessible.[29] In 1987, the Nobel Prize in Chemistry was awarded to Cram, Lehn, and Pedersen for their contributions to establishing supramolecular chemistry, in particular *"for their development and use of molecules with structure-specific interactions of high selectivity."* [34–37] In 1989, Desiraju authored a key monograph entitled *Crystal Engineering,* which provided the context and basis for much of the subsequent research concerned with understanding intermolecular interactions, and their utilisation to generate solids with desirable properties.[38] It was influential in concentrating attention towards deviations from simple close packing due to chemical functionality in molecules.[39]

The parallels between supramolecular chemistry and crystal engineering are evident in that both are centred on molecular recognition and intermolecular forces. Crystal engineering is often thought of as supramolecular chemistry in the solid state and crystals were described by Dunitz (1991) as "supramolecules par excellence".[40] Directional interactions were therefore studied extensively with a view towards understand the molecule-crystal relationship. Papers by Etter and Zaworotko on hydrogen bonding (H-bonding), Gavezzotti and Desiraju on aromatic interactions, and Braga on organometallic cluster compounds were, among many others, extremely influential in harnessing the potential of these directional interactions, and laid much of the foundation for crystal engineering as we understand it today.[41–48]

Advances in crystal engineering did not exclude coordination polymers.[49] Despite the difference in the strengths of the directional interactions used to control the structure of the crystal (covalent bond vs. H-bond/other weak interaction), the same principles applied. By the late 1980s, the similarities became abundantly clear. One example of this convergence

between organic crystal engineering and coordination polymer chemistry are the early achievements of designed diamondoid nets. In 1988, Ermer reported the construction of a diamondoid crystal structure based on H-bonding interactions in adamantane-1,3,5,7-tetracarboxylic acid.[50] The –COOH groups in this compound are oriented into a near-perfect tetrahedron. H-bonds between –COOH groups orient each molecule into a recognisable network composed of tetrahedra. The next year, Hoskins and Robson selected tetrahedral $C(C_6H_4CN)_4$ ligands - functionally reminiscent of the linear diamines used to construct Hofmann complexes - and complexed them to Cu(I) metal centres, which are known to strongly favour tetrahedral coordination environments.[51] This coordination polymer, too, is easily visualised as a network of connected tetrahedra. Both solids show how directional information in the molecular components of a crystal can allow the achievement of a desired architecture, a small step towards Maddox's directive (Fig. 1.1.2).

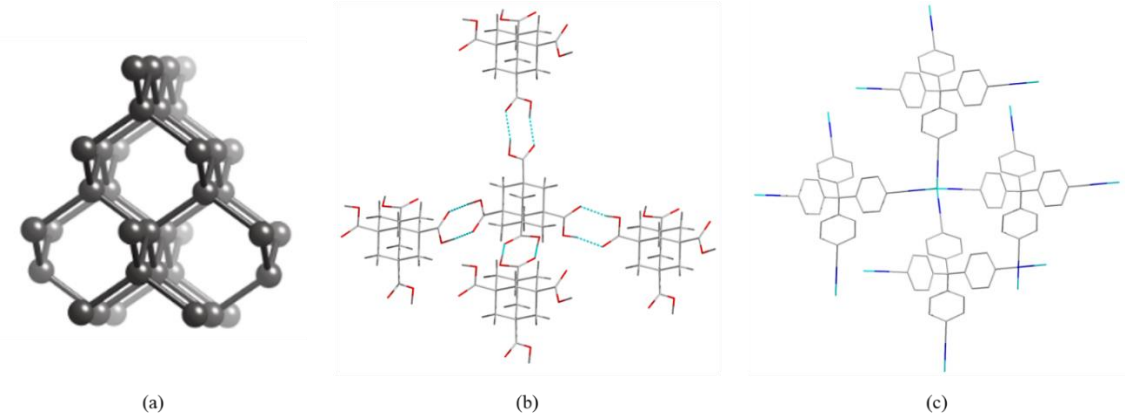

Fig. 1.1.2 – Representations of the diamondoid networks in (a) the reduced 'dia' net as given in the RCSR, from Ref. 52. (b) the H-bonded crystal structure of admantane-1,3,5,7-tetracarboxylic acid (CCDC: GEJVEW), adapted from Ref. 50. (c) the 3D coordination polymer $[Cu(C(C_6H_4CN))]$ (CCDC: JARMEU), adapted from Ref. 51.

Further, this example shows the usefulness of describing molecular architectures as networks. This approach was pioneered by Wells in 1977, in his descriptions of solid state inorganic compounds, in which directionality emerged from strong ion-ion interactions, shared oxygen atoms, and packing considerations.[53–55] The similarities between the examples above can be emphasised by describing them as diamondoid networks, owing to their resemblance to the classical diamond structure, in which each atom provides the necessary directional information for the assembly of the crystal.[56] Adopting the network approach to the design of crystalline solids reconfigures the central problem of crystal engineering into one of determining the three-dimensional (3D) pattern of connections that will form between the components of a crystal with functionality oriented in particular

directions, and the reverse, identifying components with functionality oriented appropriately for the formation of a particular 3D pattern.[57]

With these developments, the foundation had been laid for a re-evaluation of the scope of coordination polymer research. In the early 1990s a series of publications by Hoskins, Robson, and co-workers showed the rational construction of several 2D and 3D networks from metals and organic ligands.[51,58–67] In these papers, analogies were drawn between the structures of the networks obtained and patterns familiar to crystallographers, such as square and hexagonal (honeycomb) lattices, the cyclohexane boat conformation, rutile, and PtS networks, and more examples of diamond-like networks. Several of these were networks already discussed in inorganic solids by Wells, providing a basis for classification. New networks were also reported. In one of these articles (1990) Robson and Hoskins address the possible impact of these discoveries, and list some possibilities for the application of the general synthetic method they employed.[61]

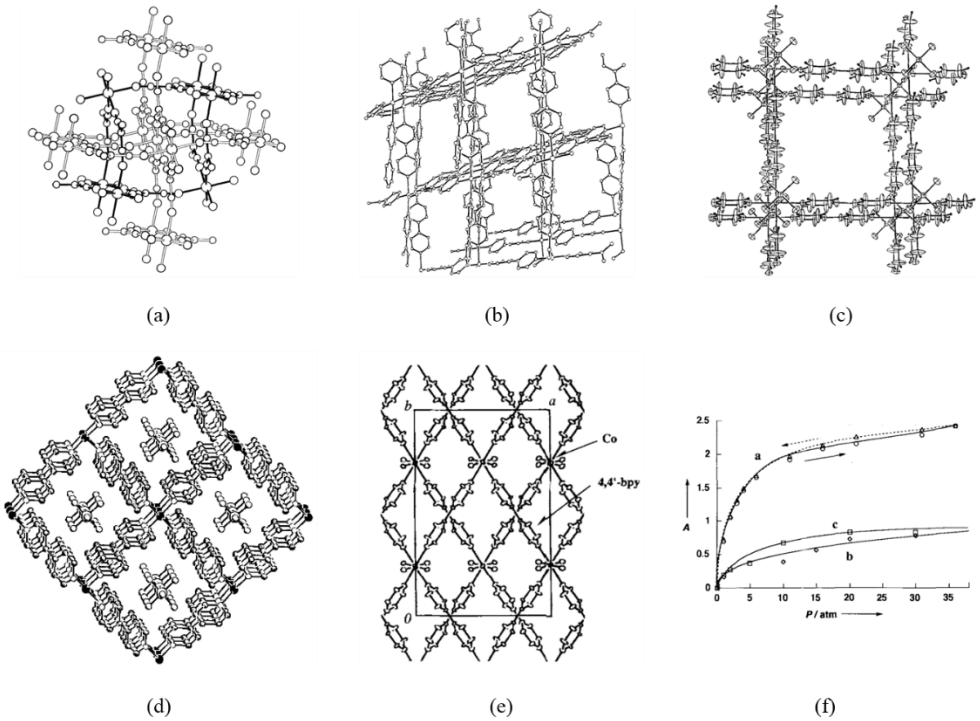

Fig. 1.1.3 – Representations of (a) the interpenetrating rutile-like frameworks of $[Zn(C(CN_3)_2]$ in Ref. 64. (b) channels formed in the 2D square framework of $[Cd(bpy)_2](NO_3)_2{\cdot}(C_6H_4Br_2)$ in Ref. 68. (c) the 3D cubic coordination polymer network in $[Zn(bpy)_2(SiF_6)]$, in Ref. 69. (d) the diamondoid 'metal-organic framework' $[Cu(bpy)_2](N(CH_3)_4)$ in Ref. 70. (e) the 'tongue-and-groove' structure in $[Co_2(bpy)_3(NO_3)_4]{\cdot}xH_2O$, in Ref. 71, and (f) adsorption isotherms of CH_4 (circles), N_2 (diamonds), and O_2 (squares) on it at 298 K in mmol/g.

The paper states "*We propose that infinite, ordered frameworks may form spontaneously, if ways can be devised of linking together centers with either a tetrahedral or an octahedral array of valencies by rod like connecting units… It may be possible to devise rods with sufficient rigidity to support the existence of solids with relatively huge empty cavities… The materials we propose here in principle offer bigger cavities, better access, a greater "concentration" of active sites and more widely variable functionalization of the matrix than cross-linked polymers or zeolites.*" Progress towards highly porous coordination polymers (and discrete metal-ligand assemblies) was made rapidly in the subsequent years, and compelling evidence was gathered that guests could be reversibly incorporated into the voids defined by the networks (Fig. 1.1.3).[68,69,72–79] The first appearance of the term "metal-organic framework" in conference proceedings was in 1994, used by Yaghi and co-workers to refer to diamondoid networks built using the 4,4'-bipyridine (bpy) ligand.[70] In 1995, Yaghi and co-workers published the selective binding and removal of pyridine guests in a cobalt(II) trimesate MOF.[80] The term MOF was used as it is today – to refer to coordination polymers based on organic ligands, with potential porosity. In 1997, 1998, and 1999, three papers by the Yaghi and Kitagawa groups demonstrated reversible gas sorption in microporous MOFs, dispelling any lingering uncertainty regarding the functional utility of coordination polymers, and consolidating the basis for the rapidly growing interest in these materials in the years to follow (Fig. 1.1.4).[71,81,82]

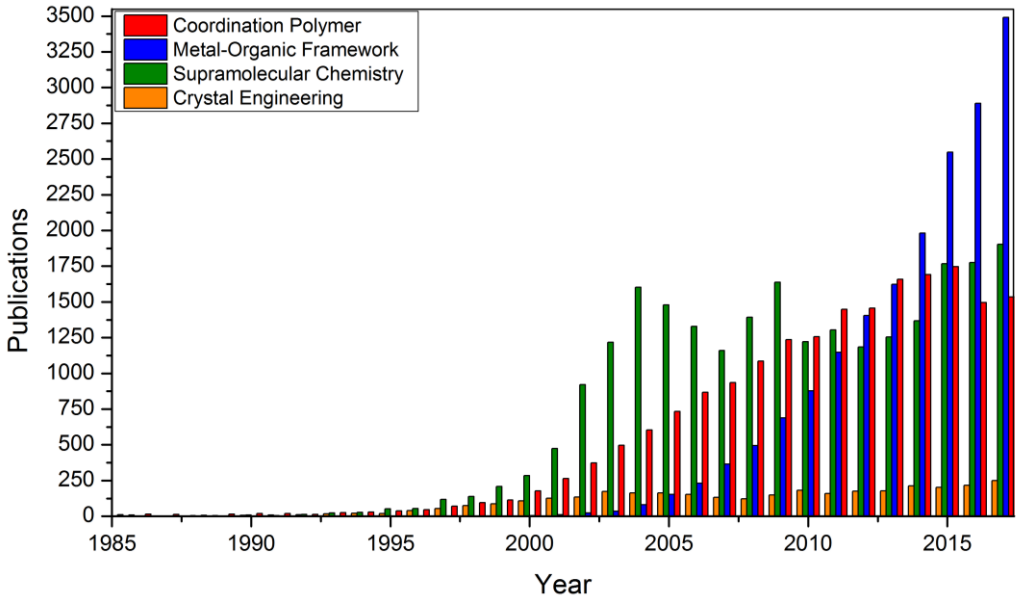

Fig. 1.1.4 – The number of unique publications appearing as Scopus search results, by year, for the search terms "coordination polymer", "metal-organic framework", "supramolecular chemistry", and "crystal engineering" in the title, abstract, or keywords, from 1986 to 2017. Up to date as of June 2018.

1.2 - Design and Synthetic Considerations

1.2.1: The Network Approach

Developments highlighting the functional attributes of MOFs brought their structural chemistry into focus. The potential of MOFs lay in the simplicity of the relationship between composition, structure and function, and elucidating the structural underpinnings of MOF chemistry became a crucial task. Hoskins and Robson's early predictions based on metal "nodes" and organic "spacers" provided the early conceptual basis for a systematic theorisation of MOF geometry and topology based on the components used, and Wells' network approach allowed comparisons to existing inorganic systems, which had been comprehensively analysed.[51,53] The network approach as applied to MOFs was the subject of two independent articles published simultaneously by the O'Keeffe and Férey groups in 2000, proposing principles for the topological classification of MOFs.[83,84] These principles developed into *reticular* chemistry (Latin: *reticulum*, "net").[85,86]

MOFs can be thought of as composed of two kinds of building units: metal ions, clusters, or oxo-clusters, and organic ligands. Directional information contained in the metal cluster or oxo-cluster determines the relative orientations of ligand groups, which act as connectors between several metal units. In analogy with zeolite topochemistry, the ligands, which provide geometrical extension, are considered the primary building units, and the metal units, which provide direction, are the secondary building units (SBUs).[87,88] Depending on the number of possible sites available for coordination, SBUs can accommodate multiple ligands and orient them in a variety of directions. Equally, the high degree of synthetic control available over organic compounds allows the selection of ligands with various functionalities, and with multiple donor atoms oriented in different directions. In general, MOF chemistry can therefore be thought of in modular terms – a chosen framework can be achieved by connecting a suitable ligand and a suitable SBU in a suitable way. Besides the benefits of the network approach already discussed, reticular analysis of MOFs was based on the topology of the framework structure. Therefore, even though there may be geometric, crystallographic, or physical differences between networks in MOFs, the topological classification remains invariant if chemical bonds connect ligands and metals in the same pattern. The topology of a MOF does not change under deformation unless

bonds are broken and re-made. In other words, topology provides a mathematical description of the structure of MOFs, based on chemical bonds.[57]

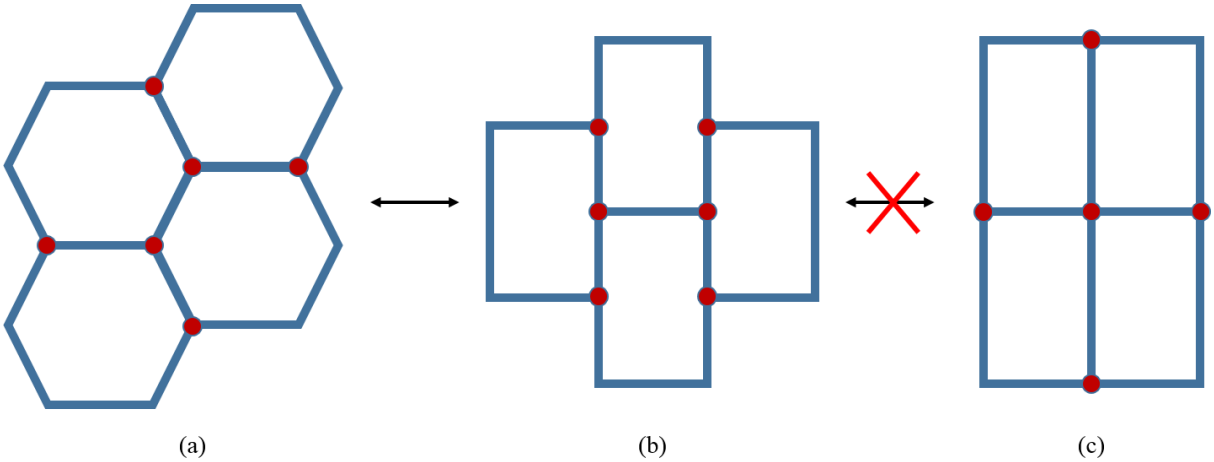

Fig. 1.2.1 – Topologically allowed (a) ↔ (b) and disallowed (b) ↔ (c) representations of the hcb (honeycomb) network. The representation in (c) is the sql (square lattice) network.

An illustration of this can be seen using 2D networks in Figure 1.2.1. Without breaking or forming any bonds, network (a) can be deformed into network (b), while network (c) cannot. Thus, despite the greater apparent geometric similarity of (b) with (c) than (a), (a) and (b) have the same topology, while (c) has a distinct topology. In fact, (a) and (b) are fragments of the well-known honeycomb (**hcb**) network, while (c) is a fragment of a square lattice network (**sql**). In **hcb** each vertex is connected to three other vertices through a spacer, while in **sql** each vertex is connected to four other vertices. Three-letter abbreviations for network topologies, such as **hcb** and **sql**, are used where available in order to classify networks without using their detailed mathematical descriptions, a practice again adopted from zeolite chemistry. This also makes network descriptions easier to retrieve and search for, a trait used extensively in the Reticular Chemistry Structure Resource (RCSR), which is a searchable repository of over 3000 periodic networks that has become an essential tool for the construction and analysis of MOF structures, and greatly aids the study of MOF topologies.[89]

1.2.2: MOF-5 and HKUST-1

The extremely well-studied structure of MOF-5 is a useful illustration of these ideas. The SBU in MOF-5 is constructed from an oxo-centred $\{Zn_4O\}$ unit, with the Zn atoms bound by six carboxylate groups (as in basic zinc acetate), resulting in the carboxylate C atoms adopting an octahedral geometry for the overall SBU. The linker is the linear remainder (a

p-phenylene moiety) of the benzenedicarboxylate (bdc, also called terephthalate) ligand. The octahedral orientation provided to the linear linkers by the SBUs results in a cubic 3D net in which each cube coincides with the unit cell (Fig. 1.2.2). The three-letter abbreviation assigned to such a network is **pcu**, which stands for primitive cubic. MOF-5 was discovered in 1999 by Yaghi and co-workers, and was found to be stable to solvent removal and very highly porous, with a Langmuir surface area of ca. 2900 m^2/g and a pore volume of 1.04 cm^3/g. These attributes were superior to all other porous materials, including zeolites and porous carbons, known at that time.[90]

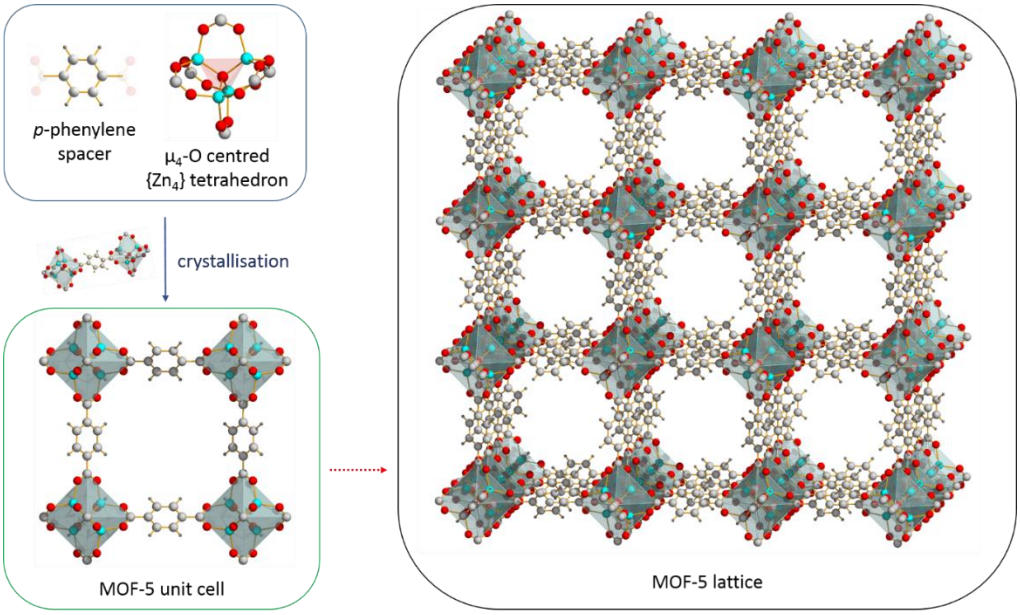

Fig. 1.2.2 – A schematic illustrating the relationship between the components of MOF-5 and its crystal structure.[90]

The reticular approach was also elegantly exemplified using functionalised and extended homologues of the bdc linker to synthesise, by design, a number of isoreticular MOFs (IRMOFs). By choosing longer linkers, larger pore volumes and gas uptakes were achieved, demonstrating the utility of the approach. Notably however, the formation of twofold interpenetrated IRMOFs upon linker extension was documented, in which void volumes were reduced by the presence of the second network.[91] Despite the robustness of the **pcu** synthetic platform, the formation of MOF-3, based on trinuclear zinc(II) "hourglass" SBUs, from the same starting materials – zinc(II) nitrate hexahydrate and terephthalic acid, also provides an example of the responsiveness of MOF syntheses to changes in conditions (Fig. 1.2.3).[90,92]

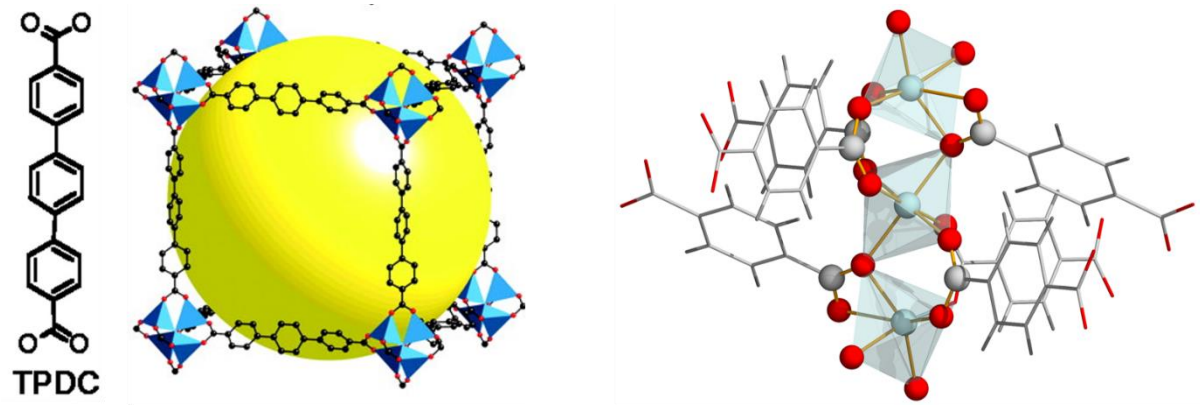

Fig. 1.2.3 (a) – A MOF isoreticular to MOF-5: IRMOF-15, based on the octahedral {Zn_4} SBU and the ditopic *p,p'*-terphenyldicarboxylate (tpdc) ligand (from Ref. 91). The yellow sphere represents the largest van der Waals sphere that the cavity shown can accommodate. (b) – A polyhedral representation of the 'hourglass' SBU in MOF-3 (CCDC: PURSOK), adapted from Ref. 92.

Linear linkers such as bdc are called ditopic, since they have donor atoms in two distinct connecting positions. Somewhat more complex structures can be achieved using tritopic ligands. In HKUST-1 (HKUST: Hong Kong University of Science and Technology), benzenetricarboxylate (btc, or trimesic acid) ligands are used as tritopic ligands that bind dinuclear copper(II) "paddle-wheel" SBUs. The paddle-wheel SBU consists of two square pyramidal Cu^{2+} environments. The Cu^{2+} ions are bound equatorially by four carboxylate groups in a *syn, syn* bidentate bridging fashion, resulting in the four carboxylate C atoms adopting a square planar geometry. The four carboxylate planes meet at the imaginary line between the Cu^{2+} ions, resembling a paddle-wheel. The axial positions of the paddle-wheel motif are occupied by labile water ligands, which can be replaced by other O- or N-donor ligands, or removed altogether - a feature that leads to desirable adsorption behaviour.[93]

The topology of HKUST-1 has the RCSR symbol **tbo** (twisted boracite). An isomeric stable topology that can result from the combination of tritopic ligands and paddle-wheel SBUs is the **pto** (Pt_3O_4) topology as shown by MOF-14 and MOF-143. These forms have the same molecular formula and can be considered isomers of one another, a phenomenon known as *framework isomerism*. Differences between **pto** and **tbo** networks can be seen in Figure 1.2.4. A number of factors determine whether the **tbo** or **pto** topology is adopted. One important factor is the planarity of the tritopic linker. Linkers such as btc and 4,4',4''-(triazine-2,4,6-triyl-tris(benzene-4,1-diyl))tribenzoate (tapb), in which the carboxylate

groups are coplanar to each other and the central phenyl ring, favour the **tbo** topology, as seen in HKUST-1. However, ligands such as 4,4',4"-benzene-1,3,5-triyl-tribenzoate (btb) and 4,4',4"-(benzene-1,3,5-triyl-tris(benzene-4,1-diyl))tribenzoate (bbc) in which peripheral benzoate moieties are pushed out of the plane of the central phenyl ring by aryl proton – aryl proton steric repulsion, show a preference for the **pto** topology.[94]

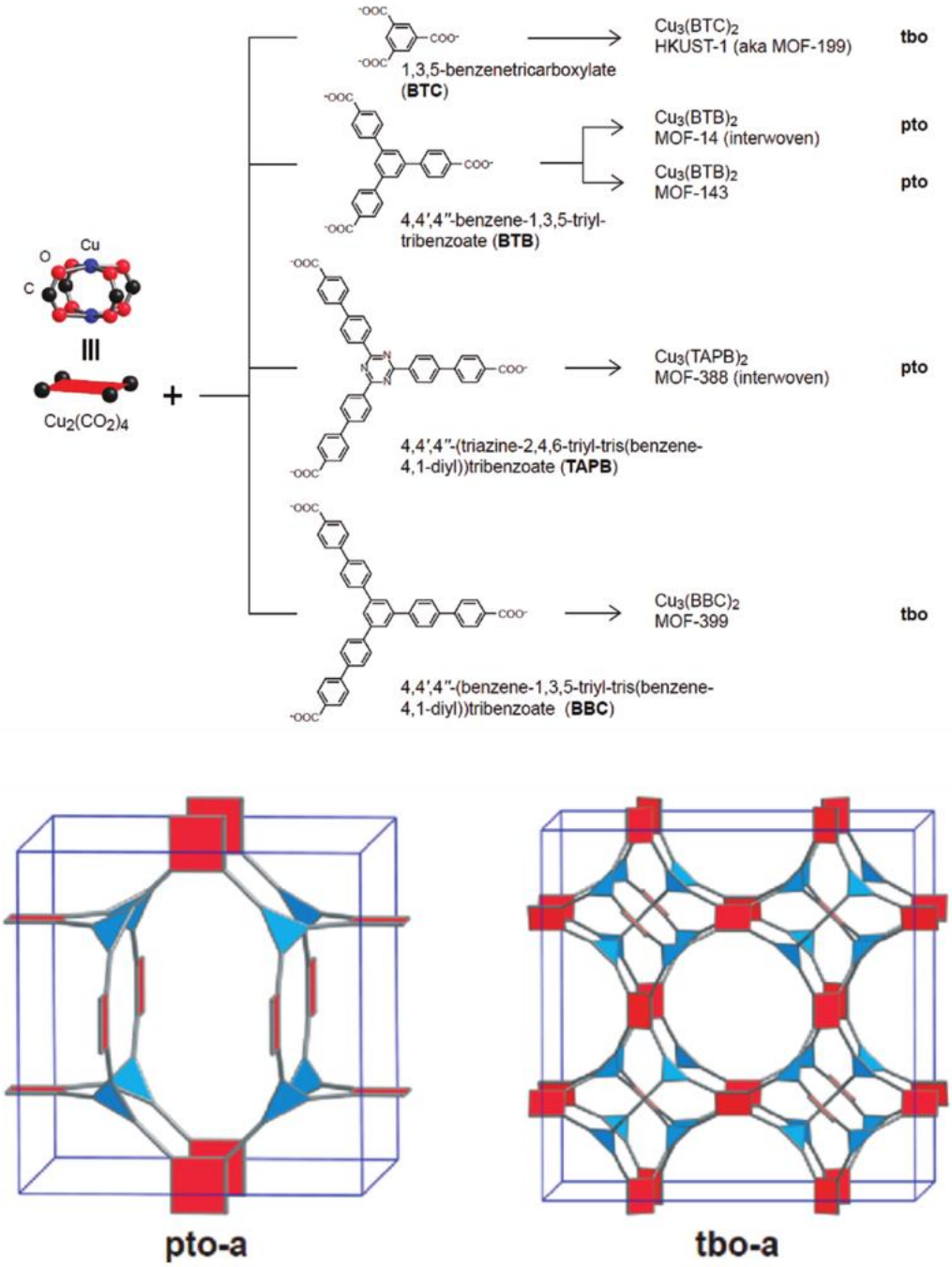

Fig. 1.2.4 (above) – A schematic diagram of the topologies obtained upon combination of the square {Cu_2} paddle-wheel SBU with various tritopic ligands into MOFs. (below) – Representations of the augmented (squares represent 4-connected nodes, triangles represent 3-connected nodes) pto and tbo network topologies adopted by these MOFs. From Ref. 94.

1.2.3: Solvents and Synthetic Conditions

These examples illustrate the power of the reticular approach to achieving desired MOF structures, but also show some of the important limitations within which it may be applied. In order to form the desired MOF in high purity, the formation of the SBU, conformations adopted by ligand molecules, and interpenetration must be controlled synthetically.

The conditions of synthesis, therefore, are vital in the design of MOFs. Due to the covalently bonded nature of MOF materials, recrystallisation and solution characterisation techniques are inaccessible, so single crystal X-ray crystallography is the most straightforward tool for structure determination. Although a number of MOF structures have been determined using PXRD techniques, the formation of single crystals directly from synthesis is highly desirable for characterisation. Metal-ligand coordination bonds are the optimum strength to provide structural support to the framework, but can still be broken and re-formed under ordinary conditions in solution. Ag-OH bonds have a bond energy of 139 kJ mol^{-1}, M-O bonds in acetylacetonate complexes have bond energies in the 170 – 250 kJ mol^{-1} range, Zr-O bonds in $Zr(OPr^{i})_4$ have a bond energy of 517 kJ mol^{-1}, and these energies illustrate the range of energies observed for metal-ligand bonds.[95–98] This allows the correction of premature terminations and cross-connections as the framework forms, and is important for the formation of a highly ordered, crystalline structure.

The solvent chosen for the synthesis must be one in which the metal salt (an ionic compound) and the ligand (an organic compound) are sufficiently soluble. Alcohols, dialkyl amides, water, and pyridine, as well as combinations of these are the most commonly used.[99] Dialkyl amides are widely used because, in addition to favourable solvation properties, they typically have sufficiently high boiling points to withstand the temperatures of MOF synthesis. Solvents help stabilise the large voids in porous structures as they form, and although no clear host-guest interactions are seen in most cases, solvents showing varying degrees of disorder are nearly always found in the crystal structures of MOFs. Varying the solvent in MOF syntheses has been shown to affect the network obtained and the degree of interpenetration.[100,101] Ionic liquids and deep eutectic solvents have been shown to have similar effects.[102,103] Chiral ionic liquids have been shown to impart chirality to MOFs grown in them using achiral building blocks.[104–106]

$$HC(O)NR_2 + H_2O \rightarrow HCO_2H + HNR_2 \rightleftharpoons HCO_2^- + H_2NR_2^+ \quad (1.2.1)$$

The decomposition pathway of dialkylamides (Equation 1) can interact with MOF syntheses as well. Secondary amines formed on decarbonylation of *N*,*N*-dimethylformamide (DMF) and *N*,*N*-diethylformamide (DEF) can template the formation of SBUs distinct from those formed by pristine solvent.[107] The dialkylammonium cation thus obtained has been shown to have a templating effect, and is an integral part of a number of SBUs synthesised in this manner.[108] Dialkyl amide solvents are also prone to decomposition upon heating, and the decomposition products – amides and carboxylic acids – can help stabilise intermediates in the metal-ligand reaction.[109] However, it should be noted that this decomposition also promotes side reactions which may be undesirable in this context.

1.2.4: Kinetics

Consider the formation of a MOF represented by the reactions in Equations 2-5. By either an associative or dissociative mechanism, the initially coordinated ligands/solvent molecules (A) on the SBU are replaced by MOF linkers (L). The dissociative process may be written as follows, with rate constants k_1 and k_{-1} for the forward and backward reactions respectively in equation 1, k_2 and k_{-2} for the forward and backward reactions respectively in equation 2, and so on.

$$MA_6 \underset{k_{-1}}{\overset{k_1}{\rightleftharpoons}} MA_5 + A \quad (1.2.2)$$

$$MA_5 + L \underset{k_{-2}}{\overset{k_2}{\rightleftharpoons}} MA_5L \quad (1.2.3)$$

And so on for subsequent substitutions.

Similarly, the associative process may be written with the same formalism for rate constants.

$$MA_6 + L \underset{k_{-1}}{\overset{k_1}{\rightleftharpoons}} MA_6L \quad (1.2.4)$$

$$MA_6L \underset{k_{-2}}{\overset{k_2}{\rightleftharpoons}} MA_5L + A \quad (1.2.5)$$

And so on.

Thus, the process of MOF formation can be approximately considered a process of stepwise substitution from MA_6 to ML_6 *via* the pathways shown. The rate of the substitution of one ligand is then represented by r_{s1}.

$$r_{s1} = k_2[MA_5][L] \tag{1.2.6}$$

And at steady state,

$$r_{prodn.[MA5]} = k_1[MA_6] \tag{1.2.7}$$

$$r_{consn.[MA5]} = k_{-1}[MA_5][A] + k_2[MA_5][L] \tag{1.2.8}$$

Thus,

$$k_1[MA_6] = k_{-1}[MA_5][A] + k_2[MA_5][L] \tag{1.2.9}$$

And,

$$[MA_5] = \frac{k_1[MA_6]}{k_2[L] + k_{-1}[A]} \tag{1.2.10}$$

And finally,

$$r_{s1} = \frac{k_2 k_1[MA_6][L]}{k_{-1}[A] + k_2[L]} \tag{1.2.11}$$

Therefore, A is a competitor to L, and the rate of bridging ligand substitution can be slowed down by increasing the concentration of A. The concentration of A is a useful synthetic handle on the speed with which crystallisation takes place, and consequently allows a degree of control over crystal quality. Slower reaction favours the formation of ordered, crystalline products, whereas at high r_{s1}, kinetically favoured, long range disordered products are likelier to form. This is due to the formation of chain terminations and cross-links by disordered metal-ligand bond formation. Correcting bonds that do not yield the long range ordered product is therefore an equally essential kinetic consideration. The rate of dissociation of a single metal-ligand bond can be written as r_{d1}.

$$r_{d1} = k_{-2}[MA_5L] \tag{1.2.12}$$

$$k_i = Ae^{\frac{-Ea}{RT}} \tag{1.2.13}$$

The E_a term in Equation 13 varies with the hardness of the metal ion in question. For relatively soft Lewis acids such as Pb^{2+}, Cd^{2+}, Cu^{2+}, and Zn^{2+}, E_a is low, and k_{-2} and r_{d1} are high, and excess solvent is sufficient competition to ensure facile crystallisations.

However, in the case of hard acids such as Al^{3+} and Zr^{4+}, the metal-ligand electrostatic interaction is stronger. So, E_a is high, and k_1 is far greater than k_{-2}, promoting the rapid formation of amorphous products. In order to lower the E_a barrier for dissociation, higher reaction temperatures are used. This approach is synthetically easy and commonly used, but is limited in that it increases both k_1 and k_{-2}. The introduction of an additional competitive Lewis base to lower the k_1 value, such as formate or acetate, can therefore be advantageous in combination with increased temperature, in these cases.[110]

1.2.5: Thermodynamics

The thermodynamics of MOF formation also indicate the need for elevated temperatures during synthesis. MOFs have extremely low densities for ordered solids, and are metastable with respect to the dense phases of the starting materials from which they are synthesised.

$$4ZnO + 3H_2(bdc) + xDEF \longrightarrow Zn_4O(bdc)_3 \cdot xDEF + 3H_2O \qquad (1.2.14)$$

The enthalpy of formation (ΔH_f) of MOF-5 as per Equation 14 has been experimentally shown to be 24.9±0.9 kJ mol^{-1} (Zn), and for the evacuated framework with no constitutional DEF molecules, 19.7±0.7 kJ mol^{-1} (Zn). The contribution of the pore solvent is therefore in the same range (4-7 kJ mol^{-1}) as in zeolites and other resilient porous materials. MOF-5 is thermally stable in dry air up to 500°C.[111] In HKUST-1, however, ΔH_f for the as synthesised MOF (in DMF) is exothermic relative to the dense phases, and is measured at -52.7±0.3 kJ mol^{-1} (Cu). Yet, ΔH_f for the desolvated MOF is positive, 16.7±0.5 kJ mol^{-1} (Cu). The interaction between DMF and HKUST-1 is therefore found to be very strong. This may be attributed to the presence of strong solvent-metal interactions at the axial positions of the paddle-wheel motif, resulting in an unsaturated metal centre (UMC) on desolvation. The very large stabilisation energy offered by the solvent helps stabilise the MOF, and partial amorphisation is observed on desolvation.[112] Therefore, the method of desolvation plays a crucial role in preserving the metastable framework for use as a porous material.[113]

The endothermic nature of framework formation further shows that elevated temperatures favour MOF synthesis. Two regimes for synthesis are commonly used - conventional elevated temperature synthesis, and solvothermal synthesis.[114] Solvothermal conditions refer to those in closed vessels at autogenous pressures above the boiling point of the solvent.[115–117] Solvothermal techniques are synthetically valuable because under these

conditions, the vapour pressure of the solvent in the vessel is raised and the dielectric properties of the solvent change, leading to increased dissociation, and enhanced effective solubilities for some reactants. For example, the pH of water measured at 453 K is ca. 5.5.[118]

1.2.6: Further Synthetic Considerations, Ligand Flexibility, and Design

The temperature used to obtain a desired product is chosen based on the process of SBU formation, the boiling point of the solvent, and the temperature of ligand decomposition. Many metal ions are capable of aggregating into various various SBUs that may all be stabilised by a given ligand system, and therefore choosing the correct temperature is vital for the formation of the desired product in high purity. In a classic example of this effect, reacting Co^{2+} with succinate in water at temperatures ranging from 60°C to 250°C yielded five distinct crystalline products at different temperatures (Fig. 1.2.5).[119] SBU nuclearity and framework dimensionality both increased with temperature. An even greater diversity of cobalt succinate coordination polymers can be obtained by varying pH and concentrations.[120] However, examples of SBUs are also known, especially for hard metal ions, which are very resilient to temperature, for instance the octahedral μ_3-O trinuclear Cr(III) hexacarboxylate unit, which is stable in solution from 25°C to 200°C.[121] Emerging alternatives to elevated-temperature syntheses include microwave-assisted, electrochemical, mechanochemical, and sonochemical methods.[122–127] However, regardless of the method employed, an understanding of the thermal behaviour of the components, and control over conditions of the system are essential for rational synthesis.

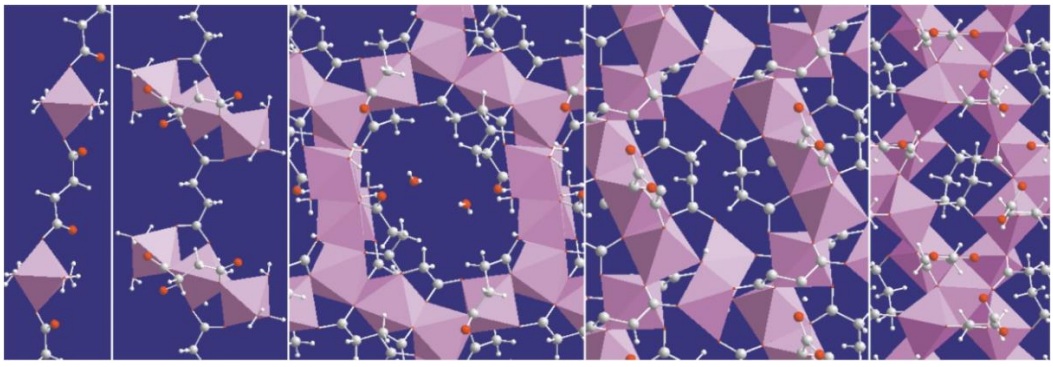

Fig. 1.2.5 – The five distinct cobalt(II) succinate phases obtained, at increasing temperature from left to right. From Ref. 119.

The auxiliary components of reactants, such as the anions in the metal salt used, also play a role in MOF formation, as can be seen in MOF-5 and compounds with related compositions.[129-131] Ligand flexibility is another important synthetic variable. The local

environments and relative conformations of donor sites in the crystallising MOF determine which topology is adopted by the framework, in cases with multiple possibilities.[131–136] Solvent-ligand interactions and ligand sterics are important determinants of structures.[137–139]

A useful general principle of the design and reticular synthesis of MOFs crystallising out of an isotropic state in solution is that, for known shapes and connectivities of nodes and spacers, the most symmetric nets are expected to form.[85] However, as illustrated by the extended homologues of HKUST-1, MOFs formed by a particular SBU and a ligands of fixed topicity may not be isoreticular to each other.[94] In theory, combinations of ligands and SBUs with particular topicities may result in a number of different structures. However in practice, *ca.* 80% of MOF structures obtained belong to a handful of high-symmetry 'default' nets, which form partly as a consequence of symmetric ligand conformations.[140] MOFs based on non-default nets are equally exciting candidates for various applications, *eg.* MOF-177, which is based on the **qom** net, rather than the 'default' **rtl** or **pyr** nets expected for a 6-connected SBU and 3-connected ligand.[141] However, predicting the formation of non-default nets requires the consideration of variables outside the standard reticular synthesis toolkit. The use of extended ligands with increased flexibility, or deliberate steric modulation, has led in some cases to the formation of non-default structures due to ligand desymmetrisation, or access to conformations restricted in shorter homologues.[142,143] However, systematic examinations of the landscape of possible non-default networks for fixed combinations of ligand and SBU connectivity are very rare.[144]

Similar factors also play a crucial role in deciding framework interpenetration. Interpenetration (or interweaving, in the case of nets minimally displaced from each other due to attractive interactions) occurs due to the thermodynamic need to form denser phases during the formation of porous MOFs (Fig. 1.2.6).[145–154] Reaction conditions have important influences on the phase formed, and ligand sterics also provide some synthetic control.[138,155–158] It is important to point out that depending on the application desired, interpenetration or interweaving can impart favourable characteristics to the material obtained.[152] An example is the dramatic improvement of the CO_2 selectivity of SIFSIX-2-Cu upon interpenetration, providing an exceptionally large physisorptive selectivity for CO_2 over N_2 (140 with interpenetration, versus 13.7).[159]

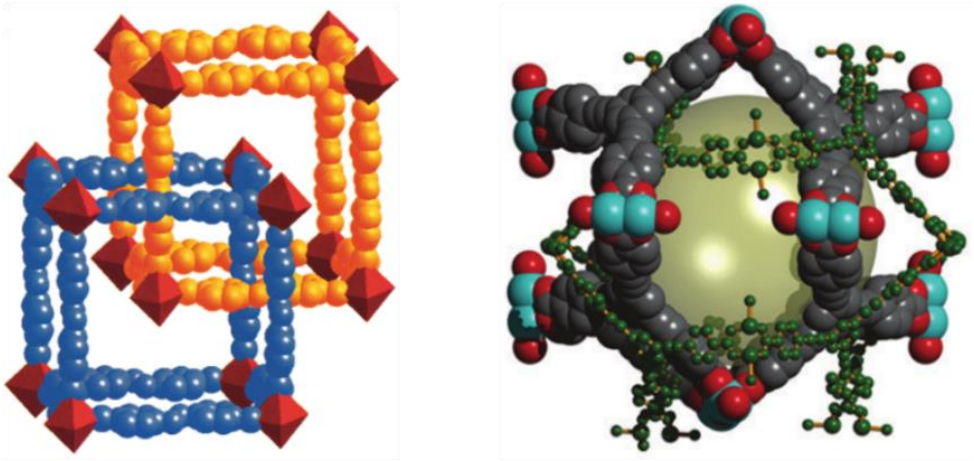

Fig. 1.2.6 (a) – Mutually interpenetrated pcu frameworks in MOF-9. From Ref. 153. (b) – Interwoven pto frameworks in TCM-4. From Ref. 160.

How possible it is to achieve total 'design' in chemical synthesis is a matter of debate.[161] However, MOF chemistry is an area in which a great deal of synthetic control may be exercised in the right circumstances, and product formation, in general, occurs according to simple rules. The modular approach of combining ligands and SBUs allows a great deal of customisability within a highly ordered, highly porous synthetic platform. Unusual and unexpected structures - that form due to apparent exceptions to the reticular concept, or due to very particular affinities within the reaction system - have advantages of their own, and their formation expands the space of possibilities available to chemists in the field. At present, technology to scale up MOF synthesis to commercially useful levels is being developed, and the promise of MOFs towards applications of many different kinds has been firmly established by a formidable body of research.[162,163]

1.3 - Applications

We are, at present, faced with technological challenges in fields as varied as carbon capture, hydrogen storage, fuel refinement and chemical purification, catalysis, and other more niche areas, in which metal-organic frameworks have prospective useful applications. Solid porous materials have become an important area of investigation aimed at the capture, release, and storage of various gases, in order to address the above challenges. Among the classes of solid porous materials, such as carbon-based solids, zeolites, porous silica, porous polymers and covalent-organic frameworks, MOFs have been established as the most tunable and structurally diverse (Table 1.3.1). They show excellent characteristics for the capture and storage of large quantities of gases, and also afford chemical platforms for customisation towards very specific applications.[164–166]

Table 1.3.1 – A comparison of classes of solid-state adsorbents, adapted from ref. 166.

Property	**Porous Organic Polymers**	**Porous Molecular Solids**	**Covalent Organic Frameworks (COFs)**	**Zeolites**	**Metal-Organic Frameworks (MOFs)**
Porosity	Usually microporous	Usually microporous, rare mesoporosity	Microporous, mesoporous	Microporous, mesoporous	Microporous, mesoporous
Pore Size Distribution	Broad	Sharp	Sharp	Sharp	Sharp
Typical Crystallinity	Amorphous	High	Moderate to high	High, occasionally amorphous	High
Stability	Good, especially hydrothermal	Modest. Isolated examples of hydrothermal stability	Low for boronates, high for imines	High thermal stability, occasionally pH sensitive	Modest, growing numbers of water-stable MOFs
Modularity	Very high	Rare, some co-crystals	In principle high, growing occurrence	High, new structures can be based on known zeotypes	Very high

Property	Porous Organic Polymers	Porous Molecular Solids	Covalent Organic Frameworks (COFs)	Zeolites	Metal-Organic Frameworks (MOFs)
Processability	Low, except PIMs*	Soluble – pro or con depending on application	Insoluble, examples of surface growth	Insoluble - films, composites, pellets well developed	Insoluble, composites and films well-known
Designability	Control over composition well developed, control over 3D organisation limited	Control over functionality within cage. Limited control over assembly	Reticular chemistry applies in principle	High, but design of organic templates often challenging	Excellent, well developed reticular chemistry
Unique Selling Points	Extended conjugation possible	Physical properties intrinsic to cages, solubility	Electronic properties	Stability, established use	High structural and chemical control for specialised application
Summary	Growing area, diverse chemistry, commercial application for PIMs*	New area, early promise for specific separations	Early promise for organic electronics	Major commercial importance, still growing	Established and highly active field, awaiting large-scale application

*PIMs – Polymers of Intrinsic Microporosity.

1.3.1: Porosity

Porosity in MOFs emerges from the combination of ligand and metal into characteristic arrangements. Just as the framework can be 'designed', the dimensions of the voids defined by the framework can also be predictably obtained. Ligands can be chosen with suitable rigidity, functionality, shape and topicity, and SBUs can be chosen with the appropriate geometry and hardness, to yield a stable MOF that is tailored for an application. The strength of the components of the framework and the metal-ligand bond must be sufficient for the metastable porous phase to remain after solvent removal – many MOFs with high acid, hydrolytic, and framework stability are based on strong metal-ligand bonds (*eg.* Materials Institute Lavoisier (MILs), and Zr^{4+}-carboxylate frameworks).[167–170] However, bonds of this strength often pose a challenge in crystallisation, and the vast majority of MOFs characterised by single-crystal X-ray studies suffer from limited stability in harsh

environments. Simple solvent removal procedures, such as low pressure and high temperature, are often ineffective if applied directly to the as-synthesised material.[171] Framework collapse affects the available porosity of the MOF, and also affects the reproducibility of evaluations of gas storage behaviour.[172]

In order to make the transition from solvent-filled to evacuated frameworks more feasible in more delicate compounds, two key empirically established strategies are applied. The first is solvent exchange, in which the original solvent (typically a high boiling, formamide-based solvent) is replaced by soaking in lower boiling solvents such as methanol or dichloromethane. This technique facilitates the removal of the new solvent at milder conditions, and in those MOFs whose collapse is triggered by the capillary action of high-surface tension solvents it allows for the introduction of lower-surface tension solvents into the MOF, facilitating the activation of some very fragile frameworks. The other technique is activation by the use of supercritical CO_2 ($scCO_2$), which has proven effective in activating many very highly porous MOFs (Table 1.3.2). However, both methods are mainly empirical, and the effect of variations in conditions, such as the rate of evacuation or temperature increase, and the time taken for solvent exchange, is poorly understood. Solvent exchange times can vary from a few minutes to several days.[173]

Table 1.3.2 – Surface tensions of common solvents used in MOF synthesis and activation.

Solvent	**Surface tension, 298 K (mN/m)**	**Ref.**
***N*,*N*-dimethylformamide**	36.0	174
***N*-methyl-2-pyrrolidone**	41.8	173
Dimethylsulfoxide	42.7	175
Dichloromethane	27.2	176
Chloroform	26.6	177
Methanol	22.1	175
n-Hexane	17.9	173
Liquid CO_2	0.59	178

The porosity of MOFs is usually experimentally characterised by N_2 sorption at 77 K and below 1 bar.[179] A useful estimation of the accessible surface area involved in gas sorption is obtained by applying BET theory to experimental isotherms, despite the theoretical

assumption that the adsorbent surface is flat.[180] The BET surface areas thus calculated are used to compare the available degree of accessible porosity in MOFs. Some high-surface area MOFs are listed below (Table 1.3.3). Theoretical maximum BET surface areas have been calculated for MOF-like systems approximated by ordered arrays of hyperextended poly-*p*-phenylene and polyyne moieties.[181] The experimental N_2 sorption isotherm also provides valuable structural information about the adsorbent – a steep increase in uptake at very low partial pressures indicates strong adsorption of N_2 molecules into small pores of < 2 nm diameter (micropores), while the presence of a shoulder after an initial steep increase, and hysteretic desorption, indicate the formation of a meniscus of condensed-phase N_2 in pores of 2-50 nm diameter (mesopores) (Fig. 1.3.1).[182,183] The effective diameter of available voids can also be calculated using DFT from the experimental isotherms to a high degree of accuracy, a feature that helps consolidate the structural model of the MOF obtained through crystallography and TGA.[184] The application of MOFs for specific uses is related strongly to the size and shape of the available pores, as well as their chemical composition, thereby linking design to function.

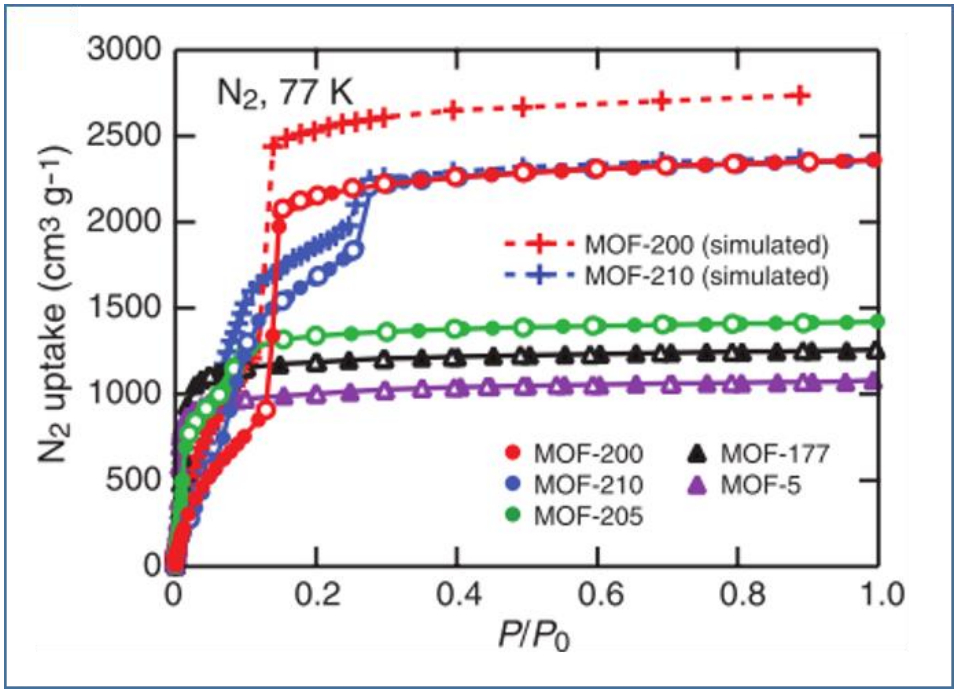

Fig. 1.3.1 – The nitrogen sorption properties of some representative MOFs at 77 K and low pressure. From Ref. 185.

Table 1.3.3 – Some high-surface area MOFs.

MOF	Year	Max. reported BET surface area (m^2/g)	Activation procedure	Ref.
MOF-5	2007	3800	CH_2Cl_2 exchange	186
NOTT-112	2009	3800	CH_2Cl_2 exchange	187
MIL-101c	2008	4230	NH_4F (aq.) exchange	188
Bio-MOF-100	2012	4300	$scCO_2$	189
DUT-6/MOF-205	2010	4460	CH_2Cl_2 exchange	185
MOF-177	2007	4750	C_6H_5Cl exchange	190
NOTT-116/PCN-68	2010	5110	CH_3OH-CH_2Cl_2 exchange	191
UMCM-2	2009	5200	CH_2Cl_2 exchange	192
NU-100/PCN-610	2010	6143	$scCO_2$	193
MOF-210	2010	6240	$scCO_2$	185
DUT-76	2015	6344	$scCO_2$	194
DUT-32	2014	6411	$scCO_2$	195
NU-109	2012	7010	$scCO_2$	196
NU-110	2012	7140	$scCO_2$	196
DUT-60	2018	7839	$scCO_2$	197
Theoretical maximum	2010	10577	-	198
Theoretical maximum	2012	14600	-	177, 192

1.3.2: Hydrogen Storage

Because of the attractiveness of hydrogen as a fuel, and its low density under ambient conditions, solid state materials for hydrogen storage have been an area of intensive research for decades.[199,200] Although pure hydrogen stored at very high pressures has already been used as a fuel in public transport systems, *eg.* in Germany and Japan, concerns regarding the weight added to vehicles and the safety of highly pressurised hydrogen have curtailed widespread application of this technology.[201] In order to offset these concerns, solid matrices have been advanced as candidates for hydrogen storage in this context, including porous carbons and metal hydrides.[202–204] In a high pressure regime, the hydrogen uptake of a solid adsorbent is found to correlate strongly with the accessible surface area.[205] Further, the energies of adsorption required for such an adsorbent to operate viably at ambient temperatures have been found to be *ca.* 22-25 kJ mol^{-1}, 3-4 times higher than the energy that would be afforded under these conditions by purely physisorptive processes.[206]

MOFs, therefore, with extremely high surface areas and functional tunability present themselves in many respects as promising materials.[207] Tailored void sizes, strategic framework catenation, and incorporation of unsaturated metal centres (UMCs) into structures have been shown to substantially enhance hydrogen uptake in MOFs, and progress continues to be made towards a critical and challenging chemical problem (Fig. 1.3.2, Table 1.3.4).[208–210]

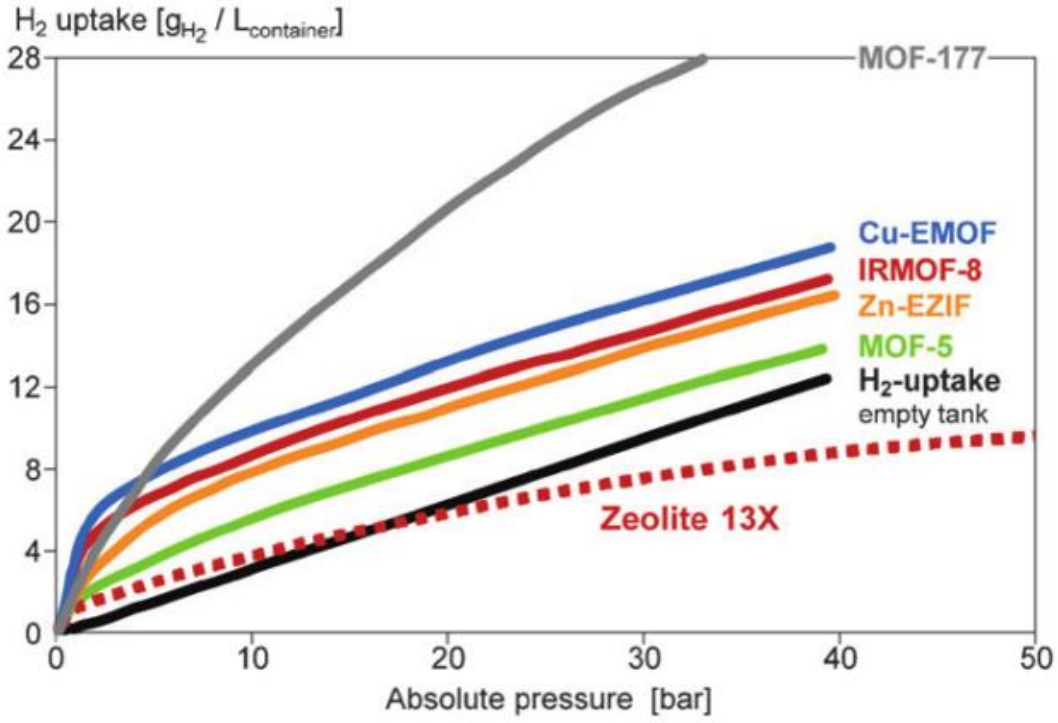

Fig. 1.3.2 – The hydrogen storage properties of some representative MOFs at high pressure in prototype trials. From Ref. 162.

Table 1.3.4 – Hydrogen storage capacities of benchmark MOFs and other materials. Storage capacity at 77 K unless specified.

Material	Hydrogen storage capacity, wt%	Pressure (bar)	H-Adsorbate interactions	Reference
MOF-5	7.1	40	Physisorption	186
	10.0	100	Physisorption	
MOF-177	11.4	78	Physisorption	211,212
PCN-610/NU-100	9.95	56	UMC, physisorption	193

Material	Hydrogen storage capacity, wt%	Pressure (bar)	H-Adsorbate interactions	Reference
PCN-68	1.87	1	UMC, physisorption	213
	7.32	50	UMC, physisorption	
PCN-12	3.05	1	UMC, physisorption	210
DUT-32	14.2	80	Physisorption	195
MOF-210	15.0	80	Physisorption	185
$Li_3Be_2H_7$	8.7 (573 K)	1	Ionic	204,214
$LiBH_4$	18.0 (653 K)	1	Covalent	203,215,216
High-Pressure C-Polymer container	7.0 (298 K)	400	Physical confinement, gas phase	202
High-Pressure Al-Fibreglass container	2.0 (298 K)	248	Physical confinement, gas phase	202,217
NH_3 (liq.)	5.9	1	Covalent	199

1.3.3: CO_2 Storage

The concentration of atmospheric CO_2 reached a maximum of 412.6 ppm in May 2018 as per the Scripps CO_2 Program measurements at Mauna Loa, Hawai'i.[218] This is in contrast to a steady value of *ca.* 270 ppm before the Industrial Revolution.[219–221] CO_2 contributes strongly to the atmospheric greenhouse effect, and human activities have led to global warming of *ca.* 0.8 K on average over the past century or so.[222–224] This warming has led to record temperatures[225], more frequent extreme weather events[226–228], food[229] and water-security[230] concerns, and ecological[231] and geopolitical precarity.[232] As greenhouse gas emissions continue, these trends are expected to intensify.[233]

Simultaneously, growing energy demands worldwide have resulted in a greater need for fuel, which are predominantly carbon based at present.[234,235] This situation, in which strong requirements exist both for the removal of CO_2 from the air and for carbon as a feedstock for fuel and materials, has led to proposals for the recycling of atmospheric CO_2, through hydrocarbon production[236], or an integrated 'methanol economy'.[237] Such a system would

lead to a degree of control over atmospheric CO_2 levels and help meet energy needs without drastically altering existing industrial infrastructure.

It is accepted that in order to stabilise atmospheric CO_2 at any level, net emissions must be brought down to zero.[238] In order to mitigate continuing emissions in the shorter term, however, technologies are required for the removal of CO_2 from air, flue gas, other industrial emissions, and emissions from dispersed sources. Photosynthetic biological systems rely on the conversion of CO_2 to fuel, but do so with efficiencies already superseded by artificial solar cells.[239] Further, the implementation of biofuel production has proven costly in terms of resources such as fertile land and water, and has resulted in non-trivial greenhouse gas emissions of its own.[240,241]An important technological frontier, therefore, is the selective capture of CO_2 at relatively low concentrations, and the facile regeneration of the capture matrix for reuse.[233]

Many solutions have been proposed for carbon capture and sequestration (CCS).[242] Gases such as nitrogen and oxygen are cryogenically distilled, a process which is impractical for CO_2 due to its low concentration and resultant high energy demand. Physical solvents such as SELEXOL® and Rectisol®, have been used for over forty years. Aqueous alkanolamine solutions, which form carbamates and bicarbonates with CO_2, are also used and capture CO_2 more effectively than physical solvents due to far stronger interactions.[243] However, the strong bonds by which CO_2 is held and the energetic cost of heating up aqueous solutions in order to regenerate the amines, as well as concerns over their corrosivity and toxicity, are serious drawbacks.[233] Some ionic liquids with task-specific functionality have recently shown promise for CO_2 capture but are relatively expensive to produce and purify.[244]

Using solid systems may help circumvent many difficulties encountered with liquid materials. $Ca(OH)_2$ and alkali metal hydroxide-based processes are extremely efficient and cost-effective routes to CO_2 capture, but regeneration only occurs at temperatures higher than 800°C, making them inefficient for CO_2 recycling.[245] Zeolites, porous carbons, and mesoporous silicas have shown excellent adsorption of pure CO_2 at low pressure.[246] However, issues remain with regard to selectivity and adsorption at ambient or higher temperatures. Functionalisation of these materials can improve selectivity, but these are

chemically challenging, and lead the material to rely on chemisorptive processes, which in turn complicate regeneration.[247] MOFs, therefore, are attractive in this context because of their very high uptakes, and facile tunability for specific streams of CO_2 in different circumstances, leading to high performance and facile recyclability.
Considering the kinetic diameter of the CO_2 molecule (3.30 Å)[248] and its significant electric quadrupole moment[249], MOFs with[188,250–257] or without UMCs,[258–272] with tailored pore sizes through ligand choice[159,267] or strategic interpenetration[159,273,274], or with voids functionalised using groups[275–282] such as –OH and $–NH_2$ have been used to demonstrate CO_2 capture.

While ultraporous MOFs are extremely effective at capturing CO_2 under high-pressure regimes, this strategy is unhelpful in the low pressure scenarios mandated by the low concentrations of CO_2 in various exhaust streams or air.[283–285] The optimal heat of adsorption of CO_2, Q_{st}, onto a solid adsorbent is in the 30-60 kJ mol^{-1} range.[286] These amount to sufficiently strong interactions for selective binding of CO_2, while still allowing regeneration of the MOF with moderate energy input. MOFs with small voids or suitable functionality can interact sufficiently strongly with CO_2 to meet this requirement.

Some examples of MOFs that show promising CO_2 uptakes are mentioned below. PCN-88 is a copper paddle-wheel based MOF in which UMCs are separated by about 7 Å, allowing a single CO_2 molecule to be adsorbed in the space between them. This is known as the single-molecule trap (SMT) approach, and leads to highly selective CO_2 uptake.[287] The SIFSIX-3-M (M = Ni, Cu, Zn) materials have cavities of *ca.* 3.8 Å diameter, allowing single CO_2 molecules to interact with nearby pore walls. This, combined with the presence of electronegative fluorine atoms in the SiF_6^{2-} inorganic struts, leads to high Q_{st} values and highly selective CO_2 adsorption at low pressure.[159] M-MOF-74 are also exciting materials for CO_2 uptake. Their large pore diameters are lined with UMCs to couple high uptake with strong interactions and selectivity.[288] Further, the UMCs in these MOFs can be post-synthetically modified, *e.g.* with 1,2-dimethylethylenediamine (mmen), resulting in a MOF with very high uptakes at low pressures.[289] These (Fig. 1.3.3) and some other benchmark solid materials for CO_2 adsorption are listed in Table 1.3.5 below.

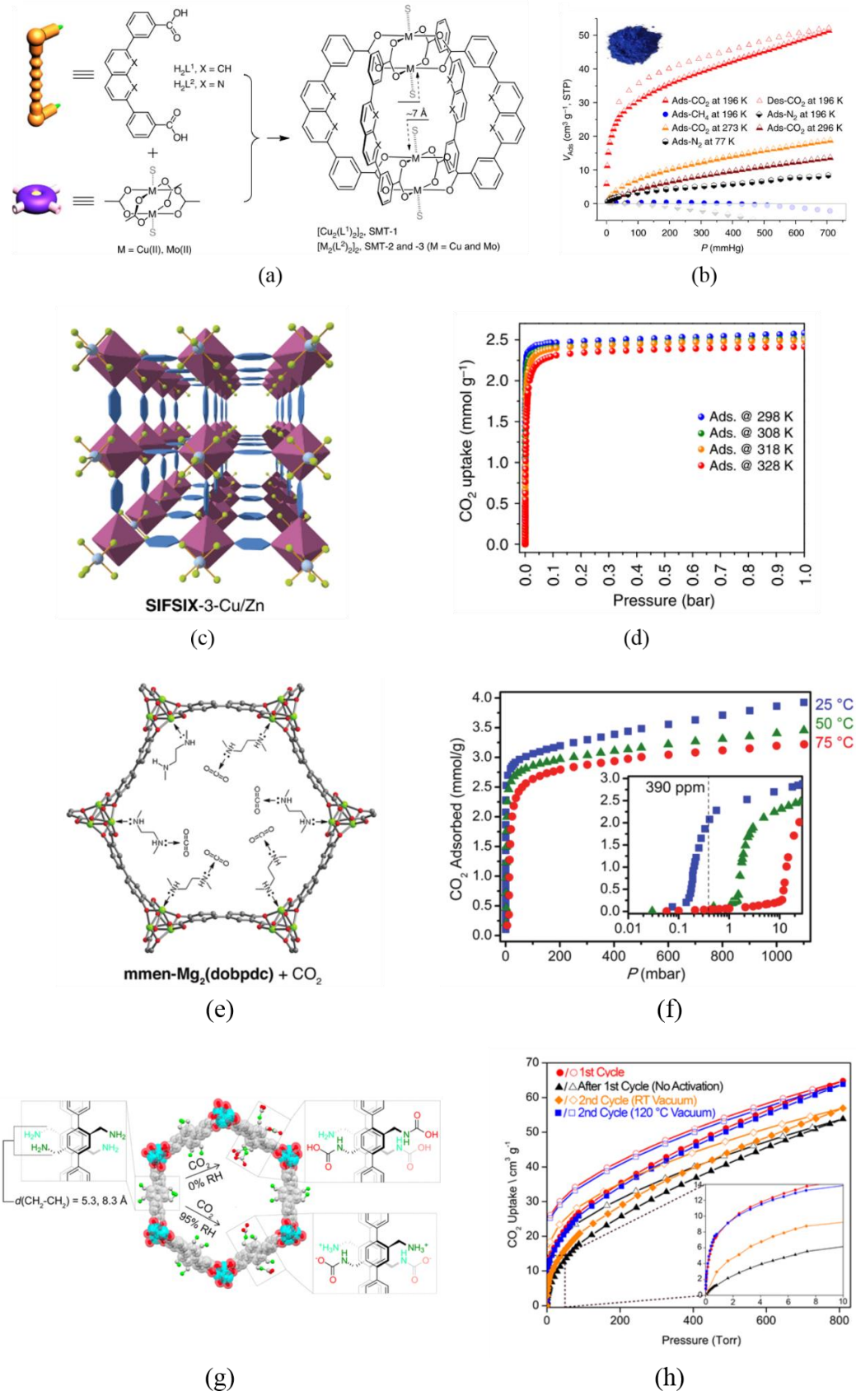

Fig. 1.3.3 – Structural models (a), (c), (e), (g) of PCN-88, SIFSIX-3-M, mmen-Mg_2(dobpdc), IRMOF-74-III-$(CH_2NH_2)_2$, and CO_2 isotherms (298 K unless specified) (b), (d), (f), (h), respectively. From Refs. 281, 287, 289, 290.

Table 1.3.5 – CO_2 uptake behaviour of benchmark MOFs and other materials. Storage capacity at 298 K and 1 bar unless specified.

Material	CO_2 uptake at 1 bar, 298 K (mmol/g)	Relevant features	Reference
Zeolite 13X	4.89 (2.41 at 0.1 bar)	Microporous	290
Activated carbon (Maxsorb)	(*ca.* 0.2 at 0.1 bar)	Microporous-mesoporous	291–293
TRI-PE-MCM-41	2.51	Amine-functionalised, mesoporous	294
MOF-5	1.5 (18.7 at 40 bar)	Microporous	295
MOF-177	1.81 (33.5 at 42 bar)	High pore volume	258
MIL-101(Cr)	2.33	High pore volume	188
PCN-88	4.2	SMTs	287
UTSA-16	4.2	H-bonds, small pores	288,296
Y-fcu-MOF-1	4.1	-F substituents, UMCs,	257
rht-MOF-7	3.8	Amine- and triazine-functionalised	297
Cu(Me-4py-trz-ia)	6.1	UMCs, small pores	298,299
ZnAtzOx	3.8 (293 K)	Amine functionalised, small pores	300,301
Mg-MOF-74	4.1	UMCs,	288,302
mmen-Mg_2(dobpdc)	3.86 (2.0 at 0.0039 bar)	Amine functionalised	289
SIFSIX-2-Cu-i	5.44	Interpenetration for small pores, pore F atoms	159
SIFSIX-3-Cu	2.58 (2.4 at 0.1 bar)	Small pores, pore F atoms	303
SIFSIX-3-Zn	2.73	Small pores, pore F atoms	159

1.3.4: Addressable MOFs

In 1998, Kondo and Kitagawa proposed the classification of porous coordination polymers into three generations.[304] First generation PCPs were classified as those unstable to the loss of inclusions (such as solvent molecules). Second generation PCPs were those that were stable to framework evacuation and could reversibly adsorb guests. The third generation consisted of frameworks that showed dynamic or stimulus responsive behaviour in addition to reversible adsorption of guests. This proved to be extraordinary foresight, early in the development of MOFs as a field of research. Indeed, the article in which this classification was published was aimed at the predictable synthesis of second-generation frameworks. Subsequently, while second generation frameworks now represent a substantial portion of the chemical literature, the potential of more dynamic MOFs, also known as ‘soft porous crystals’ has become clear.[163,305]

The description of ligands in MOFs as rigid became an accepted practice in order to ensure structural predictability and robustness, and because of the difficulty of crystallising MOFs with flexible ligands.[306] However, as MOF chemistry progressed, examples of dynamic behaviour and the use of flexible ligands became frequent.[307,308] Landmark research by Férey and contemporaries unearthed a category of MOFs in which unconventional isotherms were observed due to structural changes brought about by interactions between the adsorbate and the framework at certain threshold pressures. Subsequently, 'breathing', 'gating', 'buckling' and 'swelling' effects have been reported in several 3rd-generation MOFs.[309–313] Adsorbate-induced structural flexibility has been demonstrated even in ZIF-8, a MOF built with small, rigid, imidazolate linkers, under very high external pressure.[314,315]

Physical uptake of guests other than the adsorbate of interest is also known to trigger structural transitions in frameworks, by altering void shapes or relative orientations of interpenetrating nets.[316–320] Chemical reactions of frameworks with substrates, or the application of chemical stimuli such as reduction/oxidation or pH can also yield 3rd-generation behaviour, and these transitions may occur in a fashion that preserves single crystallinity (single crystal – single crystal transitions).[321–323] Stimuli in the form of temperature, electric field,[324] magnetic field,[325] and incident light can also be used to alter the structure and properties of specific MOFs.[326,327] Light, in particular, is an attractive stimulus by which structural transitions might be modulated in MOFs; it is ubiquitous in the form of solar radiation and its incidence upon a system can easily be controlled at low cost.[328] The absorption of incident light in MOFs, and the nature of the response to light can be chosen by selecting appropriate chromophoric components in a modular fashion. Light-harvesting, photoactive MOFs, built by the use of, photo-sensitizer ligands or metal centres, have been developed for applications such as sensing and catalysis.[329,330] Ligands that display photoresponsive behaviour when incorporated in MOFs are mainly based on azobenzene and dithienylethene moieties, which are well-known species used in molecular switches.[331–335] In addition, the photochemical [2+2] cycloaddition of proximate C=C moieties in the solid state has been extensively used to modify the dimensionality of coordination polymers addressably.[336]

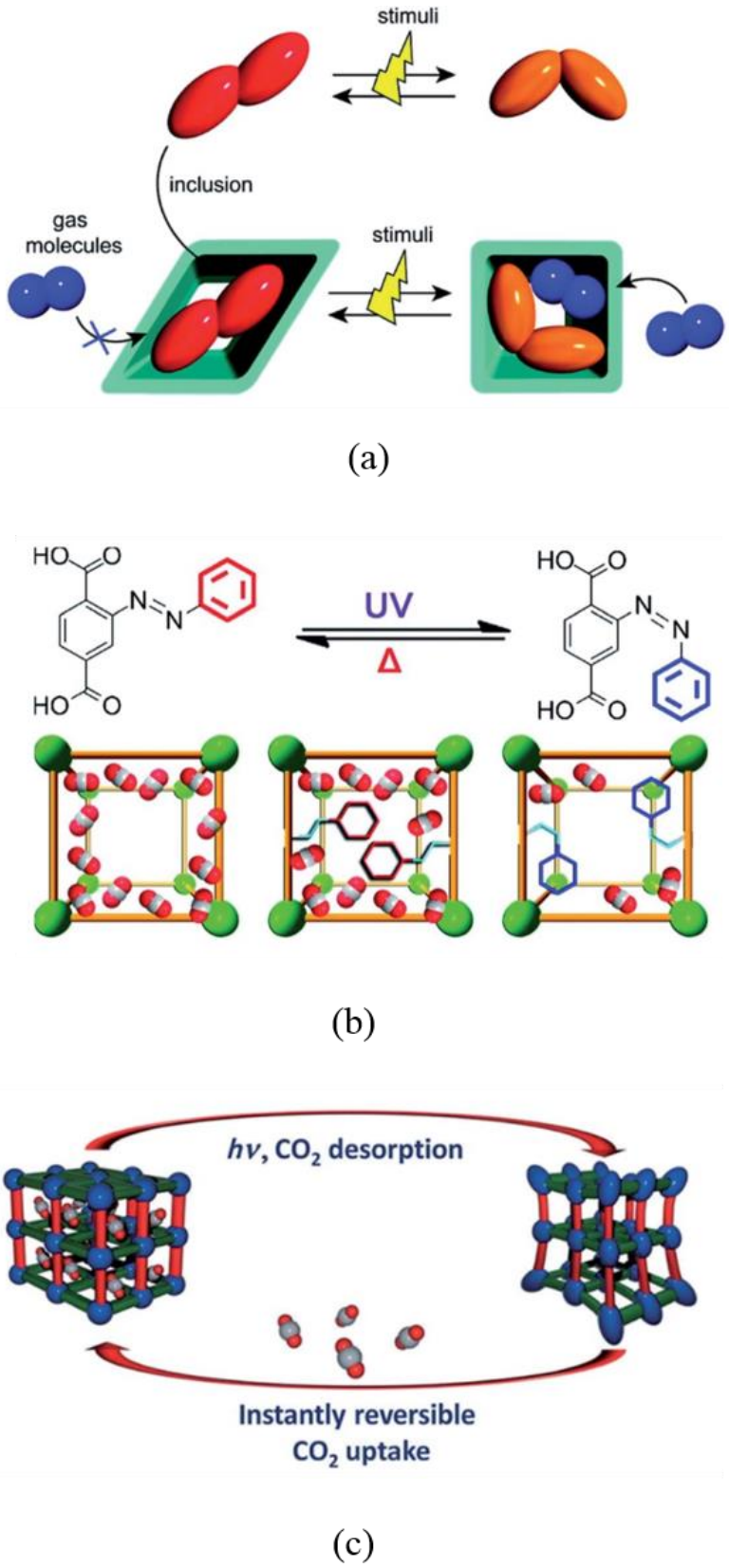

Fig. 1.3.4 – Graphical schematic representations of structural photoresponse for CO_2 uptake modulation in MOFs, by (a) guest incorporation (adapted from Ref. 337), (b) pendant group functionalisation (adapted from Ref. 338), (c) photoresponsive functionalisation of the MOF backbone (adapted from Ref. 339).

Structural photoresponse in MOFs is particularly applicable to CO_2 uptake modulation, since CO_2 sorption can take place at ordinary temperatures and pressures, and no additional apparatus is required. MOFs with light-induced changes in porosity are primarily of three types – those containing photosensitive guest molecules, nanoparticles or surface coatings,[337,340–342] those with photo-isomerisable pendant groups built into their ligands,[338,343–346] and those with photoresponsive groups built integrally into the ligand backbone of the MOF (Fig. 1.3.4).[339,347–349] With the exception of the third technique, these methods require partially restricting or blocking the MOF pores, resulting in reduced gas uptakes. Further, building these photo-responsive groups into the backbone of the framework allows real-time responses to light, allowing for high-speed release of the adsorbate gas, whereas with guests or pendant groups that isomerise in response to light, various factors such as steric and kinetic hindrance within each cavity lead to relatively slow responses. Suppressed bending or pedal-like motion of ligands have been shown to produce significant dynamic changes in uptake despite the modest magnitude of the induced structural change.[350]

1.3.5: Other Applications

In addition to the applications mentioned, MOFs are excellent candidates for other problems pertaining to chemicals in the gas phase, such as methane adsorption,[351–357] storage[358–360] and separation[361–366] of hydrocarbons, detection of specific gases and volatile organic compounds (VOCs),[367–370] and toxic gas removal and sequestration.[371–374]

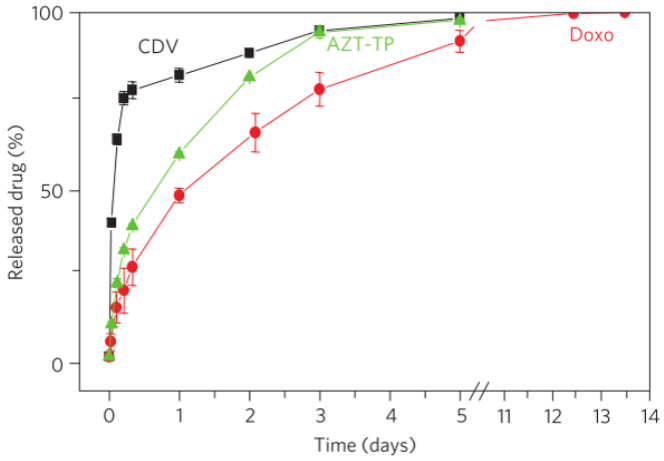

Fig. 1.3.5 –Release of standard drug molecules from MIL-100 nanoparticles in phosphate buffer solution, at 37°C. From Ref. 375.

The simplicity of MOF structures allows for function to be derived from various aspects of their form. The interpretation of MOF structures as a means by which to customisably

organise void space lends itself to MOFs being used as host matrices for intricate separations[376–378] and delicate chemical reactions.[379–381] Large molecules, including some natural products, have been immobilised in the crystalline phase within MOF pores in order to determine their structures using X-ray crystallography, as an alternative to growing pure single crystals.[380,382,383] This interpretation of MOF structures also forms the basis for their use in biomolecule protection[384,385], drug delivery[375,386–388], and other sustained-release applications (Fig. 1.3.5).[389,390]

Likewise, MOFs may be thought of as ordered arrays of accessible catalytically active metal centres or organic ligands. Their tunability in terms of composition and void dimensions allows their application to specific types of transformation, and allows them to operate in a size/shape selective or enantioselective manner.[391–394] MOFs are limited by their stability to harsh conditions, but in moderate conditions a number of instances of exceptional catalytic performance have been reported.[395] Various possibilities for customisation – such as post-synthetic modifiability,[396–399] incorporation of catalytically active guests,[169,400–403] using choromophoric ligands[404–407] or metalloligands,[408,409] or engineered defects[410,411] – provide a platform by which MOFs can be tailored to chemical demands for specific chemical reactions or synthesis of value-added compounds.[412] Similarly, using organic ligands to space paramagnetic metal centres is an approach that has had a strong impact in magnetic materials synthesis,[413] spin-crossover chemistry,[414,415] and quantum information storage materials.[416]

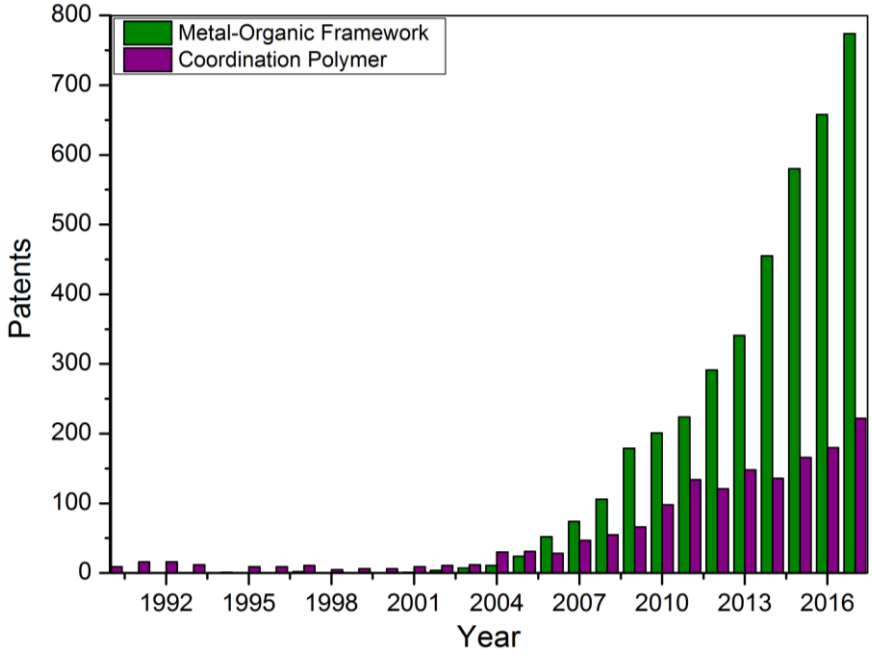

Fig. 1.3.6 – The number of unique patents appearing as Scopus search results, by year, for the search terms "coordination polymer", and "metal-organic framework" in the title, abstract, or keywords, from 1990 to 2017. Up to date as of June 2018.

A holistic approach to the MOF structure, utilising the tunability of void dimensions as well as the modular incorporation of luminescent SBUs or ligands, or specialised guests, yields selective and responsive porous materials in which luminescence may be modulated by the uptake of certain guests for applications in sensing devices.[106,417–420] A number of other applications for MOFs exist and more are likely to emerge in the coming years.[421–430] The scalability of MOF synthesis is an active area of research[431–433], and several MOF-based commercial products have become available in recent years for gas storage and other, more specialised, applications (Fig. 1.3.6).[434,435]

1.4: Objectives

The objective of the work described in this thesis has been to synthesise and characterise novel metal-organic framework and coordination polymer compounds, in order to analyse the effects of various kinds of structural flexibility and functional group incorporation on their topologies and porosities. The term 'flexibility' is used to describe conformational freedom in the ligands used - leading to structural diversity, as well as emergent dynamic behaviour in frameworks. Particular emphasis is given to the topological and supramolecular impact of this flexibility on the crystal structures of the resultant coordination polymers, and the implications for properties such as porosity and gas storage capacity. A number of metal-ligand combinations are studied.

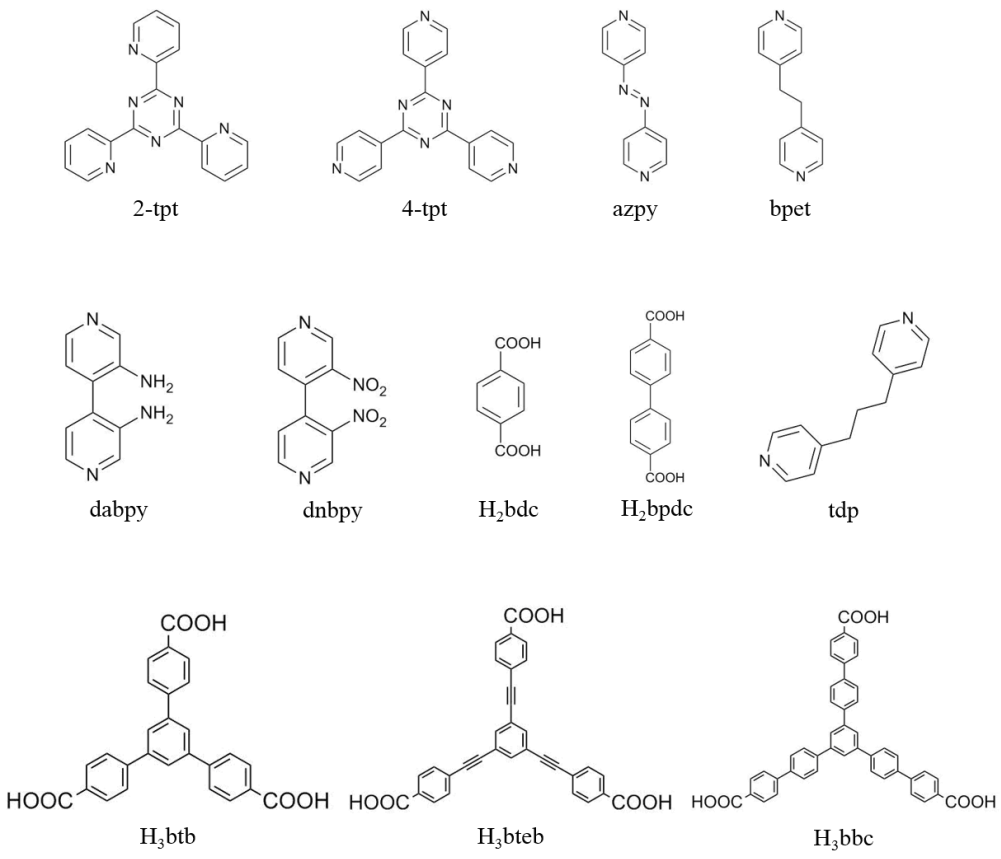

Fig. 1.4.1 – Carboxylate and pyridyl-based ligands used for coordination polymer formation in this study: 2-tpt - 2,4,6-tris(2-pyridyl)-1,3,5-triazine; 4-tpt - 2,4,6-tris(4-pyridyl)-1,3,5-triazine; azpy – 4,4'-azopyridine; bpet - 1,2-bis(4-pyridyl)ethane; dabpy - 3,3'-diamino-4,4'-bipyridine; dnbpy - 3,3'-dinitro-4,4'-bipyridine; H_2bdc - benzene-1,4-dicarboxylate; H_2bpdc - biphenyl-4,4'-dicarboxylate; tdp - trimethylenedipyridine/1,2-Bis(4-pyridyl)propane; H_3btb - 4,4',4''-benzene-1,3,5-triyl-tribenzoic acid; H_3bteb - 4,4',4''-(benzene-1,3,5-triyltris(ethyne-2,1-diyl)tribenzoate; H_3bbc - 4,4',4''-(benzene-1,3,5-triyl-tris(benzene-4,1-diyl))tribenzoate.

In the first part of the work, we set out to explore the supramolecular assemblies produced when M^{2+} ions are combined with a tritopic N-donor and a tricarboxylate ligand. Two synthetic strategies are applied. First, the 2-tpt ligand is used, in which a chelating binding mode is dominant. This mode hinders oxo-cluster formation, and forces the resultant coordination polymer to adopt similar low-dimensional structures with a variety of M^{2+} ions. We examine the effects of differing ionic radii on the overall supramolecular assembly. The second strategy is to use a tritopic N-donor ligand with no chelating modes available. With SBU formation now allowed, the adoption of a capping mode with pendant functional groups was envisioned.

The second part of the project focuses on another mixed ligand strategy - the use of ditopic N-donor ligands with various functionalities and degrees of flexibility in combination with short anionic linkers and M^{2+} centres. The synthetic objectives are twofold – pore dimensions on the order of the kinetic diameter of CO_2, in order to enable high enthalpies of adsorption and selectivity, and an exploration of the potential of conformationally flexible and photoswitchable ligands for the formation of 2D and 3D materials with attractive CO_2 sorption properties.

The installation of similar functional and addressable ditopic N-donor ligands as auxiliary building blocks into **pto** MOFs is then described. These MOFs have a porous 3-dimensional structure with unsaturated metal centres located favourably for the incorporation of ditopic neutral linkers of appropriate length. The generality of this principle is tested with linkers of varying lengths and different M^{2+} centres. In addition, the possibility of photoswitchable CO_2 adsorption is investigated.

As discussed in the introduction, extended ligands create possibilities for unusual ligand conformations and resultant MOFs with unusual topologies. Extensions such as ethynyl and *p*-phenylene moieties confer varying degrees of conformational flexibility upon ligands. Extended tritopic ligands containing these spacers are employed for the synthesis of MOFs with potential ‘non-default’ structures. Simulations are carried out in order to estimate the potential porosities of these materials. Auxiliary ligands may be incorporated where appropriate.

Finally, we aim to synthesise some MOFs using these extended tritopic ligands according to conventional design principles. An important advantage of using these ligands is the enhanced porosity of 'default' MOFs obtained. A number of SBUs are chosen based on potential applications and MOFs are synthesised. Their porosity and properties are then evaluated by a combination of experimental and computational techniques.

These experiments were intended to provide insight into the impact of flexibility on the design of MOFs and coordination polymers, and on their applications. The interplay of small conformational changes and the various interactions and bonds that compose the crystal structure of a coordination polymer is crucial to their rational design. Conformational possibilities available to ligands, as well as emergent flexibility within assembled MOFs, have important, often favourable, consequences in various contexts. Addressable changes and responses to stimuli are contingent upon the accommodation of dynamic behaviour in MOFs, and represent an important development within the field. Understanding these factors helps build a more comprehensive theory of synthetic MOF chemistry, and adds nuance to important discussions pertaining to design and applications.

1.5: References

1 A. Hantzsch and A. Werner, *Chem. Ber.*, 1890, **23**, 11–30.

2 A. Werner, *Zeitschrift für Anorg. Chemie*, 1893, **3**, 267–330.

3 G. B. Kauffman, *Coord. Chem. Rev.*, 1975, **15**, 1–92.

4 E. C. Constable and C. E. Housecroft, *Chem. Soc. Rev.*, 2013, **42**, 1429–1439.

5 M. Nic, L. Hovorka, J. Jirat, B. Kosata and J. Znamenacek, *IUPAC Compendium of Chemical Terminology-The Gold Book*, International Union of Pure and Applied Chemistry, 2005.

6 J. Berzelius, *Jahresberichte über die Fortschritte der Phys. der Wissenschaften*, 1833, **12**, 63–67.

7 W. B. Jensen, *J. Chem. Educ.*, 2008, **85**, 624–625.

8 H. Staudinger and J. Fritschi, *Helv. Chim. Acta*, 1922, **5**, 785–806.

9 Y. Shibata, *J. Coll. Sci. Imp. Univ. Tokyo*, 1916, **37**, 1–17.

10 A. Kraft, *Bull. Hist. Chem.*, 2008, **32**, 61–67.

11 J. F. Keggin and F. D. Miles, *Nature*, 1936, **137**, 577–578.

12 H. J. Buser, A. Ludi, D. Schwarzenbach and W. Petter, *Inorg. Chem.*, 1977, **16**, 2704–2710.

13 K. A. Hofmann and F. Küspert, *Zeitschrift für Anorg. Chemie*, 1897, **15**, 204–207.

14 J. H. Rayner and H. M. Powell, *J. Chem. Soc.*, 1952, 319–328.

15 S. Kanda and Y. Saito, *Bull. Chem. Soc. Jpn.*, 1956, **30**, 192–193.

16 Y. Kinoshita, I. Matsubara, T. Higuchi and Y. Saito, *Bull. Chem. Soc. Jpn.*, 1959, **32**, 1221–1226.

17 T. Iwamoto, T. Miyoshi, T. Miyamoto, Y. Sasaki and S. Fujiwara, *Bull. Chem. Soc. Jpn.*, 1967, **40**, 1174–1178.

18 G. F. Walker and D. G. Hawthorne, *Trans. Faraday Soc.*, 1967, **63**, 166–174.

19 H. M. Powell and J. H. Rayner, *Nature*, 1949, **163**, 566–567.

20 W. L. Jolly, *Preparative Inorganic Reactions*, Interscience Publishers, 1964, vol. 1.

21 G. B. Kauffman, G. S. Girolami and D. H. Busch, *Coord. Chem. Rev.*, 1993, **128**, 1–48.

22 C. E. Carraher, *J. Chem. Educ.*, 1981, **58**, 921–934.

23 Y. Mathey, C. Mazieres and R. Setton, *Inorg. Nucl. Chem. Lett.*, 1977, **13**, 1–3.

24 S. Nishikori, T. Iwamoto and Y. Yoshino, *Bull. Chem. Soc. Jpn.*, 1980, **53**, 2236–2240.

25 S. Nishikori and T. Iwamoto, *Chem. Lett.*, 1983, 1129–1130.

26 S. Nishikori and T. Iwamoto, *Chem. Lett.*, 1984, 319–322.

27 T. Iwamoto, *J. Mol. Struct.*, 1981, **75**, 51–65.

28 G. M. Sheldrick, *Acta Crystallogr. Sect. A*, 2008, **64**, 112–122.

29 F. H. Allen, *Acta Crystallogr. Sect. B*, 2002, **58**, 380–388.

30 G. M. J. Schmidt, *Pure Appl. Chem.*, 1971, **27**, 647–678.

31 A. I. Kitaigorodsky, *Chem. Soc. Rev.*, 1978, **7**, 133–163.

32 L. Leiserowitz, *Acta Crystallogr. Sect. B* , 1976, **32**, 775–802.

33 J. Maddox, *Nature*, 1988, **335**, 201.

34 J. -M Lehn, *Angew. Chem. Int. Ed. Engl.*, 1988, **27**, 89–112.

35 D. J. Cram, *Angew. Chem. Int. Ed. Engl.*, 1988, **27**, 1009–1120.

36 C. J. Pedersen, *Angew. Chem.*, 1988, **100**, 1053–1059.

37 R. M. Izatt, *Chem. Soc. Rev.*, 2007, **36**, 143–147.

38 G. R. Desiraju and G. W. Parshall, *Mater. Sci. Monogr.*, 1989, **54**, 85–113.

39 M. J. Zaworotko, *Nat. Chem.*, 2011, **3**, 653.

40 J. D. Dunitz, *Pure Appl. Chem.*, 1991, **63**, 177–185.

41 M. C. Etter, *Acc. Chem. Res.*, 1990, **23**, 120–126.

42 M. C. Etter, J. C. MacDonald and J. Bernstein, *Acta Crystallogr. Sect. B*, 1990, **46**, 256–262.

43 S. Subramanian and M. J. Zaworotko, *Coord. Chem. Rev.*, 1994, **137**, 357–401.

44 A. Gavezzotti and G. R. Desiraju, *Acta Crystallogr. Sect. B*, 1988, **44**, 427–434.

45 G. R. Desiraju and A. Gavezzotti, *Acta Crystallogr. Sect. B*, 1989, **45**, 473–482.

46 G. R. Desiraju and A. Gavezzotti, *J. Chem. Soc. Chem. Commun.*, 1989, 621–623.

47 D. Braga, F. Grepioni, P. Milne and E. Parisini, *J. Am. Chem. Soc.*, 1993, **115**, 5115–5122.

48 D. Braga, F. Grepioni, K. Biradha, V. R. Pedireddi and G. R. Desiraju, *J. Am. Chem. Soc.*, 1995, **117**, 3156–3166.

49 J. M. Lehn, *Polym. Int.*, 2002, **51**, 825–839.

50 O. Ermer, *J. Am. Chem. Soc.*, 1988, **110**, 3747–3754.

51 B. F. Hoskins and R. Robson, *J. Am. Chem. Soc.*, 1989, **111**, 5962–5964.

52 L. Öhrström, *Crystals*, 2015, **5**, 154–162.

53 A. F. Wells, *Three Dimensional Nets and Polyhedra*, Wiley, 1977.

54 A. F. Wells, *Further Studies of Three-Dimensional Nets*, American Crystallographic Association, 1979.

55 A. F. Wells, *Structural Inorganic Chemistry*, Oxford University Press, 2012.

56 W. H. Bragg and W. L. Bragg, *Proc. R. Soc. A*, 1913, 277–291.

57 L. Öhrström and K. Larsson, *Molecule-Based Materials: The Structural Network Approach*, Elsevier, 2005.

58 B. F. Hoskins, R. Robson and P. Smith, *J. Chem. Soc. Chem. Commun.*, 1990, 488–489.

59 R. W. Gable, B. F. Hoskins and R. Robson, *J. Chem. Soc. Chem. Commun.*, 1990, 762–763.

60 R. W. Gable, B. F. Hoskins and R. Robson, *J. Chem. Soc. Chem. Commun.*, 1990, 1677–1678.

61 B. F. Hoskins and R. Robson, *J. Am. Chem. Soc.*, 1990, **112**, 1546–1554.

62 B. F. Abrahams, B. F. Hoskins and R. Robson, *J. Chem. Soc. Chem. Commun.*, 1990, 60–61.

63 B. F. Abrahams, B. F. Hoskins and R. Robson, *J. Am. Chem. Soc.*, 1991, **113**, 3606–3607.

64 S. R. Batten, B. F. Hoskins and R. Robson, *J. Chem. Soc. Chem. Commun.*, 1991, 445–447.

65 B. F. Abrahams, M. J. Hardie, B. F. Hoskins, R. Robson and E. E. Sutherland, *J. Chem. Soc. Chem. Commun.*, 1994, **2**, 1049–1050.

66 R. Robson, B. F. Abrahams, S. R. Batten, R. W. Gable, B. F. Hoskins and J. Liu, in *Supramolecular Architecture*, ed. T. Bein, American Chemical Society, 1992, pp. 256–273.

67 B. F. Abrahams, B. F. Hoskins, D. M. Michail and R. Robson, *Nature*, 1994, **369**, 727–729.

68 M. Fujita, D. Oguro, M. Miyazawa, H. Oka, K. Yamaguchi and K. Ogura, *Nature*, 1995, **378**, 469–471.

69 S. Subramanian and M. J. Zaworotko, *Angew. Chem. Int. Ed. Engl.*, 1995, **34**, 2127–2129.

70 O. M. Yaghi, D. A. Richardson, G. Li, C. E. Davis and T. L. Groy, *MRS Online Proc. Libr. Arch.*

71 M. Kondo, T. Yoshitomi, H. Matsuzaka, S. Kitagawa and K. Seki, *Angew. Chem. Int. Ed. Engl.*, 1997, **36**, 1725–1727.

72 M. J. Zaworotko, *Chem. Soc. Rev.*, 1994, **23**, 283–288.

73 L. R. MacGillivray, S. Subramanian and M. J. Zaworotko, *J. Chem. Soc. Chem. Commun.*, 1994, 1325–1326.

74 L. Carlucci, G. Ciani, D. M. Proserpio and A. Sironi, *Angew. Chem. Int. Ed. Engl.*, 1995, **34**, 1895–1898.

75 L. Carlucci, G. Ciani, D. M. Proserpio and A. Sironi, *J. Am. Chem. Soc.*, 1995, **117**, 4562–4569.

76 O. M. Yaghi and H. Li, *J. Am. Chem. Soc.*, 1995, **117**, 10401–10402.

77 M. Fujita, S. Washizu, K. Ogura and Y. J. Kwon, *J. Am. Chem. Soc.*, 1994, **116**, 1151–1152.

78 G. B. Gardner, D. Venkataraman, J. S. Moore and S. Lee, *Nature*, 1995, **374**, 792–795.

79 D. Venkataraman, J. S. Moore, G. B. Gardner and S. Lee, *J. Am. Chem. Soc.*, 1995, **117**, 11600–11601.

80 O. M. Yaghi, G. Li and H. Li, *Nature*, 1995, **378**, 703–706.

81 H. Li, M. Eddaoudi, T. L. Groy and O. M. Yaghi, *J. Am. Chem. Soc.*, 1998, **120**, 8571–8572.

82 M. Kondo, T. Okubo, A. Asami, S. Noro, T. Yoshitomi, S. Kitagawa, T. Ishii, H. Matsuzaka and K. Seki, *Angew. Chem. Int. Ed.*, 1999, **38**, 140–143.

83 M. O'Keeffe, M. Eddaoudi, H. Li, T. Reineke and O. M. Yaghi, *J. Solid State Chem.*, 2000, **152**, 3–20.

84 G. Férey, *J. Solid State Chem.*, 2000, **152**, 37–48.

85 O. M. Yaghi, M. O'Keeffe, N. W. Ockwig, H. K. Chae, M. Eddaoudi and J. Kim, *Nature*, 2003, **423**, 705–714.

86 D. Alezi, I. Spanopoulos, C. Tsangarakis, A. Shkurenko, K. Adil, Y. Belmabkhout, M. O'Keeffe, M. Eddaoudi and P. N. Trikalitis, *J. Am. Chem. Soc.*, 2016, **138**, 12767–12770.

87 J. V. Smith, *Chem. Rev.*, 1988, **88**, 149–182.

88 D. W. Breck, *Zeolite Molecular Sieves: Structure, Chemistry and Use*, 1974.

89 M. O. Keeffe, M. A. Peskov, S. J. Ramsden and O. M. Yaghi, *Acc. Chem. Res.*, 2008, **41**, 1782–1789.

90 H. Li, M. Eddaoudi, M. O'Keeffe and O. M. Yaghi, *Nature*, 1999, **402**, 276–279.

91 M. Eddaoudi, J. Kim, N. Rosi, D. Vodak, J. Wachter, M. O. Keeffe and O. M. Yaghi, *Science*, 2002, **295**, 469–472.

92 H. Li, C. E. Davis, T. L. Groy, D. G. Kelley and O. M. Yaghi, *J. Am. Chem. Soc.*, 1998, **120**, 2186–2187.

93 S. S. Y. Chui, S. M. F. Lo, J. P. H. Charmant, a G. Orpen and I. D. Williams, *Science*, 1999, **283**, 1148–1150.

94 H. Furukawa, Y. B. Go, N. Ko, Y. K. Park, F. J. Uribe-Romo, J. Kim, M. O'Keeffe and O. M. Yaghi, *Inorg. Chem.*, 2011, **50**, 9147–9152.

95 I. Dance, *New J. Chem.*, 2003, **27**, 1–2.

96 B. S. Freiser, *Organometallic Ion Chemistry*, Springer Science & Business Media, 2012, vol. 15.

97 M. A. V Ribeiro da Silva, *New J. Chem.*, 1997, **21**, 671–680.

98 H. A. Skinner and J. A. Connor, *Pure Appl. Chem.*, 1985, **57**, 79–88.

99 G. Férey, *Chem. Soc. Rev.*, 2008, **37**, 191–214.

100 T. Ahnfeldt, N. Guillou, D. Gunzelmann, I. Margiolaki, T. Loiseau, G. Férey, J. Senker and N. Stock, *Angew. Chem. Int. Ed.*, 2009, **48**, 5163–5166.

101 P. Long, H. Wu, Q. Zhao, Y. Wang, J. Dong and J. Li, *Microporous Mesoporous Mater.*, 2011, **142**, 489–493.

102 E. R. Cooper, C. D. Andrews, P. S. Wheatley, P. B. Webb, P. Wormald and R. E. Morris, *Nature*, 2004, **430**, 1012–1016.

103 E. R. Parnham and R. E. Morris, *Acc. Chem. Res.*, 2007, **40**, 1005–1013.

104 L. Xu, E. Y. Choi and Y. U. Kwon, *Inorg. Chem.*, 2007, **46**, 10670–10680.

105 J. Zhang, S. Chen and X. Bu, *Angew. Chem. Int. Ed.*, 2008, **47**, 5434–5437.

106 S. Chen, J. Zhang and X. Bu, *Inorg. Chem.*, 2008, **47**, 5567–5569.

107 A. D. Burrows, K. Cassar, R. M. W. Friend, M. F. Mahon, S. P. Rigby and J. E. Warren, *CrystEngComm*, 2005, **7**, 548–550.

108 N. Zhu, G. Tobin and W. Schmitt, *Chem. Commun.*, 2012, **48**, 3638–3640.

109 E. Biemmi, T. Bein and N. Stock, *Solid State Sci.*, 2006, **8**, 363–370.

110 D. Feng, K. Wang, Z. Wei, Y. P. Chen, C. M. Simon, R. K. Arvapally, R. L. Martin, M. Bosch, T. F. Liu, S. Fordham, D. Yuan, M. A. Omary, M. Haranczyk, B. Smit and H. C. Zhou, *Nat. Commun.*, 2014, **5**, 5723.

111 J. T. Hughes and A. Navrotsky, *J. Am. Chem. Soc.*, 2011, **133**, 9184–9187.

112 M. K. Bhunia, J. T. Hughes, J. C. Fettinger and A. Navrotsky, *Langmuir*, 2013, **29**, 8140–8145.

113 D. Wu and A. Navrotsky, *J. Solid State Chem.*, 2015, **223**, 53–58.

114 N. Stock and S. Biswas, *Chem. Rev.*, 2012, **112**, 933–969.

115 K. Namratha and K. Byrappa, *Prog. Cryst. Growth Charact. Mater.*, 2012, **58**, 14–42.

116 K. Byrappa, in *Springer Handbook of Crystal Growth*, Springer, 2010, pp. 599–653.

117 A. Rabenau, *Angew. Chem. Int. Ed. Engl.*, 1985, **24**, 1026–1040.

118 C. Gerardin, M. In, L. Allouche, M. Haouas and F. Taulelle, *Chem. Mater.*, 1999, **11**, 1285–1292.

119 P. M. Forster, A. R. Burbank, C. Livage, G. Ferey and A. K. Cheetham, *Chem. Commun.*, 2004, **5**, 368–369.

120 P. M. Forster, N. Stock and A. K. Cheetham, *Angew. Chem. Int. Ed.*, 2005, **44**, 7608–7611.

121 C. Serre, F. Millange, S. Surblé and G. Férey, *Angew. Chem. Int. Ed.*, 2004, **43**, 6286–6289.

122 J. Klinowski, F. A. Almeida Paz, P. Silva and J. Rocha, *Dalton Trans.*, 2011, **40**, 321–330.

123 M. Schlesinger, S. Schulze, M. Hietschold and M. Mehring, *Microporous Mesoporous Mater.*, 2010, **132**, 121–127.

124 K. Užarević, T. C. Wang, S. Y. Moon, A. M. Fidelli, J. T. Hupp, O. K. Farha and T. Friščić, *Chem. Commun.*, 2016, **52**, 2133–2136.

125 A. Pichon, A. Lazuen-Garay and S. L. James, *CrystEngComm*, 2006, **8**, 211–214.

126 S. L. James, C. J. Adams, C. Bolm, D. Braga, P. Collier, T. Friscić, F. Grepioni, K. D. M. Harris, G. Hyett, W. Jones, A. Krebs, J. Mack, L. Maini, A. G. Orpen, I. P. Parkin, W. C. Shearouse, J. W. Steed and D. C. Waddell, *Chem. Soc. Rev.*, 2012, **41**, 413–447.

127 Z. Q. Li, L. G. Qiu, T. Xu, Y. Wu, W. Wang, Z. Y. Wu and X. Jiang, *Mater. Lett.*, 2009, **63**, 78–80.

128 E. Biemmi, S. Christian, N. Stock and T. Bein, *Microporous Mesoporous Mater.*, 2009, **117**, 111–117.

129 N. L. Rosi, J. Kim, M. Eddaoudi, B. Chen, M. O'Keeffe and O. M. Yaghi, *J. Am. Chem. Soc.*, 2005, **127**, 1504–1518.

130 C. McKinstry, E. J. Cussen, A. J. Fletcher, S. V. Patwardhan and J. Sefcik, *Cryst. Growth Des.*, 2013, **13**, 5481–5486.

131 D. Frahm, F. Hoffmann and M. Fröba, *Cryst. Growth Des.*, 2014, **14**, 1719–1725.

132 A. Dikhtiarenko, P. Serra-Crespo, S. Castellanos, A. Pustovarenko, R. Mendoza-Merono, S. García-Granda and J. Gascon, *Cryst. Growth Des.*, 2016, **16**, 5636–5645.

133 Y. Takashima, S. Furukawa and S. Kitagawa, *CrystEngComm*, 2011, **13**, 3360–3363.

134 F. Carson, J. Su, A. E. Platero-Prats, W. Wan, Y. Yun, L. Samain and X. Zou, *Cryst. Growth Des.*, 2013, **13**, 5036–5044.

135 P. Jensen, S. R. Batten, G. D. Fallon, D. C. R. Hockless, B. Moubaraki, K. S. Murray and R. Robson, *J. Solid State Chem.*, 1999, **145**, 387–393.

136 B. K. Saha, R. K. R. Jetti, L. S. Reddy, S. Aitipamula and A. Nangia, *Cryst. Growth Des.*, 2005, **5**, 887–899.

137 R. Ding, C. Huang, J. Lu, J. Wang, C. Song, J. Wu, H. Hou and Y. Fan, *Inorg. Chem.*, 2015, **54**, 1405–1413.

138 B. Liu, L. Y. Pang, L. Hou, Y. Y. Wang, Y. Zhang and Q. Z. Shi, *CrystEngComm*, 2012, **14**, 6246–6251.

139 L. R. MacGillivray, J. L. Reid and J. A. Ripmeester, *Chem. Commun.*, 2001, 1034–1035.

140 N. W. Ockwig, O. Delgado-Friedrichs, M. O'Keeffe and O. M. Yaghi, *Acc. Chem. Res.*, 2005, **38**, 176–182.

141 H. Chae, J. Kim and Y. Go, *Nature*, 2004, **427**, 523–527.

142 J. K. Schnobrich, O. Lebel, K. A. Cychosz, A. Dailly, A. G. Wong-Foy and A. J. Matzger, *J. Am. Chem. Soc.*, 2010, **132**, 13941–13948.

143 D. Frahm, F. Hoffmann and M. Fröba, *CrystEngComm*, 2013, **15**, 9429–9436.

144 Y. B. Zhang, H. Furukawa, N. Ko, W. Nie, H. J. Park, S. Okajima, K. E. Cordova, H. Deng, J. Kim and O. M. Yaghi, *J. Am. Chem. Soc.*, 2015, **137**, 2641–2650.

145 S. R. Batten and R. Robson, *Angew. Chem. Int. Ed.*, 1998, **37**, 1460–1494.

146 H. Wu, J. Yang, Z. M. Su, S. R. Batten and J. F. Ma, *J. Am. Chem. Soc.*, 2011, **133**, 11406–11409.

147 X. H. Bu, M. L. Tong, H. C. Chang, S. Kitagawa and S. R. Batten, *Angew. Chem. Int. Ed.*, 2003, **43**, 192–195.

148 J. Yang, J. F. Ma, S. R. Batten and Z. M. Su, *Chem. Commun.*, 2008, 2233–2235.

149 M. Du, X. H. Bu, Y. M. Guo, H. Liu, S. R. Batten, J. Ribas and T. C. W. Mak, *Inorg. Chem.*, 2002,

41, 4904–4908.

150 H. L. Jiang, T. A. Makal and H. C. Zhou, *Coord. Chem. Rev.*, 2013, **257**, 2232–2249.

151 Y. P. He, Y. X. Tan and J. Zhang, *CrystEngComm*, 2012, **14**, 6359–6361.

152 Y. N. Gong, D. C. Zhong and T. B. Lu, *CrystEngComm*, 2016, **18**, 2596–2606.

153 M. Eddaoudi, D. B. Moler, H. Li, B. Chen, T. M. Reineke, M. O'Keeffe and O. M. Yaghi, *Acc. Chem. Res.*, 2001, **34**, 319–330.

154 S. R. Batten, *CrystEngComm*, 2001, **18**, 91–130.

155 T. Gadzikwa, B. S. Zeng, J. T. Hupp and S. T. Nguyen, *Chem. Commun.*, 2008, 3672–3674.

156 A. J. Blake, N. R. Champness, S. S. M. Chung, W. Li and M. Schröder, *Chem. Commun.*, 1997, 1005–1006.

157 R. Mondal, M. K. Bhunia and K. Dhara, *CrystEngComm*, 2008, **10**, 1167–1174.

158 R. K. Deshpande, G. I. N. Waterhouse, G. B. Jameson and S. G. Telfer, *Chem. Commun.*, 2012, **48**, 1574–1576.

159 P. Nugent, Y. Belmabkhout, S. D. Burd, A. J. Cairns, R. Luebke, K. Forrest, T. Pham, S. Ma, B. Space, L. Wojtas, M. Eddaoudi and M. J. Zaworotko, *Nature*, 2013, **495**, 80–84.

160 N. Zhu, M. J. Lennox, T. Düren and W. Schmitt, *Chem. Commun.*, 2014, **50**, 4207–4210.

161 M. Jansen and J. C. Schön, *Angew. Chem. Int. Ed.*, 2006, **45**, 3406–3412.

162 A. U. Czaja, N. Trukhan and U. Müller, *Chem. Soc. Rev.*, 2009, **38**, 1284–1293.

163 S. Kitagawa, *Acc. Chem. Res.*, 2017, **50**, 514–516.

164 S. Kitagawa, *Angew. Chem. Int. Ed.*, 2015, **54**, 10686–10687.

165 A. Schoedel, Z. Ji and O. M. Yaghi, *Nat. Energy*, 2016, **1**, 16034.

166 A. G. Slater and A. I. Cooper, *Science*, 2015, **348**, aaa8075.

167 J. E. Mondloch, M. J. Katz, N. Planas, D. Semrouni, L. Gagliardi, J. T. Hupp and O. K. Farha, *Chem. Commun.*, 2014, **50**, 8944–8946.

168 K. S. Park, Z. Ni, A. P. Cote, J. Y. Choi, R. Huang, F. J. Uribe-Romo, H. K. Chae, M. O. Keeffe and O. M. Yaghi, *Proc. Natl. Acad. Sci.*, 2006, **103**, 10186–10191.

169 G. Ferey, C. Mellot-Draznieks, C. Serre, F. Millange, J. Dutour, S. Surble and I. Margiolaki, *Science*, 2005, **309**, 2040–2042.

170 J. H. Cavka, S. Jakobsen, U. Olsbye, N. Guillou, C. Lamberti, S. Bordiga and K. P. Lillerud, *J. Am. Chem. Soc.*, 2008, **6**, 13850–13851.

171 A. J. Howarth, A. W. Peters, N. A. Vermeulen, T. C. Wang, J. T. Hupp and O. K. Farha, *Chem. Mater.*, 2017, **29**, 26–39.

172 J. Park, J. D. Howe and D. S. Sholl, *Chem. Mater.*, 2017, **29**, 10487–10495.

173 J. Ma, A. P. Kalenak, A. G. Wong-Foy and A. J. Matzger, *Angew. Chem. Int. Ed.*, 2017, **56**, 14618–14621.

174 H. Kahl, T. Wadewitz and J. Winkelmann, *J. Chem. Eng. Data*, 2003, **48**, 1500–1507.

175 C. M. Kinart, W. J. Kinart and A. Bald, *Phys. Chem. Liq. An Int. J.*, 1999, **37**, 317–321.

176 J. Aracil, G. Luengo, B. S. Almeida, M. M. Telo, R. G. Rubio and M. D. Peña, *J. Phys. Chem.*, 1989, **93**, 3210–3218.

177 C. Wohlfarth and B. Wohlfarth, in *Surface Tension of Pure Liquids and Binary Liquid Mixtures*, Springer, 1997, pp. 1–435.

178 E. L. Quinn, *J. Am. Chem. Soc.*, 1927, **49**, 2704–2711.

179 L. J. Barbour, *Chem. Commun.*, 2006, 1163–1168.

180 K. S. Walton and R. Q. Snurr, *J. Am. Chem. Soc.*, 2007, **129**, 8552–8556.

181 L. Sarkisov, *Adv. Mater.*, 2012, **24**, 3130–3133.

182 M. Thommes, K. Kaneko, A. V. Neimark, J. P. Olivier, F. Rodriguez-Reinoso, J. Rouquerol and K. S. W. Sing, *Pure Appl. Chem.*, 2015, **87**, 1051–1069.

183 K. A. Cychosz and M. Thommes, *Engineering*, 2018, **4**, 559–566.

184 P. I. Ravikovitch, G. L. Haller and A. V. Neimark, *Adv. Colloid Interface Sci.*, 1998, **76**, 203–226.

185 H. Furukawa, N. Ko, Y. B. Go, N. Aratani, S. B. Choi, J. Kim and O. M. Yaghi, *Science*, 2010, **329**, 424–429.

186 S. S. Kaye, A. Dailly, O. M. Yaghi and J. R. Long, *J. Am. Chem. Soc.*, 2007, **129**, 14176–14177.

187 Y. Yan, X. Lin, S. Yang, A. J. Blake, A. Dailly, N. R. Champness and M. Schröder, *Chem. Commun.*, 2009, 1025–1027.

188 P. L. Llewellyn, S. Bourrelly, C. Serre, A. Vimont, M. Daturi, L. Hamon, G. De Weireld, J. Chang, D. Hong, Y. K. Hwang and S. H. Jhung, 2008, 7245–7250.

189 J. An, O. K. Farha, J. T. Hupp, E. Pohl, J. I. Yeh and N. L. Rosi, *Nat. Commun.*, 2012, **3**, 604–606.

190 Y. Li and R. T. Yang, *Langmuir*, 2007, **23**, 12937–12944.

191 Y. Yan, S. Yang, A. J. Blake, W. Lewis, E. Poirier, S. A. Barnett, N. R. Champness and M. Schröder, *Chem. Commun.*, 2011, **47**, 9995–9997.

192 K. Koh, A. G. Wong-Foy and A. J. Matzger, *J. Am. Chem. Soc.*, 2009, **131**, 4184–4185.

193 O. K. Farha, A. O. Yazaydın, I. Eryazici, C. D. Malliakas, B. G. Hauser, M. G. Kanatzidis, S. T. Nguyen, R. Q. Snurr and J. T. Hupp, *Nat. Chem.*, 2010, **2**, 944–948.

194 U. Stoeck, I. Senkovska, V. Bon, S. Krause and S. Kaskel, *Chem. Commun.*, 2015, **51**, 1046–1049.

195 R. Grunker, V. Bon, P. Muller, U. Stoeck, S. Krause, U. Mueller, I. Senkovska and S. Kaskel, *Chem. Commun.*, 2014, **50**, 3450–3452.

196 O. K. Farha, I. Eryazici, N. C. Jeong, B. G. Hauser, C. E. Wilmer, A. A. Sarjeant, R. Q. Snurr, S. T. Nguyen, A. Ö. Yazaydin and J. T. Hupp, *J. Am. Chem. Soc.*, 2012, **134**, 15016–15021.

197 I. Hönicke, I. Senkovska, V. Bon, I. Baburin, N. Boenisch, S. Raschke and J. D. Evans, *Angew. Chem. Int. Ed.*, 2018, **57**, 13780–13783.

198 J. K. Schnobrich, K. Koh, K. N. Sura and A. J. Matzger, *Langmuir*, 2010, **26**, 5808–5814.

199 L. Schlapbach and A. Züttel, *Nature*, 2001, **414**, 353–358.

200 S. Sharma and S. K. Ghoshal, *Renew. Sustain. Energy Rev.*, 2015, **43**, 1151–1158.

201 L. Schlapbach, *Nature*, 2009, **460**, 809–811.

202 A. C. Dillon, K. M. Jones, T. A. Bekkedahl, C. H. Kiang, D. S. Bethune and M. J. Heben, *Nature*, 1997, 386, 377–379.

203 A. Züttel, P. Wenger, S. Rentsch, P. Sudan, P. Mauron and C. Emmenegger, *J. Power Sources*, 2003, **118**, 1–7.

204 A. Zaluska, L. Zaluski and J. O. Ström-Olsen, *J. Alloys Compd.*, 2000, **307**, 157–166.

205 M. G. Nijkamp, J. E. M. J. Raaymakers, A. J. van Dillen and K. P. de Jong, *Appl. Phys. A*, 2001, **72**, 619–623.

206 E. Garrone, B. Bonelli and C. Otero Areán, *Chem. Phys. Lett.*, 2008, **456**, 68–70.

207 L. J. Murray, M. Dinc and J. R. Long, *Chem. Soc. Rev.*, 2009, **38**, 1294–1314.

208 Q. Wang and J. K. Johnson, *J. Chem. Phys.*, 1999, **110**, 577–586.

209 S. Ma, D. Sun, M. Ambrogio, J. A. Fillinger, S. Parkin and H. C. Zhou, *J. Am. Chem. Soc.*, 2007, **129**, 1858–1859.

210 X. S. Wang, S. Ma, P. M. Forster, D. Yuan, J. Eckert, J. J. López, B. J. Murphy, J. B. Parise and H. C. Zhou, *Angew. Chem. Int. Ed.*, 2008, **47**, 7263–7266.

211 H. Furukawa, M. A. Miller and O. M. Yaghi, *J. Mater. Chem.*, 2007, **17**, 3197–3204.

212 A. G. Wong-Foy, A. J. Matzger and O. M. Yaghi, *J. Am. Chem. Soc.*, 2006, **128**, 3494–3495.

213 D. Yuan, D. Zhao, D. Sun and H. C. Zhou, *Angew. Chem. Int. Ed.*, 2010, **49**, 5357–5361.

214 A. Zaluska, L. Zaluski and J. O. Ström-Olsen, *Appl. Phys. A*, 2001, **72**, 157–165.

215 H. I. Schlesinger and H. C. Brown, *J. Am. Chem. Soc.*, 1940, **62**, 3429–3435.

216 K. Miwa, N. Ohba, S. I. Towata, Y. Nakamori and S. I. Orimo, *Phys. Rev. B*, 2004, **69**, 1–8.

217 R. Povel, K. Feucht, W. Gelse and G. Withalm, *Interdiscip. Sci. Rev.*, 1989, **14**, 365–373.

218 C. D. Keeling, S. C. Piper, R. B. Bacastow, M. Wahlen, T. P. Whorf, M. Heimann and H. A. Meijer, in *A History of Atmospheric CO_2 and its Effects on Plants, Animals, and Ecosystems*, Springer, 2005, pp. 83–113.

219 D. Lüthi, M. Le Floch, B. Bereiter, T. Blunier, J. M. Barnola, U. Siegenthaler, D. Raynaud, J. Jouzel, H. Fischer, K. Kawamura and T. F. Stocker, *Nature*, 2008, **453**, 379–382.

220 P. Falkowski, *Science*, 2000, **290**, 291–296.

221 T. R. Karl and K. E. Trenberth, *Science*, 2003, **302**, 1719–1723.

222 J. Fourier, in *Annales de Chemie et de Physique*, 1824, vol. 27, pp. 136–167.

223 S. Arrhenius, *Philos. Mag. Ser. 5*, 1896, **41**, 237–276.

224 *America's Climate Choices*, National Research Council, National Academies Press, 2011.

225 P. D. Jones, T. M. L. Wigley and P. B. Wright, *Nature*, 1986, **322**, 430–434.

226 D. Barriopedro, E. M. Fischer, J. Luterbacher, R. M. Trigo and R. García-Herrera, *Science*, 2011, **332**, 220–224.

227 P. A. Stott, D. A. Stone and M. R. Allen, *Nature*, 2004, **432**, 610–614.

228 A. Jentsch, J. Kreyling and C. Beierkuhnlein, *Front. Ecol. Environ.*, 2007, **5**, 365–374.

229 B. G. Meerburg, A. Verhagen, R. E. E. Jongschaap, A. C. Franke, B. F. Schaap, T. A. Dueck and A. van der Werf, *Proc. Natl. Acad. Sci.*, 2009, **106**, 15594–15598.

230 C. J. Vörösmarty, P. B. McIntyre, M. O. Gessner, D. Dudgeon, A. Prusevich, P. Green, S. Glidden, S. E. Bunn, C. A. Sullivan, C. R. Liermann and P. M. Davies, *Nature*, 2010, **467**, 555–561.

231 G.-R. Walther, E. Post, P. Convey, A. Menzel, C. Parmesan, T. J. C. Beebee, J.-M. Fromentin, O. Hoegh-Guldberg and F. Bairlein, *Nature*, 2002, **416**, 389–395.

232 R. Reuveny, *Polit. Geogr.*, 2007, **26**, 656–673.

233 A. Goeppert, M. Czaun, G. K. Surya Prakash and G. A. Olah, *Energy Environ. Sci.*, 2012, **5**, 7833–7853.

234 S. Shafiee and E. Topal, *Energy Policy*, 2009, **37**, 181–189.

235 N. Bauer, J. Hilaire, R. J. Brecha, J. Edmonds, K. Jiang, E. Kriegler, H. H. Rogner and F. Sferra, *Energy*, 2016, **111**, 580–592.

236 G. A. Olah, A. Goeppert and G. K. S. Prakash, *J. Org. Chem.*, 2009, **74**, 487–498.

237 G. A. Olah, A. Goeppert and G. K. S. Prakash, *Angew. Chem. Int. Ed.*, 2005, **44**, 2636–2639.

238 A. J. Weaver, *Science*, 2011, **332**, 795–796.

239 C. H. Chiang, M. K. Nazeeruddin, M. Grätzel and C. G. Wu, *Energy Environ. Sci.*, 2017, **10**, 808–817.

240 J. P. W. Scharlemann and W. F. Laurance, *Science*, 2008, **319**, 43–45.

241 T. Searchinger, R. Heimlich, R. A. Houghton, F. Dong, A. Elobeid, J. Fabiosa, S. Tokgoz, D. Hayes and T. Yu, *Science*, 2008, **319**, 1238–1241.

242 J. C. M. Pires, F. G. Martins, M. C. M. Alvim-Ferraz and M. Simões, *Chem. Eng. Res. Des.*, 2011, **89**, 1446–1460.

243 A. L. Kohl and R. Nielsen, *Gas Purification*, Elsevier, 1997.

244 K. Y. A. Lin and A. H. A. Park, *Environ. Sci. Technol.*, 2011, **45**, 6633–6639.

245 F. Zeman, *Environ. Sci. Technol.*, 2007, **41**, 7558–7563.

246 R. V. Siriwardane, M.-S. Shen, E. P. Fisher and J. A. Poston, *Energy & Fuels*, 2001, **15**, 279–284.

247 Y. Belmabkhout, R. Serna-Guerrero and A. Sayari, *Ind. Eng. Chem. Res.*, 2010, **49**, 359–365.

248 A. F. Ismail, K. C. Khulbe and T. Matsuura, *Gas separation membranes*, Springer, 2015, vol. 7.

249 A. D. Buckingham and R. L. Disch, *Proc. R. Soc. A*, 1962, **273**, 275–289.

250 L.-C. Lin, J. Kim, X. Kong, E. Scott, T. M. McDonald, J. R. Long, J. A. Reimer and B. Smit, *Angew. Chem. Int. Ed.*, 2013, **52**, 4410–4413.

251 X. Kong, E. Scott, W. Ding, J. A. Mason, J. R. Long and J. A. Reimer, *J. Am. Chem. Soc.*, 2012, **134**, 14341–14344.

252 Z. R. Herm, R. Krishna and J. R. Long, *Microporous Mesoporous Mater.*, 2012, **151**, 481–487.

253 J. A. Mason, K. Sumida, Z. R. Herm, R. Krishna and J. R. Long, *Energy Environ. Sci.*, 2011, **4**, 3030–3040.

254 K. Sumida, S. Horike, S. S. Kaye, Z. R. Herm, W. L. Queen, C. M. Brown, F. Grandjean, G. J. Long, A. Dailly and J. R. Long, *Chem. Sci.*, 2010, **1**, 184–191.

255 D. Britt, H. Furukawa, B. Wang, T. G. Glover and O. M. Yaghi, *Proc. Natl. Acad. Sci.*, 2009, **106**, 20637–20640.

256 E. Soubeyrand-Lenoir, C. Vagner, J. W. Yoon, P. Bazin, F. Ragon, Y. K. Hwang, C. Serre, J. S. Chang and P. L. Llewellyn, *J. Am. Chem. Soc.*, 2012, **134**, 10174–10181.

257 D. X. Xue, A. J. Cairns, Y. Belmabkhout, L. Wojtas, Y. Liu, M. H. Alkordi and M. Eddaoudi, *J. Am. Chem. Soc.*, 2013, **135**, 7660–7667.

258 A. R. Millward and O. M. Yaghi, *J. Am. Chem. Soc.*, 2005, **127**, 17998–17999.

259 R. Banerjee, A. Phan, B. Wang, C. Knobler, H. Furukawa, M. O'Keeffe and O. M. Yaghi, *Science*,

2008, **319**, 939–943.

260 B. Wang, A. P. Côté, H. Furukawa, M. O'Keeffe and O. M. Yaghi, *Nature*, 2008, **453**, 207–211.

261 Y. S. Bae, B. G. Hauser, O. K. Farha, J. T. Hupp and R. Q. Snurr, *Microporous Mesoporous Mater.*, 2011, **141**, 231–235.

262 A. D. Wiersum, J. S. Chang, C. Serre and P. L. Llewellyn, *Langmuir*, 2013, **29**, 3301–3309.

263 P. L. Llewellyn, S. Bourrelly, C. Vagner, N. Heymans, H. Leclerc, A. Ghoufi, P. Bazin, A. Vimont, M. Daturi, T. Devic, C. Serre, G. De Weireld and G. Maurin, *J. Phys. Chem. C*, 2013, **117**, 962–970.

264 P. Nugent, V. Rhodus, T. Pham, B. Tudor, K. Forrest, L. Wojtas, B. Space and M. Zaworotko, *Chem. Commun.*, 2013, **49**, 1606–1608.

265 N. A. Ramsahye, G. Maurin, S. Bourrelly, P. L. Llewellyn, C. Serre, T. Loiseau, T. Devic and G. Férey, *J. Phys. Chem. C*, 2008, **112**, 514–520.

266 W. Yang, A. J. Davies, X. Lin, M. Suyetin, R. Matsuda, A. J. Blake, C. Wilson, W. Lewis, J. E. Parker, C. C. Tang, M. W. George, P. Hubberstey, S. Kitagawa, H. Sakamoto, E. Bichoutskaia, N. R. Champness, S. Yang and M. Schröder, *Chem. Sci.*, 2012, **3**, 2993–2999.

267 S. D. Burd, S. Ma, J. A. Perman, B. J. Sikora, R. Q. Snurr, P. K. Thallapally, J. Tian, L. Wojtas and M. J. Zaworotko, *J. Am. Chem. Soc.*, 2012, **134**, 3663–3666.

268 A. D. Wiersum, E. Soubeyrand-Lenoir, Q. Yang, B. Moulin, V. Guillerm, M. Ben Yahia, S. Bourrelly, A. Vimont, S. Miller, C. Vagner, M. Daturi, G. Clet, C. Serre, G. Maurin and P. L. Llewellyn, *Chem. Asian J.*, 2011, **6**, 3270–3280.

269 M. H. Mohamed, S. K. Elsaidi, L. Wojtas, T. Pham, K. A. Forrest, B. Tudor, B. Space and M. J. Zaworotko, *J. Am. Chem. Soc.*, 2012, **134**, 19556–19559.

270 G. D. Pirngruber, L. Hamon, S. Bourrelly, P. L. Llewellyn, E. Lenoir, V. Guillerm, C. Serre and T. Devic, *ChemSusChem*, 2012, **5**, 762–776.

271 S. I. Noro, Y. Hijikata, M. Inukai, T. Fukushima, S. Horike, M. Higuchi, S. Kitagawa, T. Akutagawa and T. Nakamura, *Inorg. Chem.*, 2013, **52**, 280–285.

272 Q. Yang, V. Guillerm, F. Ragon, A. D. Wiersum, P. L. Llewellyn, C. Zhong, T. Devic, C. Serre and G. Maurin, *Chem. Commun.*, 2012, **48**, 9831–9833.

273 B. Kesanli, Y. Cui, M. R. Smith, E. W. Bittner, B. C. Bockrath and W. Lin, *Angew. Chem. Int. Ed.*, 2005, **44**, 72–75.

274 J. L. C. Rowsell and O. M. Yaghi, *J. Am. Chem. Soc.*, 2006, **128**, 1304–1315.

275 T. Devic, F. Salles, S. Bourrelly, B. Moulin, G. Maurin, P. Horcajada, C. Serre, A. Vimont, J. C. Lavalley, H. Leclerc, G. Clet, M. Daturi, P. L. Llewellyn, Y. Filinchuk and G. Férey, *J. Mater. Chem.*, 2012, **22**, 10266–10273.

276 B. Zheng, J. Bai, J. Duan, L. Wojtas and M. J. Zaworotko, *J. Am. Chem. Soc.*, 2011, **133**, 748–751.

277 P. Cui, Y. G. Ma, H. H. Li, B. Zhao, J. R. Li, P. Cheng, P. B. Balbuena and H. C. Zhou, *J. Am. Chem. Soc.*, 2012, **134**, 18892–18895.

278 V. Benoit, R. S. Pillai, A. Orsi, P. Normand, H. Jobic, F. Nouar, P. Billemont, E. Bloch, S. Bourrelly, T. Devic, P. A. Wright, G. De Weireld, C. Serre, G. Maurin and P. L. Llewellyn, *J.*

Mater. Chem. A, 2016, **4**, 1383–1389.

279 Q. Yang, S. Vaesen, F. Ragon, A. D. Wiersum, D. Wu, A. Lago, T. Devic, C. Martineau, F. Taulelle, P. L. Llewellyn, H. Jobic, C. Zhong, C. Serre, G. De Weireld and G. Maurin, *Angew. Chem. Int. Ed.*, 2013, **52**, 10316–10320.

280 E. Stavitski, E. A. Pidko, S. Couck, T. Remy, E. J. M. Hensen, B. M. Weckhuysen, J. Denayer, J. Gascon and F. Kapteijn, *Langmuir*, 2011, **27**, 3970–3976.

281 R. W. Flaig, T. M. Osborn Popp, A. M. Fracaroli, E. A. Kapustin, M. J. Kalmutzki, R. M. Altamimi, F. Fathieh, J. A. Reimer and O. M. Yaghi, *J. Am. Chem. Soc.*, 2017, **139**, 12125–12128.

282 S. Vaesen, V. Guillerm, Q. Yang, A. D. Wiersum, B. Marszalek, B. Gil, A. Vimont, M. Daturi, T. Devic, P. L. Llewellyn, C. Serre, G. Maurin and G. De Weireld, *Chem. Commun.*, 2013, **49**, 10082–10084.

283 K. Sumida, D. L. Rogow, J. A. Mason, T. M. McDonald, E. D. Bloch, Z. R. Herm, T. H. Bae and J. R. Long, *Chem. Rev.*, 2012, **112**, 724–781.

284 V. Krungleviciute, K. Lask, A. D. Migone, J.-Y. Lee and J. Li, *AIChE J.*, 2008, **54**, 918–923.

285 Y. Liu, J. F. Eubank, A. J. Cairns, J. Eckert, V. C. Kravtsov, R. Luebke and M. Eddaoudi, *Angew. Chem. Int. Ed.*, 2007, **46**, 3278–3283.

286 Y. Belmabkhout, V. Guillerm and M. Eddaoudi, *Chem. Eng. J.*, 2016, **296**, 386–397.

287 J. R. Li, J. Yu, W. Lu, L. B. Sun, J. Sculley, P. B. Balbuena and H. C. Zhou, *Nat. Commun.*, 2013, **4**, 1358.

288 S. Xiang, Y. He, Z. Zhang, H. Wu, W. Zhou, R. Krishna and B. Chen, *Nat. Commun.*, 2012, **3**, 954–959.

289 T. M. McDonald, W. R. Lee, J. A. Mason, B. M. Wiers, C. S. Hong and J. R. Long, *J. Am. Chem. Soc.*, 2012, **134**, 7056–7065.

290 S. Cavenati, C. A. Grande and A. E. Rodrigues, *J. Chem. Eng. Data*, 2004, **49**, 1095–1101.

291 S. Himeno, T. Komatsu and S. Fujita, *J. Chem. Eng. Data*, 2005, **50**, 369–376.

292 T. Otowa, R. Tanibata and M. Itoh, *Gas Sep. Purif.*, 1993, **7**, 241–245.

293 C. J. Major, B. J. Sollami and K. Kammermeyer, *Ind. Eng. Chem. Process Des. Dev.*, 1965, **4**, 327–333.

294 Y. Belmabkhout, R. Serna-Guerrero and A. Sayari, *Chem. Eng. Sci.*, 2010, **65**, 3695–3698.

295 J. S. Choi, W. J. Son, J. Kim and W. S. Ahn, *Microporous Mesoporous Mater.*, 2008, **116**, 727–731.

296 S. Xiang, X. Wu, J. Zhang, R. Fu, S. Hu and X. Zhang, *J. Am. Chem. Soc.*, 2005, **127**, 16352–16353.

297 R. Luebke, J. F. Eubank, A. J. Cairns, Y. Belmabkhout, L. Wojtas and M. Eddaoudi, *Chem. Commun.*, 2012, **48**, 1455–1457.

298 D. Lässig, J. Lincke, J. Moellmer, C. Reichenbach, A. Moeller, R. Gläser, G. Kalies, K. A. Cychosz, M. Thommes, R. Staudt and H. Krautscheid, *Angew. Chem. Int. Ed.*, 2011, **50**, 10344–10348.

299 K. A. Forrest, T. Pham, K. McLaughlin, A. Hogan and B. Space, *Chem. Commun.*, 2014, **50**, 7283–

7286.

300 R. Vaidhyanathan, S. S. Iremonger, G. K. H. Shimizu, P. G. Boyd, S. Alavi and T. K. Woo, *Science*, 2010, **330**, 650–653.

301 A. Banerjee, S. Nandi, P. Nasa and R. Vaidhyanathan, *Chem. Commun.*, 2016, **52**, 1851–1854.

302 Z. R. Herm, J. A. Swisher, B. Smit, R. Krishna and J. R. Long, *J. Am. Chem. Soc.*, 2011, **133**, 5664–5667.

303 O. Shekhah, Y. Belmabkhout, Z. Chen, V. Guillerm, A. Cairns, K. Adil and M. Eddaoudi, *Nat. Commun.*, 2014, **5**, 1–7.

304 S. Kitagawa and M. Kondo, *Bull. Chem. Soc. Jpn.*, 1998, **71**, 1739–1753.

305 S. Horike, S. Shimomura and S. Kitagawa, *Nat. Chem.*, 2009, **1**, 695–704.

306 C. Janiak, *Dalton Trans.*, 2003, 2781–2804.

307 A. Schneemann, V. Bon, I. Schwedler, I. Senkovska, S. Kaskel and R. A. Fischer, *Chem. Soc. Rev.*, 2014, **43**, 6062–6096.

308 G. Férey, *J. Chem. Soc. Dalt. Trans.*, 2009, 4400–4415.

309 C. Serre, F. Millange, C. Thouvenot, M. Noguès, G. Marsolier, D. Louër and G. Férey, *J. Am. Chem. Soc.*, 2002, **124**, 13519–13526.

310 C. Serre, C. Mellot-Draznieks, S. Surblé, N. Audebrand, Y. Filinchuk and G. Férey, *Science*, 2007, 1828–1831.

311 R. Kitaura, K. Seki, G. Akiyama and S. Kitagawa, *Angew. Chem. Int. Ed.*, 2003, **42**, 428–431.

312 L. Hamon, P. L. Llewellyn, T. Devic, A. Ghoufi, G. Clet, V. Guillerm, G. D. Pirngruber, G. Maurin, C. Serre, G. Driver, W. Van Beek, E. Jolimaître, A. Vimont, M. Daturi and G. Férey, *J. Am. Chem. Soc.*, 2009, **131**, 17490–17499.

313 S. Krause, V. Bon, I. Senkovska, U. Stoeck, D. Wallacher, D. M. Többens, S. Zander, R. S. Pillai, G. Maurin, F. X. Coudert and S. Kaskel, *Nature*, 2016, **532**, 348–352.

314 S. A. Moggach, T. D. Bennett and A. K. Cheetham, *Angew. Chem. Int. Ed.*, 2009, **48**, 7087–7089.

315 D. Fairen-Jimenez, S. A. Moggach, M. T. Wharmby, P. A. Wright, S. Parsons and T. Düren, *J. Am. Chem. Soc.*, 2011, **133**, 8900–8902.

316 K. Chapman, *J. Am. Chem. Soc.*, 2008, **130**, 10524–10526.

317 S. H. Lapidus, G. J. Halder, P. J. Chupas and K. W. Chapman, *J. Am. Chem. Soc.*, 2013, **135**, 7621–7628.

318 M. Kondo, S. Furukawa, K. Hirai, T. Tsuruoka, J. Reboul, H. Uehara, S. Diring, Y. Sakata, O. Sakata and S. Kitagawa, *J. Am. Chem. Soc.*, 2014, **136**, 4938–4944.

319 D. Tanaka, A. Henke, K. Albrecht, M. Moeller, K. Nakagawa, S. Kitagawa and J. Groll, *Nat. Chem.*, 2010, **2**, 410–416.

320 Y. Sakata, S. Furukawa, M. Kondo, K. Hirai, N. Horike, Y. Takashima, H. Uehara, N. Louvain, M. Meilikhov, T. Tsuruoka, S. Isoda, W. Kosaka, O. Sakata and S. Kitagawa, *Science*, 2013, **339**, 193–196.

321 H. L. Jiang, D. Feng, K. Wang, Z. Y. Gu, Z. Wei, Y. P. Chen and H. C. Zhou, *J. Am. Chem. Soc.*, 2013, **135**, 13934–13938.

322 M. Meilikhov, K. Yusenko, A. Torrisi, B. Jee, C. Mellot-Draznieks, A. Pöppl and R. A. Fischer, *Angew. Chem. Int. Ed.*, 2010, **49**, 6212–6215.

323 C. F. Leong, T. B. Faust, P. Turner, P. M. Usov, C. J. Kepert, R. Babarao, A. W. Thornton and D. M. D'Alessandro, *Dalton Trans.*, 2013, **42**, 9831–9839.

324 C. A. Fernandez, P. C. Martin, T. Schaef, M. E. Bowden, P. K. Thallapally, L. Dang, W. Xu, X. Chen and B. P. McGrail, *Sci. Rep.*, 2014, **4**, 6114.

325 H. Li, M. M. Sadiq, K. Suzuki, R. Ricco, C. Doblin, A. J. Hill, S. Lim, P. Falcaro and M. R. Hill, *Adv. Mater.*, 2016, **28**, 1839–1844.

326 D. Bradshaw, J. E. Warren and M. J. Rosseinsky, *Science*, 2007, **315**, 977–980.

327 F. X. Coudert, *Chem. Mater.*, 2015, **27**, 1905–1916.

328 H. Li and M. R. Hill, *Acc. Chem. Res.*, 2017, **50**, 778–786.

329 M. C. So, G. P. Wiederrecht, J. E. Mondloch, J. T. Hupp and O. K. Farha, *Chem. Commun.*, 2015, **51**, 3501–3510.

330 L. E. Kreno, K. Leong, O. K. Farha, M. Allendorf, D. Van Richard P. and J. T. Hupp, *Chem. Rev.*, 2012, **112**, 1105–1125.

331 M. Takeuchi, M. Ikeda, A. Sugasaki and S. Shinkai, *Acc. Chem. Res.*, 2001, **34**, 865–873.

332 W. R. Browne and B. L. Feringa, *Nat. Nanotechnol.*, 2006, **1**, 25–35.

333 M. Irie, *Chem. Rev.*, 2000, **100**, 1685–1716.

334 C. B. Fan, L. L. Gong, L. Huang, F. Luo, R. Krishna, X. F. Yi, A. M. Zheng, L. Zhang, S. Z. Pu, X. F. Feng, M. B. Luo and G. C. Guo, *Angew. Chem. Int. Ed.*, 2017, **56**, 7900–7906.

335 C. B. Fan, Z. Q. Liu, L. L. Gong, A. M. Zheng, L. Zhang, C. S. Yan, H. Q. Wu, X. F. Feng and F. Luo, *Chem. Commun.*, 2017, **53**, 763–766.

336 J. J. Vittal, *Coord. Chem. Rev.*, 2007, **251**, 1781–1795.

337 N. Yanai, T. Uemura, M. Inoue, R. Matsuda, T. Fukushima, M. Tsujimoto, S. Isoda and S. Kitagawa, *J. Am. Chem. Soc.*, 2012, **134**, 4501–4504.

338 J. Park, D. Yuan, K. T. Pham, J. R. Li, A. Yakovenko and H. C. Zhou, *J. Am. Chem. Soc.*, 2012, **134**, 99–102.

339 R. Lyndon, K. Konstas, B. P. Ladewig, P. D. Southon, P. C. J. Kepert and M. R. Hill, *Angew. Chem. Int. Ed.*, 2013, **52**, 3695–3698.

340 R. Lyndon, K. Konstas, R. A. Evans, D. J. Keddie, M. R. Hill and B. P. Ladewig, *Adv. Funct. Mater.*, 2015, **25**, 4405–4411.

341 H. Li, M. R. Hill, C. Doblin, S. Lim, A. J. Hill and P. Falcaro, *Adv. Funct. Mater.*, 2016, **26**, 4815–4821.

342 H. Q. Wu, C. S. Yan, F. Luo and R. Krishna, *Inorg. Chem.*, 2018, **57**, 3679–3682.

343 A. Modrow, D. Zargarani, R. Herges and N. Stock, *Dalton Trans.*, 2011, **40**, 4217–4222.

344 S. Bernt, M. Feyand, A. Modrow, J. Wack, J. Senker and N. Stock, *Eur. J. Inorg. Chem.*, 2011, 5378–5383.

345 A. Modrow, D. Zargarani, R. Herges and N. Stock, *Dalton Trans.*, 2012, **41**, 8690–8696.

346 J. W. Brown, B. L. Henderson, M. D. Kiesz, A. C. Whalley, W. Morris, S. Grunder, H. Deng, H.

Furukawa, J. I. Zink, J. F. Stoddart and O. M. Yaghi, *Chem. Sci.*, 2013, **4**, 2858–2864.

347 F. Luo, C. Bin Fan, M. B. Luo, X. L. Wu, Y. Zhu, S. Z. Pu, W. Y. Xu and G. C. Guo, *Angew. Chem. Int. Ed.*, 2014, **53**, 9298–9301.

348 H. Li, M. R. Martinez, Z. Perry, H.-C. Zhou, P. Falcaro, C. Doblin, S. Lim, A. J. Hill, B. Halstead and M. R. Hill, *Chem. Eur. J.*, 2016, **22**, 11176–11179.

349 L. L. Gong, X. F. Feng and F. Luo, *Inorg. Chem.*, 2015, **54**, 11587–11589.

350 W. C. Song, X. Z. Cui, Z. Y. Liu, E. C. Yang and X. J. Zhao, *Sci. Rep.*, 2016, **6**, 1–8.

351 S. Ma, D. Sun, J. M. Simmons, C. D. Collier, D. Yuan and H. C. Zhou, *J. Am. Chem. Soc.*, 2008, **130**, 1012–1016.

352 F. Gándara, H. Furukawa, S. Lee and O. M. Yaghi, *J. Am. Chem. Soc.*, 2014, **136**, 5271–5274.

353 Y. He, W. Zhou, G. Qian and B. Chen, *Chem. Soc. Rev.*, 2014, **43**, 5657–5678.

354 J. A. Mason, J. Oktawiec, M. K. Taylor, M. R. Hudson, J. Rodriguez, J. E. Bachman, M. I. Gonzalez, A. Cervellino, A. Guagliardi, C. M. Brown, P. L. Llewellyn, N. Masciocchi and J. R. Long, *Nature*, 2015, **527**, 357–361.

355 D. Alezi, Y. Belmabkhout, M. Suyetin, P. M. Bhatt, L. J. Weseliński, V. Solovyeva, K. Adil, I. Spanopoulos, P. N. Trikalitis, A. H. Emwas and M. Eddaoudi, *J. Am. Chem. Soc.*, 2015, **137**, 13308–13318.

356 C. M. Simon, J. Kim, D. A. Gomez-Gualdron, J. S. Camp, Y. G. Chung, R. L. Martin, R. Mercado, M. W. Deem, D. Gunter, M. Haranczyk, D. S. Sholl, R. Q. Snurr and B. Smit, *Energy Environ. Sci.*, 2015, **8**, 1190–1199.

357 Y. He, W. Zhou and B. Chen, in *Metal-Organic Frameworks: Applications in Separations and Catalysis*, eds. H. García and S. Navalón, Wiley-VCH Verlag, 2018, pp. 163–198.

358 Y. He, W. Zhou, R. Krishna and B. Chen, *Chem. Commun.*, 2012, **48**, 11813–11831.

359 F. Chen, Y. Wang, D. Bai, M. He, X. Gao and Y. He, *J. Mater. Chem. A*, 2018, **6**, 3471–3478.

360 S. Mukherjee, A. V. Desai and S. K. Ghosh, *Coord. Chem. Rev.*, 2018, **367**, 82–126.

361 L. Pan, D. H. Olson, L. R. Ciemnolonski, R. Heady and J. Li, *Angew. Chem. Int. Ed.*, 2006, **45**, 616–619.

362 E. D. Bloch, W. L. Queen, R. Krishna, J. M. Zadrozny, C. M. Brown and J. R. Long, *Science*, 2012, **335**, 1606–1610.

363 H. Wu, Q. Gong, D. H. Olson and J. Li, *Chem. Rev.*, 2012, **112**, 836–868.

364 T. L. Hu, H. Wang, B. Li, R. Krishna, H. Wu, W. Zhou, Y. Zhao, Y. Han, X. Wang, W. Zhu, Z. Yao, S. Xiang and B. Chen, *Nat. Commun.*, 2015, **6**, 1–9.

365 A. Cadiau, K. Adil, P. M. Bhatt, Y. Belmabkhout and M. Eddaoudi, *Science*, 2016, **353**, 137–140.

366 X. Cui, K. Chen, H. Xing, Q. Yang, R. Krishna, Z. Bao, H. Wu, W. Zhou, X. Dong, Y. Han, B. Li, Q. Ren, M. J. Zaworotko and B. Chen, *Science*, 2016, **353**, 141–144.

367 M. D. Allendorf, R. J. T. Houk, L. Andruszkiewicz, A. A. Talin, J. Pikarsky, A. Choudhury, K. A. Gall and P. J. Hesketh, *J. Am. Chem. Soc.*, 2008, **130**, 14404–14405.

368 S. Achmann, G. Hagen, J. Kita, I. M. Malkowsky, C. Kiener and R. Moos, *Sensors*, 2009, **9**, 1574–1589.

369 A. Venkatasubramanian, J.-H. Lee, R. J. Houk, M. D. Allendorf, S. Nair and P. J. Hesketh, *ECS Trans.*, 2010, **33**, 229–238.

370 A. H. Khoshaman and B. Bahreyni, *Proc. IEEE Sensors*, 2011, **162**, 1101–1104.

371 E. Barea, C. Montoro and J. A. R. Navarro, *Chem. Soc. Rev.*, 2014, **43**, 5419–5430.

372 M. J. Katz, J. E. Mondloch, R. K. Totten, J. K. Park, S. T. Nguyen, O. K. Farha and J. T. Hupp, *Angew. Chem. Int. Ed.*, 2014, **53**, 497–501.

373 P. M. Bhatt, Y. Belmabkhout, A. H. Assen, Ł. J. Weseliński, H. Jiang, A. Cadiau, D. X. Xue and M. Eddaoudi, *Chem. Eng. J.*, 2017, **324**, 392–396.

374 N. S. Bobbitt, M. L. Mendonca, A. J. Howarth, T. Islamoglu, J. T. Hupp, O. K. Farha and R. Q. Snurr, *Chem. Soc. Rev.*, 2017, **46**, 3357–3385.

375 P. Horcajada, T. Chalati, C. Serre, B. Gillet, C. Sebrie, T. Baati, J. F. Eubank, D. Heurtaux, P. Clayette, C. Kreuz, J. S. Chang, Y. K. Hwang, V. Marsaud, P. N. Bories, L. Cynober, S. Gil, G. Férey, P. Couvreur and R. Gref, *Nat. Mater.*, 2010, **9**, 172–178.

376 S. Han, Y. Wei, C. Valente, J. J. Gassensmith, A. Coskun, J. F. Stoddart and B. A. Grzybowski, *J. Am. Chem. Soc.*, 2010, **132**, 16358–16361.

377 Z. L. Fang, S. R. Zheng, J. B. Tan, S. L. Cai, J. Fan, X. Yan and W. G. Zhang, *J. Chromatogr. A*, 2013, **1285**, 132–138.

378 S. Bhattacharjee, M. Khan, X. Li, Q.-L. Zhu and X.-T. Wu, *Catalysts*, 2018, **8**, 120–144.

379 M. Yoshizawa and M. Fujita, *Pure Appl. Chem.*, 2005, **77**, 1107–1112.

380 Y. Inokuma, M. Kawano and M. Fujita, *Nat. Chem.*, 2011, **3**, 349–358.

381 B. Dhara, S. S. Nagarkar, J. Kumar, V. Kumar, P. K. Jha, S. K. Ghosh, S. Nair and N. Ballav, *J. Phys. Chem. Lett.*, 2016, **7**, 2945–2950.

382 Y. Inokuma, S. Yoshioka, J. Ariyoshi, T. Arai, Y. Hitora, K. Takada, S. Matsunaga, K. Rissanen and M. Fujita, *Nature*, 2013, **495**, 461–466.

383 K. Yan, R. Dubey, T. Arai, Y. Inokuma and M. Fujita, *J. Am. Chem. Soc.*, 2017, **139**, 11341–11344.

384 K. Liang, R. Ricco, C. M. Doherty, M. J. Styles, S. Bell, N. Kirby, S. Mudie, D. Haylock, A. J. Hill, C. J. Doonan and P. Falcaro, *Nat. Commun.*, 2015, **6**, 1–8.

385 X. Lian, Y. Fang, E. Joseph, Q. Wang, J. Li, S. Banerjee, C. Lollar, X. Wang and H. C. Zhou, *Chem. Soc. Rev.*, 2017, **46**, 3386–3401.

386 K. M. L. Taylor-Pashow, J. Della Rocca, Z. Xie, S. Tran and W. Lin, *J. Am. Chem. Soc.*, 2009, **131**, 14261–14263.

387 M. X. Wu and Y. W. Yang, *Adv. Mater.*, 2017, **29**, 1–20.

388 M. Kotzabasaki and G. E. Froudakis, *Inorg. Chem. Front.*, 2018, **5**, 1255–1272.

389 Washington, DC: U.S. Patent and Trademark Office., U.S. Patent No. 9,375,394, 2016.

390 Washington, DC: U.S. Patent and Trademark Office., U.S. Patent No. 9,816,049., 2017.

391 L. Ma, C. Abney and W. Lin, *Chem. Soc. Rev.*, 2009, **38**, 1248–1256.

392 S. M. J. Rogge, A. Bavykina, J. Hajek, H. Garcia, A. I. Olivos-Suarez, A. Sepúlveda-Escribano, A. Vimont, G. Clet, P. Bazin, F. Kapteijn, M. Daturi, E. V. Ramos-Fernandez, F. X. I. Llabrés Xamena, V. Van Speybroeck and J. Gascon, *Chem. Soc. Rev.*, 2017, **46**, 3134–3184.

393 L. Zhu, X. Q. Liu, H. L. Jiang and L. B. Sun, *Chem. Rev.*, 2017, **117**, 8129–8176.

394 M. B. Majewski, A. W. Peters, M. R. Wasielewski, J. T. Hupp and O. K. Farha, *ACS Energy Lett.*, 2018, **3**, 598–611.

395 J. Lee, O. K. Farha, J. Roberts, K. A. Scheidt, S. T. Nguyen and J. T. Hupp, *Chem. Soc. Rev.*, 2009, **38**, 1450–1459.

396 A. D. Burrows, C. G. Frost, M. F. Mahon and C. Richardson, *Angew. Chem. Int. Ed.*, 2008, **120**, 8610–8614.

397 B. Li, Y. Zhang, D. Ma, L. Li, G. Li, G. Li, Z. Shi and S. Feng, *Chem. Commun.*, 2012, **48**, 6151–6153.

398 J. D. Evans, C. J. Sumby and C. J. Doonan, *Chem. Soc. Rev.*, 2014, **43**, 5933–5951.

399 Y. Luan, Y. Qi, H. Gao, R. S. Andriamitantsoa, N. Zheng and G. Wang, *J. Mater. Chem. A*, 2015, **3**, 17320–17331.

400 S. Hermes, M. K. Schröter, R. Schmid, L. Khodeir, M. Muhler, A. Tissler, R. W. Fischer and R. A. Fischer, *Angew. Chem. Int. Ed.*, 2005, **44**, 6237–6241.

401 M. Sabo, A. Henschel, H. Fröde, E. Klemm and S. Kaskel, *J. Mater. Chem.*, 2007, **17**, 3827–3832.

402 P. Müller, R. Grünker, V. Bon, M. Pfeffermann, I. Senkovska, M. S. Weiss, X. Feng and S. Kaskel, *CrystEngComm*, 2016, **18**, 8164–8171.

403 F. Schröder, D. Esken, M. Cokoja, M. W. E. Van Den, O. I. Lebedev, G. Van Tendeloo, B. Walaszek, H. Limbach, B. Chaudret and R. A. Fischer, *J. Am. Chem. Soc.*, 2008, **130**, 6119–6130.

404 T. Zhang and W. Lin, *Chem. Soc. Rev.*, 2014, **43**, 5982–5993.

405 Z. M. Zhang, T. Zhang, C. Wang, Z. Lin, L. S. Long and W. Lin, *J. Am. Chem. Soc.*, 2015, **137**, 3197–3200.

406 Z.-H. Yan, M.-H. Du, J. Liu, S. Jin, C. Wang, G.-L. Zhuang, X.-J. Kong, L.-S. Long and L.-S. Zheng, *Nat. Commun.*, 2018, 1–9.

407 G. Lan, Z. Li, S. S. Veroneau, Y.-Y. Zhu, Z. Xu, C. Wang and W. Lin, *J. Am. Chem. Soc.*, 2018, **140**, 12369–12373.

408 M. H. Alkordi, Y. Liu, R. W. Larsen, J. F. Eubank and M. Eddaoudi, *J. Am. Chem. Soc.*, 2008, **130**, 12639–12641.

409 M. C. Das, S. Xiang, Z. Zhang and B. Chen, *Angew. Chem. Int. Ed.*, 2011, **50**, 10510–10520.

410 Z. Fang, B. Bueken, D. E. De Vos and R. A. Fischer, *Angew. Chem. Int. Ed.*, 2015, **54**, 7234–7254.

411 J. Canivet, M. Vandichel and D. Farrusseng, *Dalton Trans.*, 2016, **45**, 4090–4099.

412 A. Herbst and C. Janiak, *CrystEngComm*, 2017, **19**, 4092–4117.

413 G. Mínguez Espallargas and E. Coronado, *Chem. Soc. Rev.*, 2018, **47**, 533–557.

414 J. A. Real, E. Andrés, M. C. Muñoz, M. Julve, T. Granier, A. Bousseksou and F. Varret, *Science*, 1995, **268**, 265–267.

415 G. J. Halder, C. J. Kepert, B. Moubaraki, K. S. Murray and J. D. Cashion, *Science*, 2002, **298**, 1762–1765.

416 J. M. Zadrozny, A. T. Gallagher, T. D. Harris and D. E. Freedman, *J. Am. Chem. Soc.*, 2017, **139**, 7089–7094.

417 B. Chen, L. Wang, Y. Xiao, F. R. Fronczek, M. Xue, Y. Cui and G. Qian, *Angew. Chem. Int. Ed.*, 2009, **48**, 500–503.

418 Z. Hu, B. J. Deibert and J. Li, *Chem. Soc. Rev.*, 2014, **43**, 5815–5840.

419 Y. Cui, B. Chen and G. Qian, *Coord. Chem. Rev.*, 2014, **273**–**274**, 76–86.

420 G. Tobin, S. Comby, N. Zhu, R. Clérac, T. Gunnlaugsson and W. Schmitt, *Chem. Commun.*, 2015, **51**, 13313–13316.

421 U. Mueller, M. Schubert, F. Teich, H. Puetter, K. Schierle-Arndt and J. Pastré, *J. Mater. Chem.*, 2006, **16**, 626–636.

422 Z.-Y. Gu, C.-X. Yang, N. Chang and X.-P. Yan, *Acc. Chem. Res.*, 2012, **45**, 734–745.

423 S. M. Cohen, *Chem. Rev.*, 2012, **112**, 970–1000.

424 A. Morozan and F. Jaouen, *Energy Environ. Sci.*, 2012, **5**, 9269–9290.

425 M. Alvaro, E. Carbonell, B. Ferrer, F. X. Llabrés i Xamena and H. Garcia, *Chem. Eur. J.*, 2007, **13**, 5106–5112.

426 M. Usman, S. Mendiratta and K. L. Lu, *Adv. Mater.*, 2017, **29**, 1–5.

427 Z. Hasan and S. H. Jhung, *J. Hazard. Mater.*, 2015, **283**, 329–339.

428 H. Jasuja, G. W. Peterson, J. B. Decoste, M. A. Browe and K. S. Walton, *Chem. Eng. Sci.*, 2015, **124**, 118–124.

429 S. K. Henninger, H. A. Habib and C. Janiak, *J. Am. Chem. Soc.*, 2009, **131**, 2776–2777.

430 H. Kim, S. Yang, S. R. Rao, S. Narayanan, E. A. Kapustin, H. Furukawa, A. S. Umans, O. M. Yaghi and E. N. Wang, *Science*, 2017, **434**, 430–434.

431 P. W. Dunne, E. Lester and R. I. Walton, *React. Chem. Eng.*, 2016, **1**, 352–360.

432 M. Rubio-Martinez, T. D. Hadley, M. P. Batten, K. Constanti-Carey, T. Barton, D. Marley, A. Mönch, K. S. Lim and M. R. Hill, *ChemSusChem*, 2016, **9**, 938–941.

433 A. Garcia Marquez, P. Horcajada, D. Grosso, G. Ferey, C. Serre, C. Sanchez and C. Boissiere, *Chem. Commun.*, 2013, **49**, 3848–3850.

434 T. Faust, *Nat. Chem.*, 2016, **8**, 990–991.

435 M. Rubio-Martinez, C. Avci-Camur, A. W. Thornton, I. Imaz, D. Maspoch and M. R. Hill, *Chem. Soc. Rev.*, 2017, **46**, 3453–3480.

Chapter 2

Supramolecular Structure and Flexibility in Mixed-Tripodal Ligand Coordination Polymers

2.1: Introduction

One-dimensional coordination polymers (1D CPs), are the simplest class of coordination polymer materials topologically, and are of interest due to their electronic, magnetic, optic and catalytic properties.[1–4] From a supramolecular point of view, 1D CPs are a class of materials in which bonding and non-bonding interactions both play a key role in influencing connectivity in their respective dimensions, and therefore the functions of the materials.[5,6] 1D chains may possess straight, zigzag, or more intricate ladder or ribbon conformations.[2,7] The overall crystal structures are determined by the non-bonding interactions between individual chains, commonly involving H-bonding or π-π stacking interactions.[8–10] Various interwoven structural motifs and entanglements between chains can be promoted by these interactions, and dynamic changes in these arrangements can be engineered.[11] Similarly, in 2D CPs, the overall crystal structure is determined by both the strong coordination bonds that form the framework, and the weak interactions that govern the supramolecular orientation of frameworks relative to each other in the crystalline state.[12]

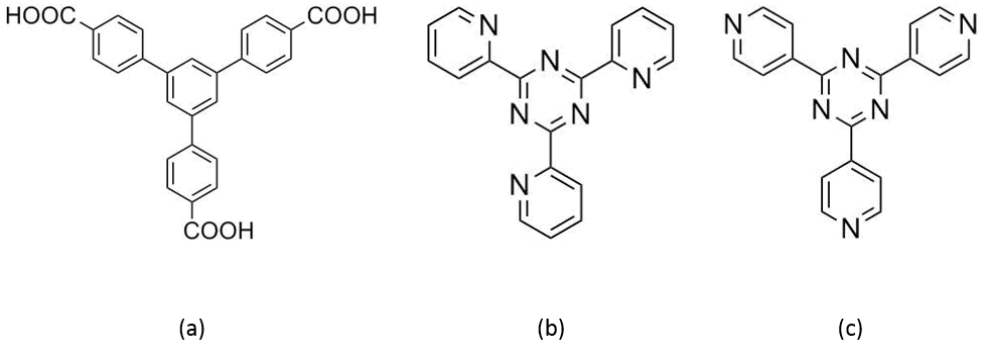

Figure 2.1 (a) - The H_3btb ligand; (b) - the 2-tpt ligand; (c) - the 4-tpt ligand.

1,3,5-Tris(4-carboxyphenyl)benzene (H_3btb), 2,4,6-tris(2-pyridyl)-1,3,5-triazine (2-tpt), and 2,4,6-tris(4-pyridyl)-1,3,5-triazine (4-tpt) are examples of typical tritopic ligands used in coordination chemistry (Fig 2.1).[13,14] The H_3btb ligand has previously been combined with N-donors, and 2-tpt and 4-tpt with carboxylate ligands, to yield a number of extended mixed-ligand materials.[15–17] Combinations of these ligands present attractive synthetic possibilities due to the availability of N- and O-donor functionalities, as well as extensive π-conjugation. These features confer stability and functionality to the resulting coordination polymers, and can result in synergistic structure directing effects.[18–21]

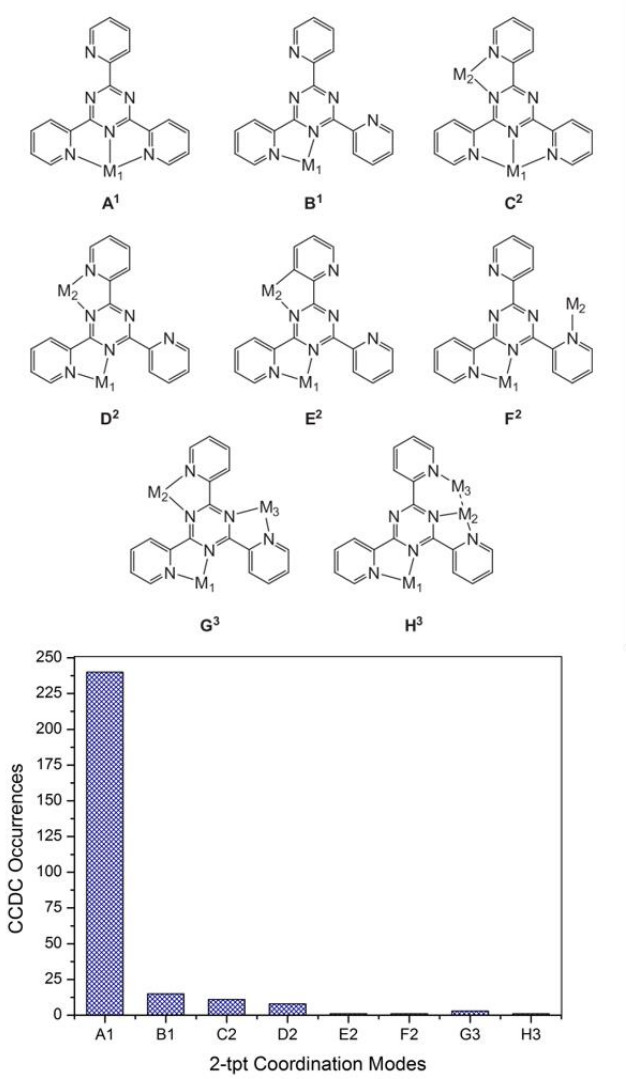

Figure 2.2 – The coordination modes (above, adapted from ref. 22) in reported crystal structures containing 2-tpt complexes (nuclearity in superscript), and a bar graph of the frequency of their occurrence in the CCDC (below).

The charge neutrality of the 4-tpt ligand allows full or partial utilisation as a tritopic linker, allowing it to be used as a ditopic linker, or simply a capping group, resulting in the potential for diverse structures incorporating mixed ligands. The prevalence of the chelating 2,2′:6′,2″- terpyridine-type coordination mode (A^1) by the 2-tpt ligand allows the conception of a polymer system in which three coordinative positions on the metal centre are occupied by N-donor atoms (Fig. 2.2). This would impair the formation of oligonuclear secondary building units (SBUs) and lead to structures based on mononuclear metal centres.[22] In this scenario, the variability between metal centres in terms of SBU formation becomes greatly reduced, giving rise to systems in which various metal centres could be applied for the formation of structurally related coordination polymers. Flexibility in the

ligands accommodates different metal centres within the same polymer motif, but the resulting conformational changes change the 3D packing of the polymer chains. Thereby, combinations of H_3btb with 2-tpt or 4-tpt into coordination polymers yield elegant structural platforms in which the hierarchical organisation of 1D, 2D, and 3D structure can be studied by rational comparison, and the effect of small changes in synthetic conditions or the identity of the metal ion used is evident in the supramolecular structure. Use of the 4-tpt ligand, in which the extensive π-conjugation is retained, but chelating modes are not available, was expected to allow the formation of oligonuclear SBUs. The structure directing effect of 4-tpt could then be compared to that of 2-tpt in similar systems.

2.2: Compounds **1-4**, [M(Hbtb)(2-tpt)], M = Zn, Ni, Mn, Cd

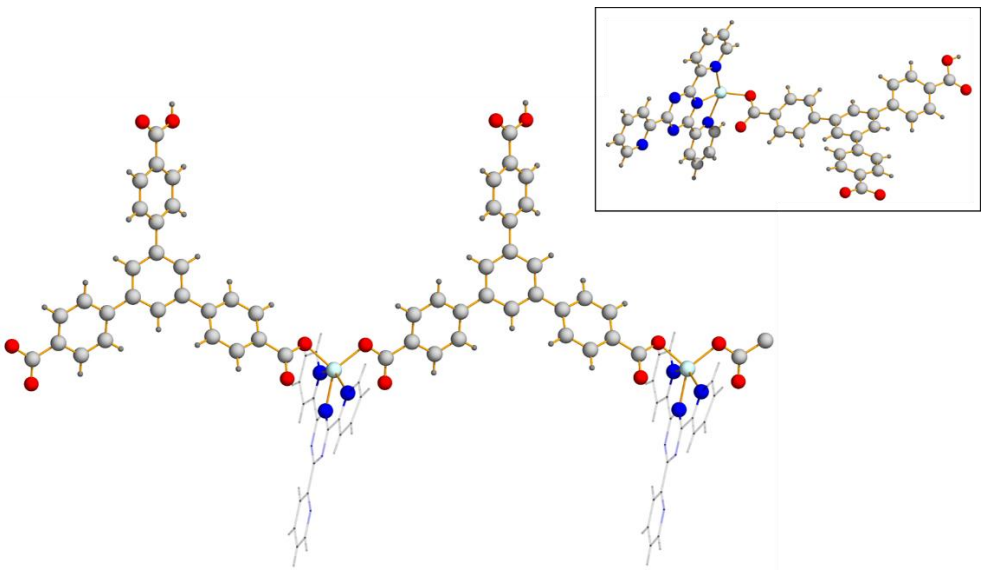

Figure 2.3 – A representation of the 1D coordination polymer chain in 1. Inset: asymmetric unit. Colour scheme: light turquoise, Zn; blue, N; red, O; grey, C; dark grey, H.

Compound **1**, [Zn(Hbtb)(2-tpt)]·DMF, was synthesised by adding zinc(II) nitrate hexahydrate to H_3btb and 2-tpt in DMF to form a slurry, which was then agitated until clarification. On heating for 4 days at 100°C, colourless single crystals of **1** were obtained. Single crystal X-ray diffraction experiments showed that **1** crystallises in the in the monoclinic crystal system and the *C*2/*c* space group, with cell dimensions of a = 33.908(2) Å, b = 17.5051(13) Å, c = 15.7559(13) Å, and $\alpha = \gamma = 90°$, β = 115.591(5)° (Fig. 2.3).

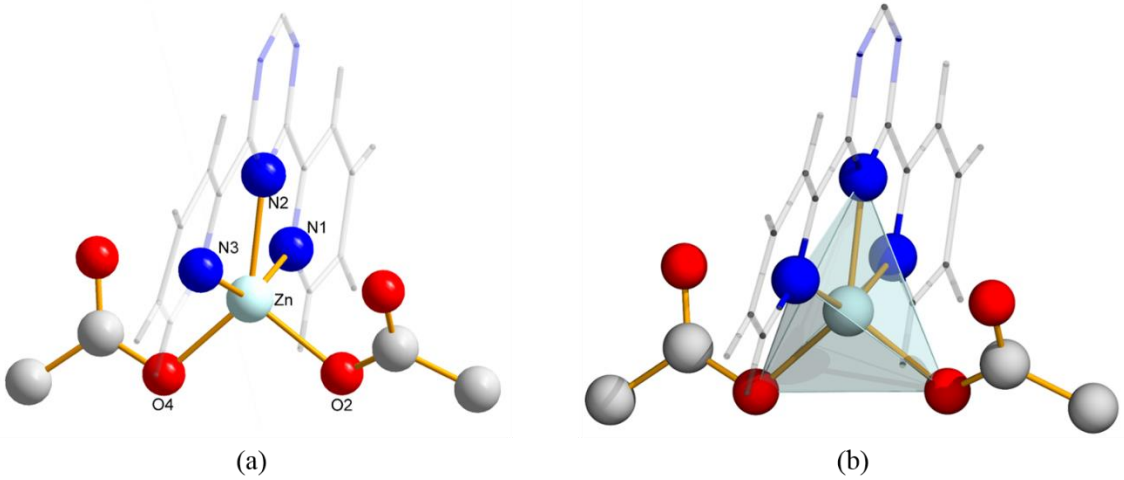

Figure 2.4 - The coordination environment in 1 with labelled atoms (a); and a polyhedral representation of the coordination environment (b).

1 is a one-dimensional coordination polymer in which the carboxylate groups of two $Hbtb^{2-}$ ligands are bound to each Zn(II) centre in a *syn*-monodentate fashion, and each zinc centre is bound to a 2-tpt ligand in a tridentate chelating fashion. This creates a slightly distorted trigonal bipyramidal Zn(II) coordination environment in which two nitrogen donor atoms from the 2-tpt ligand are located in the axial positions (Fig. 2.4). The Zn-O distances are 1.948(3) Å and 1.963(3) Å. Some important interatomic distances and angles are reported below (Table 2.1).

Table 2.1 - Selected interatomic distances and angles in 1.

Atoms	Distance		Atoms	Angle
Zn-O1	2.821(4) Å		O2-Zn-O4	100.8(1)°
Zn-O2	1.948(3) Å		N1-Zn-N3	146.7(2)°
Zn-O3	2.742(3) Å		N1-Zn-O2	93.5(1)°
Zn-O4	1.963(3) Å		N1-Zn-O4	99.8(1)°
Zn-N1	2.268(5) Å			
Zn-N2	2.056(3) Å			
Zn-N3	2.249(5) Å			

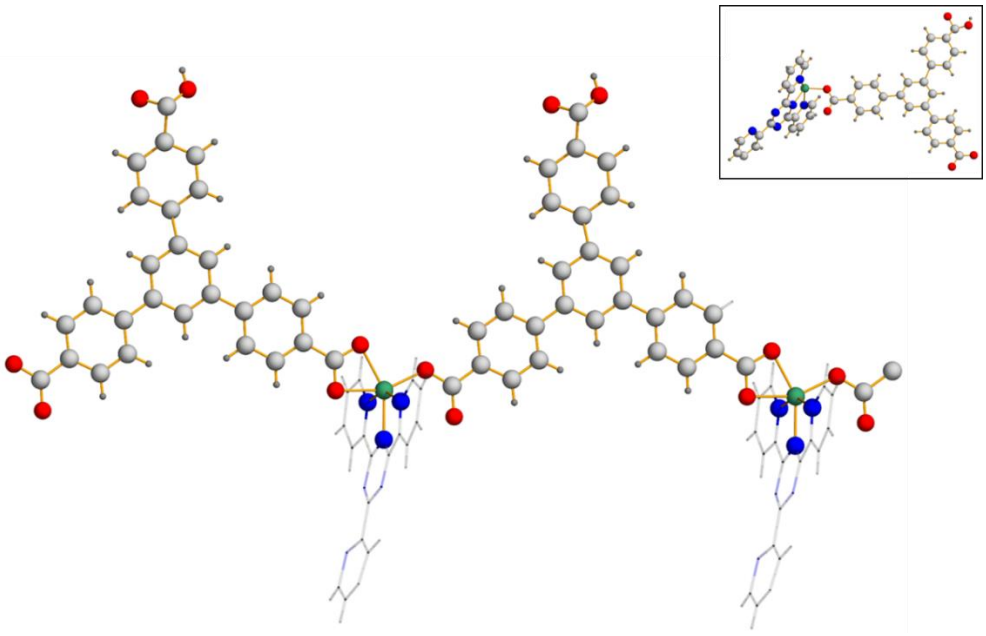

Figure 2.5 – A representation of the 1D coordination polymer chain in 2. Inset: asymmetric unit. Colour scheme: green, Ni; blue, N; red, O; grey, C; dark grey, H.

Compound **2**, [Ni(Hbtb)(2-tpt)]·0.5DMF, was synthesised by adding nickel(II) nitrate hexahydrate to H_3btb and 2-tpt in DMF to form a slurry, which was then agitated until clarification. On heating for 4 days at 100°C, some green single crystals of **2** were obtained along with a brown polycrystalline co-product. Single crystal X-ray diffraction experiments showed that **2** crystallises in the in the monoclinic crystal system and the *C*2/*c* space group, with cell dimensions of a = 34.7205(18) Å, b = 17.3089(6) Å, c = 15.8202(7) Å, and $\alpha = \gamma = 90°$, β = 115.923(2)° (Fig 2.5).

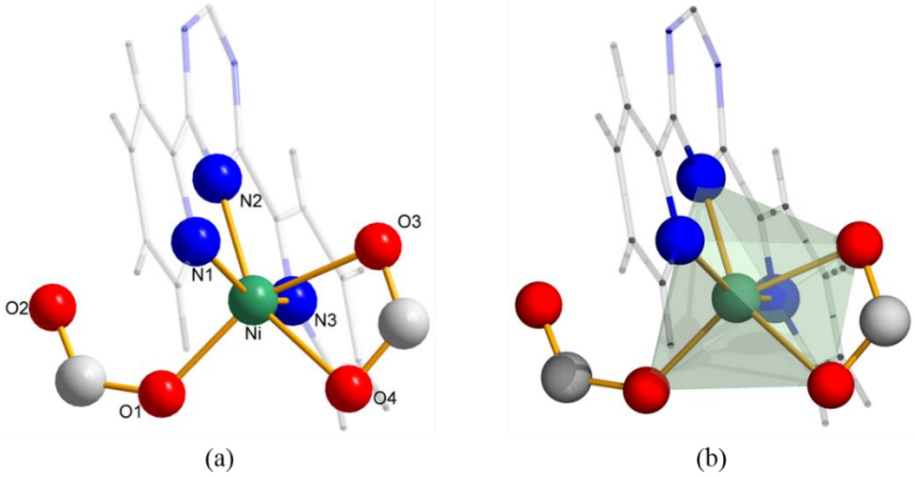

Figure 2.6 - The coordination environment in 2 with labelled atoms (a); and a polyhedral representation of the coordination environment (b).

2 is a one-dimensional coordination polymer in which one carboxylate group from a $Hbtb^{2-}$ ligand is bound to the Ni(II) centre in a *syn-syn* symmetric bidentate chelating fashion, and the other in a *syn*-monodentate fashion. Each nickel centre is bound to a 2-tpt ligand in a tridentate chelating mode, resulting in a distorted octahedral coordination environment overall. The Ni-O distances are 2.0860(387) Å and 2.0456(467) Å for the chelating mode, and 1.9230(306) Å for the monodentate mode (Fig. 2.6). Due to the presence of structural disorder, interatomic distances and angles reported are based on part A from the final crystallographic model (Table 2.2). The contribution from highly disordered solvent molecules was removed using the Squeeze routine (PLATON).[23]

Table 2.2 - Selected interatomic distances and angles in 2.

Atoms	Distance		Atoms	Angle
Ni-O1	2.09(4) Å		O1-Ni-N1	96.3(5)°
Ni-O2	3.18(1) Å		O1-Ni-O4	94.1(4)°
Ni-O3	2.05(5) Å		O3-Ni-O4	62.0(3)°
Ni-O4	1.92(3) Å		N1-Ni-N3	154.4(5)°
Ni-N1	1.88(6) Å		O1-Ni-N2	114.5(5)°
Ni-N2	1.99(3) Å			
Ni-N3	2.12(2) Å			

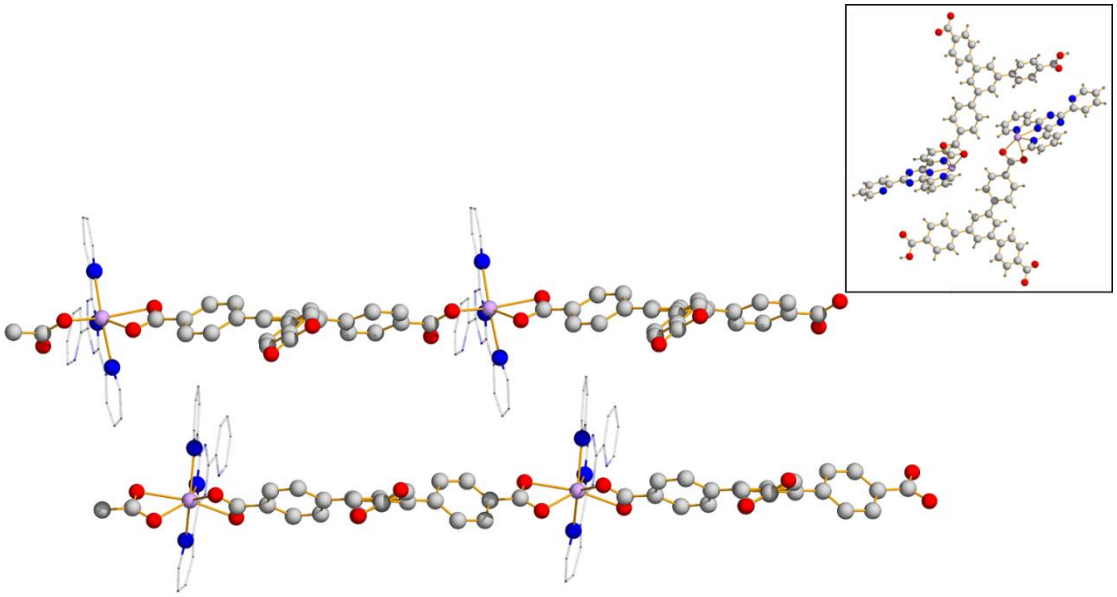

Figure 2.7 – A representation of the two distinct 1D coordination polymer chains in 3. Inset: asymmetric unit. Colour scheme: lavender, Mn; blue, N; red, O; grey, C. Hydrogen atoms removed for clarity

Compound **3**, [Mn(Hbtb)(2-tpt)]·1.25DMF, was synthesised by adding manganese(II) chloride tetrahydrate to H_3btb and 2-tpt in DMF to form a slurry, which was then agitated until clarification. On heating for 4 days at 100°C, pale orange single crystals of **3** were obtained. Single crystal X-ray diffraction experiments showed that **3** crystallises in the in the monoclinic crystal system and the $P2_1/c$ space group, with cell dimensions of a = 16.2604(6) Å, b = 17.3810(6) Å, c = 30.3417(10) Å, and $\alpha = \gamma = 90°$, β = 101.280(2)°.

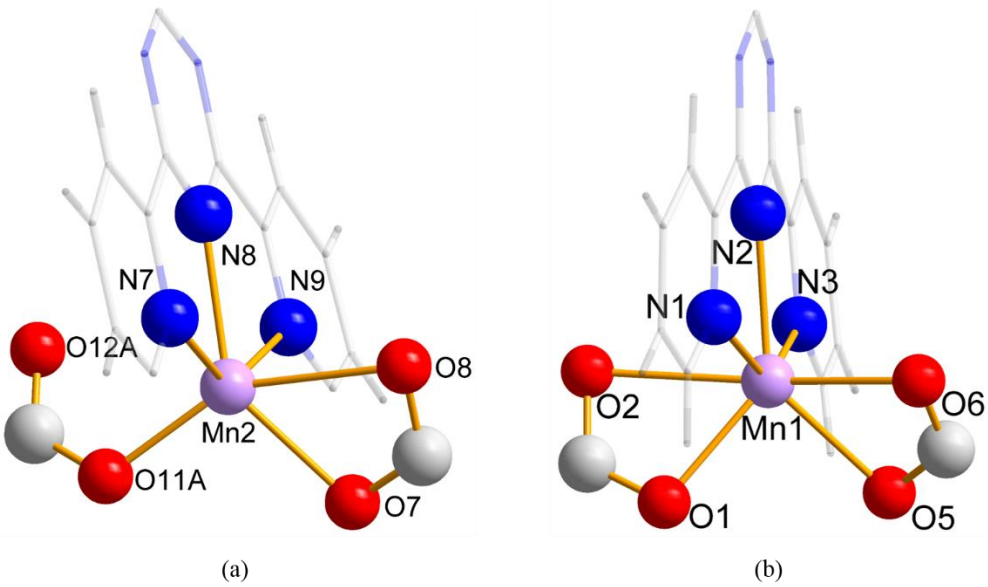

Figure 2.8 - The coordination environment in 3 around the 7-coordinate Mn centre (a); and around the 6-coordinate Mn centre (right).

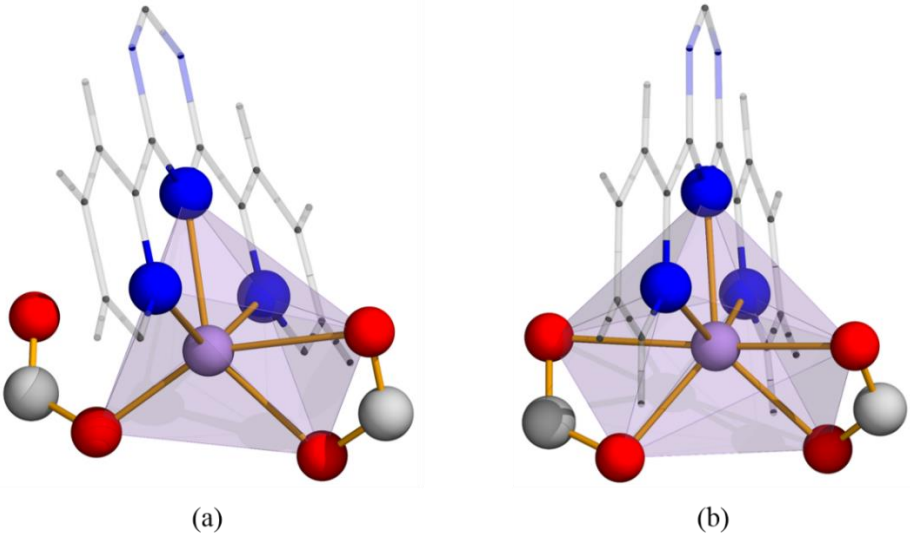

Figure 2.9 - Polyhedral representations of the coordination environment in 3 around the 7-coordinate Mn centre (left); and around the 6-coordinate Mn centre (b).

3 is a one-dimensional coordination polymer, and the asymmetric unit consists of two monomeric fragments from separate 1D chains (Fig. 2.7). In one of these, the fragment containing Mn2, the Mn(II) centre is 6-coordinated with one *syn-syn* symmetric carboxylate chelating mode, and one *syn*-monodentate mode resulting in a distorted octahedral geometry. In the other fragment the Mn(II) centre is 7-coordinated and both carboxylates show *syn-syn* symmetric chelating modes forming a capped octahedral geometry (Fig. 2.8, 2.9). In both fragments the 2-tpt ligand acts as a tridentate chelating

ligand around the Mn(II) centre. Due to some disorder associated with the btb ligand moiety in the Mn2 centred fragment, interatomic distances and angles reported are based on part A from the structural model (Table 2.3).

Table 2.3 - Selected interatomic distances and angles in 3.

Atoms	Distance		Atoms	Angle
Mn1-O1	2.132(2) Å		O2-Mn1-O6	167.24(8)°
Mn1-O2	2.467(2) Å		N1-Mn1-N3	139.6(1)°
Mn1-O5	2.249(2) Å		O6-Mn1-N1	82.86(9)°
Mn1-O6	2.229(2) Å		O2-Mn1-N3	85.66(9)°
Mn1-N1	2.350(3) Å		O1-Mn1-O2	56.72(8)°
Mn1-N2	2.223(2) Å		O5-Mn1-O6	58.39(8)°
Mn1-N3	2.360(3) Å			
Mn2-O7	2.1794(2) Å		O8-Mn2-O11A	150.5(2)°
Mn2-O8	2.4086(3) Å		O8-Mn2-O7	56.48(9)°
Mn2-O11A	1.97(6) Å		N7-Mn2-N9	139.4(1)°
Mn2-O12A	2.966(6) Å		N8-Mn2-O8	93.02(9)°
Mn2-N7	2.336(3) Å		O7-Mn2-N9	81.2(1)°
Mn2-N8	2.222(3) Å			
Mn2-N9	2.326(3) Å			

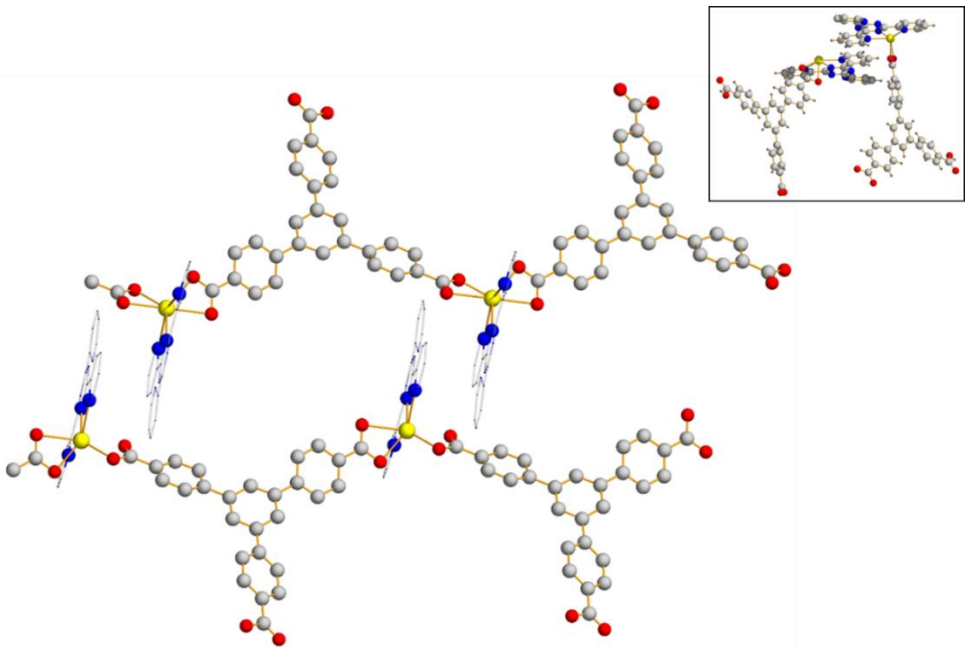

Figure 2.10 – A representation of the asymmetric unit of 4. Colour scheme: Yellow, Cd; blue, N; red, O; grey, C. Hydrogen atoms removed for clarity.

Compound **4**, [Cd(Hbtb)(2-tpt)]·DMF, was synthesised by adding cadmium(II) nitrate tetrahydrate to H_3btb and 2-tpt in DMF to form a slurry, which was then agitated until clarification. On heating for 4 days at 100°C, colourless single crystals of **4** were obtained. Single crystal X-ray diffraction experiments showed that **4** crystallises in the in the monoclinic crystal system and the $P2_1/c$ space group, with cell dimensions of a = 16.281(3)Å, b = 17.516(3) Å, c = 30.291(4) Å, and $\alpha = \gamma = 90°$, β = 100.546(3)°.

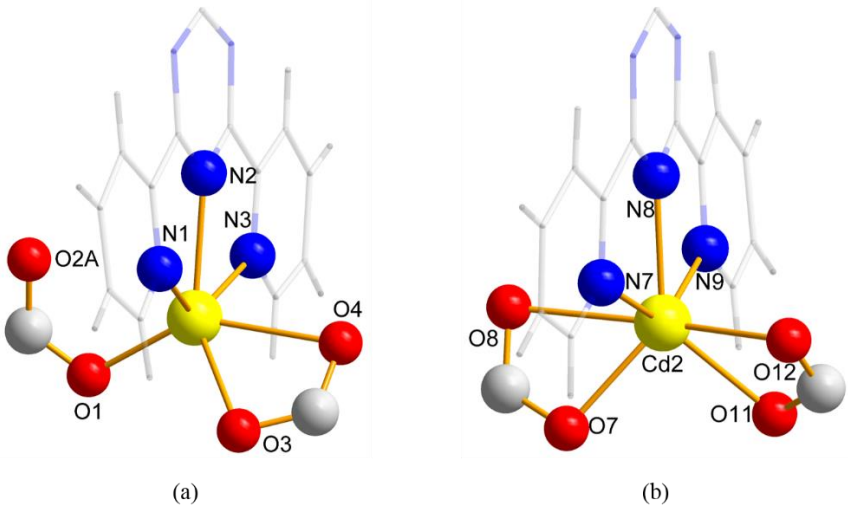

Figure 2.11 - The coordination environment in 4 around the 6-coordinate Cd centre (a); and around the 7-coordinate Cd centre (b).

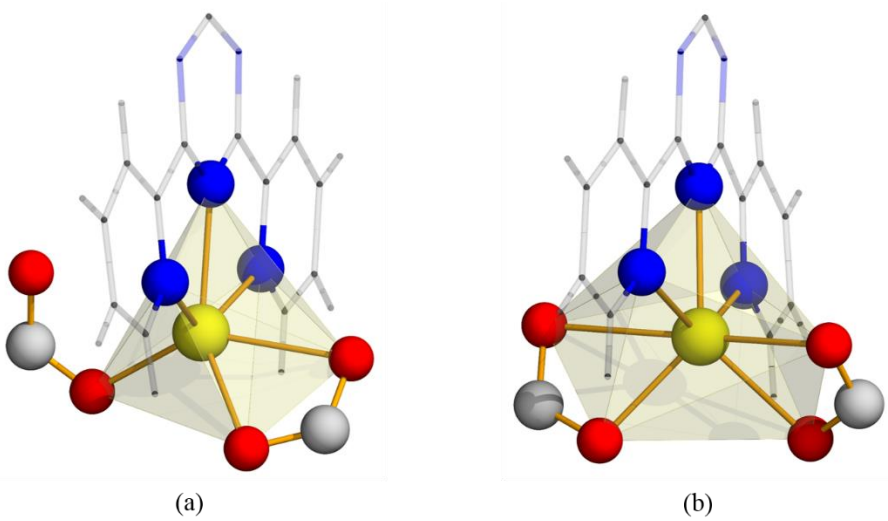

Figure 2.12 - Polyhedral representations of the coordination environment in 4 around the 6-coordinate Cd centre (left); and around the 7-coordinate Cd centre (right).

4 forms as a one-dimensional coordination polymer, and as in **3**, the asymmetric unit consists of two monomeric fragments from separate 1D chains (Fig. 2.10). In one of these, the fragment containing Cd1, the Cd(II) centre is 6-coordinated with one *syn-syn* symmetric carboxylate chelating mode, and one *syn*-monodentate mode resulting in a distorted octahedral geometry. In the other fragment the Cd(II) centre is 7-coordinated and both carboxylates show *syn-syn* symmetric chelating modes forming a capped trigonal prismatic geometry (Fig. 2.11, 2.12). In both fragments, the 2-tpt ligand acts as a tridentate chelating ligand around the Cd(II) centre. Due to disorder associated with the btb ligand moiety in the Cd1 centred fragment, interatomic distances and angles reported are based on part A from the structural model (Table 2.4).

Table 2.4 - Selected interatomic distances and angles in 4.

Atoms	Distance		Atoms	Angle
Cd1-O7	2.234(9) Å		O1-Cd1-O4	143.7(8)°
Cd1-O8	2.569(9) Å		O1-Cd1-N3	99.2(7)°
Cd1-O11	2.346(9) Å		N1-Cd1-N3	135.6(4)°
Cd1-O12	2.342(9) Å		O3-Cd1-O4	54.7(3)°
Cd1-N1	2.43(1) Å		O4-Cd1-N2	94.6(3)°
Cd1-N2	2.315(9) Å		N1-Cd1-O4	89.6(3)°
Cd1-N3	2.42(1) Å			
Cd2-O1A	2.10(3) Å		O8-Cd2-O12	168.0(3)°
Cd2-O2	2.82(3) Å		O11-Cd2-O12	56.5(3)°
Cd2-O3	2.28(9) Å		O7-Cd2-O8	54.7(3)°
Cd2-O4	2.486(9) Å		N7-Cd2-N9	136.2(4)°
Cd2-N1	2.43(1) Å		N8-Cd2-O12	95.3(3)°
Cd2-N2	2.33(1) Å		N7-Cd2-O12	83.9(3)°
Cd2-N3	2.41(1) Å			

1, **2**, **3**, and **4**, therefore are shown to consist of infinite one-dimensional coordination polymer chains. Each metal centre is bound to two $Hbtb^{2-}$ ligands *via* the carboxylate groups, as well as one 2-tpt ligand. Two of the peripheral benzoate groups of each $Hbtb^{2-}$ ligand bind to a metal centre, leaving one protonated benzoic acid group unbound and pendant in the structure. The 2-tpt ligand, in which one pyridyl ring remains uncoordinated, acts as a capping group for the metal centres through a chelating coordination mode (A^1, Fig. 2.2). This impairs the formation of oligonuclear secondary building units (SBUs) and leads to structures based on mononuclear metal centres, providing a valuable platform to assess the impact of the characteristics of single metal ions as nodes around which supramolecular architectures are built. Together, the two ligands give rise to 1D polymeric chains with uncoordinated N- and O- donors. All four structures form honeycomb-like 2D networks which are stabilised by hydrogen bonds between the protonated moiety of the $Hbtb^{2-}$ ligand and the carboxylate group of a deprotonated $Hbtb^{2-}$ arm (Fig. 2.13).

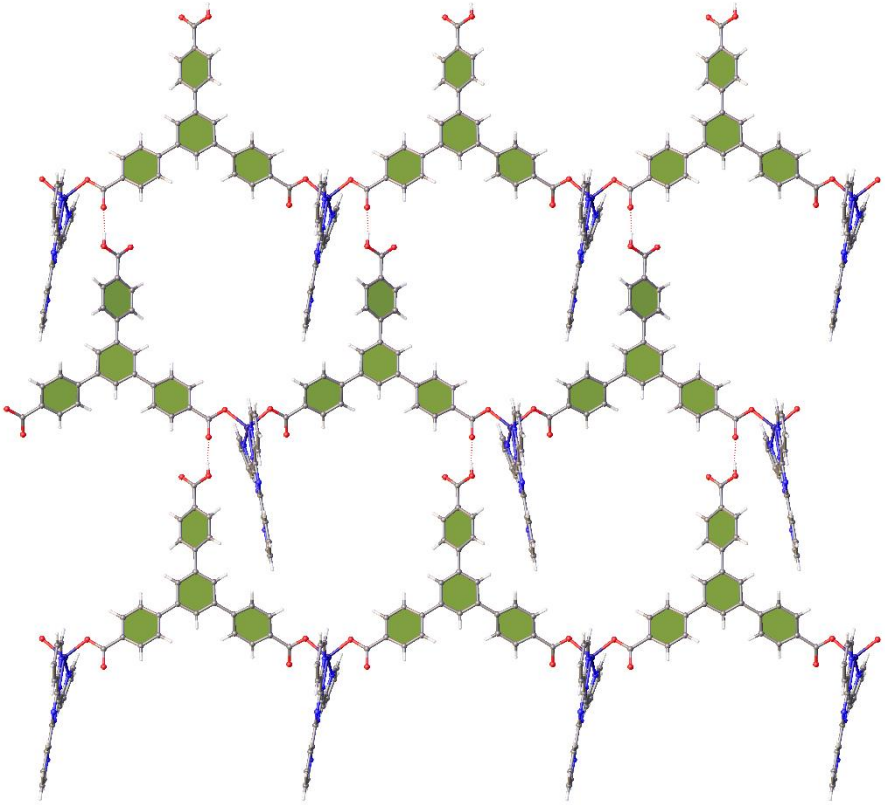

Figure 2.13 – The H-bonded 2D honeycomb motif in 1 as viewed down the crystallographic c-axis, which is representative of the structure present in all four 1D CPs – 1, 2, 3, and 4.

The geometries of coordination environments around the metal centres in **1**, **2**, **3**, and **4**, were analysed using *Shape V2.1*.[24] The results of the analysis are given in Table 2.5 below, and confirm the initial assessments of coordination geometry in the coordination polymers.

Table 2.5 - Results of the geometrical analysis of the coordination environment in 1, 2, 3, and 4, with *Shape V2.1*. Continuous shape measure values are given. Lower values correspond to more appropriate assignment of geometry.

1	Square pyramid	Trigonal bipyramid	Vacant octahedron
	3.418	4.893	5.009
2	Octahedron	Trigonal prism	
	4.873	8.861	
3	Capped octahedron	Capped trigonal prism	
	2.933	3.258	
4	Capped trigonal prism	Capped octahedron	
	3.312	4.566	

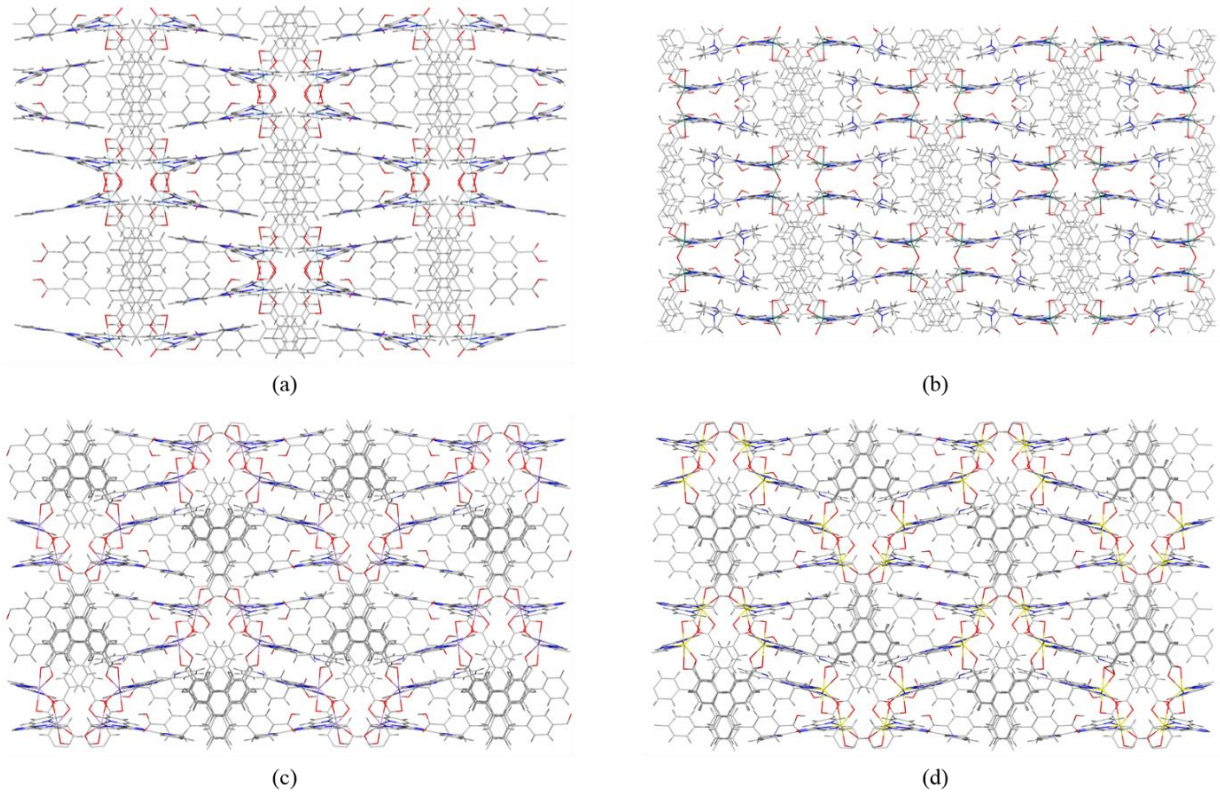

Figure 2.14 (a – d) – Representations of the overall packing in 1, 2, 3, and 4 respectively, viewed along the approximate 2-tpt planes and perpendicular to the approximate $Hbtb^{2-}$ planes (*c*-direction in 1, 2; *a*-direction in 3, 4). The differences in alignment of phenyl rings are apparent. Solvent molecules omitted for clarity.

The packing in all four CPs is stabilised by extensive aromatic interaction between the $Hbtb^{2-}$ ligands (Fig. 2.14). For the compounds containing the smaller metal ions, **1** (Zn^{2+}) and **2** (Ni^{2+}), two different stacking modes occur in the crystal structures, which we name *type 1* and *type 2* (Figure 2.15, Table 2.6). *Type 1* stacking occurs between two $Hbtb^{2-}$ ligands that are rotated 180° to each other leading to pairwise, somewhat offset, aromatic interactions between pairs of central and peripheral phenyl rings. In *type 2* stacking the $Hbtb^{2-}$ ligands are rotated 180° relative to each other and there is an offset overlap between two pairs of peripheral phenyl rings. Further, in **1** and **2**, the $Hbtb^{2-}$ ligands are stacked in a *1-2-1-2* fashion adopting alternating *type 1* and *type 2* stacking, in sequence, throughout the structure. Pairs of CP chains participating in *type 2* stacking are additionally weakly associated through aromatic interactions of the 2-tpt ligands which are aligned perpendicular to the $Hbtb^{2-}$-based sheets (Fig. 2.16). *Type 1* stacking CP pairs do not show stabilising interactions between 2-tpt ligands.

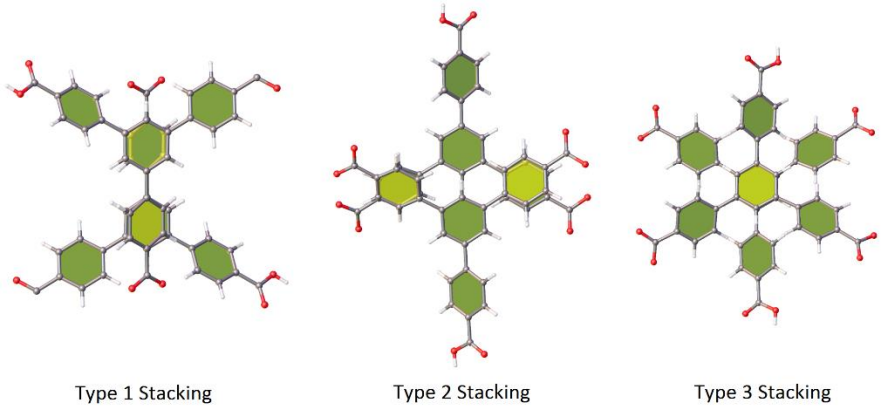

Figure 2.15 – The classification of aromatic stacking interaction modes used to distinguish between the supramolecular structures of 1, 2, 3, and 4.

In general, the strength of aromatic interactions is understood to be dependent on the angle between the two π-systems and is related to the magnitude of the inter-plane distance between aromatic systems.[25,26] Misalignments, tilting effects, and the consequent increased inter-plane distances hinder aromatic interactions, and therefore, they become less favourable within a supramolecular arrangement. π-conjugation within a benzoate group aligns the carboxylate plane with the phenyl plane.[27] The phenyl rings of the $Hbtb^{2-}$ ligand, however, are naturally non-coplanar with respect to each other because of the steric repulsion from aryl protons on adjacent rings (H_{Ar} - H_{Ar} repulsion). Torsion angles *ca.* 35°-45° between phenyl rings in biphenyl-type pairs are energetically the most favourable and are typically encountered in the literature.[28]

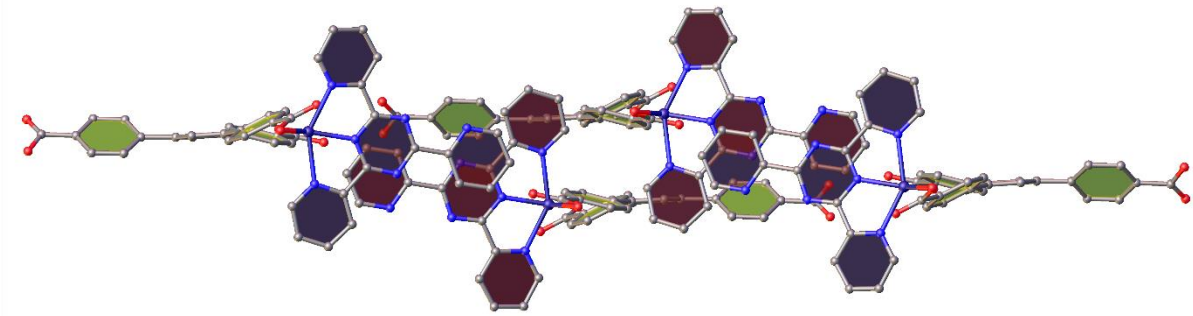

Figure 2.16 – Aromatic interactions between 2-tpt ligands (aromatic systems highlighted in navy blue), viewed along the crystallographic *b*-direction in 1.

In **1** and **2,** in which monodentate carboxylates are present in every CP chain, angles between phenyl ring planes are within this limit, as the uncoordinated carboxylate oxygen

atom enables the facile rotation of the benzoate group to accommodate this preferred geometry, ensuring the accommodation of preferred angles both in the coordination environment of the metal and between phenyl planes. Only in the case of the larger M(II) ions, Mn (**3**) and Cd (**4**), the bidentate binding mode and subsequent steric repulsion of the oxygen atoms leads to an increase of the angle between the two carboxylate groups bound to the same (7-coordinate) metal ion from 41° up to 69°. Thus, the modified coordination environment of the metal ions extends to the aromatic system of the ligand and influences the relative orientations of the phenyl rings, leading to less favourable aromatic interactions between the 2D sheets. Centroid-centroid distances and interplanar angles between phenyl rings in the case of *type 2* stacking increase from 3.6 Å and 14.8° in **1** to 5.0 Å and 46.4° (outside the range of conventional π- π interactions) in **3** as a result of the steric repulsion from the coordination environment. While *type 1* and *type 2* stacking modes are observed in **3** and **4**, reduced favourability for stabilising π-π interactions forces the structures to accommodate a third, distinct stacking arrangement that governs the packing of the 2D sheets. This *type 3* stacking arrangement is facilitated by two $Hbtb^{2-}$ ligands that are rotated 180° to each other around the perpendicular axis of the central benzene ring (Fig. 2.15). Consequently, the honeycomb type sheets in **3** and **4** stack in *1-2-1-3* fashion instead of *1-2-1-2*. Thus, this flexibility in packing enables the system to accommodate various metal ions with relatively large differences in ionic radius (Figure 2.17, Table 2.6).

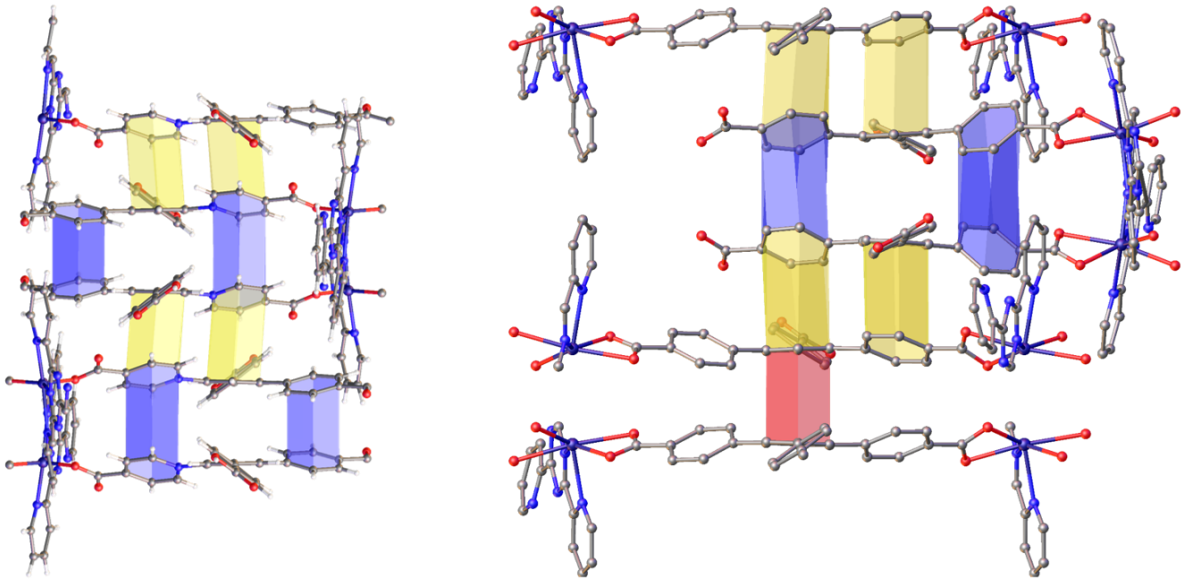

(a) (b)

Figure 2.17 – The *1-2-1-2* stacking mode in 1 (left); the *1-2-1-3* stacking mode in 3.

The challenge posed by unfavourable steric effects due to ion size in the 1D polymeric structure is overcome by rearrangements in the three dimensional packing illustrating a hierarchical supramolecular response to a local modification created at the metal centre. Hirshfeld surface analyses (Appendix 9.1) were carried out in order to gain a better understanding of the locations of the short contacts associated with these interactions.[29,30] Decomposed fingerprint plots for percent values corresponding to C···C and C···H interactions were used as an indicator of the prevalence of the π-π interactions and the π-system overlap. Tilting of the benzene rings results in a higher C···H and lower C···C contribution and therefore raises the C···H/C···C ratio (an *ad hoc* measure of the extent to which pairwise π-stacking is offset), as stacking phenyl rings become more misaligned. This ratio is positively correlated with the ion size of the transition metal (Appendix 9.1.3). The ratios increase from 3.9 for the smallest to 6.1 for the largest metal ion in the series. (Table 2.6). Importantly, the locations of C···C contacts and O···H contacts as shown by Hirshfeld surface analysis agree very well with the identified stacking sequences and hydrogen bonds (Fig. 2.18).

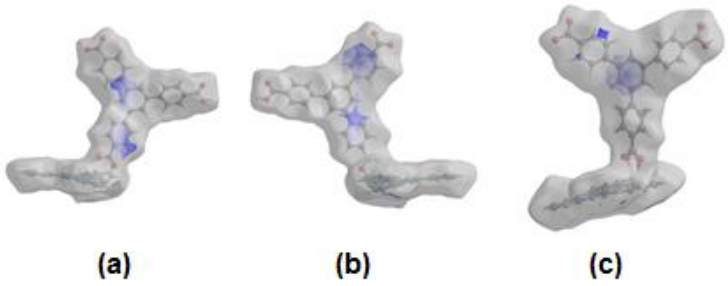

Figure 2.18 – C··· C contacts corresponding to (a) *type 1*, (b) *type 2*, (c) *type 3* stacking modes mapped on to Hirshfeld surfaces generated for the asymmetric units of 1 (a, b) and 3 (c) respectively.

Table 2.6 - Comparison of structural features in 1-4.

	1 – Zn	**2 – Ni**	**3 – Mn**	**4 - Cd**
Coordination	5-c	6-c	6,7-c	6,7-c
COO^- denticity	Mono	Mono, bi	Mono, bi	Mono, bi
Ionic radii[31]	0.68	0.69	0.9	1.03
Crystal radii[31]	0.82	0.83	1.04	1.17
Stacking modes	A,B	A,B	A,B,C	A,B,C
Stacking sequence	*1-2-1-2*	*1-2-1-2*	*1-2-1-3*	*1-2-1-3*
M-O distances	1.94	1.95	2.17 – 2.41	2.14 – 2.56
M-N distances	2.06 – 2.27	1.89 – 2.10	2.22 – 2.35	2.29 – 2.40
Shape analysis	Square pyramidal	Octahedral	Capped octahedral	Capped trigonal prismatic
Plane angle (°)	41.164	14.097/48.081	45.019(47.624)/69.299	45.594/69.412
Hirshfeld C···C (%)	6.8	5	5.3	5.3
Hirshfeld C···H (%)	26.7	22.8	28.1	32.2
C···C/C···H ratio	3.9	4.6	5.3	6.1

In addition, Hirshfeld surface analysis also confirms the role of the pendant protonated carboxylic acid moiety in forming short H-bonding interactions with oxygen atoms from deprotonated carboxylate groups, resulting in the aforementioned 2D honeycomb-like motifs in all four compounds. The constitutional DMF solvent molecules do not play any apparent structural role in **1-4**, explaining the high degree of solvent disorder.

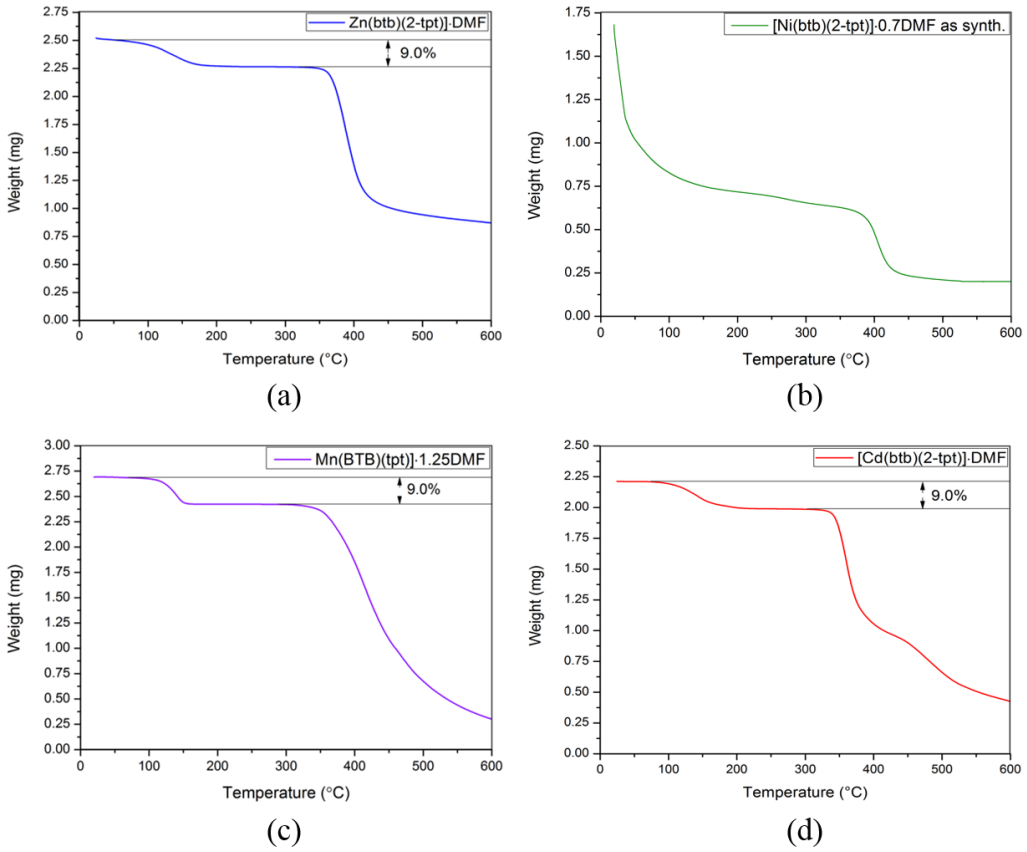

Figure 2.19 (a – d) – Thermogravimetric analysis for 1, 2, 3, and 4 respectively.

The thermal stability of the compounds was evaluated by thermogravimetric analysis, revealing stability up to 370°C upon which the organic ligands undergo degradation (Fig. 2.19). A preceding step corresponding to the loss of trapped DMF molecules at 120°C is observed for all investigated compounds. The relatively high temperature for the onset of solvent loss agrees well with the observation that in both kinds of packing arrangement, disordered DMF molecules are contained in inaccessible voids. Therefore, solvent loss can only occur with a related structural deformation. Phase-purity of the as-synthesised crystalline materials was assessed by powder X-ray diffraction studies (Fig. 2.20). While **1** and **4** appear phase pure, PXRD patterns from **2** and **3** indicate the presence of impurities in significant quantity.

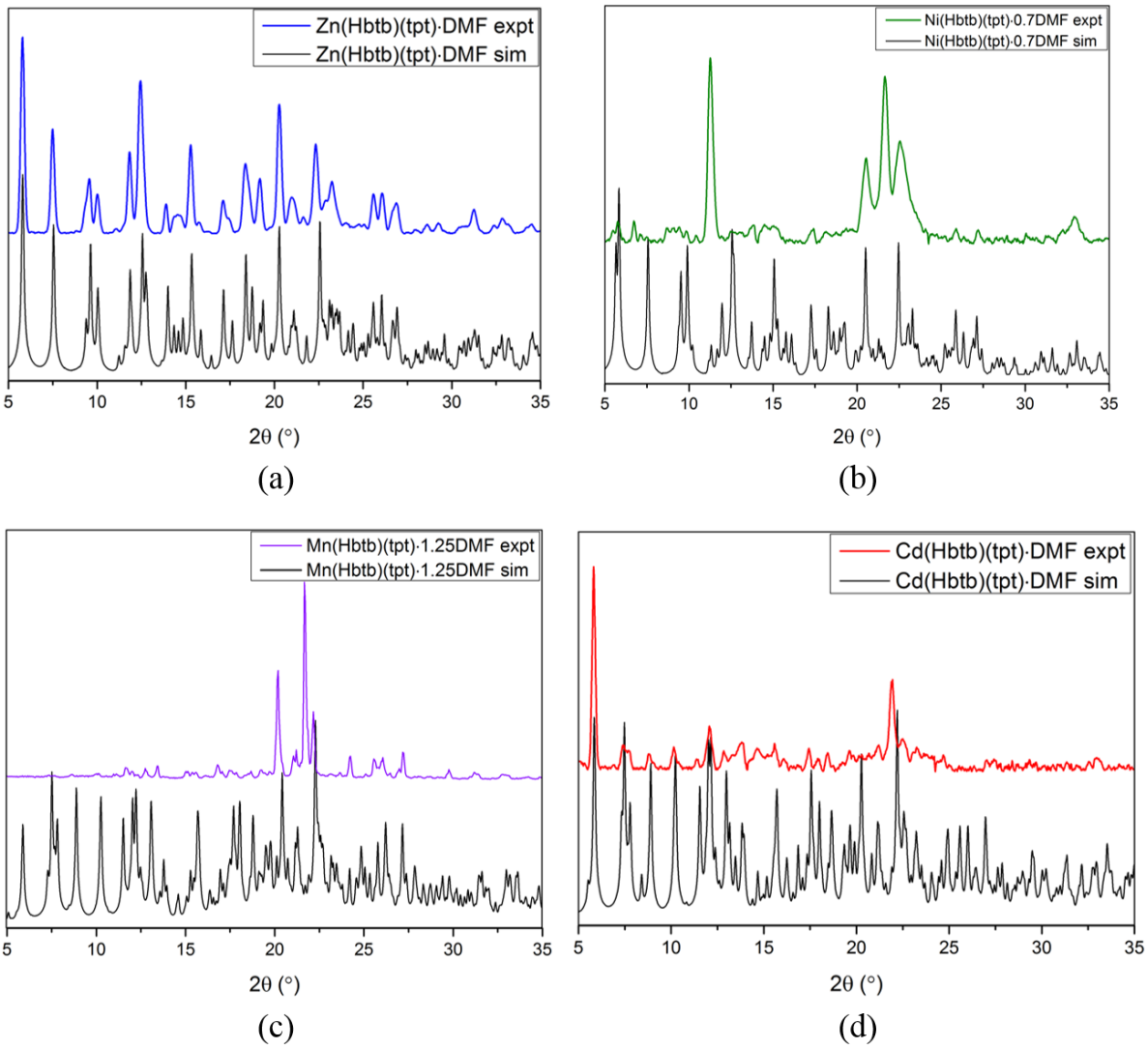

Figure 2.20 (a – d) – X-ray powder patterns of compounds 1 (blue: experimental; black: calculated), 2 (green: experimental; black: calculated), 3 (purple: experimental; black: calculated) and 4 (red: experimental; black: calculated) respectively.

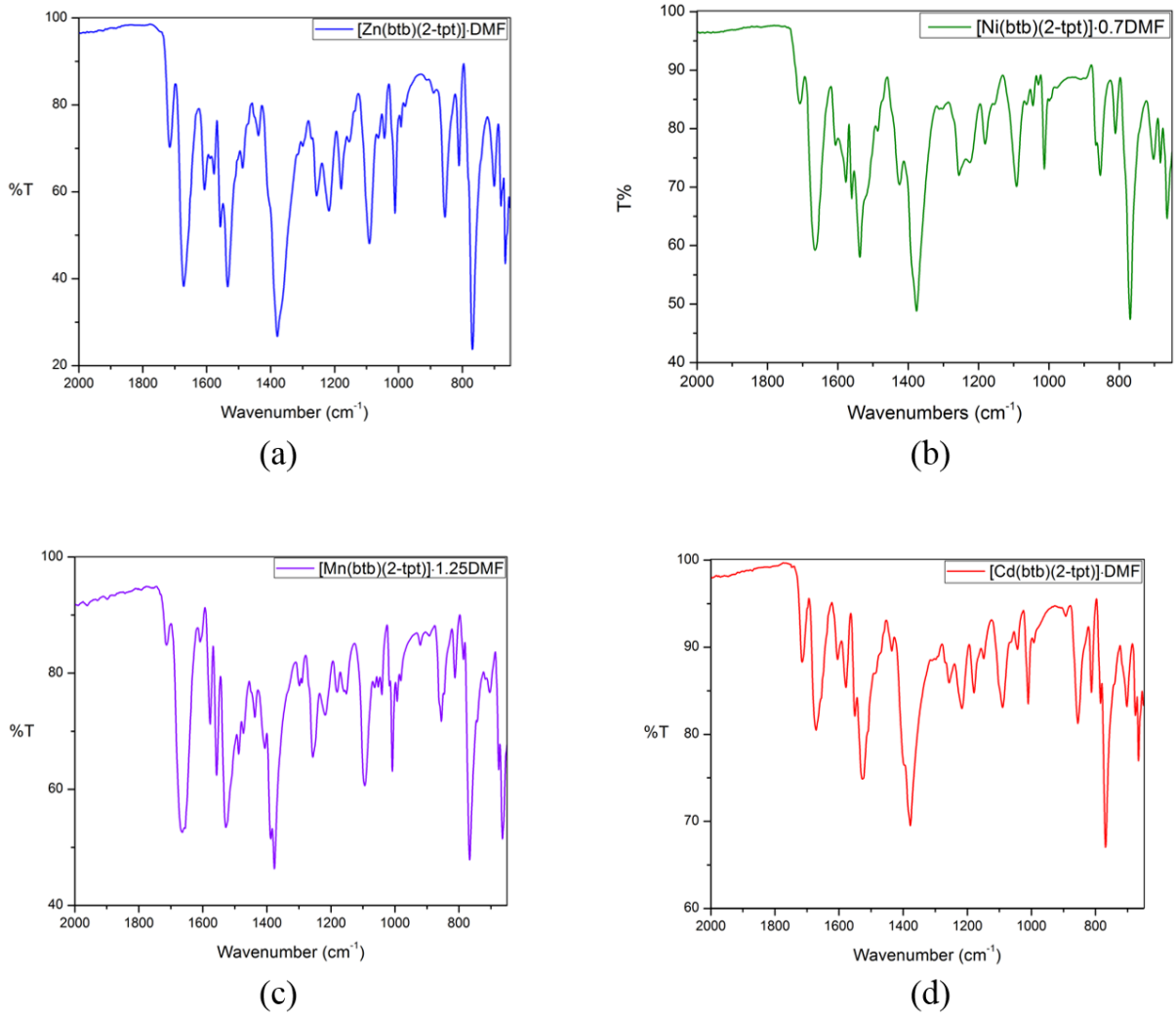

Figure 2.21 (a – d) - FTIR spectra of compounds 1, 2, 3, and 4 respectively.

Bulk characterisations for **1**, **3**, and **4** was carried out. FTIR spectroscopy resulted in remarkably similar spectra for **1**–**4**. The strong peak at *ca.* 1690 cm^{-1} is due to the C=O stretch in the constitutional DMF molecules, and the strong peak at *ca.* 1380 is assigned to the stretching vibrations of the triazine and pyridyl rings of the 2-tpt ligand (Fig. 1.21). Unambiguous peak assignment for the remaining peaks between 1570 and 1350 cm^{-1} is complicated by adjacent occurrence of the modes associated with the free carboxylic acid group, the symmetric carboxylate stretch due to the bound carboxylate groups, C=C and C=N stretching modes, and the co-existence of 6- and 7- coordinate modes in **3** and **4**. The sharp peak at ca. 790 cm^{-1} is assigned to the characteristic C-H bending mode in the coordinated 2-tpt ligand.[32]

In compound **2**, supplementary characterisation does not agree with the structural model obtained by single crystal X-ray diffraction. Examination of the product mixture showed that the major component was a brown polycrystalline phase, in which green single crystals of **2** were distinctly visible. FTIR studies of the as-synthesised product mixture showed only minor deviations and intensity differences to those obtained from **1**, **3**, and **4**, suggesting that the polycrystalline phase also consists of Ni, and both btb and 2-tpt ligands. The early onset and large magnitude of solvent loss in the thermogravimetric trace suggest a porous structure. PXRD peaks do not correspond to any reported complex of Ni with either btb or 2-tpt ligands, or the crystal structures of the free ligands H_3btb or 2-tpt.

We postulate that the synthetic difficulty in the case of **2** is due to the outer $3d^8$ electronic configuration in Ni^{2+}, as opposed to the half-filled $3d^5$ configuration in Mn^{2+}, and the fully filled $3d^{10}$ and $4d^{10}$ in Zn^{2+} and Cd^{2+} respectively. While ligand field stabilisation effects are negligible in **1**, **3**, and **4**, the highly distorted octahedral geometry in **2** is destabilised relative to ideal octahedral or other geometries that could be afforded by solvation, or undistorted octahedral ligand coordination on the Ni^{2+} ions. This effect is likely to contribute to the observed phase impurity which is formed with **2**, and the low yield of **2** overall. Crystallographic details for **1**-**4** are given below (Table 2.7).

Table 2.7 - Crystallographic details for 1-4.

Identification code	1	2	3	4
Empirical formula	$C_{48}H_{35}N_7O_7Zn$	$C_{47.1}H_{32.9}N_{6.7}NiO_{6.7}$	$C_{48.75}H_{36.75}MnN_{7.25}O_{7.25}$	$C_{48}H_{35}CdN_7O_7$
Formula weight	887.20	858.61	895.04	934.23
Temperature/K	100(2)	100(2)	100(2)	100(2)
Crystal system	monoclinic	monoclinic	monoclinic	monoclinic
Space group	*C*2/*c*	*C*2/*c*	$P2_1/c$	$P2_1/c$
***a*/Å**	33.908(2)	34.7205(18)	16.2604(6)	16.281(3)
***b*/Å**	17.5051(13)	17.3089(6)	17.3810(6)	17.516(3)
***c*/Å**	15.7559(13)	15.8202(7)	30.3417(10)	30.291(4)
***α*/°**	90	90	90	90
***β*/°**	115.591(5)	115.923(2)	101.280(2)	100.546(3)
***γ*/°**	90	90	90	90
Volume/Å^3	8434.6(12)	8550.9(7)	8409.6(5)	8492(2)
Z	8	8	8	8
ρ_{calc}g/cm^3	1.397	1.333	1.414	1.461
μ/mm^{-1}	1.325	1.093	3.088	0.576
F(000)	3664.0	3316.0	3704.0	3808.0
Crystal size/mm^3	0.14 × 0.06 × 0.02	0.16 × 0.06 × 0.05	0.16 × 0.09 × 0.08	0.3 × 0.25 × 0.15
Radiation/Å	CuKα (λ = 1.54178)	CuKα (λ = 1.54178)	CuKα (λ = 1.54178)	MoKα (λ = 0.71073)
2θ range for data collection/°	5.78 to 116.178	5.66 to 137.15	5.084 to 136.946	2.326 to 50.852
Index ranges	-37 ≤ h ≤ 37, -17 ≤ k ≤ 19, -17 ≤ l ≤ 13	-36 ≤ h ≤ 41, -20 ≤ k ≤ 20, -19 ≤ l ≤ 18	-17 ≤ h ≤ 19, -20 ≤ k ≤ 20, -36 ≤ l ≤ 35	-19 ≤ h ≤ 14, -21 ≤ k ≤ 19, -33 ≤ l ≤ 36
Reflections collected	20659	53655	58048	73384
Independent reflections	5802 [R_{int} = 0.0549, R_{sigma} = 0.0541]	7864 [R_{int} = 0.0912, R_{sigma} = 0.0508]	15442 [R_{int} = 0.0460, R_{sigma} = 0.0370]	15578 [R_{int} = 0.0714, R_{sigma} = 0.0747]
Data/restraints/parameters	5802/57/583	7864/2095/999	15442/422/1334	15578/492/1300
Goodness-of-fit on F^2	1.029	1.045	1.029	1.186
Final R indexes [I>=2σ (I)]	R_1 = 0.0623, wR_2 = 0.1664	R_1 = 0.0996, wR_2 = 0.2742	R_1 = 0.0636, wR_2 = 0.1723	R_1 = 0.1267, wR_2 = 0.2510
Final R indexes [all data]	R_1 = 0.0829, wR_2 = 0.1826	R_1 = 0.1612, wR_2 = 0.3409	R_1 = 0.0781, wR_2 = 0.1847	R_1 = 0.1881, wR_2 = 0.2798
Largest diff. peak/hole / e Å^{-3}	1.19/-0.67	0.48/-0.33	0.85/-0.72	2.87/-2.42

2.3: Compound **5**, $[Co_3(btb)_2(4\text{-tpt})_2(DMF)_2]$

In order to assess the effect of using the 4-tpt ligand as a capping group rather than the chelating 2-tpt ligand, together with M^{2+} and H_3btb, elevated temperature syntheses were attempted. Compound **5**, $[Co_3(4\text{-tpt})_2(btb)_2(DMF)_2]$, was synthesised by heating a solution of cobalt(II) nitrate hexahydrate with 4-tpt and H_3btb in DMF at 85°C for two days. Single crystal X-ray diffraction shows that **5** crystallises in the monoclinic crystal system and the *C*2/*c* space group, with cell dimensions of a = 21.6326(11) Å, b = 25.9274(11) Å, c = 16.7966(7) Å, and $\alpha = \gamma = 90°$, β = 98.702(3)°. The compound is a coordination polymer which extends in two dimensions. The structure is composed of trinuclear $\{Co_3\}$ secondary building units (SBUs), linked to six carboxylate groups from six distinct btb ligands. The central Co ion has an octahedral $\{CoO_6\}$ coordination environment and is surrounded by six carboxylate oxygens, while the exterior Co ions have distorted octahedral $\{CoO_5N\}$ environments and are supported by four carboxylate oxygen atoms, an O-donor atom from a terminal DMF ligand, and an N-donor atom from a 4-tpt pyridyl ring (Fig. 2.22). The $\{Co_3\}$ unit is symmetric to inversion through the central Co^{2+} ion.

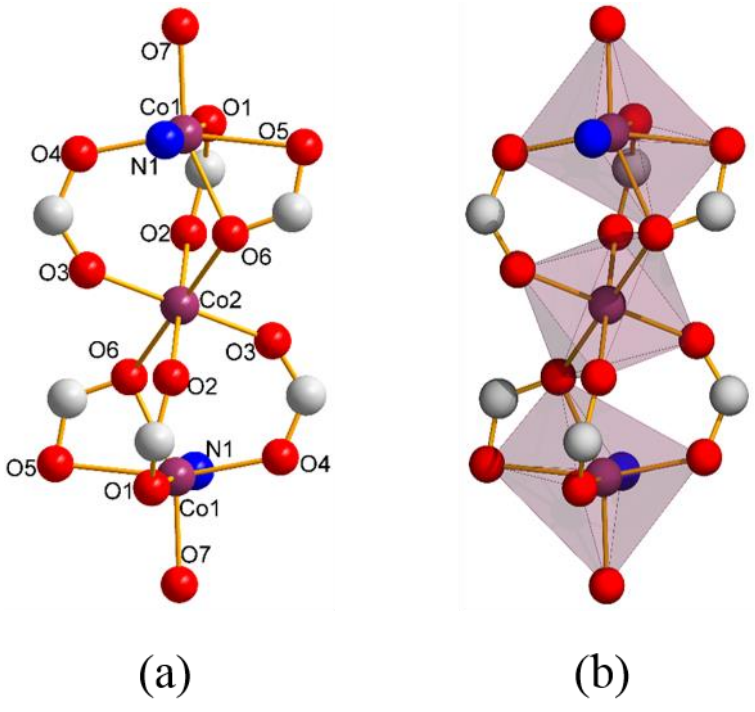

Figure 2.22 - The SBU in 5 with labelled atoms (a); and a polyhedral representation of the SBU (b).

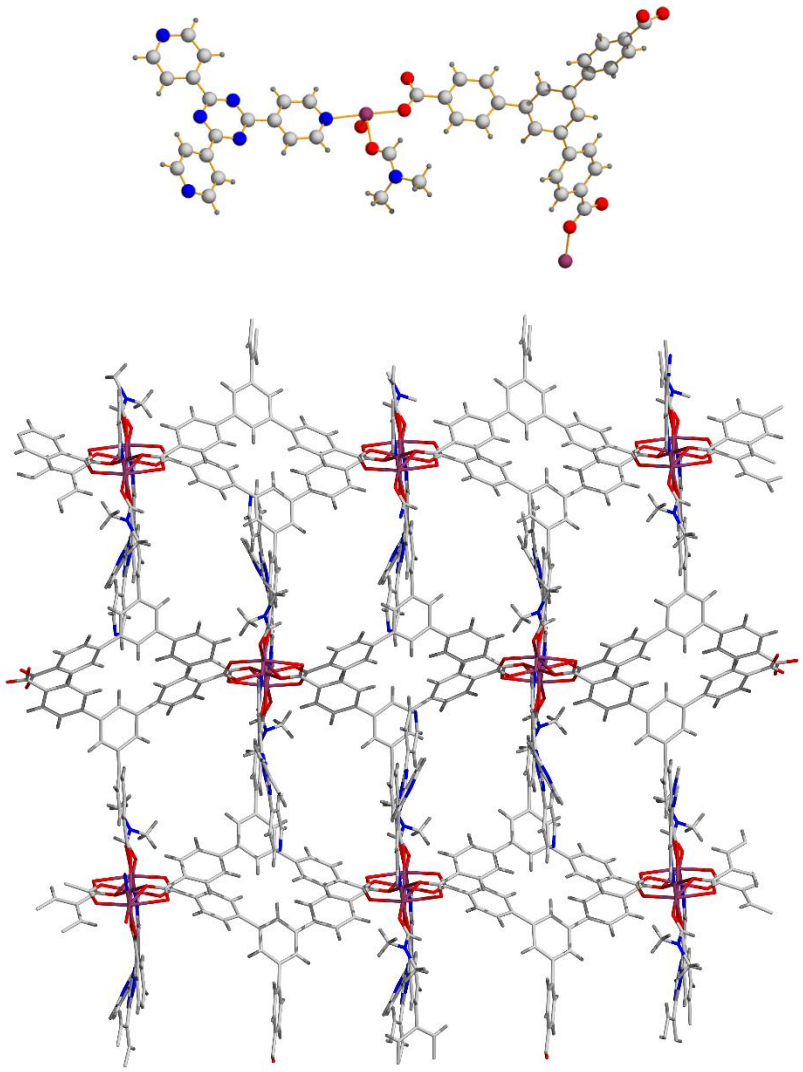

Figure 2.23 – A representation of the asymmetric unit of 5 (above), and a representation of a single 2D sheet of 5 (below). Colour scheme: violet, Co; blue, N; red, O; grey, C; dark grey, H.

The asymmetric unit of **5** consists of two crystallographically independent Co^{2+} centres, Co1 and Co2, one fully deprotonated btb^{3-} ligand, and one 4-tpt ligand, where Co2 represents the symmetry-related terminal metal centres of the SBU. The Co1-Co2-Co1' angle is 180.00°, and the Co1-Co2 distance is 3.4524(8) Å (Fig. 1.23). The contribution from the highly disordered constitutional solvent molecules was removed using the Squeeze routine (PLATON).[23]

The Co(II) centre at the core of the SBU (Co2) is coordinated to six O-donor atoms from six different btb ligands, and adopts octahedral geometry. The peripheral Co1 centres are coordinated to four O-donor atoms from btb ligands that also bind to Co2 in bridging μ_2-(O1, O2) and μ_2-(O4, O3) modes. O5 and O6 are O-donors from the same carboxylate

group and bind in a chelating fashion to Co1. O6 also binds to Co2, resulting in an overall bridging chelate μ_2-(O5, O6, O6) mode. O6 occupies the internal apex of the Co1 coordination environment. The external apex is occupied by O7, an O-donor atom from a coordinated *N*,*N*-dimethylformamide (DMF) ligand. The final equatorial position is occupied by N1, from the 4-tpt ligand. Selected interatomic distances and angles are listed in Table 1.8.

Table 2.8 - Selected interatomic distances and angles in 5.

Atoms	Distance		Atoms	Angle
Co2-O2	2.102(3) Å		Co1-Co2-Co1′	180°
Co2-O3	2.102(3) Å		O1-Co1-O7	88.1(2)°
Co2-O6	2.126(4) Å		N1-Co1-O7	89.0(2)°
Co1-O6	2.107(3) Å		O5-Co1-O6	58.4(1)°
Co1-O5	2.345(4) Å		O1-Co1-O4	95.8(1)°
Co1-O4	2.047(4) Å		O1-Co1-O6	155.2(2)°
Co1-O7	2.059(4) Å		O2-Co2-O3	83.5(1)°
Co1-O1	2.024(4) Å		O2-Co2-O2′	180.0(1)°
Co1-N1	2.146(5) Å		O6-Co2-O3	88.1(1)°

Each btb ligand is linked to three {Co_3} SBUs. Each 4-tpt ligand, however, is only bonded to a single Co atom, and acts as a monotopic, π-electron rich capping group rather than a linker. The structure is thus linked into two dimensional sheets based on 6-connected SBUs and 3-connected ligands. The overall net is a (3,6)-connected kagome-dual **kgd** net with a (3-c)$_2$(6-c) stoichiometry and an overall point symbol of $\{4^3\}_2\{4^6.6^6.8^3\}$ (Fig. 2.24).

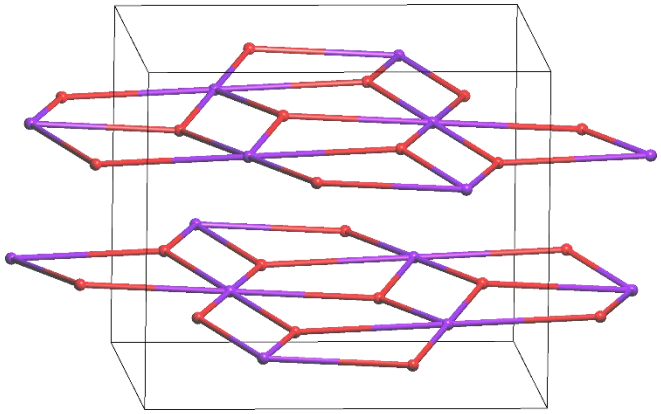

Figure 2.24 - The topological reduction of 5 into kgd networks. 3-connected nodes representing ligands are in red. 6-connected nodes representing {Co_3} SBUs are in purple.

On closer examination of the crystal structure, weak interactions are found to play a key role in organising the structure in **5**, at both the 2D and the 3D levels. The overall packing is illustrated in Fig. 2.25. The organisation of adjacent hourglass SBUs bridged by a pair of btb ligands is stabilised by aromatic stacking interaction between both pairs of peripheral btb phenyl rings (centroid – centroid distance = 3.9397(1) Å). This helps provide the coplanar arrangement of btb ligands necessary for the formation of **kgd** sheets. In addition, the capping pyridyl moieties on adjacent **kgd** nets also participate in pairwise aromatic stacking interactions along the crystallographic *c*-axis (centroid – centroid distance = 4.0167(1) Å), determining the spatial relationship of each 2D net with the two nets above and below (Fig. 2.26). The overall 3D structure of **5** is therefore assembled based on both strong coordination bonds and weak aromatic stacking interactions. Hirshfeld surface analysis applied to the asymmetric unit of **5** shows C···C short contacts corresponding to the stacking modes observed (Appendix 9.1).[29] Approximately 6% of the overall Hirshfeld surface can be assigned to C···C contacts, with another 24.9% assigned to C···H and H···C contacts.

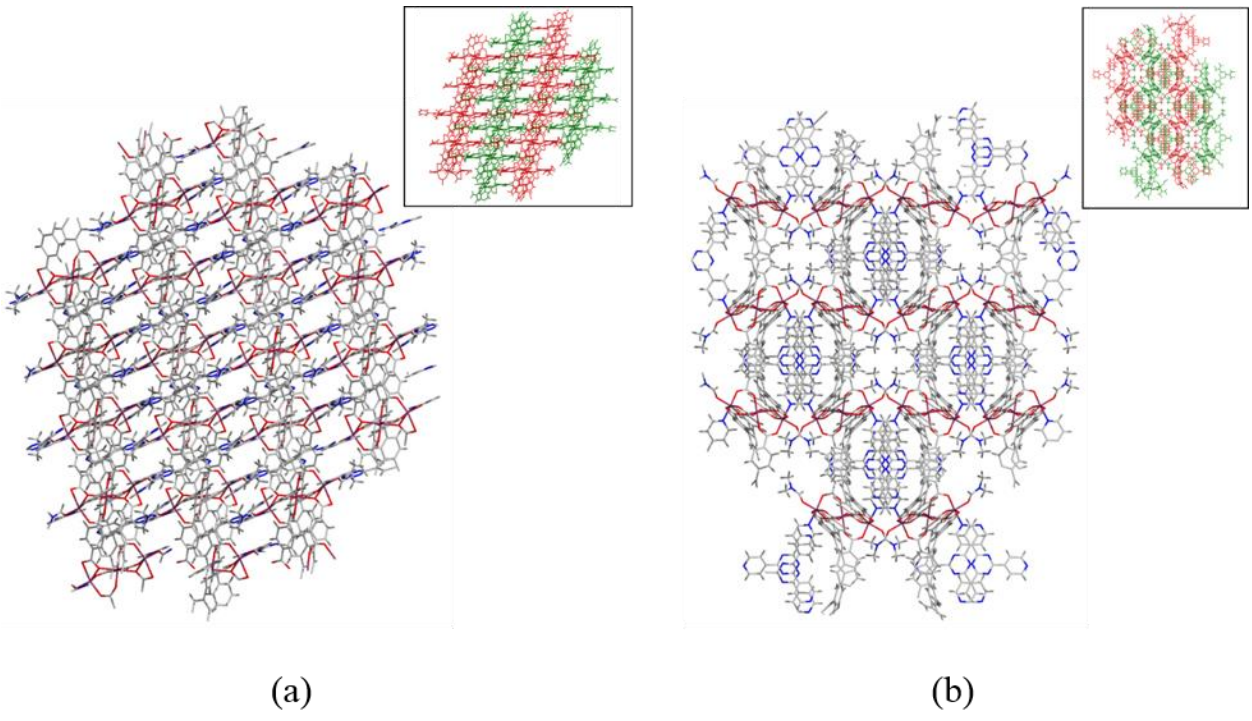

Figure 2.25 – Wireframe representations of 2x2x2 supercells of 5 viewed along the crystallographic *b*- (a) and *c*- (b) directions. Insets: relative orientations of alternating 2D sheets coloured red and green respectively.

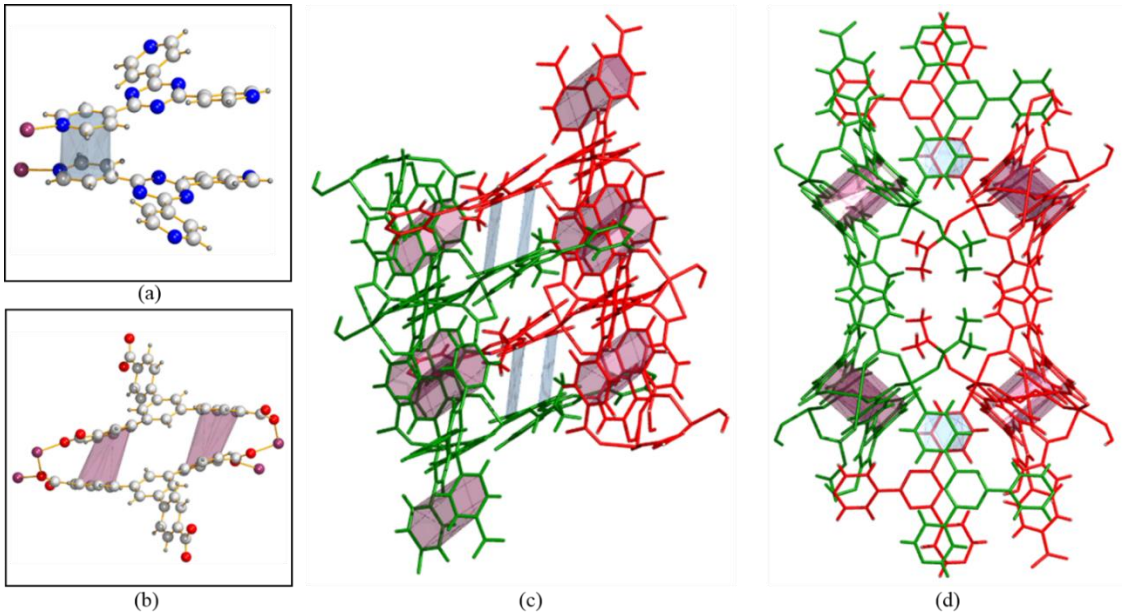

Figure 2.26 – Aromatic interactions between bonding terminal pyridyl rings of the 4-tpt ligands, highlighted in light blue (a) and between btb ligands, highlighted in maroon (b) in 5; and representations of these interactions in the extended structure of 1 along the crystallographic *b*- (c) and *c*- (d) directions.

Due to the interplay of a number of structure-directing factors, comparisons to two published structures in particular are relevant. In 2016, Zhang et al. reported the synthesis of a 3D coordination polymer based on btb and 4-tpt ligands, and a triangular, μ_3-OH centred $\{Co_3\}$ SBU (CCDC: IMAJUD).[33] This coordination polymer adopts the **sit** topology, and the difference in SBU formation can be attributed to the use of MeOH as a co-solvent and the high temperature (120°C) and long reaction time (5 days) applied (Fig. 2.27).

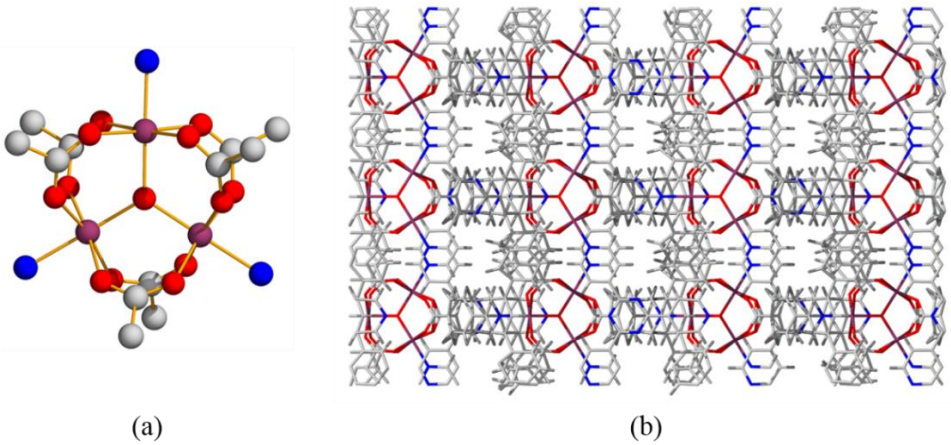

Figure 2.27 (a) – Ball-and-stick representation of the SBU in IMAJUD; (b) Wireframe representation of the *sit* net in IMAJUD (adapted from ref. 25).

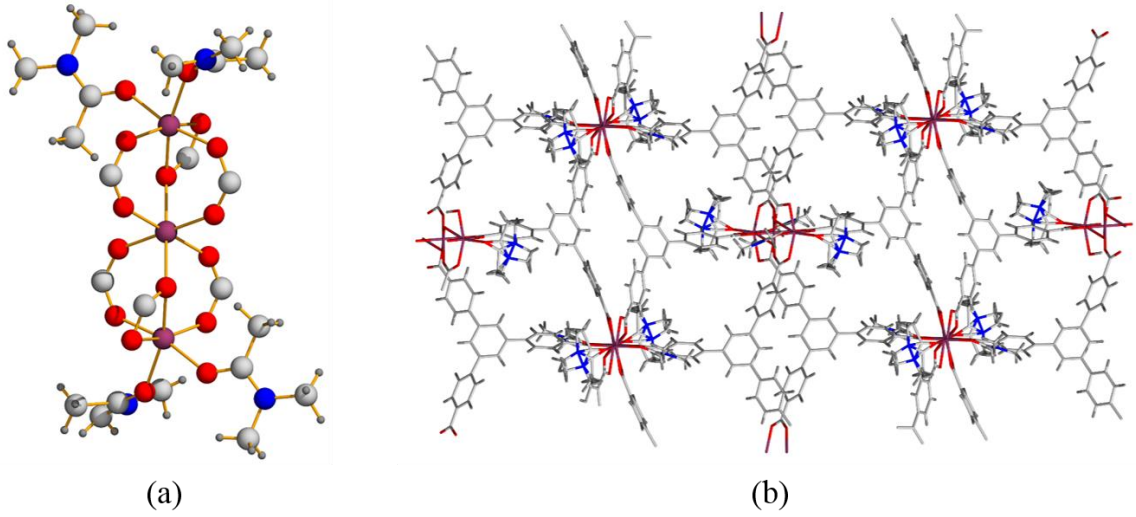

Figure 2.28 (a) – Ball-and-stick representation of the SBU in HELDIN; (b) Wireframe representation of the *kgd* net in HELDIN (adapted from ref. 26).

Kim et al. have reported a related MOF based on the single ligand approach, built with {Co_3} and btb (CCDC: HELDIN) which also has a **kgd** net, and is thus a useful reference to judge the role of the 4-tpt capping group, which is not a part of this structure (Fig. 2.28).[34] This framework is synthesised in DMA at 100°C in 10 days, resulting in a 39% yield. These synthetic conditions are a more thermodynamically forcing route to arrive at the **kgd** structure, with a significantly lower yield. Frameworks composed of Co^{2+} and H_3btb are common (40 entries in the CCDC at the time of writing). Synthetic conditions and concentrations for DUT-28 (CCDC: AXINAX; 90°C, DMF, 5 days) and SUMOF-1-Co (CCDC: CAVPEW; 85°C, DMF, 2 days; 4,4′-bipyridine co-ligand) are comparable, but result in different 3D nets.[35,36]

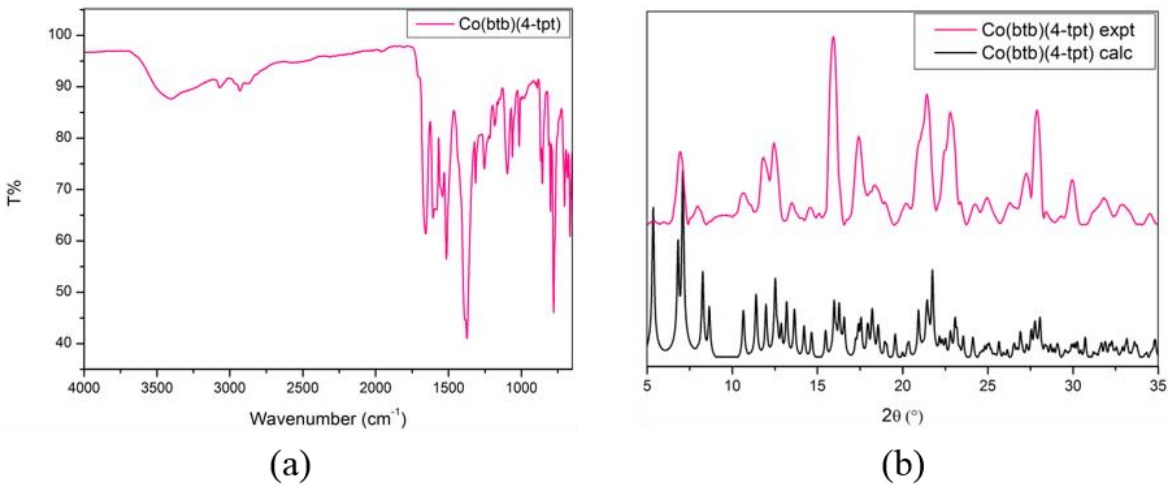

Figure 2.29 – (a) FTIR spectrum; (b) X-ray powder pattern for compound 5.

The phase purity of the crystalline sample obtained was investigated using powder x-ray diffraction (PXRD). The PXRD analysis is in reasonable agreement with the single crystal analysis, indicating bulk purity. Differences in peak intensities between measured and calculated patterns are attributed to preferred orientation effects due to the use of single crystals for data collection. FTIR spectroscopy was also carried out on compound **5** to investigate bulk purity. The spectrum is in good agreement with the structure as determined by X-ray diffraction, showing C=O stretching frequencies, as well as aromatic C=C and C=N stretching vibrations between 1659 and 1512 cm^{-1}. The strong peak at 1374 cm^{-1} is due to the prominent symmetric carboxylate stretching mode (ν_sCOO) (Fig. 2.29 (a)). The broad peak centred around 3401 cm^{-1} is due to hydrogen bonding interactions between pore DMF solvent and aryl protons in the framework (Fig. 2.29 (b)).

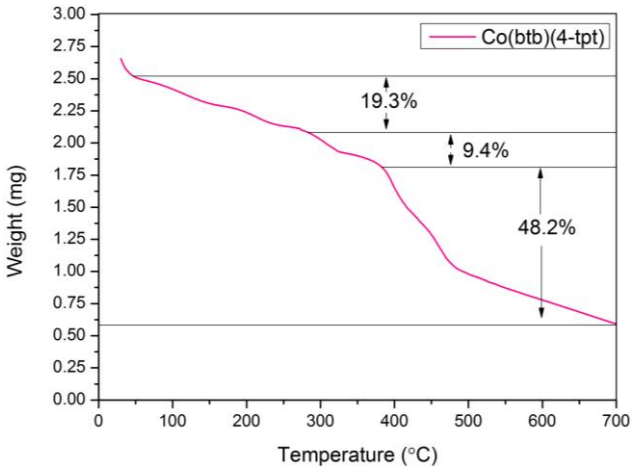

Figure 2.30 – TGA trace for compound 5.

The thermal stability was assessed using thermogravimetric analysis (TGA) under a nitrogen stream (Fig. 2.30). TGA reveals that some (ca. 2 wt.%) surface solvent evaporates before 40°C. Following this a steady decline in weight is observed corresponding to the loss of pore solvent accompanied by necessary structural deformations, since the pore windows in **5** are not sufficiently large to allow the loss of guests without framework deformation. This decline ends at 290°C, at which point a sharp ligand decomposition step is observed. Another such step is observed at 380°C.

Crystallographic details for **5** are given below (Table 2.9).

Table 2.9 - Crystallographic details for 5.

Identification code	5
Empirical formula	$C_{96}H_{68}Co_3N_{14}O_{14}$
Formula weight	1818.43
Temperature/K	100(2)
Crystal system	monoclinic
Space group	*C*2/*c*
***a*/Å**	21.6326(11)
***b*/Å**	25.9274(11)
***c*/Å**	16.7966(7)
***α*/°**	90
***β*/°**	98.702(3)
***γ*/°**	90
Volume/Å^3	9312.4(7)
Z	4
ρ_{calc}g/cm^3	1.297
μ/mm^{-1}	4.706
F(000)	3740.0
Crystal size/mm^3	0.08 × 0.07 × 0.06
Radiation/Å	CuKα (λ = 1.54178)
2θ range for data collection/°	5.356 to 118.128
Index ranges	$-24 \leq h \leq 23$, $-19 \leq k \leq 28$, $-13 \leq l \leq 18$
Reflections collected	20961
Independent reflections	6694 [R_{int} = 0.0528, R_{sigma} = 0.0666]
Data/restraints/parameters	6694/0/576
Goodness-of-fit on F^2	0.999
Final R indexes [I>=2σ (I)]	R_1 = 0.0723, wR_2 = 0.1988
Final R indexes [all data]	R_1 = 0.1011, wR_2 = 0.2187
Largest diff. peak/hole / e Å^{-3}	0.46/-0.45

2.4: Conclusion

Mixed tritopic ligand-based coordination polymer compounds **1**-**5** were synthesised, characterised and structurally analysed. The H_3btb ligand common to all five compounds is responsible for charge-balance of the SBU and structural extension in each case. In **1**, **2**, **3**, and **4**, the tridentate chelating mode of the 2-tpt ligand hinders the formation of polynuclear assemblies, leading to the recurrence of structurally related 1D motifs in all four compounds. This characteristic of the 2-tpt ligand provides a valuable synthetic handle over SBU formation and restricts the number of available coordination sites on the metal centre, thus playing a crucial structural role.

1, **2**, **3**, and **4** derive linear extension from the $Hbtb^{2-}$ ligand. The underlying structural flexibility of the polymer motif, derived from changes in tilt angles associated with coordinating benzoate groups, allows various coordination geometries around the M(II) centres to result in similar 1D polymers. The orientations of individual 1D CPs relative to each other is mediated by H-bonds from the protonated carboxylate of the $Hbtb^{2-}$ ligand to carboxylate oxygen atoms in adjacent chains, organising a 2D honeycomb structure in all four compounds. However, the 3D structures adopted by **1** and **2** are significantly different from those adopted by **3** and **4**, accompanied by differences in crystal parameters and space group. This is attributed to the coordination environments of the metal centres, in which steric effects result in tilting of ligand phenyl rings due to the flexibility of the btb ligand, affecting the relative stacking orientations of adjacent 2D honeycomb motifs.

In **5**, the 2-tpt ligand is replaced by 4-tpt, which does not have a chelating coordination mode, and Co^{2+} ions are used. The 4-tpt ligand acts as a π-electron rich capping group bound to the $\{Co_3\}$ hourglass-shaped SBU, and plays a vital role in structure direction, *via* aromatic interactions between adjacent 2D sheet CPs. **5** adopts the 2D **kgd** network based on the 6-connected $\{Co_3\}$ SBU and 3-connected, fully deprotonated btb linker. Free pyridyl groups from the 4-tpt ligand are pendant in the structure, while the bound pyridyl rings participate in pairwise aromatic interactions which orient the 2D sheets relative to each other.

Therefore, our initial hypothesis – that the use of the chelating 2-tpt ligand to hinder SBU formation in **1**-**4** was likely to result in a low-dimensional motif with a variety of metal

centres – was confirmed. The use of 4-tpt in **5** resulted in the adoption of a capping mode in a 2D CP based on {Co_3} SBUs. The 1D and 2D structures of **1**-**4** were compared and showed only minor differences. However, marked differences in the 3D crystal structures were traced back to the ionic radii of the metals used, and the resultant orientations of benzoate groups in $Hbtb^{2-}$ ligands, which in turn participated in the aromatic interactions governing 3D structure. In addition, the use of the 4-tpt ligand as a capping group was found to promote the formation of the **kgd** network, through favourable aromatic interactions.

2.5: References

1 C. T. Chen and K. S. Suslick, *Coord. Chem. Rev.*, 1993, **128**, 293–322.

2 W. L. Leong and J. J. Vittal, *Chem. Rev.*, 2011, **111**, 688–764.

3 C. Janiak, *Dalton Trans.*, 2003, 2781–2804.

4 T. J. Prior and M. J. Rosseinsky, *CrystEngComm*, 2000, **2**, 128–133.

5 J. M. Lehn, *Polym. Int.*, 2002, **51**, 825–839.

6 A. M. Ako, C. S. Hawes, B. Twamley and W. Schmitt, *CrystEngComm*, 2017, **19**, 994–1000.

7 K. Biradha, C. Seward and M. J. Zaworotko, *Angew. Chem. Int. Ed.*, 1999, **38**, 492–495.

8 C.-B. Ma, C.-N. Chen and Q.-T. Liu, *CrystEngComm*, 2005, **7**, 650–655.

9 X.-M. Zhang, M.-L. Tong, M.-L. Gong and X.-M. Chen, *Eur. J. Inorg. Chem.*, 2003, **2003**, 138–142.

10 L. Carlucci, G. Ciani, A. Gramaccioli, D. M. Proserpio and S. Rizzato, *CrystEngComm*, 2000, **2**, 154–163.

11 J. J. Vittal, *Coord. Chem. Rev.*, 2007, **251**, 1781–1795.

12 A. Y. Robin and K. M. Fromm, *Coord. Chem. Rev.*, 2006, **250**, 2127–2157.

13 H. Chae, J. Kim and Y. Go, *Nature*, 2004, **427**, 523–527.

14 P. Paul, B. Tyagi, A. K. Bilakhiya, P. Dastidar and E. Suresh, *Inorg. Chem.*, 2000, **39**, 14–22.

15 J. Wang, F. Yuan, H. M. Hu, B. Xu and G. L. Xue, *Inorg. Chem. Commun.*, 2016, **71**, 19–22.

16 N. Klein, I. Senkovska, I. A. Baburin, R. Grünker, U. Stoeck, M. Schlichtenmayer, B. Streppel, U. Mueller, S. Leoni, M. Hirscher and S. Kaskel, *Chem. Eur. J.*, 2011, **17**, 13007–13016.

17 L. Zhang, W. Yang, X. Y. Wu, C. Z. Lu and W. Z. Chen, *Chem. Eur. J.*, 2016, **22**, 11283–11290.

18 N. Zhu, M. J. Lennox, G. Tobin, L. Goodman, T. Düren and W. Schmitt, *Chem. Eur. J.*, 2014, **20**, 3595–3599.

19 A. C. Kathalikkattil, D.-W. Kim, J. Tharun, H.-G. Soek, R. Roshan and D.-W. Park, *Green Chem.*, 2014, **16**, 1607–1616.

20 N. Zhu, M. J. Lennox, T. Düren and W. Schmitt, *Chem. Commun.*, 2014, **50**, 4207–4210.

21 N. Zhu, D. Sensharma, P. Wix, M. J. Lennox, T. Düren, W.-Y. Wong and W. Schmitt, *Eur. J. Inorg. Chem.*, 2016, 1939–1943.

22 B. Therrien, *J. Organomet. Chem.*, 2011, **696**, 637–651.

23 A. L. Spek, *Acta Crystallogr. Sect. C*, 2015, **71**, 9–18.

24 M. Llunell, D. Casanova, J. Cirera, P. Alemany and S. Alvarez, *SHAPE, Version 2.1*, Universitat de Barcelona, 2013.

25 C. A. Hunter and J. K. M. Sanders, *J. Am. Chem. Soc.*, 1990, **112**, 5525–5534.

26 G. R. Desiraju and A. Gavezzotti, *J. Chem. Soc. Chem. Commun.*, 1989, 621–623.

27 G. A. Sim, J. M. Robertson and T. H. Goodwin, *Acta Crystallogr.*, 1955, **8**, 157–164.

28 M. P. Johansson and J. Olsen, *J. Chem. Theory Comput.*, 2008, **4**, 1460–1471.

29 M. A. Spackman and D. Jayatilaka, *CrystEngComm*, 2009, **11**, 19–32.

30 S. K. Wolff, D. J. Grimwood, J. J. McKinnon, M. J. Turner, D. Jayatilaka and M. A. Spackman, *Crystal Explorer*, University of Western Australia, 2012.

31 R. D. Shannon, *Acta Crystallogr. Sect. A*, 1976, **32**, 751–767.

32 K. Abdi, H. Hadadzadeh, M. Salimi, J. Simpson and A. D. Khalaji, *Polyhedron*, 2012, **44**, 101–112.

33 L. Zhang, W. Yang, X. Y. Wu, G. H. Zhang, C. Z. Lu and W. Z. Chen, *Inorg. Chem. Commun.*, 2016, **68**, 60–62.

34 D. Kim, X. Song, J. H. Yoon and M. S. Lah, *Cryst. Growth Des.*, 2012, **12**, 4186–4193.

35 P. Wollmann, M. Leistner, U. Stoeck, R. Grünker, K. Gedrich, N. Klein, O. Throl, W. Grählert, I. Senkovska and F. Dreisbach, *Chem. Commun.*, 2011, **47**, 5151–5153.

36 Q. Yao, J. Sun, K. Li, J. Su, M. V Peskov and X. Zou, *Dalton Trans.*, 2012, **41**, 3953–3955.

Chapter 3

Flexibility and Functional Approaches to Tuning of CO_2 Uptake in Ditopic N-donor MOFs

3.1: Introduction

Linear, ditopic, dipyridyl-based organic ligands have been crucial to the development of coordination polymer chemistry.[1] 4,4′-bipyridine (bpy), the simplest and most widely-used of these, is a building block in nearly 4000 coordination polymer structures in the CCDC at the time of writing.[2] One of the most important uses of these ligands is as 'pillars' in mixed ligand MOFs, incorporated into 1D chains or 2D layer structures in order to provide connectivity and structural support into higher dimensions.[3–10]

This approach is synthetically elegant - the charge balance requirement of the positively charged metal centres can be satisfied by organic ligands that define individual chains or layers, usually carboxylates, or inorganic counter-ions. Then, the lower bond energy of the pyridyl-metal bond allows facile incorporation of the second ligand, and brings with it many exciting possibilities for functional group incorporation, post-synthetic modification, and linker exchange.[11–16]

The well-understood and facile organic chemistry of pyridyl-based molecules allows the conception of functionalised ligands for rational incorporation as pillars. We identify the amino-functionalised 3,3′-diamino-4,4′-bipyridine (dabpy) ligand and the 4,4′-azopyridine (azpy) ligand as electron rich pillars that can be incorporated into novel frameworks with the objective of enhanced interaction with CO_2 molecules, and therefore favourable CO_2 storage behaviour.[17] In addition, the resemblance of azpy to the well-known *cis-trans* photoisomerisable azobenzene moiety presents the possibility of stimulus responsive behaviour upon incorporation into metal-organic frameworks (see Introduction).[18,19]

Further, the 1,2-bis(4-pyridyl)ethane (bpet) and 1,2-bis(4-pyridyl)propane (or 4,4′-trimethylenedipyridine, tdp) ligands were chosen for their mechanical and conformational flexibility (Fig. 3.1).[20,21] Such flexibility is an impediment to conventional pillaring, and therefore would provide a simple synthetic platform with which to evaluate the impact of increasing flexibility on coordination polymer structure, and therefore dimensionality and porosity.

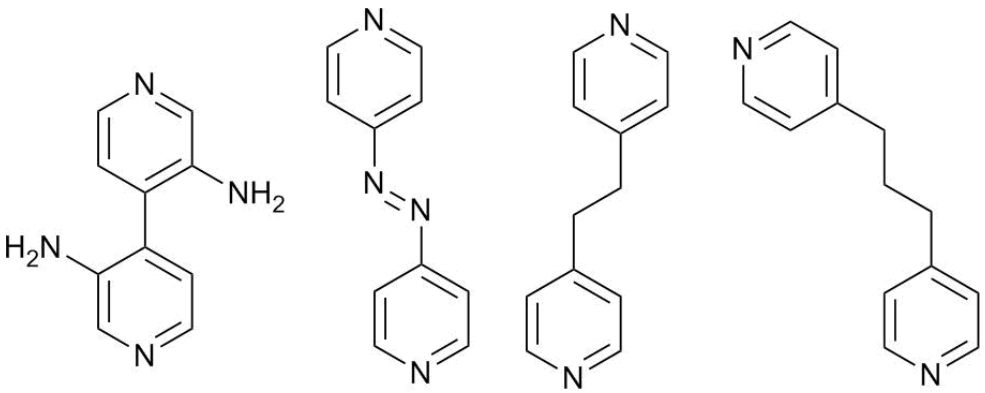

Figure 3.1 – From left, the dabpy, azpy, bpet, and tdp ligands.

In this chapter, the use of dabpy is described with 2D layers based on Co(II) and Zn(II), in conjunction with rigid, ditopic carboxylate ligands – terephthalic acid (H_2bdc) and biphenyl-4,4′-dicarboxylic acid (H_2bpdc) – to yield MOFs with amino-functionalities available along pillaring linkers, *i.e.*, on the channel walls. Further, compounds based on Cu(II) chains formed with the inorganic hexafluorosilicate (SiF_6^{2-}) ion, are synthesised using azpy, bpet, and tdp, in order to assess the impacts of various kinds of modular and emergent flexibility on coordination network formation, and to evaluate the impact of these deviations from rigidity on the gas storage behaviour of these MOFs, particularly with regard to CO_2 (Fig. 3.2). Single crystal X-ray structures and physicochemical characterisations are reported for each compound.

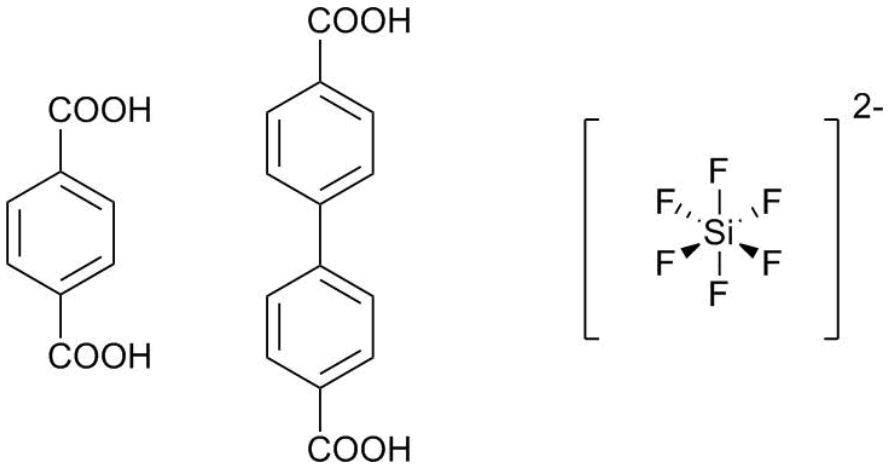

Figure 3.2 – From left, the H_2bdc, H_2bpdc, and SiF_6^{2-} ligands.

3.2: Compound **6**, $[Zn_3(bdc)_3(dabpy)]$

Compound **6**, $[Zn_3(bdc)_3(dabpy)]$, was synthesised by heating zinc(II) nitrate hexahydrate, H_2bdc, and 3,3′-diamino-4,4′-bipyridine (dabpy) dissolved in DMF, at 90°C for 24 hours, and was obtained as pale yellow block crystals. Single crystal X-ray diffraction was carried out and the structure of **6** was solved in the monoclinic *P*2/*m* space group. The cell dimensions of the crystal structure of **6** were found to be a = 9.5375(4) Å, b = 18.5463(8) Å, c = 17.2607(6) Å, and $\alpha = \gamma = 90°$, $\beta = 106.053(2)°$.

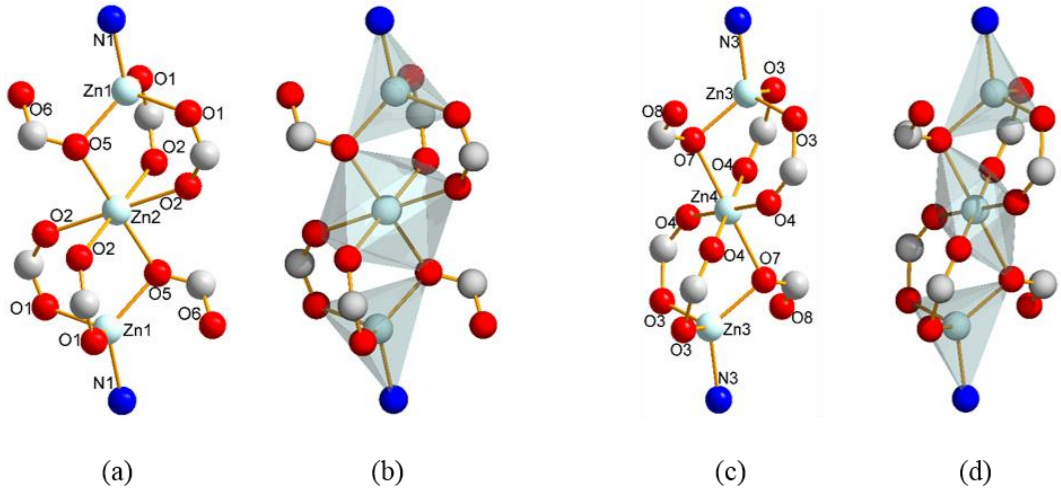

Figure 3.3 – The coordination environment in one SBU of 6 (a) and a polyhedral representation of the SBU in 6 (b), as well as the coordination environment in the other SBU (c) and a polyhedral representation (d).

6 shows a three-dimensional coordination polymer structure, composed of trinuclear $\{Zn_3\}$ SBUs and bdc^{2-} and dabpy linkers, resulting in a mixed-ligand MOF. Two crystallographically distinct $\{Zn_3\}$ SBUs are found in the asymmetric unit, and consist of three co-linear Zn^{2+} ions, which define an hourglass-shaped formation in conjunction with the six carboxylate groups bound to them. The SBUs are symmetric to inversion about the internal zinc(II) centre (Zn2, Zn4) (Fig. 3.3).

The peripheral Zn^{2+} ions (Zn1, Zn3) are bound in a monodentate pillaring fashion to an N-donor atom from the dabpy ligand, and have a tetrahedral $\{ZnO_3N\}$ coordination environment, while the internal Zn^{2+} centres are octahedrally coordinated to six O-donor atoms from bdc^{2-} carboxylate groups forming a $\{ZnO_6\}$ environment. In both trinuclear SBUs, the fully deprotonated bdc^{2-} ligands bind to Zn^{2+} centres using a combination of modes. *Syn, syn*-bidentate bridging is the most common, with the occurrence of

bidentate-(O1, O2) and bidentate-(O3, O4) modes linking Zn1 and Zn2, and Zn3 and Zn4 respectively. However, these pairs of metal centres are also linked by bridging-(O5, O5) and bridging-(O7, O7) monodentate bridging modes, completing the 8-connected 'hourglass' SBUs (Table 3.1).

Table 3.1 - Selected interatomic distances and angles in 6.

Atoms	**Distance**		**Atoms**	**Angle**
Zn1-N1	2.007(6) Å		N1-Zn1-O1	104.4(1)°
Zn1-O1	1.944(4) Å		O1-Zn1-O1′	112.0(2)°
Zn1-O5	1.944(6) Å		O1-Zn1-O5	107.1(1)°
Zn1-O6	2.76(1) Å		Zn1-Zn2-Zn1′	180°
Zn1-Zn2	3.189(1) Å		O2-Zn2-O2′ (ax.)	180°
Zn2-O2	2.037(8) Å		O2-Zn2-O2′ (eq.)	66.4(3)°
Zn2-O5	2.158(4) Å		O2-Zn2-O5	93.8(2)°
Zn3-N3	1.998(7) Å		Zn3-Zn4-Zn3′	180°
Zn3-O3	1.945(4) Å		N3-Zn3-O3	104.8(1)°
Zn3-O8	2.749(7) Å		O7-Zn3-O8	47.8(2)°
Zn3-O7	1.938(4) Å		O3-Zn3-O3′	112.1(2)°
Zn3-Zn4	3.191(1) Å		O3-Zn3-O8	88.5(2)°
Zn4-O4	2.071(7) Å		O4-Zn4-O4′ (eq.)	122.7(3)°
Zn4-O7	2.177(6) Å		O4-Zn4-O4′ (ax.)	180°
			O7-Zn4-O7′	180°
			O7-Zn4-O4	85.2(2)°

The six carboxylate groups around the {Zn_3} SBU extend in a linear ditopic fashion to adjacent SBUs and act as μ_4 bridging moieties overall, similar to the structure of the archetypal MOF-3 (see Introduction).[22] Pairs of Zn^{2+} centres in each SBU are linked by three carboxylate groups each, which adopt staggered positions about the axis of the linear SBU. The ditopic dabpy linkers (pyridyl N-donor atoms *ca.* 7.03 Å apart) are incorporated as pillars between the charge-neutral 2D Zn-carboxylate sheets, in two distinct inclined modes (Fig. 3.4). The possibility for a single pillaring mode perfectly perpendicular to the plane of the 2D sheet was noted (see compound **7**). Thus, **6** has an 8-connected network with the rare **bcg** topology, and an overall point symbol of {$3^6.4^{14}.5^7.6$} (Fig. 3.5).

Importantly, the carboxylate groups to which O5 and O7 belong are crystallographically characterised by half atom occupancy and are split over a mirror plane. The distances reported in Table 3.1 consider only a single part of the disordered group. The Platon-Squeeze routine was applied to remove the contribution of disordered pore solvent molecules to the crystal structure.[23]

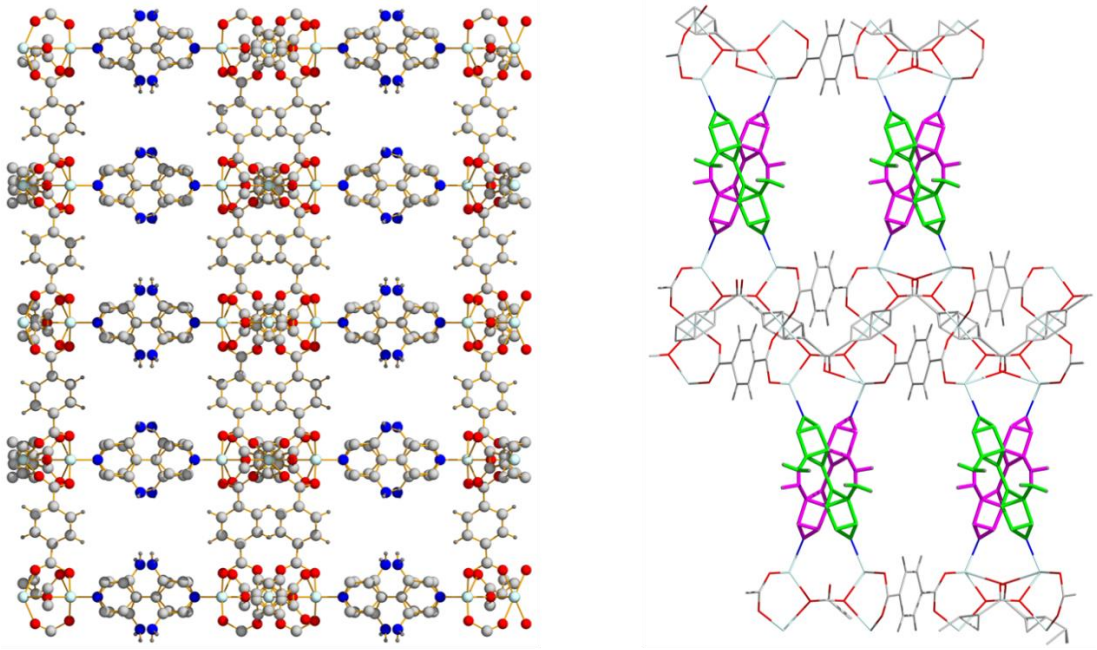

Figure 3.4 – (a) A representation of the crystal structure of 6 viewed along the crystallographic *a*-axis. Colour scheme: light turquoise, Zn; blue, N; grey, C; red, O; dark grey, H. (b) A representation of the mutually oblique dabpy pillars (pink and green) linking Zn-bdc sheets in 6.

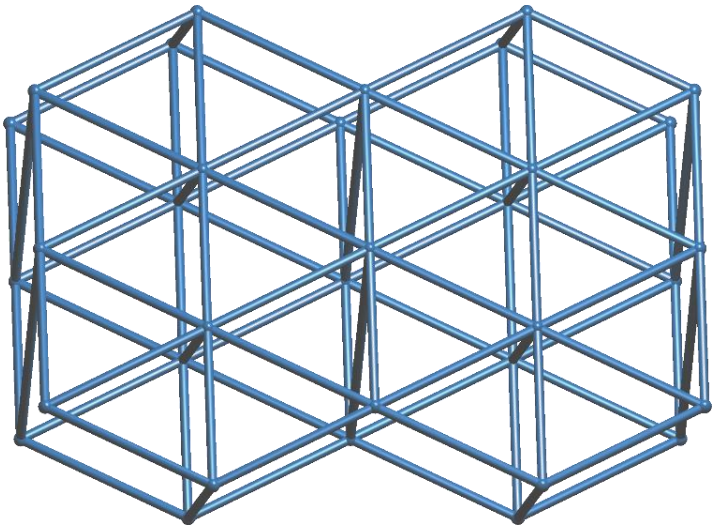

Figure 3.5 – Topological reduction of 6 into a bcg net.

The structure is porous, with a void volume estimated to be 1169.92 $Å^3$ (39.9%), as estimated using CCDC-Mercury. The limiting diameter of channels along the crystallographic *a*-direction is calculated to be 4.0 Å, and along the *b*-direction, 3.6 Å, using Olex2.[24] The radius of the largest spherical void is found to be 2.4 Å. These values suggest modest gas uptakes, but definite porosity to standard adsorbates such as CO_2 (kinetic diameter = 3.30 Å) and N_2 (kinetic diameter = 3.64 Å).

Physicochemical characterisation further confirms the purity of **6**. Thermogravimetric analysis under a N_2 stream shows an initial solvent loss of 28.8% wt. below 120°C due to pore solvent, and a further slow decline of 8.8% above 120°C owing to strongly interacting DMF molecules, through H-bonding to the framework atoms. At 370°C a decline is observed due to ligand decomposition (Fig. 3.6).

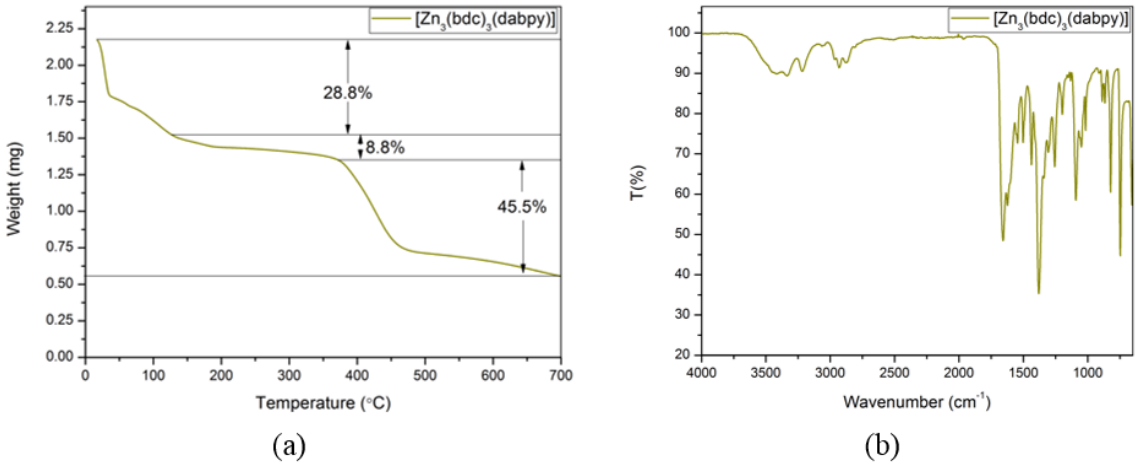

Figure 3.6 – TGA trace (a) and FTIR spectrum (b) for 6.

FTIR spectroscopy reveals signals at 3424 cm^{-1} (ν_s NH_2) and 3339 cm^{-1} (ν_s NH) due to the amino-substituents on the dabpy ligand. The signal at 3216 cm^{-1} and that at 1658 (ν_s C=O) are due to pore DMF molecules. C-H stretching vibrations are observed at 2966-2850 cm^{-1}, and a vibration associated with the aromatic C-H bending mode is found at 822 cm^{-1}. The asymmetric carboxylate (ν_{as} COO) stretching mode is found at 1624 cm^{-1}, and the corresponding symmetric mode is at 1437 cm^{-1}. Applying the criterion outlined by Deacon and Phillips, the Δ value corresponding to the coordination mode, here 187 cm^{-1}, corresponds to the observed bidentate-bridging mode.[25] The signals corresponding to aromatic C=C and C=N stretching vibrations and the monodentate bridging COO mode are

in close proximity to each other between 1557 cm^{-1} and 1502 cm^{-1} and are not individually assigned (Fig. 3.6). Powder X-ray diffraction confirms the phase purity of as-synthesised **6**, and validates the structural model obtained by single-crystal diffraction studies (Fig. 3.7).

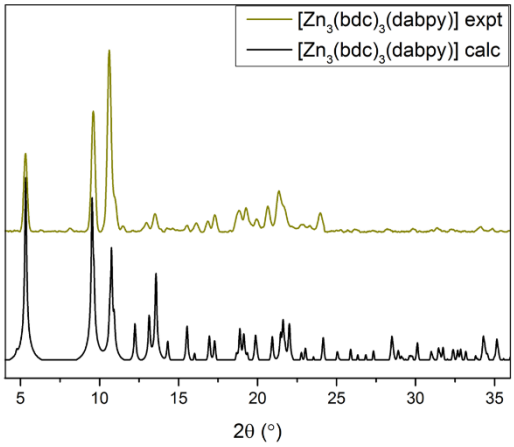

Figure 3.7 – PXRD pattern of 6.

Having found **6** to be porous and phase-pure, its sorption behaviour was investigated. A crystalline sample of as-synthesised **6** was washed by exchanging the mother liquor with fresh, dry DMF twice daily for three days. This was replaced with dry dichloromethane, which was also exchanged twice daily for three days. The solid compound was dried from dichloromethane at 120°C under high vacuum (*ca.* 10^{-3} atm pressure) for 12 hours.

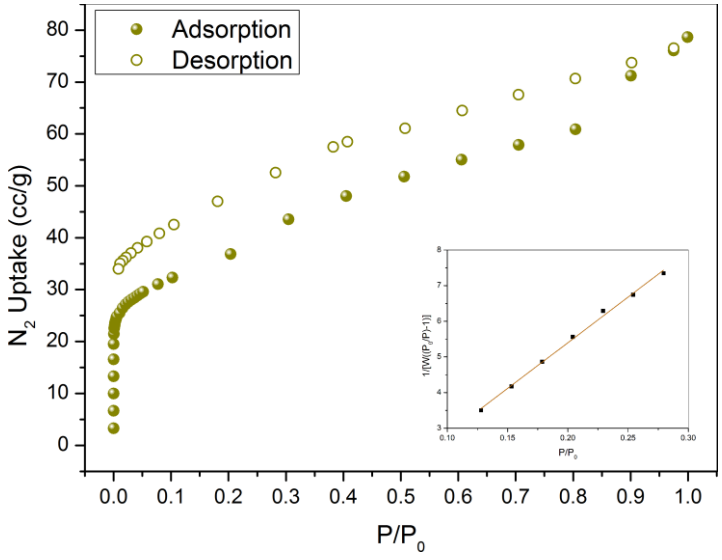

Figure 3.8 – N_2 isotherm measured at 77 K for 6. Inset: Multi-point BET fit; slope = 25.623, intercept = 2.737 x 10^{-1}, correlation coefficient, r = 0.998401, C (constant) = 94.605, surface area = 134.5 m^2/g.

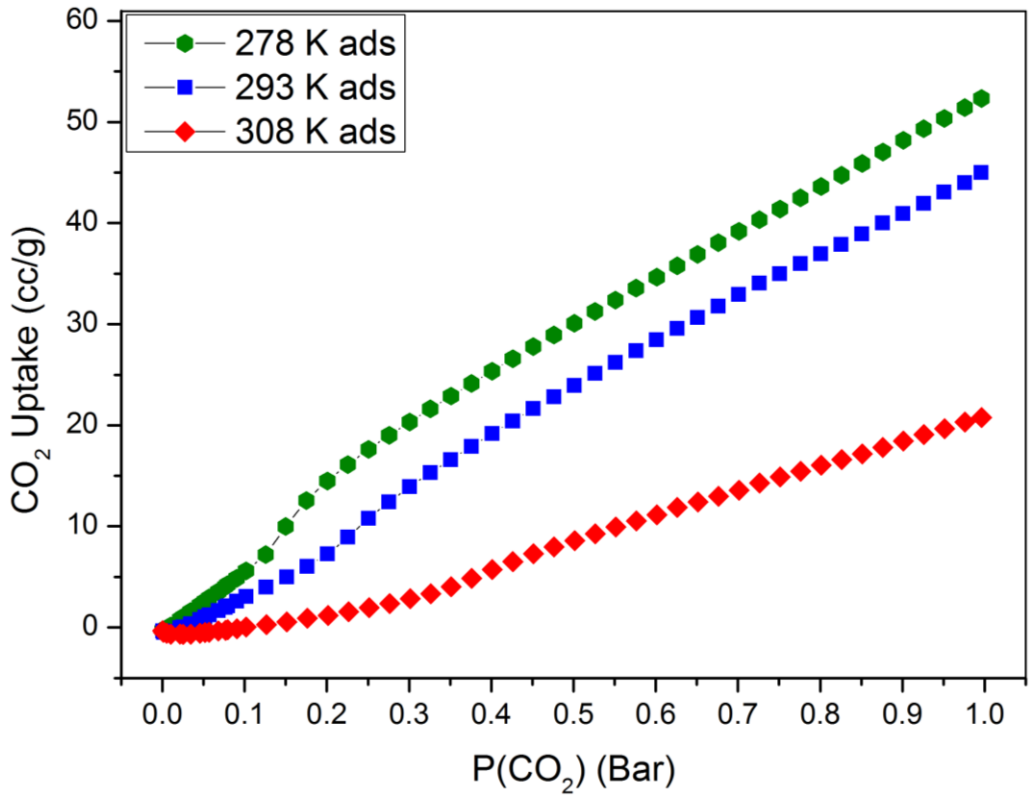

Figure 3.9 - CO_2 adsorption isotherms for 6 measured at 278 K (green), 293 K (blue), 308 K (red).

N_2 sorption experiments at 77 K revealed a steep adsorption step due to micropore filling at low pressure, and a relatively low surface area of 134 m^2/g (Fig. 3.8). N_2 uptake at 293 K was found to be 9.15 cc/g. CO_2 sorption experiments showed uptakes of 52.32, 45.01 cc/g, and 22.16 cc/g at 278 K, 293 K, and 308 K respectively (Fig. 3.9). The heats of adsorption could not be calculated due to a very small common volume range. However, the near-linear shape of the CO_2 adsorption isotherms implies weak interactions between the framework and CO_2 molecules at low pressures, suggesting that the amino groups play a minor role in adsorption. This is likely to be due to the small size of the pores, which becomes the limiting criterion for adsorption, and restricts the orientational freedom of adsorbed CO_2 by which the energy of prospective interactions might be maximised.

The crystallographic details for the single crystal X-ray studies of **6** are given below in Table 3.2.

Table 3.2 - Crystallographic details for 6.

Identification code	6
Empirical formula	$C_{34}H_{20}N_4O_{12}Zn_3$
Formula weight	872.65
Temperature/ K	100(2)
Crystal system	monoclinic
Space group	*P*2/*m*
***a*/Å**	9.5375(4)
***b*/Å**	18.5463(8)
***c*/Å**	17.2607(6)
***α*/°**	90
***β*/°**	106.053(2)
***γ*/°**	90
Volume/Å^3	2934.1(2)
Z	2
ρ_{calc}/ g/cm^3	0.988
μ/mm^{-1}	1.791
F(000)	876.0
Crystal size/mm^3	0.11 × 0.06 × 0.06
Radiation	CuKα (λ = 1.54178)
2θ range for data collection/°	4.764 to 137.2
Index ranges	$-11 \leq h \leq 11$, $-22 \leq k \leq 20$, $-19 \leq l \leq 20$
Reflections collected	23054
Independent reflections	5580 [R_{int} = 0.0754, R_{sigma} = 0.0672]
Data/restraints/parameters	5580/35/420
Goodness-of-fit on F^2	1.040
Final R indexes [I>=2σ (I)]	R_1 = 0.0485, wR_2 = 0.1403
Final R indexes [all data]	R_1 = 0.0593, wR_2 = 0.1469
Largest diff. peak/hole / e Å^{-3}	0.53/-0.63

3.3: Compound 7, $[Co_3(bpdc)_3(dabpy)(H_2O)]$

The mixed-ligand strategy adopted to synthesise **6** was extended using the H_2bpdc ligand in conjunction with dabpy. Co(II) was used in order to form a mixed ligand MOF based on the 'hourglass' SBU. Compound **7**, $[Co_3(bpdc)_3(dabpy)(H_2O)]\cdot 4DMF$, was synthesised by heating cobalt(II) nitrate hexahydrate, H_2bpdc, and 3,3′-diamino-4,4′-bipyridine (dabpy) dissolved in DMF, at 150°C for 3 days, and was obtained as violet crystals. Single crystal X-ray diffraction was carried out and the structure of **7** was solved in the monoclinic $P2_1/n$ space group. The cell dimensions of the crystal structure of **7** were found to be a = 13.852(3) Å, b = 18.077(4) Å, c = 25.918(6) Å, and $\alpha = \gamma = 90°$, β = 90.644(4)°.

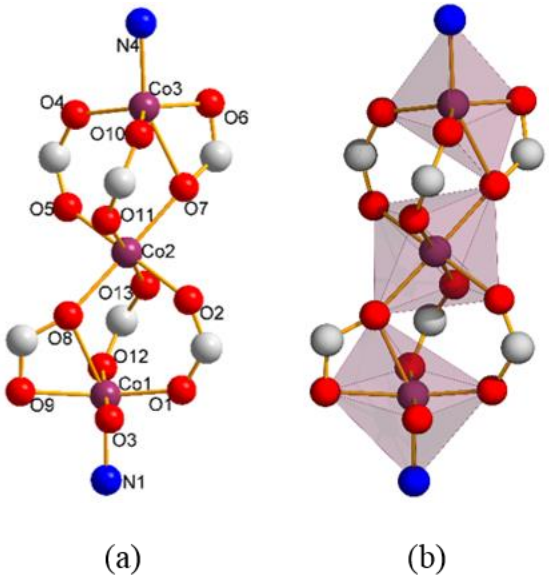

Figure 3.10 – The coordination environment in 7 (a) and a polyhedral representation of the SBU in 7 (b).

The compound adopts a three-dimensional network structure, and is composed of trinuclear $\{Co_3\}$ SBUs, linked by ditopic $bpdc^{2-}$ and dabpy ligands, resulting in a mixed-ligand 3D MOF. The $\{Co_3\}$ SBU, as in compound **5**, resembles an hourglass and has six carboxylate groups bound to it. However, in this case all three Co(II) coordination environments are unique. The central Co ion has an octahedral $\{CoO_6\}$ coordination environment consisting of bonds from six distinct carboxylate groups from six $bpdc^{2-}$ ligands (Table 3.10). The outer Co ions have distinct coordination environments. Co3 displays distorted trigonal bipyramidal $\{CoO_4N\}$ geometry, while Co1 incorporates an additional H_2O ligand into its coordination sphere to generate a $\{CoO_5N\}$ coordination sphere. Co1 is coordinated to three O-donor atoms from $bpdc^{2-}$ carboxylate groups that are also bound to Co2, in bridging bidentate-(O1, O2), bidentate-(O12, O13), and bridging chelate bidentate-(O9, O8, O8) modes. Coordination to a water molecule, (O3), completes the Co1 environment. Co3 is

also coordinated to three O-donor atoms from $bpdc^{2-}$ carboxylate groups which are also bound to Co2, in bridging bidentate-(O4, O5), bidentate-(O10, O11), and bridging chelate κ^3-(O6, O7, O7) modes. The dabpy linkers are bound to outer axial positions on Co1 and Co3, resulting in an 8-connected SBU overall. Table 3.3 lists releveant interatomic distances and angles.

Table 3.3 - Selected interatomic distances and angles in 7.

Atoms	**Distance**		**Atoms**	**Angle**
Co3-N4	2.054(6) Å		N4-Co3-O6	97.97(2)°
Co3-O6	2.056(6) Å		N4-Co3-O4	101.0(3)°
Co3-O4	1.954(6) Å		O6-Co3-O7	60.8(2)°
Co3-O10	1.979(6) Å		Co1-Co2-Co3	177.02(1)°
Co3-O7	2.243(6) Å		O5-Co2-O2	175.7(2)°
Co3-Co2	3.513(1) Å		O11-Co2-O8	86.0(2)°
Co2-Co1	3.450(1) Å		O2-Co2-O8	90.8(2)°
Co2-O7	2.073(6) Å		N4-Co3-O7	156.2(2)°
Co2-O5	2.032(6) Å		O9-Co1-O3	81.6 (5)°
Co2-O11	2.065(5) Å		N1-Co1-O8	155.8(2)°
Co2-O2	2.040(5) Å		N1-Co1-O1	97.5(3)°
Co2-O8	2.091(6) Å		O9-Co1-O12	98.2(3)°
Co2-O13	2.064(6) Å			
Co1-O8	2.215(6) Å			
Co1-O1	1.92(1) Å			
Co1-O9	2.064(7) Å			
Co1-O12	2.001(6) Å			
Co1-O3	2.284(2) Å			
Co1-N1	2.068(6) Å			

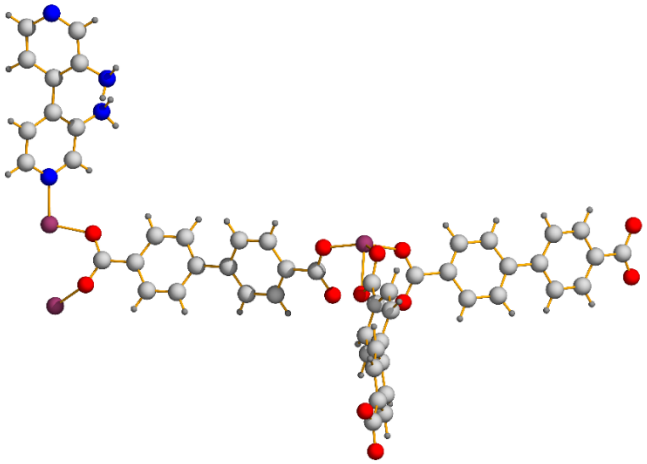

Figure 3.11 – The asymmetric unit in 7.

The asymmetric unit of **7** consists of three independent Co(II) ions, three fully deprotonated $bpdc^{2-}$ ligands, and one dabpy ligand, arranged as shown in Fig 3.11. Each $bpdc^{2-}$ and dabpy ligand are bound to two separate metal centres. The axial sites on the SBU are arranged such that three points of extension emerge from Co1 and Co2, and three more from Co2 and Co3, in a staggered fashion, resulting in a 6-connected vertex of a 2D hexagonal arrangement. These vertices are pillared by the dabpy ligand into a two-fold interwoven structure, built from 8-connected SBUs and ditopic linkers. Each net can be described as a **hex** net with a point symbol of $\{3^6.4^{18}.5^3.6\}$ (Fig. 3.12).

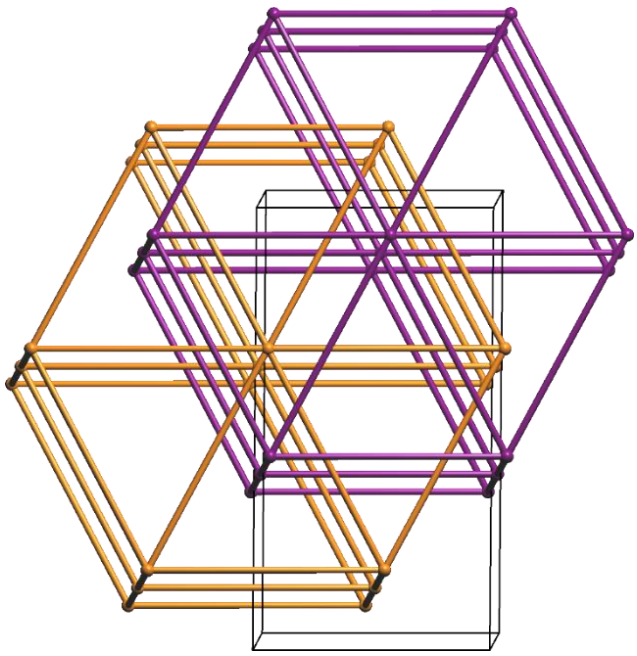

Figure 3.12 – Topological reduction of 7 into two interwoven hex nets. Unit cell edges are shown for reference.

Ligand torsions in the $bpdc^{2-}$ and dabpy ligands accommodate the aryl proton – aryl proton repulsion between adjacent aromatic rings, and the relevant angles of torsion between the planes of adjacent phenyl rings are *ca.* 33.05°, 33.56°, and 17.20° for $bpdc^{2-}$ ligands, and 48.93° for the dabpy ligand in which the bulky amino-substituents are present. The short N···H distance between the two proximate amino-groups is 2.215(9) Å. The interweaving nets are stabilised by π···π interactions (centroid-centroid distance: 3.803(1) Å) between the $bpdc^{2-}$ ligand of one net and the dabpy ligand of the other (and *vice versa*) oriented perpendicular to each other in terms of their lengthwise axes. There are four constitutional DMF molecules per formula unit occupying the pores, as well as one coordinated H_2O molecule, resulting in an overall formula of $[Co_3(bpdc)_3(dabpy)(H_2O)]\cdot 4DMF$.

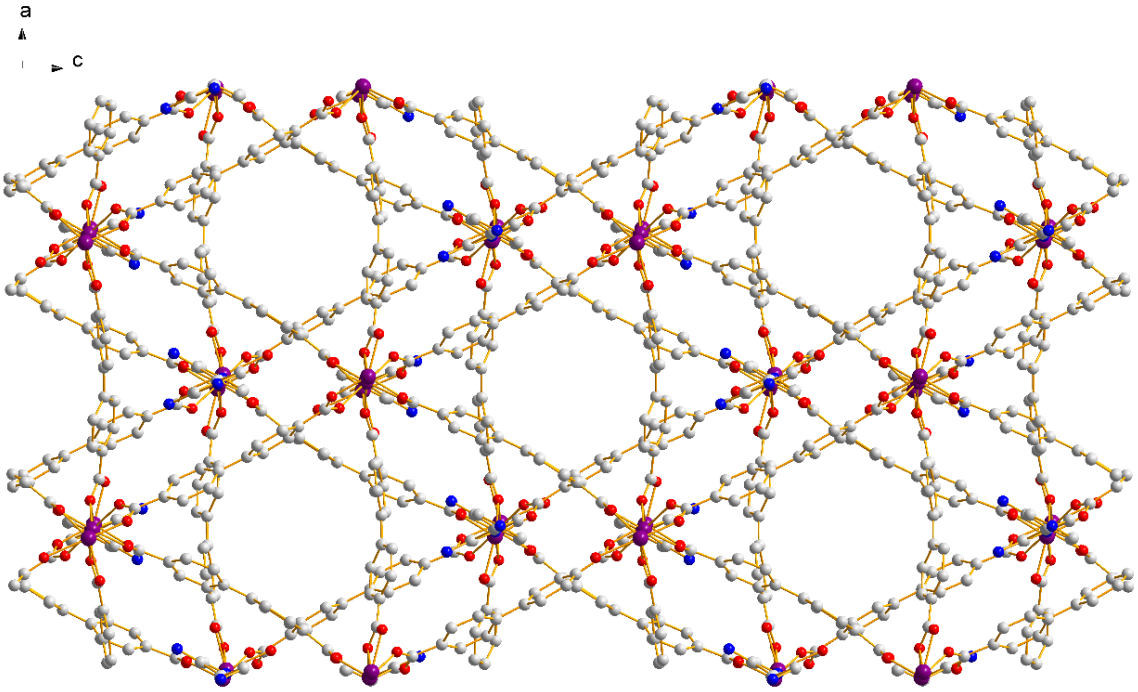

Figure 3.13 – A representation of the crystal structure of 7 viewed along the crystallographic *b*-axis. Colour scheme: violet, Co; blue, N; grey, C; red, O. H atoms and solvent molecules are omitted for clarity.

Voids, in which DMF guests are contained in **7**, are defined by both interpenetrating **hex** nets, and the most prominent voids are channels along the crystallographic *b*-axis (Fig. 3.13, 3.14). Voids account for 34.5% of the cell volume (2239.15 $Å^3$), while the framework structure occupies the rest. The effective limiting channel diameter in **7** was found to be 4.4 Å, while the maximum pore width was found to be 6.0 Å, determined using Olex2.[24] The dabpy ligands are oriented lengthwise along the crystallographic *b*-direction, enabling amino-functionalities to point into the channels.

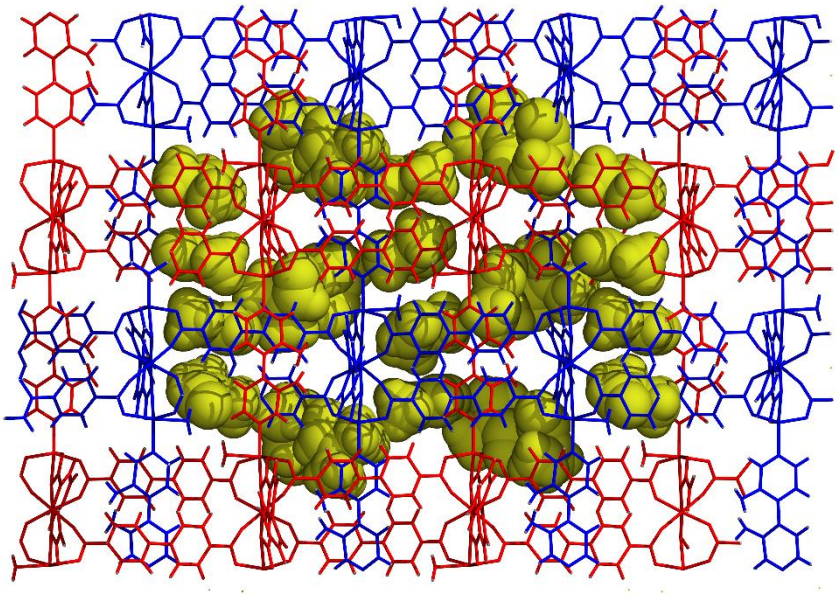

Figure 3.14 – A wireframe representation of the crystal structure of 7 viewed along the crystallographic *a*-axis. Solvent molecules are coloured yellow. Individual nets are coloured blue and red, respectively.

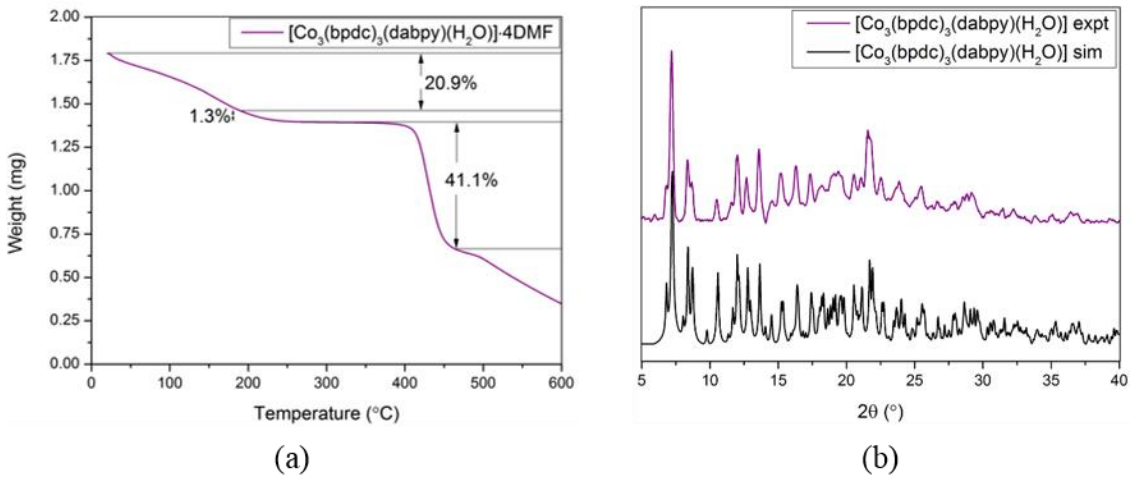

Figure 3.15 – TGA trace (a) and PXRD pattern (b) for 7.

The thermal stability of **7** was evaluated by thermogravimetric analysis, revealing stability under nitrogen upto *ca.* 380°C, at which ligand decomposition begins to occur. Preceding solvent steps corresponding to removal of four pore DMF molecules per formula unit (20.9%) and one coordinated water molecule (1.3%) take place below 240°C, in a stepwise fashion, in close agreement with the formula assigned. The phase purity of **7** was evaluated using PXRD measurement, and the single crystal structural model was validated by a close match in patterns (Fig. 3.15).

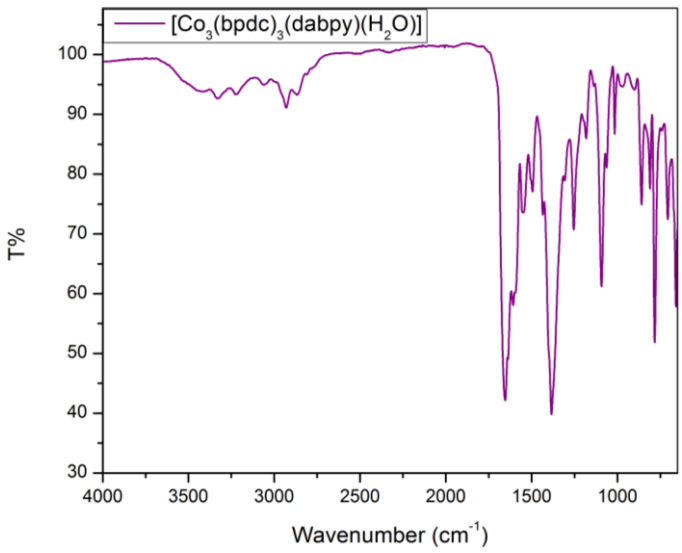

Figure 3.16 – FTIR spectrum of 7.

FTIR spectroscopy was also carried out, and revealed several overlapping bands between 1655 cm^{-1} (DMF C=O stretch) and 1385 cm^{-1} (ν_s C=C), due to aromatic C=C and C=N stretching frequencies and the various carboxylate binding modes present in **7**. Frequencies corresponding to the symmetric and asymmetric stretching carboxylates in the dominant bridging mode are assigned as 1435 cm^{-1} and 1608 cm^{-1}. Therefore we obtain a Deacon-Phillips Δ value equal to 173 cm^{-1}, which is in good agreement with empirical observations for this binding mode.[25] The weaker signal associated with the symmetric carboxylate stretching mode of the bridging chelate mode is not assigned, but is expected to be among the overlapping bands between 1460 cm^{-1} and 1490 cm^{-1}. It is important to note that the bridging chelate modes also present in **7** are likely overlapping with the modes listed, and are not assigned here. The broad signal centred around 3500 cm^{-1} is due to hydrogen bonded DMF molecules present in the framework channels. Signals at 3333 cm^{-1}, 3370 cm^{-1} (both ν_s NH) and 3455 cm^{-1} (ν_s NH_2) are assigned to the H-bonded amino groups. The band at 3216 cm^{-1} is due to the strongly interacting pore DMF molecules (Fig. 3.16). The single crystal X-ray details are given in Table 3.4.

Table 3.4 - Crystallographic details for 7.

Identification code	7
Empirical formula	$C_{31.25}H_{29.75}Co_{1.5}N_{3.75}O_8$
Formula weight	674.23
Temperature/ K	100(2)
Crystal system	Monoclinic
Space group	$P2_1/n$
***a*/Å**	13.852(3)
***b*/Å**	18.077(4)
***c*/Å**	25.918(6)
***α*/°**	90
***β*/°**	90.644(4)
***γ*/°**	90
Volume/Å^3	6490(2)
Z	8
ρ_{calc}/ g/cm^3	1.380
μ/mm^{-1}	0.829
F(000)	2784.0
Crystal size/mm^3	0.24 x 0.19 x 0.10
Radiation	MoKα (λ = 0.71073)
20 range for data collection/°	1.572 to 55.49
Index ranges	$-18 \leq h \leq 15$, $-23 \leq k \leq 23$, $-30 \leq l \leq 33$
Reflections collected	49074
Independent reflections	15106 [R_{int} = 0.0571, R_{sigma} = 0.0654]
Data/restraints/parameters	15106/74/841
Goodness-of-fit on F^2	1.121
Final R indexes [I>=2σ (I)]	R_1 = 0.1010, wR_2 = 0.2426
Final R indexes [all data]	R_1 = 0.1182, wR_2 = 0.2524
Largest diff. peak/hole / e Å^{-3}	1.98/-1.33

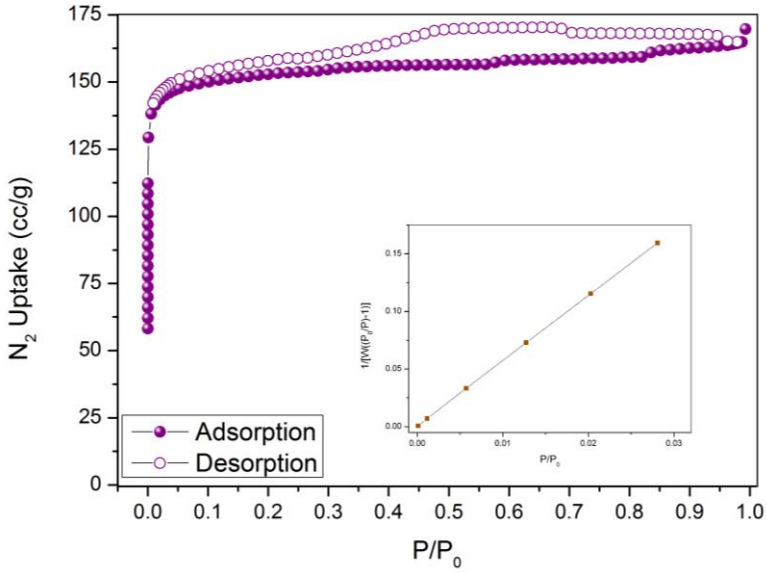

Figure 3.17 – N_2 isotherm measured at 77 K for 7. Inset: Multi-point BET fit; slope = 5.666, intercept = 5.784 x 10^{-4}, correlation coefficient, r = 0.999990, C (constant) = 9796.556, surface area = 614.6 m^2/g.

The porosity of **7** was experimentally determined after activating it by a procedure of solvent exchange with dichloromethane followed by outgassing under high vacuum at 80°C. N_2 sorption carried out at 77 K showed a type 1 isotherm in which the steep uptake increase at low pressure confirms the microporosity of **7** (Fig. 3.17). The BET surface area of 7 was determined to be 615 m^2/g. The micropore volume was determined to be 0.24 cc/g by the DFT method. Pore sizes obtained by the DFT method correspond well with the maximum diameter obtained crystallographically for voids, which is ca. 6.0 Å (Fig. 3.18).[26] N_2 sorption was also performed at 293 K and showed very low uptake at 1 bar (*ca.* 5.8 cc/g).

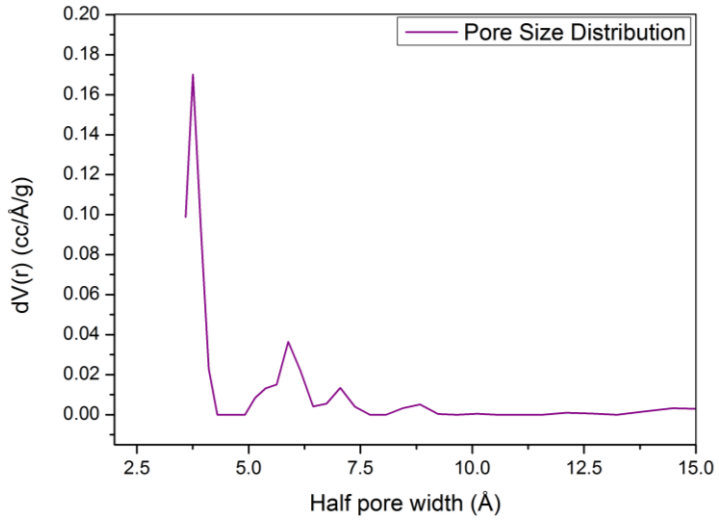

Figure 3.18 –DFT pore size distribution of 7 from N_2 adsorption data.

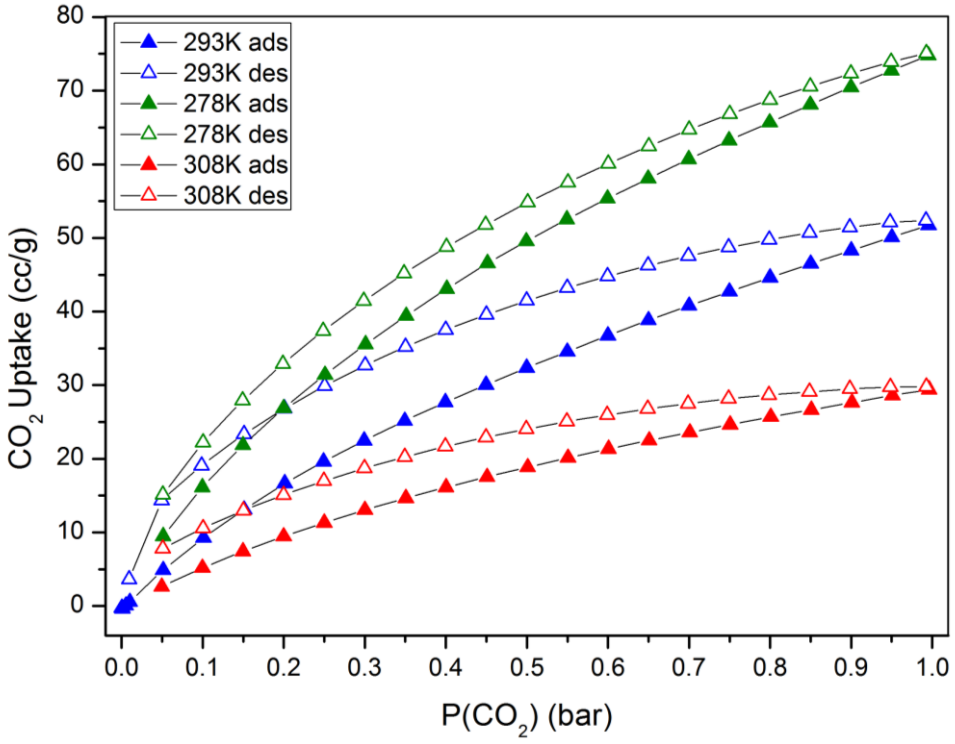

Figure 3.19 - CO_2 sorption isotherms for 7 measured at 278 K (green), 293 K (blue), 308 K (red); solid symbols: adsorption; open symbols: desorption.

CO_2 sorption experiments were also carried out on **7**. CO_2 uptakes at 1 bar were found to be 74.78 cc/g, 51.75 cc/g, and 29.41 cc/g at 278 K, 293 K, and 308 K respectively (Fig. 3.19). Isosteric heat of adsorption values were calculated using a Clausius-Clapeyron treatment to be 27.5-32.5 kJ/mol (Fig. 3.20).[27] Hysteretic desorption was observed in both N_2 and CO_2 measurements.

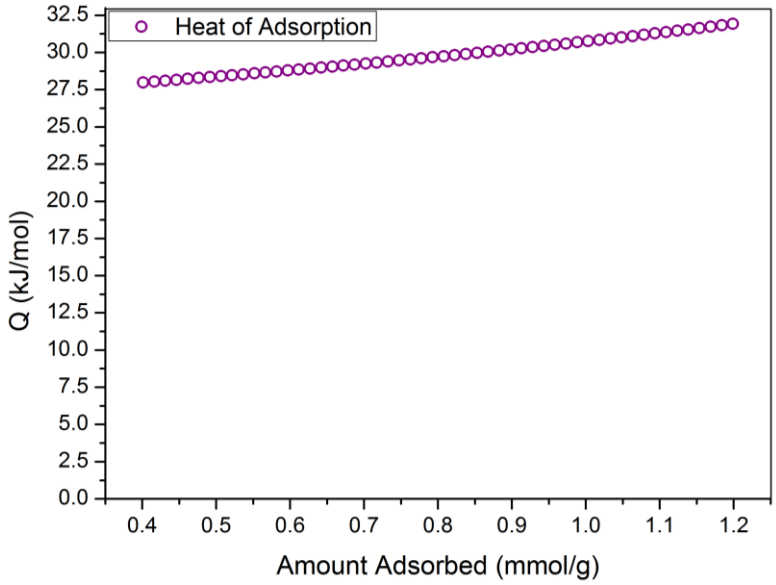

Figure 3.20 – Isosteric heats of adsorption on 7 from CO_2 adsorption data.

Structurally, **7** bears a number of important similarities to a reported MOF, RPM-1 (CCDC: WUTCET), which is composed of {Co_3} SBUs, $bpdc^{2-}$, and 4,4′-bipyridine.[28] RPM-1 also consists of doubly interpenetrated **hex** nets, and has a similar arrangement of voids (Fig. 3.21). However, the {Co_3} SBU in RPM-1 is not coordinated to water molecules and is symmetric about the central Co(II) centre. Importantly, CO_2 sorption behaviour has not been measured for RPM-1.

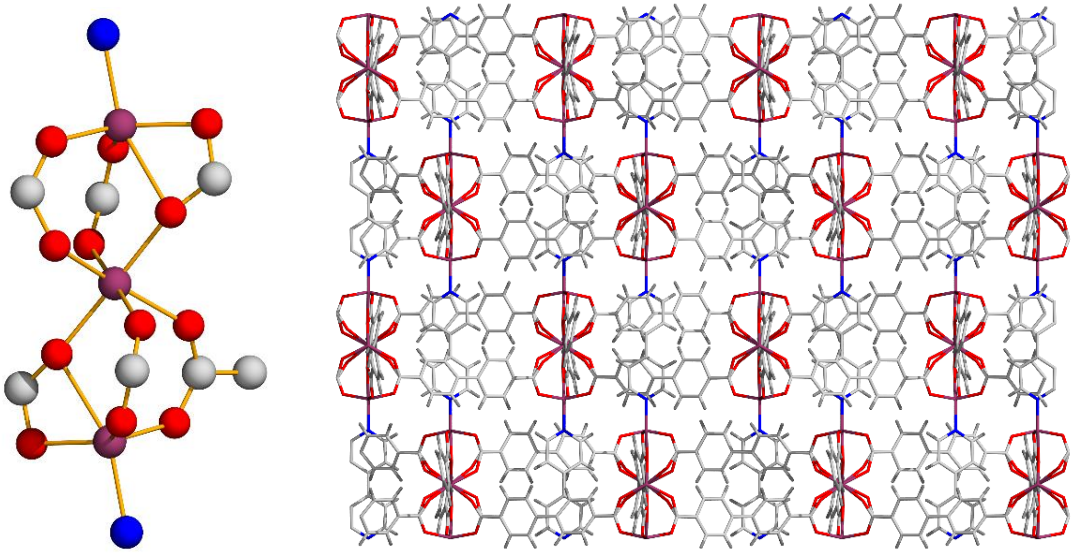

Figure 3.21 – Ball and stick representation of the SBU in RPM-1 (left); wireframe representation of the crystal structure of RPM-1 (right). Solvent molecules omitted for clarity.

3.4: Compound 8, $[Cu(bpet)_2SiF_6]$

The short inorganic SiF_6^{2-} spacers are valuable for modulating CO_2 uptake in coordination polymers based on ditopic N-donors, due to the presence of F atoms and the small spacer length. Here the SiF_6^{2-} moiety is combined with the flexible bpet linker and Cu(II) centres to form a coordination polymer, whose CO_2 uptake properties are of interest. Compound **8**, $[Cu(bpet)_2SiF_6]$, was crystallised using a MeOH solution of the bpet ligand carefully layered over a DMSO solution of $CuSiF_6{\cdot}H_2O$. The assembly was left sealed and undisturbed for 14 days under ambient conditions after which pale purple, rod-shaped single crystals were obtained. A procedure involving stoichiometric amounts of bpet and $CuSiF_6{\cdot}H_2O$ stirred at room temperature was optimised, which allowed high yields of $[Cu(bpet)_2SiF_6]{\cdot}x$MeOH to be produced at a higher scale.

Single crystal X-ray diffraction studies were carried out on **8**. The structure was solved in the monoclinic crystal system and the *C*2/*c* space group, with unit cell dimensions of a = 20.2389(12) Å, b = 8.3612(6) Å, c = 18.9778(16) Å, and $\alpha = \gamma = 90°$, $\beta = 117.267(4)°$. **8** was found to be composed of Cu^{2+} metal centres which are bound to hexafluorosilicate (SiF_6^{2-}) ions and ditopic, neutral bispyridylethane (bpet) linkers (Table 3.6).

The SiF_6^{2-} ion is a well-documented pillar in **pcu** networks, providing linkages in the third dimension between positively charged **sql** sheets based on M^{2+} ions and ditopic N-donor ligands, such as the SIFSIX series of compounds.[29–33] However, in the case of **8**, the flexible ethyl backbone of the bpet ligand allows the ligand to adopt a *gauche* conformation in which square-grid type metal-ligand networks are not formed (Fig. 3.22).[20] Instead, two bpet ligands bind adjacent Cu(II) centres through a monodentate N-donor binding mode, defining a rhombic cavity between each pair of ligands. This arrangement continues between the next pair of Cu(II) centres and so forth, and therefore, four roughly equivalent, coplanar positions on each Cu(II) centre are occupied by coordinating nitrogen atoms. The octahedral environment on each Cu(II) centre is completed by coordinating fluorine atoms from SiF_6^{2-} ions.

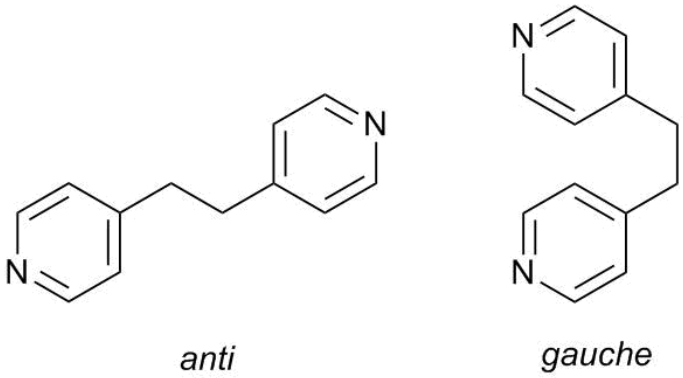

Figure 3.22 – *anti* and *gauche* conformations of the bpet ligand.

Table 3.5 - Selected interatomic distances and angles in 8.

Atoms	Distance		Atoms	Angle
Cu1-F3	2.435(4) Å		F3-Cu1-N8	90.3(1)°
Cu1-F4	2.531(4) Å		F4-Cu1-N8	89.7(1)°
Cu1-N7	2.017(3) Å		N8-Cu1-N7	88.5(2)°
Cu1-N8	2.016(5) Å		F3-Cu1-F4	180°

Cu-F bonds form along the Jahn-Teller elongated axis, resulting in an elongated octahedral geometry overall (Fig. 3.23). Selected interatomic distances and angles are given in Table 3.5. SiF_6^{2-} ions are thus incorporated as ditopic pillars between the one-dimensional, vertex-sharing rhombic arrangements, resulting in a 2D structure with extended Cu-F-SiF_4-F-Cu motifs along the pillaring direction.

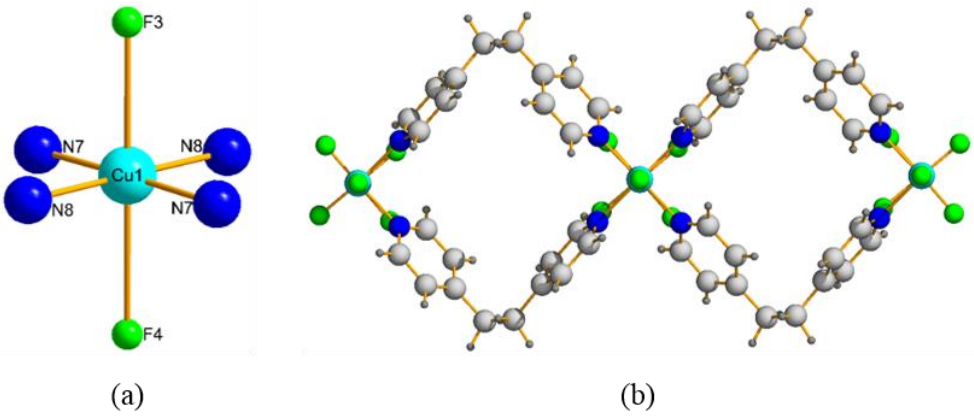

Figure 3.23 – The coordination environment in 8 (a); A representation of the channels present in a single 2D layer of 8 (b). Colour scheme: light blue, Cu; blue, N; grey, C; light grey, H; light green, F; dark green, Si.

Thus, the structure can be thought to consist of Cu^{2+} metal centres, *gauche* bpet ligands, and pillaring SiF_6^{2-} ions; or an infinite 1D SBU composed of repeating $CuSiF_6$ units, linked to two other such SBUs by pairs of *gauche* bpet ligands. The packing arrangement of these 2D sheets is determined by C-H···F interactions and results in an *ABAB* type packing pattern. The network formed is therefore an **sql** type 4-connected network in which pairs of *gauche* bpet ligands act as one kind of single spacer between Cu^{2+} centres, and SiF_6^{2-} ions act as another kind. The overall vertex symbol is $\{4^4.6^2\}$ and the topological reduction is shown in Fig. 3.24.

Table 3.6 – Crystallographic details for 8.

Identification code	8
Empirical formula	$C_{24}H_{24}CuF_6N_4Si$
Formula weight	574.10
Temperature/ K	100(1)
Crystal system	monoclinic
Space group	*C*2/*c*
***a*/Å**	20.2389(12)
***b*/Å**	8.3612(6)
***c*/Å**	18.9778(16)
***α*/°**	90
***β*/°**	117.267(4)
***γ*/°**	90
Volume/Å^3	2854.6(4)
Z	4
ρ_{calc}/ g/Cm^3	1.336
μ/mm^{-1}	2.003
F(000)	1172.0
Crystal size/mm^3	0.09 × 0.02 × 0.02
Radiation	CuKα (λ = 1.54178)
2θ range for data collection/°	9.832 to 114.616
Index ranges	$-21 \leq h \leq 21$, $-7 \leq k \leq 9$, $-20 \leq l \leq 15$
Reflections collected	6718
Independent reflections	1902 [R_{int} = 0.0691, R_{sigma} = 0.0642]
Data/restraints/parameters	1902/0/165
Goodness-of-fit on F^2	1.114
Final R indexes [I>=2σ (I)]	R_1 = 0.0537, wR_2 = 0.1285
Final R indexes [all data]	R_1 = 0.0778, wR_2 = 0.1366
Largest diff. peak/hole / e Å^{-3}	0.33/-0.29

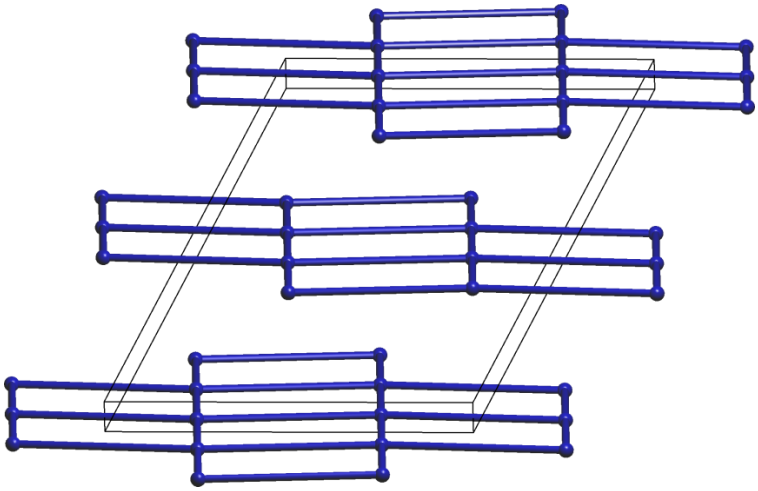

Figure 3.24 – Topological reduction of 8 into sql networks. Unit cell edges are shown for clarity.

The Platon-Squeeze routine was applied for structure solution and the electron density removed on application of the solvent mask roughly corresponds to 3 MeOH molecules per unit cell. The solvent accessible void volume in the structure is 566.58 Å^3, corresponding to 19.8% of the unit cell (using a probe radius of 1.2 Å, and the CCDC-Mercury program) (Fig. 3.25). Application of the 'calcvoid' routine in the Olex2 program shows that the largest spherical void in the crystal structure of **8** has a radius of 2.2 Å and shows that the structure can be permeated in the crystallographic *b*-direction by a sphere of 1.4 Å radius.[24]

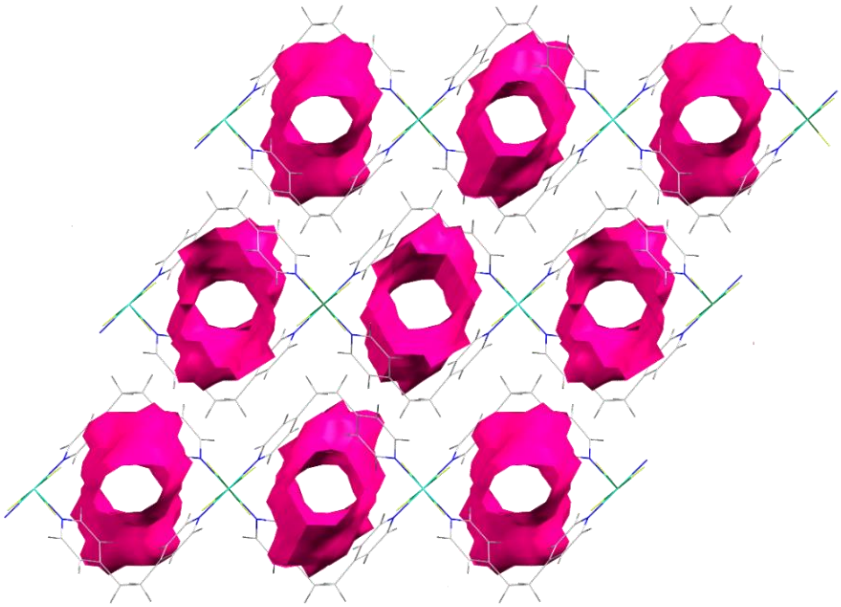

Figure 3.25 – Wireframe representation of 8 highlighting the *ABAB* stacking pattern and voids along the *b*-direction (generated using CCDC-Mercury). Colour scheme: light blue, Cu; blue, N; grey, C; light grey, H; light green, F; dark green, Si.

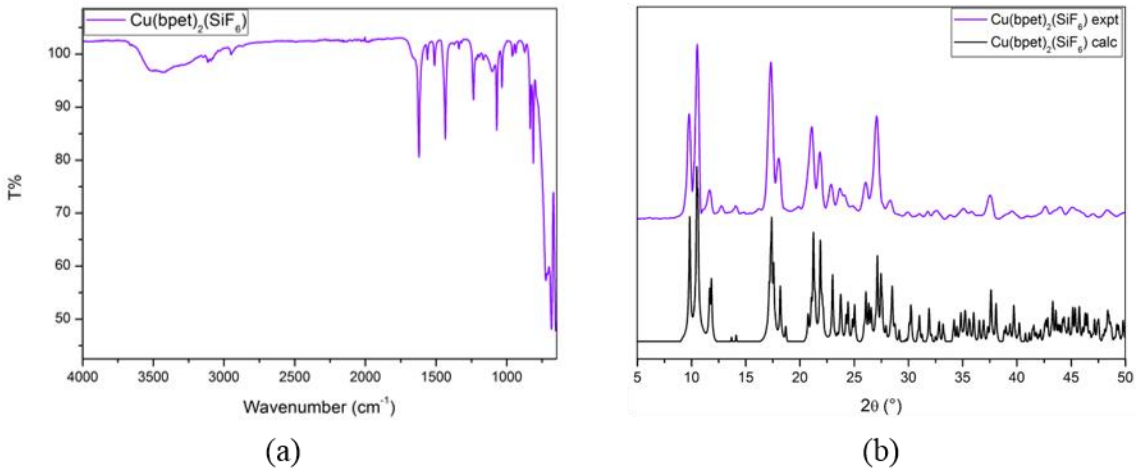

Figure 3.26 – FTIR spectrum (left) and PXRD pattern (right; purple: experimental pattern, black: calculated pattern) for 8.

Physicochemical characterisation of **8** was carried out to support the structural model obtained by single crystal X-ray crystallography. FTIR spectroscopy showed a characteristic broad band between 3500 and 3200 cm^{-1} corresponding to the O-H stretching mode of guest MeOH molecules. The strong signal due to SiF_6^{2-} stretching is seen at 724 cm^{-1}. Signals at 809 and 835 cm^{-1} are assigned to C-H bending modes, and signals from 1620-900 cm^{-1} are also associated with the bpet ligand. The PXRD pattern confirms the phase purity of polycrystalline **8**, synthesised at relatively larger scales, and validates the single-crystal structural model (Fig. 3.26).

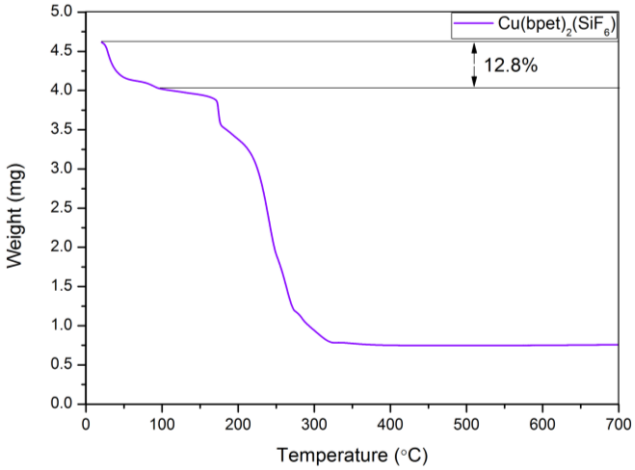

Figure 3.27 – Thermogravimetric analysis for 8.

Thermogravimetric analysis shows a decline associated with removal of guest MeOH molecules of 12.8 wt. % below 100°C, which corresponds to *ca.* 3 MeOH molecules per unit cell, in agreement with X-ray crystallography (Fig. 3.27).

Theoretical studies of the closely related bibenzyl molecule in the gas phase and in solution show a very small maximum energy difference (*ca.* 2 kcal/mol, depending on the level of theory applied) and a significant minimum energy barrier (*ca.* 4.2 kcal/mol) between *anti* and *gauche* conformations.[34] Therefore, the phase purity and absence of framework isomerism observed in the bulk synthesis of **8**, without the application of any elaborate synthetic constraints, is remarkable. Possible framework isomers include the pcu network obtained by analogy with the SIFSIX series based on the *anti* conformation of bpet, or combinations of *anti* and *gauche* conformations as seen in other bpet-based coordination polymers.

Further evaluation of the bulk sample of **8** was carried out by scanning electron microscopy (SEM), providing an assessment of the nature and habit of the microcrystalline phase. SEM images are in line with the phase purity of **8**, and reveal the prevalence of a uniform, laminar biconvex crystal morphology as seen in Fig 3.28.

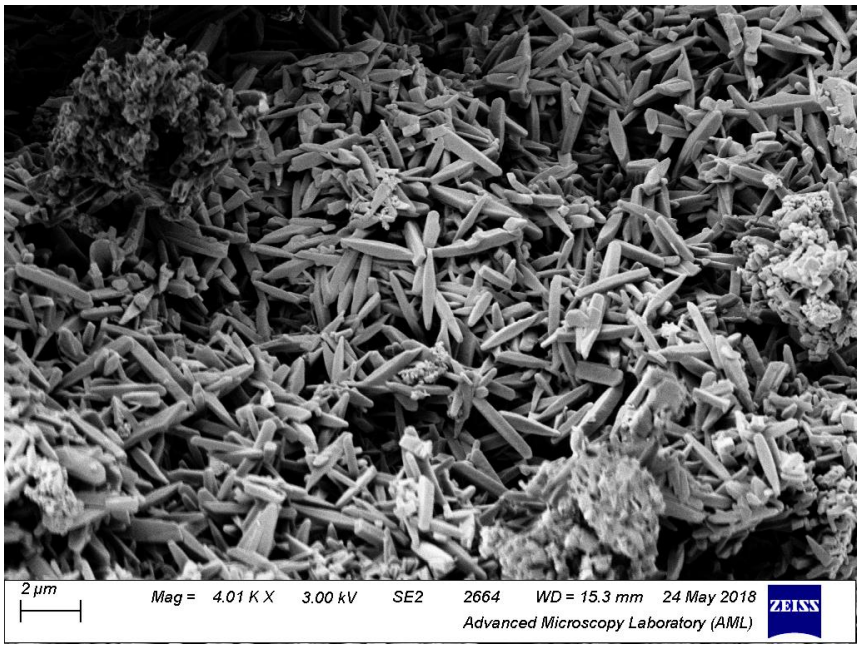

Figure 3.28 – Scanning electron micrograph of 8 synthesised in bulk.

The porosity in **8**, unlike most 2D porous coordination polymers, is intrinsic to each layer, *i.e.* it is independent of the relative orientation of 2D sheets to each other.[35] This is a rare occurrence amongst 2D CPs, and is promising for a variety of applications, as 1D channels run through each layer. The channels are constricted at the rhombic windows defined by

coordinating bpet ligands. Thus, while the diameter of the largest spherical void is 4.4 Å, the channel-limiting diameter is 2.8 Å, as determined using Olex2 (Fig. 3.29).

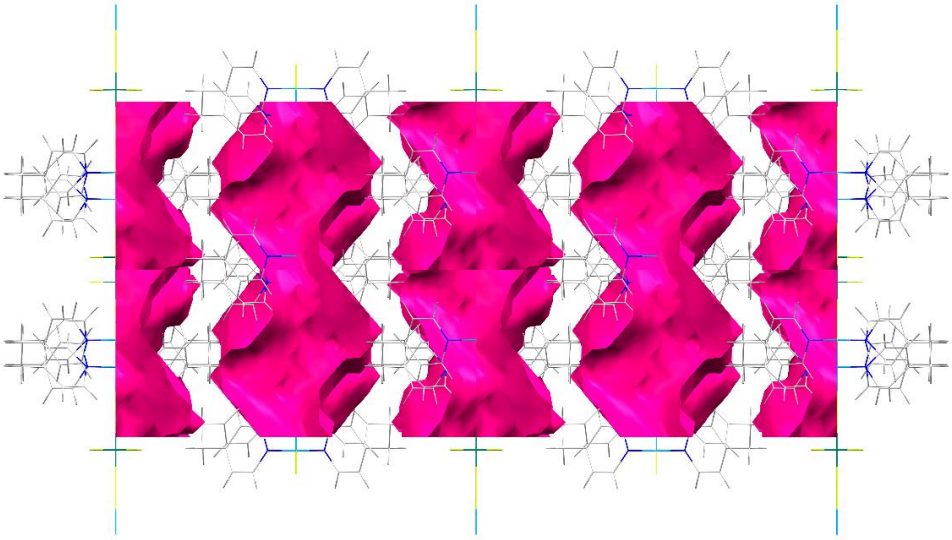

Figure 3.29 – Wireframe representation of 8 along the *c*-direction. A cross-section of the channels is shown (generated using CCDC-Mercury) to highlight the constrictions present. Colour scheme: light blue, Cu; blue, N; grey, C; light grey, H; light green, F; dark green, Si.

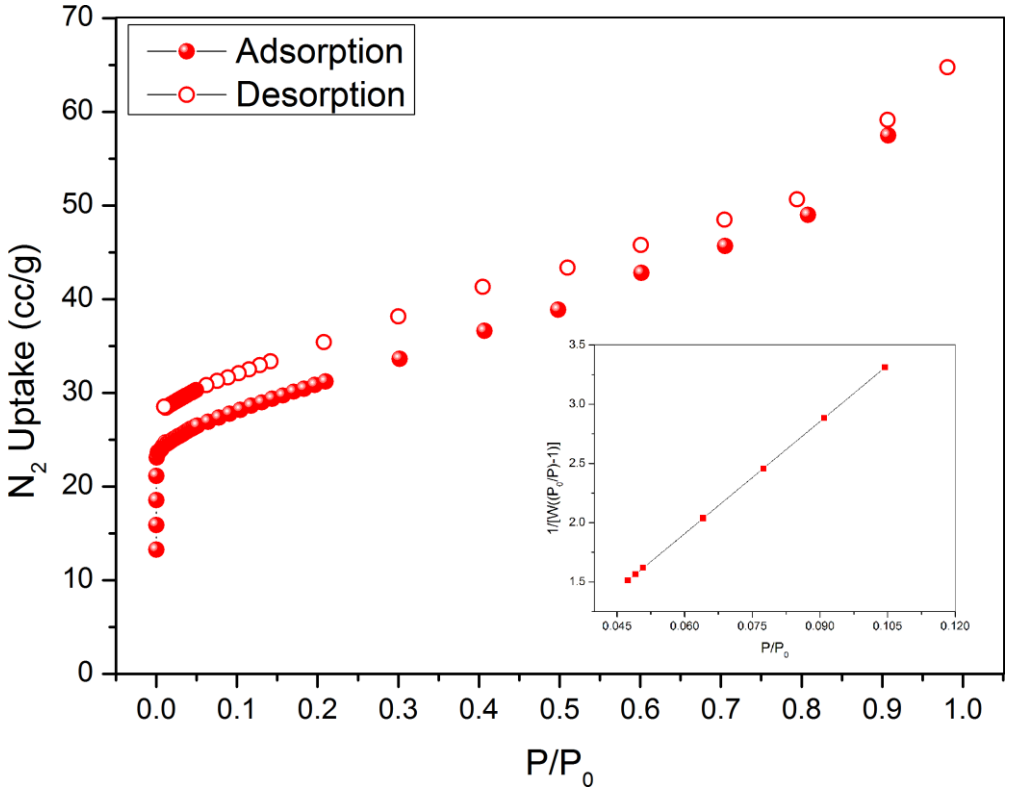

Fig. 3.30 – N_2 isotherm of 8 at 77 K. Inset: Multi-point BET fit; slope = 31.759, intercept = 1.654 x 10^{-2}, correlation coefficient, r = 0.999998, C (constant) = 1907.686, surface area = 110.4 m^2/g.

Gas sorption experiments were carried out on **8** after activation by heating at 120°C under high vacuum for 12 hours. Activation temperatures of 80°C and below were found to be ineffective, while temperatures of 150°C or higher led to a degradation of the sample. N_2 and CO_2 sorption experiments confirmed the porous nature of **8**. The N_2 isotherm measured at 77 K shows a small, steep adsorption step at very low partial pressure. The compound is characterised by a BET surface area of 110.4 m^2/g and a micropore volume of 0.091 cc/g as calculated by using the DFT method, and implying very modest microporosity (Fig. 3.30). N_2 sorption experiments carried out at 293 K show a low uptake of *ca.* 3 cc/g.

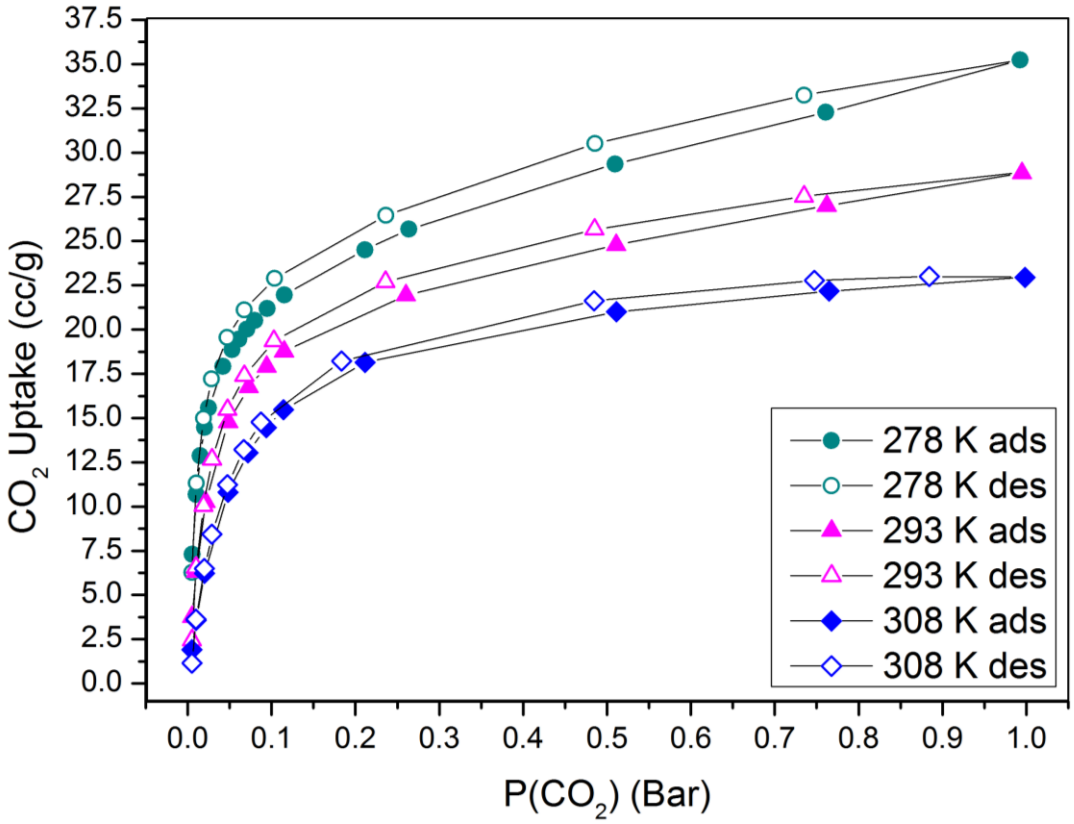

Fig. 3.31 – CO_2 isotherm of 8 at 278 K, 293 K, and 308 K.

CO_2 sorption experiments revealed steep adsorption at very low pressures, type 1 sorption behaviour, and relatively high uptakes of 35.23 cc/g, 28.84 cc/g, and 22.96 cc/g at 1 bar at 278 K, 293 K, and 308 K respectively (Fig. 3.31). The curves were fitted to a Langmuir-Henry model and the heats of adsorption were determined to be in the 35-40 kJ/mol range (Fig. 3.32). The selectivity of **8** for CO_2 over N_2 was determined to be 212 from Henry coefficients, which is comparable to benchmark MOFs.

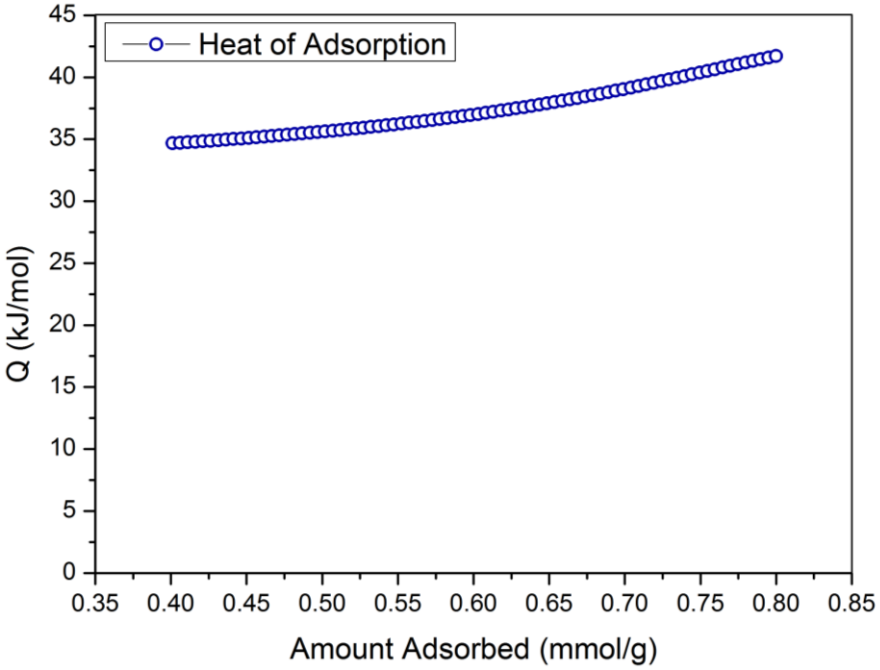

Figure 3.32 – Isosteric heats of adsorption on 8 from CO_2 adsorption data.

The kinetic diameters of N_2 and CO_2 at 293 K are 3.64 Å and 3.30 Å respectively, which are both smaller than the limiting channel diameter in the crystal structure of **8**. In addition, the limiting van der Waals diameter for a CO_2 molecule considered in isolation is 3.1 Å.[36,37] Thus, the adsorption in **8** can occur only if the flexible bpet ligand adopts a conformation upon activation in which the limiting channel diameter increases to ca. 3.1 Å or greater.

The pyridyl rings in **8** are connected to the rest of the structure by C-C and N-Cu bonds about which rotation is possible. Indeed, we find that upon artificially aligning the pyridyl planes to the *b*-axis in a modified crystallographic model of **8** (Olex2), the limiting channel diameter can increase to as much as 3.2 Å. Further flexibility is available through distortions of the alkyl backbone of the ligand. Therefore, we postulate that the flexibility of the bpet ligand is crucial not only to the synthesis of **8**, but also the porosity observed in **8**.

3.5: Compound 9, $[Cu(tdp)_2SiF_6]$

The approach used to synthesise **8** was extended to the even longer tdp ligand, in order to synthesise coordination polymers in which the ligand backbone provides a minimum of structural support, and may adopt a wide variety of conformations. Compound **9**, $[Cu(tdp)_2SiF_6]$, was crystallised using a MeOH solution of the tdp ligand carefully layered over a $CHCl_3$ solution of $CuSiF_6{\cdot}H_2O$. The assembly was left sealed and undisturbed for 9 weeks under ambient conditions after which pale purple, rod-shaped single crystals were obtained.

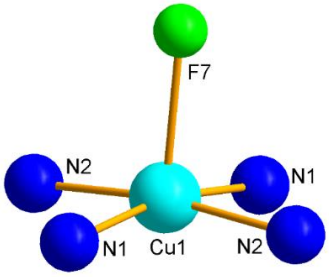

Figure 3.33 – The coordination environment in 9.

Single crystal X-ray diffraction studies were carried out. The structure of **9** was solved in the tetragonal crystal system and the $P4_32_12$ space group, with unit cell dimensions of a = 13.3069(4) Å, b = 13.3069(4) Å, c = 15.1563(6) Å, and $\alpha = \beta = \gamma = 90°$ (Table 3.8). **9** is composed of Cu^{2+} metal centres which are bound to hexafluorosilicate (SiF_6^{2-}) ions and ditopic, neutral 4,4'-trimethylenedipyridine (tdp) linkers. The asymmetric unit of the crystal structure of **9** consists of one tdp ligand, and one SiF_6^{2-} ion, both bound to one Cu^{2+} ion. The Cu^{2+} ion inhabits a square pyramidal coordination environment, with four Cu-N bonds to four distinct tdp ligands forming the base of the pyramid and a Cu-F bond to a SiF_6^{2-} moiety forming the apex (Fig. 3.33). The tdp ligand adopts the *ag* conformation, in which there is one *anti* and one *gauche* conformation on the propyl backbone of tdp (Fig. 3.34). Interatomic distances and bonds in the coordination environment of **9** are given below in Table 3.7.

Table 3.7 - Selected interatomic distances and angles in 9.

Atoms	Distance		Atoms	Angle
Cu1-N1	1.995(5) Å		F7-Cu1-N1	96.9(3)°
Cu1-N2	2.025(5) Å		F7-Cu1-N2	88.2(2)°
Cu1-F7	2.189(6) Å		N1-Cu1-N2	89.3(2)°

Table 3.8 – Crystallographic details for 9.

Identification code	9
Empirical formula	$C_{25.61}H_{27.9}CuF_6N_{4.07}O_2Si$
Formula weight	630.25
Temperature/ K	100(2)
Crystal system	tetragonal
Space group	$P4_32_12$
***a*/Å**	13.3069(4)
***b*/Å**	13.3069(4)
***c*/Å**	15.1563(6)
***α*/°**	90
***β*/°**	90
***γ*/°**	90
Volume/Å^3	2683.78(19)
Z	4
ρ_{calc}/ g/Cm^3	1.560
μ/mm^{-1}	2.245
F(000)	1292.0
Crystal size/mm^3	0.18 × 0.04 × 0.04
Radiation	CuKα (λ = 1.54178)
2θ range for data collection/°	8.842 to 136.658
Index ranges	$-16 \leq h \leq 15$, $-14 \leq k \leq 16$, $-17 \leq l \leq 18$
Reflections collected	20009
Independent reflections	2468 [R_{int} = 0.0607, R_{sigma} = 0.0307]
Data/restraints/parameters	2468/92/181
Goodness-of-fit on F^2	0.992
Final R indexes [I>=2σ (I)]	R_1 = 0.0575, wR_2 = 0.1611
Final R indexes [all data]	R_1 = 0.0609, wR_2 = 0.1657
Largest diff. peak/hole / e Å^{-3}	1.35/-0.34

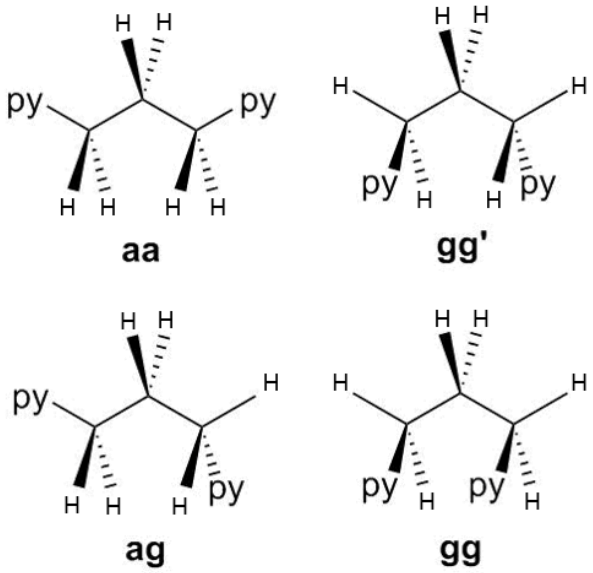

Figure 3.34 – Various conformations of the tdp ligand.

Each tdp ligand is bound to two Cu^{2+} ions, and each Cu^{2+} ion is bound to four tdp ligands, resulting in a two-dimensional **sql** network. Each square in each square grid network is passed through by a spacer from a perpendicularly oriented **sql** net resulting in infinite entangled motifs in a 2D → 3D topology known as **sql-c*** (Fig. 3.35). The point symbol for each 4-connected network in **9** was found to be $\{4^4.6^2\}$.

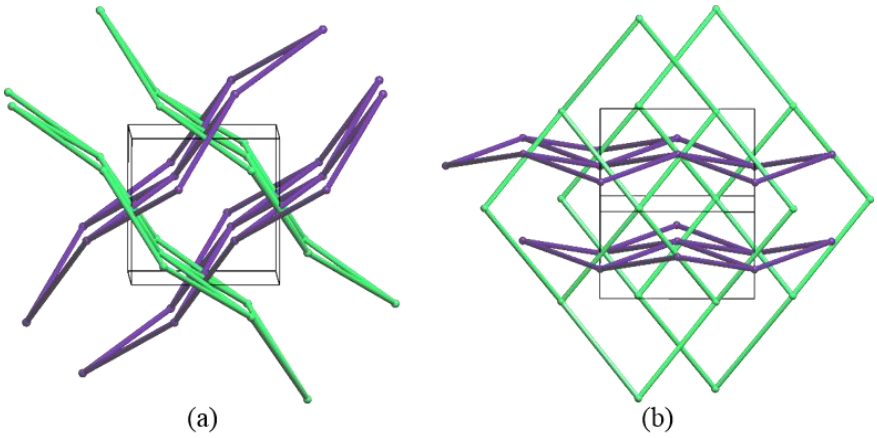

Figure 3.35 – Topological reduction of 9 into a sql-c* network in two orientations (a), (b). Unit cell edges are shown for clarity.

The capping coordination mode adopted by the SiF_6^{2-} group is unusual – there are 10 reported instances of this mode in the CCDC, while there are 113 of the more conventional bidentate bridging mode, as well as 2 of a bidentate chelating mode. However, the

conditions for charge balance are satisfied and there are no counter-ions in the structure. The *ag* conformation of the tdp ligands defines roughly biconcave octagonal repeating motifs consisting of four Cu^{2+} centres and four tdp ligands (Fig. 3.36). These motifs are extended in two dimensions resulting in sheets which are arranged relative to each as shown in Fig. 3.38, and the dense packing arrangement is stabilised by F···H interactions.

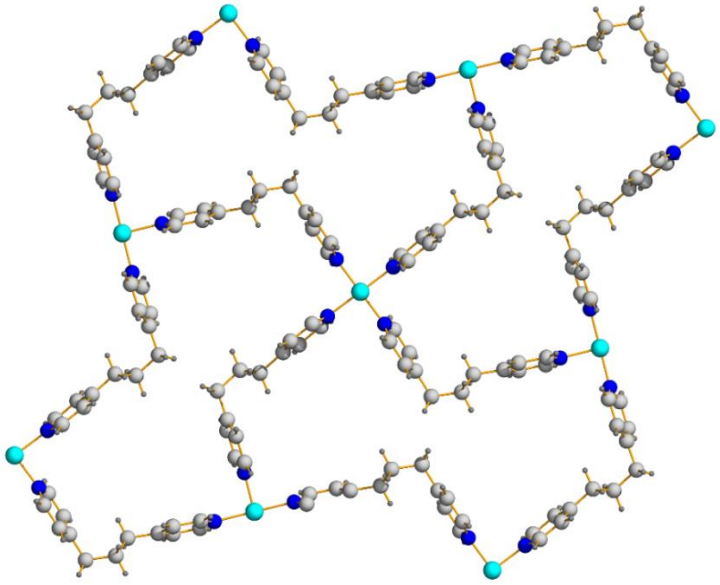

Figure 3.36 – A fragment of the $[Cu(tdp)]_n^{2n+}$ sheet in 9 showing the orientations of individual biconcave octagonal motifs.

The crystal structure shows no accessible void volume. However, trapped solvent molecules occupy inaccessible voids, which account for 1% of the unit cell volume. The identity of the solvent molecules could not be determined crystallographically due to disorder, and the Platon-Squeeze routine was applied.[24]

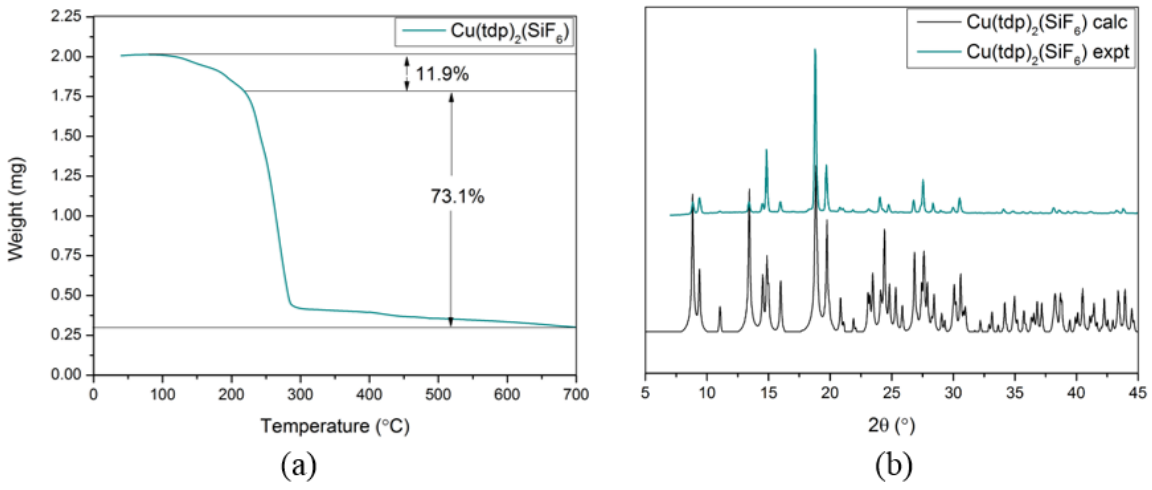

Figure 3.37 – Thermogravimetric analysis (left) and PXRD pattern (right; cyan: experimental pattern, black: calculated pattern) for 9.

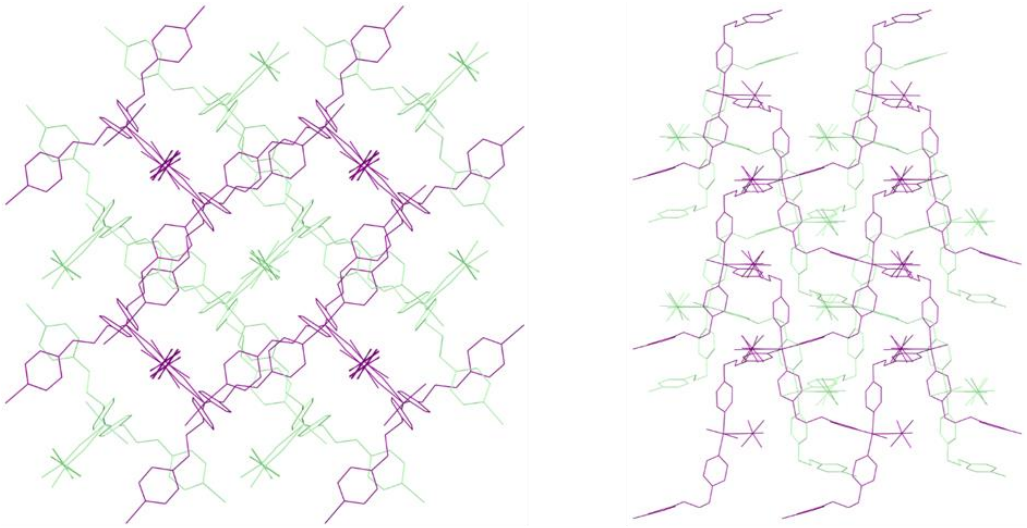

Figure 3.38 – Wireframe representations showing the packing of 2D sheets in 9 in 2x2x2 supercells along the crystallographic *c*-axis (a) and *b*-axis (b) respectively.

Thermogravimetric analysis shows a steady removal of solvent upon application of heat, which must be accompanied by the necessary structural deformations necessary to facilitate the removal of solvent. The initial weight loss step accounts for 11.9 wt% below 220°C, at which point the onset of ligand decomposition becomes clear. The poorly defined solvent loss step agrees with the structural model in which solvent molecules contribute to the weight of the structure, but accessible voids are not present. PXRD studies were also carried out on single crystals of **9**. These confirm the phase purity of the as-synthesised material, and validate the single-crystal structural model (Fig. 3.37). Preferred orientation effects due to large crystal size account for the minor differences in intensity observed between the experimental and calculated PXRD patterns.

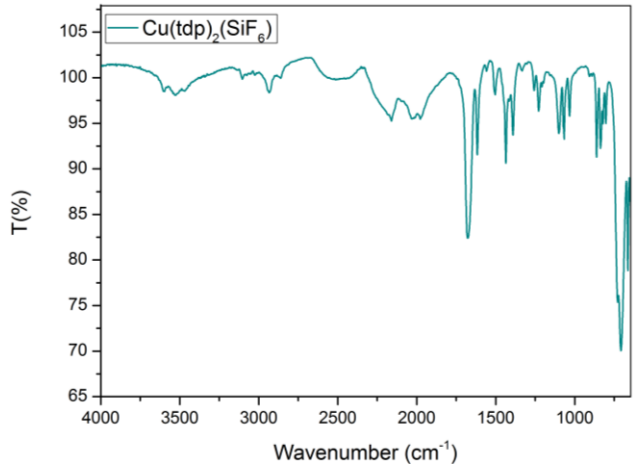

Figure 3.39 – FTIR spectrum of 9.

FTIR spectroscopy shows a pronounced signal at 707 cm^{-1} which is assigned to the SiF_6^{2-} stretching in the monodentate capping mode. Signals at 804 cm^{-1} and 839 cm^{-1} are assigned to C-H bending vibrations. Signals at 1500 cm^{-1}, 1615 cm^{-1}, and 1677 cm^{-1} are assigned to C=C and C=N modes from the tdp pyridyl rings. Signals at 2860 cm^{-1}, 2934 cm^{-1}, and 3104 cm^{-1} are due to C-H stretches, while those at 3467 cm^{-1}, 3521 cm^{-1}, and 3594 cm^{-1} are due to trapped, H-bonding H_2O or MeOH solvent molecules. Signals within the range 1031 cm^{-1} - 1434 cm^{-1} are due to the alkyl backbone of the tdp ligand (Fig. 3.39).

We attribute the long crystallisation time of **9** to the flexibility inherent to the tdp ligand. This flexibility results in numerous possibilities for coordination polymer formation. Notable examples of compounds based on Cu(II)-tdp motifs include those synthesised by Carlucci *et al.* (CCDC: FAGCOG), in which the ligand adopts a *gg* conformation resulting in a non-polymeric ring structure, and two by Plater *et al.* in which the tdp ligands adopt a combination of *aa* and *ag* conformations, yielding 2D **sql** sheet structures (CCDC: CUHZOU, CUHZIO).[38,39] These structures serve as evidence that a variety of conformations are accessible in solution, and that metal complexes may be formed by a diversity of such tdp conformations.

The flexibility of the tdp ligand differentiates it from the ditopic N-donors used in the SIFSIX series, and underlies the formation of the densely packed, non-porous structure of **9**, rather than the porous **pcu** networks that characterise the series. In fact, we find that the dense packing is sufficiently stabilising for the SiF_6^{2-} ion to adopt an unusual capping mode, foregoing the stabilisation offered by an additional Cu-F bond. Nonetheless, it is remarkable that with a number of possible conformations and combinations thereof available to the tdp ligand, **9** forms in high purity based only on the *ag* conformation. In comparison with **8**, the additional methylene group in the alkyl backbone of the ligand appears to be a threshold beyond which porosity is no longer available in the resultant coordination polymer.

3.6: Compound 10, $[Cu(azpy)_2SiF_6]$

A three-dimensional SiF_6^{2-}-based coordination polymer built using a rigid aromatic ligand would only show monodentate coordination at two points, allowing a degree of rotational flexibility within the framework. In order to ascertain whether this flexibility might impact CO_2 uptake, compound **10**, $[Cu(azpy)_2SiF_6]$, was synthesised by heating copper(II) hexafluorosilicate and 4,4′-azopyridine (azpy) in dry methanol in a closed container to yield a polycrystalline product. Appropriately-sized crystals, suitable for single-crystal X-ray diffraction studies were grown by layering techniques using DMSO and MeOH. The resulting crystal structure of **10** contains constitutional MeOH guests, and the identified framework is consistent with previously reported SIFSIX-Cu homologues. We find the isolated MOF crystallises in the tetragonal crystal system in the space group *I*4/*m* with unit cell axes lengths of 13.0690(3) and 8.3940(3) Å and is doubly interpenetrated. (Table 3.10).

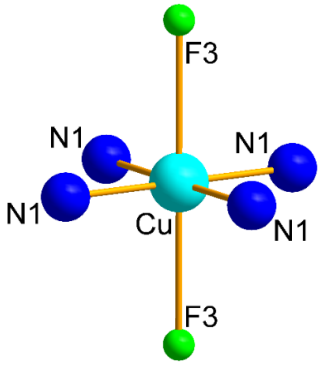

Figure 3.40 – The coordination environment in 10.

The square-grid motif in the structure is characterised by Cu(II)-N bond distances of 2.0201(25) Å involving the equatorially binding azpy ligands. The pillaring hexafluorosilicate anions that bind in the apical positions of the Cu(II) centres give rise to a Cu-F bond distance of 2.4888(34) Å (Fig. 3.40, Table 3.9).

Table 3.9 - Selected interatomic distances and angles in 10.

Atoms	Distance		Atoms	Angle
Cu1-N1	2.020(2) Å		F3-Cu1-F3′	180°
Cu1-F3	2.489(3) Å		N1-Cu1-N1′	90.0(1)°
			F3-Cu1-N1	90.000(1)°

In **10**, N-donor atoms from azpy ligands are bound to all four equatorial positions, while SiF_6^{2-} bridging anions pillar the sheets thus formed into a three-dimensional **pcu** network,

by forming Jahn-Teller elongated Cu-F bonds at the apical positions of each Cu^{2+} centre. Therefore azpy and SiF_6^{2-} are both ditopic struts, by which the overall pillared-sheet structure is obtained. Two networks composed as described are mutually catenated, and are maximally displaced from each other, resulting in the cuboidal channels created by a single network being divided into four smaller channels. The overall point symbol for each 6-connected network is $\{4^{12}.6^3\}$ (Fig. 3.41).

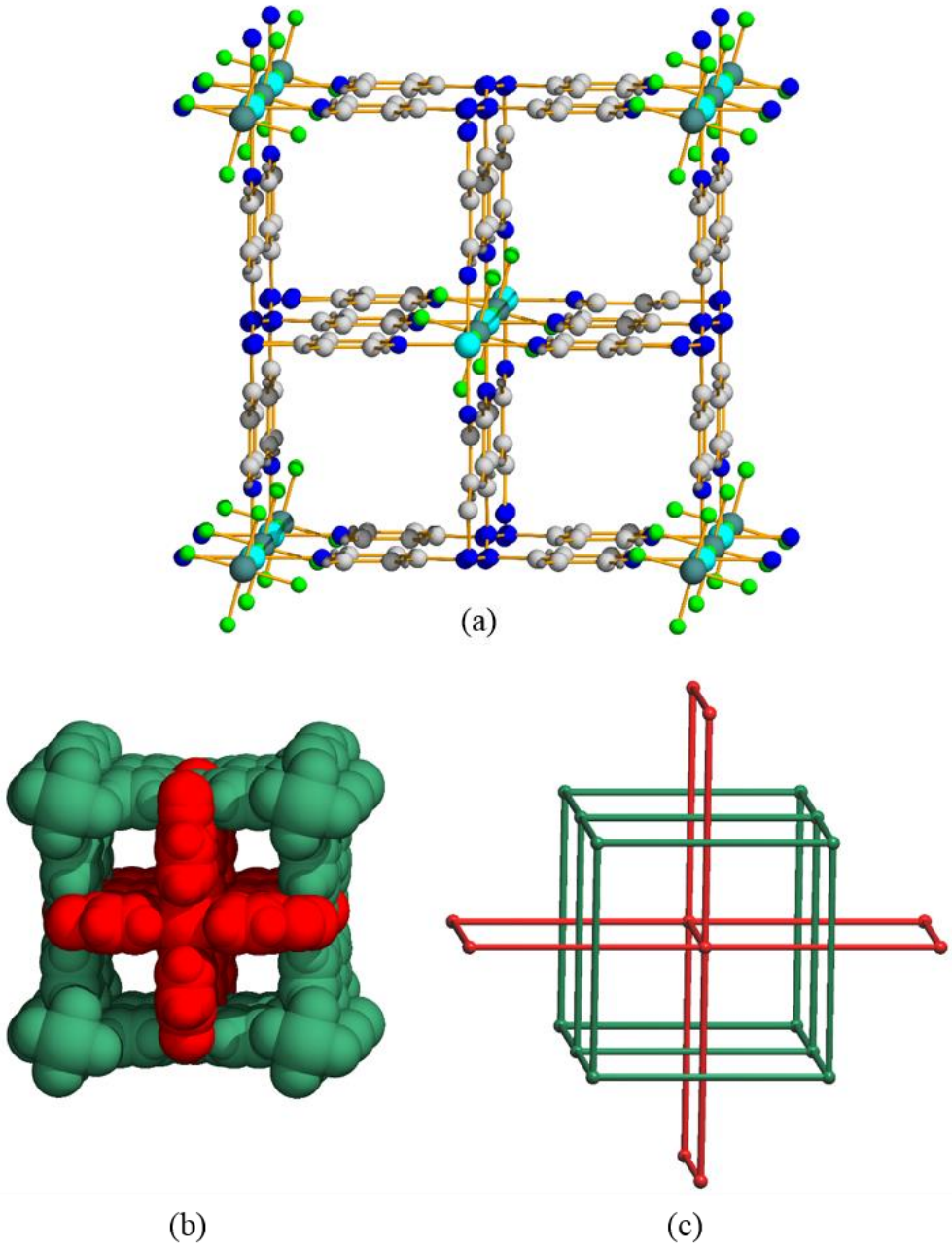

Figure 3.41 (a) – A representation of the crystal structure of 10. Colour scheme: light blue, Cu; blue, N; grey, C; light grey, H; light green, F; dark green, Si; (b) – Space-filling model of a unit cell of 10, with nets coloured individually. Channels are visible along the crystallographic *c*-direction; (c) – Topological reduction of interpenetrating pcu nets.

During attempts to synthesise **10** from MeOH/H_2O solvent mixtures, it was observed that previously established synthetic methods for other Cu-SIFSIX materials only led to the formation of the hydrated **sqI** network in $[Cu(H_2O)_2(azpy)_2]SiF_6 \cdot H_2O$ (**10′**), confirmed by single-crystal unit cell determination (CCDC: XEFGEU).[40] The open-framework **pcu** topology of **10** differs significantly from the non-porous **sqI** structure of **10′** which may be loosely regarded as an ionisation isomer of the former structure (Fig. 3.42).

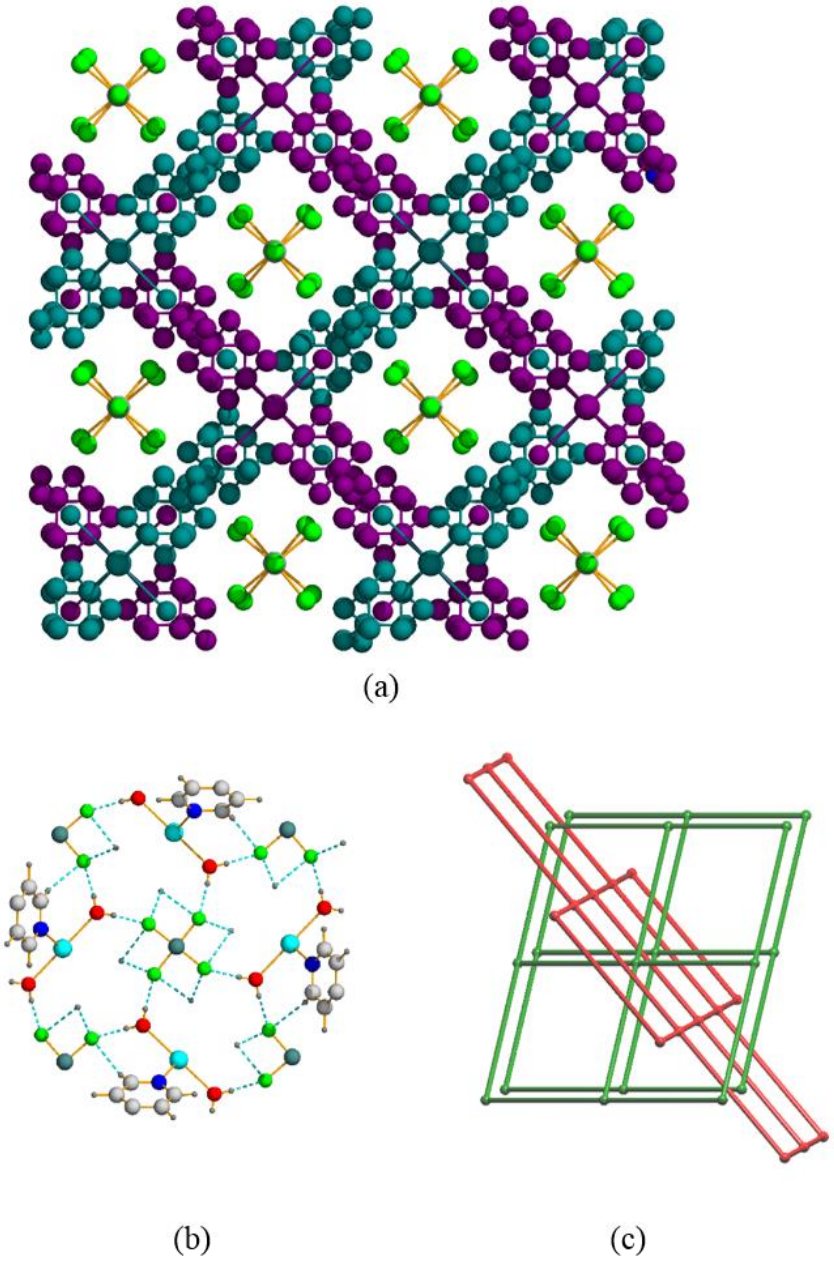

Figure 3.42 (a) – A representation of the crystal structure of 10′. Nets are coloured individually and interstitial SiF_6^{2-} ions are shown; (b) – The H-bonding network in 10′ (dashed blue bonds); (c) – Topological reduction of interpenetrating sql nets.

Table 3.10 - Crystallographic details for 10.

Identification code	10
Empirical formula	$C_{24}H_{32}CuF_6N_8O_4Si$
Formula weight	702.20
Temperature/ K	100(2)
Crystal system	Tetragonal
Space group	*I* 4/*m*
***a*/Å**	13.0690(3)
***b*/Å**	13.0690(3)
***c*/Å**	8.3940(3)
***α*/°**	90
***β*/°**	90
***γ*/°**	90
Volume/Å^3	1433.68(8) Å^3
Z	2
ρ_{calc}/ g/Cm^3	1.627
μ/mm^{-1}	2.261
F(000)	722
Crystal size/mm^3	0.090 x 0.020 x 0.020
Radiation	CuKα (λ = 1.54178 Å)
2θ range for data collection/°	4.785 to 68.100°.
Index ranges	-15<=h<=15, -15<=k<=15, -10<=l<=8
Reflections collected	8312
Independent reflections	711 [R(int) = 0.0429]
Data/restraints/parameters	711 / 34 / 87
Goodness-of-fit on F^2	1.045
Final R indexes [I>=2σ (I)]	R_1 = 0.0553, wR_2 = 0.1526
Final R indexes [all data]	R_1 = 0.0578, wR_2 = 0.1562
Largest diff. peak/hole / e Å^{-3}	0.427/-0.484

In **10′** two axially coordinated H_2O ligands occupy the Jahn-Teller elongated positions on each Cu^{2+} centre. Infinite, positively charged, square grid-like sheets with the composition $[Cu(H_2O)_2(4,4'\text{-azpy})_2]_n^{2n+}$ are charge-balanced by SiF_6^{2-} ions, which are situated in the spaces between interpenetrating sheets. The hexafluorosilicate ions interact with the coordinated water molecules (F···O distance: 2.6826(17) Å) and constitutional pore water molecules (F···O distance: 2.7274(49) Å), forming an intricate H-bonded network and resulting in a stable, non-porous structure (Fig. 2.42).

10 is susceptible to hydrolytic degradation in the presence of H_2O. On exposure to air under ambient humidity, green colouration of the original red/brown crystalline material is observed, as **10** converts quantitatively to **10′** over a time period of a few hours. A more rapid structural transition from **10** to **10′** can be triggered through the addition of liquid H_2O. The phase transition entails a large-scale structural re-ordering, involving a substitution of Cu-F bonds with Cu-O bonds, migration of SiF_6^{2-} ions into voids, and an overall change in the mode of interpenetration - a total re-organisation of networks involving the breaking and re-forming of Cu-N bonds.

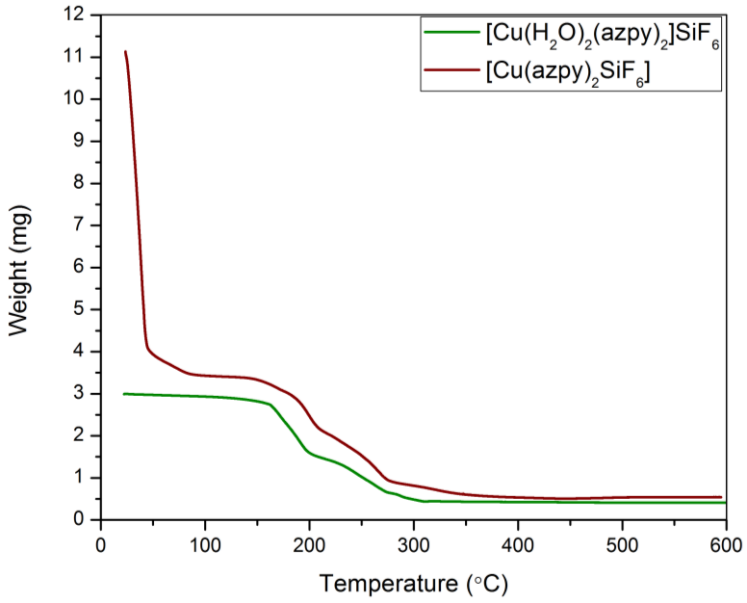

Figure 3.43 – Thermogravimetric analysis for 10 (maroon) and 10′ (green).

The differences in porosity can be seen in the TGA traces of **10** and **10′**. In other respects the traces are similar, and the onset of ligand decomposition can be seen at 160°C in both (Fig. 3.43). PXRD patterns obtained from polycrystalline samples of **10** and **10′** show that the as-synthesised samples are phase pure, and allow the interconversion between them to

be followed analytically. FT-IR analysis shows the expected signals from the two compounds. Sharp signals in the 800-1700 cm^{-1} region are associated with the azpy ligand. The signals at *ca.* 735 and 745 cm^{-1} are associated with SiF_6^{2-} stretching vibrations while the signal at *ca.* 475 cm^{-1} is associated with SiF_6^{2-} bending vibrations. The signal associated with Cu-F vibrations appears at 676 cm^{-1} for **10**. Upon transformation to **10′**, this signal shifts to 690 cm^{-1}. Concurrently, the Cu-N vibration at 635 cm^{-1} shifts to 618 cm^{-1}, indicating variation in bond strengths due to a different coordination environment (Fig. 3.44).

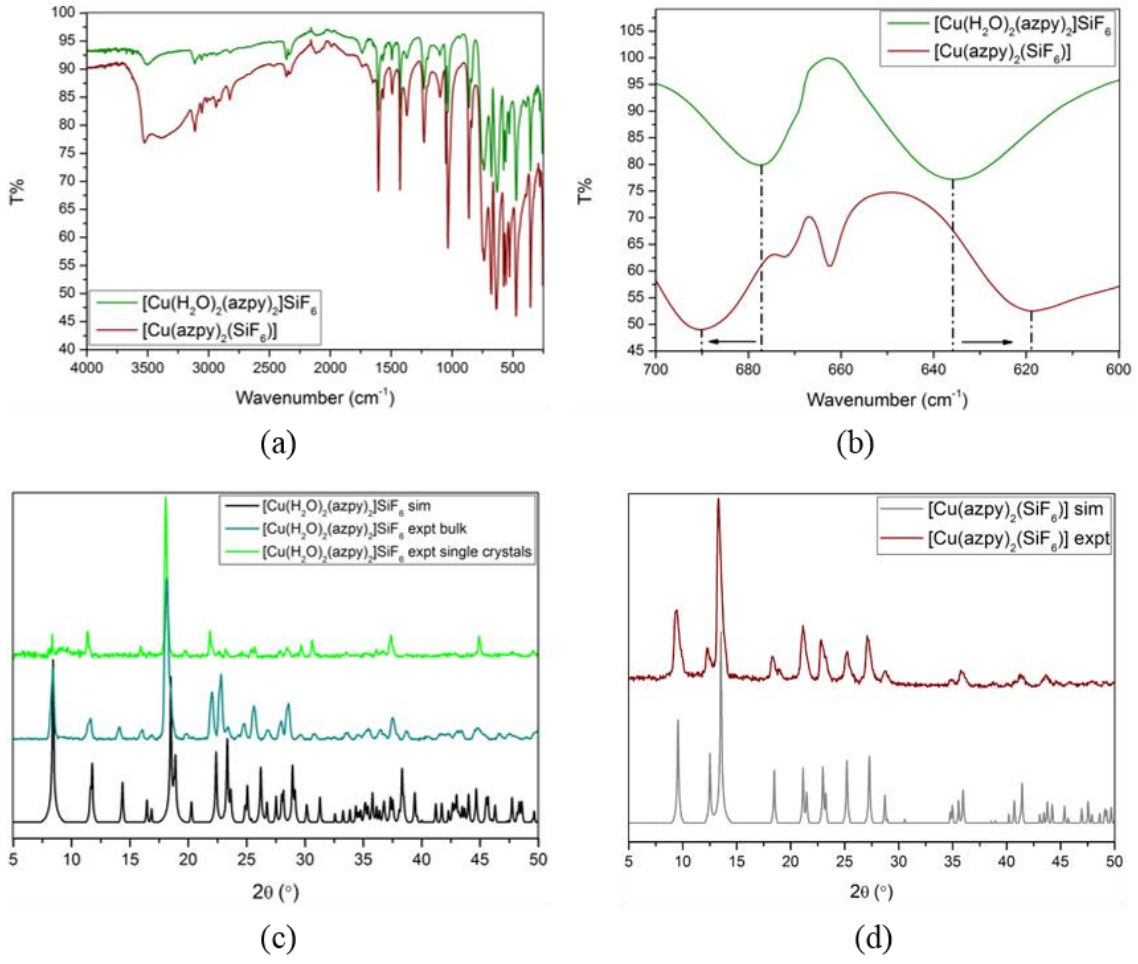

Figure 3.44 (a) – FTIR spectra of 10 (maroon) and 10′ (green); (b) – Differences in the FTIR spectra of 10 and 10′ between 700 cm^{-1} and 600 cm^{-1}; (c) – PXRD patterns of 10′ (light green: experimental pattern measured with 10′ single crystals; teal: experimental pattern measured with polycrystalline 10′; black: calculated pattern for 10′); (d) – PXRD patterns of 10 (maroon: experimental pattern measured with polycrystalline 10; black: calculated pattern for 10).

Gas sorption experiments were carried out on **10** and **10′** after activation under high vacuum at 30°C for 24 h. N_2 and CO_2 sorption experiments on **10′** confirm that it is a non-porous

material with negligible gas uptake (BET surface area of *ca.* 3 m^2/g). In contrast, the N_2 adsorption isotherm for **10** at 77 K shows steep micropore adsorption at low partial pressure (Fig. 3.45). The compound is characterised by a BET surface area of 436 m^2/g and a micropore volume of 0.16 cc/g as calculated using the DFT method.[26] These values are lower but consistent with those reported for SIFSIX-2-Cu-i (735 m^2/g BET surface area and 0.26 cc/g micropore volume), a homologous material that is stabilised by bispyridylethyne linkers.[30]

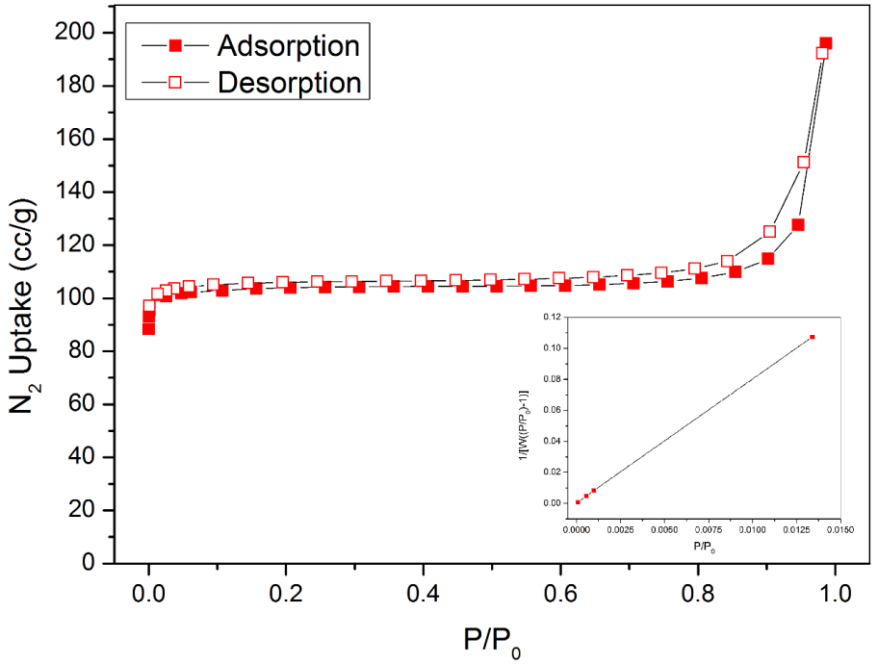

Figure 3.45 – N_2 isotherm measured at 77 K for 10. Inset: Multi-point BET fit; slope = 7.991, intercept = 3.645 x 10^{-4}, correlation coefficient, r = 1.000000, C (constant) = 21925.613, surface area = 435.8 m^2/g.

CO_2 sorption experiments on **10** revealed high low-temperature uptake, with similar isotherms to the reported dipyridylethyne-based analogue, SIFSIX-Cu-2-i. Previously reported calculations on SIFSIX materials conclude that the adsorption mechanism is based on the relatively strong interactions between the partial positive charge on the CO_2 carbon atom and the partial negative charge on the electronegative equatorial fluorine atoms of the SiF_6^{2-} pillar.[30] However, a number of remarkable features distinguish compound **10** from materials in the SIFSIX series as well as other benchmark MOFs for CO_2 adsorption. On measuring CO_2 isotherms across a range of temperatures, a distinct step in the isotherms was observed, becoming more pronounced at higher $P(CO_2)$ at higher temperatures (Fig. 3.46).

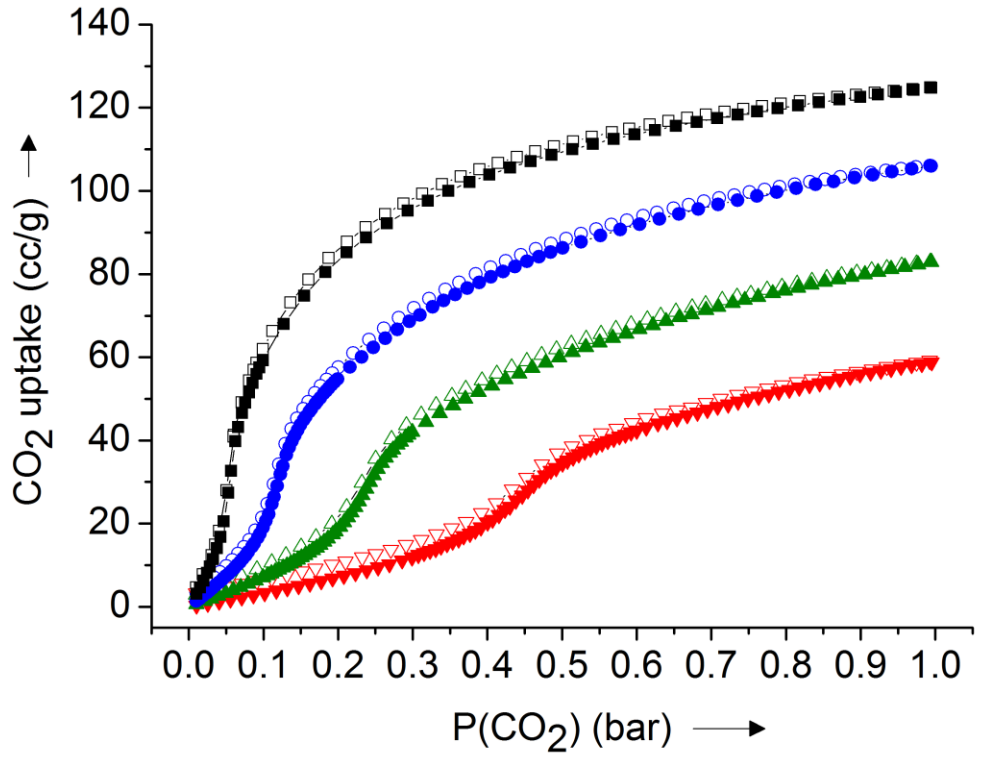

Figure 3.46 - CO_2 sorption isotherms for 10 measured at 278 K (black), 293 K (blue), 308 K (green), 323 K (red); solid symbols: adsorption; open symbols: desorption.

In terms of adsorption capacity, 1 cc of **10** adsorbs 131.7 cc of CO_2 at 1 bar at 293 K. This value compares very well with other benchmark adsorbents for CO_2 capture, such as Zeolite 13X,[41] SIFSIX-2-Cu-i,[30] MIL-101,[42,43] and Mg-MOF-74[44] (Table 3.11). On the other hand, due to the inflection in the isotherm, the CO_2 quantity adsorbed at 0.1 bar is very low. In fact, of the listed benchmark materials only MOF-177[45] and MIL-101(Cr)[42], which are both mesoporous MOFs, adsorb less CO_2 in this pressure range. Thus, the observed change in the sign of the isotherm curvature results in an exceptionally high working capacity of 114.3 cc/cc between 0.1 and 1 bar. This is, to the best of our knowledge, the highest reported CO_2 working capacity in this pressure range and thus, renders **10** an interesting material for use in pressure swing adsorption (PSA) technologies. No photo-response was observed upon UV irradiation following the procedure to be described for compounds **11** and **12**.

Table 3.11. CO_2 sorption characteristics of a number of benchmark materials.

	Uptake (mmol/g)		Uptake (cc/cc)		Uptake (cc /cc)	(g/cc)	
Adsorbent	**1 bar**	**0.1 bar**	**1 bar**	**0.1 bar**	**Working capacity (1 – 0.1 bar)**	**Crystal density**	**Ref**
10	4.42	0.582	131.7	17.3	114.3	1.33	This work
SIFSIX-3-Cu	2.58	2.47	92.5	88.5	3.9	1.60	46
SIFSIX-2-Cu-i	5.44	1.72	152.3	48.2	104.2	1.25	30
Zeolite 13X	4.89	2.98	211.4	128.8	82.6	1.93	41
HKUST-1	3.48	0.75	95.1	20.5	74.6	1.22	47
Mg-MOF74	4.07	2.73	83.1	55.7	27.3	0.91	44
MOF-177	1.81	0.181	41.0	4.1	36.9	1.01	45
MIL-101(Cr)	2.33	0.405	23.0	4.0	19.0	0.44	42, 43
Cu(Me-4py-trz-ia)	6.1	1.2	126.8	24.9	101.9	0.93	48
TRI-PE-MCM-41	2.51	2	52.3	41.7	10.6	0.93	49

10 shows no significant adsorption of N_2 at 293 K (Fig. 3.47). Using the Henry coefficients of the corresponding CO_2 isotherm and we calculate very high experimental CO_2/N_2 selectivities of 108 and 335 corresponding to fitted curves of the pre-inflection and post-inflection parts of the CO_2 isotherm (at 293 K), respectively.[50]

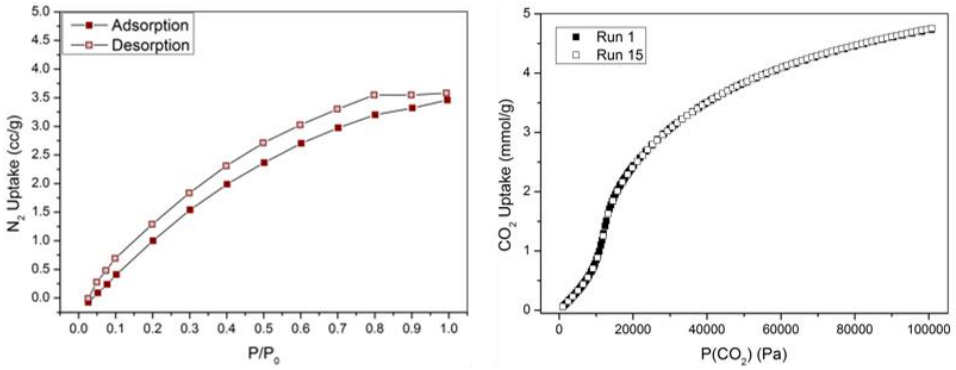

(a) (b)

Figure 3.47 (left) – N_2 isotherm measured at 293 K for 10; (right) - Comparison of CO_2 uptake isotherms after 15 cycles at 293 K.

The inflection in the CO_2 isotherms implies a structural framework transition upon which a 'closed framework' with low CO_2 uptake capacity opens up to form an 'open framework' structure with a high CO_2 storage capacity. The transition occurs over a very small pressure range and is triggered by the adsorption of a specific amount of CO_2. The onset of the inflection is temperature-dependent and occurs at higher pressures for isotherms that were recorded at higher temperatures. The reversibility of the uptake mechanism is strongly demonstrated as the adsorption and desorption curves are superimposed and no differences are observed after 15 measurements without activation (Figure 3.47). The reversibility is further consistent with the calculated isosteric heats of adsorption. Calculations using a Clausius-Clapeyron treatment based on the 278, 293, and 308 K isotherms, give moderate values that vary between 35-37 kJ/mol and which are expected to translate to reversible physisorption phenomena. Parametrisation of the inflected isotherms is non-standard, and is given in Appendix 9.2.

Through computation of the derivative of the experimental isotherms and expressing these as a function of the number of CO_2 molecules per unit cell, we determine that at the inflection point, 1.5 CO_2 molecules are accommodated per unit cell in the structure of **10** (Figure 3.48). From this, we infer that initial adsorption of CO_2 stabilises a framework modification that is more amenable to CO_2 uptake than the empty framework.

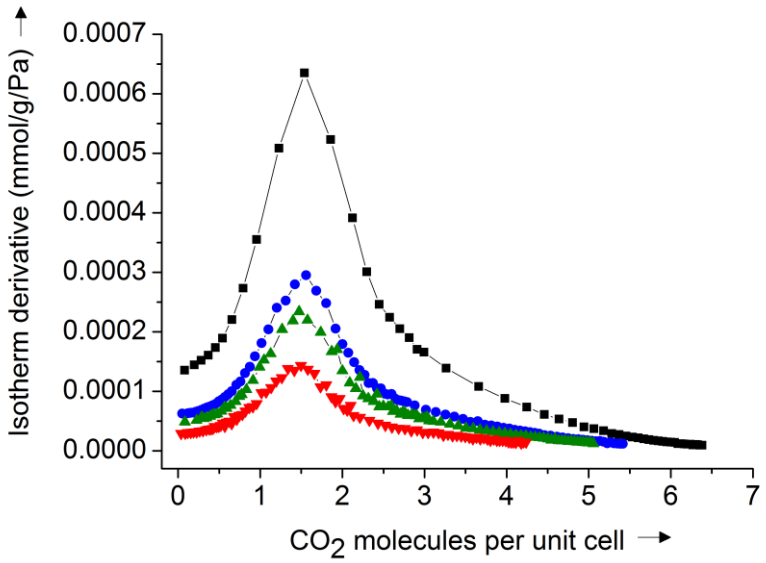

Figure 3.48 - 1st derivatives of CO_2 sorption isotherms measured at 278 K (black), 293 K (blue), 308 K (green), 323 K (red).

Conventional gating,[51] breathing,[52] and swelling phenomena[53] can be ruled out on the basis of the absence of hysteretic desorption. The azpy ligand is a single aromatic system, and therefore the effect of rotation about the Cu-N bonds is reflected across the entire ligand. This, together with the reversible and consistent characteristics of the desorption isotherms, leads to the conclusion that the relevant structural change is associated with a particular ordering of the azpy ligands defining the channel axis after guest adsorption and leading to more accessible voids. A crystallographic determination of the channel diameter using the 'calcvoid' routine in the Olex 2 program indicates an effective limiting channel diameter of 3.2 Å in the structure, a value sufficiently close to the kinetic diameter of CO_2 (3.30 Å) for minor changes in ligand orientation to have marked effects.[54] The diameter of the largest spherical pore available is 3.6 Å. On the basis of the evidence presented, a simple parallel ordering of ligands to the channel axis, or a stabilisation of suitable non-parallel ligand conformations is suggested (subject to the complication that there are no distinct 'cages' in **10,** because of the emergence of the channels from framework interpenetration).[55] The difference in the free energies between frameworks before and after the inflection, using the method developed by Coudert *et al.*, ΔF_{host}, is equal to 2.7 kJ/mol and agrees well with expected energies for this type of structural transition (Appendix 9.2).[56]

The hydrolytic conversion of **10** to **10′** could be reversed by heating **10′** in MeOH. MeOH effects a transformation by removing the kinetically labile, Jahn-Teller elongated, axial H_2O ligands from the Cu(II) centres. This destabilises the H-bonding network that holds the SiF_6^{2-} ions in place in the square pore windows by removing the axially coordinated H_2O groups that participate in H···F interactions. As a consequence, the SiF_6^{2-} ions migrate to bridge adjacent Cu(II) centres, and force a reconfiguration of the network into a porous 3D structure. The reverse occurs when H_2O molecules bind to axial positions on the Cu(II) centres in the dry 3D network: SiF_6^{2-} ions are displaced, occupy H-bonded positions in the pore windows, and the non-porous 2D framework is formed – this is the most stable arrangement in wet conditions. Hence the 2D ↔ 3D transformation occurs reversibly with the introduction or removal of H_2O, assisted by temperature, acting as a stimulus.

Unlike many of the paradigm-defining recyclable MOFs, the **10** – **10′** pair represents a system of two distinct structures both of which contain identical (non-solvent) components; in the process of converting one to the other, no building blocks need to be re-added.[28,57,58]

In agreement with the translational scale of the molecular re-arrangements that facilitate the transition, we were unable to observe any evidence of the transformation proceeding in a single crystal – single crystal fashion under the applied conditions.[59] The conversion-reconversion process is limited by leaching, and has an approximate half-life of two cycles.

The very high CO_2 uptake capacity of **10** and the contrasting non-porous nature of **10′**, in combination with the conversion between the compounds, are properties that we combined to develop a stimulus–responsive system for the instantaneous release of large volumes of CO_2.[19,60] Thus, samples of **10** were evacuated, saturated with CO_2, exposed to ambient air for a few seconds, and sealed in a flask.

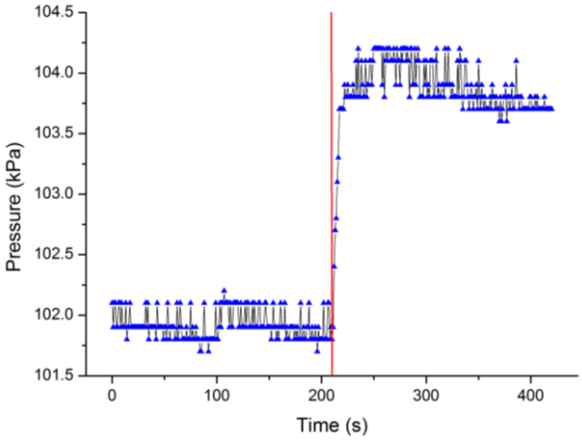

Figure 3.49 - Pressure versus time for the release of loaded CO_2 from 10. Excess liquid water was allowed to make contact with the sample at *t* = 210 s.

On contact with liquid H_2O, a large increase in CO_2 pressure was observed (Figure 2.49). Upon addition of a small quantity of MeOH and heating, **10′** could be reconverted to **10** and reused. CO_2 is forcibly excluded from the framework, leading to significantly faster release than would be seen by simple diffusion or displacement processes. Further, the large differences between the CO_2 sorption capacities of the porous and non-porous forms, lead to significantly larger gas uptake/release volumes in comparison to those of previously described materials.

3.7: Conclusions

In this chapter, the syntheses, single crystal X-ray structures, physicochemical characterisations, and low pressure gas sorption behaviour (where applicable), have been presented for the following five coordination polymers, $[Zn_3(bdc)_3(dabpy)]$ (**6**), $[Co_3(bpdc)_3(dabpy)(H_2O]\cdot 4DMF$ (**7**), $[Cu(bpet)_2SiF_6]$ (**8**), $[Cu(tdp)_2SiF_6]$ (**9**), and $[Cu(azpy)_2SiF_6]$ (**10**).

6 and **7** are the first MOFs built with the dabpy linker. Both **6** and **7** form mixed-ligand networks that can be categorised as pillared layers, in which the dapby linker pillars sheets formed by trinuclear 'hourglass' SBUs and linear dicarboxylate linkers. **6** is based on pillared $\{Zn_3\}$-bdc sheets, while **7** is based on $\{Co_3\}$-bpdc sheets. The synthetic strategy places amino-substituents at the 3-position on 4,4′-bipyridine pyridyl rings, allowing amino-groups to line the cylindrical pores. **6** shows the unusual **bcg** topology, and indicates that use of a longer dicarboxylate will allow the formation of a more symmetric **hex** net. Indeed, we find in **7** that the use of the H_2bpdc ligand allows the **hex** net to form. Despite substantial uptakes at low pressure, CO_2 sorption data reveals energies of adsorption in the range of pure physisorption in **7**, suggesting that the amino groups play a minimal role in adsorption. We postulate that this is due to the limiting effect of small pore diameters in **6** and **7**.

8 and **9** are novel coordination polymers based on hexafluorosilicate anion-linked Cu^{2+} chain motifs. **8** consists of *gauche* bpet ligands which bind adjacent Cu^{2+} centres in pairs defining 2D structures with 1D rhombic channels running parallel to the Cu-SiF_6 chain motif. The porosity of **8** was experimentally determined, and the occurrence of rare intrinsic porosity in each 2D sheet of **8** was thus confirmed. **8** was found to have excellent CO_2 sorption characteristics, and is highly selective for CO_2 over N_2. The flexibility of bpet ligands was shown to be crucial to the porosity of the structure. In **9,** the highly flexible tdp ligand forms an interpenetrated **sql-c*** network. The Cu^{2+} ion adopts a square pyramidal geometry, and the SiF_6^{2-} ion adopts an unfamiliar capping monodentate binding mode. The tdp ligand adopts the *ag* conformation. The structure is non-porous, owing to the high degree of flexibility intrinsic to the ligand, and the interpenetration present in the structure. Remarkably, despite the large number of possible ligand conformations, **8** and **9** can be synthesised at a relatively high scale, and are phase pure.

10 is an interpenetrated **pcu** network homologous to the SIFSIX series of materials. The rigid aromatic azpy linker is used to build square sheets with Cu^{2+} ions, which are pillared into a 3D structure by SiF_6^{2-} anions. The 1D channels in the structure are approximately of the same width as the kinetic diameter of CO_2, making CO_2 sorption strongly contingent on the exact orientation of azpy ligands, which can access a degree of rotational freedom about their lengthwise axis within the structure. CO_2 sorption experiments show that a structural transition occurs from a 'closed' to an 'open' structure upon the adsorption of 1.5 molecules of CO_2 per unit cell, after which the uptake increases to high values. As a result of this transition, **10** has the highest working capacity for CO_2 sorption at room temperature between 0.1 bar and 1 bar. Further, we show that the reversible transition between **10** and **10′** ($[Cu(H_2O)_2(azpy)_2]SiF_6 \cdot H_2O$) upon hydration or dehydration – and the consequent transition between porosity, topology, and modes of interpenetration – can be harnessed for instant release of adsorbed CO_2.

Therefore, we have illustrated the versatility of ditopic N-donor ligands in coordination polymer synthesis, for bearing functional groups and introducing them into frameworks, for the introduction of flexible ligand backbones, and consequent mechanical and conformational flexibility, into the SiF_6^{2-}-pillared synthetic platform, resulting in porous (**8**) and non-porous (**9**) structures. Flexibility resulting from the arrangement of rigid components into a coordination polymer is seen in **10**, in which rotational flexibility about the Cu-N bond allows a structural transition upon the adsorption of 1.5 molecules of CO_2 per unit cell. Another response to stimuli occurs in the form of a reversible water-mediated transition between **10** and the non-porous **10′**, which can be harnessed for the instantaneous release of CO_2, and subsequent regeneration of **10**.

3.8: References

1 A. Y. Robin and K. M. Fromm, *Coord. Chem. Rev.*, 2006, **250**, 2127–2157.

2 P. Z. Moghadam, A. Li, S. B. Wiggin, A. Tao, A. G. P. Maloney, P. A. Wood, S. C. Ward and D. Fairen-Jimenez, *Chem. Mater.*, 2017, **29**, 2618–2625.

3 K. Seki, *Chem. Commun.*, 2001, **1**, 1496–1497.

4 K. Seki and W. Mori, *J. Phys. Chem. B*, 2002, **106**, 1380–1385.

5 A. Pichon, C. M. Fierro, M. Nieuwenhuyzen and S. L. James, *CrystEngComm*, 2007, **9**, 449–451.

6 S. Dalai, P. S. Mukherjee, E. Zangrando, F. Lloret and N. R. Chaudhuri, *J. Chem. Soc. Dalton Trans.*, 2002, **675**, 822.

7 D. N. Dybtsev, H. Chun and K. Kim, *Angew. Chem. Int. Ed.*, 2004, **43**, 5033–5036.

8 B. Rather, M. J. Zaworotko, *Chem. Commun.*, 2003, 830–831.

9 B. Chen, S. Ma, F. Zapata, F. R. Fronczek, E. B. Lobkovsky and H. C. Zhou, *Inorg. Chem.*, 2007, **46**, 1233–1236.

10 S. H. Cho, B. Ma, S. B. T. Nguyen, J. T. Hupp and T. E. Albrecht-Schmitt, *Chem. Commun.*, 2006, 2563–2565.

11 J. T. Culp, C. Madden, K. Kauffman, F. Shi and C. Matranga, *Inorg. Chem.*, 2013, **52**, 4205–4216.

12 S. Takaishi, E. J. Demarco, M. J. Pellin, O. K. Farha and J. T. Hupp, *Chem. Sci.*, 2013, **4**, 1509–1513.

13 Y. Xu, N. A. Vermeulen, Y. Liu, J. T. Hupp and O. K. Farha, *Eur. J. Inorg. Chem.*, 2016, **2016**, 4345–4348.

14 O. Karagiaridi, W. Bury, E. Tylianakis, A. A. Sarjeant, J. T. Hupp and O. K. Farha, *Chem. Mater.*, 2013, **25**, 3499–3503.

15 K. K. Tanabe and S. M. Cohen, *Chem. Soc. Rev.*, 2011, **40**, 498–519.

16 P. Deria, J. E. Mondloch, O. Karagiaridi, W. Bury, J. T. Hupp and O. K. Farha, *Chem. Soc. Rev.*, 2014, **43**, 5896–5912.

17 R. W. Flaig, T. M. Osborn Popp, A. M. Fracaroli, E. A. Kapustin, M. J. Kalmutzki, R. M. Altamimi, F. Fathieh, J. A. Reimer and O. M. Yaghi, *J. Am. Chem. Soc.*, 2017, **139**, 12125–12128.

18 C. L. Jones, A. J. Tansell and T. L. Easun, *J. Mater. Chem. A*, 2016, **4**, 6714–6723.

19 H. Li and M. R. Hill, *Acc. Chem. Res.*, 2017, **50**, 778–786.

20 T. L. Hennigar, D. C. MacQuarrie, P. Losier, R. D. Rogers, M. J. Zaworotko and D. Kogers, *Angew. Chem. Int. Ed.*, 1997, **36**, 972–973.

21 L. Carlucci, G. Ciani, A. Gramaccioli, D. M. Proserpio and S. Rizzato, *CrystEngComm*, 2000, **2**, 154–163.

22 M. Eddaoudi, H. Li and O. M. Yaghi, *J. Am. Chem. Soc.*, 2000, **122**, 1391–1397.

23 A. L. Spek, *Acta Crystallogr. Sect. C Struct. Chem.*, 2015, **71**, 9–18.

24 O. V. Dolomanov, L. J. Bourhis, R. J. Gildea, J. A. K. Howard and H. Puschmann, *J. Appl. Crystallogr.*, 2009, **42**, 339–341.

25 R. J. Phillips and G. B. Deacon, *Coord. Chem. Rev.*, 1980, **33**, 227–250.

26 P. I. Ravikovitch, G. L. Haller and A. V. Neimark, *Adv. Colloid Interface Sci.*, 1998, **76**, 203–226.

27 S. Sircar, *J. Chem. Soc. Trans. 1*, 1985, **81**, 1527–1540.

28 L. Pan, H. Liu, X. Lei, X. Huang, D. H. Olson, N. J. Turro and J. Li, *Angew. Chem. Int. Ed.*, 2003, **42**, 542–546.

29 S. D. Burd, P. S. Nugent, M. H. Mohamed, S. K. Elsaidi and M. J. Zaworotko, *Chimia*, 2013, **67**, 372–378.

30 P. Nugent, Y. Belmabkhout, S. D. Burd, A. J. Cairns, R. Luebke, K. Forrest, T. Pham, S. Ma, B. Space, L. Wojtas, M. Eddaoudi and M. J. Zaworotko, *Nature*, 2013, **495**, 80–84.

31 A. Bajpai, M. Lusi and M. J. Zaworotko, *Chem. Commun.*, 2017, **53**, 3978–3981.

32 S. K. Elsaidi, M. H. Mohamed, H. T. Schaef, A. Kumar, M. Lusi, T. Pham, K. A. Forrest, B. Space, W. Xu, G. J. Halder, J. Liu, M. J. Zaworotko and P. K. Thallapally, *Chem. Commun.*, 2015, **51**, 15530–15533.

33 S. K. Elsaidi, M. H. Mohamed, C. M. Simon, E. Braun, T. Pham, K. A. Forrest, W. Xu, D. Banerjee, B. Space, M. J. Zaworotko and P. K. Thallapally, *Chem. Sci.*, 2017, **8**, 2373–2380.

34 C. Latouche and V. Barone, *J. Chem. Theory Comput.*, 2014, **10**, 5586–5592.

35 N. Reimer, H. Reinsch, A. K. Inge and N. Stock, *Inorg. Chem.*, 2015, **54**, 492–501.

36 A. F. Ismail, K. C. Khulbe and T. Matsuura, *Gas Separation Membranes: Polymeric and Inorganic*, Springer, 2015.

37 J. Koresh, *J. Colloid Interface Sci.*, 1982, **88**, 398–406.

38 L. Carlucci, G. Ciani, D. M. Proserpio and S. Rizzato, *CrystEngComm*, 2002, **4**, 121–129.

39 M. J. Plater, M. R. S. J. Foreman and A. M. Z. Slawin, *J. Chem. Res. - Part S*, 1999, **6**, 74–75.

40 M. A. Withersby, A. J. Blake, N. R. Champness, P. A. Cooke, P. Hubberstey, A. L. Realf, S. J. Teat and M. Schröder, *J. Chem. Soc. Dalton Trans.*, 2000, **2**, 3261–3268.

41 S. Cavenati, C. A. Grande and A. E. Rodrigues, *J. Chem. Eng. Data*, 2004, **49**, 1095–1101.

42 P. L. Llewellyn, S. Bourrelly, C. Serre, A. Vimont, M. Daturi, L. Hamon, G. De Weireld, J. Chang, D. Hong, Y. K. Hwang and S. H. Jhung, *Langmuir*, 2008, 7245–7250.

43 Z. Zhou, L. Mei, C. Ma, F. Xu, J. Xiao, Q. Xia and Z. Li, *Chem. Eng. Sci.*, 2016, **147**, 109–117.

44 D. Britt, H. Furukawa, B. Wang, T. G. Glover and O. M. Yaghi, *Proc. Natl. Acad. Sci.*, 2009, **106**, 20637–20640.

45 D. Saha and Z. Bao, *Environ. Sci. Technol.*, 2010, **44**, 1820–1826.

46 O. Shekhah, Y. Belmabkhout, Z. Chen, V. Guillerm, A. Cairns, K. Adil and M. Eddaoudi, *Nat. Commun.*, 2014, **5**, 1–7.

47 S. Ye, X. Jiang, L. W. Ruan, B. Liu, Y. M. Wang, J. F. Zhu and L. G. Qiu, *Microporous Mesoporous Mater.*, 2013, **179**, 191–197.

48 D. Lässig, J. Lincke, J. Moellmer, C. Reichenbach, A. Moeller, R. Gläser, G. Kalies, K. A. Cychosz, M. Thommes, R. Staudt and H. Krautscheid, *Angew. Chem. Int. Ed.*, 2011, **50**, 10344–10348.

49 Y. Belmabkhout, R. Serna-Guerrero and A. Sayari, *Ind. Emg. Chem. Res.*, 2010, **49**, 359–365.

50 L. Hamon, P. L. Llewellyn, T. Devic, A. Ghoufi, G. Clet, V. Guillerm, G. D. Pirngruber, G.

Maurin, C. Serre, G. Driver, W. Van Beek, E. Jolimaître, A. Vimont, M. Daturi and G. Férey, *J. Am. Chem. Soc.*, 2009, **131**, 17490–17499.

51 R. Kitaura, K. Seki, G. Akiyama and S. Kitagawa, *Angew. Chem. Int. Ed.*, 2003, **42**, 428–431.

52 C. Serre, F. Millange, C. Thouvenot, M. Noguès, G. Marsolier, D. Louër and G. Férey, *J. Am. Chem. Soc.*, 2002, **124**, 13519–13526.

53 C. Serre, C. Mellot-Draznieks, S. Surblé, N. Audebrand, Y. Filinchuk and G. Férey, *Science*, 2007, 1828–1831.

54 S. Sircar, *Ind. Eng. Chem. Res.*, 2006, **45**, 5435–5448.

55 P. Kanoo, S. K. Reddy, G. Kumari, R. Haldar, C. Narayana, S. Balasubramanian and T. K. Maji, *Chem. Commun.*, 2012, **48**, 8487.

56 F.-X. Coudert, M. Jeffroy, A. H. Fuchs, A. Boutin and C. Mellot-Draznieks, *J. Am. Chem. Soc.*, 2008, **130**, 14294–14302.

57 A. Lan, K. Li, H. Wu, L. Kong, N. Nijem, D. H. Olson, T. J. Emge, Y. J. Chabal, D. C. Langreth, M. Hong and J. Li, *Inorg. Chem.*, 2009, **48**, 7165–7173.

58 J. Li, D. J. Timmons and H. Zhou, 2009, 6368–6369.

59 I. Halasz, *Cryst. Growth Des.*, 2010, **10**, 2817–2823.

60 S. Horike, S. Shimomura and S. Kitagawa, *Nat. Chem.*, 2009, **1**, 695–704.

Chapter 4

Rational Functionalisation and Stimulus Responsive CO_2 Uptake in **pto**-Derived MOFs

4.1: Introduction

The **pto** topology, based on the structure of Pt_3O_4, was first reported in a MOF by Chen *et al.* in 2001, after being described by O'Keeffe *et al.* in 2000.[1,2] Analogous to the network structure of Pt_3O_4, **pto** networks are built using 3-connected and 4-connected nodes. In practice, most **pto** MOFs are composed of dinuclear paddle-wheel SBUs and rigid tritopic linkers, although exceptions are known.[3]

A large number of MOFs that are stabilised by polytopic carboxylates contain metal sites capped with labile neutral ligands (often solvent molecules) that can easily be removed or replaced to yield UMCs. For some specific MOF topologies, for instance **pto** or **pts** (assuming the use of only one kind of polytopic carboxylate ligand), such sites are located diametrically across voids from each other, hence allowing the conception of suitable bridging secondary linkers introduced across the void space to functionalise the material, as shown by Kaskel and co-workers, as well as by previous results from our group.[4–7] These secondary linkers can be used to incorporate functional groups suitable for various applications.

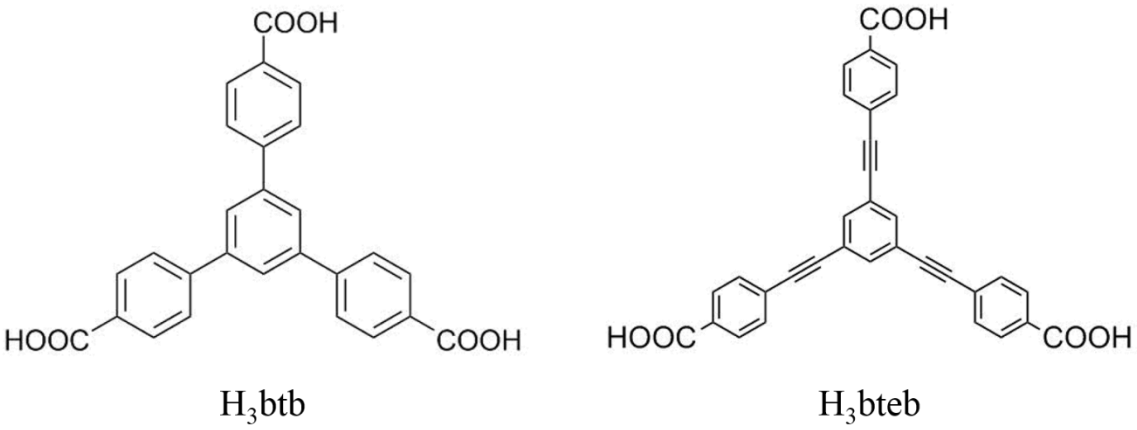

Figure 4.1 – The H_3btb and H_3bteb ligands.

In this chapter the use of H_3btb and H_3bteb ligands (Fig. 4.1) in combination with paddle-wheel SBUs in order to obtain **pto** nets and their further modification using auxiliary linkers is described. The H_3btb ligand is the most commonly used tritopic ligand in the synthesis of **pto** MOFs. The orientation of peripheral benzoate groups at torsion angles of *ca.* 33° to the plane of the central phenyl ring in the final btb^{3-} moiety is crucial to the formation of **pto** networks. When these torsion angles are *ca.* 0°, the isomeric **tbo** network forms (see Introduction).[8] The aryl proton – aryl proton (H_{Ar}-H_{Ar}) repulsion between phenyl rings in

the H_3btb ligand ensures that the **tbo** network cannot form and the **pto** network is favoured. In addition, using H_3btb and period 4 metals (*eg.* Cu(II), Zn(II), Co(II), Ni(II)) to form **pto** networks results in distances of *ca.* 11 Å between opposite SBUs – a length suitable for the incorporation of 4,4′-bipyridine (N to N length = *ca.* 7.0 Å), and its functionalised variants (Fig. 4.2).

H_3bteb is an extended tritopic ligand which is significantly more flexible than H_3btb in two respects. First, the acetylene moieties lengthen each arm, resulting in mechanical flexibility manifested as ligand bowing, which can be seen in crystal structures of MOFs based on H_3bteb.[9] Second, the acetylene moieties remove the H_{Ar}-H_{Ar} repulsion restricting rotation of peripheral benzoate moieties relative to the central phenyl ring. Therefore bteb^{3-} can form both **pto** and **tbo** networks, and the use of auxiliary ligands can direct the formation of phase pure **pto** MOFs, as demonstrated by prior work in our group.[4,5]

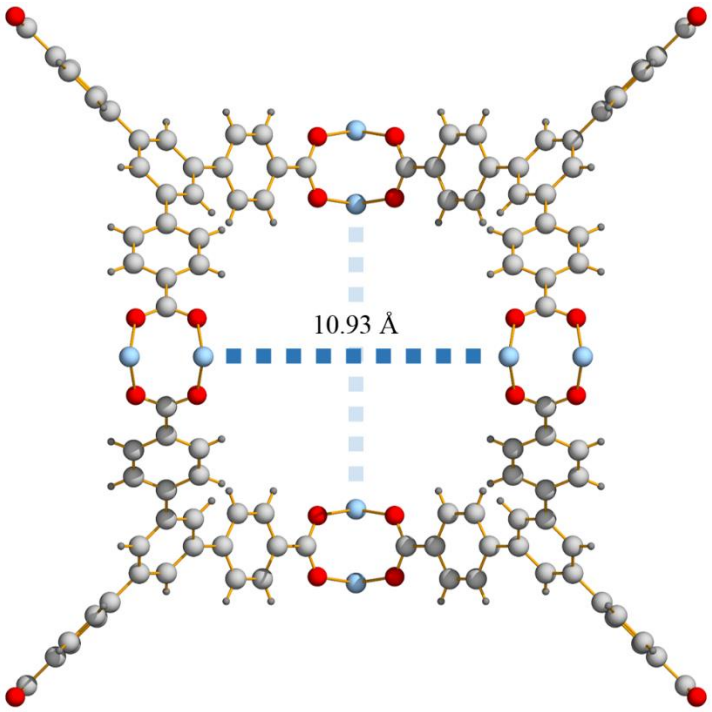

Figure 4.2 – The btb^{3-}/{M$^{II}_2$}-based pto network, with the distances between opposite paddle-wheel units highlighted.

In this chapter, the tunability of the **pto** arrangement outlined above is utilised, and functionalities are incorporated into the MOF pore. In compounds **11** and **12**, the H_3bteb ligand is combined with {Cu_2} paddle-wheel SBUs, and the **pto** framework formed (distance between opposite SBUs *ca.* 13.45 Å) is decorated with auxiliary 4,4′-azopyridine (azpy) ligands. These azpy ligands (distance between terminal N-donor atoms *ca.* 9.1 Å)

are chosen for their photo-responsive behaviour upon irradiation using UV-light. **11** and **12** are characterised by single crystal X-ray diffraction and physicochemical techniques, and their photo-response is evaluated in the context of gas sorption. A number of MOFs have been reported based on azobenzene-based carboxylates or on diarylethylene moieties (see Introduction).[10–12] **11** and **12** are the first constructed using azpy, as well as the first based on a mixed active-inactive ligand approach to show photo-responsive sorption behaviour.

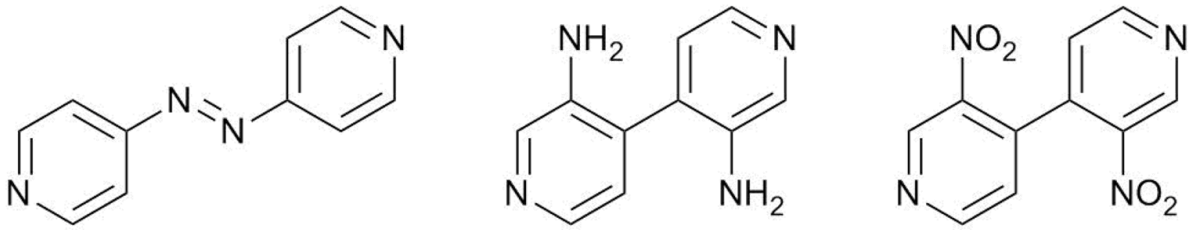

Figure 4.3 – The azpy, dabpy, and dnbpy ligands.

13-16 are built with H_3btb and $\{M^{II}_2\}$ paddle-wheel SBUs (M = Zn, Co, Ni). The auxiliary ligands used are dabpy (3,3′-diamino-4,4′-bipyridine) and dnbpy (3,3′-dinitro-4,4′-bipyridine), which are amino- and nitro-functionalised, respectively (Fig. 4.3). The incorporation of these functional groups into MOF voids has been shown to have favourable influences on gas sorption.[13–15] The distance between terminal N-donor atoms in dabpy is *ca.* 7.09 Å, and in dnbpy, *ca.* 6.98 Å. **13-16** are studied by single-crystal X-ray crystallography and thoroughly characterised.

4.2: $[Cu_3(bteb)_2(azpy)(H_2O)]$ (**11**) and $[Cu_3(bteb)_2(azpy)_{0.5}(H_2O)_2]$ (**12**)

The syntheses of **11** and **12** were carried out at 85°C by reacting solutions of 0.73 mmol $Cu(NO_3)_2 \cdot 3H_2O$ and 0.5 mmol H_3bteb with 0.018 mmol and 0.006 mmol of azpy in 1 mL of DMF, respectively. Higher concentrations of azpy resulted in phase-pure, green block crystals of **11**. At lower concentrations green rod-shaped single crystals of **12** were obtained along with some minor quantities of amorphous by-products, which were separated manually.

Single crystal X-ray diffraction studies carried out on **11** and **12** show the adoption of doubly-interwoven structures based on the **pto** net. The frameworks are constituted by dinuclear Cu^{2+} paddle-wheel SBUs bound by *syn*, *syn* bidentate carboxylate groups from the fully deprotonated $bteb^{3-}$ ligand (Fig. 4.4, 4.5). Each ligand is connected to three $\{Cu_2\}$ paddlewheel units, and each $\{Cu_2\}$ paddlewheel is connected to four $bteb^{3-}$ ligands to form a (4,3)-connected net, in which torsions of *ca.* 33° between central and peripheral phenyl rings stabilise the **pto** arrangement.

The **pto** networks in both MOFs have Cu^{2+}-Cu^{2+} axes aligned into three perpendicular directions, which are coincident to the three crystallographic axes. Both can be considered substituted versions of the archetype **pto** framework reported in TCM-4 and modified in TCM-5.[5] The 4,4′-azopyridine linker (terminal-N to terminal-N length: *ca*. 9.1 Å), despite its slight non-linearity, is a highly suitable auxiliary ligand for incorporation into the TCM-4 structure. In contrast to polytopic carboxylates, the incorporation of ditopic N-donor bridges allows rotational freedom for the auxiliary ligand about the terminal N - terminal N axis, provided suitable sterics. Mismatches in length are compensated by the highly extended $bteb^{3-}$ ligand, which shows a great capacity for bowing, and some stabilization is afforded by weak interactions between the two interwoven frameworks.

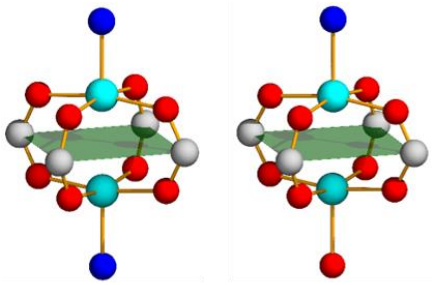

(a) (b)

Figure 4.4 – Representations of Cu(II) paddle-wheel SBUs in 11. (a) - the SBU aligned along the *c*-axis, which has N-donor atoms from azpy ligands at both apical Cu(II) positions; (b) is an SBU to which one H_2O and one azpy ligand are bound.

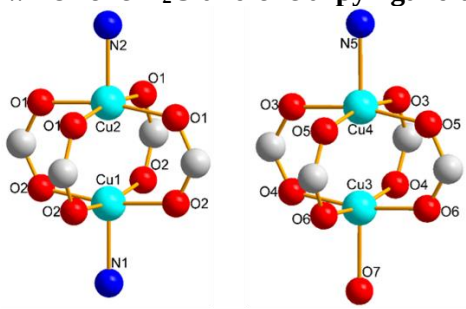

(a) (b)

Figure 4.5 – Labelled representations of Cu(II) paddle-wheel SBUs in 11.

11 crystallises in the space group *P*42/*nmc* - the deviation from the cubic symmetry seen in TCM-4 results in adoption of the tetragonal crystal system. The asymmetric unit of **11** contains a fully deprotonated $bteb^{3-}$ ligand, with two of the carboxylate groups bound to four Cu^{2+} centres. Three of these Cu^{2+} centres are bound to N-donor atoms from azpy ligands, and one is bound to an O-donor atom from water at the apical positions of the square pyramidal geometry exhibited by these Cu^{2+} centres. Along the crystallographic *a* and *b* axes, alternate inter-SBU spaces are bridged by azpy ligands, leaving water molecules coordinated to half the Cu^{2+} centres. However, along the crystallographic *c*-direction, all SBUs are bridged. This results in an overall molecular formula of $[Cu_3(bteb)_2(azpy)(H_2O)]$, whereby dual interpenetration prevails throughout the structure (Fig. 4.6).

Hence, there are two distinct coordination environments adopted by the dinuclear paddle-wheel SBUs in **11** – one in which both axial positions are bound to N-donor atoms that derive from azpy ligands, and one in which one of the axial positions is bound to an O-donor atom of a coordinated water molecule (Fig. 4.10). The geometrical parameters and binding environment of the dinuclear SBUs in **11** are characterised by Cu^{2+}-Cu^{2+} distances of *ca*. 2.65 Å, Cu-O carboxylate bond lengths of 1.93-1.97 Å, axial Cu-O and Cu-N bond lengths of *ca.* 2.17 Å (Table 4.1).

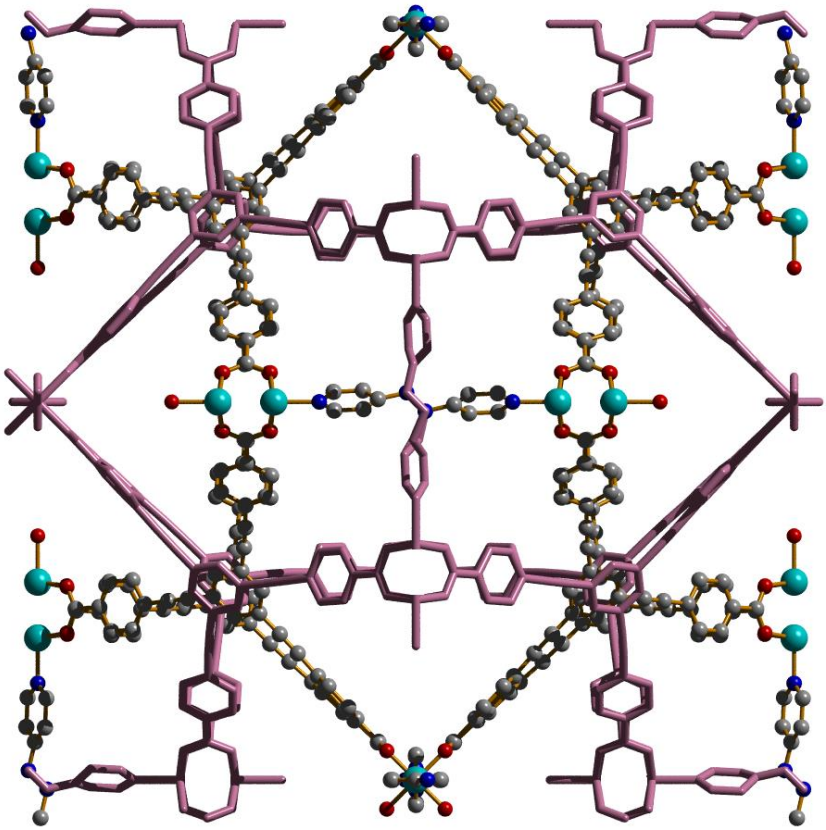

Figure 4.6 – A representation of the crystal structure of 11, with framework interweaving highlighted by colouring one net in pink.

The unit cell volume of **11**, *ca.* 40882 $Å^3$, is greater than that of the un-functionalised corresponding TCM-4 structure, which has a unit cell volume of 39725 $Å^3$. However, the introduction of groups diametrically across the existing channels results in a decreased solvent accessible void volume (53 vol.%, in **11** compared to 78 vol.% in TCM-4).[4,5]

Table 4.1 - Selected interatomic distances and angles in 11.

Atoms	Distance		Atoms	Angle
Cu1-O2	1.958(4) Å		O2-Cu1-N1	96.0(2)°
Cu1-N1	2.09(1) Å		O2-Cu1-O2′	88.9(2)°
Cu1-Cu2	2.648(2) Å		N1-Cu1-Cu2	180°
Cu2-O1	1.953(4) Å		N2-Cu2-Cu1	180°
Cu2-N2	2.04(1) Å		N2-Cu2-O1	95.7(2)°
			O1-Cu2-O1′	89.5(2)°
Cu3-O7	2.169(6) Å		O4-Cu3-O7	96.2 (2)°
Cu3-O6	1.934(4) Å		O6-Cu3-O7	95.5(2)°
Cu3-O4	1.957(4) Å		O4-Cu3-O6	89.0(2)°
Cu4-O3	1.967(4) Å		O7-Cu3-Cu4	178.7(1)°
Cu4-O5	1.953(4) Å		Cu3-Cu4-N5	177.7(2)°
Cu4-N5	2.167(6) Å		O3-Cu4-N5	95.3(2)°
			O5-Cu4-N5	97.8(2)°
			O3-Cu4-O5	88.3(2)°

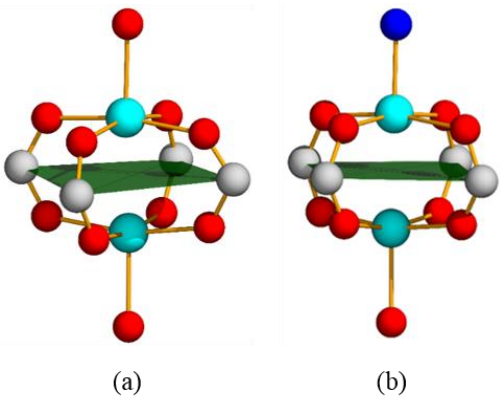

Figure 4.7 – Representations of Cu(II) paddle-wheel SBUs in 12. (a) the SBU aligned along the *c*-axis, which has O-donor atoms from H_2O at both apical Cu(II) positions; (b) the SBU to which one H_2O and one azpy ligand are bound.

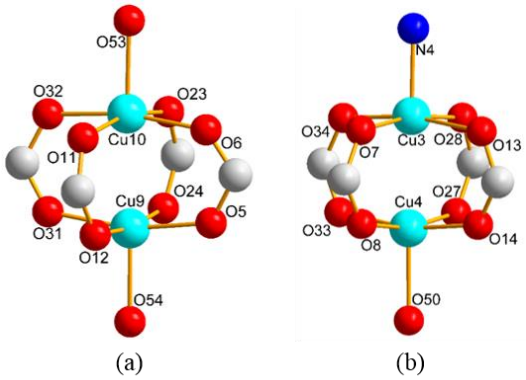

Figure 4.8 – Labelled representations of Cu(II) paddle-wheel SBUs in 12.

From this perspective, **12** (Figures 1b and 1d) offers a more desirable compromise between porosity and the incorporation of switching functionality *via* the azpy ligand. The compound crystallises in the triclinic crystal system (space group $P\bar{1}$). As in **11** the structure is based on dinuclear Cu^{2+} paddlewheel SBUs (Cu^{2+}-Cu^{2+} distance *ca.* 2.64 Å) and $bteb^{3-}$ ligands (Table 4.2). The asymmetric unit in this case is more elaborate than that for **11**, and consists of eight fully deprotonated $bteb^{3-}$ ligands bound to six $\{Cu_2\}$ SBUs. Two SBUs are bridged by azpy ligands, which are bound to the apical sites on square pyramidal Cu^{2+} centres. The remaining apical positions are bound to O-donor atoms from water molecules (Fig. 4.7, 4.8). The accessible void volume per unit cell is not much larger than in **11**, 22430 $Å^3$ (55.5%). However, the presence of fewer azpy bridging ligands results in permanent channels which are characterised by a cross-sectional diameter of 8.8 Å at their narrowest, which extend in the direction of the crystallographic *c* axis. Alternate inter-SBU spaces along the crystallographic *a* and *b* axis are bridged by azpy ligands, while SBUs along the *c*-direction retain axially coordinated water ligands (Fig. 4.9).

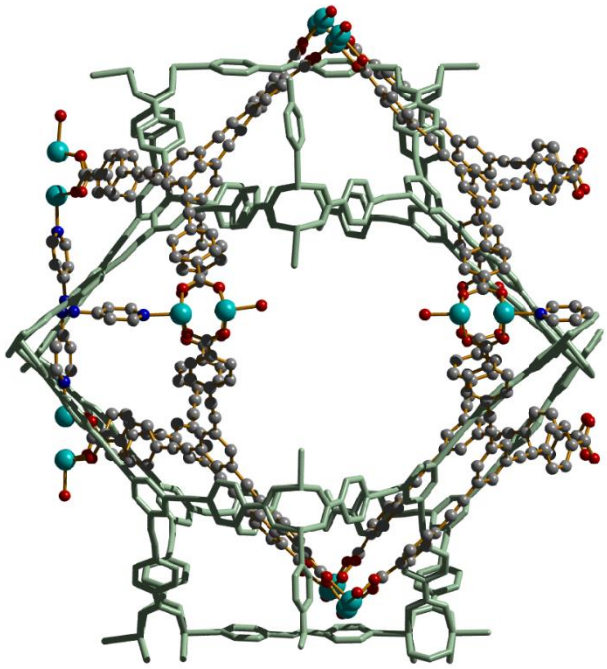

Figure 4.9 – A representation of the crystal structure of 12, with framework interweaving highlighted by colouring one net in light green.

Once again, this results in two distinct coordination environments – SBUs may either be axially linked to one N-donor and one O-donor, or two O-donor groups (axial Cu-O distance: *ca.* 2.16 Å, axial Cu-N distance: *ca.* 2.07 Å, equatorial Cu-O distance: 1.92-2.14

Å). This arrangement results in significantly greater channel availability and a larger number of potential unsaturated metal centres (UMCs) on activation, which are expected to interact with guests, for instance with CO_2 adsorbate molecules. Thus, in contrast to **11**, in **12**, the {Cu_2} units are not linked into a continuous 1-D arrangement by azpy ligands in any direction. Therefore, the composition of **12** is [$Cu_3(bteb)_2(azpy)_{0.5}(H_2O)_2$], with dual interpenetration (Fig. 4.10).

Table 4.2 - Selected interatomic distances and angles in 12.

Atoms	**Distance**		**Atoms**	**Angle**
Cu9-O54	2.110(7) Å		O54-Cu9-O5	95.7(4)°
Cu9-O5	1.98(1) Å		O54-Cu9-O24	98.4(4)°
Cu-9-O12	1.93(1) Å		O5-Cu9-24	89.3(5)°
Cu9-O24	1.94(1) Å		O12-Cu9-O31	87.6(5)°
Cu9-O31	2.00(1) Å		O54-Cu9-Cu10	175.3(2)°
Cu9-Cu10	2.621(3) Å		Cu9-Cu10-O53	177.2(2)°
Cu10-O11	1.97(1) Å		O53-Cu10-O32	96.2(5)°
Cu10-O6	1.99(1) Å		O53-Cu10-O11	97.7(4)°
Cu10-O32	1.99(2) Å		O6-Cu10-O23	87.6(5)°
Cu10-O23	1.96(1) Å		O32-Cu10-O11	86.2(6)°
Cu10-O53	2.130(8) Å			
Cu4-O50	2.167(8) Å		O50-Cu4-O14	94.7(4)°
Cu4-O27	1.970(9) Å		O50-Cu4-O27	96.5(4)°
Cu4-O14	1.93(1) Å		O27-Cu4-O14	87.4(5)°
Cu4-O8	1.97(1) Å		O8-Cu4-O33	93.4(4)°
Cu4-O3	2.08(1) Å		O50-Cu4-Cu3	178.0(2)°
Cu4-Cu3	2.641(3) Å		Cu4-Cu3-N4	177.7(3)°
Cu3-O28	1.97(1) Å		N4-Cu3-O28	96.7(5)°
Cu3-O13	2.15(1) Å		N4-Cu4-O13	93.6(4)°
Cu3-O7	1.95(1) Å		O13-Cu-O28	92.3(5)°
Cu3-O34	1.99(1) Å		O34-Cu3-O7	88.5(5)°
Cu3-N4	2.07(1) Å			

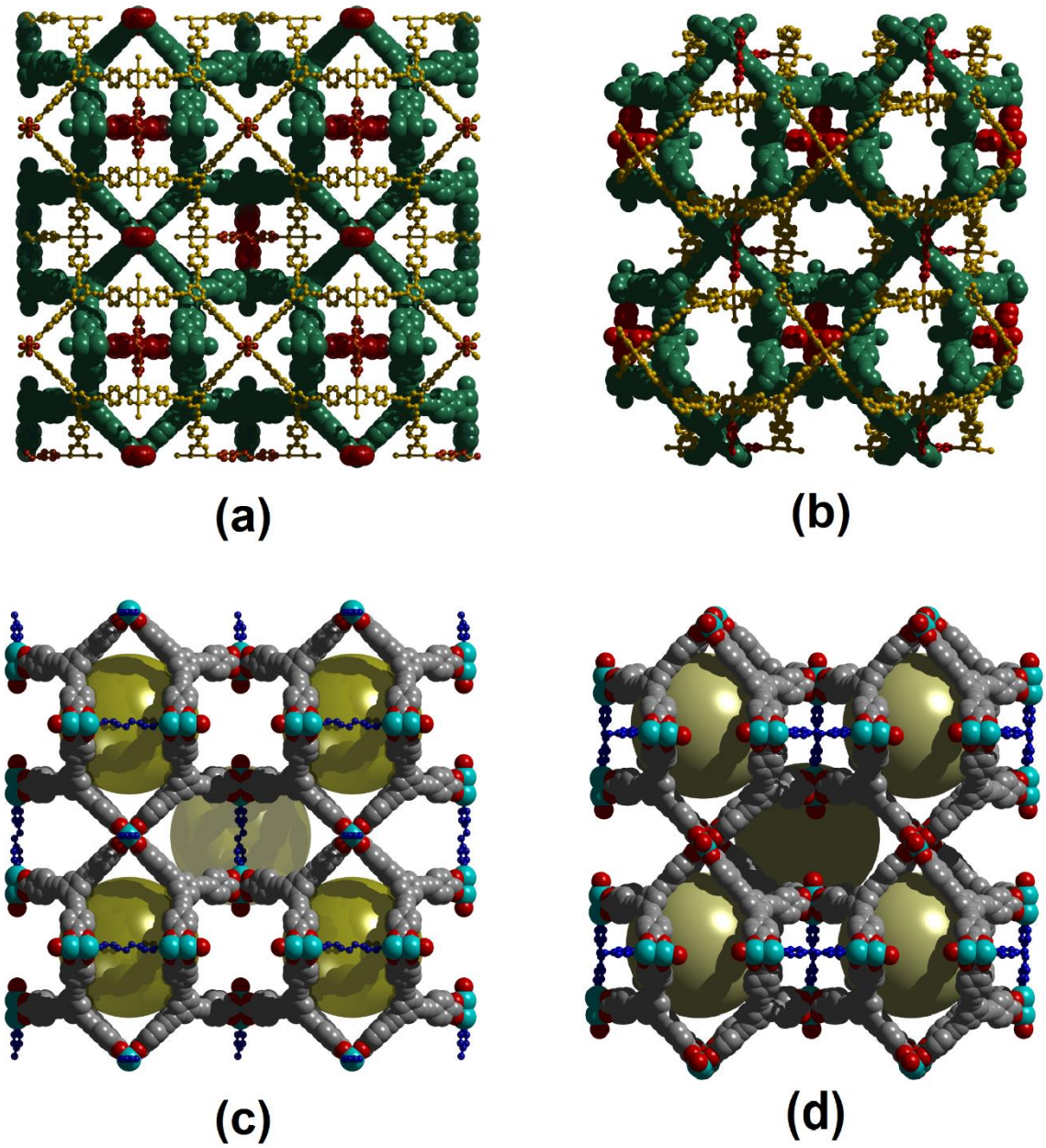

Figure 4.10 – a) and b) Framework structures of 11 and 12, respectively (azopyridine moieties highlighted in blue; Cu teal, O red, C grey, H atoms omitted; void volumes indicated as yellow spheres); c) and d) Dual interpenetrated structures of 11 and 12, respectively (azopyridine moieties highlighted in red; respective interwoven frameworks are shown in space-filling {green} and ball-stick {orange} modes).

Topological analysis reveals that the framework in **11** consists of two identical, interpenetrating (3,5,6)-connected 3-nodal nets. The overall point symbol for each of these nets is $\{5^{12}\cdot8^3\}\{5^2\cdot8\}_4\{5^6\cdot8^4\}_2$ (Figure 4.11 (a)). Similarly, **12** consists of two identical, interpenetrating (3,4,5)-connected 3-nodal nets, with point symbol $\{5\cdot8^2\}_4\{5^6\cdot8^4\}_2\{8^6\}$ (Figure 4.11 (b)). The presence of 6-connected nodes in **11**, and 4-connected nodes in **12**

are consistent with the observed degrees of azpy incorporation. These two nets can be considered intermediates between the 'empty' **pto** net, and the 'fully bridged' **ith-d** net, and can be considered to be derived from the **pto** archetype by the incorporation of **azpy** ligands.[16]

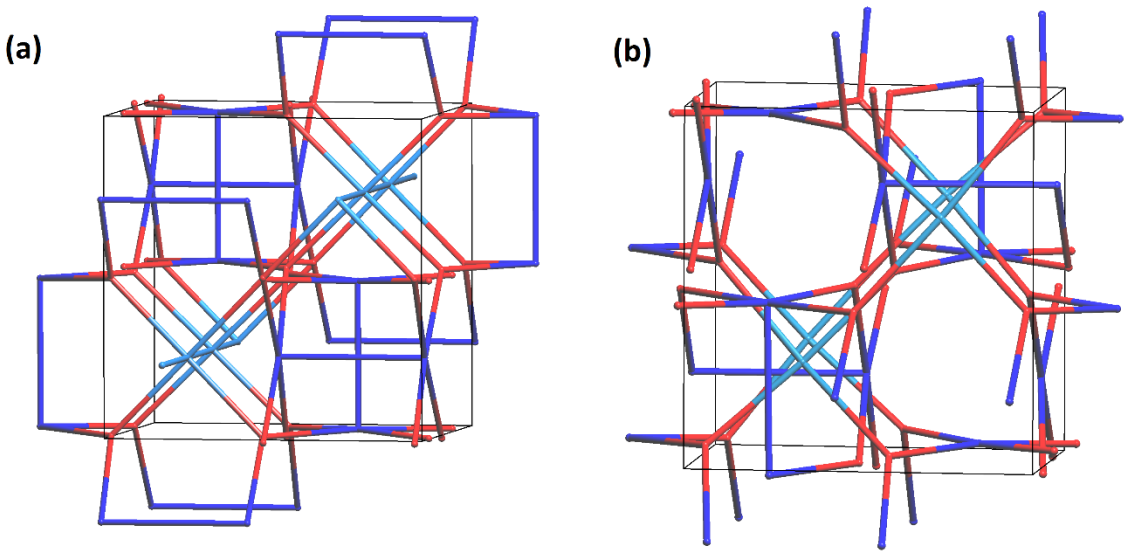

Figure 4.11 – Topological reduction of unit cells of (a) 11 and (b) 12.

The void volumes in **11** and **12,** correspond well with the thermogravimetric analyses under N_2, which reveal a loss of constitutional solvent molecules below 120°C, equivalent to *ca.* 54 wt. % for **11** and 62 wt. % for **12** (Fig. 4.12, 4.13). Above 120°C, coordinated water molecules leave the structure. The framework structures are stable up to *ca.* 280°C, after which degradation of the organic ligand occurs. Phase purity was confirmed by powder X-ray diffraction measurements using as-synthesised crystals in rotating capillaries, due to which some preferred orientation effects were observed (Fig. 4.12, 4.13).

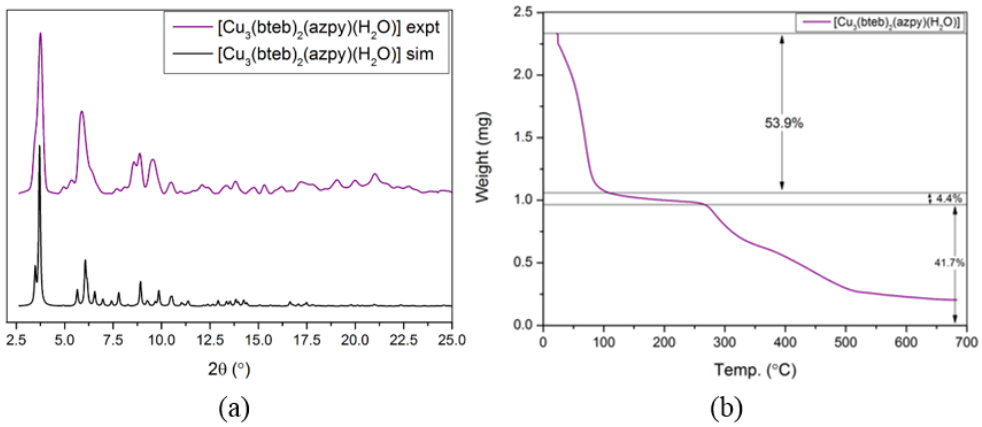

Figure 4.12 – PXRD pattern (a) and TGA trace (b) for 11.

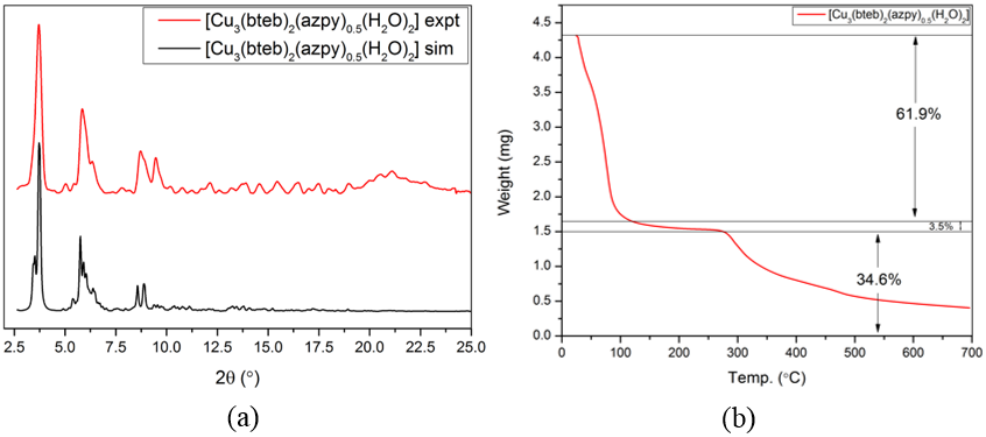

Figure 4.13 – PXRD pattern (a) and TGA trace (b) for 12.

Having confirmed the thermal stability and possible porosity of the compounds, both MOFs were activated for gas sorption analysis. Activation was performed under high vacuum at 120°C following solvent exchange with CH_2Cl_2. CO_2 adsorption experiments were carried out on both samples at 293 K and the measurement temperature was maintained carefully using a recirculating water bath. While partial framework collapse had a clear effect on the overall magnitude of the CO_2 uptakes, the measurements carried out in the dark confirmed a substantial degree of CO_2 physisorption within the materials (Fig. 4.14).

Using a UV lamp (Spectroline ENF-280C/FE) with a wavelength centred at $\lambda = 365$ nm and in-built filter, and the sample contained in a quartz cell, adsorption experiments were carried out. Under these conditions **11** and **12** both exhibit photo-responses under static and dynamic light irradiation (Figure 4.3).

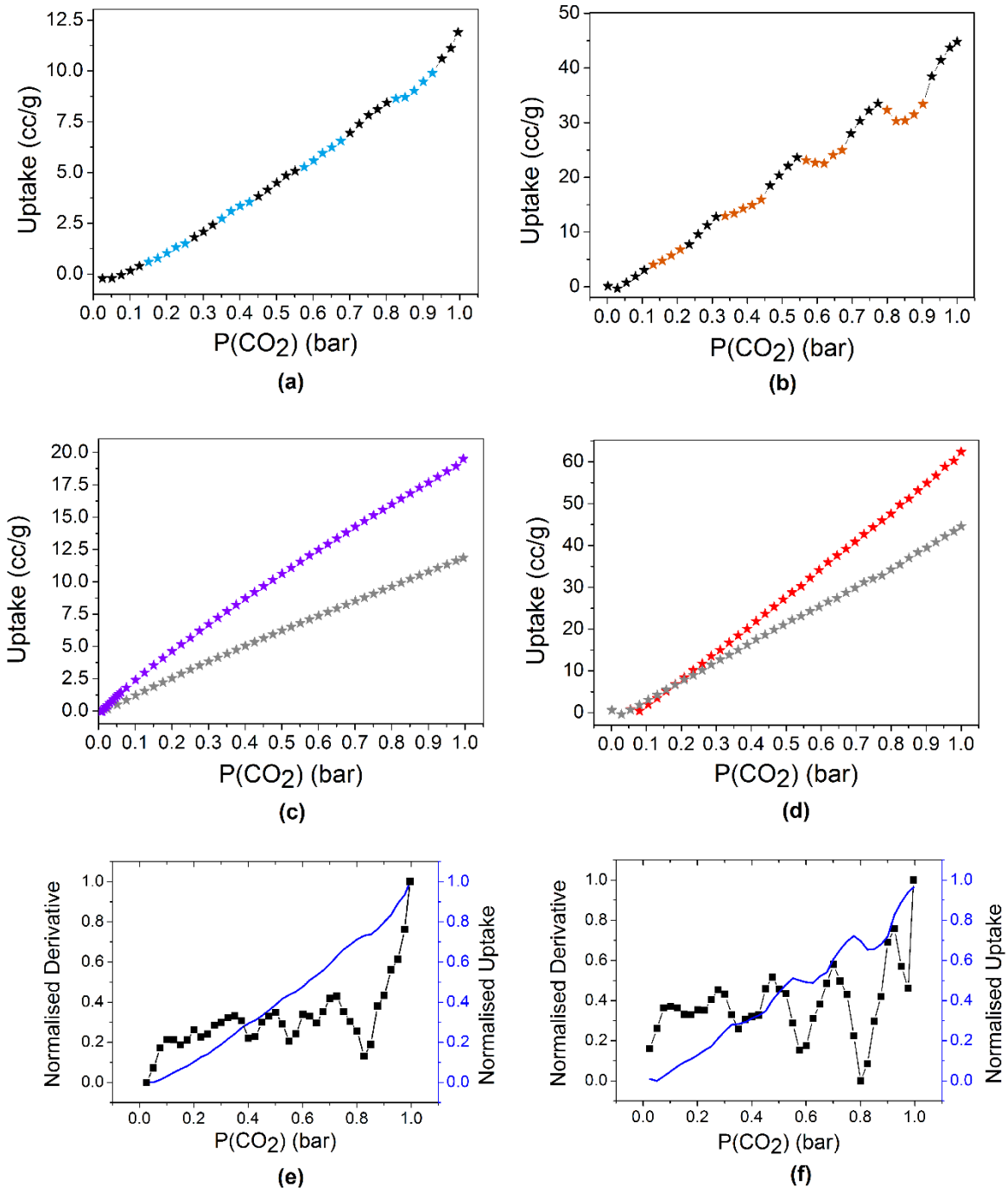

Figure 4.14 –CO_2 adsorption isotherms (293 K) for (a) 11 under dynamic irradiation (black: dark, light blue: under UV light irradiation); derivative plot in inset; (b) 12 under dynamic irradiation (black: dark, pink: under UV); derivative plot in inset; (c) 11 under static irradiation (purple: dark, grey: under UV light irradiation); (d) 12 under static irradiation (red: dark, grey: under UV light irradiation); (e) 11 (blue) plotted with the derivative (black) of the isotherm; (f) 12 (blue) plotted with the derivative (black) of the isotherm.

11 shows relatively low CO_2 uptake overall, and very small dynamic changes in uptake are observed. However, under static conditions (in the dark or under continuous UV

irradiation) a CO_2 uptake difference of 37% at 1 bar is observed. **12** performs far better than **11**, revealing a significantly larger CO_2 uptake at 293 K (CO_2 uptake of 62.3 cc/g at 1 bar). A dynamic response of up to 40% compared to the dark isotherm, and a static response of 29% at 1 bar are observed. Under static, continuous UV-irradiation, lower CO_2 quantities are adsorbed; dynamic irradiation/dark cycles facilitate desorption and CO_2 release upon light irradiation. The first derivatives of the dynamic switching isotherms show that the inflections observed correspond to irradiation events, and show that the magnitude of the photo-response increases at higher P(CO_2) in both materials, and is more pronounced for **12**, in which incorporation of bridging azpy linkers is reduced, and therefore channel availability and framework flexibility are greater.

In order to rule out other effects contributing to the observed changes in uptake, control experiments were carried out using a sample containing TCM-4 and TCM-5, which are non-photo-responsive, and structurally related to **11** and **12**. In control samples, no dynamic photo-response was observed, and the change in uptake under static irradiation was negligible (Fig. 4.15).

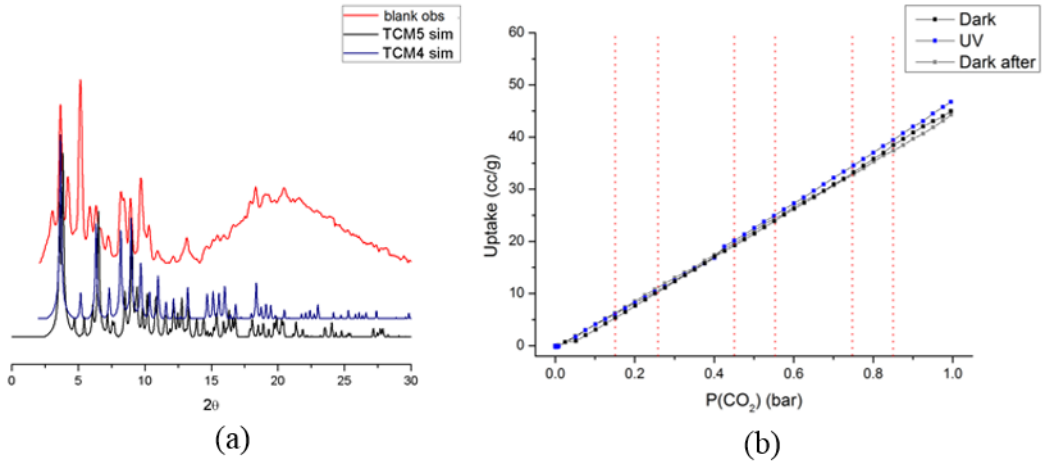

Figure 4.15 - (a) Experimental PXRD pattern of TCM-4/TCM-5 blank compared to simulated PXRD pattern of TCM-4 and TCM-5; (b) 293 K CO_2 adsorption isotherms of the blank sample under dark, static irradiation, and dynamic irradiation conditions. Red dotted lines show the regions of the isotherms measured under dynamic irradiation.

The bulk purity of **11** and **12** as characterised by elemental analysis and powder X-ray crystallography precluded any contribution from free ligands in the MOF pores. FTIR spectroscopy was also carried out on **11** and **12** (Fig. 4.16). The FTIR spectra of **11** and **12** both exhibit broad signals centred at around 3300 cm^{-1} due to H-bonded DMF molecules in the MOF pores. In **11**, the IR spectrum is characterised by strong bands at 1537 cm^{-1} and

1380 cm^{-1}, corresponding to asymmetric ($\nu_{as}COO$) and symmetric ($\nu_{s}COO$) carboxylate stretching modes respectively. A number of overlapping signals between 1651 cm^{-1} and 1402 cm^{-1} are observed due to C=O, C=N, and C=C vibrations. Similarly in **12**, bands at 1553 cm^{-1} and 1387 cm^{-1} may be assigned to $\nu_{as}COO$ and $\nu_{s}COO$ respectively. Deacon-Phillips Δ values for **11** and **12** are therefore 157 cm^{-1} and 166 cm^{-1}, which are consistent with the bidentate bridging carboxylate binding mode observed in the paddle-wheel SBUs.[17]

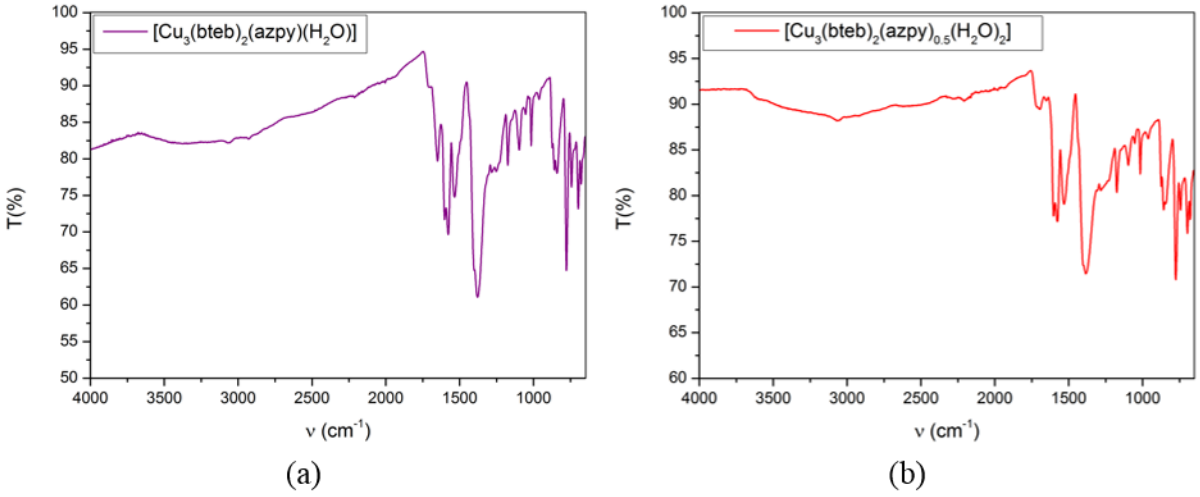

Figure 4.16 – FTIR spectra (a) for 11 and (b) for 12.

ATR-FTIR spectroscopy was carried out at lower wavenumbers on **12** to understand the nature of structural responses corresponding to the observed change in CO_2 sorption (Fig. 4.17). No significant intensity increases of vibrational bands in the 600-500 cm^{-1} window, corresponding to the C-N bending modes of azpy moieties, were observed, contrary to previous reports on dynamic behaviour in MOFs containing azobenzene-based ligands.[10] However, upon UV-irradiation a degree of suppression of the vibrational mode at 528 cm^{-1} is apparent and is associated with a very small shift or the emergence of a weak new signal at 531 cm^{-1}. Therefore despite dominant restrictions on movement of the azpy moiety, we infer that UV-irradiation induced distortions do take place. These distortions appear to involve very small changes in bond length, and do not consist of the suppressed bending mechanism reported for the azobenzenetetracarboxylic acid (abtc) ligand. Relaxation to the ground state takes place within one minute as confirmed by these IR studies, as well as desorption observed during the interval between the measurements of successive points on the dynamically irradiated adsorption isotherm. PXRD studies comparing powder patterns

obtained for **12** before and immediately after UV irradiation show no observable difference. The photo-response should therefore be local and non-periodic, but does not rely on the localised bending mechanism. Further, this confirms that simple *cis-trans* isomerisations of the bridging azpy ligands do not take place.

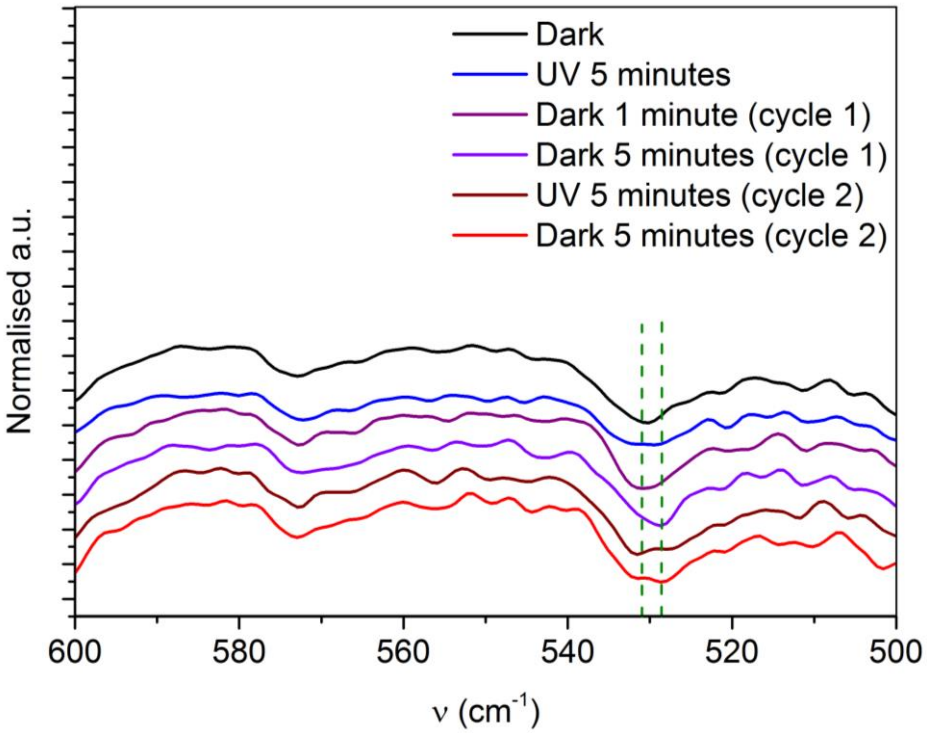

Figure 4.17 - IR spectra at various stages during irradiation of 12.

Time dependent density functional theory (DFT) calculations were performed on a model system using Gaussian 09 and the CAMB3LYP functional.[18,19] These calculations reveal a π-π* transition at 280 nm in reasonable agreement with the observation given the model system and the methodology (see Appendix 9.3 for details). The orbitals involved in this transition are almost completely localized on the azopyridine ligand with a small contribution from the Cu(II) centres directly attached to the azopyridine ligand (Fig. 4.18). Such an excitation may be expected to trigger a *cis-trans* ligand isomerisation but this is restricted in **11** and **12** due to the constraints imposed by the 3D structure. However, the flexibility of the bteb^{3-} ligand makes the framework in **12** capable of withstanding a degree of induced distortion. One important point of difference between the azpy and abtc^{2-} ligands is that the azpy ligands bind using monodentate N-donors and can rotate freely about the Cu-N bonds, subject to steric constraints. We therefore propose that the photo-response in these materials may be due to a mechanism that facilitates small torsions about the {Cu_2}-

azpy-{Cu_2} bridged system. These torsions may be occasioned by strain within the azpy ligand due to excitation and have the effect of partially obscuring the available void space (Figure 4.4). Such a mechanism is supported by the small changes observed in the IR spectra and the rapid response time observed in IR and CO_2 adsorption experiments.

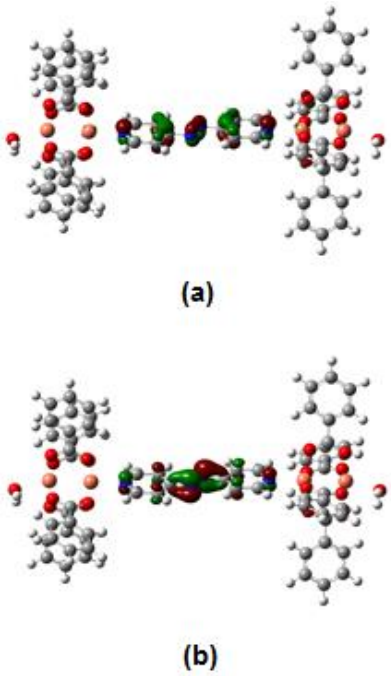

Figure 4.18 - Time-dependent DFT-derived molecular orbital (MO) representations of a simplified {Cu_2}-azpy-{Cu_2} model unit in 11 and 12. a) MO representation upon π- π^* transition results in a localisation of the MOs at the azopyridine ligand and contribution from binding Cu(II) centres; b) MO representation of the 'dark' state.

Details of the single crystal X-ray data obtained for **11** and **12** are given in Table 4.3, below.

Table 4.3 – Crystallographic details for 11 and 12.

Identification code	11	12
Empirical formula	$C_{76}H_{40}Cu_3O_{13}N_4$	$C_{71}H_{38}Cu_3N_2O_{14}$
Formula weight	1407.74	1333.65
Temperature/ K	220(2)	215(2)
Crystal system	Tetragonal	Triclinic
Space group	*P*42/*nmc*	$P\bar{1}$
a/Å	35.831(6)	32.947(3)
b/Å	35.831(6)	34.133(3)
c/Å	31.843(5)	36.130(3)
α/°	90	94.63(4)
β/°	90	93.84(4)
γ/°	90	90.82(4)
Volume/Å^3	40882(15)	40400(7)
Z	8	8
ρ_{calc}/ g/Cm^3	0.457	0.439
μ/mm^{-1}	0.546	0.543
F(000)	5720	5416
Crystal size/mm^3	0.25 x 0.15 x 0.15	0.35 x 0.20 x 0.15
Radiation/Å	CuKα (λ = 1.54178)	CuKα (λ = 1.54178)
2θ range for data collection/°	1.744 to 39.618	1.888 to 35.616
Index ranges	-29<=h<=29, -29<=k<=29, -23<=l<=26	-7<=h<=24, -25<=k<=24, -27<=l<=26
Reflections collected	122469	44015
Independent reflections	6381 [R(int) = 0.0575]	31414 [R(int) = 0.0422]
Data/restraints/parameters	6381 / 421 / 478	31414 / 1884 / 2809
Goodness-of-fit on F^2	1.077	1.376
Final R indexes [I>=2σ (I)]	R_1 = 0.0954, wR^2 = 0.2922	R_1 = 0.1177, wR^2 = 0.3368
Final R indexes [all data]	R_1 = 0.1015, wR^2 = 0.2994	R_1 = 0.1469, wR^2 = 0.3624
Largest diff. peak/hole / e Å^{-3}	0.654 and -0.568	1.488 and -0.490

4.3: Compounds **13-15,** $[M_6(btb)_4(dabpy)_3]$ (M = Ni, Co, Zn), and **16**, $[Zn_6(btb)_4(dnbpy)_3]$

In compounds **13-16**, the btb^{3-}/$\{M^{II}_2\}$-based **pto** network was used as the structural basis for the rational incorporation of ditopic, functionalised dabpy and dnbpy ligands along the pore diameter.

13 was synthesised by reacting $Ni(NO_3)_2 \cdot 6H_2O$ with H_3btb and dabpy in DMF at 120°C for two days. The product, $[Ni_6(btb)_4(dabpy)_3]$ was obtained as large, green, cubic crystals suitable for single crystal X-ray studies. X-ray crystallography reveals the adoption of a single-framework **pto**-based structure. The crystal structure was refined in the cubic crystal system and the $Pm\bar{3}n$ space group, and cell parameters were found to be $a = b = c =$ 27.598(3) Å, and $\alpha = \beta = \gamma = 90°$.

The Ni^{2+} metal centres that form the dinuclear paddle-wheel SBU are related to each other by symmetry (Ni1), as are the carboxylate O-donor atoms that compose the coordination environment (O1) (Fig. 4.19). Interatomic distances and angles are listed in Table 4.4.

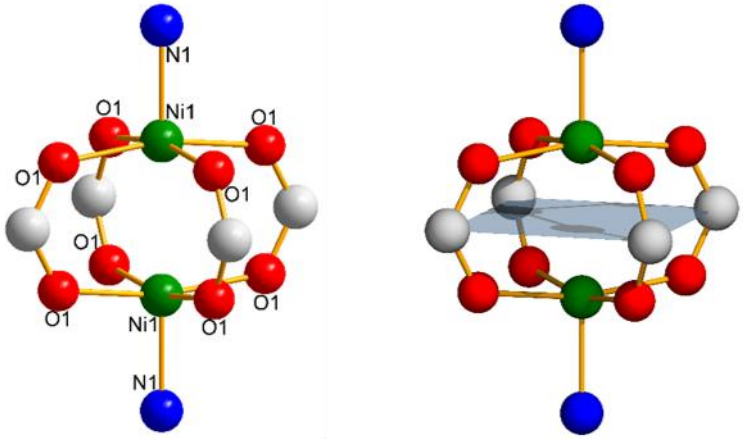

Figure 4.19 – The coordination environment (a), and a representation of the square $\{Ni_2\}$ paddle-wheel SBU in 13 (b).

Table 4.4 - Selected interatomic distances and angles in 13.

Atoms	Distance		Atoms	Angle
Ni1-Ni1′	2.6842(3) Å		N1-Ni1-Ni1′	180°
Ni1-N1	2.0075(2) Å		N1-Ni1-O1	96.56(4)°
Ni1-O1	1.998(1) Å		O1-Ni1-O1′	89.48(6)°

The isostructural Co(II) compound, **14** was synthesised by reacting $Co(NO_3)_2 \cdot 6H_2O$ with H_3btb and dabpy in DMF at 85°C for three days. The product, $[Co_6(btb)_4(dabpy)_3]$ was obtained as rod-shaped, violet crystals suitable for single crystal X-ray studies. X-ray crystallography reveals the adoption of a single-framework **pto**-based structure. The crystal structure was refined in the cubic crystal system and the $Pm\bar{3}n$ space group, and cell parameters were found to be $a = b = c = 27.6860(8)$ Å, and $\alpha = \beta = \gamma = 90°$.

The Co^{2+} metal centres that form the dinuclear paddle-wheel SBU are related to each other by symmetry (Co1), as are the carboxylate O-donor atoms that compose the coordination environment (O1) (Fig. 4.20). Interatomic distances and angles are listed in Table 4.5.

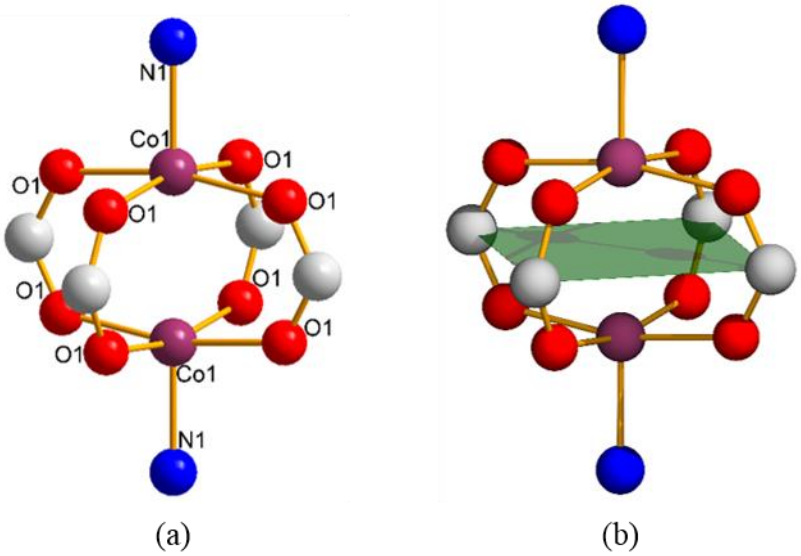

Figure 4.20 – The coordination environment (a), and a representation of the square $\{Co_2\}$ paddle-wheel SBU in 14 (b).

Table 4.5 - Selected interatomic distances and angles in 14.

Atoms	Distance		Atoms	Angle
Co1-Co1′	2.6922(1) Å		N1-Co1-Co1′	180°
Co1-N1	2.0496(1) Å		N1-Co1-O1	96.6(6)°
Co1-O1	2.026(2) Å		O1-Co1-O1′	89.1(8)°

The isostructural Zn(II) compound, **15** was synthesised by reacting $Zn(NO_3)_2 \cdot 6H_2O$ with H_3btb and dabpy in DMF at 85°C for two days. The product, $[Zn_6(btb)_4(dabpy)_3]$ was obtained as pale yellow, rod-shaped crystals suitable for single crystal X-ray studies. X-ray crystallography reveals the adoption of a single-framework **pto**-based structure. The crystal

structure was refined in the cubic crystal system and the $Pm\bar{3}n$ space group, and cell parameters were found to be $a = b = c = 27.6709(9)$ Å, and $\alpha = \beta = \gamma = 90°$.

The Zn^{2+} metal centres that form the dinuclear paddle-wheel SBU are related to each other by symmetry (Zn1), as are the carboxylate O-donor atoms that compose the coordination environment (O1) (Fig. 4.21). Interatomic distances and angles are listed in Table 4.6.

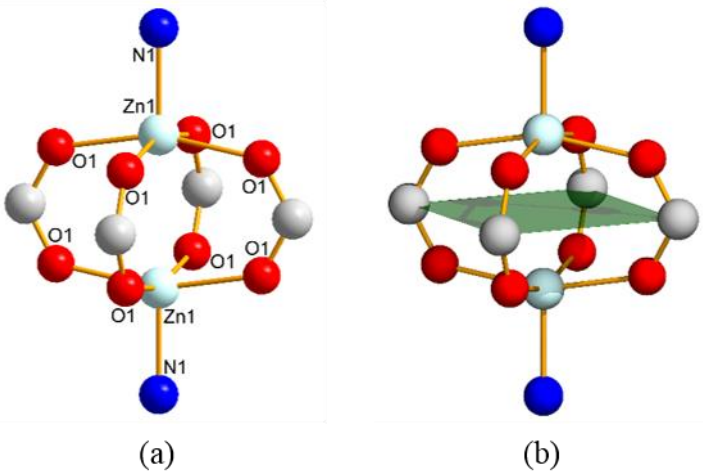

Figure 4.21 – The coordination environment (a), and a representation of the square {Zn_2} paddle-wheel SBU in 15 (b).

Table 4.6 - Selected interatomic distances and angles in 15.

Atoms	Distance		Atoms	Angle
Zn1-Zn1′	2.898(2) Å		N1-Zn1-Zn1′	180°
Zn1-N1	2.012(8) Å		N1-Zn1-O1	99.7(1)°
Zn1-O1	2.052(4) Å		O1-Zn1-O1′	88.3(2)°

16, the 3,3′-dinitro-4,4′-bipyridine derivative of **15** was synthesised by reacting $Zn(NO_3)_2 \cdot 6H_2O$ with H_3btb and dnbpy in DMF at 90°C for two days. The product, $[Zn_6(btb)_4(dnbpy)_3]$ was obtained as pale orange, cubic crystals suitable for single crystal X-ray studies. X-ray crystallography reveals the adoption of a single-framework **pto**-based structure. The crystal structure was refined in the cubic crystal system and the $Pm\bar{3}n$ space group, and cell parameters were found to be $a = b = c = 27.6646(8)$ Å, and $\alpha = \beta = \gamma = 90°$.

The Zn^{2+} metal centres that form the dinuclear paddle-wheel SBU are related to each other by symmetry (Zn1), as are the carboxylate O-donor atoms that compose the coordination environment (O1) (Fig. 4.22). Interatomic distances and angles are listed in Table 4.7.

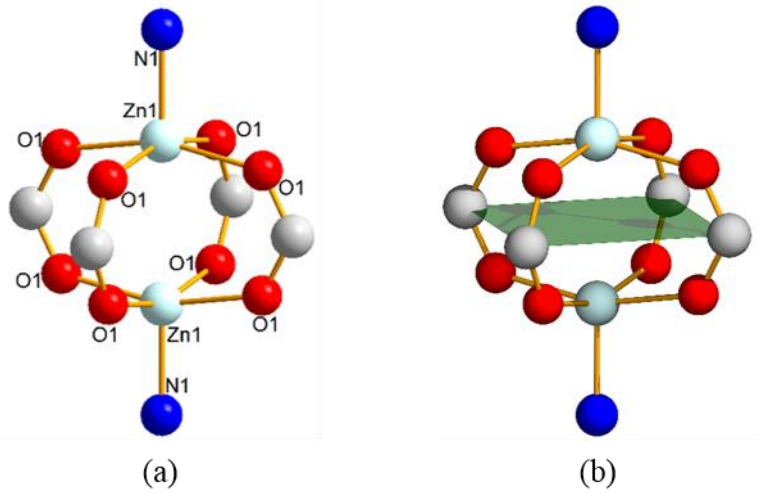

Figure 4.22 – The coordination environment (a), and a representation of the square {Zn_2} paddle-wheel SBU in 16 (b).

Table 4.7 - Selected interatomic distances and angles in 16.

Atoms	Distance		Atoms	Angle
Zn1-Zn1′	2.9009(1) Å		N1-Zn1-Zn1′	180°
Zn1-N1	1.9717(1) Å		N1-Zn1-O1	99.71(8)°
Zn1-O1	2.030(3) Å		O1-Zn1-O1′	88.0(1)°

In **13**, **14**, and **15**, the dabpy ligand (dnbpy in **16**) acts as a connecting ligand between opposite {M_2} paddle-wheel SBUs. Each SBU is connected to four *syn*, *syn*–bidentate bridging carboxylate groups from four distinct btb^{3-} ligands. Each btb^{3-} ligand connects three SBUs, thus forming a **pto** scaffold into which the auxiliary ditopic ligand is incorporated. The incorporation of the auxiliary ligands is 'complete' in all four compounds – every pair of opposite SBUs accommodates a ligand, and every apical position on the M^{2+} centres composing the paddle-wheel unit is occupied by an N-donor atom from a dabpy or dnbpy pyridyl ring (Fig. 4.24).

The networks formed in **13-16** are topologically identical. The SBU can be reduced to a 6-connected node and the ligand can be reduced to a 3-connected node, resulting in an overall stoichiometry of $(6\text{-c})_3(3\text{-c})_4$. The point symbol of the overall (3,6)-connected net is

$\{5^{12}.8^3\}_3\{5^3\}_4$, with a corresponding three-letter code of **ith-d** in the RCSR database. The topological reduction of the structures is shown in Figure 4.23.

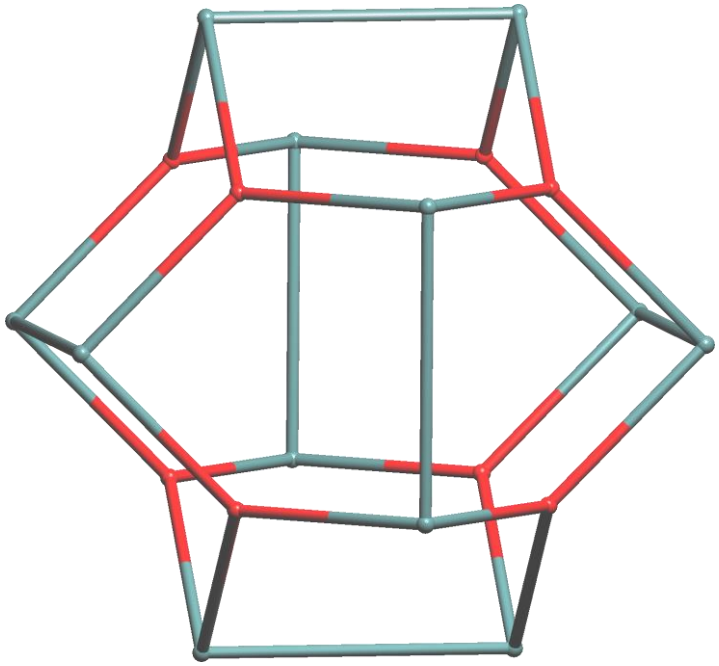

Figure 4.23 – Topological reduction of the networks in 13-16 to the ith-d net. 3-c nodes are coloured in red and 6-c nodes are coloured in teal.

Single crystal X-ray structural models for **13-16** showed significant disorder about the auxiliary ligand, and crystallographic restraints were required for the modelling of these ligands and the functional groups on them. The btb^{3-} ligands in 13-16 showed torsions between the central phenyl rings and the peripheral benzoate groups in the range of 34.59° - 35.16°. Values for void volume and pore diameter are as shown in Table 4.8.

Table 4.8 – Structural features of 13-16.

Compound	btb^{3-} ring torsion (°)	Void vol. (%)	Limiting channel diameter (Å),	Max. pore diameter (Å)	Simulated surface area (m^2/g)[20]
13	34.86	77.5	7.6	20.4	3054
14	35.16	77.3	7.6	20.0	2369
15	34.59	78.9	7.6	20.0	3034
16	34.86	78.2	7.6	20.0	2763

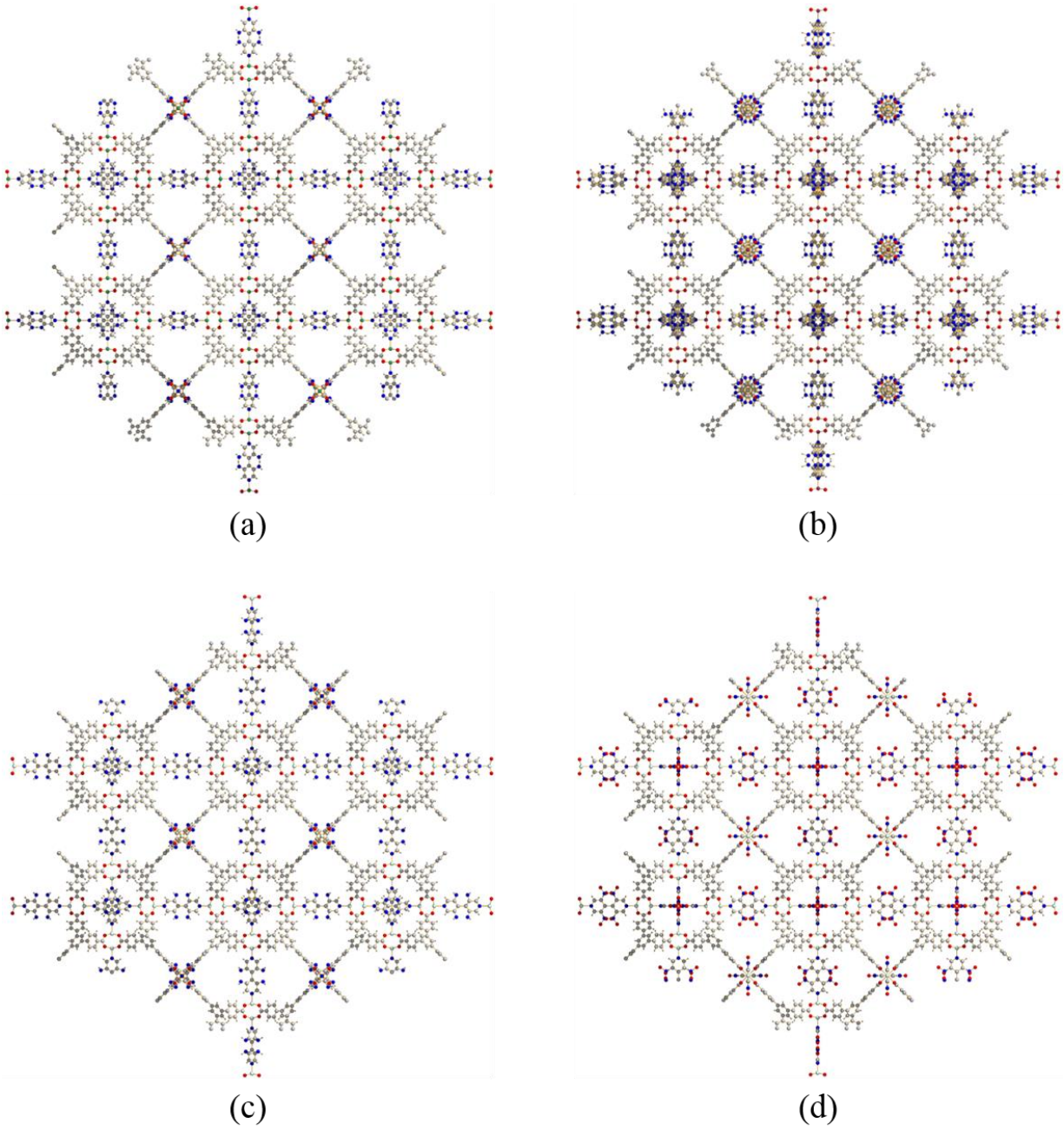

Figure 4.24 – 2x2x2 supercell representations of (a) 13, (b) 14, (c) 15, (b) 16. Colour scheme: green, Ni; violet, Co; light turquoise, Zn; blue, N; grey, C; light grey, H; red, O.

Thermogravimetric analysis of **13-16** confirms the large volume of pore solvent and is in line with expected behaviour (Fig. 4.25). All four compounds are observed to be thermally stable up to 360°C under nitrogen, at which point the onset of a ligand decomposition step takes place.

We attribute the variability in the slopes of the solvent loss step and the ligand decomposition step to variability in crystal sizes. Small crystals of **14** and **16** are conducive to the observation of sharp steps, and solvent loss is complete at 120°C, while for the large crystals of **13** and **15** the step is complete only at 180°C.

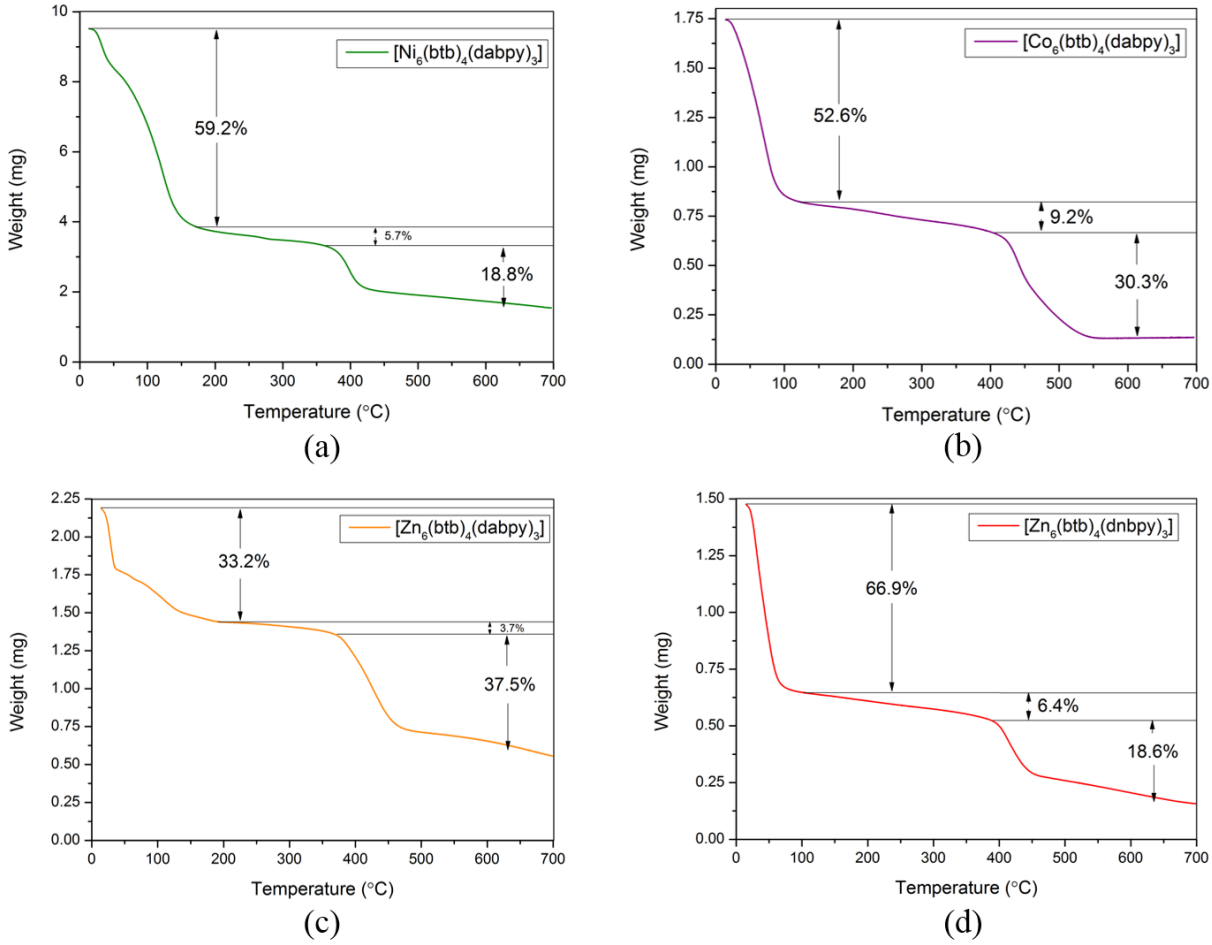

Figure 4.25 – TGA traces for (a) 13, (b) 14, (c) 15, and (d) 16.

Powder X-ray crystallography confirms the phase purity of all four compounds and validates the structural model (Fig. 4.26). Preferred orientation effects on peak intensity are significant in **13** and **15** due to the use of large crystals in the rotating capillary method. The broad background signal between $2\theta = 15°$ to $2\theta = 25°$ is due to scattering from the glass capillary.

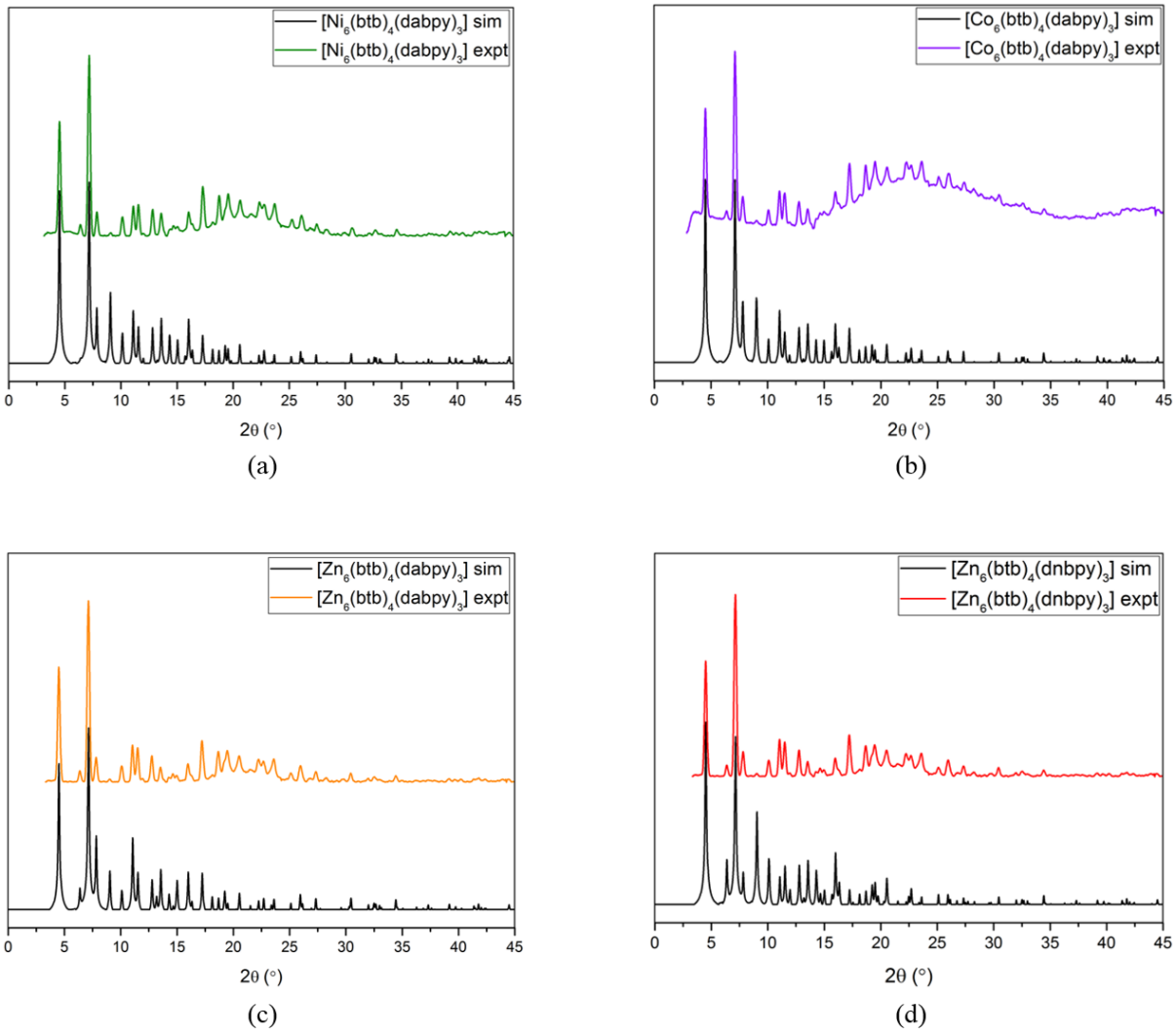

Figure 4.26 – PXRD patterns for (a) 13, (b) 14, (c) 15, and (d) 16.

FTIR spectroscopy carried out on **13-16** reveal strong bands at *ca.* 1385 cm^{-1} and *ca.* 1550 cm^{-1} (ν_sCOO and ν_{as}COO respectively) in each case (Fig. 4.27). This leads to an approximate Deacon-Phillips Δ value of 165 cm^{-1}, in line with expectations for the bidentate carboxylate bridging mode revealed by single-crystal X-ray studies.[9] Signals at *ca.* 3425 cm^{-1} (ν_sNH_2) and 3334 cm^{-1} (ν_sNH) confirm the presence of amino-groups in **13**, **14** and **15**. The ν_sNO_2 band in **16** is expected at 1350-1290 cm^{-1} and overlaps with the ν_sCOO band. The ν_sNO_2 band is observed at 1496 cm^{-1}, confirming the presence of nitro-groups. The band at *ca.* 1655 cm^{-1} is assigned to the C=O stretch in pore DMF molecules in **13-16**.

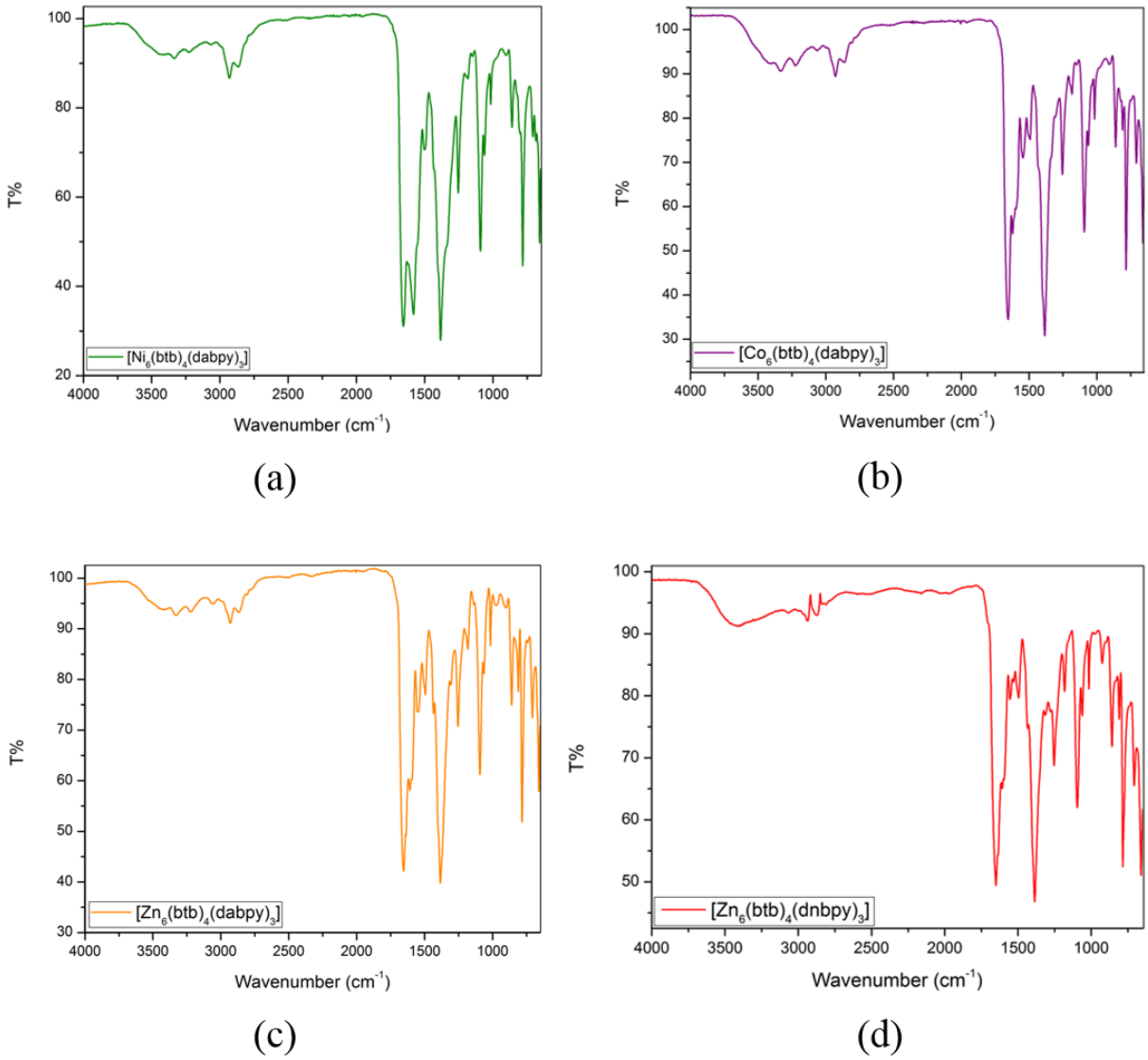

Figure 4.27 – FTIR spectra for (a) 13, (b) 14, (c) 15, and (d) 16.

Samples of **13**, **14**, **15**, and **16**, were exchanged with fresh DMF, followed by dichloromethane, and treated under high vacuum for 8 hours at 120°C. However, the samples were found to have negligible gas uptake due to framework collapse and amorphisation. Activation using supercritical CO_2 was also ineffective. Values of N_2 accessible surface areas simulated from the single crystal X-ray structures of **13-16** are listed in Table 4.8 above.

Crystallographic details of the single crystal X-ray measurements are listed in Table 4.9.

Table 4.9 –Crystallographic details for 13-16.

Identification code	13	14	15	16
Empirical formula	$C_{23}H_{14}NNiO_4$	$C_{23}H_{14}CoNO_4$	$C_{23}H_{14}NO_4Zn$	$C_{23}H_{14}NO_4Zn$
Formula weight	427.06	427.28	433.72	433.72
Temperature/K	230(2)	220(2)	220(2)	220(2)
Crystal system	cubic	cubic	cubic	cubic
Space group	$Pm\bar{3}n$	$Pm\bar{3}n$	$Pm\bar{3}n$	$Pm\bar{3}n$
a/Å	27.598(3)	27.6860(8)	27.6709(9)	27.6646(8)
b/Å	27.598(3)	27.6860(8)	27.6709(9)	27.6646(8)
c/Å	27.598(3)	27.6860(8)	27.6709(9)	27.6646(8)
α/°	90	90	90	90
β/°	90	90	90	90
γ/°	90	90	90	90
Volume/Å^3	21020(7)	21221.7(18)	21187(2)	21172.6(18)
Z	12	12	12	12
ρ_{calc}g/cm^3	0.405	0.401	0.408	0.408
μ/mm^{-1}	0.470	1.972	0.553	0.553
F(000)	2628.0	2616.0	2652.0	2652.0
Crystal size/mm^3	0.32 × 0.25 × 0.18	0.2 × 0.2 × 0.06	0.12 × 0.1 × 0.06	0.18 × 0.17 × 0.17
Radiation	CuKα (λ = 1.54178)	CuKα (λ = 1.54178)	CuKα (λ = 1.54178)	CuKα (λ = 1.54178)
2θ range for data collection/°	4.528 to 136.544	4.514 to 136.794	4.516 to 91.314	4.516 to 124.646
Index ranges	-32 ≤ h ≤ 31, -33 ≤ k ≤ 33, -30 ≤ l ≤ 33	-29 ≤ h ≤ 32, -33 ≤ k ≤ 20, -33 ≤ l ≤ 32	-25 ≤ h ≤ 25, -25 ≤ k ≤ 23, -25 ≤ l ≤ 25	-30 ≤ h ≤ 31, -31 ≤ k ≤ 31, -31 ≤ l ≤ 31
Reflections collected	65628	61405	64168	195104
Independent reflections	3442 [R_{int} = 0.0652, R_{sigma} = 0.0234]	3482 [R_{int} = 0.1226, R_{sigma} = 0.0606]	1615 [R_{int} = 0.2946, R_{sigma} = 0.0553]	3000 [R_{int} = 0.2544, R_{sigma} = 0.0361]
Data/restraints/parameters	3442/29/96	3482/39/102	1615/11/84	3000/62/96
Goodness-of-fit on F^2	1.004	1.003	0.874	0.991
Final R indexes [I>=2σ (I)]	R_1 = 0.0598, wR_2 = 0.2027	R_1 = 0.0798, wR_2 = 0.2163	R_1 = 0.0635, wR_2 = 0.2097	R_1 = 0.0917, wR_2 = 0.2502
Final R indexes [all data]	R_1 = 0.0660, wR_2 = 0.2128	R_1 = 0.0945, wR_2 = 0.2360	R_1 = 0.0815, wR_2 = 0.2321	R_1 = 0.1108, wR_2 = 0.2767
Largest diff. peak/hole / e Å^{-3}	0.36/-0.40	1.37/-0.44	0.21/-0.35	0.76/-0.52

4.4: Conclusions

In this chapter, six new metal-organic frameworks (**11-16**) are reported and physicochemically characterised. **11-16** are based on the structural blueprint provided by the **pto** topology, built using $\{M_2\}$ paddle-wheel SBUs and tritopic carboxylate ligands. The location of pairs of SBUs diametrically across voids, and the availability and correct orientation of axial sites in the M^{2+} coordination environment, facilitate the incorporation of auxiliary neutral, ditopic ligands across the pore diameter. This provides an excellent synthetic platform for the bespoke incorporation of functionality into the void space.

11-16 exhibit different degrees of auxiliary ligand incorporation, and therefore, different topologies obtained as modifications of the 'parent' **pto** net. **11** and **12** show partial incorporation of auxiliary ligands onto axial sites on SBUs, and their nets are represented by the point symbols $\{5^{12}\cdot8^3\}\{5^2\cdot8\}_4\{5^6\cdot8^4\}_2$ and $\{5\cdot8^2\}_4\{5^6\cdot8^4\}_2\{8^6\}$ respectively. In **13-16**, every pair of opposite SBUs is linked to give 'fully substituted' **ith-d** nets, with point symbol $\{5^{12}.8^3\}_3\{5^3\}_4$.

The synthetic procedures for **11-16** are optimised, and importantly for mixed-ligand systems, the MOFs are obtained phase-pure. In **11** and **12**, the flexible $bteb^{3-}$ ligand was used together with $\{Cu_2\}$ paddle-wheel SBUs to form the **pto** scaffold, into which photo-responsive azpy ligands were incorporated. Coupled gas sorption – irradiation experiments show that **11** and **12** respond to the stimulus of incident light, with observable decreases in uptake when irradiated. The magnitude of the photo-response is greater in **12** than in **11**, due to the flexibility that arises from more incomplete substitution along the crystallographic axes. Indeed, an instantaneous desorption corresponding to *ca.* 40% of adsorbed CO_2 (by volume) is observed in **12**. FTIR studies and DFT calculations provide some insights into the mechanism of the photo-response, and the flexibility of $bteb^{3-}$ is vital to the stimulus responsive behaviour of the MOFs.

13-16 were synthesised using the rigid btb^{3-} ligand and $\{M_2\}$ paddle-wheel SBUs, with the objective of incorporating the electron-rich $-NH_2$ and $-NO_2$ functional groups into the MOF pore, using the auxiliary dabpy and dnbpy ligands. These functional groups have been shown to enhance the uptake of specific gases in MOFs and are also useful as anchors for post-synthetic modifications.[21] Although activation procedures invariably led to structural

collapse in **13-16**, these compounds were synthesised in an optimised, phase-pure manner, and thoroughly characterised, illustrating the versatility and generality of the synthetic strategy adopted in this chapter.

4.5: References

1 M. Eddaoudi, D. B. Moler, H. Li, B. Chen, T. M. Reineke, M. O'Keeffe and O. M. Yaghi, *Acc. Chem. Res.*, 2001, **34**, 319–330.

2 M. O'Keeffe, M. Eddaoudi, H. Li, T. Reineke and O. M. Yaghi, *J. Solid State Chem.*, 2000, **152**, 3–20.

3 M. Lusi, P. B. A. Fechine, K. J. Chen, J. J. Perry and M. J. Zaworotko, *Chem. Commun.*, 2016, **52**, 4160–4162.

4 N. Zhu, M. J. Lennox, T. Düren and W. Schmitt, *Chem. Commun.*, 2014, **50**, 4207–4210.

5 N. Zhu, M. J. Lennox, G. Tobin, L. Goodman, T. Düren and W. Schmitt, *Chem. Eur. J.*, 2014, **20**, 3595–3599.

6 N. Klein, I. Senkovska, I. A. Baburin, R. Grünker, U. Stoeck, M. Schlichtenmayer, B. Streppel, U. Mueller, S. Leoni, M. Hirscher and S. Kaskel, *Chem. Eur. J.*, 2011, **17**, 13007–13016.

7 P. Müller, R. Grünker, V. Bon, M. Pfeffermann, I. Senkovska, M. S. Weiss, X. Feng and S. Kaskel, *CrystEngComm*, 2016, **18**, 8164–8171.

8 H. Furukawa, Y. B. Go, N. Ko, Y. K. Park, F. J. Uribe-Romo, J. Kim, M. O'Keeffe and O. M. Yaghi, *Inorg. Chem.*, 2011, **50**, 9147–9152.

9 N. Zhu, G. Tobin and W. Schmitt, *Chem. Commun.*, 2012, **48**, 3638–3640.

10 H. Li, M. R. Martinez, Z. Perry, H.-C. Zhou, P. Falcaro, C. Doblin, S. Lim, A. J. Hill, B. Halstead and M. R. Hill, *Chem. Eur. J.*, 2016, **22**, 11176–11179.

11 F. X. Coudert, *Chem. Mater.*, 2015, **27**, 1905–1916.

12 C. L. Jones, A. J. Tansell and T. L. Easun, *J. Mater. Chem. A*, 2016, **4**, 6714–6723.

13 J. An, S. J. Geib and N. L. Rosi, *J. Am. Chem. Soc.*, 2009, **132**, 38–39.

14 R. W. Flaig, T. M. Osborn Popp, A. M. Fracaroli, E. A. Kapustin, M. J. Kalmutzki, R. M. Altamimi, F. Fathieh, J. A. Reimer and O. M. Yaghi, *J. Am. Chem. Soc.*, 2017, **139**, 12125–12128.

15 D. K. Maity, A. Halder, B. Bhattacharya, A. Das and D. Ghoshal, *Cryst. Growth Des.*, 2016, **16**, 1162–1167.

16 V. A. Blatov, A. P. Shevchenko and D. M. Proserpio, *Cryst. Growth Des.*, 2014, **14**, 3576–3586.

17 R. J. Phillips and G. B. Deacon, *Coord. Chem. Rev.*, 1980, **33**, 227–250.

18 Gaussian 09, Revision D.01, M. J. Frisch, G. W. Trucks, H. B. Schlegel, G. E. Scuseria, M. A. Robb, J. R. Cheeseman, G. Scalmani, V. Barone, B. Mennucci, G. A. Petersson, H. Nakatsuji, M. Caricato, X. Li, H. P. Hratchian, A. F. Izmaylov, J. Bloino, G. Zheng, J. L. Sonnenberg, M. Hada, M. Ehara, K. Toyota, R. Fukuda, J. Hasegawa, M. Ishida, T. Nakajima, Y. Honda, O. Kitao, H. Nakai, T. Vreven, J. A. Montgomery Jr., J. E. Peralta, F. Ogliaro, M. Bearpark, J. J. Heyd, E. Brothers, K. N. Kudin, V. N. Staroverov, R. Kobayashi, J. Normand, K. Raghavachari, A. Rendell, J. C. Burant, S. S. Iyengar, J. Tomasi, M. Cossi, N. Rega, J. M. Millam, M. Klene, J. E. Knox, J. B. Cross, V. Bakken, C. Adamo, J. Jaramillo, R. Gomperts, R. E. Stratmann, O.Yazyev, A. J. Austin, R. Cammi, C. Pomelli, J. W. Ochterski, R. L. Martin, K. Morokuma, V. G. Zakrzewski, G. A. Voth, P. Salvador, J. J. Dannenberg, S. Dapprich, A. D. Daniels, Ö. Farkas, J. B. Foresman, J. V. Ortiz, J. Cioslowski, D. J. Fox, *Gaussian Inc.*, Wallingford CT, **2009**.

19 T. Yanai, D. P. Tew and N. C. Handy, *Chem. Phys. Lett.*, 2004, **393**, 51–57.

20 L. Sarkisov and A. Harrison, *Mol. Simul.*, 2011, **37**, 1248–1257.

21 Z. Wang and S. M. Cohen, *J. Am. Chem. Soc*, 2007, **129**, 12368–12369.

Chapter 5

Non-Default Topologies *via* Ligand Extension in MOFs

5.1: Introduction

A useful general principle of the design and reticular synthesis of MOFs crystallising out of an isotropic state in solution is that, for known shapes and connectivities of nodes and spacers, the most symmetric nets are expected to form.[1] An early study in the development of the field showed that over 80% of MOF structures exhibit a handful of such "default" nets.[2] The remainder, the "non-default" nets, form despite the possibility of a more symmetric net with the same connectivity. Systematic studies of the formation of such nets are rare, but conformations within the ligand during crystallisation have been shown to be crucial to their formation.[3]

An example of a MOF with one such "non-default" topology is MOF-177, in which octahedral $[Zn_4O]^{6+}$-based SBUs and tritopic btb^{3-} linkers form the **qom** net.[4] The default nets for the (3,6)-connected triangle-octahedron system are the high symmetry **rtl** (rutile) and **pyr** (pyrite) nets. These arrangements can also be accessed by btb^{3-}-based ligands, but only upon steric modulation by substituent groups, which effect small conformational adjustments.[5] Typically, however, the btb^{3-} ligand is incorporated into default nets, *e.g.*, the **kgd** net in combination with $\{Cd_3\}$ SBUs.[6] With $\{Cu_2\}$ SBUs, btb^{3-} ligands yield MOF-14, which has the **pto** topology.[7]

The approximation of ligands as rigid is important for the generalisation toward symmetric networks. However, in extended ligands, conformations are determined locally by a number of contingencies, which can be utilised to yield a plurality of networks from only a few starting components. The H_3btb ligand can be thought of as consisting of biphenyl moieties, in which the lowest energy conformation consists of dihedral angles between the central phenyl ring and peripheral benzoate groups of 36-42°.[8,9] This is due to repulsion between hydrogen atoms on adjacent phenyl rings (H_{Ar}-H_{Ar} repulsion).

The default structures for MOFs composed of square paddle-wheel SBUs and triangular tricarboxylate linkers are the **pto** and **tbo** nets (see Introduction).[10] Whether the **pto** or **tbo** network is formed has been shown to depend on the dihedral angles in the tricarboxylate ligand. Coplanarity between the peripheral benzoate groups and the central phenyl ring (a dihedral angle of 0°) in the tricarboxylate ligand results in the **tbo** network. The **tbo**

network is seen in HKUST-1 which is based on trimesic acid, and MOF-399, in which the bbc^{3-} linker adopts dihedral angles of 0°.[11]

Notably, the H_3bbc ligand allows the adoption of a dihedral angle of 0° through two successive *ca.* 35° torsions owing to two successive H_{Ar}-H_{Ar} repulsions. Considering the relatively low energy barrier for torsions past coplanarity in biphenyl (*ca.* 8 kJ mol^{-1}), it follows that bbc^{3-} linkers can exhibit approximate torsions of both 0° and *ca.* 70°, allowing for a great diversity of possible structures.[8]

Similarly, earlier work in the Schmitt group showed that using an acetylene spacer moiety in order to remove H_{Ar}-H_{Ar} repulsion and the consequent restriction on rotation, such as in the H_3bteb ligand, can result in a system that can form both the **pto** net (TCM-4) and the **tbo** net (TCM-8).[12] This free relative orientation of the terminal carboxylate can, in principle, facilitate the formation of non-default nets as well.

In this chapter, results of investigations into the combination of $\{Cd_3\}$ and $\{Cu_2\}$ SBUs with H_3bbc and H_3bteb to yield MOFs with non-default networks are detailed. The azpy ligand is also introduced into these systems in order to harness new topological platforms for novel MOFs. These compounds are characterised by single crystal X-ray crystallography, and simulations are carried out to assess the porosity and surface areas of these MOFs.

5.2: Compound **17**, $[Cu_3(bteb)_2(H_2O)_2(DMF)]$

Cu^{2+}-$bteb^{3-}$ systems are known to show both **pto** and **tbo** nets, implying that steric constraints favouring particular topologies are ineffective. In order to obtain non-default MOFs based on this system, elevated temperature reactions were carried out under a variety of conditions. Compound **17**, $[Cu_3(bteb)_2(H_2O)_2(DMF)]$, was synthesised using the conventional elevated temperature method. It co-crystallises reproducibly in a modest yield, along with major products TCM-4 and TCM-5 when H_3bteb and $Cu(NO_3)_2{\cdot}3H_2O$ are reacted in DMF in the presence of 4,4′-bipyridine at 85°C. Crystals of **17** were separated manually and single-crystal X-ray diffraction analysis demonstrates that the compound crystallises in the monoclinic space group $P2_1/c$. The cell parameters were found to be a = 17.116(2) Å, b = 36.686(5) Å, c = 25.647(3) Å, and $\alpha = \gamma = 90°$, β = 101.44(2)° (Table 5.2).

The asymmetric unit of **17** contains two fully deprotonated $bteb^{3-}$ ligand moieties coordinated to three Cu(II) ions, by which two distinct SBUs are composed – one formed by Cu1 and Cu2, and the other by Cu3 and its symmetry equivalent (Fig. 5.1). The structural parameters of dinuclear SBUs in **17** are as expected for $\{Cu_2\}$ paddle-wheels. O-donor atoms of *syn*, *syn*-bidentate carboxylate groups provide the bases of the square pyramidal coordination polyhedra of each Cu(II) centre, and O-donor atoms of H_2O and DMF molecules bind in the apical positions. The Cu–Cu distances in the dinuclear $\{Cu_2\}$ SBUs are *ca.* 2.6 Å (Table 5.1). Cu1 and Cu2 are axially coordinated to O-donor atoms from H_2O molecules, while Cu3 is coordinated to the O-donor atom in DMF.

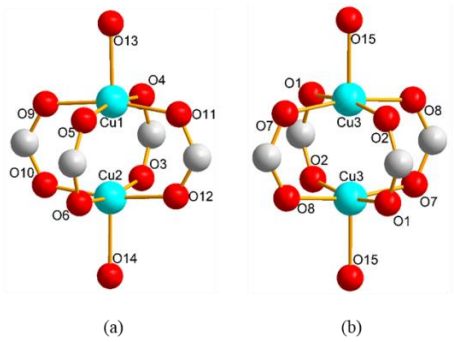

Figure 5.1 – Representations of the two crystallographically distinct $\{Cu_2\}$ SBUs in 17.

Each $\{Cu_2\}$ SBU is coordinated by four tritopic $bteb^{3-}$ ligands, and each $bteb^{3-}$ moiety connects to three $\{Cu_2\}$ SBUs giving rise to a neutral network structure. It is observed that one of the peripheral carboxylate groups of the $bteb^{3-}$ ligand is oriented coplanar to the

central benzene ring while the other two peripheral carboxylate functionalities adopt a conformation staggered by *ca.* 33° relative to the central benzene ring. On adopting the former 0°-binding mode, the central phenyl and the outer benzoate ring systems are approximately co-planar whilst the 33°-binding mode results in a tilted conformation between central and outer phenyl rings.

Table 5.1 - Selected interatomic distances and angles in 17.

Atoms	**Distance**		**Atoms**	**Angle**
Cu1-O13	2.134(4) Å		O13-Cu1-O4	95.1(1)°
Cu1-O4	1.961(4) Å		O13-Cu1-O9	94.5(2)°
Cu1-O5	1.984(4) Å		O4-Cu1-O11	88.6(1)°
Cu1-O9	1.969(4) Å		O5-Cu1-O9	88.7(2)°
Cu1-O11	1.957(4) Å		O13-Cu1-Cu2	177.4(1)°
Cu1-Cu2	2.6339(9) Å		Cu1-Cu2-O14	178.9(1)°
Cu2-O14	2.142(4) Å		O14-Cu2-O3	96.3(2)°
Cu2-O3	1.960(4) Å		O14-Cu2-O6	95.2(2)°
Cu2-O6	1.956(4) Å		O6-Cu2-O10	88.4(2)°
Cu2-O10	1.950(4) Å		O3-Cu2-O12	88.5(2)°
Cu2-O12	1.960(4) Å			
Cu3-O15	2.136(4) Å		O15-Cu3-Cu3’	176.0(1)°
Cu3-O1	1.961(3) Å		O15-Cu3-O1	98.2(1)°
Cu3-O2	1.965(3) Å		O15-Cu3-O2	93.6(1)°
Cu3-O7	1.944(3) Å		O8-Cu3-O1	90.0(1)°
Cu3-O8	1.942(3) Å		O7-Cu3-O2	90.3(1)°
Cu3-Cu3’	2.638(1) Å			

The two benzoate moieties that facilitate the 33° angles bridge in [010] parallel aligned {Cu_2} SBUs units, whereas the third benzoate links orthogonally aligned {Cu_2} SBUs in the direction of the crystallographic *c*-axis. The $bteb^{3-}$ ligand shows a tendency towards bowing which is crucial to the stabilisation of the framework (Fig. 5.2). In the corresponding **pto** and **tbo** structures that are formed by $bteb^{3-}$ and {Cu_2} SBUs, the angles between the central phenyl and each peripheral carboxylate group are identical, either *ca.* 33° for the **pto** or *ca.* 0° for the **tbo** structure (Fig. 5.3). In both cases the organic ligands adopt C_3 symmetry. Thus, **17** is not isoreticular to HKUST-1 or MOF-14 and may be regarded as an isomeric ‘intermediate’ between the **tbo** and **pto** topologies.

Table 5.2 – Crystallographic details for 17.

Identification code	17
Empirical formula	$C_{69}H_{41}Cu_3NO_{15}$
Formula weight	1314.65
Temperature/ K	220(2)
Crystal system	monoclinic
Space group	$P2_1/c$
***a*/Å**	17.116(2)
***b*/Å**	38.686(5)
***c*/Å**	25.647(3)
***α*/°**	90
***β*/°**	101.44(2)°
***γ*/°**	90
Volume/Å^3	16645(4)
Z	4
ρ_{calc}/ g/cm^3	0.525
μ/mm^{-1}	0.658
F(000)	2676
Crystal size/mm^3	0.40 x 0.35 x 0.25
Radiation/Å	CuKα (λ = 1.54178)
2θ range for data collection/°	4.20 to 102.08
Index ranges	$-16 \leq h \leq 14$, $-32 \leq k \leq 37$, $-16 \leq l \leq 25$
Reflections collected	33007
Independent reflections	15447 [R_{int} = 0.0383, R_{sigma} = 0.0552]
Data/restraints/parameters	15447/2/797
Goodness-of-fit on F^2	1.041
Final R indexes [I>=2σ (I)]	R_1 = 0.0681, wR_2 = 0.2072
Final R indexes [all data]	R_1 = 0.0878, wR_2 = 0.2208
Largest diff. peak/hole / e Å^{-3}	0.50/-0.41

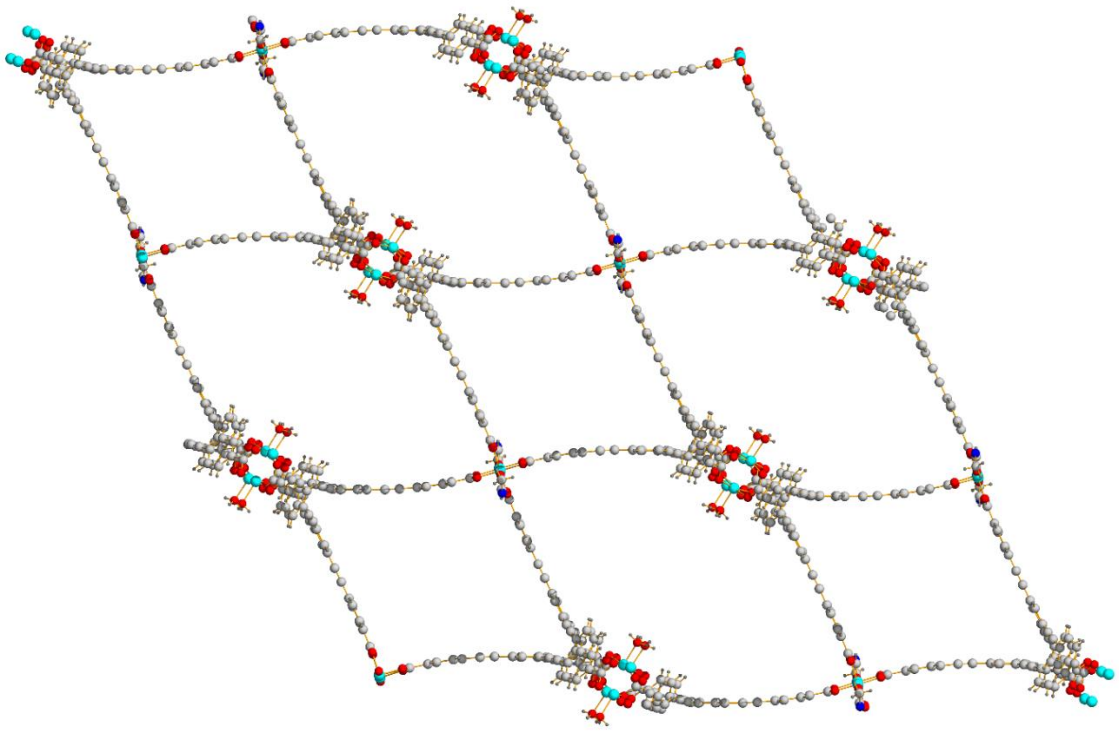

Figure 5.2 – A single net of 17 viewed along the crystallographic *b*-direction.

A more detailed topological consideration reflects the different binding arrangement of the benzoate groups of the bteb^{3-} ligands in **17** (Figure 5.3). The topological analysis shows that the net can indeed be described as a (3,4,4)-connected, trinodal net with two topologically distinct 4-connected nodes. The overall point symbol is $\{4.8^2\}_4\{4^2.8^2.10^2\}_2\{8^4.12^2\}$. The 4-connected vertex with the point symbol $\{4^2.8^2.10^2\}$ represents the $\{Cu_2\}$ SBUs in which the four adjacent terminal phenyl rings of the ligand are all tilted against their respective central ring (33° angle). The 4-connected vertex with the point symbol $\{8^4.12^2\}$ represents the Cu(II) dimer in the structure where the terminal phenyl rings of the ligand are coplanar to the respective central ring (90° angle).

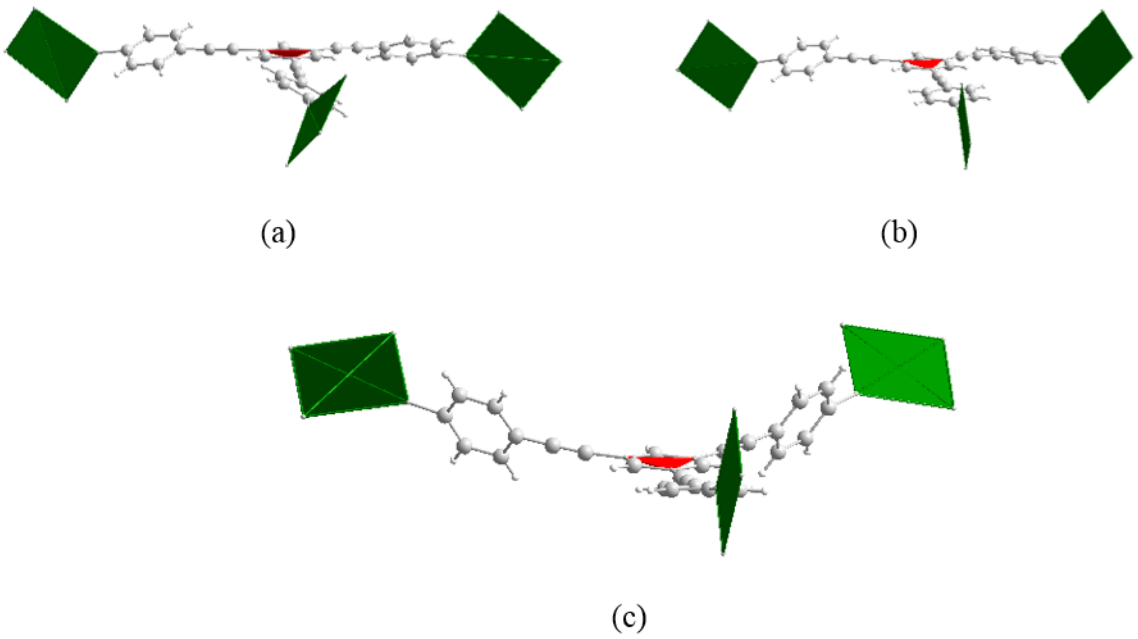

Figure 5.3 - Graphical representation of square-triangle torsions in (a) TCM-4, (b) TCM-8, (c) TCM-10.

Thus, the network in **17** represents a less-symmetrical (3,4)-connected net topology that is only represented once in the *Topos Topological Database* (TTD) (3,4,4T84) and that distinctively differs from the nets in TCM-4 and TCM-8.[13,14] The corresponding augmented analogue can be represented by the point symbol $\{3.16^2\}\{3.8.9\}_2\{4.16^2\}\{4.8.10\}_2$. The simplified structural representations that highlight the binding modes of the organic ligands are shown in Figure 5.4.

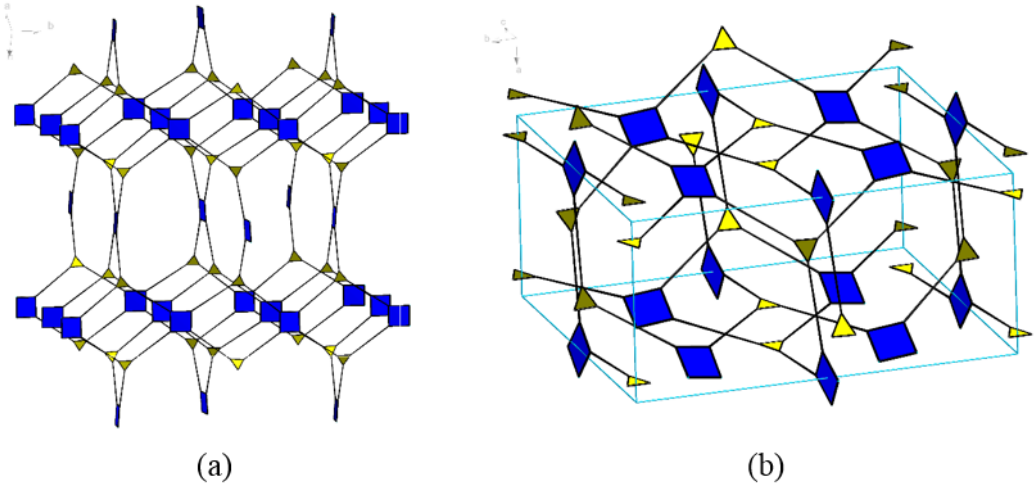

Figure 5.4 – Augmented topological reductions of a single net of 17 (a), and a unit cell of 17 (b). Cell edges are shown in light blue.

The observed triple-interweaving of the nets in **17** (Figure 5.5) can also be attributed to the extended and flexible nature of the bteb^{3-} ligand. π-π stacking of the central benzene rings from different sub-nets and bowing of the bteb^{3-} ligands stabilize the interwoven structure. The observed type of interpenetration and connectivity results in cylindrical/hexagonal channels that extend in the direction of the crystallographic *c*-axis. Significantly sized openings can also be noticed in the *b*-direction. Packing diagrams that highlight the channels and the interpenetration of the three symmetry-equivalent networks are displayed along the unit cell directions in Figure 5.8. Despite the interwoven nature of the MOF, the unit cell of **17** has a solvent-accessible void volume of ca. 72% (corresponding to 11925 Å^3).[15] Channels along the *b*- and *c*-directions were determined to have limiting minimum diameters of 8.4 Å.[16]

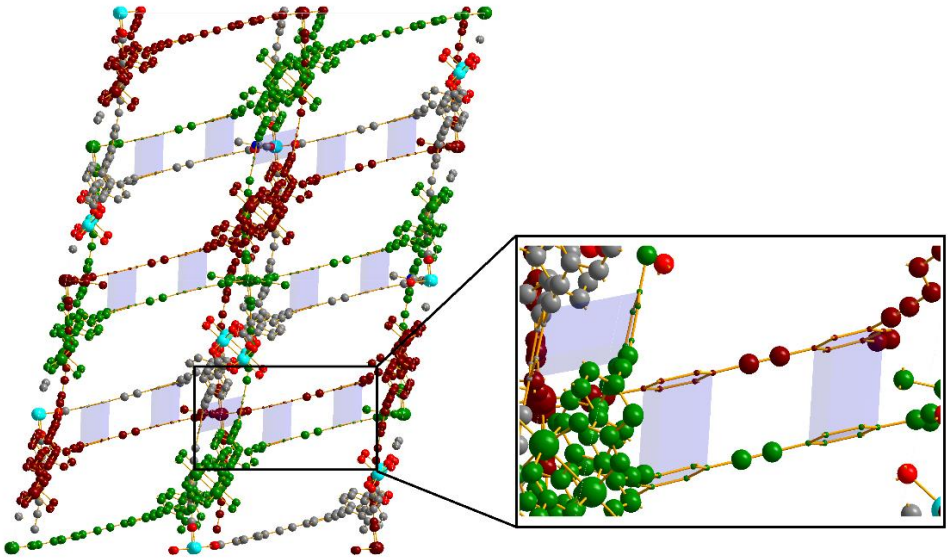

Figure 5.5 – The three interwoven nets in 17 – atoms coloured in green, maroon, and grey respectively. Aromatic interactions between nets are highlighted.

FTIR spectroscopy carried out on **17** shows a broad signal centred at 3455 cm^{-1} due to constitutional DMF molecules interacting with the framework (Fig. 5.6). The strong band at 1652 cm^{-1} is assigned to the C=O stretching vibration in DMF. The asymmetric carboxylate stretching mode was found at 1551 cm^{-1}, and the symmetric carboxylate stretching mode was found at 1386 cm^{-1}. This gives a Deacon-Phillips Δ value of 165 cm^{-1}, which agress well with the observed bidentate bridging binding mode in **17**.[17] The phase purity of manually collected crystals of **17** was assessed using powder X-ray diffraction,

which also validated the structural model obtained from single crystal measurements (Fig. 5.6).

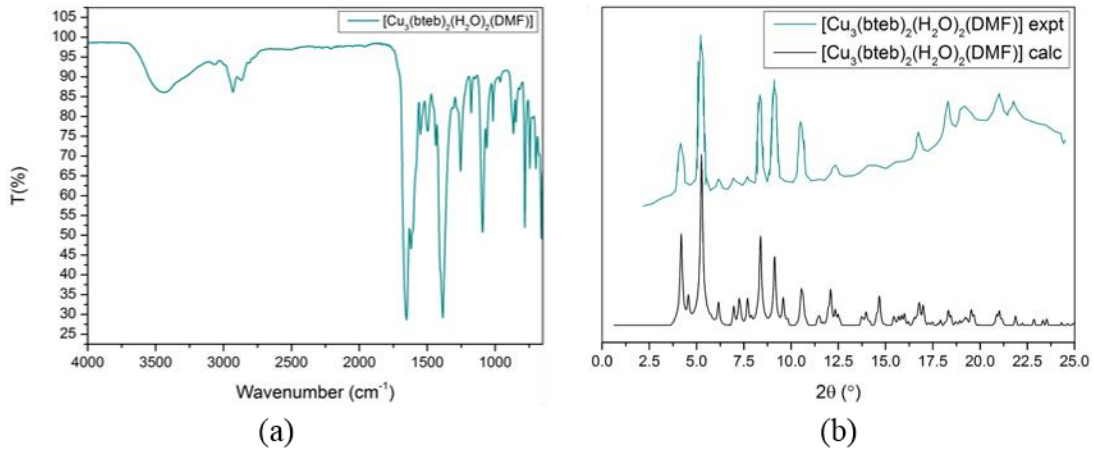

Figure 5.6 – FTIR spectrum (a) and PXRD pattern (b) of manually separated 17.

The significant solvent-accessible void volume in **17** is underlined by the thermogravimetric analysis carried out in a N_2 atmosphere (Fig. 5.7). The thermogravimetric step associated with the loss of constitutional solvent molecules occurs up to 110°C. The weight loss of *ca.* 5% above 110°C is caused by the removal of coordinated H_2O/DMF molecules before the decomposition of the $bteb^{3-}$ moieties destroys the network structure above 280°C.

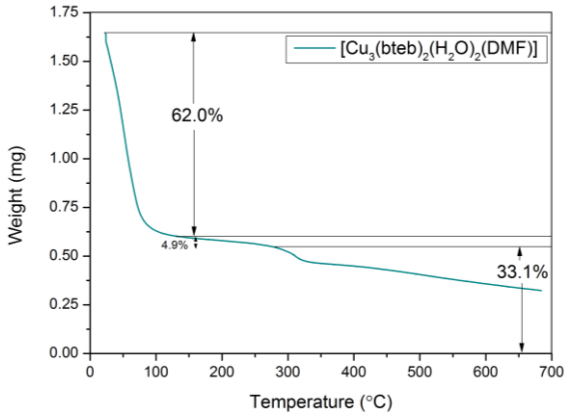

Figure 5.7 – TGA trace of manually separated 17.

Theoretical calculations were conducted to evaluate the possible surface areas and gas storage capacity of **17** and to compare these with TCM-4/8. A theoretical approach that

calculates the largest solid sphere that can be inserted into the cavities whilst avoiding any overlap with framework atoms was used to determine the pore size distribution (PSD) as shown in Figure 5.9.[18]

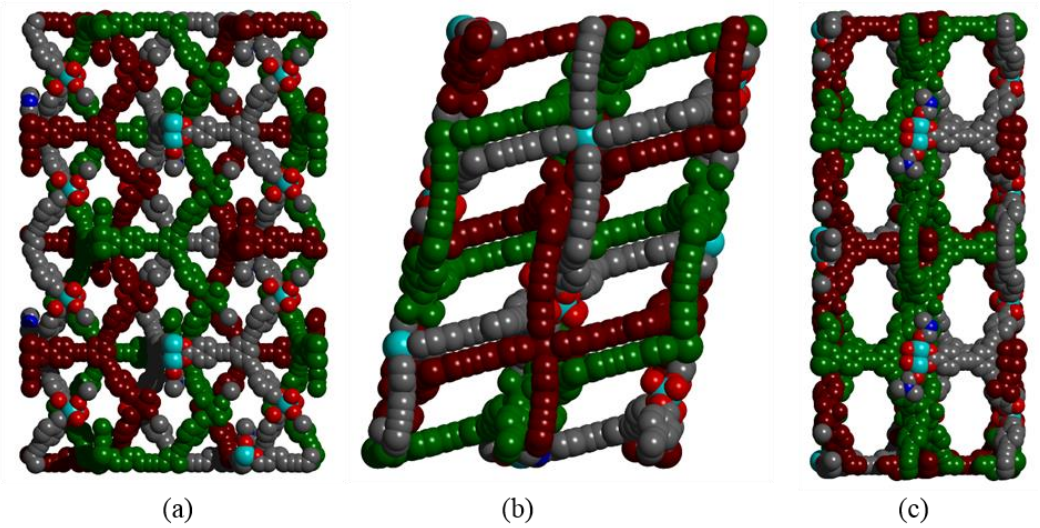

Figure 5.8 –Packing representations of 17 along the *a*- (a), *b*- (b), and *c*- (c) directions.

This analysis confirmed that **17** contains well-defined micropores with cross-sectional diameters of *ca.* 12.3 Å and smaller, narrow cavities of *ca*. 9.8 Å in diameter. This distribution is distinct to that of the corresponding dual interpenetrated **pto** and **tbo** structures that contain either distinct micropores of 12.3, 14.5 and 18.5 Å in diameter (TCM-8) or mesopores with diameters >20 Å (TCM-4 or TCM-4'). The surface area of **17** was calculated to be *ca.* 3900 m^2/g which is noteworthy considering the triply interpenetrated nature of the compound (Table 5.3).[19]

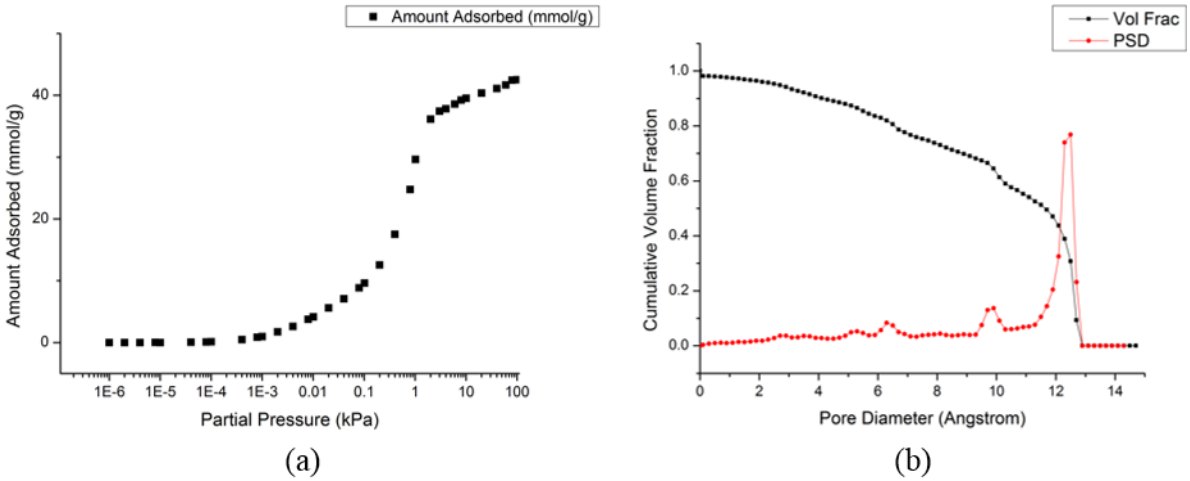

Figure 5.9 (a) – Calculated N_2 adsorption isotherm for 17; (b) – pore size distribution calculated for 17.

Table 5.3 – A comparison of $\{Cu_2\}$-$bteb^{3-}$ MOFs.

	TCM-4	**TCM-8**	**17**
Interpenetration	Dual	Dual	Triple
Cell volume ($Å^3$)/Z	80939/16	105620/16	16645/4
Void volume (%)/ unit cell	78	84	72
Calculated surface area	3820	5441	3907

5.3: Compound **18**, $[Cu_6(bbc)_4(H_2O)_5(DMF)]$, and Compound **19**, $[Cu_3(bbc)_2(azpy)_2]$

Extending the approach used in the synthesis of 17 to the bbc^{3-} ligand, compound **18** was synthesised at elevated temperature and high concentrations, close to the saturation concentration of the H_3bbc ligand in DMF. The conventional elevated temperature method was used and blue single crystals of **18** were obtained along with a microcrystalline blue bulk phase, on reaction of H_3bbc and $Cu(NO_3)_2{\cdot}3H_2O$ in DMF. Crystals of **18** were removed manually and studied by single-crystal X-ray diffraction.

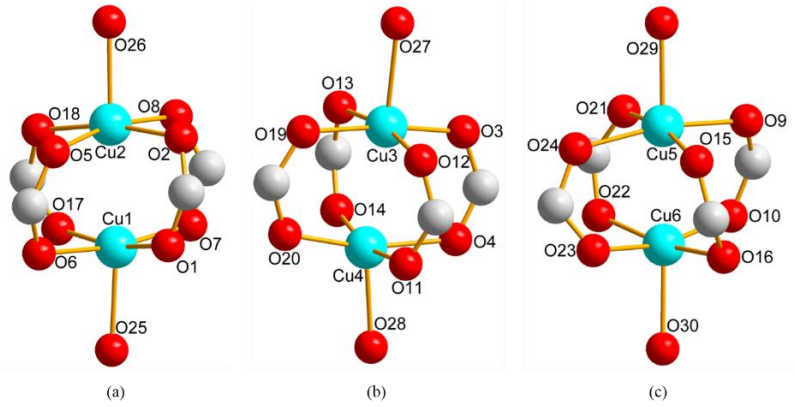

Figure 5.10 – Representations of the three crystallographically distinct $\{Cu_2\}$ SBUs in 18.

The crystal structure of **18** was solved and refined in the monoclinic crystal system and the $P2_1/n$ space group, with the cell parameters a = 19.299(2) Å, b = 64.486(7) Å, c = 24.613(3) Å, $\alpha = \gamma = 90°$, $\beta = 100.51(3)°$. The asymmetric unit of **18** contains 6 Cu^{2+} centres, in the form of three dimeric $\{Cu_2\}$ paddle-wheel units, and 4 fully deprotonated bbc^{3-} linkers. O-donor atoms of *syn*, *syn*-bidentate carboxylate groups provide the bases of the square pyramidal coordination polyhedra of each Cu(II) centre. Two of the $\{Cu_2\}$ are capped at the Jahn-Teller elongated apical positions of respective Cu^{2+} centres by H_2O ligands, while the third $\{Cu_2\}$ unit is capped at one apex by H_2O and at the other by DMF. Each $\{Cu_2\}$ SBU is coordinated by four tritopic bbc^{3-} ligands, and each bbc^{3-} moiety connects to three $\{Cu_2\}$ SBUs giving rise to a neutral network structure with the formula $[Cu_6(bbc)_4(H_2O)_5(DMF)]$. The $\{Cu_2\}$ paddle-wheels in **18** show unusually high degrees of distortion, as evidenced by the deviations from square pyramidal geometry around Cu^{2+} centres and the deviation from linear alignment of capping O-donor atoms along the Cu-Cu axis (Fig 5.10, bond angles are listed in Table 5.4). O-donor atoms of *syn*, *syn*-bidentate

carboxylate groups provide the bases of the square pyramidal coordination polyhedra of each Cu(II) centre.

Table 5.4 - Selected interatomic distances and angles in 18.

Atoms	Distance		Atoms	Angle
Cu1-O25	2.21(5) Å		O25-Cu1-O1	101.0(5)°
Cu1-O1	1.98(1) Å		O25-Cu1-O7	99.9(5)°
Cu1-O7	1.95(1) Å		O6-Cu1-O17	88.5(6)°
Cu1-O6	2.01(2) Å		O17-Cu1-O7	91.5(6)°
Cu1-O17	2.00(2) Å		O25-Cu1-Cu2	174.8(4)°
Cu1-Cu2	2.616(4) Å		Cu1-Cu2-O26	177.9(4)°
Cu2-O26	2.19(1) Å		O26-Cu2-O2	92.6(6)°
Cu2-O26	1.94(2) Å		O26-Cu2-O5	92.2(6)°
Cu2-O2	1.94(2) Å		O5-Cu2-O18	98.5(5)°
Cu2-O5	1.99(1) Å		O18-Cu2-O8	99.1(5)°
Cu2-O8	2.02(1) Å		O27-Cu3-O3	94.1(5)°
Cu2-O18	1.97(1) Å		O27-Cu3-O12	97.4(8)°
Cu3-O27	2.29(1) Å		O13-Cu3-O19	92.0(6)°
Cu3-O3	1.89(2) Å		O19-Cu3-O12	89.0(6)°
Cu3-O12	2.01(1) Å		O27-Cu3-Cu4	83.4(6)°
Cu3-O13	1.99(1) Å		Cu3-Cu4-O28	167.2(4)°
Cu3-O19	1.99(2) Å		O28-Cu4-O11	92.4(6)°
Cu3-Cu4	2.628(6) Å		O28-Cu4-O20	107.4(6)°
Cu4-O28	2.17(1) Å		O14-Cu4-O4	85.8(8)°
Cu4-O4	2.03(2) Å		O4-Cu4-O11	87.5(7)°
Cu4-O11	1.98(1) Å		O11-Cu4-O20	90.6(6)°
Cu4-O14	2.00(1) Å		O29-Cu5-O9	92.7(5)°
Cu4-O20	1.92(2) Å		O29-Cu5-O21	91.0(6)°
Cu5-O29	2.20(1) Å		O21-Cu5-O24	84.1(6)°
Cu5-O9	2.01(1) Å		O24-Cu5-O15	91.0(6)°
Cu5-O15	1.96(1) Å		O29-Cu5-Cu6	172.4(4)°
Cu5-O21	1.98(2) Å		Cu5-Cu6-O30	169.2(5)°
Cu5-O24	1.97(1) Å		O30-Cu6-O23	91.4(7)°
Cu5-Cu6	2.643(5) Å		O30-Cu6-O10	103.4(6)°
Cu6-O30	2.21(2) Å		O22-Cu6-O23	85.3(6)°
Cu6-O22	1.96(1) Å		O23-Cu6-O16	85.8(6)°
Cu6-O23	1.97(2) Å			
Cu6-O10	1.95(1) Å			
Cu6-O16	2.10(2) Å			

The default net expected for the combination of the 'square' $\{Cu_2\}$ SBU and the 'triangular' tritopic bbc^{3-} linker is the **tbo** net, shown by MOF-399, in which the ligand adopts a conformation in which each terminal benzoate moiety is coplanar with the central phenyl ring. Topological analysis of **18** shows that the network adopted is not **tbo**, or the alternative highly symmetric **pto** net adopted in cases where the ligand adopts a conformation in which each terminal benzoate group is tilted by a dihedral angle of ca. 33° to the central phenyl ring.

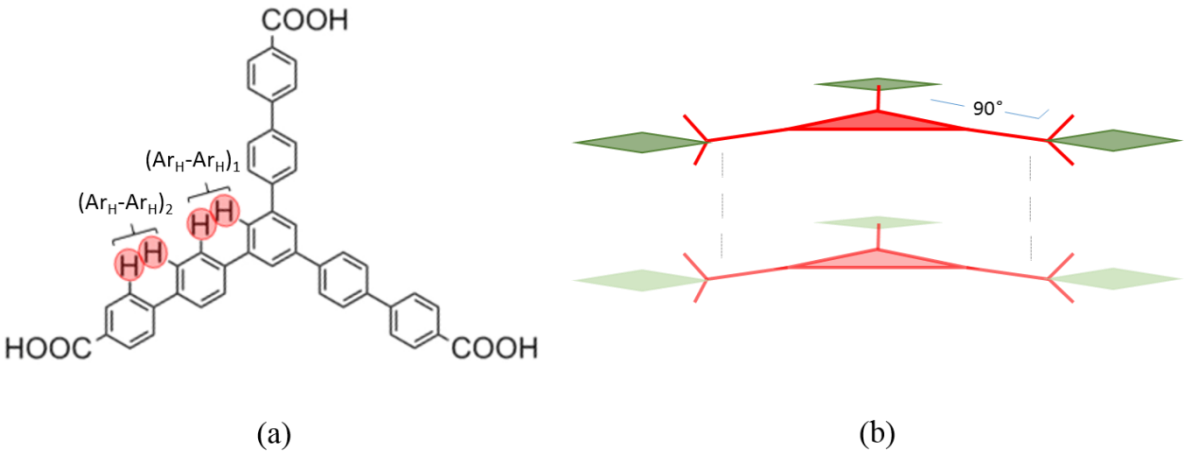

Figure 5.12 (a) – The H_{Ar}-H_{Ar} repulsions in the H_3bbc ligand; (b) – A schematic representation of a $\{Cu_2\}$-tricarboxlylate complex in which the dihedral angle between the central phenyl ring and peripheral carboxylate -CO moiety is 90°, showing the coplanarity of augmented 3- and 4-connected nodes.

Upon considering an imaginary tricarboxylate ligand in which all peripheral benzoate moieties adopted a dihedral angle of 90°, we can see that if $\{Cu_2\}$ units were bound to these carboxylate groups, they would be oriented coplanar to each other and the central phenyl ring (Fig. 5.12). Such an orientation would rule out three-dimensionality in the observed structure, and encourage sheet-like formations. The bbc^{3-} ligands used in **18** consist of a central phenyl ring, followed by a phenyl spacer, to which the peripheral benzoate moieties are bonded. This results in H_{Ar}-H_{Ar} repulsions between the central phenyl ring and the phenyl spacer, as well as H_{Ar}-H_{Ar} repulsions between each phenyl spacer and the adjacent peripheral benzoate moiety. The possible dihedral angles, assuming an angle of ca. 33° necessitated by each pair of repulsive interactions, between the central phenyl ring and the peripheral benzoate moieties are 0° ((H_{Ar}-H_{Ar})$_1$ = +33°, (H_{Ar}-H_{Ar})$_2$ = -33°), or *ca.* 66° ((H_{Ar}-H_{Ar})$_1$ = +33°, (H_{Ar}-H_{Ar})$_2$ = +33°, Fig. 5.13)). The adoption of the 0° dihedral angle leads to the more symmetric, edge-transitive **tbo** network of MOF-399.[10] However,

adoption of the *ca.* 66° dihedral angle, as well as distortion of the {Cu_2} SBUs allows the formation of a framework isomer of MOF-399, with a lower symmetry structure.

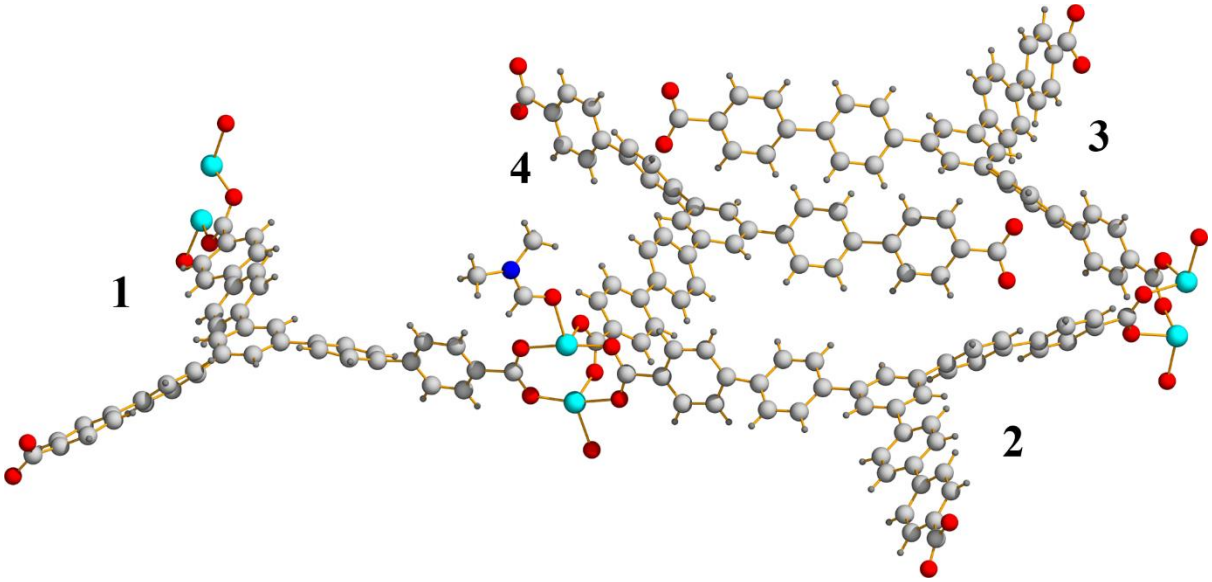

	Angle (°)	Angle (°)	Angle (°)
1	58.58	56.55	89.84
2	80.95	69.40	61.45
3	72.18	86.99	72.40
4	85.82	72.84	55.75

Figure 5.13 – The asymmetric unit of the crystal structure of 18, and the torsion angles measured between carboxylate carbon and oxygen atoms and adjacent carbon atoms of the central phenyl rings.

18 has a structure which compensates for the loss of symmetry and from the 'default' net and induced strain, by a large increase in density over MOF-399 (ρ_{18} = 0.706 cm^3/g, $\rho_{MOF-399}$ = 0.126 cm^3/g), which is thermodynamically favoured. Packing along the crystallographic *a*- and *c*- axes show an increased sheet-like arrangement compared to MOF-399 (Fig. 5.14). However, torsion angles between the central phenyl ring and the peripheral benzoate moieties remain well below 90°, and the network formed is three-dimensional.

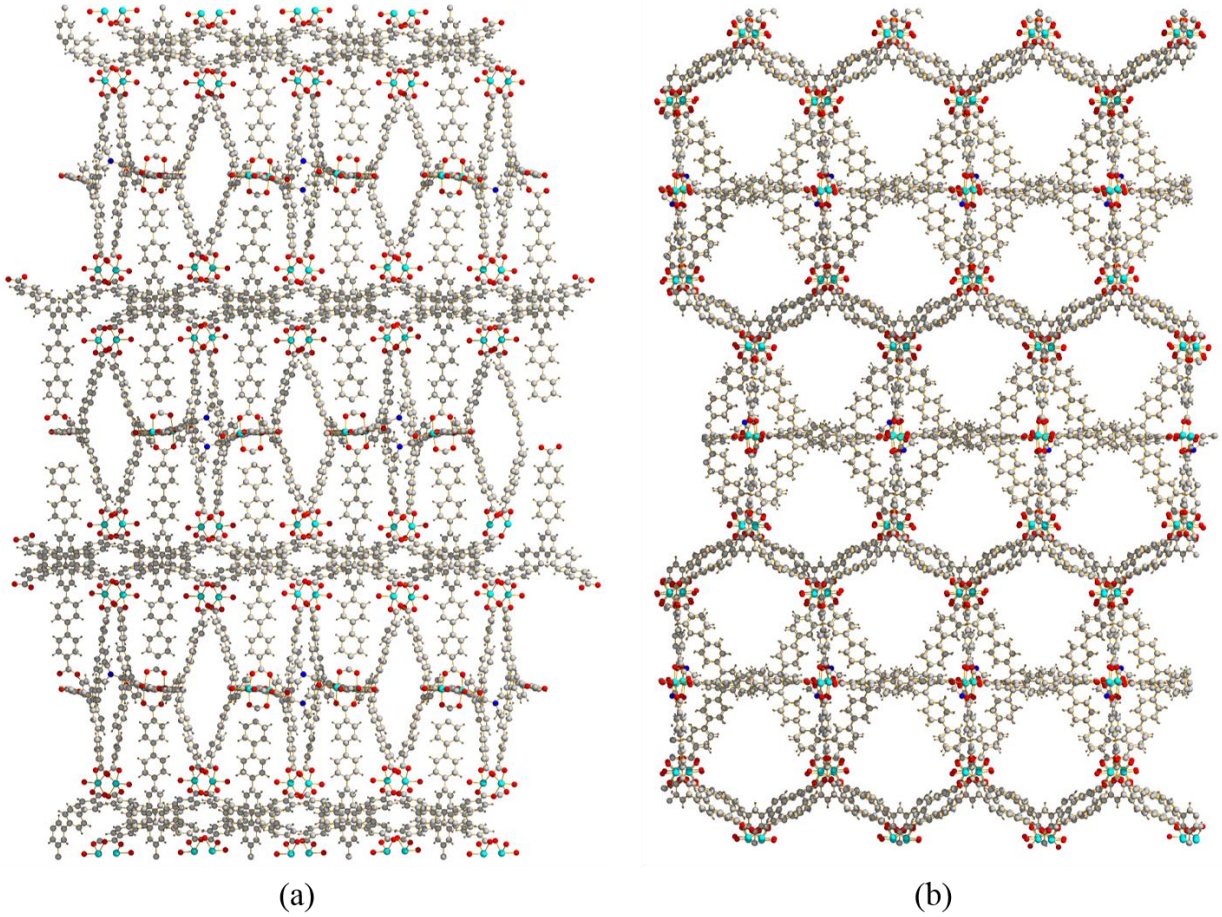

Figure 5.14 – Packing representations of 18 along the crystallographic (a) – *a*-, and (b) *c*-directions.

Detailed topological analysis using the *TopoxPro* suite shows that the net in **18** is a 4-nodal (3,3,4,4)-connected net, with an overall point symbol of $\{4.8^2\}_2\{4.8^5\}_2\{8^3\}_2\{8^5.12\}$.[14] This is a previously unreported net to the best of our knowledge, and is not listed in the RCSR database. The two types of 3-connected node represent non-identical bbc^{3-} linkers, and the two types of 4-connected node represent non-identical $\{Cu_2\}$ SBUs (Fig. 5.15). The overall stoichiometry, as reflected in the point symbol, is $(3\text{-c})_2(3\text{-c})_2(4\text{-c})(4\text{-c})_2$.

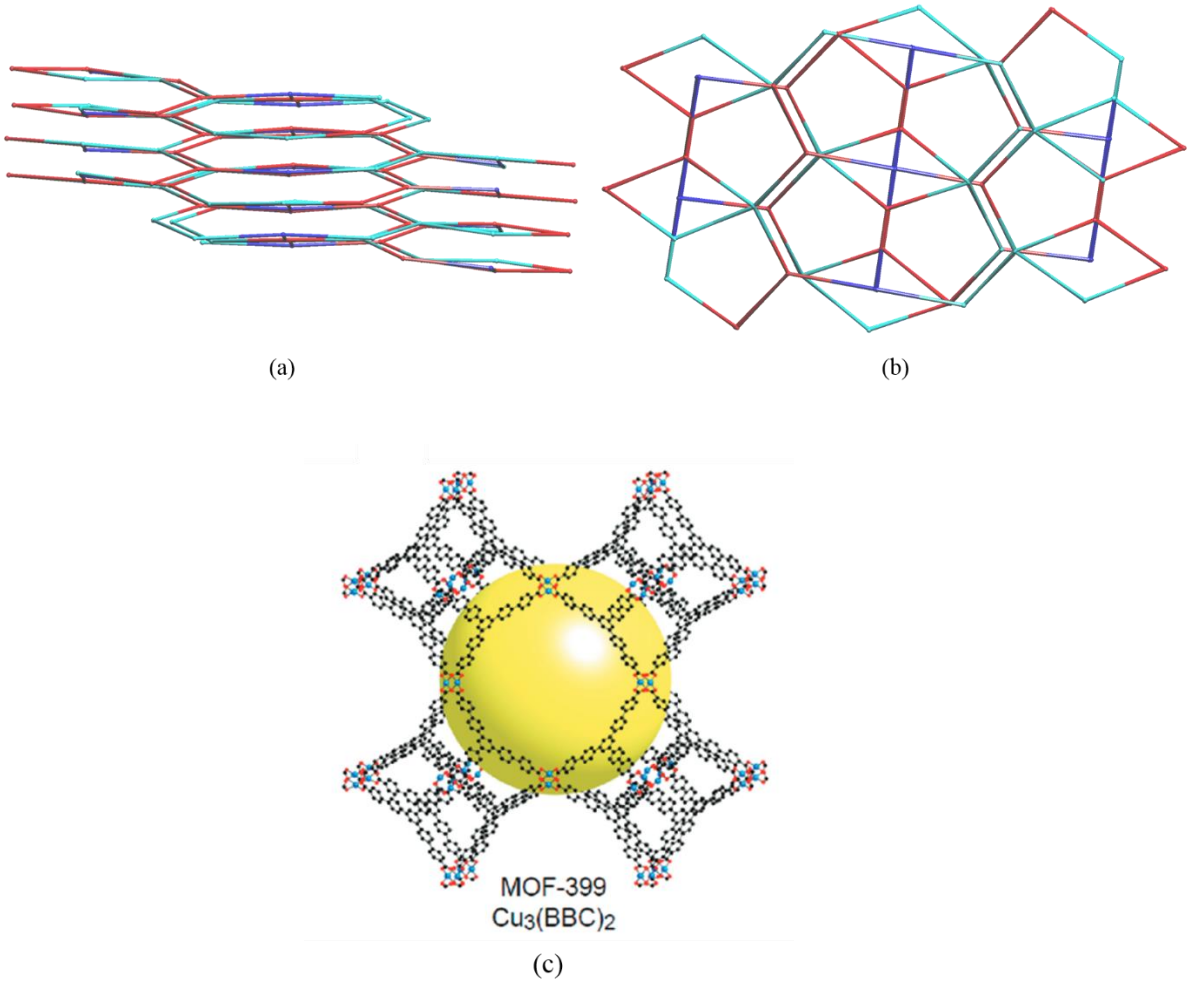

Figure 5.15 – Topological reductions of 18 viewed along the crystallographic (a) *a*- , and (b) *c*-directions. 3-connected nodes are coloured red, and 4-connected nodes are coloured shades of blue; (c) – A representation of the structure of MOF-399, taken from Ref. 10, shown for contrast.

Dihedral angles of *ca*. 66° - *ca*. 75° are dominant, and this results in cascading pairs of approximately helical motifs in the structure, reconciling the increased coplanarity of the 'square' SBUs with the three-dimensionality and achirality of the crystal structure. The pairs of helices consist of one right-handed (Δ) and one left-handed (Λ) helix, as shown in Fig. 5.16. The helices have an idealised pitch of *ca.* 6.2 – 6.5 Å, and define one-dimensional channels along the crystallographic *c*-axis. The structure in **18** is estimated to have a void volume of 57.4% (CCDC:Mercury) of the total volume and a limiting channel diameter along the *c*-axis of 9.2 Å (Olex2).[15,16] The diameter of the largest spherical void in the structure was calculated to be 12.0 Å.

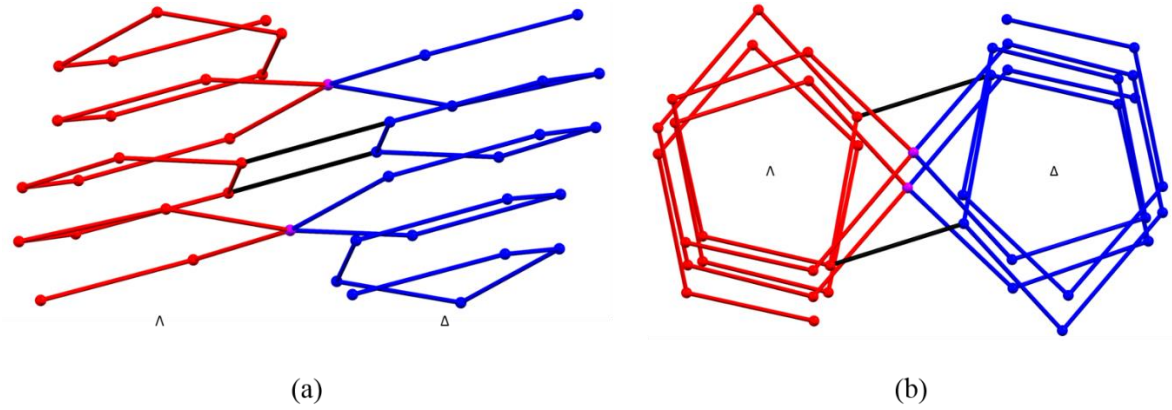

Figure 5.16 – Topological reductions of 18 viewed along the crystallographic (a) *a*- , and (b) *c*-directions, with helical motifs highlighted in red (left-handed) and blue (right-handed).

Physicochemical characterisation and sorption experiments could not be carried out on **18**. The experimental powder X-ray pattern on the microcrystalline bulk sample shows traces of **18** and MOF-399, but is primarily unidentified (Fig. 5.17). The yield of isolated single crystals of **18** is too low for harvesting of crystals manually to be fruitful.

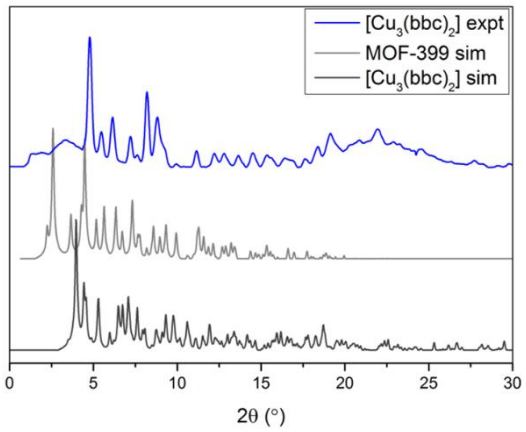

Figure 5.17 – PXRD pattern of the bulk product obtained along with 18, compared to simulations of the PXRD patterns of MOF-399 and 18 obtained from single crystal structures.

Therefore, simulations of the pore size distribution and accessible surface area were carried out on the crystal structure of **18**, using the Poreblazer suite.[20] The simulations reveal a He pore volume of 0.943 cm^3/g, a limiting channel diameter of 8.81 Å, and a maximum pore diameter of 12.04 Å, in excellent agreement with their crystallographic estimations. The pore size distribution obtained is shown in Fig 5.18. The accessible surface area was calculated to be 2088 m^2/g. Therefore **18** can be said to be potentially highly porous despite its 'non-default' network structure.

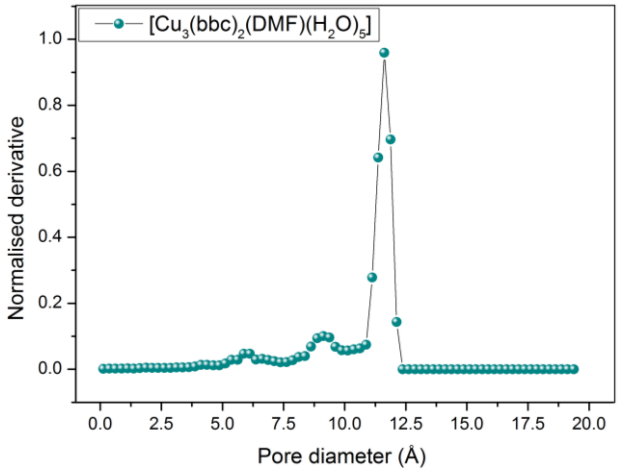

Figure 5.18 – Pore size distribution simulated from the crystal structure of 18.

Compound **19**, $[Cu_3(bbc)_2(azpy)_2]$, was synthesised by reacting H_3bbc, $Cu(NO_3)_2{\cdot}3H_2O$, and 4,4′-azopyridine (azpy), at high concentrations in DMF at 85°C. Isolated blue-green single crystals of **19** were obtained along with a microcrystalline blue bulk phase. Crystals of **19** were removed manually and studied by single-crystal X-ray diffraction.

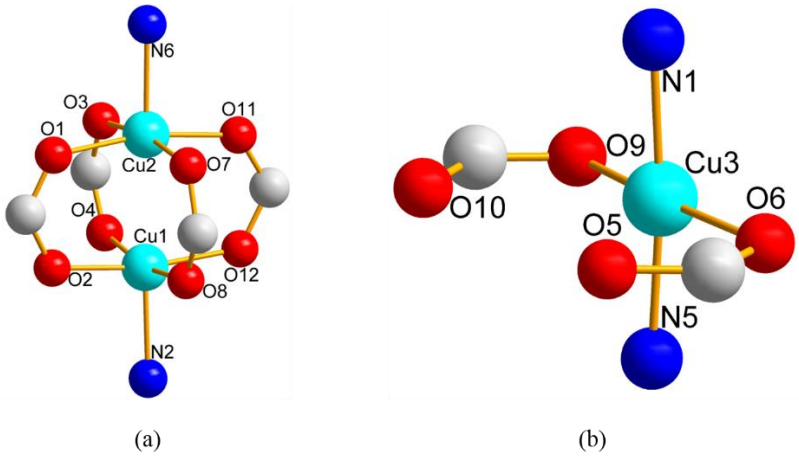

Figure 5.19 – Representations of two distinct Cu SBUs in 19 – (a) {Cu_2} paddle-wheel, and (b) mononuclear {Cu}.

The crystal structure of **19** was solved and refined in the triclinic $P\bar{1}$ space group, with the cell parameters a = 21.997(6) Å, b = 27.374(8) Å, c = 28.724(8) Å, α = 113.20(4)°, β = 95.05(4)°, γ = 113.08(3)°. The structure of **19** shows three-fold interpenetration. Each interpenetrated net is built by fully deprotonated bbc^{3-} linkers, azpy linkers, and Cu(II) centres. Cu(II) centres are present as {Cu_2} paddle-wheel SBUs. However, unlike most Cu(II) MOFs, an equal number of square planar mononuclear Cu^{2+} centres are also present

(Fig. 5.19). Each bbc^{3-} linker is connected to two $\{Cu_2\}$ units and a mononuclear metal centre. Each paddle-wheel unit is composed of square pyramidal coordination environment around pairs of Cu^{2+} ions, in which O-donor atoms of *syn, syn*-bidentate carboxylate groups provide the bases of the square pyramidal coordination polyhedra of each Cu(II) centre. The apical positions of the square pyramid are occupied by N-donor atoms form azpy ligands. The mononuclear Cu^{2+} centres are bound to two O-donors from carboxylate groups from two distinct bbc^{3-} which bind in monodentate fashion. The two O-donors are situated *trans* to each other on the square plane, and the non-bonded oxygens are oriented on the same side of the Cu^{2+} centre. Two N-donor atoms from azpy ligands complete the square planar geometry are are also oriented trans to each other (Table 5.5). Each azpy ligand connects a mononuclear Cu^{2+} centre to a $\{Cu_2\}$ paddle-wheel (Fig. 5.20).

Table 5.5 - Selected interatomic distances and angles in 19.

Atoms	**Distance**		**Atoms**	**Angle**
Cu2-O1	1.955(7) Å		N6-Cu2-O1	96.6(4)°
Cu2-O3	1.96(1) Å		N6-Cu2-O11	95.4(4)°
Cu2-O7	1.96(1) Å		O11-Cu2-O3	90.5(4)°
Cu2-O11	1.938(6) Å		O1-Cu2-O3	89.0(4)°
Cu2-N6	2.14(1) Å		N6-Cu2-Cu1	177.3(2)°
Cu1-Cu2	2.617(3) Å		Cu2-Cu1-N2	174.9(2)°
Cu1-O2	1.939(7) Å		N2-Cu1-O2	95.7(3)°
Cu1-O4	1.97(1) Å		N2-Cu1-O12	94.7(3)°
Cu1-O8	1.98(1) Å		O2-Cu2-O4	90.5(4)°
Cu1-O12	1.965(7) Å		O12-Cu2-O8	89.2(4)°
Cu1-N2	2.145(9) Å			
Cu3-O6	1.99(1) Å		N1-Cu3-N5	174.7(3)°
Cu3-O9	1.943(9) Å		N1-Cu3-O9	88.6(4)°
Cu3-N5	1.98(1) Å		O9-Cu3-O6	171.6(5)°
Cu3-N1	1.96(1) Å		N5-Cu3-O6	90.2(4)°
Cu3-O5	2.92(1) Å		O9-Cu3-O10	52.5(4)°
Cu3-O10	2.82(1) Å		O6-Cu3-O5	51.2(4)°

Torsions in the bbc^{3-} linker show the loss of the three-fold rotational symmetry seen in the **pto** and **tbo** nets – the two carboxylates bound to $\{Cu_2\}$ are twisted by about 80° relative to the central phenyl ring, while the carboxylate bound to the mononuclear Cu^{2+} is nearly coplanar to it. The $\{Cu_2\}$ units bound to bbc^{3-} ligands adopt a sheet-like orientation, due to the torsion within the ligand approaching 90°, and these sheets are oriented perpendicular to the crystallographic *c*-direction. Two adjacent paddle-wheels are bound to two arms of the same two bbc^{3-} linkers, resulting in a rhombus-shaped cavity. The pillaring azpy linkers are oriented parallel to the *c*-direction whereby the sheets stack in *abab* fashion.

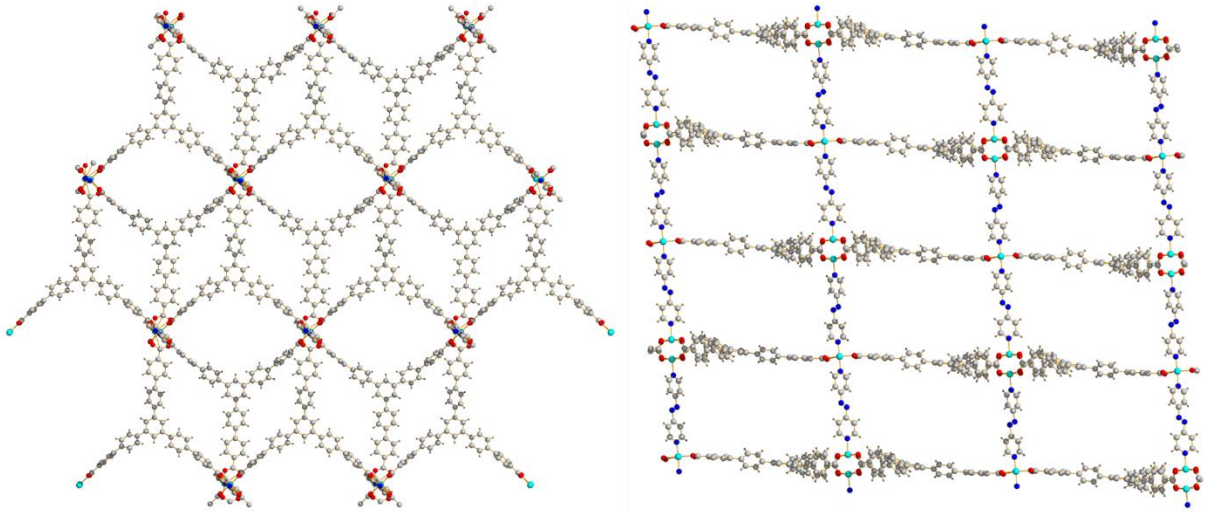

(a) (b)

Figure 5.20 – Packing representations of a single net of 19 along the crystallographic (a) – *c*-, and (b) *a*-directions.

Topological analysis shows that each net is a 3-nodal, (3, 4, 6)-connected net. The point symbol for the net is $\{4.6^2\}_2\{4^2.6^8.8^3.10^2\}\{6^4.8^2\}$ corresponding to a stoichiometry of (3-c)$_2$(4-c)(6-c) (Fig 5.21). This is a previously unreported net to the best of our knowledge, and is not listed in the RCSR database. Two of these nets are minimally displaced from each other and can be said to be interwoven, while the third is maximally displaced from the other two. This results in a rare 2+1 mode of non-equivalent interpenetration (Fig. 5.22).[21]

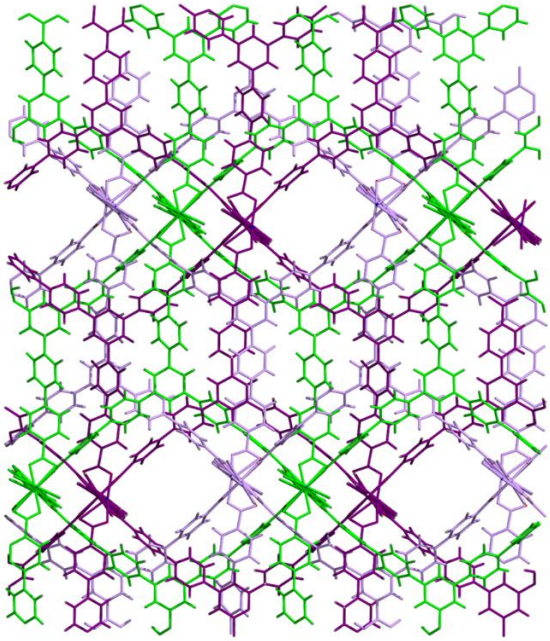

Figure 5.21 – Wireframe representation of 19 highlighting the interpenetrating nets. Interwoven nets are coloured in shades of purple, and the interpenetrating net that completes the 2+1 mode is coloured in green.

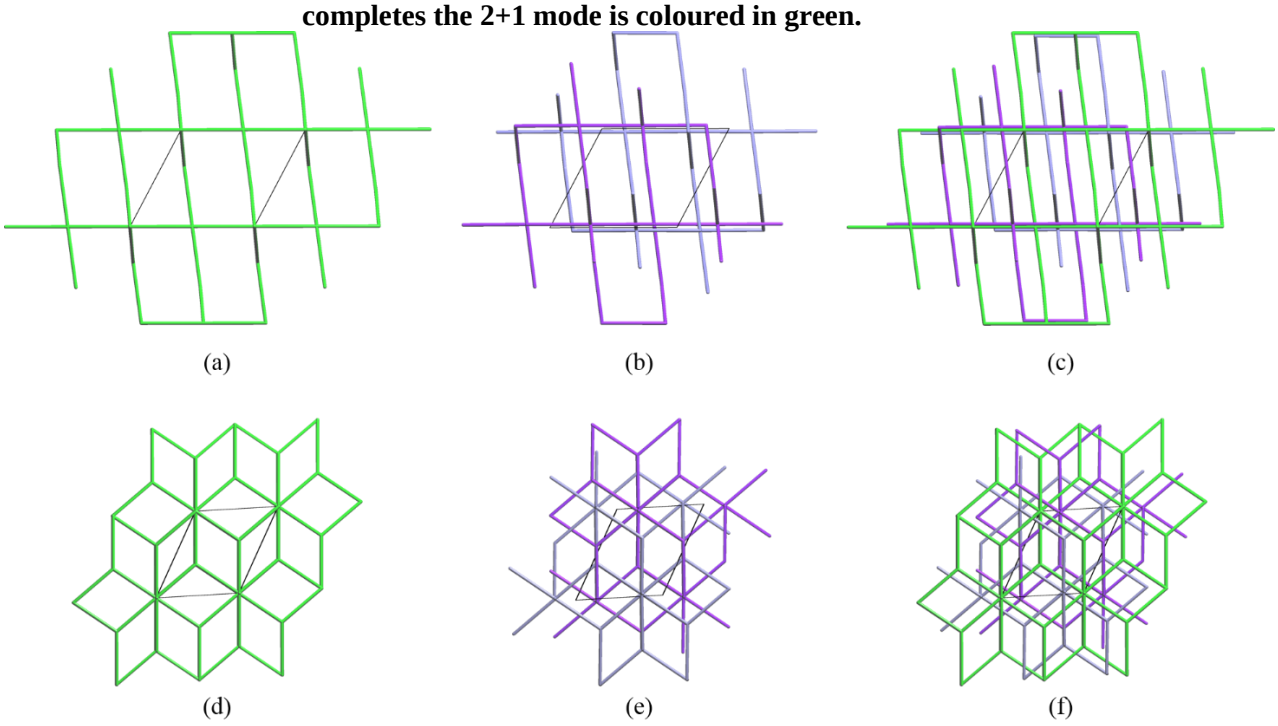

Figure 5.22 – Topological reductions of 19 viewed along the crystallographic (a, b, c) *a*- , and (d, e, f) *c*-directions. Interwoven nets are coloured in shades of purple, and the interpenetrating net that completes the 2+1 mode is coloured in green.

Despite the three-fold interpenetration observed in **19**, the structure is still substantially porous. The solvent accessible void volume is calculated to be 58.7% (CCDC:Mercury) of the total volume. The limiting channel diameter along the *c*-axis is 5.2 Å, corresponding to

the rhombic windows described earlier (Olex2). The diameter of the largest spherical void was calculated to be 12.4 Å. As with **18**, the microcrystalline bulk sample in **19** was found by powder X-ray spectroscopy to primarily consist of unidentified phases (Fig. 5.23). The yield from isolated single crystals was too low for usable quantities of **19** to be harvested. Physicochemical characterisation and experimental sorption could not be carried out.

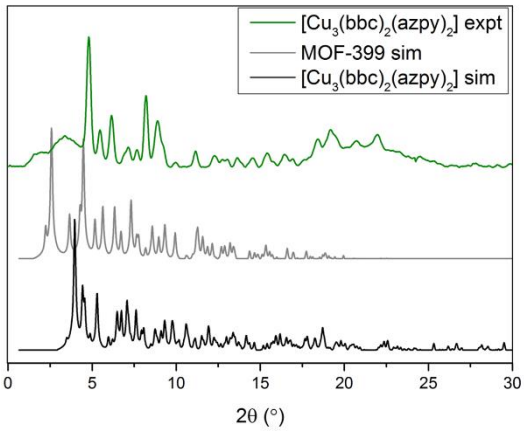

Figure 5.23 – PXRD pattern of the bulk product obtained along with 19, compared to simulations of the PXRD patterns of MOF-399 and 19 obtained from single crystal structures.

Therefore, using the Poreblazer suite, simulations of the pore size distribution and surface area were carried out on the crystal structure of **19**.[20] The simulations reveal a He pore volume of 0.969 cm^3/g, a limiting channel diameter of 7.33 Å, and a maximum pore diameter of 11.85 Å, in agreement with their crystallographic estimations. The pore size distribution obtained is shown in Fig 5.24. The accessible surface area was found to be 2303 m^2/g. Therefore the structure of **19** is shown to be potentially highly porous despite its 'non-default' and highly interpenetrated network.

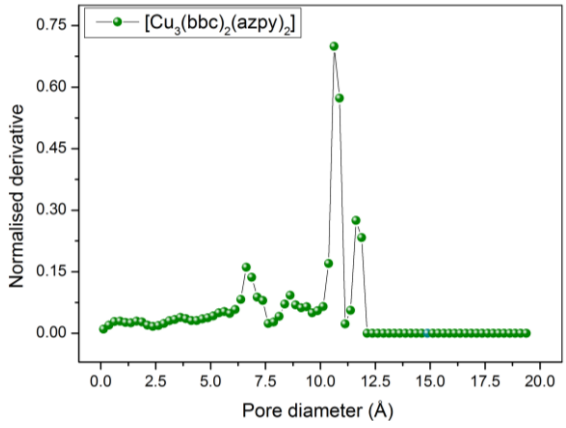

Figure 5.24 – Pore size distribution simulated from the crystal structure of 19.

Crystallographic details for the structures determined for **18** and **19** are given in Table 5.6.

Table 5.6 - Crystallographic details for 18 and 19.

Identification code	18	19
Empirical formula	$C_{183}H_{125}Cu_6NO_{30}$	$C_{41.25}H_{26.25}Cu_{1.12}N_3O_{4.5}$
Formula weight	3199.07	707.38
Temperature/ K	215(2)	215(2)
Crystal system	monoclinic	triclinic
Space group	$P2_1/n$	$P\bar{1}$
***a*/Å**	19.299(2)	21.997(3)
***b*/Å**	64.486(7)	27.374(4)
***c*/Å**	24.613(3)	28.724(4)
***α*/°**	90	113.201(4)
***β*/°**	100.51(3)	95.052(4)
***γ*/°**	90	113.082(3)
Volume/Å^3	30118(6)	14010(4)
Z	4	8
ρ_{calc}/ g/cm^3	0.706	0.671
μ/mm^{-1}	0.779	0.672
F(000)	6576.0	2907.0
Crystal size/mm^3	0.33 × 0.10 × 0.08	0.20 × 0.10 × 0.10
Radiation/Å	CuKα (λ = 1.54184)	CuKα (λ = 1.54184)
2θ range for data collection/°	3.9 to 81.188	4.434 to 76.882
Index ranges	$-15 \leq h \leq 16$, $-37 \leq k \leq 53$, $-20 \leq l \leq 16$	$-17 \leq h \leq 17$, $-21 \leq k \leq 21$, $-23 \leq l \leq 22$
Reflections collected	52329	23459
Independent reflections	18846 [R_{int} = 0.1094, R_{sigma} = 0.2322]	13593 [R_{int} = 0.0360, R_{sigma} = 0.0664]
Data/restraints/parameters	18846/320/575	13593/2/499
Goodness-of-fit on F^2	1.184	1.296
Final R indexes [I>=2σ (I)]	R_1 = 0.1692, wR_2 = 0.4251	R_1 = 0.1071, wR_2 = 0.3320
Final R indexes [all data]	R_1 = 0.2627, wR_2 = 0.4619	R_1 = 0.1334, wR_2 = 0.3504
Largest diff. peak/hole / e Å^{-3}	1.99/-0.67	0.63/-0.54

5.4: Compound **20**, $[Cd_3(bbc)_2(DMF)_3(H_2O)]$, and Compound **21**, $[Cd_6(bbc)_4(DEF)_3(H_2O)_9]$

A similar approach to that adopted for **17-19** was applied to frameworks based on slightly softer Cd^{2+} metal centres. Compound **20**, $[Cd_3(bbc)_2(DMF)_3(H_2O)]$, was synthesised by the conventional elevated temperature method in DMF at 100°C, using H_3bbc and $Cd(NO_3)_2{\cdot}4H_2O$. Colourless single crystals of **20** were obtained which were suitable for single-crystal X-ray diffraction.

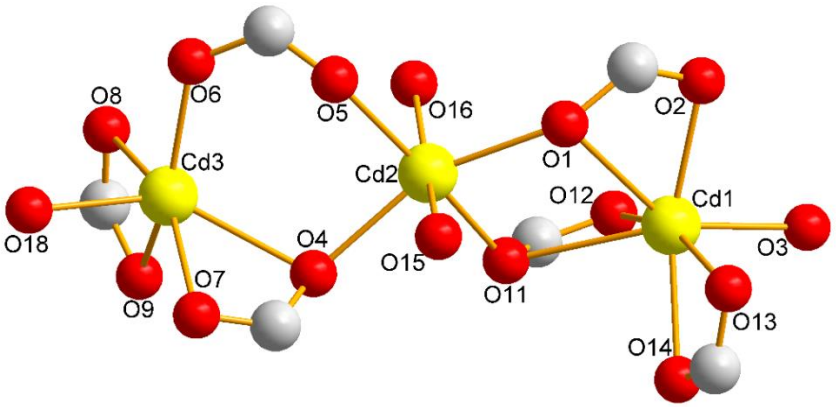

Figure 5.25 – A representation of the SBU in 20.

The crystal structure of **20** was solved and refined as a racemic twin in the orthorhombic crystal system and the chiral $P2_12_12$ space group, with the cell parameters a = 42.019(4) Å, b = 16.9283(16) Å, c = 24.574(2) Å, $\alpha = \beta = \gamma = 90°$. The asymmetric unit of **20** contains three Cd^{2+} centres, aligned into a single $\{Cd_3\}$ SBU, and two fully deprotonated bbc^{3-} linkers. The hourglass-shaped $\{Cd_3\}$ SBU is composed of three nearly co-linear Cd^{2+} centres interconnected by four carboxylate croups from bbc^{3-}, three of which exhibit bidentate bridging chelate modes, and the other exhibits a bidentate bridging mode (Fig 5.25). One bidentate chelating carboxylate each are bound to both outer Cd^{2+} centres, Cd1 and Cd3. One DMF ligand each are bound to Cd1 and Cd3, and two are bound to Cd2, resulting in coordination environments which are distorted octahedral around Cd3, octahedral around Cd2, and capped trigonal prismatic around Cd1. The angle between the three cadmium centres is *ca.* 154.8°. Degrees of compliance to ideal geometries can be assessed from the bond distances and angles listed in Table 5.7. The torsion angles in the bbc^{3-} ligands of **20** are given in Table 5.8.

Table 5.7 - Selected interatomic distances and angles in 20.

Atoms	Distance		Atoms	Angle
Cd5-O24	2.27(1) Å		O33-Cd5-O30	172.0(7)°
Cd5-O28	2.54(1) Å		O28-Cd5-O29	90.4(4)°
Cd5-O29	2.28(1) Å		O28-Cd5-O24	53.0(4)°
Cd5-O30	2.50(2) Å		O31-Cd5-O30	105.1(5)°
Cd5-O31	2.31(2) Å		O24-Cd5-O32	87.1(6)°
Cd5-O32	2.34(2) Å			
Cd5-O33	2.25(2) Å			
Cd1-O3	2.21(1) Å		O3-Cd1-Cd2	167.7(3)°
Cd1-O7	2.26(2) Å		O3-Cd1-O7	79.6(6)°
Cd1-O12	2.23(1) Å		O3-Cd1-O2	145.3(5)°
Cd1-O15	2.17(6) Å		O7-Cd1-O15	85.3(6)°
Cd1-O2	2.27(1) Å		O15-Cd1-O12	96.0(5)°
Cd1-O37	2.38(1) Å		O2-Cd1-O37	53.4(4)°
Cd1-O14	2.95(3) Å			
Cd1-Cd2	3.51(2) Å			
Cd2-O12	3.65(2) Å		O4-Cd2-O4	123.2(6)°
Cd2-O2	2.24(1) Å		O14-Cd2-O4	177.0(7)°
Cd2-O6	2.16(1) Å		O2-Cd2-O13	93.0(6)°
Cd2-O14	2.37(2) Å		O6-Cd2-O13	174.0(1)°
Cd2-O13	2.29(4) Å		O5-Cd2-O6	75.9(8)°
Cd2-O4	2.51(2) Å			
Cd2-O5	2.59(4) Å			

Table 5.8 – Dihedral angles between the central phenyl and peripheral benzoate planes in 20.

	Angle (°)	Angle (°)	Angle (°)
1	67.5	0.2	77.3
2	80.0	5.4	84.1

Thus, the SBU formed is 6-connected overall, and the connections as represented by the carboxylate carbon atoms can be considered as a pair of 3-connected nodes between each pair of Cd atoms in the {Cd_3} SBU. Each SBU is connected to six carboxylate groups from six distinct bbc^{3-} ligands. Each bbc^{3-} linker links three {Cd_3} SBUs. The overall structure thus obtained is a two-dimensional coordination polymer network based on bilayered hexagonal motifs (Fig. 5.26). Each SBU directs organic ligands into three coplanar directions along two planes corresponding to inter-Cd space in the SBU.

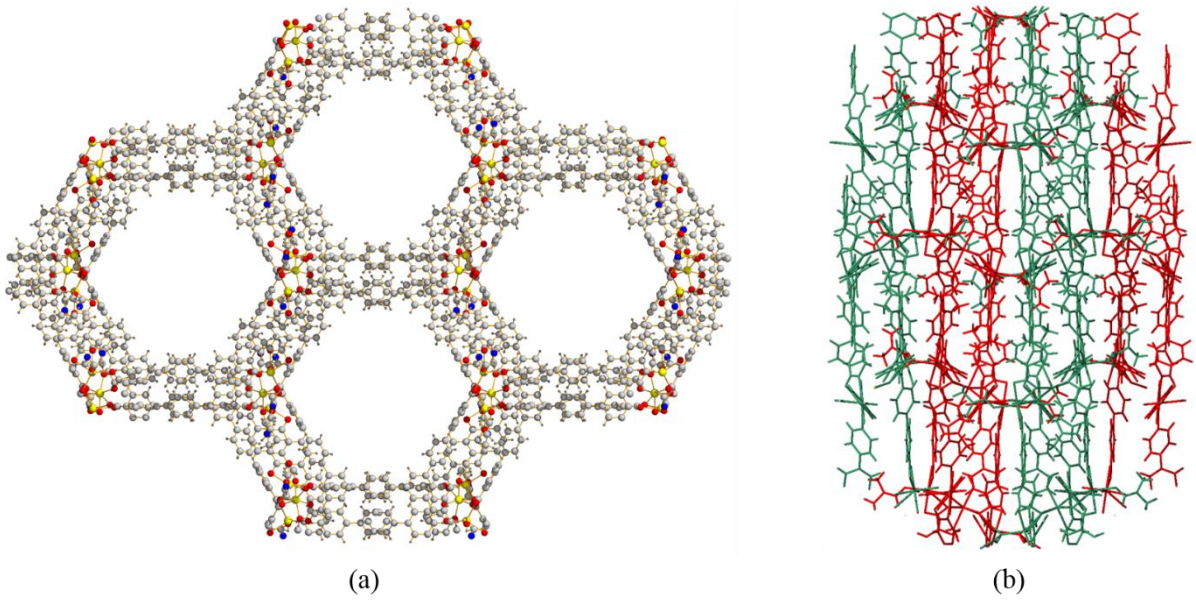

Figure 5.26 (a) – Ball and stick representation of the crystal structure of 20 viewed along the crystallographic *b*-direction. Colour scheme: yellow, Cd; blue, N; grey, C; light grey, H; red, O; (b) – A wireframe representation of 20 along the crystallographic *b*-direction with alternating bilayers coloured in red and green.

The orientation of hexagonal monolayers within each bilayer is crucial to the overall topology of the framework. In this regard, in **20**, monolayers are effectively eclipsed with respect to each other viewed along the approximate Cd-Cd axis of the SBUs. Therefore in this respect, the network in **20** is isoreticular to that observed in the MOF DUT-41 reported by Hauptvogel *et al.*, and not isoreticular to the common **kgd** structure obtained for the Cd-btb MOF reported by Mu *et al.*, in which hexagonal monolayers are effectively staggered with respect to each other.[6] Topological reduction shows that the net in **20** is a binodal net, which is represented by the point symbol $\{4^3.6^{12}\}\{4^3\}_2$ (Fig. 5.27).

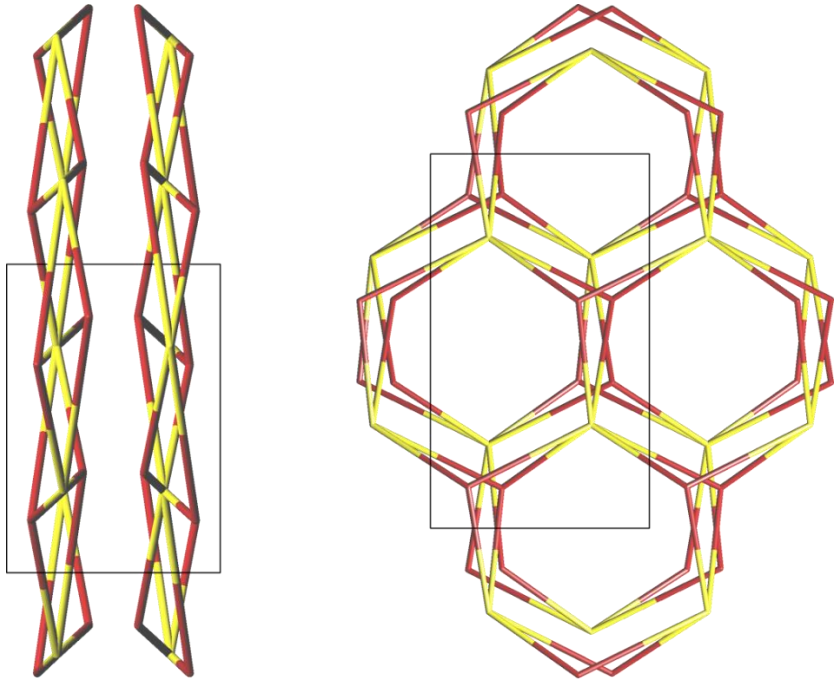

Figure 5.27 – Topological reduction of 20 viewed along the crystallographic (a) *a*-, and (b) *b*-directions. 6-connected nodes are coloured in yellow and 3-connected nodes are coloured in red.

The bilayer sheets in **20** pack in a fashion that allows the hexagonal cavities produced to align nearly unobstructed into channels along the crystallographic *b*-axis (Fig. 5.26). The solvent accessible void volume in the structure was determined to be 57.1% (CCDC:Mercury). The limiting diameter of the one-dimensional channels along the crystallographic *b*-axis was determined to be 14.8 Å, and the diameter of the largest spherical void in the structure was determined to be 15.6 Å (Olex2).[15,16]

Evidence of this porosity is experimentally strengthened by thermogravimetric analysis. The TGA trace of **20** collected under an N_2 stream shows a steep weight loss step from 30°C to 120°C due to the loss of constitutional DMF solvent molecules corresponding to 46% of the weight of the as-synthesised compound. Further weight loss of 8.7% occurs due to the removal of coordinated DMF molecules from the SBUs of the structure up to 380°C, when ligand decomposition takes place. Powder X-ray diffraction confirms the phase purity of the as-synthesised compound and validates the structural model (Fig. 5.28)

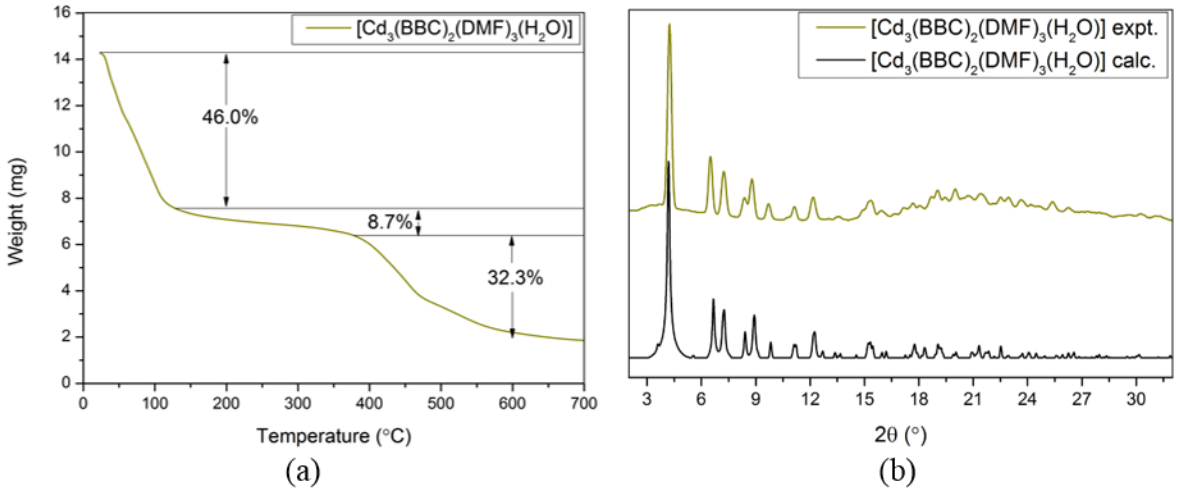

Figure 5.28 – The TGA trace (a) and PXRD pattern (b) of as-synthesised 20.

FTIR spectroscopy carried out on **20** showed a broad signal centred at 3400 cm^{-1}, due to the intermolecular interactions between solvent molecules and with the pore wall (Fig. 5.29). C=O stretching vibrations in constitutional DMF molecules result in the strong band at 1647 cm^{-1}. A number of overlapping signals between 1605 cm^{-1} and 1254 cm^{-1} are observed due to C=O, C=N, and C=C vibrations. Strong bands at 1560 cm^{-1} and 1384 cm^{-1} may be assigned to $\nu_{as}COO$ and $\nu_{s}COO$ respectively. Bands at 1525 cm^{-1} and 1585 cm^{-1} are also assigned to $\nu_{as}COO$, due to the plurality of carboxylate binding modes observed.

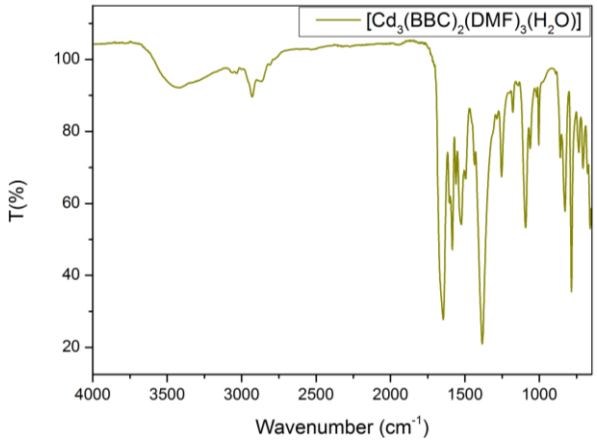

Figure 5.29 – The FTIR spectrum of as-synthesised 20.

Simulations were carried out on **20** in order to explore the porosity of the framework. Using the Poreblazer suite on the framework with DMF and H_2O molecules still coordinated to SBUs, simulations carried out reveal a He pore volume of 0.870 cm^3/g, a limiting channel diameter of 14.56 Å, and a maximum pore diameter of 15.40 Å, in excellent agreement

with their crystallographic estimations.[20] The geometrical surface area was calculated to be 1482 m^2/g. Similar simulations carried out on the framework of **20** after the removal of DMF and H_2O molecules to generate UMCs show a He pore volume of 1.178 cm^3/g. The accessible surface area was found to be 2138 m^2/g. The pore size distributions obtained in both simulations are shown in Fig 5.30.

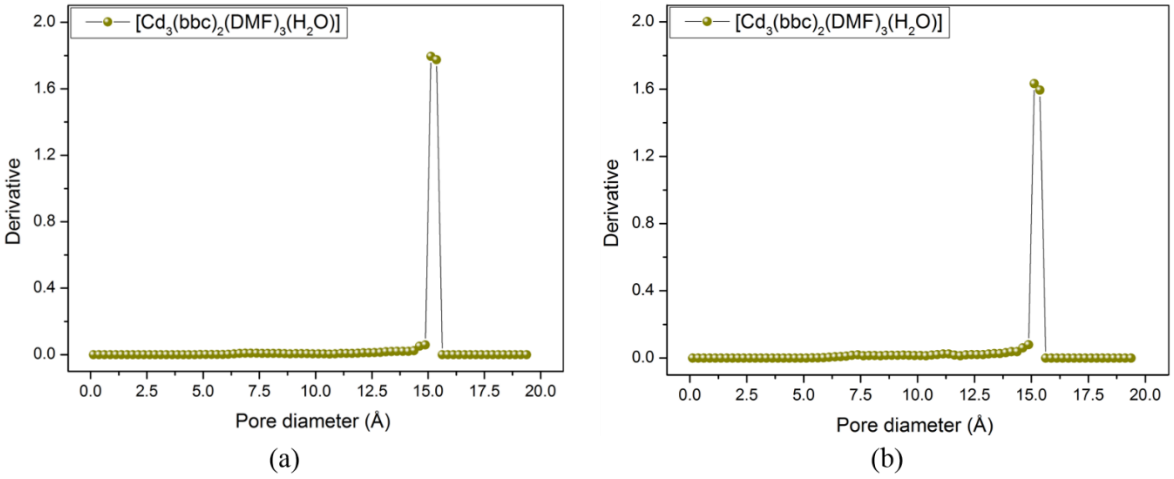

Figure 5.30 – Simulated pore size distributions of 20 (a) before and (b) after generation of UMCs.

The phase purity in **20** precluded the presence of the **kgd** net. Further experiments on the influence of the synthetic conditions of the Cd-bbc system were carried out. Compound **21** was synthesised by the conventional elevated temperature method in DEF at 100°C, using H_3bbc and $Cd(NO_3)_2 \cdot 4H_2O$. The H_3bbc concentration used was lower than in the case of **20**. Colourless single crystals of **21**, $[Cd_6(bbc)_4(DEF)_3(H_2O)_9]$ were obtained which were suitable for single-crystal X-ray diffraction.

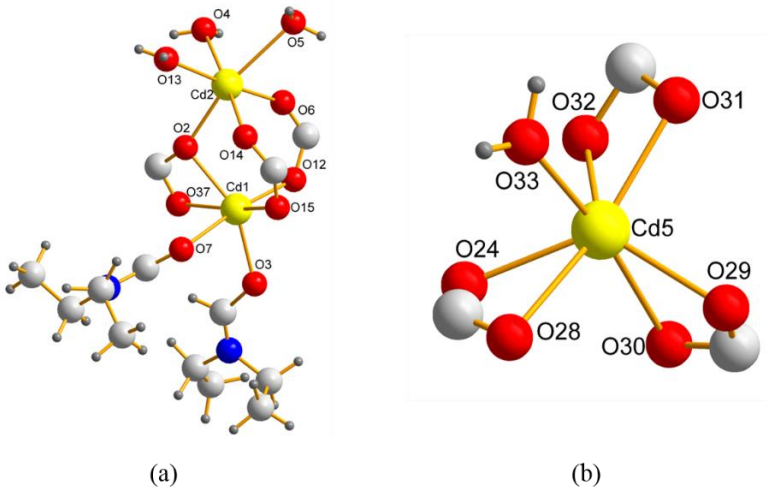

Figure 5.31 – Representations of one each of the (a) dinuclear and (b) mononuclear SBUs in 21.

The crystal structure of **21** was solved and refined as a racemic twin in the chiral orthorhombic $P2_12_12$ space group, with the cell parameters a = 80.001(3) Å, b = 18.4569(16) Å, c = 25.0174(10) Å, $\alpha = \beta = \gamma = 90°$. The asymmetric unit of **21** contains six Cd^{2+} centres, and 4 fully deprotonated bbc^{3-} linkers. Two types of SBU are present in the structure. The first type is a mononuclear 7-coordinate Cd^{2+} centre to which three bidentate chelating carboxylates from bbc^{3-} are bound. A coordinated H_2O ligand completes an approximate capped trigonal prismatic geometry.

The second type of SBU is a dinuclear $\{Cd_2\}$ unit, in which the two Cd^{2+} centres are linked by three carboxylates from bbc^{3-} - two of which adopt bidentate bridging binding modes, while the third adopts a bridging chelating mode (Fig. 5.31). Distorted octahedral geometry on one atom of the $\{Cd_2\}$ unit is completed by a coordinated DEF molecule and coordinated H_2O molecule (or two DEF molecules). The other atom has an octahedral environment completed by three coordinated H_2O molecules.

Each SBU therefore bears 3 points of structural extension through bbc^{3-} linkers, independent of nuclearity. Notably, the mononuclear SBU bears an overall charge of -1, while the dinuclear SBU bears an overall charge of +1, resulting in a neutral framework. Degrees of compliance to ideal geometries can be assessed from the bond distances and angles listed in Table 5.9.

The torsion angles in the bbc^{3-} ligands of **21** are given in Table 5.9.

Table 5.9 - Selected interatomic distances and angles in 21.

Atoms	Distance		Atoms	Angle
Cd5-O24	2.274(1) Å		O33-Cd5-O30	172.0(7)°
Cd5-O28	2.539(1) Å		O28-Cd5-O29	90.4(4)°
Cd5-O29	2.277(1) Å		O28-Cd5-O24	53.0(4)°
Cd5-O30	2.500(2) Å		O31-Cd5-O30	105.1(5)°
Cd5-O31	2.306(2) Å		O24-Cd5-O32	87.1(6)°
Cd5-O32	2.337(2) Å			
Cd5-O33	2.250(2) Å			
Cd1-O3	2.21(1) Å		O3-Cd1-Cd2	167.7(3)°
Cd1-O7	2.26(2) Å		O3-Cd1-O7	79.6(6)°
Cd1-O12	2.23(1) Å		O3-Cd1-O2	145.3(5)°
Cd1-O15	2.17(2) Å		O7-Cd1-O15	85.3(6)°
Cd1-O2	2.27(1) Å		O15-Cd1-O12	96.0(5)°
Cd1-O37	2.38(1) Å		O2-Cd1-O37	53.4(4)°
Cd1-O14	2.95(3) Å			
Cd1-Cd2	3.510(2) Å			
Cd2-O12	3.65(2) Å		O4-Cd2-O4	123.2(6)°
Cd2-O2	2.24(1) Å		O14-Cd2-O4	177.0(7)°
Cd2-O6	2.16(1) Å		O2-Cd2-O13	93.0(6)°
Cd2-O14	2.37(2) Å		O6-Cd2-O13	174.0(1)°
Cd2-O13	2.29(4) Å		O5-Cd2-O6	75.9(8)°
Cd2-O4	2.51(2) Å			
Cd2-O5	2.59(4) Å			

Table 5.10 – Dihedral angles between the central phenyl and peripheral benzoate planes in 21.

	Angle (°)	Angle (°)	Angle (°)
1	82.5	69.0	53.1
2	89.7	61.4	46.6
3	72.7	65.8	34.4
4	88.1	66.0	69.2

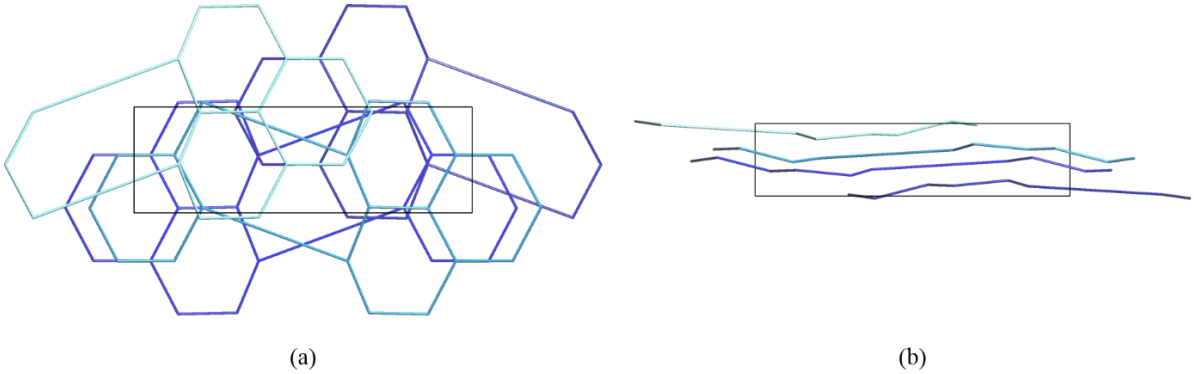

Figure 5.32 – Topological reduction of 21 into hcb layers viewed along the crystallographic (a) *b*-, and (b) *c*-directions.

Each SBU therefore is bound to three carboxylate groups from three distinct bbc^{3-} ligands, and each bbc^{3-} ligand is linked to three SBUs. The overall structure is composed of 2D honeycomb-like sheet motifs, in which sheets are oriented approximately along the plane parallel to the *B*-face. The arrangement of SBUs in each sheet is illustrated in Fig. 5.33. Topological analysis of the structure shows that the network adopted is the 2D, uninodal, 3-connected **hcb** (honeycomb) network, with a point symbol of $\{6^3\}$ (Fig. 5.32).

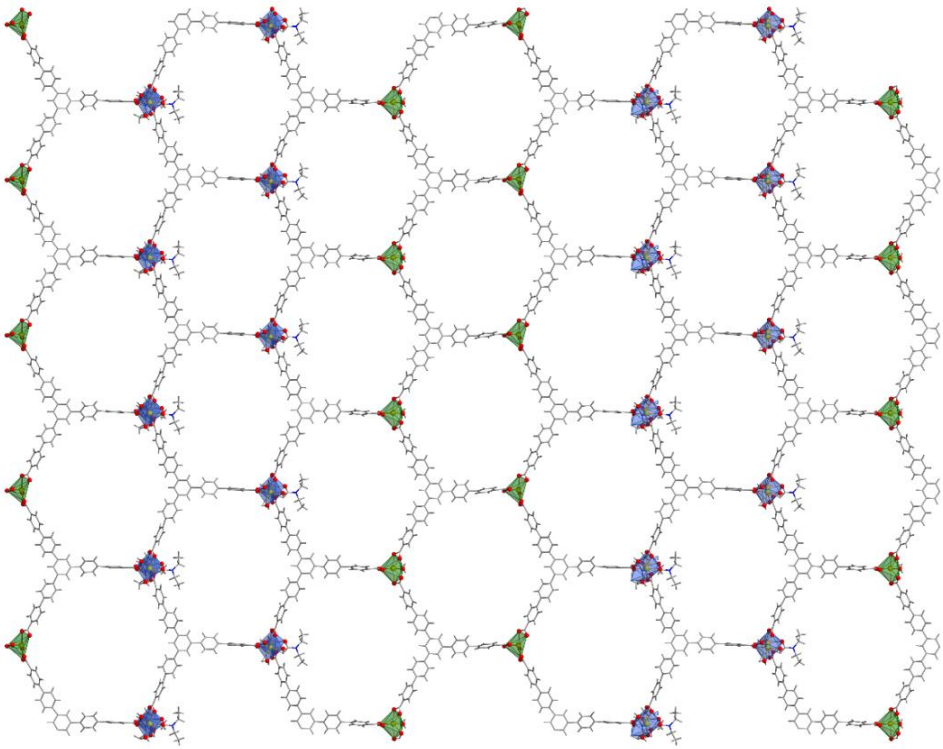

Figure 5.33 – The distribution of SBUs in a single hcb net of 21 with mononuclear SBUs highlighted in green and dinuclear SBUs in red. The vertical axis is the crystallographic *c*-direction, while the *b*-axis is perpendicular to the page.

SBUs repeat along the *c*-axis in each sheet in a {Cd}-{Cd}-{Cd} and $\{Cd_2\}$-$\{Cd_2\}$-$\{Cd_2\}$ fashion. Along the *a*-axis, SBUs repeat in pairs, with an overall $\{Cd_2\}$-$\{Cd_2\}$-{Cd}-{Cd}-$\{Cd_2\}$-$\{Cd_2\}$ arrangement. As a result, the three SBUs that define individual hexagons may be exclusively $\{Cd_2\}$ or {Cd}, or 2:1 combinations of both.

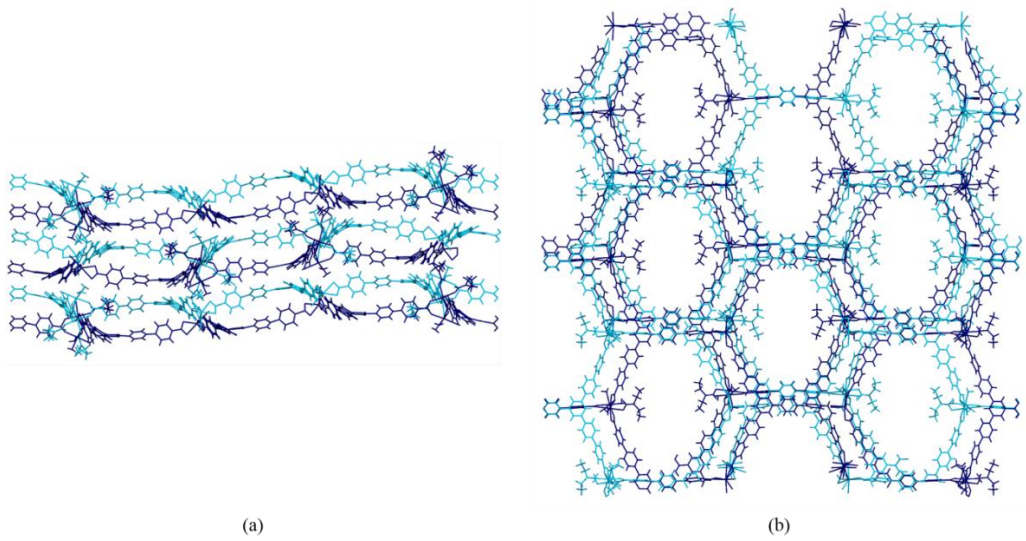

Figure 5.34 – Wireframe representation of layers in 21 viewed along the crystallographic (a) *c*-, and (b) *b*-axis. Alternate layers are coloured in light blue and dark blue.

In order to minimise the separation of opposite electrostatic charges on SBUs, $\{Cd_2\}$ units bearing excess positive charge and {Cd} units bearing excess negative charge align in a nearly co-linear fashion along the *b*-axis, with some allowance made for the capping solvent ligands. This packing arrangement results in the majority of the hexagonal cavity in each sheet remaining unobscured along the *b*-axis, giving rise to 1D channels (Fig. 5.34). The structure viewed along the *b*-axis is strikingly similar to that of **20**, and the charge separated structure in **21** could provide insights into the mechanism of formation of **20** - in particular, the trinuclear SBUs and the $\{4^3.6^{12}\}\{4^3\}_2$ net. If the framework of **21** is understood to be an intermediate *en route* to the framework of **20**, with the bilayer as the thermodynamic minimum, then the need to minimise charge separation between $\{Cd_2\}$ and {Cd} SBUs is an explanation as to why $\{Cd_3\}$ SBUs in **20** are aligned with other $\{Cd_3\}$ SBUs. Therefore, the porosity in **21** is extrinsic to the 2D structure and maintained by local electrostatic interactions between sheets. The solvent accessible void volume of the structure in **21** is 59.6% of the total volume (CCDC:Mercury).[15] The limiting minimum channel diameter is 10.0 Å, and the diameter of the largest spherical void is 12.0 Å (Olex2).[16] If the structure is considered to have been 'fully' activated, such that all the

coordinated solvent molecules are removed, the void volume increases to 66.6%, and the limiting channel diameter and diameter of the largest spherical void increase to 14.8 Å and 15.6 Å respectively.

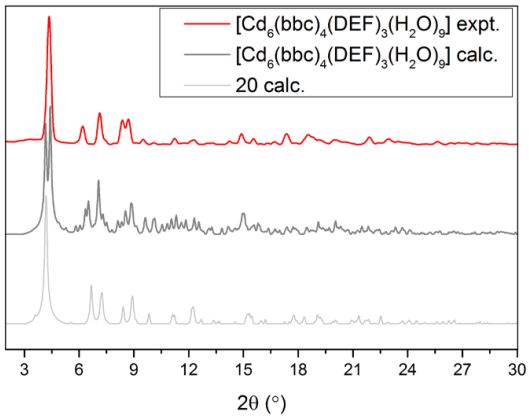

Figure 5.35 – The PXRD pattern of as-synthesised 21.

Powder X-ray diffraction experiments carried out on **21** indicate that the as-synthesised sample is present in substantial proportion, together with the DEF-capped homologue of **20**, however minor mismatches are observed (*e.g.* at 2θ = 6°) which cannot be attributed to **20** and **21** (Fig. 5.35). Therefore, simulations were carried out in order to ascertain the porosity of **21**. Using the Poreblazer suite, it was determined by simulation that the nitrogen-accessible surface area of **21** is 2188 m^2/g, and the surface area of the framework upon UMC generation is 2267 m^2/g.[20] The helium pore volume was found to increase from 0.998 cm^3/g to 1.273 cm^3/g upon UMC generation, and the maximum pore diameter and limiting pore diameter increased from 9.51 Å and 11.89 Å to 14.61 Å and 15.35 Å, respectively. These values are in excellent agreement with crystallographic determinations. Pore size distributions simulated are shown in Figure 5.36. **21** is therefore potentially a highly porous framework.

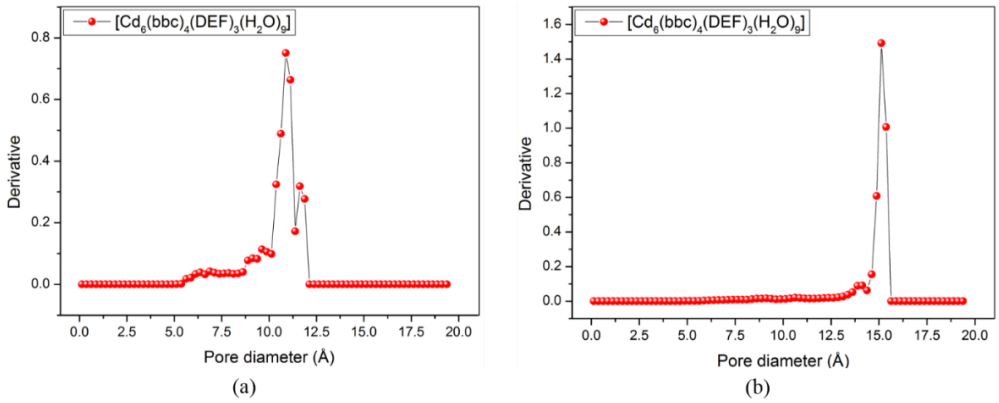

Figure 5.36 – Simulated pore size distributions of 21 (a) before and (b) after generation of UMCs.

The crystallographic details of the structures determined for **20** and **21** are as given in Table 5.11.

Table 5.11 - Crystallographic details for 20 and 21.

Identification code	20	21
Empirical formula	$C_{98.5}H_{75.83}Cd_3N_{2.83}O_{16.33}$	$C_{195}H_{159}Cd_6N_3O_{36}$
Formula weight	1897.62	3794.64
Temperature/ K	100(1)	100(1)
Crystal system	orthorhombic	orthorhombic
Space group	$P2_12_12$	$P2_12_12$
***a*/Å**	42.019(4)	80.001(3)
***b*/Å**	16.9823(16)	18.4569(8)
***c*/Å**	24.574(2)	25.0174(10)
***α*/°**	90	90
***β*/°**	90	90
***γ*/°**	90	90
Volume/Å^3	17535(3)	36940(3)
Z	4	4
ρ_{calc}/ g/cm^3	0.719	0.682
μ/mm^{-1}	0.395	3.011
F(000)	3845.0	7704.0
Crystal size/mm^3	0.25 × 0.16 × 0.139	0.20 × 0.15 × 0.10
Radiation/Å	MoKα (λ = 0.71073)	CuKα (λ = 1.54178)
2θ range for data collection/°	3.072 to 44.978	2.208 to 95.922
Index ranges	$-44 \le h \le 45$, $-18 \le k \le 14$, $-26 \le l \le 16$	$-77 \le h \le 72$, $-17 \le k \le 16$, $-22 \le l \le 23$
Reflections collected	77499	141512
Independent reflections	22766 [R_{int} = 0.0814, R_{sigma} = 0.0852]	34328 [R_{int} = 0.0784, R_{sigma} = 0.0765]
Data/restraints/parameters	22766/272/1013	34328/386/1616
Goodness-of-fit on F^2	0.993	1.009
Final R indexes [I>=2σ (I)]	R_1 = 0.0577, wR_2 = 0.1440	R_1 = 0.0869, wR_2 = 0.2310
Final R indexes [all data]	R_1 = 0.0782, wR_2 = 0.1527	R_1 = 0.1061, wR_2 = 0.2507
Largest diff. peak/hole / e Å^{-3}	0.83/-0.61	1.03/-1.23
Flack parameter	0.09(3)	0.320(10)

5.5: Compund **22**, $[Cd_3(bteb)_2(DMF)_3(H_2O)]\cdot 3DMF\cdot 0.5H_2O$, and Compound **23**, $[Cd_3(bteb)_2(DMF)_3(azpy)_{0.5}]\cdot 1.75DMF$

Applying a similar synthetic technique to Cd^{2+} and the acetylene-spaced H_3bteb ligand, compound **22**, $[Cd_3(bteb)_2(DMF)_3(H_2O)]\cdot 3DMF\cdot 0.5H_2O$, was synthesised by the elevated temperature method in DMF at 100°C, using H_3bteb and $Cd(NO_3)_2\cdot 4H_2O$. Colourless single crystals of **22** were obtained which were suitable for single-crystal X-ray diffraction.

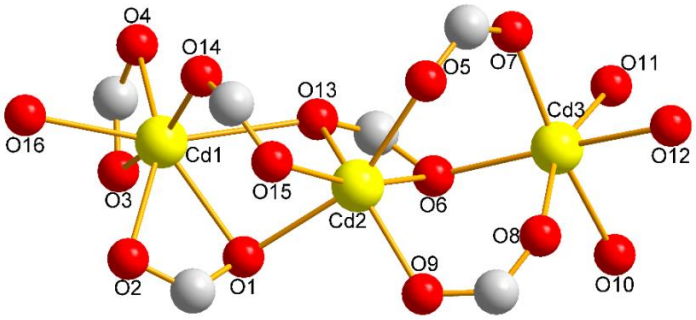

Figure 5.37 – A representation of the SBU in 22.

The crystal structure of **22** was solved in the triclinic space group $P\bar{1}$, with the cell parameters a = 12.9874(5) Å, b = 20.7015(8) Å, c = 20.7145(8) Å, and α = 108.9940(10)°, β = 104.3340(10)°, γ = 103.4960(10)°. The asymmetric unit of **22** contains three Cd^{2+} centres, and two fully deprotonated bbc^{3-} linkers. The SBU in **22** contains three Cd^{2+} centres linked by five carboxylate groups from $bteb^{3-}$ linkers – three *via* bidentate bridging modes, and two *via* bidentate bridging chelate modes – and a sixth carboxylate group bound in a chelating fashion to Cd1 (Fig. 5.37). Three DMF ligands are bound to Cd3, and an H_2O ligand caps Cd1. Thus, Cd2 and Cd3 have approximately octahedral coordination environments, while Cd1 has a 7-coordinate distorted edge-capped octahedral environment. In contrast to the usual 'hourglass' trinuclear SBU, the three Cd^{2+} nuclei in SBU in **22** are not co-linear, with a Cd1-Cd2-Cd3 angle of 136.506(16)° (Table 5.12).

Each tritopic $bteb^{3-}$ linker connects three $\{Cd_3\}$ SBUs, and each $\{Cd_3\}$ SBU extends geometrically through six $bteb^{3-}$ ligands. The nature of extension, however, is unlike that in **20** and **21**, due to the different relative orientations of carboxylate ligands within each $bteb^{3-}$ linker. The availability of a greater degree of rotational freedom in $bteb^{3-}$, as compared to bbc^{3-}, is due to the presence of an acetylene moiety instead of the *p*-phenylene spacer in bbc^{3-}. This removes the H_{Ar}-H_{Ar} repulsions that constrain bbc^{3-} to adopt torsions

between the central phenyl ring and peripheral benzoate groups within restricted ranges. The asymmetric unit of **22**, contains three Cd^{2+} centres and two distinct $bteb^{3-}$ linkers, with torsion angles listed below (Table 5.13). It can be seen that angles close to 45° - sterically restricted in bbc^{3-} or btb^{3-} homologues - represent roughly half the total number of possible angles.

Table 5.12 - Selected interatomic distances and angles in 22.

Atoms	Distance		Atoms	Angle
Cd1-O1	2.390(3) Å		O16-Cd1-O4	80.6(2)°
Cd1-O2	2.382(3) Å		O3-Cd1-O4	56.5(1)°
Cd1-O3	2.290(4) Å		O2-Cd1-O4	99.2(6)°
Cd1-O4	2.362(2) Å		O3-Cd1-O14	157.9(5)°
Cd1-O13	2.823(4) Å		O16-Cd1-O13	159.5(2)°
Cd1-O14	1.98(2) Å		O16-Cd1-O2	153.8(2)°
Cd1-O16	2.385(9) Å			
Cd1-O15	3.33(2) Å		O15-Cd2-O6	163.9(5)°
Cd1-Cd2	3.5211(6) Å		O15-Cd2-O13	111.2(5)°
Cd2-O1	2.392(3) Å		O1-Cd2-O15	80.3(5)°
Cd2-O5	2.249(4) Å		O1-Cd2-O6	99.2(1)°
Cd2-O6	2.572(3) Å		O9-Cd2-O6	89.8(1)°
Cd2-O9	2.184(3) Å		O13-Cd2-O6	53.8(1)°
Cd2-O13	2.283(2) Å		O1-Cd2-O5	156.4(1)°
Cd2-O15	2.348(25) Å		Cd3-Cd2-O12	129.0(5)°
Cd2-Cd3	3.6911(6) Å			
Cd3-O6	2.307(4) Å		O12-Cd3-O11	88.6(5)°
Cd3-O7	2.210(4) Å		O12-Cd3-O10	91.5(5)°
Cd3-O8	2.257(3) Å		O10-Cd3-O8	86.3(3)°
Cd3-O5	3.297(4) Å		O6-Cd3-O12	172.4(5)°
Cd3-O9	3.831(3) Å		O10-Cd3-O7	166.0(3)°
Cd3-O10	2.39(1) Å		O6-Cd3-O7	89.1(1)°
Cd3-O11	2.30(3) Å			
Cd3-O12	2.24(2) Å		Cd1-Cd2-Cd3	136.5(2)°
Cd1-Cd3	6.6992(6) Å			

Table 5.13 – Dihedral angles between the central phenyl and peripheral benzoate planes in 22.

	Angle (°)	Angle (°)	Angle (°)
1	48.6	13.9	48.6
2	49.1	10.2	89.9/64.6

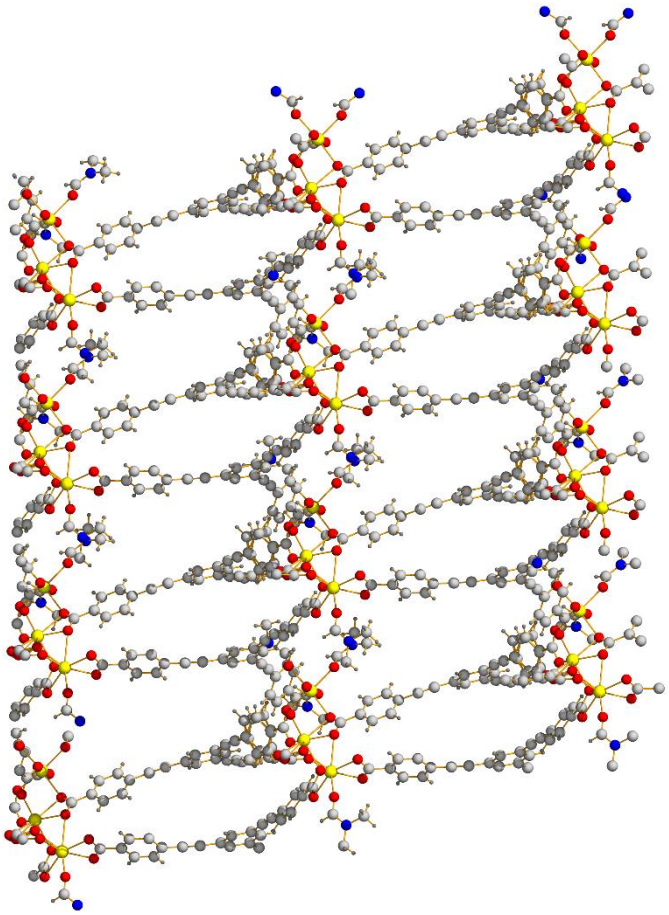

Figure 5.38 – Ball-and-stick representation of a single net of 22 viewed along the crystallographic *b*-axis. Colour scheme: yellow, Cd; blue, N; grey, C; light grey, H; red, O.

As a result, the (3,6)-connected net in **22** is unlike that in **20**. The structure in **22** is a three dimensional net, and shows a cascading motif outlining hexagonal channels along the crystallographic *a*-direction (Fig. 5.38). The structure is doubly-interwoven, resulting in the channels becoming partially obscured (Fig. 5.39). Despite this, crystallographic calculations show that the solvent accessible void volume is 30.6% of the structure (CCDC:Mercury). The limiting diameter of the channels along the *a*-direction is 4.8 Å (5.2

Å after UMC generation), and the diameter of the largest spherical void in the structure is 6.0 Å (8.0 Å after UMC generation), as calculated using Olex2.

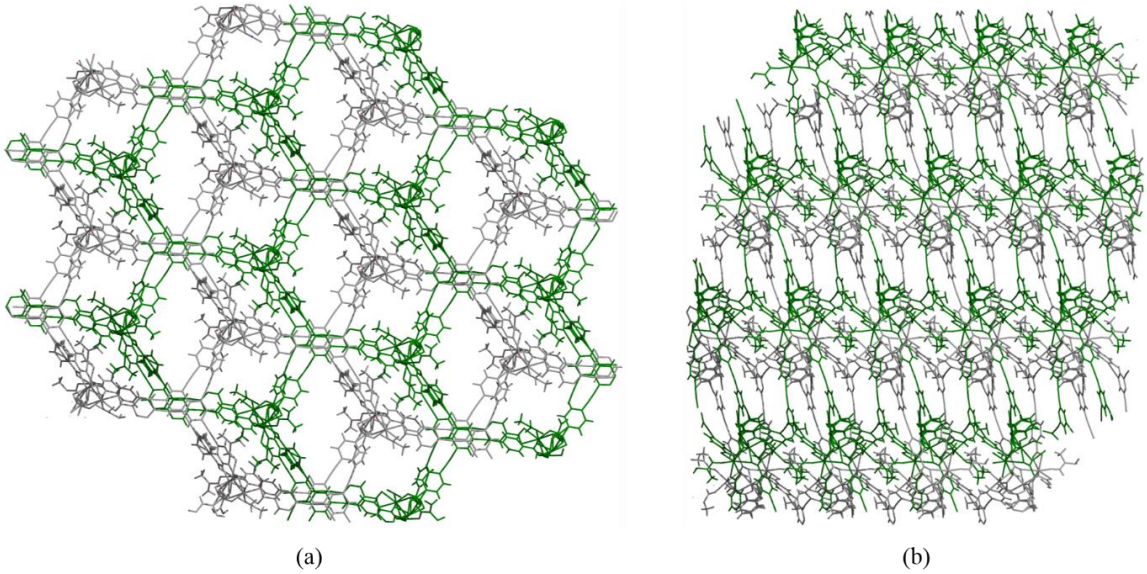

Figure 5.39 – Wireframe representations of the crystal structure of 22, with interwoven sit nets highlighted in green and grey.

Topological reduction of **22** shows that both interwoven nets are binodal, (3,6)-connected nets with the stoichiometry $(3\text{-c})_2(6\text{-c})$ (Fig. 5.40). The point symbol for the nets is $\{4.6^2\}_2\{4^2.6^{10}.8^3\}$, and the three-letter RCSR symbol is **sit** (**sit-c** for the interwoven pair). The **sit** net is a rare occurrence (29 examples in the *Topos Topological Database*), but notably it has been reported by Yang *et al.*, using $\{Cd_3\}$ SBUs and the rigid, tritopic 1,3,5-tris[2-(4-carboxyphenyl)-1-ethynyl]-2,4,6-trimethylbenzene ligand.[22]

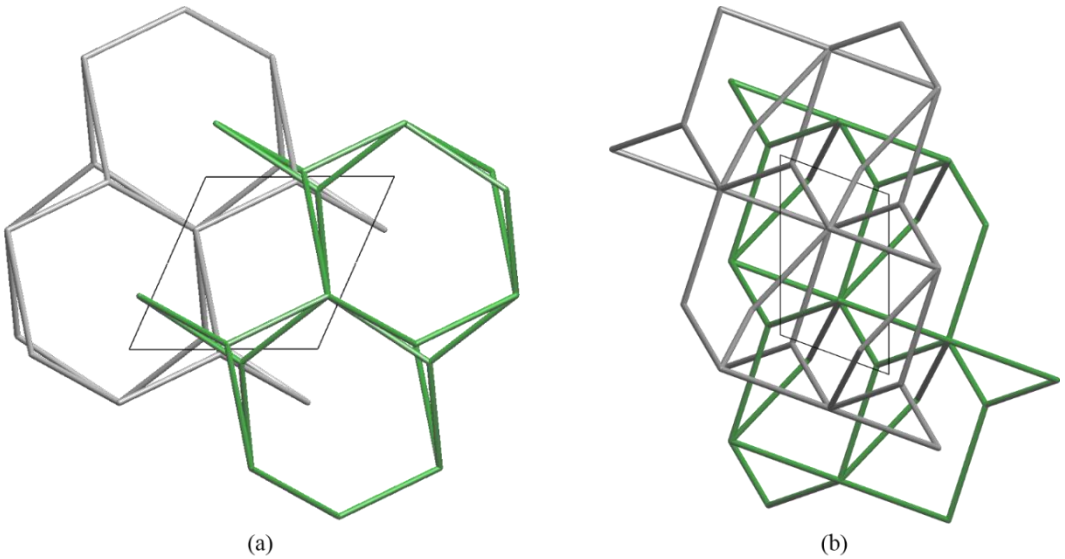

Figure 5.40 – Topological reduction of 22 into interwoven sit nets viewed along the crystallographic (a) *a*-, and (b) *c*-directions.

The crystalline product obtained from the synthesis of **22** contained more than one type of single crystal, as well as microcrystalline phases. A second type of single crystal, **22′** was manually removed from the product mixture, and studied by single crystal X-ray diffraction.

22′ is also assigned the formula $[Cd_3(bteb)_2(DMF)_3(H_2O)]$, and as in **22**, the structure is composed of two interwoven **sit** nets, with the same mode of interpenetration. However, the $\{Cd_3\}$ SBU in **22′** is slightly different to that in **22**. The SBU is composed of three pentagonal bipyramidal Cd atoms, and the greater number of capping solvent ligands results in a crowding of carboxylate groups about the SBU (Fig. 5.41). The Cd-Cd-Cd angle in **22′** is 128.929(107), which is significantly more acute than that observed for **22**. As a result, the packing of adjacent $bteb^{3-}$ linkers oriented along the approximate *ac*-plane is slightly denser. However, X-ray data obtained for **22′** is poor (see Table 5.16), and further analysis of the structure was not carried out.

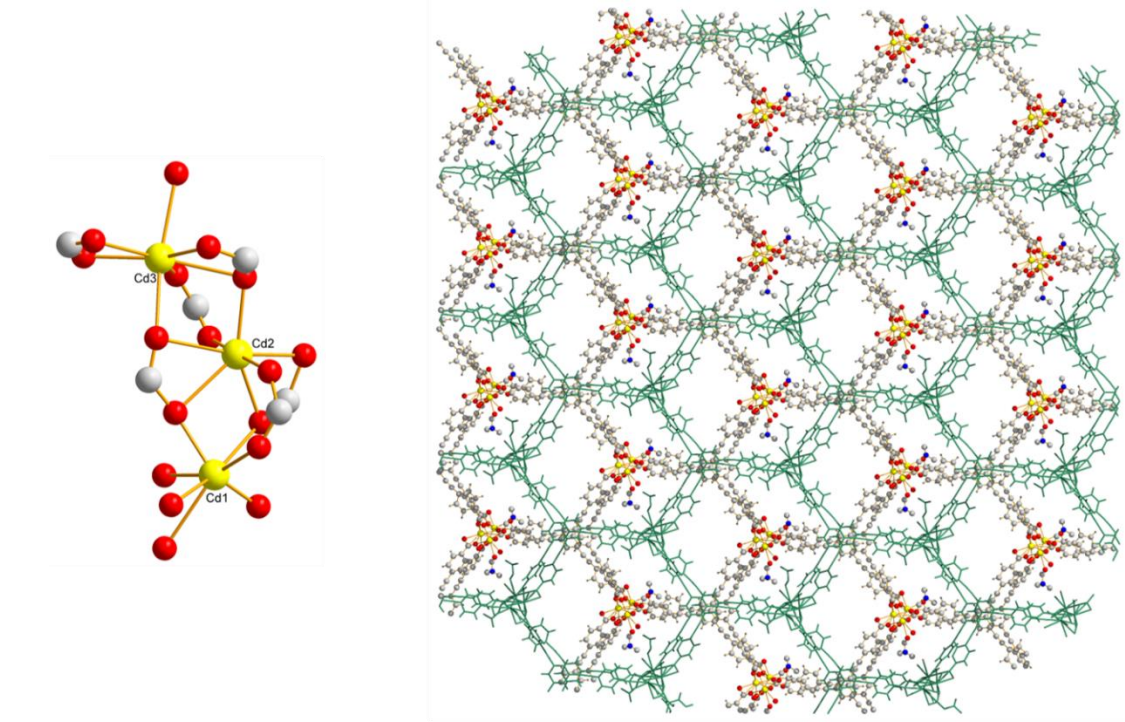

Figure 5.41 – Representations of (a) the SBU; (b) the interweaving sit nets in 22′.

The PXRD pattern of the as-synthesised microcrystalline mixture showed the presence of both **22** and **22′** (Fig. 5.42). Manual separation of phases was not feasible due to the

similarity in colour and morphology of the single crystals of **22** and **22′**, and therefore physicochemical characterisation techniques could not be applied.

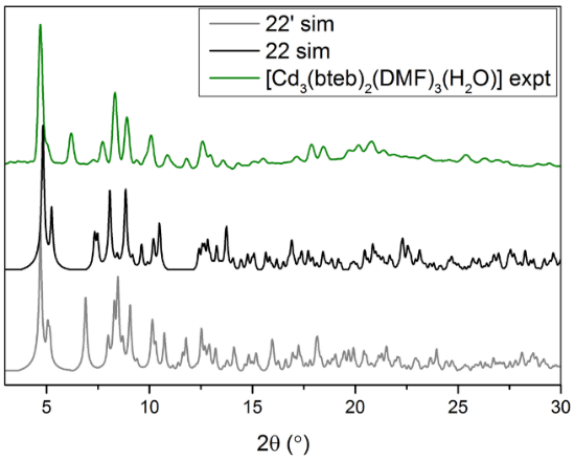

Figure 5.42 – The PXRD pattern of as-synthesised 22.

Simulations carried out on the structure using the Poreblazer suite helped determine the porosity of the structure precisely. The He pore volume was determined to be 0.318 cm^3/g (0.620 cm^3/g after UMC generation).[20] The N_2 accessible surface area was determined to be 485 m^2/g (1249 m^2/g after UMC generation). The pore limiting diameter for **22** with capping solvents still bound to the SBU was found to be 4.36 Å and the maximum pore diameter was found to be 5.73 Å. Similarly, for the structure after UMC generation, the pore limiting diameter was found to be 4.91 Å and the maximum pore diameter was found to be 8.68 Å. These values are in agreement with crystallographic determinations. The pore size distributions simulated before and after UMC generation are shown in Figure 5.43. While interweaving in **22** results in moderate porosity relative to **20** and **21**, the structure is porous, and the flexibility of the $bteb^{3-}$ligand allows access to three-dimensionality in the framework structure.

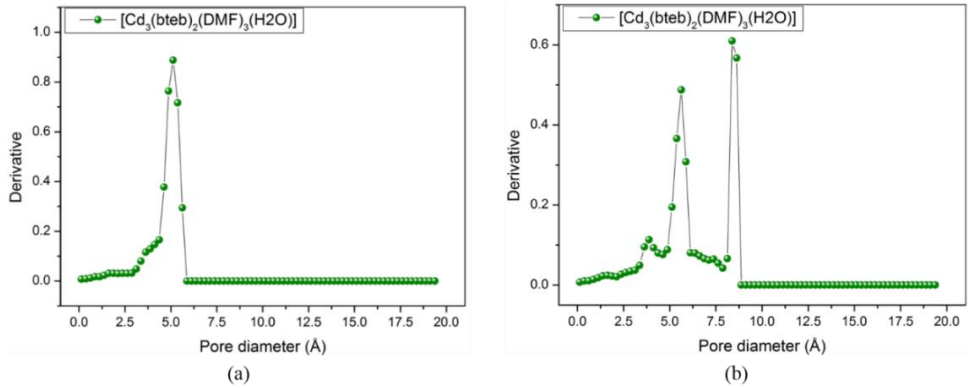

Figure 5.43 – Simulated pore size distributions of 22 (a) before and (b) after generation of UMCs.

Having noted the presence of labile coordinated solvent moieties on Cd centres in **20**, **21**, and **22**, the possibilities of using a ditopic N-donor ligand to substitute these ligands and act as pillars or auxiliary struts were explored. Post-synthetic procedures using 4,4'-bipyridine (bpy) and 4,4′-azopyridine (azpy), as shown in Zhang *et al.* (2014) for a $\{Cd_3\}$-btb MOF, were unsuccessful.[23] However, upon incorporating azpy into the synthetic procedure for **22**, a new MOF, **23**, with the formula $[Cd_3(bteb)_2(DMF)_3(azpy)_{0.5}]\cdot 1.75DMF$, was obtained.

Orange-red single crystals of **23** were obtained along with crystals of **22** and microcrystalline phases. Single crystal X-ray studies showed the incorporation of azpy linkers into the dual framework structure of **22**. The crystal structure of **22** was solved in the triclinic space group $P\bar{1}$. The cell parameters obtained are a = 13.1008(6) Å, b = 20.5691(5) Å, c = 20.7220(9) Å, and α = 115.7400(15)°, β = 100.8110(16)°, γ = 99.7070(16)°, which are close to those obtained in **22**.

The asymmetric unit of **23** contains three Cd^{2+} centres, forming a $\{Cd_3\}$ SBU, 2 fully deprotonated $bteb^{3-}$ linkers, and half an azpy ligand. The SBU in **23** contains three Cd^{2+} centres linked by five carboxylate groups from $bteb^{3-}$ linkers – three *via* bidentate bridging modes, and two *via* bidentate bridging chelate modes – and a sixth carboxylate group bound in a chelating fashion to Cd1. Three DMF ligands are bound to Cd3, and the N-donor atom from the azpy ligand caps Cd1. Thus, Cd2 and Cd3 have approximately octahedral coordination environments, while Cd1 has a 7-coordinate distorted edge-capped octahedral environment (Fig. 5.44). In this respect **23** is similar to **22**.

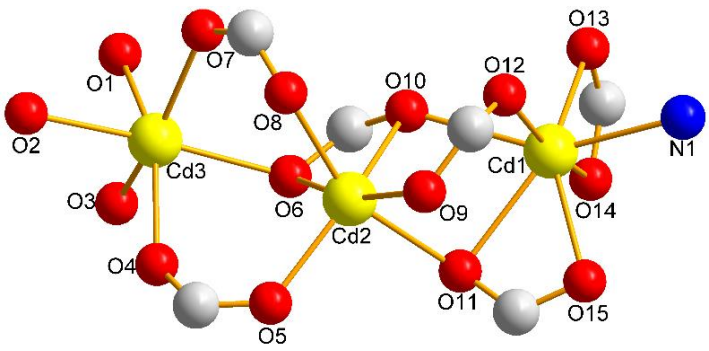

Figure 5.44 – A representation of the SBU in 23.

The three Cd^{2+} nuclei in SBU in **23** are not co-linear, with a Cd1-Cd2-Cd3 angle of 128.559(21)°, even more acute than in **22** (Table 5.14). The torsion angles in the $bteb^{3-}$ ligands of **23** are given in Table 5.1

Table 5.14 - Selected interatomic distances and angles in 23.

Atoms	Distance		Atoms	Angle
Cd1-N1	2.398(7) Å		N1-Cd1-O14	98.1(2)°
Cd1-O13	2.379(3) Å		N1-Cd1-O15	81.5(2)°
Cd1-O14	2.299(5) Å		N1-Cd1-O12	84.0(2)°
Cd1-O15	2.371(5) Å		O13-Cd1-O14	56.3(1)°
Cd1-O9	3.580(5) Å		O12-Cd1-O14	166.2(2)°
Cd1-O10	2.561(6) Å		N1-Cd1-O10	151.5(2)°
Cd1-O11	2.450(6) Å		N1-Cd1-Cd2	141.9(2)°
Cd1-O12	2.228(7) Å			
Cd1-Cd2	3.5124(8) Å			
Cd2-O5	2.162(5) Å		O9-Cd2-O6	165.2(2)°
Cd2-O6	2.378(6) Å		O9-Cd2-O10	111.1(2)°
Cd2-O8	2.219(7) Å		O9-Cd2-O11	85.8(2)°
Cd2-O9	2.233(6) Å		O11-Cd2-O5	97.4(2)°
Cd2-O10	2.448(4) Å		O11-Cd2-O8	156.3(2)°
Cd2-O11	2.330(5) Å		O8-Cd2-O10	91.0(2)°
Cd2-Cd3	3.6913(9) Å			
Cd3-O1	2.285(6) Å		Cd2-Cd3-O2	133.0(2)°
Cd3-O2	2.30(1) Å		O2-Cd3-O1	85.3(3)°
Cd3-O3	2.08(6) Å		O2-Cd3-O3	96(1)°
Cd3-O4	2.24(3) Å		O3-Cd3-O4	84(2)°
Cd3-O6	2.34(6) Å		O4-Cd3-O1	151(1)°
Cd3-O7	2.22(8) Å		O2-Cd3-O6	171.5(3)°
Cd3-O5	3.78(6) Å			
Cd3-O8	3.405(7) Å		Cd3-Cd2-Cd1	128.56(2)°
Cd1-Cd3	6.4905(9) Å			

Table 5.15 – Dihedral angles between the central phenyl and peripheral benzoate planes in 23.

	Angle (°)	Angle (°)	Angle (°)
1	52.1	78.2	4.6
2	16.9	38.7	43.7/18.0

Similar to **22**, each tritopic bteb^{3-} linker connects three {Cd_3} SBUs, and each {Cd_3} SBU extends geometrically through six bteb^{3-} ligands, while each azpy ligand connects two {Cd_3} SBUs (Fig. 5.45). Ligand torsions are also similar to those seen in **22**. Importantly, the azpy linkers link {Cd_3} SBUs that are not connected, *i.e.*, they act as bridging ligands from one **sit** net to another. The pillaring procedure adopted for the pillaring of **kgd** net was termed 'stitching' by Zhang *et al.*, and by the same token the insertion of auxiliary ligands to connect two interwoven 3D nets may be termed 'cross-stitching'.[23]

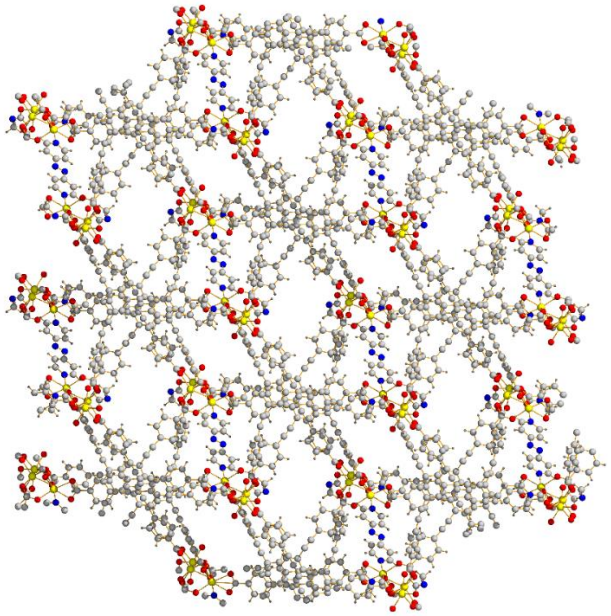

Figure 5.45 – Ball-and-stick representation of the crystal structure of 23. Colour scheme: yellow, Cd; blue, N; grey, C; light grey, H; red, O.

As a consequence, the two interwoven 3D nets seen in **22** are connected to give a single 3D net in **23**. The overall net is a binodal (3,7)-connected net with the stoichiometry $(3\text{-c})_2(7\text{-c})$, and the point symbol $\{4.6^2\}_2\{4^2.6^{16}.8^3\}$ (Fig. 5.46).[14] Nets with (3,7)-connectivity are rare, and there are only five examples of binodal (3,7)-connected nets listed in the RCSR database.[24] The $\{4.6^2\}_2\{4^2.6^{16}.8^3\}$ net is new, to the best of our knowledge, and is not listed on the RCSR.

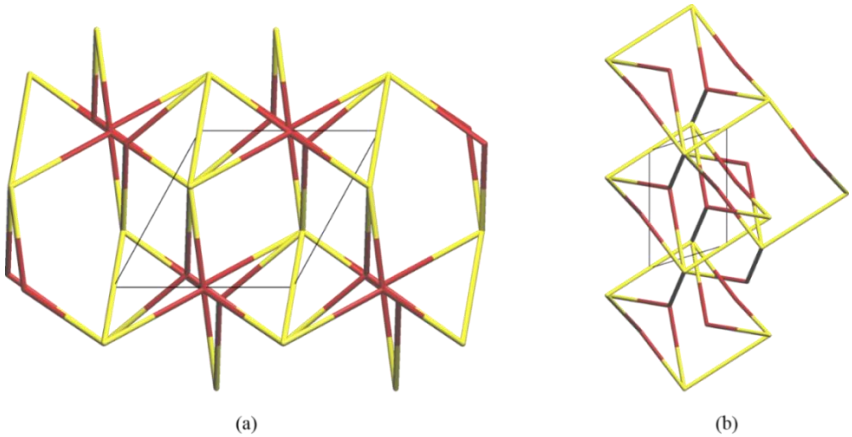

Figure 5.46 – Topological reduction of 23 viewed along the crystallographic (a) *a*-, and (b) *b*-directions.

The framework, besides the bridging azpy ligands, is oriented very similarly to the interwoven nets in **22** (Fig. 5.47). 1D channels are observed along the crystallographic *a*-axis, which have a limiting minimum diameter of 3.6 Å. The diameter of the largest spherical void in the structure is 6.4 Å (Olex 2).[16] The solvent accessible void volume in the structure of **23** was calculated to be 26% of the total volume (CCDC:Mercury).[15]

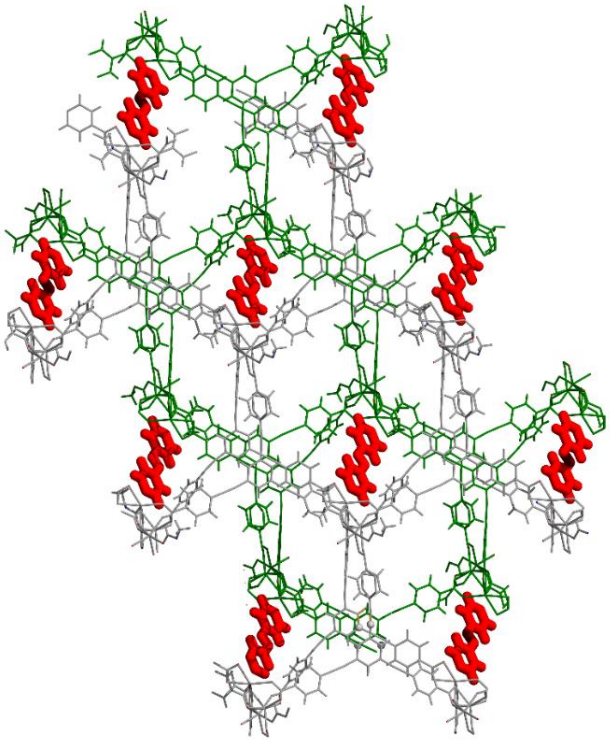

Figure 5.47 – Wireframe representation of the framework in 23 disconnected into two interwoven sit nets, grey and green, and bridging azpy ligands, red.

Powder X-ray diffraction experiments show that **23** co-crystallises as the major product with **22** and a number of unidentified phases under the applied conditions (Fig. 5.48).

Physicochemical characterisation techniques were not utilised, and simulations were carried out to evaluate the porosity of **23**.

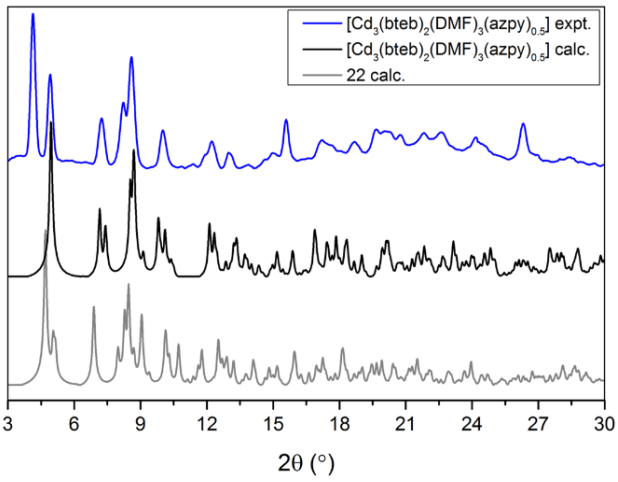

Figure 5.48 – The PXRD pattern of as-synthesised 23.

Using the Poreblazer suite, the He pore volume was determined to be 0.260 cm^3/g (0.467 cm^3/g after UMC generation).[20] The N_2 accessible surface area was determined to be 185 m^2/g (531 m^2/g after UMC generation). The pore limiting diameter for **23** with capping solvents still bound to the SBU was found to be 3.43 Å and the maximum pore diameter was found to be 6.47 Å. Similarly, for the structure after UMC generation, the pore limiting diameter was found to be 4.84 Å and the maximum pore diameter was found to be 6.84 Å. These values are in agreement with crystallographic determinations. Notably, the structure has comparable porosity along all three crystallographic directions before UMC generation. After UMC generation, 1D channels along the *a*-axis account for the porosity in the structure. The pore size distributions simulated before and after UMC generation are shown in Figure 5.49.

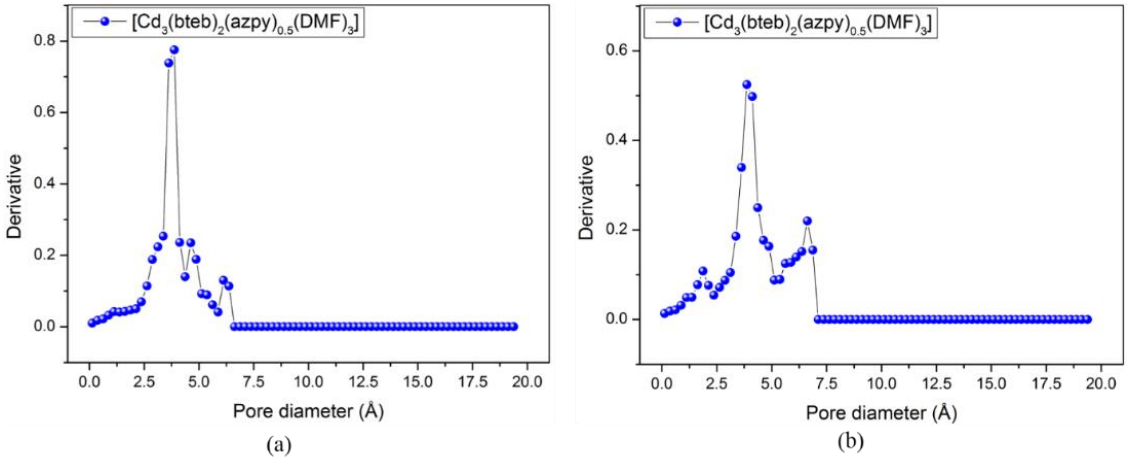

Figure 5.49 – Simulated pore size distributions of 23 (a) before and (b) after generation of UMCs.

Table 5.16 - Crystallographic details for 22, 22′, and 23.

Identification code	22	22′	23
Empirical formula	$C_{84}H_{75}Cd_3N_{6.1}O_{19.95}$	$C_{73.75}H_{29}Cd_3N_{2.25}O_{17.25}$	$C_{21.31}H_{16.81}Cd_{0.75}N_{1.69}O_{4.19}$
Formula weight	1826.30	1559.69	447.85
Temperature/ K	100(2)	100(2)	100(2)
Crystal system	triclinic	triclinic	triclinic
Space group	$P\bar{1}$	$P\bar{1}$	$P\bar{1}$
***a*/Å**	12.9874(5)	12.9076(6)	13.101(6)
***b*/Å**	20.7015(8)	19.5818(6)	20.569(5)
***c*/Å**	20.7145(8)	21.0220(7)	20.722(9)
***α*/°**	108.9940(10)	116.056(2)	115.74(15)
***β*/°**	104.3340(10)	92.736(3)	100.81(16)
***γ*/°**	103.4960(10)	94.295(3)	99.71(16)
Volume/Å^3	4793.1(3)	4740.6(3)	4739.2(3)
Z	2	2	8
ρ_{calc}/ g/cm^3	1.265	1.093	1.255
μ/mm^{-1}	0.723	5.771	0.728
F(000)	1851.0	1538.0	1808.0
Crystal size/mm^3	0.170 × 0.090 × 0.050	0.09 × 0.05 × 0.02	0.15 × 0.15 × 0.07
Radiation/Å	MoKα (λ = 0.71073)	CuKα (λ = 1.54178)	MoKα (λ = 0.71073)
2θ range for data collection/°	3.38 to 50.836	4.698 to 110.348	3.3 to 52.152
Index ranges	-15 ≤ h ≤ 15, -24 ≤ k ≤ 24, -25 ≤ l ≤ 25	-13 ≤ h ≤ 13, -20 ≤ k ≤ 20, -22 ≤ l ≤ 21	-16 ≤ h ≤ 11, -25 ≤ k ≤ 25, -25 ≤ l ≤ 25
Reflections collected	86390	34168	104469
Independent reflections	17554 [R_{int} = 0.0529, R_{sigma} = 0.0465]	11385 [R_{int} = 0.0752, R_{sigma} = 0.0829]	18687 [R_{int} = 0.0904, R_{sigma} = 0.0945]
Data/restraints/parameters	17554/318/1248	11385/328/795	18687/294/1070
Goodness-of-fit on F^2	1.015	1.490	1.037
Final R indexes [I>=2σ (I)]	R_1 = 0.0429, wR_2 = 0.1168	R_1 = 0.1491, wR_2 = 0.4184	R_1 = 0.0699, wR_2 = 0.1726
Final R indexes [all data]	R_1 = 0.0742, wR_2 = 0.1323	R_1 = 0.2103, wR_2 = 0.4646	R_1 = 0.1251, wR_2 = 0.1983
Largest diff. peak/hole / e Å^{-3}	0.81/-0.72	1.92/-1.93	2.68/-2.01

5.6: Conclusion

In this chapter we report the syntheses and single crystal X-ray structures of seven novel metal-organic frameworks based on the $\{Cu_2\}$ or $\{Cd_3\}$ SBUs, the H_3bbc and H_3bteb ligands, and the azpy ligands as auxiliary linkers. These are as follows: **17** ($[Cu_3(bteb)_2(H_2O)_2(DMF)]$), **18** ($[Cu_6(bbc)_4(H_2O)_5(DMF)]$), **19** ($[Cu_3(bbc)_2(azpy)_2]$), **20** ($[Cd_3(bbc)_2(DMF)_3(H_2O)]$), **21** ($[Cd_6(bbc)_4(DEF)_3(H_2O)_9]$), **22** ($[Cd_3(bteb)_2(DMF)_3(H_2O)]\cdot 3DMF\cdot 0.5H_2O$, and **22′** with the same formula), and **23** ($[Cd_3(bteb)_2(DMF)_3(azpy)_{0.5}]\cdot 1.75DMF$).

The $bteb^{3-}$-$\{Cu_2\}$ system can exhibit both the **pto** and **tbo** network topologies, due to the rotational flexibility in the ligand. The synthesis of **17**, with the rare $\{4.8^2\}_4\{4^2.8^2.10^2\}_2\{8^4.12^2\}$ net using only $bteb^{3-}$ and $\{Cu_2\}$ paddle-wheel units, is a landmark as the only known instance of three polymorphic MOFs formed from paddle-wheel SBUs and tricarboxylate ligands. The synthesis, single crystal structure, and physicochemical characterisation of **17** are described.

18 is a framework isomer of the well-known MOF-399, which is obtained as a trace product due to the occurrence of high dihedral angles between the central phenyl ring and peripheral benzoate groups in the bbc^{3-} linker. This results in the new $\{4.8^2\}_2\{4.8^5\}_2\{8^3\}_2\{8^5.12\}$ net. In **19**, the new $\{4.6^2\}_2\{4^2.6^8.8^3.10^2\}\{6^4.8^2\}$ net is obtained, due to the incorporation of auxiliary azpy ligands into the structure. **19** shows two distinct SBUs, the $\{Cu_2\}$ paddle-wheel and mononuclear $\{Cu\}$ centres. In addition, an unusual (2+1) mode of interpenetration is observed. Both MOFs are obtained as minor products, and characterised by single crystal X-ray studies. Simulations of surface areas show that both MOFs are potentially highly porous.

In **20**, trinuclear $\{Cd_3\}$ SBUs are combined with bbc^{3-} linkers in DMF to form a 2-dimensional MOF based on hexagonal bilayers with the $\{4^3.6^{12}\}\{4^3\}_2$ topology as exemplified in DUT-41, rather than the **kgd** net as seen for the $\{Cd_3\}$-btb^{3-} system. **20** was synthesised phase-pure, and characterised by single crystal X-ray as well as physicochemical techniques. **21**, synthesised from the same components in DEF, forms honeycomb (**hcb**) hexagonal monolayers, with some structural parallels to **20**.

In **22**, the H_3bteb ligand is used with {Cd_3} SBUs to form the uncommon **sit-c** topology with two interwoven nets. A variant of **22**, **22′** was also subjected to single crystal X-ray studies and its structure was obtained. These MOFs show a non-default (6,3)-connected net, which forms a 3D MOF, rather than the 2D **kgd** net. Incorporation of the auxiliary azpy ligand into the {Cd_3}-bteb^{3-} system results in **23**, which shows the previously unreported (3,7)-connected $\{4.6^2\}_2\{4^2.6^{16}.8^3\}$ net. The net is achieved by the incorporation of azpy as a bridging ligand between the interwoven **sit** nets in **22**, linking the interwoven nets into a single, more complex net.

In summation, we report the syntheses and crystal structures of seven novel MOFs with non-default nets, among which three new topologies are observed. These MOFs are constructed using conventional SBUs and extended ligands, and we show that the flexibility of the ligand is a key factor in the net of the resultant MOF. These effects are further accommodated by distortions in the SBU, and in **19,** the formation of the unexpected {Cu} unit. The neutral, ditopic, azpy ligand was further incorporated into these systems as an auxiliary linker to exploit the variability of these systems to yield new nets.

These examples illustrate the importance of a nuanced view of coordination polymer design, with due consideration made of the flexible and dynamic behaviour of components during crystallisation. This work also opens up avenues of future studies, such as controlled desymmetrisation and steric modulations of ligands, towards phase pure synthesis and experimental characterisation of ‘non-default’ MOFs.

5.7: References

1 O. M. Yaghi, M. O'Keeffe, N. W. Ockwig, H. K. Chae, M. Eddaoudi and J. Kim, *Nature*, 2003, **423**, 705–714.

2 N. W. Ockwig, O. Delgado-Friedrichs, M. O'Keeffe and O. M. Yaghi, *Acc. Chem. Res.*, 2005, **38**, 176–182.

3 D. Frahm, F. Hoffmann and M. Fröba, *CrystEngComm*, 2013, **15**, 9429–9436.

4 H. Chae, J. Kim and Y. Go, *Nature*, 2004, **427**, 523–527.

5 Y. B. Zhang, H. Furukawa, N. Ko, W. Nie, H. J. Park, S. Okajima, K. E. Cordova, H. Deng, J. Kim and O. M. Yaghi, *J. Am. Chem. Soc.*, 2015, **137**, 2641–2650.

6 B. Mu, Y. Huang and K. S. Walton, *CrystEngComm*, 2010, **12**, 2347–2349.

7 B. Chen, M. Eddaoudi, S. T. Hyde, M. O'Keeffe and O. M. Yaghi, *Science*, 2001, **291**, 1021–1023.

8 M. P. Johansson and J. Olsen, *J. Chem. Theory Comput.*, 2008, **4**, 1460–1471.

9 F. Grein, *J. Mol. Struct.*, 2003, **624**, 23–28.

10 H. Furukawa, Y. B. Go, N. Ko, Y. K. Park, F. J. Uribe-Romo, J. Kim, M. O'Keeffe and O. M. Yaghi, *Inorg. Chem.*, 2011, **50**, 9147–9152.

11 S. S. Y. Chui, S. M. F. Lo, J. P. H. Charmant, A. G. Orpen and I. D. Williams, *Science*, 1999, **283**, 1148–1150.

12 N. Zhu, M. J. Lennox, T. Düren and W. Schmitt, *Chem. Commun.*, 2014, **50**, 4207–4210.

13 S. Xiang, J. Huang, L. Li, J. Zhang, L. Jiang, X. Kuang and C. Y. Su, *Inorg. Chem.*, 2011, **50**, 1743–1748.

14 V. A. Blatov, A. P. Shevchenko and D. M. Proserpio, *Cryst. Growth Des.*, 2014, **14**, 3576–3586.

15 C. F. Macrae, P. R. Edgington, P. McCabe, E. Pidcock, G. P. Shields, R. Taylor, M. Towler and J. Van De Streek, *J. Appl. Crystallogr.*, 2006, **39**, 453–457.

16 O. V. Dolomanov, L. J. Bourhis, R. J. Gildea, J. A. K. Howard and H. Puschmann, *J. Appl. Crystallogr.*, 2009, **42**, 339–341.

17 R. J. Phillips and G. B. Deacon, *Coord. Chem. Rev.*, 1980, **33**, 227–250.

18 L. D. Gelb and K. E. Gubbins, *Langmuir*, 1998, **14**, 2097–2111.

19 T. Düren, F. Millange, G. Férey, K. S. Walton and R. Q. Snurr, *J. Phys. Chem. C*, 2007, **111**, 15350–15356.

20 L. Sarkisov and J. Kim, *Chem. Eng. Sci.*, 2015, **121**, 322–330.

21 E. V. Alexandrov, V. A. Blatov, A. V. Kochetkov and D. M. Proserpio, *CrystEngComm*, 2011, **13**, 3947–3958.

22 J. Yang, X. Wang, R. Wang, L. Zhang, F. Liu, F. Dai and D. Sun, *Cryst. Growth Des.*, 2014, **14**, 6521–6527.

23 Z. X. Zhang, N. N. Ding, W. H. Zhang, J. X. Chen, D. J. Young and T. S. A. Hor, *Angew. Chem. Int. Ed.*, 2014, **53**, 4628–4632.

24 M. O. Keeffe, M. A. Peskov, S. J. Ramsden and O. M. Yaghi, *Acc. Chem. Res.*, 2008, **41**, 1782–1789

Chapter 6

Targeted Synthesis of MOFs Based on Extended Tritopic Carboxylate Ligands

6.1: Introduction

The use of extended linkers for the synthesis of high-surface area MOFs is a well-documented strategy that has yielded excellent results.[1,2] Rational design principles and reticular chemistry allow the conception of frameworks with desired geometries, topologies, and properties for specific applications, and extended ligands can allow the synthesis of MOFs with very low densities and high porosities by this method.[3,4] Here, we apply first the extended tritopic H_3bteb and then the H_3bbc ligands mentioned earlier to specific SBUs, in order to achieve highly porous MOFs with particular geometric properties based on 'default' nets. In this chapter the synthesis of particular MOFs based on the aforementioned ligands is described, based on rational strategies, and with the objective of obtaining novel compounds with accessible metal centres with significant porosity and of possible catalytic interest.

Earlier work in the Schmitt group led to the synthesis of zinc frameworks TCM-1 and TCM-2, following which a Co-MOF, $(Me_2NH_2)[Co_5(bteb)_3(\mu_3\text{-}OH)_2(DMF)_2]$, isostructural to TCM-2 was reported.[5,6] It is evident that for the formation of TCM-2 or (Co)TCM-2, the decomposition of DMF to yield the stabilising $(Me_2NH_2)^+$ cation is necessary. In addition, the 'hourglass' SBU adopted by Zn^{2+} centres in TCM-1 is also favoured by Co^{2+} in MOF structures under suitable conditions.[7–9] Co-MOFs have been an area of growing interest owing to their catalytic capabilities.[10,11] Therefore, the synthesis of (Co)TCM-1 through control of synthetic conditions was an intriguing objective. The synthesis and crystal structure of (Co)TCM-1, compound **24**, are reported in this chapter.

Zr^{4+} based SBUs are increasingly common as nodes in MOFs, and confer stability to MOFs due to their high oxophilicity and the resultant strength of metal-ligand bonds. However, this property also makes crystallisations challenging, and tends to result in coordinatively saturated metal centres as seen in archetypal Zr-MOFs such as UiO-66, and NU-1000.[12,13] The highly Lewis acidic nature of the Zr^{4+} centre makes it an attractive target as an accessible node in a MOF structure for catalytic applications. Examples of Zr-MOFs in which potential UMCs are available show landmark catalytic characteristics, as demonstrated recently by Sawano *et al.*[14] The highly extended H_3bteb ligand, by analogy with the $\{Hf_6\}$-bteb MOF reported by Cao *et al.*, would be expected to generate UMCs on the $\{Zr_6\}$ SBU, due to its tritopic nature, and consequent low linker connectivity.[15] We

describe here the synthesis and characterisation of the {Zr_6}-bteb MOF, **25**. The UMC-free {Zr_6}-bteb MOF was reported recently by Lee *et al*.[16]

Further, the novel {Mn_3}-bbc MOF, **26**, is synthesised and characterised, showing the default **kgd** net expected for the combination of hourglass-shaped SBUs and the extended tritopic H_3bbc ligands. Simulations are carried out in order to assess the porosity of the structure.

Finally, two main group MOFs are synthesised and characterised, based on Pb^{2+} (**27**) and In^{3+} (**28**) SBUs and H_3bbc. Pb^{2+} centres are known to form polymeric 1D rod-shaped SBUs, and are known to exhibit hemidirected coordination environments in conjunction with hard ligands.[17–20] Therefore, a net similar to that seen in MIL-103 was expected, in which tritopic linkers are bound to 1D SBUs in parallel planes, outlining hexagonal channels. In^{3+} centres are Lewis acidic and catalytically useful.[21,22] However the 2D In-MOFs reported show very moderate porosities, with the highest to date exhibiting a surface area of 301 m^2/g, reported recently by Li *et al.* for a 4,4′-sulfonyldibenzoic acid and 2-amino-1,4-terephthalic acid based mixed-ligand MOF.[23] We reasoned that mononuclear In^{3+} centres in combination with bbc^{3-} linkers would yield a substantially more porous framework. However, the usual 8-coordinate In^{3+} geometry would be unfavourable. The synthesis and characterisation of **27** and **28** are reported in this chapter. Simulations are carried out to determine porosity.

6.2: Compound **24**, $[Co_3(bteb)_2(H_2O)_2]$

In order to synthesise the Co(II) analogue of TCM-1, a variety of synthetic conditions were experimented with. Upon combination of $Co(NO_3)_2 \cdot 6H_2O$ and H_3bteb under dilute conditions in DMF at 85°C, violet single crystals of **24**, $[Co_3(bteb)_2(H_2O)_2]$, were obtained, together with deep purple block crystals of $(Me_2NH_2)[Co_5(\mu_3\text{-}OH)_2(bteb)_3(DMF)_2]$. Single crystal X-ray studies were carried out, which showed that the compound crystallises in the chiral tetragonal $P4_122$ space group. The cell parameters were found to be $a = b = 20.963(3)$ Å, c = 38.757(13) Å, and $\alpha = \beta = \gamma = 90°$. The Platon Squeeze routine was applied to account for disordered pore solvent.

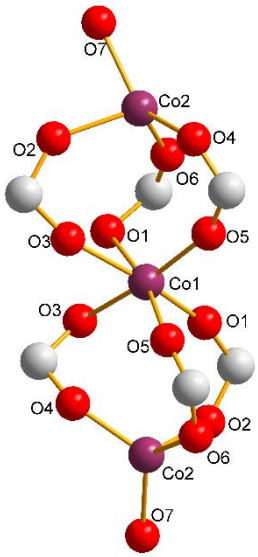

Figure 6.1 – A representation of the {Co_3} SBU in 24.

The asymmetric unit of **24** contains two distinct Co^{2+} ions, one fully deprotonated $bteb^{3-}$ ligand, and one coordinated DMF molecule. The Co^{2+} centres – Co1 and Co2 – are linked *via* three bidentate bridging carboxylate moieties from three distinct $bteb^{3-}$ linkers. Similarly Co2 and Co1', a third Co^{2+} centre in the SBU generated through symmetry operations, are also linked *via* three bidentate bridging carboxylates. This results in a six-connected {Co_3} hourglass-shaped SBU overall (Fig. 6.1). The coordination environment of Co1 is tetrahedral, and is completed by a capping H_2O molecule at the apical position. The Co2 coordination environment is octahedral, and the three Co^{2+} centres are nearly collinear (Table 6.1).

Table 6.1 - Selected interatomic distances and angles in 24.

Atoms	Distance		Atoms	Angle
Co2-O7	1.98(3) Å		O7-Co2-O4	130(2)°
Co2-O2	1.93(4) Å		O7-Co2-O6	116(2)°
Co2-O4	2.07(4) Å		O4-Co2-O6	108(2)°
Co2-O6	1.84(4) Å		O4-Co2-O2	101(1)°
Co2-O3	3.08(3) Å		Co1-Co2-O7	152(1)°
Co2-O5	3.09(4) Å			
Co2-O1	3.29(3) Å		Co2-Co1-Co2′	176.0(3)°
Co2-	3.57(1) Å			
Co1-O1	1.93(2) Å		O1-Co1-O1′	83(1)°
Co1-O5	2.00(3) Å		O5-Co1-O5′	72(1)°
Co1-O3	2.25(3) Å		O1-Co1-O5	102(1)°
Co1-O2	3.56(4) Å		O1-Co1-O3	75(1)°
Co1-O6	3.58(4) Å			
Co1-O4	2.94(4) Å			

Each {Co_3} SBU is therefore connected to six $bteb^{3-}$ ligands, and each bteb ligand is connected to three {Co_3} SBUs. The overall structure is doubly interwoven, with pairwise aromatic interactions between symmetry-related nets. Each individual net is chiral, as two $bteb^{3-}$ carboxylate groups link SBUs along a 4_3 screw axis along the crystallographic *c*-direction. The remaining carboxylate group connects these helical chains according to the four-fold screw axis into a three dimensional structure (Fig. 6.2, 6.3). This structure is therefore isostructural to [$Zn_3(bteb)_2(DMF)_2$], also known as TCM-1.[5]

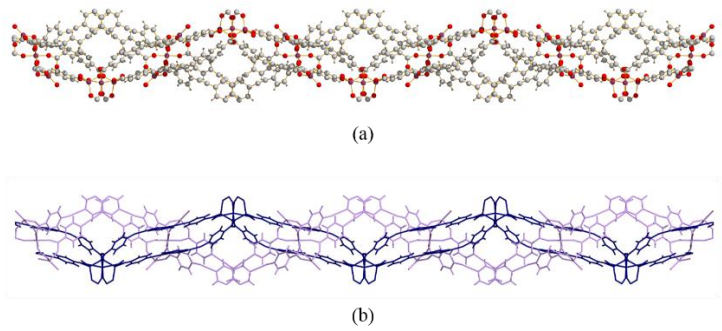

Figure 6.2 – Interwoven helical motifs along the *c*-axis in 24, (a) overall, and (b) interwoven nets highlighted in lavender and dark blue.

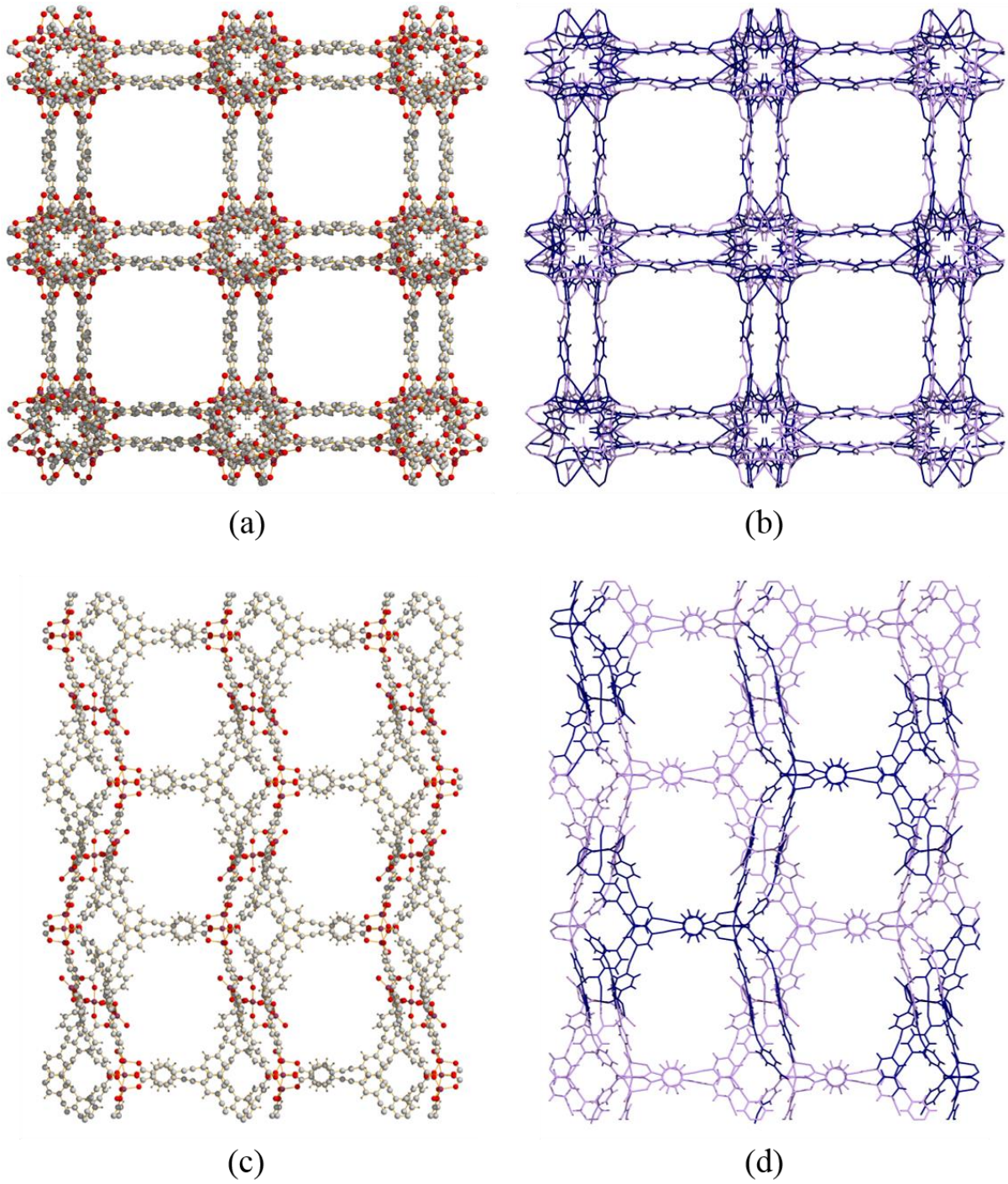

Figure 6.3 – Representations of the crystal structure of 24 along the crystallographic (a) *b*-axis, (b) *b*-axis, with interwoven nets highlighted in lavender and dark blue, (c) *c*-axis, (d) *b*-axis, (b) *c*-axis, with interwoven nets highlighted in lavender and dark blue. Colour scheme: violet, Co; grey, C; light grey, H; red, O.

The topology of TCM-1 has been described as a $\{10^3\}$ **srs**-type net based on solely three-connected nodes. However, **24** is best described as a (6,3)-connected net. Treating the $\{Co_3\}$ SBU as a single 6-connected node, we arrive at a topological reduction with the point

symbol $\{4^3.10^{12}\}\{4^3\}_2$ for each individual net. This is listed in the RCSR as the rare, binodal **cys** net (Fig. 6.4).[24,25]

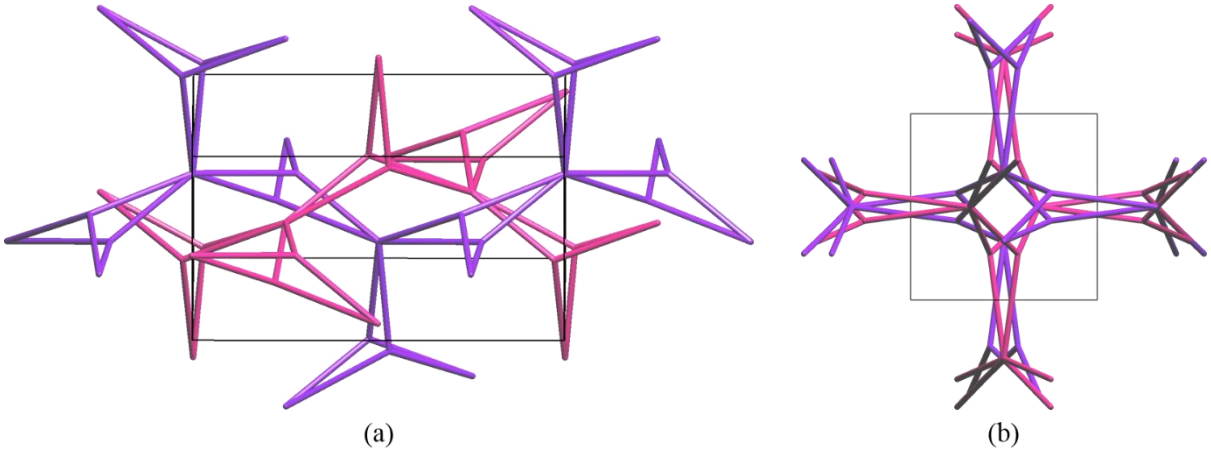

Figure 6.4 – Topological reduction of 24 into interwoven cys nets viewed along the approximate crystallographic (a) (101), and (b) *c*-directions.

The tightly interwoven networks in the dual-framework structure **24** result in minimal obstruction of the porosity in individual nets. The solvent accessible void volume after application of the Platon Squeeze routine is found to be 72.8% of the overall structure (CCDC:Mercury).[26,27] The structure is porous in all three crystallographic directions, with limiting diameters of 10.4 Å in the *a*- and *b*-directions, and 12.4 Å in the *c*-direction. The diameter of the largest spherical void was found to be 15.2 Å (Olex2).[28]

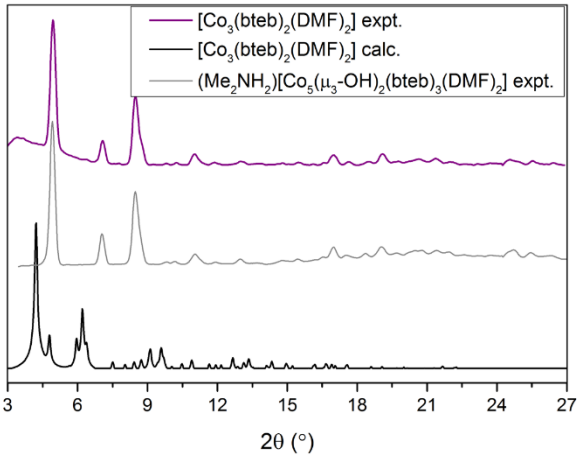

Figure 6.5 – The PXRD pattern of as-synthesised 24.

PXRD studies on the bulk of the as-synthesised sample clarify that **24** is a trace product, and the dominant product under the applied conditions is the related $(Me_2NH_2)[Co_5(\mu_3\text{-}OH)_2(bteb)_3(DMF)_2]$, which has been synthesised concurrently in our group and by Yu *et al* (Fig. 6.5).[6] Spectroscopic and thermochemical characterisation was

therefore not carried out on **24**. Simulations of porosity were carried out using the Poreblazer suite.[29] The nitrogen-accessible surface area of **24** was found to be 2934 m^2/g. The helium pore volume was found to be 1.623 cm^3/g, and the maximum pore diameter and limiting pore diameter are 13.93 Å and 14.82 Å, respectively. These values are in agreement with crystallographic determinations. The pore size distribution was simulated, and is shown in Figure 6.6. **24** is therefore potentially a highly porous framework.

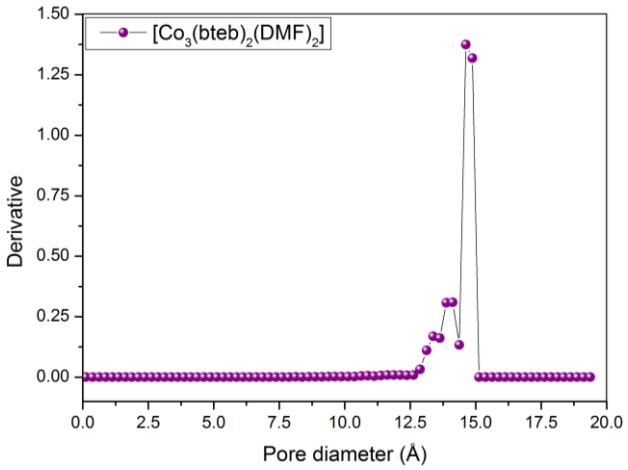

Figure 6.6 – Simulated pore size distribution of 24.

Optimisation of synthetic conditions for phase-pure **24** is ongoing. Preliminary investigations show that **24** is a promising candidate for use as an electrochemically driven water oxidation catalyst. Crystallographic details for **24** are given in Table 6.2.

Table 6.2 – Crystallographic details for 24.

Identification code	24
Empirical formula	$C_{66}H_{34}Co_3O_{14}$
Formula weight	1227.72
Temperature/ K	215(2)
Crystal system	tetragonal
Space group	$P4_122$
a/Å	20.963(3)
b/Å	20.963(3)
c/Å	38.757(13)
α/°	90
β/°	90
γ/°	90
Volume/Å^3	17032(8)
Z	4
ρ_{calc}/ g/cm^3	0.479
μ/mm^{-1}	2.452
F(000)	2492.0
Crystal size/mm^3	0.35 × 0.10 × 0.10
Radiation/Å	CuKα (λ = 1.54184)
2θ range for data collection/°	4.216 to 62.57
Index ranges	$-12 \leq h \leq 13$, $-10 \leq k \leq 13$, $-25 \leq l \leq 26$
Reflections collected	21476
Independent reflections	2699 [R_{int} = 0.3149, R_{sigma} = 0.3272]
Data/restraints/parameters	2699/139/120
Goodness-of-fit on F^2	0.844
Final R indexes [I>=2σ (I)]	R_1 = 0.1396, wR_2 = 0.2927
Final R indexes [all data]	R_1 = 0.3218, wR_2 = 0.3687
Largest diff. peak/hole / e Å^{-3}	0.24/-0.13
Flack parameter	0.21(5)

6.3: Compound **25**, $[Zr_6(bteb)_4(\mu_3\text{-}O)_4(\mu_3\text{-}OH)_4(H_2O)_4]$

Accessible Zr^{4+} centres in highly porous frameworks are an attractive synthetic target due to their potential as heterogeneous Lewis acid catalysts. In order to obtain the $\{Zr_6\}$-bteb MOF described in section 6.1, synthetic conditions were optimised for single crystal formation. A variety of modulators and modulator concentrations were used. Compound **25** was synthesised by heating a highly saturated solution of benzoic acid, with H_3bteb and $ZrCl_4$ in DMF, under autogenous pressure at 120°C for 96 hours. Transparent, rod-shaped single crystals of the pure MOF **25** were obtained.

Single crystal X-ray diffraction studies showed the adoption of a three-dimensional single-framework MOF structure composed of hexanuclear Zr^{4+} units linked by fully deprotonated $bteb^{3-}$ ligands. The overall formula for the framework is $[Zr_6(bteb)_4(\mu_3\text{-}O)_4(\mu_3\text{-}OH)_4(H_2O)_4]$. The structure of **25** was solved in the tetragonal space group *I*4/*m*, with cell dimensions of a = 33.1024(9) Å, b = 33.1024(9) Å, and c = 21.7112(7) Å.

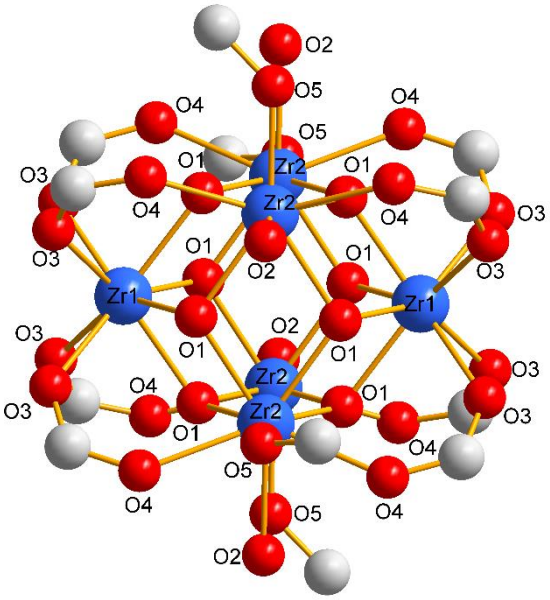

Figure 6.7 – A representation of the $\{Zr_6\}$ SBU in 25.

The SBU is based on the well-characterised $\{Zr_6\}$ oxo-cluster, in which Zr^{4+} ions are arranged at the vertices of an octahedron, and μ_3-O and μ_3-OH moieties occupy the face centres (Fig. 6.7). However, while the typical SBU as seen in MOFs such as UiO-66 or NU-1000 consists uniformly of bidentate bridging carboxylate binding modes, the SBU in

25 consists of monodentate carboxylate binding modes at four positions, where the 8-coordination of the Zr^{4+} centre is completed by H_2O ligands (Table 6.3).[14,15,30]

Table 6.3 - Selected interatomic distances and angles in 25.

Atoms	Distance		Atoms	Angle
Zr1-O1	2.169(4) Å		O3-Zr1-O3′	74.3(1)°
Zr1-O3	2.18(4) Å		O1-Zr1-O1′	108.6(2)°
Zr1-Zr1′	4.92(1) Å		O1-Zr1-O1″	70.1(1)°
Zr1-Zr2	3.5028(8) Å		O1-Zr1-O3	79.2(1)°
Zr2-Zr2′ (square edge)	3.5269(9) Å			
Zr2-Zr2″ (square diagonal)	4.9878(9) Å		Zr2-O1-Zr2′	111.8(2)°
Zr2-O1	2.125(4) Å		Zr2-O1-Zr1	109.3(2)°
Zr2-O2	2.230(5) Å		O2-Zr2-O4	71.9(1)°
Zr2-O4	2.284(4) Å		O2-Zr2-O1	88.2(1)°
Zr2-O5	2.125(6) Å		O1-Zr2-O1′	71.6(2)°

This type of coordination environment can allow access to Zr^{4+} sites when the water ligands are displaced. One of the three carboxylate groups on each ligand molecule binds in a monodentate fashion while the other two are bidentate. Each $\{Zr_6\}$ SBU is connected to 12 separate $bteb^{3-}$ ligands, and each ligand is connected to 3 $\{Zr_6\}$ SBUs. The resultant (12,3)-connected net corresponds to the uncommon **llj** topology with the point symbol $\{4^{20}.6^{28}.8^{18}\}\{4^3\}_4$, and is isostructural to the reported Hafnium analogue (Fig. 6.8).[15]

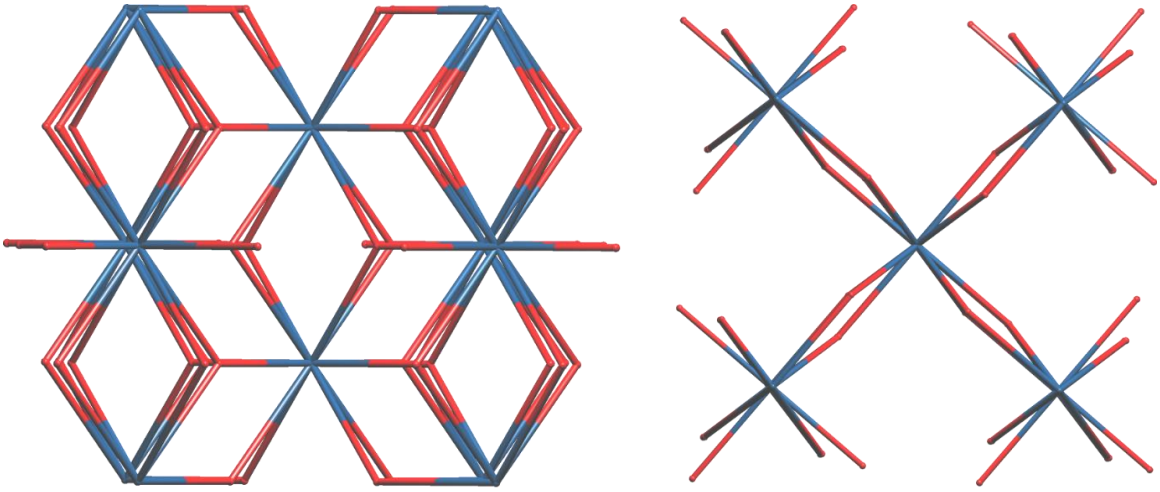

(a) (b)

Figure 6.8 – Topological reduction of 25 into the llj net viewed along the approximate crystallographic (a) *a*-, and (b) *c*-directions.

The framework is highly porous, with cuboidal channels running along the *c*-axis, bounded by four ligands and four SBUs (Fig. 6.9). The accessible diameter of the channels is 16.8 Å, and the coordinated H_2O ligands are highly accessible through these channels. The maximum void diameter is 18.0 Å, and the void volume is determined to be 79.1%.[27,28]

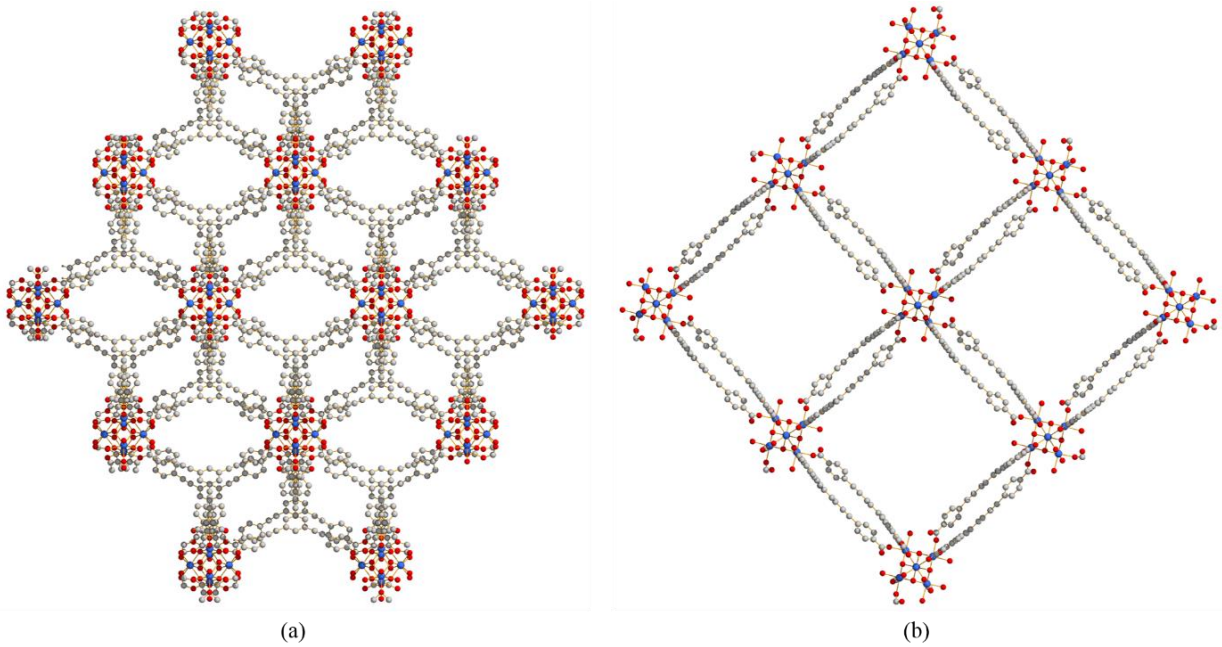

Figure 6.9 – Representations of the crystal structure of 25 viewed along the approximate crystallographic (a) *a*-, and (b) *c*-directions. Colour scheme: light blue, Zr; grey, C; light grey, H; red, O.

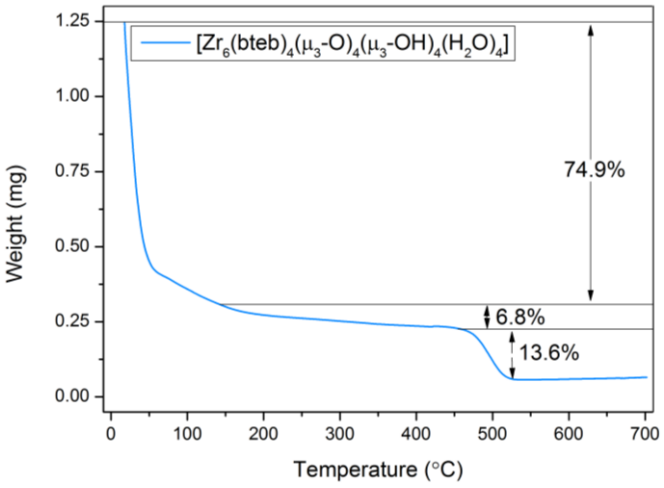

Figure 6.10 – Thermogravimetric analysis for 25.

This is in good agreement with the experimental thermogravimetric analysis of **25**, which shows a preliminary loss of solvent corresponding to 74.9% weight below 140°C, followed

by a ligand decomposition step at ca. 460°C (Fig. 6.10). Further characterisation of the phase purity of as-obtained **25** was carried out using PXRD and FTIR techniques.

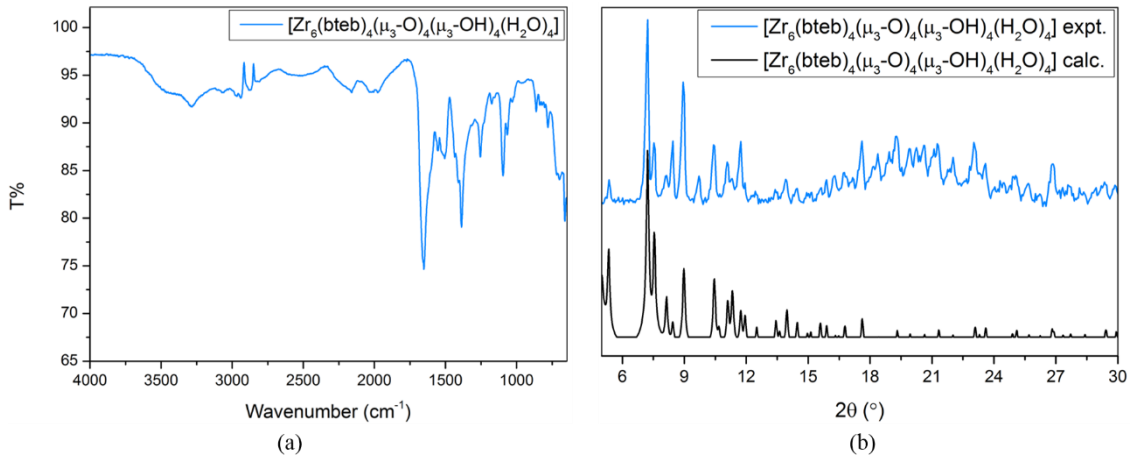

Figure 6.11 – FTIR spectrum (a) and PXRD pattern (b) for 25.

FTIR spectroscopy carried out on **25** showed a broad signal centred at 3400 cm^{-1}, due to the interactions of solvent molecules with the pore wall (Fig. 6.11). C=O stretching vibrations in constitutional DMF molecules result in the strong band at 1652 cm^{-1}. A number of overlapping signals between 1600 cm^{-1} and 1255 cm^{-1} are observed due to C=O and C=C vibrations. Strong bands at 1557 cm^{-1} and 1387 cm^{-1} may be assigned to $\nu_{as}COO$ and $\nu_{s}COO$ respectively. The bands at 1506 cm^{-1} is also assigned to $\nu_{as}COO$, due to the monodentate carboxylate binding mode observed.

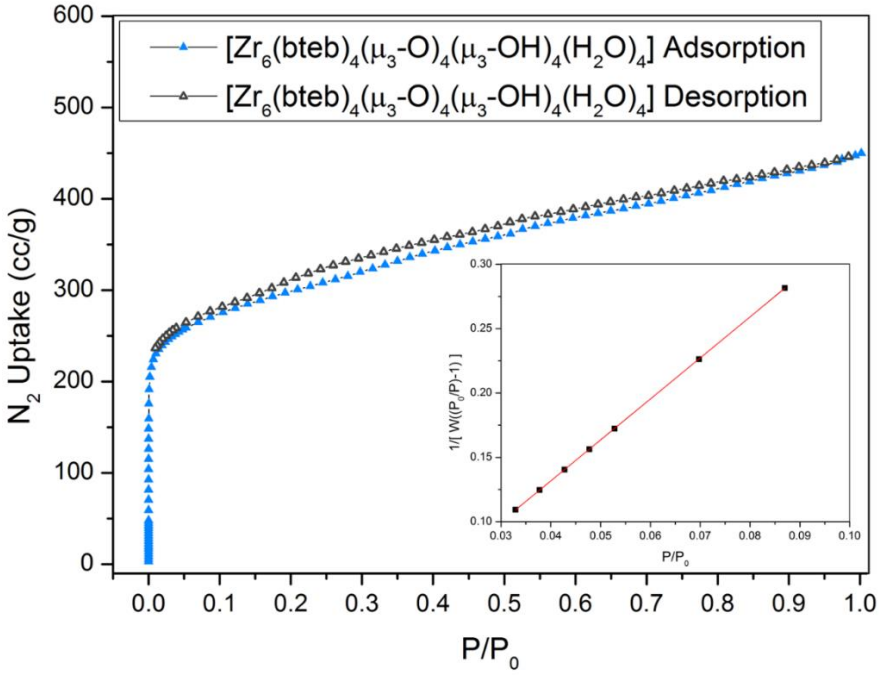

Fig. 6.12 – N_2 isotherm of 25 at 77 K. Inset: Multi-point BET fit; slope = 3.186, intercept = 4.307x 10^{-3}, correlation coefficient, r = 0.999996, C (constant) = 740.649, surface area = 1091.6 m^2/g.

The porosity of the MOF was further characterised using gas sorption analysis. N_2 sorption analysis at 77 K showed that porosity was retained even after activation, which is unusual for MOFs constructed solely using bteb^{3-} due to the magnitude of ligand extension, and for Zr-MOFs built using extended tritopic ligands than the higher-connectivity tetracarboxylate system, which is more typically used.[2,31]

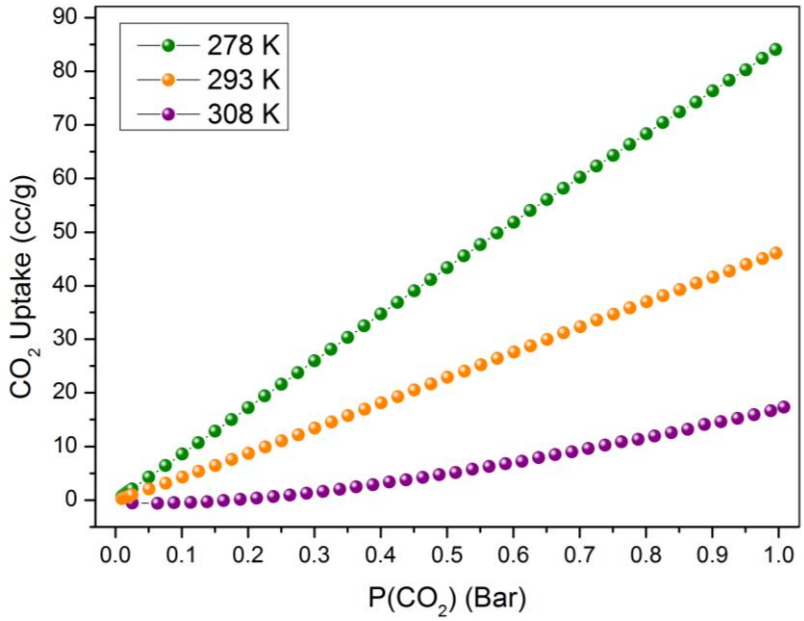

Fig. 6.13 – CO_2 adsorption isotherm of 25 at 278 K, 293 K, and 308 K.

The isotherm shows microporosity, and a surface area of 1092 m^2/g is obtained by BET analysis (compared to a calculated value of 4989 m^2/g using the Poreblazer suite) (Fig. 6.12). CO_2 sorption isotherms measured at 278 K, 293 K, and 308 K, show uptakes at 1 bar of 84 cc/g, 46 cc/g, and 17 cc/g respectively. The isosteric heat of adsorption is ca. 30 kJ/mol. This demonstrates the high physisorptive aptitude of **25** for CO_2 as a substrate (Fig. 6.13).

The discrepancy between the observed and calculated surface areas, as well as the noise in the PXRD pattern, are attributed to partial amorphisation during activation. A more delicate activation procedure may therefore be required. Preliminary investigations suggest that the accessible Lewis-acidic Zr^{4+} sites in **25** could lead to promising applications as a heterogeneous catalyst for the synthesis of cyclic carbonates from CO_2 and epoxides under moderate reaction conditions. Crystallographic details of **25** are listed in Table 6.4.

Table 6.4 – Crystallographic details for 25.

Identification code	25
Empirical formula	$C_{22}H_{7.33}O_6Zr$
Formula weight	458.83
Temperature/ K	215(2)
Crystal system	tetragonal
Space group	*I*4/*m*
a/Å	33.1024(9)
b/Å	33.1024(9)
c/Å	21.7112(7)
α/°	90
β/°	90
γ/°	90
Volume/Å^3	23790.5(15)
Z	12
ρ_{calc}/ g/cm^3	0.384
μ/mm^{-1}	1.216
F(000)	2728.0
Crystal size/mm^3	0.24 × 0.10 × 0.10
Radiation/Å	CuKα (λ = 1.54178)
2θ range for data collection/°	4.868 to 91.622
Index ranges	$-30 \leq h \leq 30$, $-26 \leq k \leq 30$, $-20 \leq l \leq 19$
Reflections collected	39895
Independent reflections	5178 [R_{int} = 0.0606, R_{sigma} = 0.0441]
Data/restraints/parameters	5178/14/185
Goodness-of-fit on F^2	1.103
Final R indexes [I>=2σ (I)]	R_1 = 0.0610, wR_2 = 0.1843
Final R indexes [all data]	R_1 = 0.0724, wR_2 = 0.1909
Largest diff. peak/hole / e Å^{-3}	0.46/-0.86

6.4: Compound **26**, $[Mn_3(bbc)_2(DMF)_4]$

Mn^{2+} metal centres in MOFs are attractive as potential sites of heterogeneous catalysis. $\{Mn_3\}$ SBUs are usually formed, and allow a reticular conception of product formation. Additionally, these SBUs are apically capped by labile solvent ligands, allowing access to the metal centres under reaction conditions. Compound **26**, $[Mn_3(bbc)_2(DMF)_4]$, was synthesised by heating a solution of H_3bbc and $MnCl_2{\cdot}4H_2O$ in DMF, under autogenous pressure at 120°C for 96 hours. Transparent, rod-shaped single crystals of **26** were obtained.

Single crystal X-ray diffraction studies showed the adoption of a two-dimensional bilayer framework MOF structure composed of trinuclear Mn^{2+} units linked by fully deprotonated bbc^{3-} ligands. The overall formula for the framework is $[Mn_3(bbc)_2(DMF)_4]$. The structure of **26** was solved in the monoclinic crystal system, and the *C*2/*c* space group, with cell dimensions of a = 40.652(8) Å, b = 24.463(4) Å, and c = 14.657(2) Å, and β = 94.58(2)°.

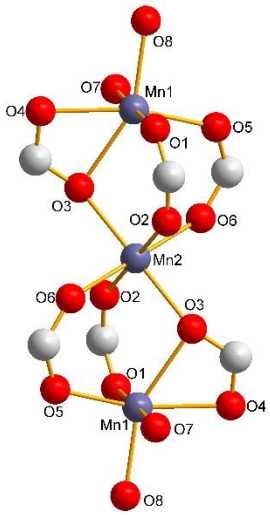

Figure 6.14 – A representation of the $\{Mn_3\}$ SBU in 26.

The SBU in **26** is hourglass shaped, and the three Mn^{2+} centres are approximately collinear (Table 6.5). The SBU is symmetric about the central Mn^{2+} ion and the three metal centres are connected by six carboxylate groups from distinct bbc^{3-} ligands. Four of these carboxylate groups adopt bidentate bridging binding modes, while the other two show bridging chelate modes. The central Mn^{2+} ion (Mn2) is in an octahedral coordination environment, while distorted octahedral environments about the peripheral Mn^{2+} ions (Mn1) are completed by two coordinated DMF molecules each (Fig. 6.14).

Table 6.5 - Selected interatomic distances and angles in 26.

Atoms	Distance		Atoms	Angle
Mn1-O1	2.098(4) Å		O8-Mn1-O1	95.4(2)°
Mn1-O2	3.248(5) Å		O8-Mn1-Mn2	170.9(1)°
Mn1-O3	2.311(4) Å			
Mn1-O4	2.225(4) Å		O5-Mn1-O1	94.5(2)°
Mn1-O4	2.126(4) Å		O8-Mn1-O3	152.5(2)°
Mn1-O7	2.271(5) Å		O7-Mn1-O1	176.9(2)°
Mn1-O8	2.121(4) Å		O3-Mn1-O3′	180°
Mn1-Mn2	3.523(1) Å		O3-Mn1-O2	87.2(2)°
Mn2-O2	2.161(4) Å		O6-Mn1-O2	88.1(2)°
Mn1-O3	2.165(4) Å		Mn1-Mn2-	180°
Mn1-O6	2.139(4) Å			

As a result of the orientation of carboxylate carbons in the SBU into an approximate trigonal antiprismatic orientation, the extension provided by ligands results in a pair of mutually obscured hexagonal networks constituting individual bilayers. The porosity in **26** is limited intrinsically due to the blocking of hexagonal cavities in each monolayer by the other monolayer in the pair. The overall 2D net obtained may be described as a binodal (3,6)-connected net (Fig. 6.15). Topological reduction of **26** shows that the point symbol of the underlying net is $\{4^3\}_2\{4^6.6^6.8^3\}$, and the associated RCSR notation is **kgd** (kagome dual).[24]

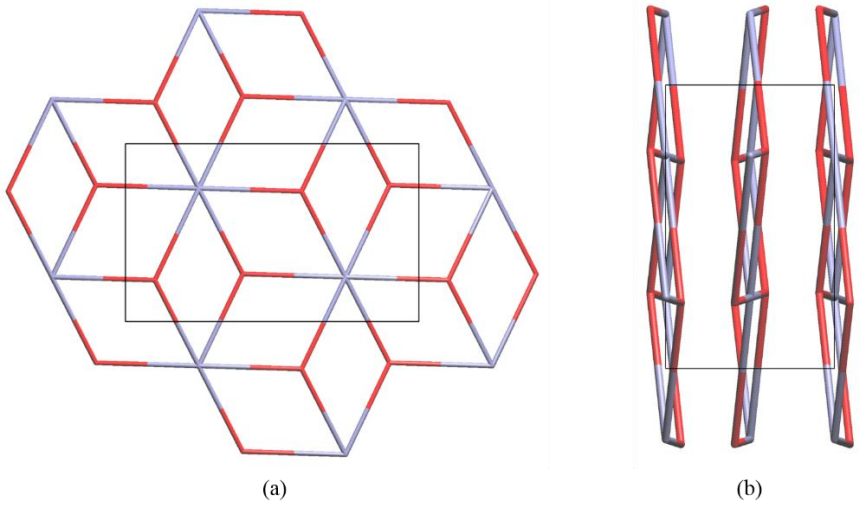

Figure 6.15 – Topological reduction of 26 into the kgd net viewed along the approximate crystallographic (a) *c*-, and (b) *a*-directions.

The porosity of the framework is due to channels along the crystallographic *c*-axis, which have a limiting diameter of 8.0 Å despite the inaccessibility of hexagonal pores. The maximum void diameter is 10.0 Å, and the void volume is determined to be 45.2% (Fig. 6.12).[27,28]

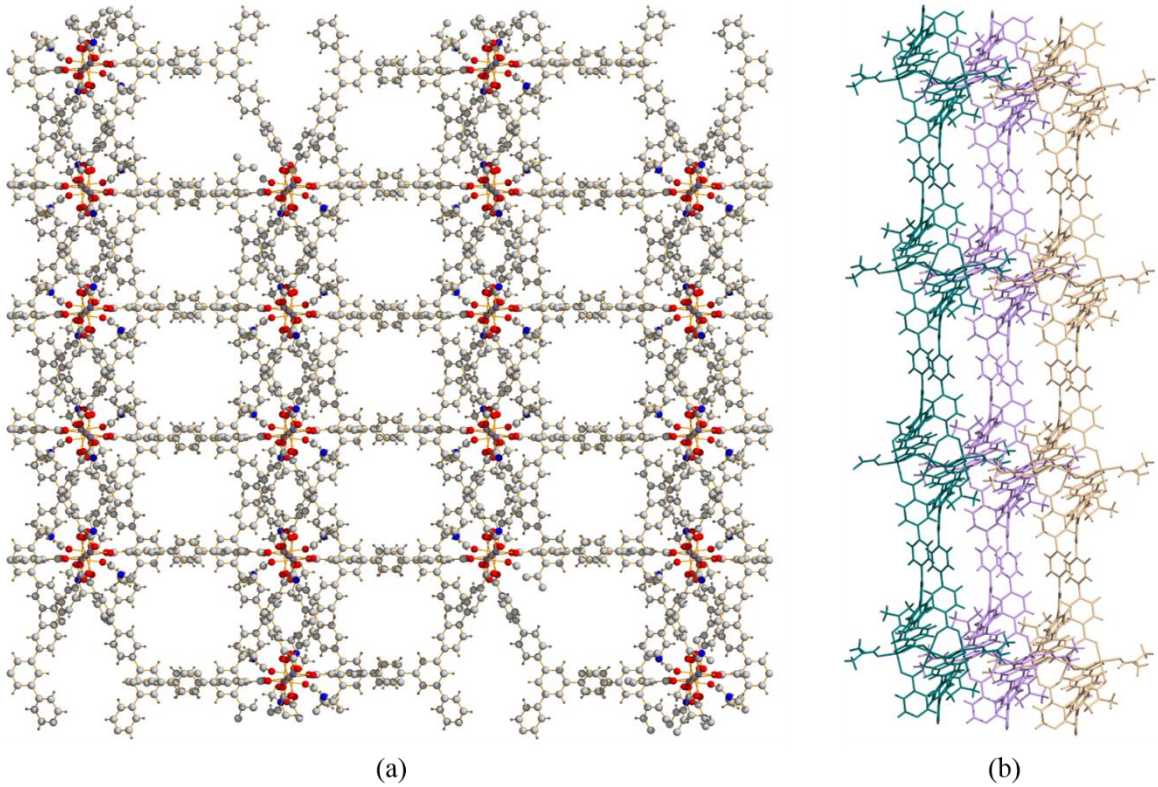

Figure 6.16 – Representations of the crystal structure of 26: (a) Packing representation viewed along the crystallographic *c*-direction. Colour scheme: lavender, Mn; blue, N; grey, C; light grey, H; red, O; (b) wireframe representation of the relative orientation of separate 2D bilayer nets (coloured separately) in 26 viewed along the crystallographic *a*-direction.

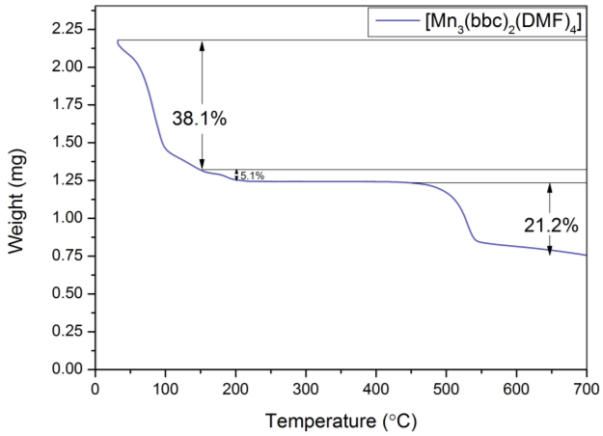

Figure 6.17 – Thermogravimetric analysis for 26.

This is corroborated by the experimental thermogravimetric analysis of **26**, which shows a preliminary loss of solvent corresponding to 38.1% weight below 140°C, followed by a ligand decomposition step at ca. 450°C (Fig. 6.17). Further characterisation of the phase purity of as-synthesised **26** was carried out using PXRD and FTIR techniques.

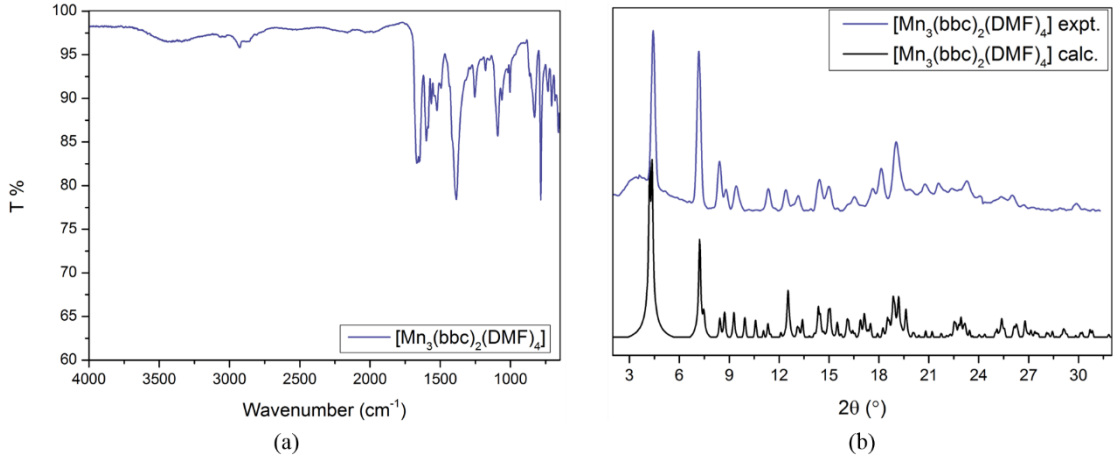

Figure 6.18 – FTIR spectrum (a) and PXRD pattern (b) for 26.

FTIR spectroscopy carried out on **26** showed a broad signal centred at 3460 cm^{-1}, due to the interactions of constitutional DMF molecules with the pore wall (Fig. 6.18). C=O stretching vibrations in DMF molecules correspond to the strong band at 1651 cm^{-1}. A number of overlapping signals between 1667 cm^{-1} and 1254 cm^{-1} are observed due to C=O and C=C vibrations. Strong bands at 1586 cm^{-1} and 1386 cm^{-1} may be assigned to ν_{as}COO and ν_{s}COO respectively. The band at 1599 cm^{-1} is also assigned to ν_{as}COO, due to the bridging chelate carboxylate binding mode observed.

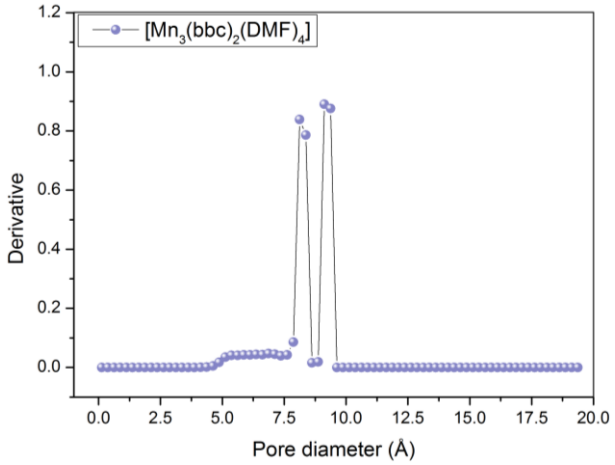

Figure 6.19 – Simulated pore size distribution of 26.

Simulations of porosity were carried out using the Poreblazer suite.[29] The nitrogen-accessible surface area of **26** was found to be 1548 m^2/g. The helium pore volume was

found to be 0.655 cm^3/g, and the maximum pore diameter and limiting pore diameter are 7.60 Å and 9.50 Å, respectively. These values are in agreement with crystallographic determinations. The pore size distribution was simulated, and is shown in Figure 6.19. Crystallographic details for **26** are listed in Table 6.6.

Table 6.6 – Crystallographic details for 26.

Identification code	26
Empirical formula	$C_{138}H_{110}Mn_3N_4O_{16}$
Formula weight	2245.11
Temperature/ K	215(2)
Crystal system	monoclinic
Space group	*C*2/*c*
a/Å	40.652(8)
b/Å	24.463(4)
c/Å	14.657(2)
α/°	90
β/°	94.58(2)
γ/°	90
Volume/$Å^3$	14529(4)
Z	4
ρ_{calc}/ g/cm^3	1.026
μ/mm^{-1}	0.311
F(000)	4676.0
Crystal size/mm^3	0.21 × 0.10 × 0.10
Radiation/Å	MoKα (λ = 0.71073)
2θ range for data collection/°	1.944 to 41.718
Index ranges	$-40 \leq h \leq 33$, $-24 \leq k \leq 24$, $-14 \leq l \leq 14$
Reflections collected	38073
Independent reflections	7617 [R_{int} = 0.0543, R_{sigma} = 0.0447]
Data/restraints/parameters	7617/108/636
Goodness-of-fit on F^2	1.054
Final R indexes [I>=2σ (I)]	R_1 = 0.0750, wR_2 = 0.2006
Final R indexes [all data]	R_1 = 0.0899, wR_2 = 0.2092
Largest diff. peak/hole / e $Å^{-3}$	0.47/-0.41

6.5: Compound **27**, $[Pb_6(bbc)_4(DMF)_2]$

The soft Pb^{2+} centre has limited application in framework chemistry due to its tendency to form variable and poorly defined SBUs, and its toxicity. However, if incorporated into MOFs, Pb^{2+} centres can be utilised in sensing and catalysis applications, as well as the preferential removal of particular substrates form mixtures, *e.g.* crude oil sweetening. Compound **27** was synthesised by heating a solution of H_3bbc and $Pb(NO_3)_2$ in DMF, under autogenous pressure at 100°C for 48 hours. Transparent, block-shaped single crystals of **27** were obtained.

Single crystal X-ray diffraction studies showed the adoption of a three-dimensional MOF structure composed of polymeric rod-shaped SBUs formed by Pb^{2+} centres linked by fully deprotonated bbc^{3-} ligands (Fig. 6.20). The overall formula for the framework is $[Pb_6(bbc)_4(DMF)_2]$. The structure of **27** was solved in the monoclinic crystal system, and the *P*n space group, with cell dimensions of a = 24.115(7) Å, b = 15.353(4) Å, and c = 41.438(11) Å, and β = 92.79(2)°.

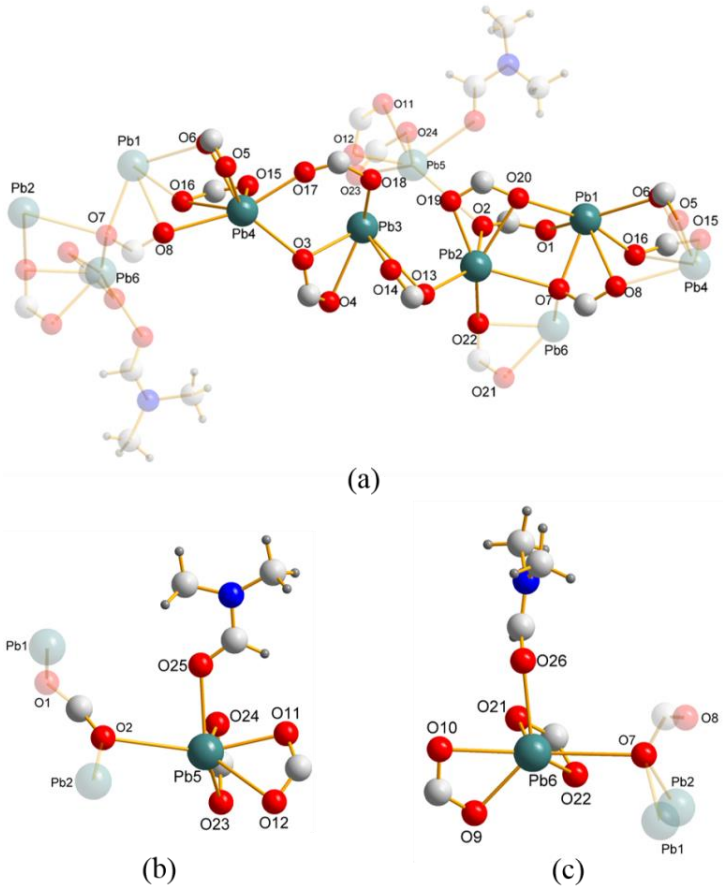

Figure 6.20 – A representation of the crystallographically unique components of the {Pb_∞} SBU in 27, with an emphasis on (a) Pb1, Pb2, Pb3, and Pb4; (b) Pb5; (c) Pb6.

The SBU in **27** is infinitely extended along the crystallographic *b*-direction, and contains six unique Pb^{2+} centres. The Pb^{2+} centres are linked through a variety of carboxylate binding modes, and coordination polyhedra are seen to share a combination of vertices and edges. The coordination environments of the six Pb^{2+} centres are hemidirected, as often observed for lead(II) complexes with hard ligands (Fig. 6.21).[19] Along the *ac*-plane, the rod SBU directs tritopic bbc^{3-} ligands outwards in an approximately coplanar, eclipsed fashion, resulting in parallel honeycomb-shaped 2D motifs stacked along the *b*-axis. Pb1, Pb2, Pb3, and Pb4 have coordination environments consisting solely of O-donor atoms from carboxylate groups. Pb5 and Pb6 bear DMF ligands in addition to carboxylate groups (Table 6.7).

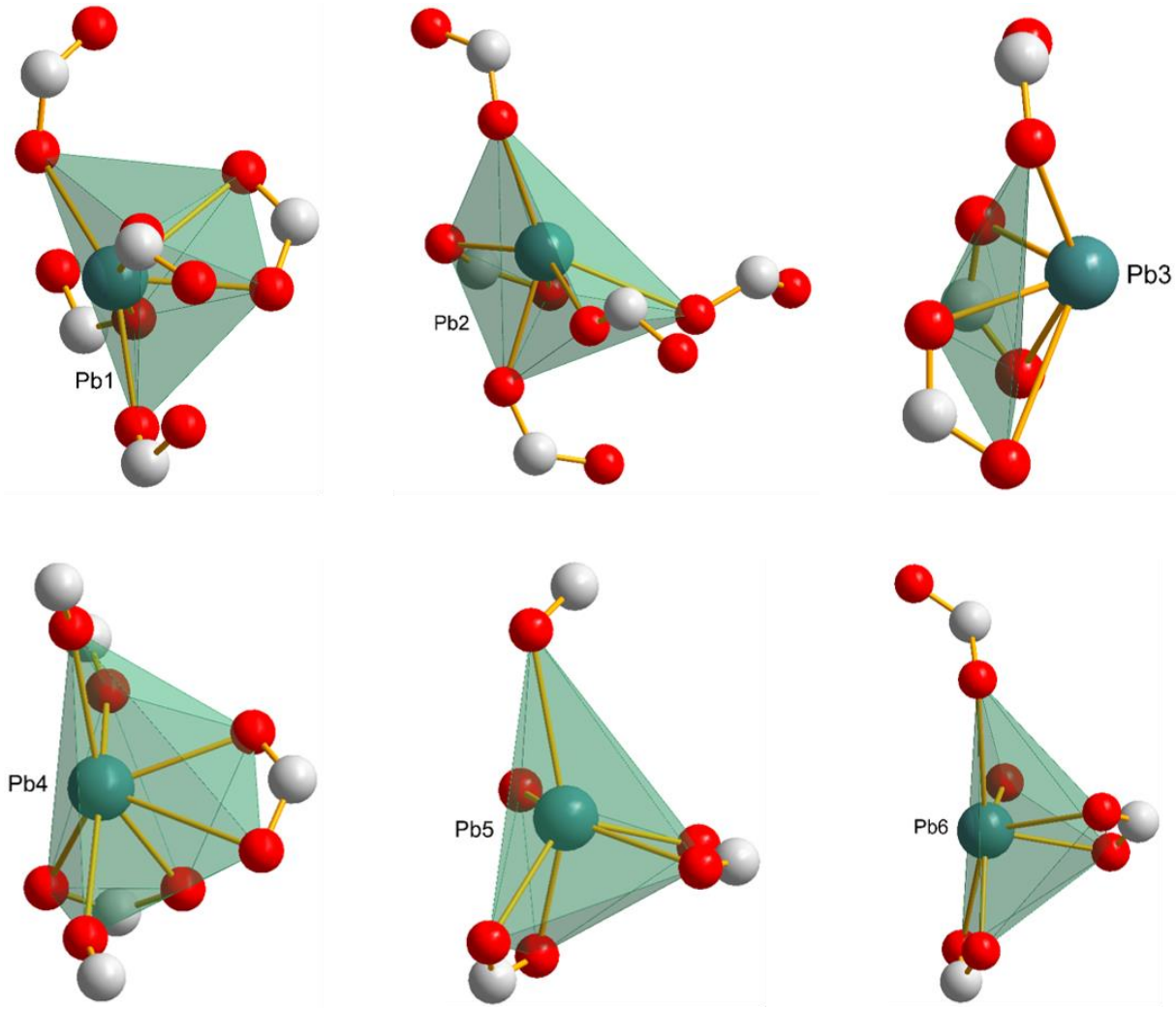

Figure 6.21 – Hemidirected coordination environments around Pb^{2+} centres in 27.

Table 6.7 - Selected interatomic distances and angles in 27.

Atoms	Distance		Atoms	Angle
Pb1-Pb4	4.011(1) Å		Pb1-Pb4-Pb3	136.26(2)°
Pb1-O6	2.766(9) Å		Pb3-Pb2-Pb1	138.79(2)°
Pb1-O16	2.347(8) Å		O1-Pb1-O6	148.1(4)°
Pb1-O8	2.896(9) Å		O7-Pb1-O1	77.8(4)°
Pb1-O7	2.474(8) Å		O20-Pb1-O1	94.4(4)°
Pb1-O1	2.42(1) Å			
Pb1-O20	2.78(1) Å			
Pb2-Pb1	4.012(1) Å		O19-Pb2-O2	79.5(3)°
Pb2-O1	3.90(1) Å		O2-Pb2-O20	73.4(3)°
Pb2-O2	2.470(8) Å		O2-Pb2-O13	142.6(3)°
Pb2-O13	2.528(9) Å			
Pb2-O19	2.408(8) Å			
Pb2-O20	2.701(9) Å			
Pb2-O22	2.913(9) Å			
Pb2-Pb3	4.305(1) Å			
Pb3-O13	2.528(9) Å		O13-Pb3-O14	47.6(3)°
Pb3-O14	2.408(2) Å		O14-Pb3-O18	79.1(4)°
Pb3-O18	2.42(1) Å		O3-Pb3-O18	92.68(4)°
Pb3-O4	2.71(1) Å			
Pb3-O3	2.455(9) Å			
Pb3-O17	3.33(1) Å			
Pb3-O12	3.10(9) Å			
Pb3-Pb4	4.436(1) Å			
Pb4-O18	4.34(1) Å		O17-Pb4-O8	152.1(4)°
Pb4-O15	2.53(1) Å		O17-Pb4-O5	81.6(3)°
Pb4-O5	2.523(1) Å		O5-Pb4-O16	113.8(3)°
Pb4-O6	2.493(9) Å		O6-Pb4-O15	77.4(3)°
Contd…				

Atoms	Distance		Atoms	Angle
Pb4-O16	3.030(9) Å			
Pb4-O8	2.74(1) Å			
Pb5-O11	2.342(9) Å		O25-Pb5-O11	80.0(4)°
Pb5-O12	2.702(9) Å		O25-Pb5-O24	81.4(4)°
Pb5-O23	2.523(1) Å		O24-Pb5-O11	81.9(3)°
Pb5-O24	2.437(9) Å		O23-Pb5-O12	86.9(3)°
Pb5-O25	2.49(1) Å			
Pb5-O2	3.04(1) Å			
Pb5-O19	3.262(8) Å			
Pb6-O22	2.707(9) Å		O26-Pb6-O21	76.5(4)°
Pb6-O21	2.340(9) Å		O26-Pb6-O10	80.6(4)°
Pb6-O26	2.56(2) Å		O21-Pb6-O10	86.6(4)°
Pb6-O9	2.36(1) Å		O22-Pb6-O9	85.6(6)°
Pb6-O11	2.56(1) Å			

The bbc^{3-} linkers in **27** link three parallel rod SBUs. Thus the net in **27** may be considered a combination of infinite 1D rod SBUs and 3-connected nodes, similar to the topology of MIL-103 (Fig. 6.22). However, the involvement of Pb^{2+} lone pairs in the coordination environment does not allow reduction to the idealised trigonal prismatic connectivity about the 1d node.

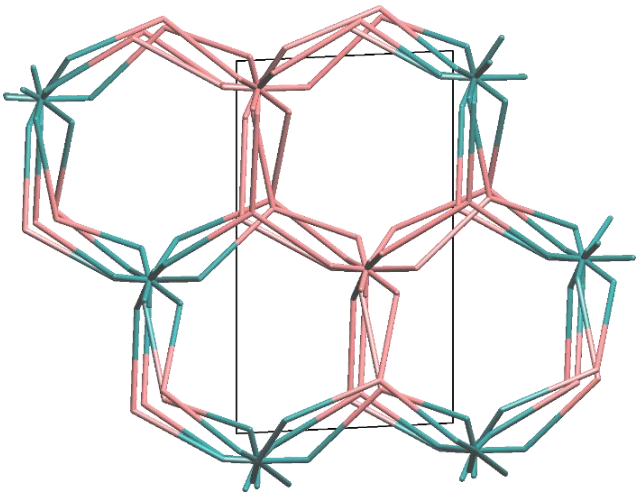

Figure 6.22 – Topological reduction of 27 into the tpr net viewed along the approximate crystallographic *c* -direction. Teal nodes correspond to SBUs and pink nodes correspond to ligands

Therefore an approximate topological reduction of **27** results in a point symbol of $\{3.8^2\}\{3.4^4.8.12^2\}$, and the associated three-letter symbol is **tpr**.

The porosity of the framework is due to hexagonal channels along the crystallographic *b*-axis, which have a limiting diameter of 14.0 Å. The maximum void diameter is 15.2 Å, and the void volume is determined to be 54.6% (Fig. 6.23).

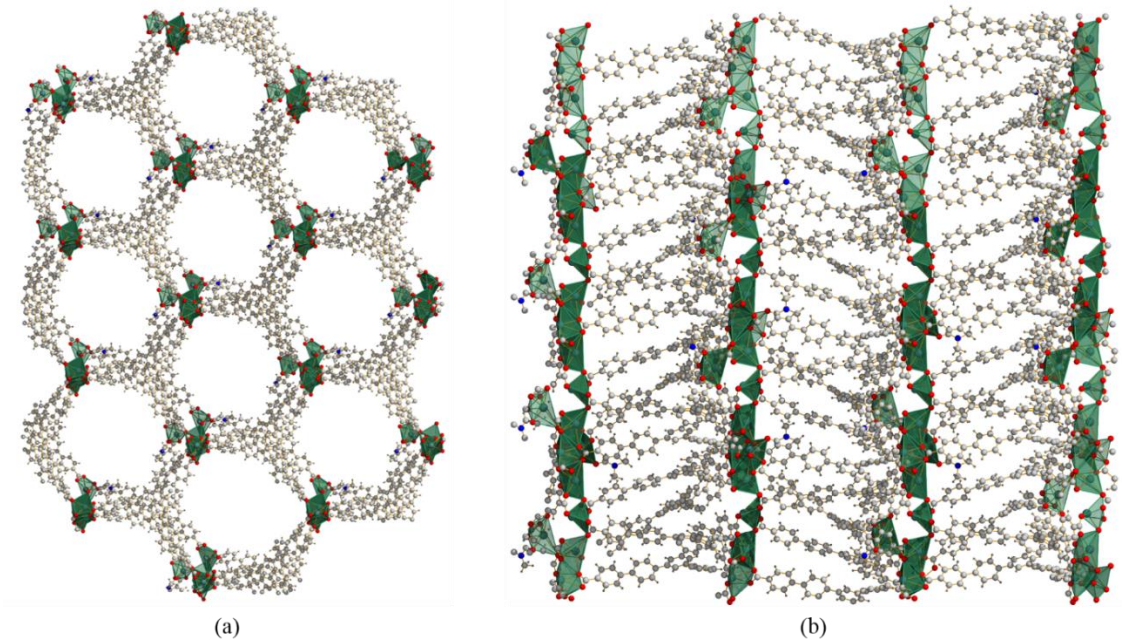

Figure 6.23 – Packing representations of the crystal structure of 27, viewed along the crystallographic (a) *b*-direction, (b) *a*-direction. Colour scheme: green polyhedra, {Pb_∞}; blue, N; grey, C; light grey, H; red, O.

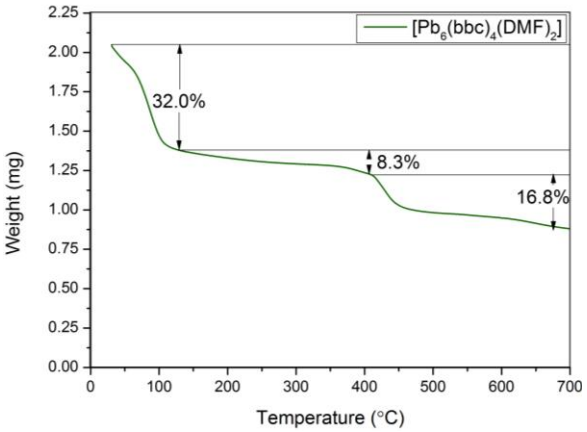

Figure 6.24 – Thermogravimetric analysis for 27.

Experimental thermogravimetric analysis of **27** shows a preliminary loss of solvent corresponding to 32.0% weight below 120°C, followed by a ligand decomposition step at ca. 410°C (Fig. 6.24). Further characterisation of the phase purity of as-synthesised **27** was carried out using PXRD and FTIR spectroscopy.

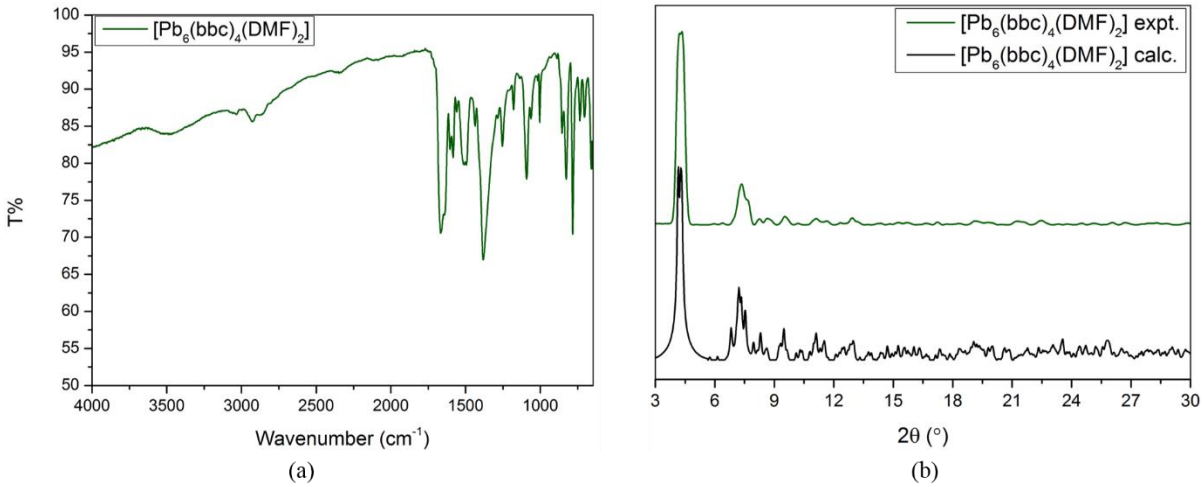

Figure 6.25 – FTIR spectrum (a) and PXRD pattern (b) for 27.

FTIR spectroscopy carried out on **27** showed a broad signal centred at 3460 cm^{-1}, due to the interactions of pore DMF molecules with the framework wall. C=O stretching vibrations in DMF molecules correspond to the strong band at 1646 cm^{-1}. A number of overlapping signals between 1668 cm^{-1} and 1254 cm^{-1} are observed due to C=O and C=C vibrations. Strong bands at 1584 cm^{-1} and 1382 cm^{-1} are be assigned to $\nu_{as}COO$ and $\nu_{s}COO$ respectively. Bands at 1559 cm^{-1} and 1501 cm^{-1} are also assigned to $\nu_{as}COO$, due to the plurality of carboxylate binding modes observed (Fig. 6.25).

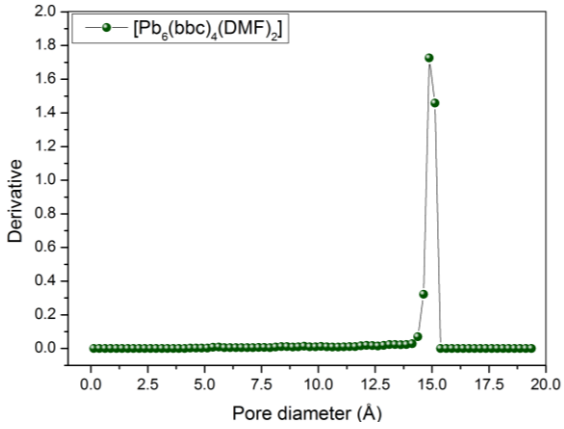

Figure 6.26 – Simulated pore size distribution of 27.

Simulations of porosity were carried out using the Poreblazer suite.[29] The nitrogen-accessible surface area of **27** was found to be 1324 m^2/g. The helium pore volume was found to be 0.744 cm^3/g, and the maximum pore diameter and limiting pore diameter are

13.52 Å and 15.08 Å, respectively. These values are in close agreement with crystallographic determinations. The pore size distribution was simulated, and is shown in Figure 6.26. Crystallographic details for **27** are listed in Table 6.8.

Table 6.8 – Crystallographic details for 27.

Identification code	**27**
Empirical formula	$C_{93}H_{60.5}NO_{13}Pb_3$
Formula weight	2021.49
Temperature/ K	215(2)
Crystal system	monoclinic
Space group	*Pn*
a/Å	24.115(7)
b/Å	15.353(4)
c/Å	41.438(11)
α/°	90
β/°	92.79(2)
γ/°	90
Volume/Å^3	15323(7)
Z	4
ρ_{calc}/ g/cm^3	0.876
μ/mm^{-1}	6.576
F(000)	3902.0
Crystal size/mm^3	0.250 × 0.100 × 0.080
Radiation/Å	CuKα (λ = 1.54178)
2θ range for data collection/°	4.27 to 125.036
Index ranges	$-27 \leq h \leq 26$, $-17 \leq k \leq 16$, $-45 \leq l \leq 47$
Reflections collected	146674
Independent reflections	44493 [R_{int} = 0.0564, R_{sigma} = 0.0631]
Data/restraints/parameters	44493/2/1919
Goodness-of-fit on F^2	1.019
Final R indexes [I>=2σ (I)]	R_1 = 0.0477, wR_2 = 0.1357
Final R indexes [all data]	R_1 = 0.0507, wR_2 = 0.1379
Largest diff. peak/hole / e Å^{-3}	1.83/-1.27

6.6: Compound **28**, (M^+)[In(bbc)Cl]

In^{3+} SBUs in MOFs are of interest due to their applicability as solid state Lewis acid catalysts. However, their applicability has been limited due to the use of small ligands in reported In-MOFs, which restricts the accessibility of the In(III) centre. Hence, the combination of In^{3+} and bbc^{3-} was used, with the expectation of a highly porous, 3-connected, two-dimensional net structure as a result. Compound **28** was synthesised by heating a solution of H_3bbc and $InCl_3{\cdot}4H_2O$ in DMF, under autogenous pressure at 120°C for 96 hours. Transparent, rod-shaped single crystals of **28** were obtained. Single crystal X-ray diffraction studies showed the adoption of a two-dimensional MOF structure composed of mononuclear In^{3+} centres linked by fully deprotonated bbc^{3-} ligands. Unlike the usual 8-coordinated environment observed around In^{3+} in MOFs, typically due to coordination by four chelating carboxylate groups, **28** shows a highly unusual Cl^- capped 7-coordinated environment, resulting in a negative charge overall on the SBU and the framework (Table 6.9).[23] We propose that this negative charged is countered by the presence of unidentified cations in the MOF pores, resulting in an overall formula of (M^+)[In(bbc)Cl]. The structure of **28** was solved in the monoclinic crystal system, and the $P2_1/n$ space group, with cell dimensions of a = 25.201(7) Å, b = 14.078(4) Å, and c = 37.757(12) Å, and β = 90.82(2)°.

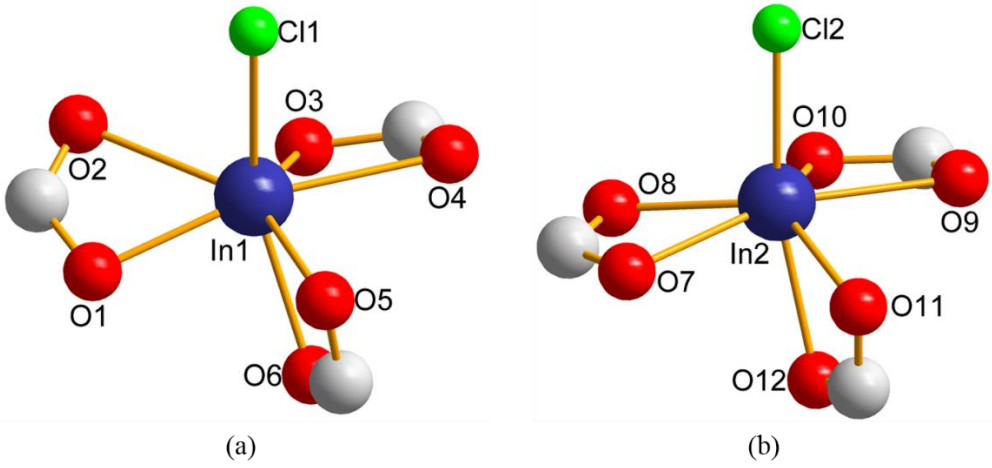

Figure 6.27 – A representation of the crystallographically distinct - (a) and (b) - {In} SBUs in 28.

Two crystallographically distinct In^{3+} centres are present in **28**, and are the SBUs for two interwoven 2D frameworks that together result in a single 2D layer (Fig. 6.27). The structure of **28** consists of layer-by-layer packing of these dual 2D nets. Each In^{3+} is bound

to three carboxylate groups from distinct bbc^{3-} linkers, and each bbc^{3-} linker is bound to three {In} SBUs.

Table 6.9 - Selected interatomic distances and angles in 28.

Atoms	Distance		Atoms	Angle
In1-Cl1	2.385(3) Å		Cl1-In1-O1	104.6(2)°
In1-O1	2.16(1) Å		Cl1-In1-O2	85.5(3)°
In1-O2	2.46(1) Å		O2-In1-O3	78.2(3)°
In1-O3	2.152(8) Å		O4-In1-O5	85.7(3)°
In1-O4	2.466(8) Å		O1-In1-O6	84.8(3)°
In1-O5	2.240(7) Å			
In1-O6	2.277(8) Å			
In2-Cl2	2.341(4) Å		Cl2-In2-O8	100.9(2)°
In2-O7	2.337(8) Å		Cl2-In2-O7	96.8(2)°
In2-O8	2.178(8) Å		O7-In2-O11	79.3(3)°
In2-O9	2.376(8) Å		O12-In2-O9	81.6(2)°
In2-O10	2.157(8) Å		O11-In2-O9	81.0(3)°
In2-O11	2.164(7) Å		O8-In2-O10	81.7(3)°
In2-O12	2.277(7) Å		O7-In2-O9	160.1(3)°

As a result of the orientation of carboxylate carbon atoms in the SBU into a triangular orientation, the extension provided by ligands results in networks with hexagonal cavities. Ligand torsions close to 90° are observed between the central phenyl ring and peripheral benzoate groups, facilitating the formation of 2D structures. Possible porosity in **28** is extrinsic to each 2D layer, and the structure packs so as to allow hexagonal channels to form. Each individual 2D net obtained may be described as a uninodal 3-connected net. Topological reduction of **28** shows that the point symbol of the underlying net is $\{6^3\}$, and the associated RCSR notation is **hcb** (honeycomb) (Fig. 6.28).

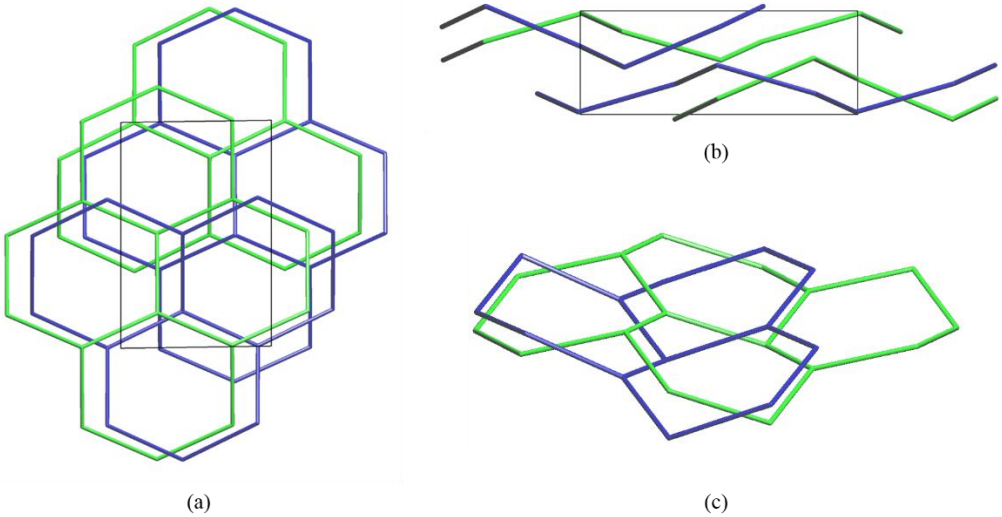

Figure 6.28 – Topological reduction of 28 into interwoven hcb nets viewed along the approximate crystallographic (a) *b*-, and (b) *a*-directions; (c) a single interwoven pair of hcb nets in 28.

The porosity of the framework is due to channels along the crystallographic *b*-axis, which have a limiting diameter of 9.6 Å despite the interweaving of nets. The maximum void diameter is 11.2 Å, and the void volume is determined to be 51.4%.[27,28]

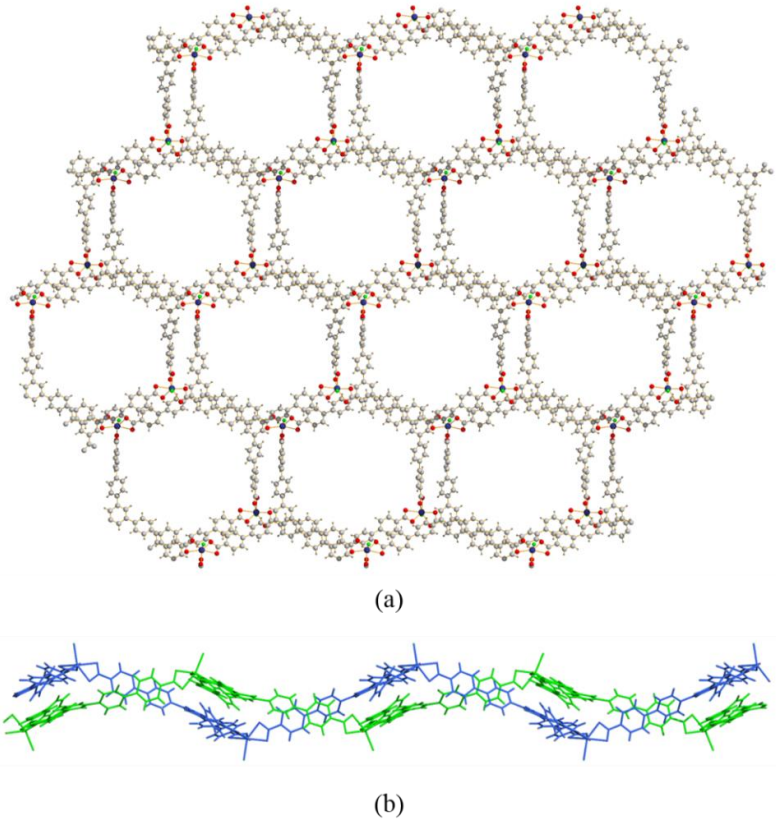

Figure 6.29 – Representations of the crystal structure of 28: (a) Packing representation viewed along the crystallographic *c*-direction. Colour scheme: indigo, In; green, Cl; grey, C; light grey, H; red, O. (b) Wireframe representation of the relative orientation of separate 2D bilayer nets (coloured separately) in 26 viewed along the crystallographic *a*-direction.

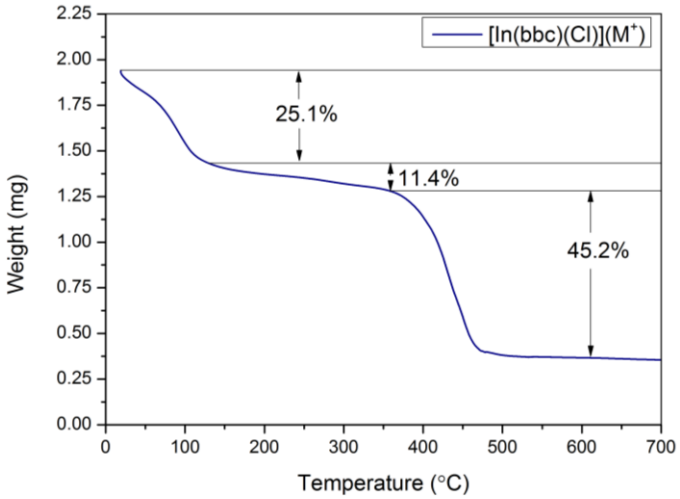

Figure 6.30 – Thermogravimetric analysis for 28.

Experimental thermogravimetric analysis of **28** shows a preliminary loss of solvent corresponding to 25.1% weight below 120°C, followed by a ligand decomposition step at ca. 380°C (Fig. 6.30). Further characterisation of the phase purity of as-synthesised **28** was carried out using PXRD and FTIR techniques. Minor mismatches between experimentally observed and simulated peak intensities are attributed to preferred orientation effects.

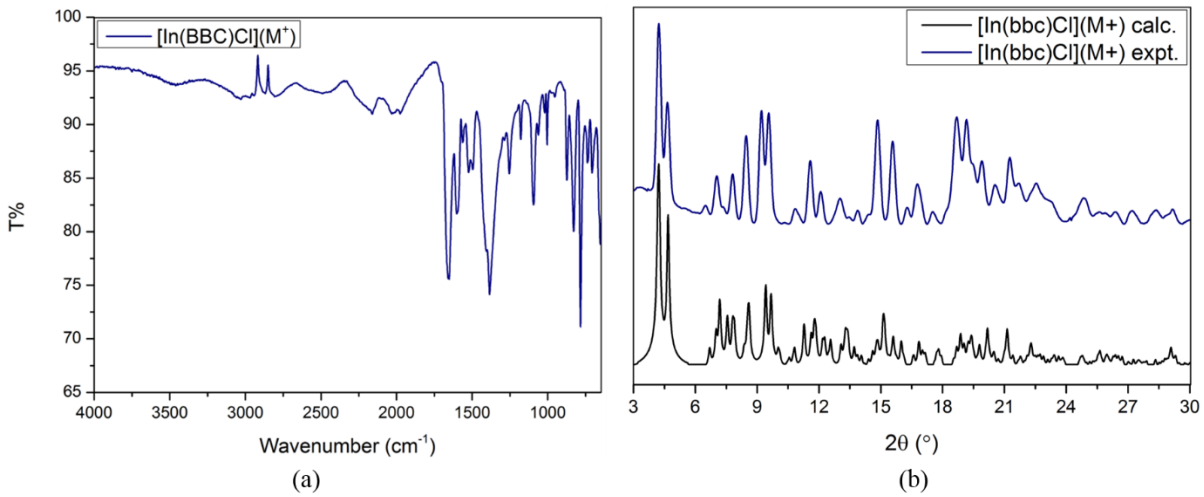

Figure 6.31 – FTIR spectrum (a) and PXRD pattern (b) for 28.

FTIR spectroscopy carried out on **28** showed a broad signal centred at 3462 cm^{-1}, due to the interactions of constitutional DMF molecules with the MOF pore. C=O stretching vibrations in DMF molecules correspond to the strong band at 1652 cm^{-1}. Overlapping signals between 1602 cm^{-1} and 1254 cm^{-1} are observed due to C=O and C=C vibrations. Strong bands at 1524 cm^{-1} and 1385 cm^{-1} are assigned to $\nu_{as}COO$ and $\nu_{s}COO$ respectively.

Therefore we obtain a Deacon-Phillips Δ value equal to 139 cm^{-1}, which agrees with empirical observations for the chelating carboxylate binding mode exhibited in **28** (Fig. 6.31).[32]

Simulations of porosity were carried out using the Poreblazer suite.[29] The nitrogen-accessible surface area of **28** was found to be 1602 m^2/g, which would be the highest surface area for a 2D indium-organic framework to the best of our knowledge. The helium pore volume was found to be 0.764 cm^3/g, and the maximum pore diameter and limiting pore diameter are 9.26 Å and 10.75 Å, respectively. These values are in agreement with crystallographic determinations. The pore size distribution was simulated, and is shown in Figure 6.32. **28** is therefore shown to be potentially highly porous.

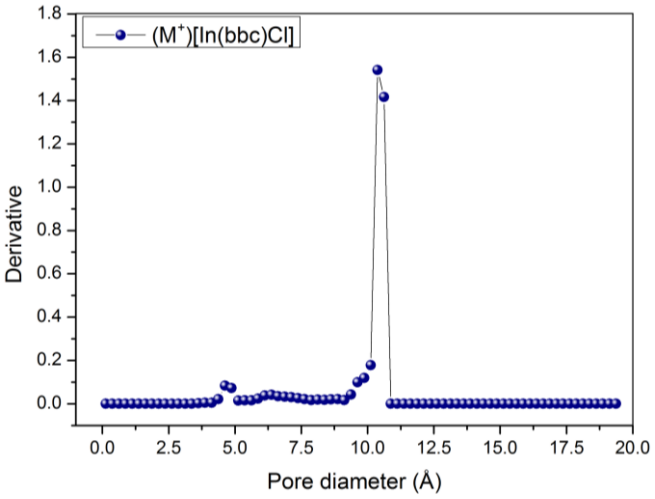

Figure 6.32 – Simulated pore size distribution of 28.

Crystallographic details for **28** are listed in Table 6.10.

Table 6.10 – Crystallographic details for 28.

Identification code	28
Empirical formula	$C_{45}H_{27}ClInO_6$
Formula weight	465.11
Temperature/ K	100(2)
Crystal system	monoclinic
Space group	$P2_1/n$
***a*/Å**	25.201(7)
***b*/Å**	14.078(4)
***c*/Å**	37.757(12)
***α*/°**	90
***β*/°**	90.82(2)
***γ*/°**	90
Volume/Å^3	13394(7)
Z	8
ρ_{calc} / g/cm^3	0.807
μ/mm^{-1}	0.420
F(000)	3288.0
Crystal size/mm^3	0.20 × 0.10 × 0.10
Radiation/Å	MoKα (λ = 0.71073)
2θ range for data collection/°	1.93 to 43.064
Index ranges	$-25 \leq h \leq 25$, $-14 \leq k \leq 14$, $-38 \leq l \leq 38$
Reflections collected	98606
Independent reflections	15303 [R_{int} = 0.1206, R_{sigma} = 0.0951]
Data/restraints/parameters	15303/12/787
Goodness-of-fit on F^2	1.084
Final R indexes [I>=2σ (I)]	R_1 = 0.0826, wR_2 = 0.2463
Final R indexes [all data]	R_1 = 0.1291, wR_2 = 0.2664
Largest diff. peak/hole / e Å^{-3}	0.90/-0.72

6.7: Conclusions

In this chapter, we report the synthesis and crystal structures of five targeted metal-organic frameworks, **24**-**28**. **24**, $[Co_3(bteb)_2(DMF)_2]$, is the Co(II) analogue of TCM-1. We report the synthesis and crystal structure of **24**, and use simulations to demonstrate that it is highly porous. UMCs available on the apical positions of the hourglass SBU allow access to Co^{2+} centres. Coupled with the high porosity, this is an attractive structural feature for the use of **24** in heterogeneous catalysis.

25, $[Zr_6(bteb)_4(\mu_3\text{-}O)_4(\mu_3\text{-}OH)_4(H_2O)_4]$, was synthesised with the objective of obtaining a highly porous Zr-bteb MOF with a sufficiently low ligand connectivity for UMCs to be present on the $\{Zr_6\}$ SBU. **25** was characterised by single crystal X-ray crystallography and physicochemical techniques, and found to be phase pure. Experimental and simulated determinations of porosity are carried out, and show that **25** is highly porous.

26, $[Mn_3(bbc)_2(DMF)_4]$, was synthesised using the H_3bbc ligand and characterised in phase-pure form. The default **kgd** net was shown to be adopted, and the porosity of **26** was shown by simulation to be high. **27**, $[Pb_6(bbc)_4(DMF)_2]$, also formed with high purity, and its synthesis, crystal structure and physicochemical characterisation are described here. Pb^{2+} centres show hemidirected coordination environments and UMCs, and are linked into a polymeric 1D rod-shaped SBU. Large hexagonal channels run through the structure, and simulations show that **27** is highly porous. **28**, $(M^+)[In(bbc)Cl]$, was synthesised and characterised, using In^{3+} metal centres in mononuclear SBUs, with an unusual Cl^- capping ligand present. This results in a negatively charged framework overall, which adopts an interpenetrated honeycomb 2D-net structure. The use of the highly extended bbc^{3-} linker results in simulations of the highest porosity for In-MOFs to date.

Therefore, rational synthetic procedures to obtain crystals of **24** and phase-pure crystalline samples of **25**-**28** are described. These MOFs have conventional topologies, but the use of the highly extended $bteb^{3-}$ and bbc^{3-} linkers leads to high porosities. The presence of UMCs in the structures of **24**-**27** presents a number of possibilities for future applications of these MOFs, and the charged framework and high porosity of **28** makes it an interesting candidate for catalytic applications as well.

The synthesis of **24** appears to depend on the presence of $(NH_2Me_2)^+$ species in solution during synthesis, and therefore obtaining phase pure samples may be approached by using lower temperature procedures, and fresh, high-grade DMF. The experimental determination of porosity for **26**-**28** is an apparent direction for future investigation.

6.8: References

1 H. Furukawa, N. Ko, Y. B. Go, N. Aratani, S. B. Choi, J. Kim and O. M. Yaghi, *Science*, 2010, **329**, 424–429.

2 T. C. Wang, W. Bury, D. A. Gómez-Gualdrón, N. A. Vermeulen, J. E. Mondloch, P. Deria, K. Zhang, P. Z. Moghadam, A. A. Sarjeant, R. Q. Snurr, J. F. Stoddart, J. T. Hupp and O. K. Farha, *J. Am. Chem. Soc.*, 2015, **137**, 3585–3591.

3 H. Furukawa, Y. B. Go, N. Ko, Y. K. Park, F. J. Uribe-Romo, J. Kim, M. O'Keeffe and O. M. Yaghi, *Inorg. Chem.*, 2011, **50**, 9147–9152.

4 I. Hönicke, I. Senkovska, V. Bon, I. Baburin, N. Boenisch, S. Raschke and J. D. Evans, *Angew. Chem. Int. Ed.*, 2018, **57**, 13780–13783.

5 N. Zhu, G. Tobin and W. Schmitt, *Chem. Commun.*, 2012, **48**, 3638–3640.

6 G. Yu and S. Gan, *J. Mol. Struct.*, 2015, **1091**, 159–162.

7 F. Luo, Y. Che and J. Zheng, *Cryst. Growth Des.*, 2009, **9**, 1066–1071.

8 Y. Wang, B. Bredenkötter, B. Rieger and D. Volkmer, *J. Chem. Soc. Dalt. Trans.*, 2006, 689–696.

9 L. Pan, H. Liu, X. Lei, X. Huang, D. H. Olson, N. J. Turro and J. Li, *Angew. Chem. Int. Ed.*, 2003, **42**, 542–546.

10 H. Y. Cho, D. A. Yang, J. Kim, S. Y. Jeong and W. S. Ahn, *Catal. Today*, 2012, **185**, 35–40.

11 M. Tonigold, Y. Tu, B. Bredenkötter, B. Rieger, S. Bahnmüller, J. Hitzbleck, G. Langstein and D. Volkmer, *Angew. Chem. Int. Ed.*, 2009, **48**, 7546–7550.

12 J. H. Cavka, S. Jakobsen, U. Olsbye, N. Guillou, C. Lamberti, S. Bordiga and K. P. Lillerud, *J. Am. Chem. Soc.*, 2008, **6**, 13850–13851.

13 J. E. Mondloch, W. Bury, D. Fairen-Jimenez, S. Kwon, E. J. Demarco, M. H. Weston, A. A. Sarjeant, S. T. Nguyen, P. C. Stair, R. Q. Snurr, O. K. Farha and J. T. Hupp, *J. Am. Chem. Soc.*, 2013, **135**, 10294–10297.

14 T. Sawano, Z. Lin, D. Boures, B. An, C. Wang and W. Lin, *J. Am. Chem. Soc.*, 2016, **138**, 9783–9786.

15 L. Cao, Z. Lin, W. Shi, Z. Wang, C. Zhang, X. Hu, C. Wang and W. Lin, *J. Am. Chem. Soc.*, 2017, **139**, 7020–7029.

16 S. Lee, H. B. Bürgi, S. A. Alshmimri and O. M. Yaghi, *J. Am. Chem. Soc.*, 2018, **140**, 8958–8964.

17 J. He, M. Zeller, A. D. Hunter and Z. Xu, *J. Am. Chem. Soc.*, 2012, **134**, 1553–1559.

18 X. P. Zhou, Z. Xu, M. Zeller and A. D. Hunter, *Chem. Commun.*, 2009, 5439–5441.

19 L. Shimoni-Livny, J. P. Glusker and C. W. Bock, *Inorg. Chem.*, 1998, **37**, 1853–1867.

20 D. K. Geiger, D. E. Parsons and P. L. Zick, *Acta Crystallogr. Sect. E* , 2014, **70**, 566–572.

21 F. Gándara, B. Gomez-Lor, E. Gutiérrez-Puebla, M. Iglesias, M. A. Monge, D. M. Proserpio and N. Snejko, *Chem. Mater.*, 2008, **20**, 72–76.

22 R. Liang, L. Shen, F. Jing, W. Wu, N. Qin, R. Lin and L. Wu, *Appl. Catal. B Environ.*, 2015, **162**, 245–251.

23 Y. H. Li, S. L. Wang, Y. C. Su, B. T. Ko, C. Y. Tsai and C. H. Lin, *Dalton Trans.*, 2018, **47**, 9474–9481.

24 M. O. Keeffe, M. A. Peskov, S. J. Ramsden and O. M. Yaghi, *Acc. Chem. Res.*, 2008, **41**, 1782–1789.

25 V. A. Blatov, A. P. Shevchenko and D. M. Proserpio, *Cryst. Growth Des.*, 2014, **14**, 3576–3586.

26 A. L. Spek, *Acta Crystallogr. Sect. C*, 2015, **71**, 9–18.

27 C. F. Macrae, P. R. Edgington, P. McCabe, E. Pidcock, G. P. Shields, R. Taylor, M. Towler and J. Van De Streek, *J. Appl. Crystallogr.*, 2006, **39**, 453–457.

28 O. V. Dolomanov, L. J. Bourhis, R. J. Gildea, J. A. K. Howard and H. Puschmann, *J. Appl. Crystallogr.*, 2009, **42**, 339–341.

29 L. Sarkisov and A. Harrison, *Mol. Simul.*, 2011, **37**, 1248–1257.

30 L. M. Aguirre-Díaz, M. Iglesias, N. Snejko, E. Gutiérrez-Puebla and M. Á. Monge, *Chem. Eur. J.*, 2016, **22**, 6654–6665.

31 S. B. Kalidindi, S. Nayak, M. E. Briggs, S. Jansat, A. P. Katsoulidis, G. J. Miller, J. E. Warren, D. Antypov, F. Corà, B. Slater, M. R. Prestly, C. Marti-Gastaldo and M. J. Rosseinsky, *Angew. Chem. Int. Ed.*, 2015, **54**, 221–226.

32 R. J. Phillips and G. B. Deacon, *Coord. Chem. Rev.*, 1980, **33**, 227–250.

Chapter 7

Experimental Section

7.1: Methods

Single Crystal X-Ray Diffraction Analysis: Single crystal X-Ray analysis and refinement were performed by Paul Wix, Friedrich Steuber, Dr. Nianyong Zhu, Dr. Amal Cherian Kathalikattil, Dr. Lauren Macreadie, or Dr. Brendan Twamley, using a Bruker APEX2 Duo diffractometer. X-Ray intensity data were measured at 100 K using a MiTeGen micromount, or 215 K – 230 K, mounted in a glass capillary containing a small amount of solvent, using an Oxford Cryosystem Cobra low temperature device. Frames were integrated with the Bruker SAINT software package and the data corrected for absorption effects using the multi-scan method (SADABS).[1] Structures were solved by intrinsic phasing using XT[2] or by direct methods (SHELXS) and refined with the programs Olex2[3] and XL[4] least squares refinement. Some structures contain large solvent accessible void volume in which solvent molecules could not be located reliably. To account for this, the Platon-SQUEEZE routine[5] was used to calculate the void volume and re-generate the reflection file by excluding the diffraction contributions of these unlocated solvent molecules. The final results are based on the new reflection data.

Pore dimensions were determined using the 'calcvoid' routine in Olex2. The van der Waals radii used in this calculation were previously reported by Bondi,[6] and Rowland and Taylor.[7] Solvent-accessible void volume was determined using the 'voids' sub-programme in CCDC:Mercury, using a pre-set probe radius of 1.2 Å, and a grid spacing of 0.7 Å.

Powder X-Ray Diffraction Analysis: For samples presumed sensitive to desolvation (**1-7**, **11-24**, **26-28**), powder XRD patterns were measured by Paul Wix, Dr. Nianyong Zhu, Dr. Amal Cherian Kathalikattil, or Dr. Brendan Twamley, by sealing crystalline samples under solvent in a glass capillary. The capillaries mounted and centred on a goniometer head on a Bruker APEX II diffractometer for data collection. The data were collected upon 360° φ rotational frames at 2θ values of 10° and 20°, with exposure times of 10 or 20 minutes per frame at a detector distance of 120 mm. Overlapping sections of data were combined and the data was processed using the Bruker APEX II routine XRD2-Eval subprogram.

For structurally robust samples (**8-10, 25**), data collection was carried out using a Bruker D2 Phaser diffractometer using Cu-Kα radiation at 30 kV and 10 mA, with a step size of 0.02° (2θ) between 5 and 55° (2θ), and data were collected at 25°C. Samples were ground

and loaded using a zero-background sample holder. Analysis and background correction were further carried out with the DIFFRAC.EVA program.[8]

Thermogravimetric Analysis: Thermogravimetric analysis (TGA) was carried out using a Perkin Elmer Pyris-1 Thermogravimetric analyser under a nitrogen stream at a flow rate of 20 mL min^{-1}. Measurements were carried out between 25°C and 600°C or 25°C and 700°C at a heating rate of 3°C or 5°C per minute.

FTIR Spectroscopy: Infrared spectroscopy was recorded on a PerkinElmer Spectrum One FT-IR spectrometer using a universal ATR sampling accessory. Data was collected and processed using Spectrum v5.0.1 (2002 PerkinElmer Instrument LLC) software. The scan rate was 16 scans per minute with a resolution of 4 scans in the range 4000-650 cm^{-1}. Standard abbreviations for spectra are used: vs, very strong; s, strong; m, medium; w, weak; vw, very weak; sh, shoulder; br, broad; vbr, very broad.

Photoswitching IR analysis on **12** was carried out using a Bruker TENSOR-II FT-IR spectrometer equipped with a diamond UATR and processed using the OPUS suite. Scans were collected from 4000-200 cm^{-1}.

Gas Sorption Analysis: Adsorption measurements were performed using a Quantachrome Autosorb-iQ instrument. The temperature was maintained at 278, 293, 298, 308, and 323 (±0.1) K using a circulating Dewar and a refrigerated/heated bath circulator (ISOTEMP 4100 R20, Fischer Scientific), and at 77 K using a liquid nitrogen bath. The samples were activated under secondary vacuum prior to the measurements and the mass of the samples was measured after the activation. The N_2, He and CO_2 gases were obtained in CP grade are from BOC Gases Ireland. Activation conditions for various compounds are as listed below.

- **6**, **13-16**, **20**, soaked in DCM for 72 hours; exchanged once every 24 hours; secondary vacuum at 120°C for 12 hours.
- **7**, soaked in DCM for 72 hours; exchanged once every 24 hours; secondary vacuum at 80°C for 12 hours.
- **8**, soaked in MeOH for 24 hours; secondary vacuum at 120°C for 12 hours.
- **10, 10′**, soaked in MeOH for 24 hours; secondary vacuum at 30°C for 12 hours.

- **11**, **12**, TCM-4/5 blanks[9] - soaked in DCM for 72 hours; exchanged once every 24 hours; secondary vacuum at 120°C for 24 hours.
- **25**, soaked in acetone for 72 hours; exchanged once every 24 hours; secondary vacuum at 120°C for 12 hours.

Photoswitching uptake measurements on **11** and **12** were done using a quartz sample cell. Sample irradiation was carried out using a Spectroline ENF-280C/FE UV lamp centred at 365 nm with an inbuilt filter. Blank samples (TCM-4/5) were synthesised as per Zhu et al.[9] Blank adsorption and static and dynamic switching experiments were carried out under identical conditions.

Water-triggered CO_2 Release: Qualitative experiments for observations of water-triggered CO_2 release were carried out with the assistance of Dr. Colm Healy by evacuating a flask containing 30 mg of activated **10**, flushing with CO_2, and maintaining a CO_2 atmosphere for 5 minutes. Following this, the sample was exposed to the ambient atmosphere for a few seconds while a Vernier LabQuest 400 pressure sensor was attached to the mouth of the flask, and 1 mL of deionised water was attached to the system in an L-shaped quick-fit glass tube (Fig. 7.1). The flask was sealed and pressure was allowed to equilibrate. At t = 210 seconds, the L-shaped tube was turned, allowing water to make contact with the sample and trigger a reformation of **10** to **10′**. The sharp pressure increase was recorded and is plotted as a function of time in Fig. 3.49 (see Chapter 3).

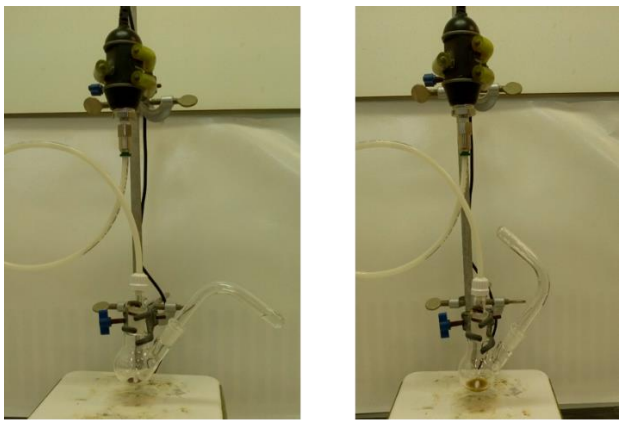

(a) (b)

Figure 7.1. Experimental set-up for the determination of the pressure increase upon liquid water-triggered transformation of 10 to 10′; before (a) and after (b) water is allowed to make contact with the sample of 10.

*Simulation Details for **17***: Simulations of adsorption were carried out by Dr. Matthew Lennox and Dr. Tina Düren at the University of Nottingham using the MuSiC software package.[10] The accessible surface area was calculated by rolling a nitrogen-sized probe sphere (diameter = 3.31 Å) is rolled along the surface of the framework atoms.[11,12]

*Simulation Details for **13-16**, **18-28**:* The Poreblazer 3.0.2 program was used, with the supervision of Dr. Sebastien Vaesen, to calculate accessible surface area (with a dinitrogen molecule as a probe), geometric pore size distribution, structure density, helium pore volume, maximum pore size, and pore limiting diameter from crystal structures rendered as Xmol files using CCDC:Mercury. Universal Force Field parameters were used as pre-set, with parameters added for Cd^{2+}, Pb^{2+}, and In^{3+} taken from Rapp*é et al*.[13,14]

NMR Spectroscopy: ^{1}H and $^{13}C\{^{1}H\}$ NMR, spectra were recorded on a Bruker DPX 400 instrument operating at 400.13 MHz by Dr. John O'Brien and Dr. Manuel Rüther. Samples were prepared in deuterated solvents as mentioned. Standard abbreviations for spectra are used: s, singlet; d, doublet; t, triplet; qt quartet; q, quaternary; m, multiplet; br broad, J, coupling constant.

Mass Spectrometry: Mass spectrometry was carried out on a Micromass LCT Electrospray mass spectrometer by Dr. Martin Feeney and Dr. Gary Hessman. Samples were dissolved in HPLC grade solvents.

Elemental Analysis: Elemental C, H, N, quantitative analysis was performed on samples for additional confirmation of phase purity (**1**, **3**, **4**, **11**, **12**, **17**, **20**) by Ann Connolly and Rónán Crowley using an Exeter Analytical CE 440 at the Analytical Laboratory, UCD Belfield, Dublin.

Hirshfeld Surface Analysis: Hirshfeld surface analysis was carried out using Crystal Explorer, using high resolution settings.[15]

Density Functional Theory calculations: Density functional theory (DFT) calculations were carried out by Swetanshu Tandon out using the Gaussian09 package (see Appendix 9.3).

7.2: Materials

All chemicals used were of reagent grade and procured from standard chemical suppliers. Solvents were supplied by in-house suppliers, and were of technical grade or higher. Water was deionised before use.

The following ligands were used as procured from commercial sources:

- 2,4,6-tris(2-pyridyl)-1,3,5-triazine (2-tpt, Sigma, 98%)
- *2*,4,6-tris(4-pyridyl)-1,3,5-triazine (4-tpt, Tokyo Chemical Industry, 97%)
- 1,4-benzenedicarboxylic acid (H_2bdc, Aldrich, 98%)
- 1,4-biphenyldicarboxylic acid (H_2bpdc, Aldrich, 98%)
- 1,2-bis(4-pyridyl)ethane (bpet, Acros, 97%)
- 1,2-bis(4-pyridyl)propane (tdp, Aldrich, 98%)
- 1,3,5-tris(4′-carboxy[1,1′-biphenyl]-4-yl)benzene (H_3bbc, Aldrich, 95%)

The remaining ligands were synthesised as per modified literature methods as follows.

3,3'-dinitro-4,4'-bipyridine (dnbpy):[16] 8.70 g of 4-chloro-3-nitropyridine (0.055 mol) and 8.40 g copper (0.132 mol) were stirred in 36 mL DMF at 100°C for 16 h. The product mixture was diluted with 300 mL of water and the precipitate was collected by filtration. The solid was washed with water (1x100 mL), ammonia (3x10 mL), ice cold ethanol (2x10 mL) and extracted with hot chloroform. The solvent was removed at reduced pressure. The crude product was recrystallised from ethanol yielding yellow needle crystals. Yield: 1.48 g (6.01 mmol, 11%). ^{1}H-NMR ($CDCl_3$, 400 MHz) δ_H (ppm): 9.53 (2H, s), 8.98 (2H, d), 7.27 (2H, d).

3,3'-diamino-4,4'-bipyridine (dabpy):[16]A solution of 4.30 g tin(II) chloride (22.7 mmol) and 600 mg of 3,3'-dinitro-4,4'-bipyridine (2.44 mmol) in 8.6 mL of hydrochloric was stirred at 100°C for 75 min. The precipitate was separated by filtration after cooling in an ice bath. The solid was dissolved in water. The solution was brought to alkaline pH using sodium hydroxide. The solid was collected by filtration and recrystallised from an ethanol water mixture (4:1) yielding a pale yellow powder. Yield: 116 mg (0.623 mmol, 25%). ESI-

MS (MeOH) *m/z* = 187.10 ($C_{10}H_{10}N_4$); ^{1}H-NMR (DMSO-d_6, 400 MHz) δ_H (ppm): 8.14 (2H, s), 7.86 (2H, d), 6.99 (2H, d).

4,4'-azopyridine (azpy):[17] A solution of 10.1 g of 4-aminopyridine (0.107 mol) in 160 mL water was chilled in an ice bath followed by the drop wise addition of 200 mL of 10% NaOCl (0.269 mol) with constant stirring. After stirring for 2.5 hours in the ice bath, the product was extracted with ether. The solvent was removed by evaporation under reduced pressure. The solid product was recrystallised from water and washed with hexane, yielding bright orange-red needles. Yield: 1.10 g (5.98 mmol, 11%). ^{1}H-NMR ($CDCl_3$, 400 MHz) δ_H (ppm): 8.87 (4H, d), 7.76 (4H, d).

1,3,5-tri(p-carboxyphenyl)benzene (H_3btb): This procedure was carried out in two steps.[18] 3.00 g of 1,3,5-tribromobenzene (9.528 mmol), 6.86 g *p*-methoxycarbonylphenylboronic acid (38.12 mmol), 5.05 g Na_2CO_3 (47.65 mmol), and 0.83 g $Pd(PPh_3)_4$ (0.71 mmol), were refluxed in solution in a toluene-methanol-water mixture (80 mL – 40 mL – 40 mL) under a nitrogen atmosphere for 48 hours. After removal of the solvent, the off-white solid was extracted with dichloromethane (100×3 mL), washed with brine (100 mL), and dried over anh. $MgSO_4$. Silica gel column chromatography was performed (hexane:dichloromethane = 1:5) to give 1,3,5-tri(*p*-methoxycarbonylphenyl)benzene, which was dried under reduced pressure. Yield: 3.70 g (81%). ^{1}H NMR ($CDC1_3$): δ_H (ppm): 3.97 (9H, s), 7.90 (2H, d), 8.07 (2H, d), 8.46 (2H, d) 8.49 (1H, t).

2.00 g, 1,3,5-tri(*p*-methoxycarbonylphenyl)benzene (4.2 mmol) was suspended in 60 mL THF-MeOH (30 mL – 30 mL), and 30 mL of 10% NaOH (aq) was added in small aliquots. The mixture was stirred overnight, and the volume of solvent was approximately halved by rotary evaporation. The pH was lowered to approximately 2 by the addition of 3 M HCl. The resulting white precipitate of 1,3,5-tri(*p*-carboxyphenyl)benzene was collected by filtration, washed with deionised water, and dried under vacuum. (1.41 g, 77%). ^{1}H-NMR (DMSO-d_6, 400 MHz) δ_H (ppm): 13.05 (3H, s), 8.10 (3H, s), 8.07 (12H, s).

4,4',4''-(benzene-1,3,5-triyltris(ethyne-2,1-diyl)tribenzoic acid *(H_3bteb):* This procedure was carried out in four steps.[19,20]

Synthesis of 1,3,5-tris(trimethylsilylethynyl)benzene: 250 mL of dry trimethylamine was added to a flask containing 9.45 g of 1,3,5-tribromobenzene (30 mmol), 0.400 g $Pd(PPh_3)_2Cl_2$ (0.57 mmol), and 0.050 g CuI (0.26 mmol) under a nitrogen atmosphere. 10.60 g of trimethylsilylacetylene (108 mmol) was added and the mixture was stirred at 60°C for 7 hours. The product mixture was filtered after cooling to room temperature, and the filtrate was dried by rotary evaporation. The brown oil obtained was dissolved in hexane and filtered through a silica plug. The filtrate was dried by rotary evaporation. Yellow crystals were obtained on standing. Yield: 10.10 g (27.6 mmol, 92%). ^{1}H-NMR ($CDCl_3$, 400MHz) δ_H (ppm): 7.49 (3H, s), 0.25 (27H, s).

Synthesis of 1,3,5-triethynylbenzene: 5.50 g of 1,3,5-tris(trimethylsilylethynyl)benzene (15.0 mmol) was added to a mixture of 11.15 g of K_2CO_3 (80 mmol), 25 mL of dichloromethane, and 250 mL of methanol, and stirred for 30 minutes. The mixture was then passed through a silica plug, and washed with 4x50 mL of methanol. The filtrate was transferred to a separating funnel and washed with a mixture of brine and dichloromethane. The dichloromethane fraction was collected and the solvent was removed. 1,3,5-triethynylbenzene was obtained as white needle crystals. Yield: 2.100 g (14.0 mmol, 93%). ^{1}H-NMR ($CDCl_3$, 400MHz) δ_H (ppm): 7.60 (3H, s), 3.14 (3H, s).

Synthesis of trimethyl 4,4',4''-(benzene-1,3,5-triyltris(ethyne-2,1-diyl))tribenzoate: 2.10 g of 1,3,5-triethynylbenzene (0.014 mmol), 11.170 g (44.6 mmol) 4-methyliodobenzoate, 0.224 g (0.117 mmol) CuI, and 0.335 g (0.446 mmol) $Pd(PPh_3)_2Cl_2$ were stirred in 180 mL of trimethylamine at 35°C for 48 hours under a nitrogen atmosphere. The solvent was removed from the product mixture and it was redissolved in dichloromethane. This solution was filtered and the filtrate was purified by column chromatography (dichloromethane, dichloromethane: ethyl acetate = 1:1) yielding a yellow powder. Yield: 4.90 g (8.8 mmol, 63%). ^{1}H-NMR ($CDCl_3$, 400MHz) δ_H (ppm): 8.06 (6H, d, J=7.8Hz), 7.71 (3H, s), 7.61 (6H, d, J=7.8Hz), 3.96 (9H, s).

Synthesis of 4,4',4''-(benzene-1,3,5-triyltris(ethyne-2,1-diyl)tribenzoic acid, *H_3bteb*: A saturated LiOH solution (5.405g, 0.129 mol, in 25 mL of deionised water) was added to a solution of 4.90 g (8.8 mmol) of trimethyl 4,4',4''-(benzene-1,3,5-triyltris(ethyne-2,1-diyl))tribenzoate in 100 mL of tetrahydrofuran and stirred overnight. The mixture was

heated at 70°C for 30 minutes and then allowed to cool. The mixture was acidified using 3 M HCl until visible precipitation stopped. The precipitate was washed with methanol and purified by column chromatography using tetrahydrofuran as eluent. The solvent was removed by rotary evaporation, and the solid obtained was dried further using a Schlenk vacuum line, yielding an off-white powder. Yield 3.37 g (6.6 mmol, 75%). ES-MS (THF) m/z = 509.10 ($C_{33}H_{18}O_6$); Decomposes ca. 270°C, melting point could not be determined; ^{1}H-NMR (DMSO-d_6, 400MHz) δ_H (ppm): 11.73 (3H, s), 7.99 (6H, d, J=8 Hz), 7.86 (3H, s), 7.71 (6H, d, J=8 Hz); ^{13}C{^{1}H}-NMR (DMSO, 100 MHz) δ_C (ppm): 166.7, 134.6, 131.8, 131.0, 129.6, 126.0, 123.3, 90.2, 89.7; FTIR (diffuse reflectance) ν_{max} cm^{-1}: 2980 (br), 2761 (br), 2558 (br) 1690 (s), 1605 (s), 1560 (m), 1420 (s), 1314 (s), 1284 (s), 1177 (m), 1111 (w), 857 (s), 769 (s).

Compounds **1**-**28** were synthesised by the following procedures. Yields are determined using the weights of air-dried samples and the crystallographically determined framework formula. These are therefore approximate.

1, *[Zn(2-tpt)(Hbtb)]·DMF:* 10.00 mg (0.034 mmol) of $Zn(NO_3)_2{\cdot}6H_2O$ was added to a slurry of 11.00 mg (0.035 mmol) of 2,4,6-tris(2-pyridyl)-1,3,5-triazine (2-tpt) and 15.00 mg (0.034 mmol) of 4,4′,4″-(benzene-1,3,5-triyl)trisbenzoic acid (H_3btb) in 1 mL of *N*,*N*-dimethylformamide in a screw-top vial. The vial was agitated for a few minutes until the slurry was clarified, then heated at 100°C for four days. The product was obtained as a pale yellow crystalline solid and dried in air. Yield: 9.40 mg, 28%. CHN analysis calculated for $C_{51}H_{42}N_8O_8Zn$ (with two constitutional DMF molecules per formula unit): C 63.79%, H 4.41%, N 11.67%; experimental: C 63.10%, H 3.76%, N 11.03%.

2, *[Ni(2-tpt)(Hbtb)]·0.5DMF:* 10.00 mg (0.034 mmol) of $Ni(NO_3)_2{\cdot}6H_2O$ was added to a slurry of 11.00 mg (0.035 mmol) of 2,4,6-tris(2-pyridyl)-1,3,5-triazine (2-tpt) and 15.00 mg (0.034 mmol) of 4,4′,4″-benzene-1,3,5-triyl-tris(benzoic acid) (H_3btb) in 1 mL of *N*,*N*-dimethylformamide in a screw-top vial. The vial was agitated for a few minutes until the slurry was clarified, then heated at 100°C for four days. The product was obtained as individual green single crystals, separated by hand, and dried in air. Yield: <5%.

3, *[Mn(2-tpt)(Hbtb)]·1.25DMF:* 7.00 mg (0.035 mmol) of $MnCl_2 \cdot 4H_2O$ was added to a slurry of 11.00 mg (0.035 mmol) of 2,4,6-tris(2-pyridyl)-1,3,5-triazine (2-tpt) and 15.00 mg (0.034 mmol) of 4,4′,4″-benzene-1,3,5-triyl-tris(benzoic acid) (H_3btb) in 1 mL of *N*,*N*-dimethylformamide in a screw-top vial. The vial was agitated for a few minutes until the slurry was clarified, then heated at 100°C for four days. The product was obtained as a pale orange crystalline solid and dried in air. Yield: 5.61 mg, 17%. CHN analysis calculated for $C_{51}H_{46}N_8O_{10}Mn$ (with two constitutional DMF molecules and two constitutional water molecules per formula unit): C 62.13%, H 4.70%, N 11.37%; experimental: C 61.98%, H 3.75%, N 12.75%.

4, *[Cd(2-tpt)(Hbtb)]·DMF:* 10.00 mg (0.032 mmol) of $Cd(NO_3)_2 \cdot 4H_2O$ was added to a slurry of 11.00 mg (0.035 mmol) of 2,4,6-tris(2-pyridyl)-1,3,5-triazine (2-tpt) and 15.00 mg (0.034 mmol) of 4,4′,4″-benzene-1,3,5-triyl-tris(benzoic acid) (H_3btb) in 1 mL of *N*,*N*-dimethylformamide in a screw-top vial. The vial was agitated for a few minutes until the slurry was clarified, then heated at 100°C for four days. The product was obtained as a clear crystalline solid and dried in air. Yield: 10.04 mg, 29%. CHN analysis calculated for $C_{51}H_{42}N_8O_8Cd$ (with two constitutional DMF molecules per formula unit): C 60.81%, H 4.20%, N 11.12%; experimental: C 60.73%, H 3.74%, N 10.66%.

5*, [Co_3(4-tpt)$_2$(btb)$_2$(DMF)$_2$]:* 10.00 mg of $Co(NO_3)_2 \cdot 6H_2O$ (0.034 mmol) was added to a mixture of 11.00 mg (0.035 mmol) of 2,4,6-tris(4-pyridyl)-1,3,5-triazine (4-tpt) and 15.00 mg (0.034 mmol) of 4,4′,4″-benzene-1,3,5-triyl-tris(benzoic acid) (H_3btb) in 1 mL of *N*,*N*-dimethylformamide. The mixture was heated to 85°C for two days. The product was obtained as pink crystals. Yield: 12.12 mg, 58.0%.

6*, [Zn_3(bdc)$_3$(dabpy)]:* 3.53 mg of $Zn(NO_3)_2 \cdot 6H_2O$ (0.012 mmol), 4.08 mg of H_2bdc (0.017 mmol) and 1.27 mg of 3,3'-diamino-4,4'-bipyridine (dabpy) (0.007 mmol) were dissolved in 0.5 mL DMF and 0.5 mL EtOH. This mixture was heated at 90°C for 24 hours in an autoclave, yielding yellow crystals. Yield: 2.64 mg, 75%.

7*, [Co_3(bpdc)$_3$(dabpy)]:* 4.00 mg of $Co(NO_3)_2 \cdot 6H_2O$ (0.014 mmol), 4.91 mg of H_2bpdc (0.020 mmol) and 1.88 mg of 3,3'-diamino-4,4'-bipyridine (dabpy) (0.010 mmol) were

dissolved in 1 mL DMF and sonicated for 10 min. This mixture was heated at 150°C for 72 hours in an autoclave, yielding violet crystals. Yield: 3.10 mg, 61%.

***8**, [Cu(bpet)$_2$SiF$_6$]:*

- Bulk material: 32 mg of $CuSiF_6 \cdot H_2O$ (0.155 mmol) dissolved in 1 mL of dry MeOH:$CHCl_3$ (9:1) was added dropwise to a solution of 22 mg of 1,2-bis(4-pyridyl)ethane (0.119 mmol) in 1 mL of dry MeOH in a glass vial. The purple precipitate was collected after being left to stand for 10 minutes and dried in air. Yield: 27.1 mg, 79%.
- Single Crystals: A solution of 1.86 mg of $CuSiF_6 \cdot H_2O$ (0.008 mmol) in 400 µl DMSO was pipetted into the bottom of a glass tube with a diameter of 3 mm. 300 µl DMSO was layered over this solution. A solution of 1.11 mg of 1,2-bis(4-pyridyl)ethane (0.006 mmol) in 400 µl of dry MeOH was layered on top of the previous two layers. Faint purple rod-like crystals were obtained after diffusion at room temperature for 2 weeks.

***9**, [Cu(tdp)$_2$SiF$_6$]:* A solution of 20.6 mg $CuSiF_6 \cdot H_2O$ (0.100 mmol) in 2 mL methanol was layered over a solution of 9.9 mg of 1,2-bis(4-pyridyl)propane (0.050 mmol) in 2 mL chloroform in a narrow vial. The vial was sealed and allowed to stand undisturbed. Purple rod crystals were collected after six weeks and dried in air. Yield: 4.3 mg, 29%.

***10**, [Cu(azpy)$_2$SiF$_6$]:*

- Bulk material: 14 mg of $CuSiF_6 \cdot H_2O$ (0.063 mmol) and 24 mg of 4,4'-azopyridine (0.130 mmol), were dissolved in 10 mL of dry MeOH in a glass vial. The vial was heated to 85°C for 90 minutes and allowed to cool to room temperature. The maroon solid was collected and dried under vacuum at room temperature. Yield: 27.0 mg, 76%.
- Single Crystals: A solution of 1.86 mg of $CuSiF_6 \cdot H_2O$ (0.008 mmol) in 400 µl DMSO was pipetted into the bottom of a glass tube with a diameter of 3 mm. 300 µl DMSO was layered over this solution. A solution of 1.06 mg of 4,4'-azopyridine (0.006 mmol) in 400 µl of dry MeOH was layered on top of the previous two layers. Maroon rod-like crystals were obtained after diffusion at room temperature for 2 weeks.

***10'**, [Cu(H$_2$O)$_2$(azpy)$_2$]SiF$_6 \cdot$H$_2$O:*

- Bulk Material: 140 mg of $CuSiF_6 \cdot H_2O$ (0.626 mmol) and 240 mg of 4,4'-azopyridine (1.30 mmol) were dissolved in 100 mL of 1:1 H_2O:MeOH. This mixture was stirred under

reflux for 12 hours and then cooled to room temperature. The green solid was collected by filtration. Yield: 266 mg, 70%.

- Single Crystals: 1.5 mg of $CuSiF_6 \cdot H_2O$ (0.007 mmol) and 2.3 mg of 4,4'-azopyridine (0.012 mmol) were dissolved in 1 mL of a 1:1 H_2O:MeOH. 500 µL of nitrobenzene were added. The mixture was sonicated for ten minutes and heated to 85°C for 12 hours, then left to cool for 12 hours. Green bipyramidal crystals of **10′** were obtained.

11, *$[Cu_3(bteb)_2(azpy)(H_2O)]$:* 0.0254 g of H_3bteb (0.050 mmol) and 0.0177 g of $Cu(NO_3)_2 \cdot 3H_2O$ (0.073 mmol) were added to 1 mL of DMF in a glass vial and sonicated for 10 minutes. 0.0033 g of 4,4'-azopyridine (0.0018 mmol) were added to the reaction mixture. The vial was sealed and heated at 85°C for 24 hours. Green block crystals of **11** were obtained. The crystals were washed with DMF and stored under DMF. Yield: 13.6 mg, 39%. CHN analysis: $C_{76}H_{40}Cu_3O_{13}N_4$ (with 8 constitutional water molecules per formula unit) - Calculated: C 58.82%, H 3.64%, N 3.61%; Found: C 58.57%, H 3.14%, N 4.14%.

12, *$[Cu_3(bteb)_2(azpy)_{0.5}(H_2O)_2]$:* 0.0254 g of H_3bteb (0.050 mmol) and 0.0177 g of $Cu(NO_3)_2 \cdot 3H_2O$ (0.073 mmol) were added to 1 mL of DMF in a glass vial and sonicated for 10 minutes. 0.0011 g of 4,4'-azopyridine (0.0006 mmol) were added to the reaction mixture. The vial was sealed and heated at 85°C for 8 hours. Green needle crystals of **12** were obtained. The crystals were separated from a minor amorphous co-product by hand, washed with DMF and stored under DMF. Yield: 3.7 mg, 11%. CHN analysis: $C_{142}H_{76}Cu_6N_4O_{28}$ (with 6 constitutional water molecules per formula unit) - Calculated: C 61.45%, H 3.20%, N 2.02%; Found: C 61.59%, H 2.56%, N 1.93%.

13, *$[Ni_6(btb)_4(dabpy)_3]$:* 31.66 mg of $Ni(NO_3)_2 \cdot 6H_2O$ (0.109 mmol), 10.84 mg of H_3btb (0.025 mmol) and 4.96 mg of 3,3'-diamino-4,4'-bipyridine (dabpy) (0.027 mmol) were dissolved in 1 mL DMF and heated at 120°C for 50 hours to obtain green crystals. Yield: 5.4 mg, 30%.

14, *$[Co_6(btb)_4(dabpy)_3]$:* 8.64 mg of $Co(NO_3)_2 \cdot 6H_2O$ (0.030 mmol), 8.41 mg of H_3btb (0.019 mmol) and 2.87 mg of 3,3'-diamino-4,4'-bipyridine (dabpy) (0.015 mmol) were

dissolved in 1 mL DMF and heated at 85°C for 72 hours to obtain green crystals. Yield: 2.3 mg, 17%.

***15**, [$Zn_6(btb)_4(dabpy)_3$]:* 4.96 mg of $Zn(NO_3)_2 \cdot 6H_2O$ (0.017 mmol), 4.84 mg of H_3btb (0.011 mmol) and 1.54 mg of 3,3'-diamino-4,4'-bipyridine (dabpy) (0.008 mmol) were dissolved in 1 mL DMF and heated at 85°C for 48 hours to obtain pale yellow crystals. Yield: 3.2 mg, 45%.

***16**, [$Zn_6(btb)_4(dnbpy)_3$]:* 4.96 mg of $Zn(NO_3)_2 \cdot 6H_2O$ (0.017 mmol), 4.84 mg of H_3btb (0.011 mmol) and 2.04 mg of 3,3'-dinitro-4,4'-bipyridine (dnbpy) (0.008 mmol) were dissolved in 1 mL DMF and heated at 85°C for 48 hours to obtain golden yellow crystals. Yield: 2.1 mg, 27%.

***17**, [$Cu_3(bteb)_2(H_2O)_2(DMF)$]:* To a solution of 65 mg (0.270 mmol) of $Cu(NO_3)_2 \cdot 3H_2O$ in DMF (2 mL), was added 94 mg of H_3bteb (0.184 mmol). The resulting mixture was sonicated for 10 min. Then, a solution of 15 mg of 4,4′-bipyridine (0.100 mmol) in DMF (0.25 mL) was added to this mixture. The resulting reaction mixture was kept in a closed vial at 85°C for 48 hours. A mixture containing light-blue, plate-like crystals (TCM-8), blue-green, polyhedral crystals (TCM-4), and aggregates of blue, block-like crystals (**17**) was obtained. Crystals of **17** are distinguishable by their colour and morphology. **17** was isolated from the mixture manually. Yield: <5 %. CHN analysis of a dried sample of **17** ($C_{69}H_{41}Cu_3NO_{15}$) with four constitutional H_2O molecules per formula unit: calcd. C 59.76, H 3.56, N 1.01; found C 59.76, H 3.39, N 1.40.

***18**, [$Cu_6(bbc)_4(H_2O)_5(DMF)$]:* 0.026 g of H_3bbc (0.039 mmol) and 0.0177 g of $Cu(NO_3)_2 \cdot 3H_2O$ (0.073 mmol) were added to 1 mL of DMF in a glass vial and sonicated for 10 minutes. The vial was sealed and heated at 85°C for 24 hours. Isolated blue crystals of **18** were obtained, along with a microcrystalline light blue phase. Yield: <5%.

***19**, [$Cu_3(bbc)_2(azpy)_2$]:* 0.026 g of H_3bbc (0.039 mmol) and 0.0177 g of $Cu(NO_3)_2 \cdot 3H_2O$ (0.073 mmol) were added to 1 mL of DMF in a glass vial. 0.0033 g of 4,4'-azopyridine (0.0018 mmol) were added and the mixture was sonicated for 10 minutes. The vial was

sealed and heated at 85°C for 24 hours. Isolated green crystals of **18** were obtained, along with a microcrystalline light blue phase. Yield: <5%.

***20**, [Cd$_3$(bbc)$_2$(DMF)$_3$(H$_2$O)]:* 0.025 g of H$_3$bbc (0.037 mmol) and 0.020 g of Cd(NO$_3$)$_2$·4H$_2$O (0.065 mmol) were added to 1 mL of DMF in a glass vial and sonicated for 10 minutes. The vial was sealed and heated at 100°C for 96 hours. Large transparent block crystals of **20** were obtained. The mother liquor was exchanged with DMF, and the crystals were stored in DMF. Yield: 14.1 mg, 40%. CHN analysis calculated for C$_{96}$H$_{76}$Cd$_3$N$_2$O$_{18}$ (with two coordinated DMF molecules and four coordinated water molecules per formula unit): C 61.24, H 4.07%, N 1.49%; experimental: C 60.94%, H 3.70%, N 1.53%.

***21**, [Cd$_6$(bbc)$_4$(DEF)$_3$(H$_2$O)$_9$]:* 0.015 g of H$_3$bbc (0.022 mmol) and 0.020 g of Cd(NO$_3$)$_2$·4H$_2$O (0.065 mmol) were added to 1 mL of DEF in a glass vial and sonicated for 10 minutes. The vial was sealed and heated at 100°C for 96 hours. Large transparent block crystals of **21** were obtained, together with minor quantities of unidentified phases. The mother liquor was exchanged with DEF, and the crystals were stored in DEF. Yield: approx. 2.1 mg, 10%.

***22** and **22′**, [Cd$_3$(bteb)$_2$(DMF)$_3$(H$_2$O)]:* 0.0254 g of H$_3$bteb (0.050 mmol) and 0.0226 g of Cd(NO$_3$)$_2$·4H$_2$O (0.073 mmol) were added to 1 mL of DMF in a glass vial and sonicated for 10 minutes. The vial was sealed and heated at 100°C for 72 hours. Pale yellow block crystals of **22** and **22′** were obtained as a product mixture. The mother liquor was exchanged with DMF, and the crystals were stored in DMF. Yields could not be determined.

***23**, [Cd$_3$(bteb)$_2$(DMF)$_3$(azpy)$_{0.5}$]·1.75DMF:* 0.0254 g of H$_3$bteb (0.05 mmol) and 0.0226 g of Cd(NO$_3$)$_2$·4H$_2$O (0.073 mmol) were added to 1 mL of DMF in a glass vial and sonicated for 10 minutes. 0.0033 g of 4,4'-azopyridine (0.0018 mmol) were added to the reaction mixture. The vial was sealed and heated at 100°C for 72 hours. Bright red crystals of 23 was obtained along with pale yellow block crystals of **22**, **22′**, and other phases as a product mixture. The mother liquor was exchanged with DMF, and the crystals were stored in DMF. Yield: <5%.

***24**, [$Co_3(bteb)_2(H_2O)_2$]:* 2.5 mg of H_3bteb (0.005 mmol) and 3.5 mg of $Co(NO_3)_2 \cdot 6H_2O$ (0.012 mmol) were added to 1 mL of DMF in a glass vial and sonicated for 10 minutes. The vial was sealed and heated at 85°C for 16 hours. Pale violet rod shaped crystals of **24** were obtained together with dark violet block crystals of $(Me_2NH_2)[Co_5(bteb)_3(\mu_3\text{-}OH)_2(DMF)_2]$. Yield: <5%.

***25**, [$Zr_6(bteb)_4(\mu_3\text{-}O)_4(\mu_3\text{-}OH)_4(H_2O)_4$]:* 28.8 mg of $ZrCl_4$ (0.12 mmol), 46.4 mg of H_3bteb (0.09 mmol), and 1465 mg (12 mmol) of benzoic acid were dissolved in 8 mL of DMF (used without drying) in a closed vial and heated at 120°C for four days. Colourless crystals were obtained, washed with acetone, and stored under acetone. Yield: 31 mg, 55%.

***26**, [$Mn_3(bbc)_2(DMF)_4$]:* 3.0 mg of $MnCl_2 \cdot 4H_2O$ (0.015 mmol) and 7.0 mg of H_3bbc (0.010 mmol) were added to 1 mL of DMF in a glass vial and sonicated for 10 minutes. The vial was sealed and heated at 120°C for 96 hours. Transparent rod shaped crystals of **26** were obtained. The mother liquor was exchanged with DMF, and the crystals were stored in DMF. Yield: 2.0 mg, 22%.

***27**, [$Pb_6(bbc)_4(DMF)_2$]:* 5.0 mg of $Pb(NO_3)_2$ (0.015 mmol) and 5.0 mg of H_3bbc (0.0075 mmol) were added to 1 mL of DMF in a glass vial and sonicated for 10 minutes. The vial was sealed and heated at 100°C for 48 hours. Transparent rod shaped crystals of **28** were obtained. The mother liquor was exchanged with DMF, and the crystals were stored in DMF. Yield: 4.2 mg, 55%.

***28**, (M+)[In(bbc)Cl]:* 5.0 mg of $InCl_3$ (0.023 mmol) and 5.0 mg of H_3bbc (0.0075 mmol) were added to 1 mL of DMF in a glass vial and sonicated for 10 minutes. The vial was sealed and heated at 120°C for 96 hours. Transparent rod shaped crystals of **28** were obtained. The mother liquor was exchanged with DMF, and the crystals were stored in DMF. Yield could not be determined.

7.3 References

1 Bruker AXS Inc., *SADABS*, Madison, Wisconsin, USA, 2001.

2 G. M. Sheldrick, *Acta Crystallogr. Sect. A*, 2015, **71**, 3–8.

3 O. V. Dolomanov, L. J. Bourhis, R. J. Gildea, J. A. K. Howard and H. Puschmann, *J. Appl. Crystallogr.*, 2009, **42**, 339–341.

4 G. M. Sheldrick, *Acta Crystallogr. Sect. A*, 2008, **64**, 112–122.

5 A. L. Spek, *Acta Crystallogr. Sect. C*, 2015, **71**, 9–18.

6 A. Bondi, *J. Phys. Chem.*, 1964, **68**, 441–451.

7 R. S. Rowland and R. Taylor, *J. Phys. Chem.*, 1996, **100**, 7384–7391.

8 Bruker AXS Inc., *DIFFRAC.EVA Version 4.1*, Karlsruhe, Germany, 2015.

9 N. Zhu, M. J. Lennox, G. Tobin, L. Goodman, T. Düren and W. Schmitt, *Chem. Eur. J.*, 2014, **20**, 3595–3599.

10 A. Gupta, S. Chempath, M. J. Sanborn, L. A. Clark and R. Q. Snurr, *Mol. Simul.*, 2003, **29**, 29–46.

11 L. D. Gelb and K. E. Gubbins, *Langmuir*, 1998, **14**, 2097–2111.

12 T. Düren, F. Millange, G. Férey, K. S. Walton and R. Q. Snurr, *J. Phys. Chem. C*, 2007, **111**, 15350–15356.

13 L. Sarkisov and A. Harrison, *Mol. Simul.*, 2011, **37**, 1248–1257.

14 A. K. Rappé, C. J. Casewit, K. S. Colwell, W. A. Goddard and W. M. Skiff, *J. Am. Chem. Soc.*, 1992, **114**, 10024–10035.

15 S. K. Wolff, D. J. Grimwood, J. J. McKinnon, M. J. Turner, D. Jayatilaka and M. A. Spackman, *Crystal Explorer*, University of Western Australia, 2012.

16 S. Kanoktanaporn and J. A. H. Macbride, *J. Chem. Soc. Perkin Trans. 1*, 1978, 1126–1131.

17 C. B. Aakeröy, S. Panikkattu, P. D. Chopade and J. Desper, *CrystEngComm*, 2013, **15**, 3125–3136.

18 Y. He, Z. Bian, C. Kang, Y. Cheng and L. Gao, *Tetrahedron*, 2010, **66**, 3553–3563.

19 E. Weber, M. Hecker, E. Koepp, W. Orlia, M. Czugler and I. Csöregh, *J. Chem. Soc. Perkin Trans. II*, 1988, 1251–1257.

20 R. K. Castellano and J. Rebek, *J. Am. Chem. Soc.*, 1998, **120**, 3657–3663.

Chapter 8

Conclusions and Outlook

In summary, synthetic procedures and single crystal X-ray structures are reported in this study for 28 (**1-28**) coordination polymers and metal organic frameworks. A number of examples of the interplay of various structural factors, key among them structural flexibility, with the properties of the frameworks formed are illustrated.

In particular, the use of a polyaromatic chelating ligand, 2-tpt, in combination with a tricarboxylate ligand (H_3btb) resulted in structurally related 1D coordination polymers, **1-4**. The comparability of their covalently bonded 1D, and H-bonded 2D structures despite the use of various metal (M^{2+}) centres owed itself to accommodation of torsional strain in the btb^{3-} ligands. This strain resulted in different mutual orientations of phenyl rings in the organic linkers, and therefore the difference in sizes of metal centres was expressed as different supramolecular packing arrangements, through the directing effects of aromatic interactions on the 3D structure. 2-tpt was also substituted for a related polyaromatic capping ligand, 4-tpt, and the 2D coordination polymer, **5**, was obtained.

Compounds **6** and **7** utilised a mixed-ligand strategy to incorporate amino-functionality into MOF pores, as substituent groups on a bipyridyl system (dabpy) which is incorporated as a neutral ligand into MOFs based on $\{M^{2+}{}_3\}$ SBUs and simple dicarboxylate linkers. Significant porosity to N_2 and CO_2 was observed in both MOFs. Compounds **8** and **9** were synthesised in order to understand the impact of ligand flexibility on the topology and dimensionality of MOF built using the [$CuSiF_6$] backbone. The bpet and tdp ligands, with alkane backbones two and three carbon atoms long, are highly flexible relative to the rigid ligands typically used for the synthesis of these materials. Prolonged crystallisations allowed the isolation of bpet- and tdp-based compounds, which were both found to be two-dimensional. **8**, based on bpet ligands was shown to be porous, and showed excellent CO_2 uptake characteristics and selectivity, transferring the most valuable qualities of 3D ($CuSiF_6$)-based MOFs into two dimensions. In **10**, the rigid azpy ligand is incorporated into the 3D structure based on bis-monodentate coordination, allowing a degree of rotational flexibility about the terminal N – terminal N axis. This flexibility results in a hindered uptake of CO_2 until 1.5 molecules are adsorbed per unit cell. At this point a transition is triggered by the adsorbed gas, forcing the azpy moieties to adopt an orientation more conducive to CO_2 uptake. As a result we obtain the highest reported working capacity for CO_2 between 0.1 bar and 1 bar. Further, the transition between **10** and its hydrated, non-

porous form **10′** was explored, and water was used as a stimulus to trigger the transition instantaneously, releasing any guest CO_2 present in **10**.

11 and **12** were synthesised using an elegant synthetic strategy by which neutral, ditopic, N-donor ligands of appropriate length, such as azpy, may be incorporated into frameworks with the **pto** topology. Labile ligands present at apical positions of paddle-wheel SBUs are substituted by these ligands in a rational manner, resulting in a platform by which desired functionality may be reliably incorporated into a known MOF cavity. **11** and **12** form upon different degrees of azpy incorporation into a $\{Cu_2\}$-bteb **pto** scaffold. The flexibility of the bteb ligand, and consequently the framework, allows the incorporated azpy ligands to respond to the stimulus of UV irradiation. CO_2 sorption experiments on **11** and **12** showed a strong response to irradiation – changes of upto 40% of the uptake under dynamic irradiation conditions, despite partial framework collapse. These are the first reported MOFs with photoresponsive gas uptake in which photoswitching ligands are not the sole organic component. This strategy was also used to synthesise **13-16**, based on $\{M^{2+}{}_2\}$-btb scaffolds, into which the dabpy and dnbpy ligands were incorporated. The porosities of these MOFs were determined by simulation.

Rotational flexibility in extended ligands allows them to adopt a far greater variety of conformations than their shorter counterparts. Acetylene spacer groups separate phenyl rings, thereby enabling them to rotate freely relative to each other, while *p*-phenylene spacers allow restricted rotations due to H_{Ar}-H_{Ar} repulsions. In the $bteb^{3-}$ ligand this rotational flexibility can lead to desymmetrisation, allowing the formation of non-default structures. In **17**, $bteb^{3-}$ is combined with the $\{Cu_2\}$ SBU, and results in the rare $\{4.8^2\}_4\{4^2.8^2.10^2\}_2\{8^4.12^2\}$ net. Consequently, **17** is a triply-interwoven framework isomer of the **pto** net shown by TCM-4, and the **tbo** net shown by TCM-8. This is the first example of three distinct topologies obtained using paddle-wheel SBUs and tricarboxylate ligands. An unconventional ligand conformation due to reinforced torsions between adjacent phenyl rings in bbc^{3-} leads to the new $\{4.8^2\}_2\{4.8^5\}_2\{8^3\}_2\{8^5.12\}$ topology observed in **18**, a framework isomer of MOF-399 in which the torsions negate each other and result in coplanarity between the central phenyl ring and peripheral benzoate groups. Introduction of azpy as an auxiliary ligand into the Cu^{2+}/bbc^{3-} synthetic system resulted in **19**, a mixed-ligand framework. **19** has a novel $\{4.6^2\}_2\{4^2.6^8.8^3.10^2\}\{6^4.8^2\}$ topology, and consists of

sheets based on Cu^{2+} and bbc^{3-} which are pillared by azpy linkers. Notably, Cu^{2+} is present both as paddle-wheel {Cu_2} SBUs and as mononuclear {Cu} centres in the MOF. In addition, **19** is a rare example of a MOF showing a rare (2+1) non-equivalent mode of framework catenation.

Rotational flexibility also leads to non-default structures when H_3bteb and H_3bbc are combined with Cd^{2+} centres. Rather than the **kgd** net seen in the {Cd_3}-btb MOF, **20** and **21** show $\{4^3.6^{12}\}\{4^3\}_2$ and **hcb** nets based on the {Cd_3}-bbc system, when DMF and DEF are used, respectively. The uncommon **sit** net is formed when the {Cd_3} SBU is bound by $bteb^{3-}$ linkers, as seen in **22** and **22′**, which both show 2-fold interpenetration. In **23**, the azpy ligand is introduced into the Cd^{2+}/$bteb^{3-}$ synthetic system as an auxiliary linker. The azpy ligands replace DMF ligands present on the {Cd_3} SBU, and 'cross-stitch' the interwoven **sit** scaffolds into a single $\{4.6^2\}_2\{4^2.6^{16}.8^3\}$ net, which is a previously unreported topology. Simulations of N_2 adsorption carried out on **17**-**23** show that despite the unusual networks of these MOFs, they are highly porous.

24 was obtained following rational synthesis using H_3bteb in controlled conditions in an attempt to realise a Co^{2+} analogue of the previously reported TCM-1. **25** was successfully synthesised with the objective of realising a highly porous {Zr_6}-based MOF with access to unsaturated Zr^{4+} Lewis acidic sites. **26** and **27** are highly porous UMC-containing MOFs based on {Mn_3} (**kgd** net) and {Pb_∞} (**tpr**-type net). **28** is based on unusual Cl-capped mononuclear {In^{3+}} SBUs, and has a doubly interwoven **hcb** topology. The use of the highly elongated bbc^{3-} linker results in simulations showing that **28** has the highest potential porosity reported for 2D In^{3+} MOFs. These MOFs couple SBUs known to be useful for catalytic applications with high porosity, and their evaluation as heterogeneous catalysts is ongoing.

Therefore, a variety of behaviours that may be described as 'flexibility' are observed. The varying accommodation of torsional strain in one- and two-dimensional motifs, the plurality of conformations accessible to ligands due to free rotations in alkyl-chain backbones, rotational flexibility about metal-ligand bonds in assembled MOFs, rotational flexibility about acetylene spacers in extended ligands, and conformational variability about *p*-phenylene spacers in extended ligands have all been explored in this work. A

variety of consequences have been observed, including the formation of non-default and novel topologies and highly porous MOFs, 2D MOFs with intrinsic porosity, supramolecular variability in the 3D packing of similar 1D motifs, and stimulus-responsive behaviour.

A number of directions for continued and derived investigation emerge from this work, some of which are listed as follows:

- Harnessing the supramolecular response to metal ion size and free pyridyl and carboxylate moieties in **1**-**4** for differential luminescent sensing applications.
- Quantifying the contribution of amino-groups in **6** and **7** to CO_2 sorption by evaluating heats of adsorption on un-functionalised versions of these MOFs
- Extending the synthetic strategy of **8** to rigid, angular ditopic linkers to systematically study the intrinsically porous platform afforded.
- Functionalising ligands in the synthetic platform of **8** to weaken interactions between 2D layers, and allow exfoliation of intrinsically porous coordination polymer sheets.
- *In situ* crystallographic measurements on **11** and **12** in order to unambiguously establish the structural changes induced upon irradiation, and the mechanism of stimulus response.
- The use of amino- and nitro- functionality in **13**-**16** as an anchor for customised post-synthetic modifications towards sensing and catalytic applications.
- Steric control over torsions in **17**-**23** and their underlying synthetic platform, by tailored functionalisation, in order to achieve particular non-default topologies by design and as phase-pure products.
- The screening of other combinations of SBU and extended ligands for non-default MOF structures, by which a number of new compounds and topologies may be realised - and the derivation of general principles in order to enhance the toolkit of the reticular chemist.
- Thorough experimental evaluations of **24** as a porous heterogeneous catalyst in electrochemical water oxidation, and **25** and **28** in the synthesis of cyclic carbonates from CO_2 and epoxides, and related Lewis acid catalysed reactions.

In conclusion, we provide here a number of illustrations of various consequences structural flexibility in metal-organic frameworks and coordination polymers may have on their supramolecular structure, network topology, porosity, and addressability. Novel and unusual frameworks, topologies, and applicable synthetic strategies have been reported, and some landmark properties have been demonstrated with regard to porosity and addressable behaviour in MOFs.

Chapter 9

Appendix

9.1: Hirshfeld Surface Analysis for Compounds 1-5

High-resolution Hirshfeld surfaces were generated using *Crystal Explorer*[1] for the individual repeating units of compounds **1 – 5** in order to illustrate the nature of the non-covalent interactions involved in the three dimensional packing of the 1D polymer chains.

9.1.1: D_{norm} Plots

D_{norm} plots for **1-5** are presented here. These plots consist of a normalised contact distance between atoms interior and exterior to the Hirshfeld surface mapped on to the surface, in which blue regions correspond to contacts longer than the sum of the van der Waals' radii and red regions correspond to contacts shorter than it for the atoms involved.

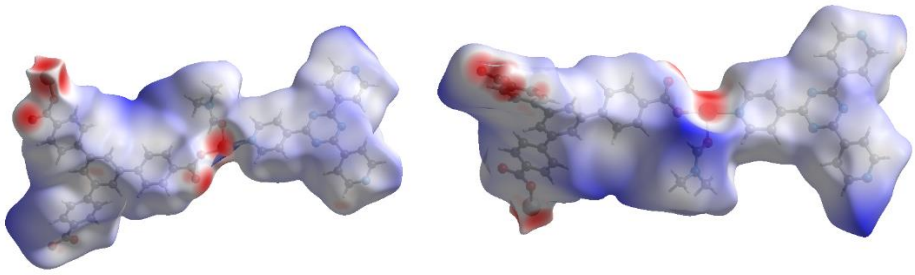

Figure 9.1.1 - D_{norm} plots of 1.

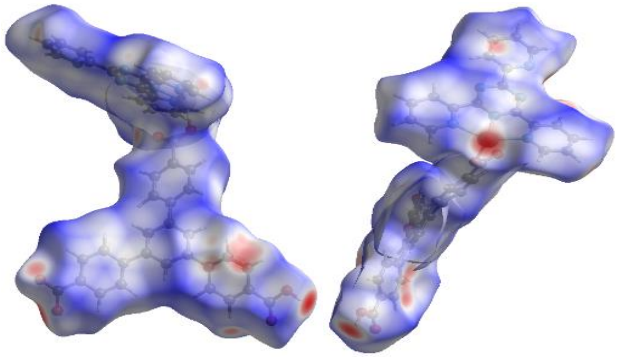

Figure 9.1.2 - D_{norm} plots of 2.

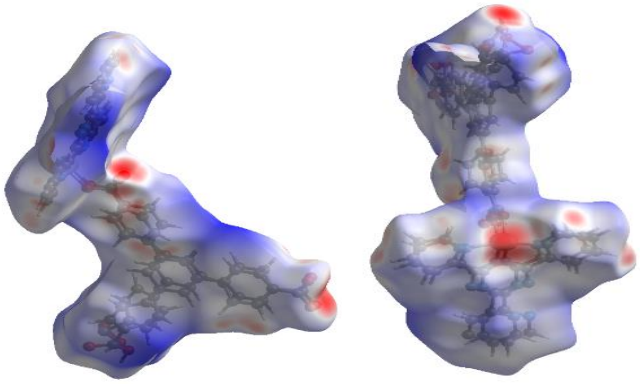

Figure 9.1.3 - D_{norm} plots of 3.

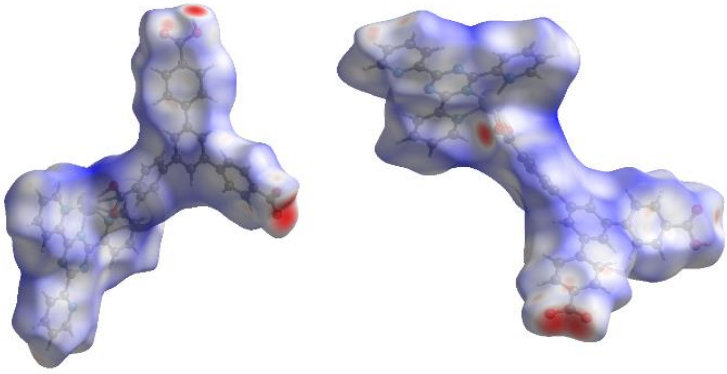

Figure 9.1.4 - D_{norm} plots of 4.

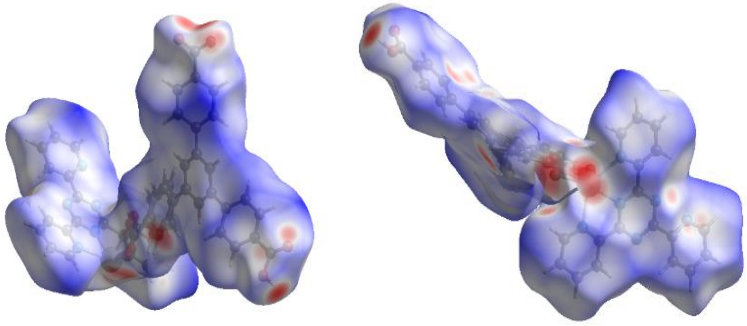

Figure 9.1.5 - D_{norm} plots of 5.

In Figs. 9.1.1-9.1.5, the red areas of the D_{norm} plot correspond to areas that have shortened contacts due to hydrogen bonding and π-π interaction. These can be distinctly identified in the following parts of the unit – the pendant carboxyl proton in **2-5**, which is strongly involved in H-bonding interactions in each case, oxygen atoms on the coordinating carboxylate groups which interact with the aforementioned protons in H-bonds, parts of the aromatic rings involved in π-π stacking, and diffuse short contacts around the metal centre and aryl protons which interact weakly with disordered solvent molecules, *eg.* in **1**.

9.1.2: Fingerprint Plots

The fingerprint plot of a Hirshfeld surface consists of the external contact distance (Å) plotted against internal contact distance for every point on the surface.[2] Interactions between similar species (e.g. C···C (π-π) interactions) appear along the diagonal since the Hirshfeld surfaces of two identical interacting species must coincide exactly halfway in between them. All asymmetry in the overall fingerprint plots of **1-5** is due to the presence of contacts to constitutional solvent molecules, which have been considered external to the Hirshfeld surfaces in this work.

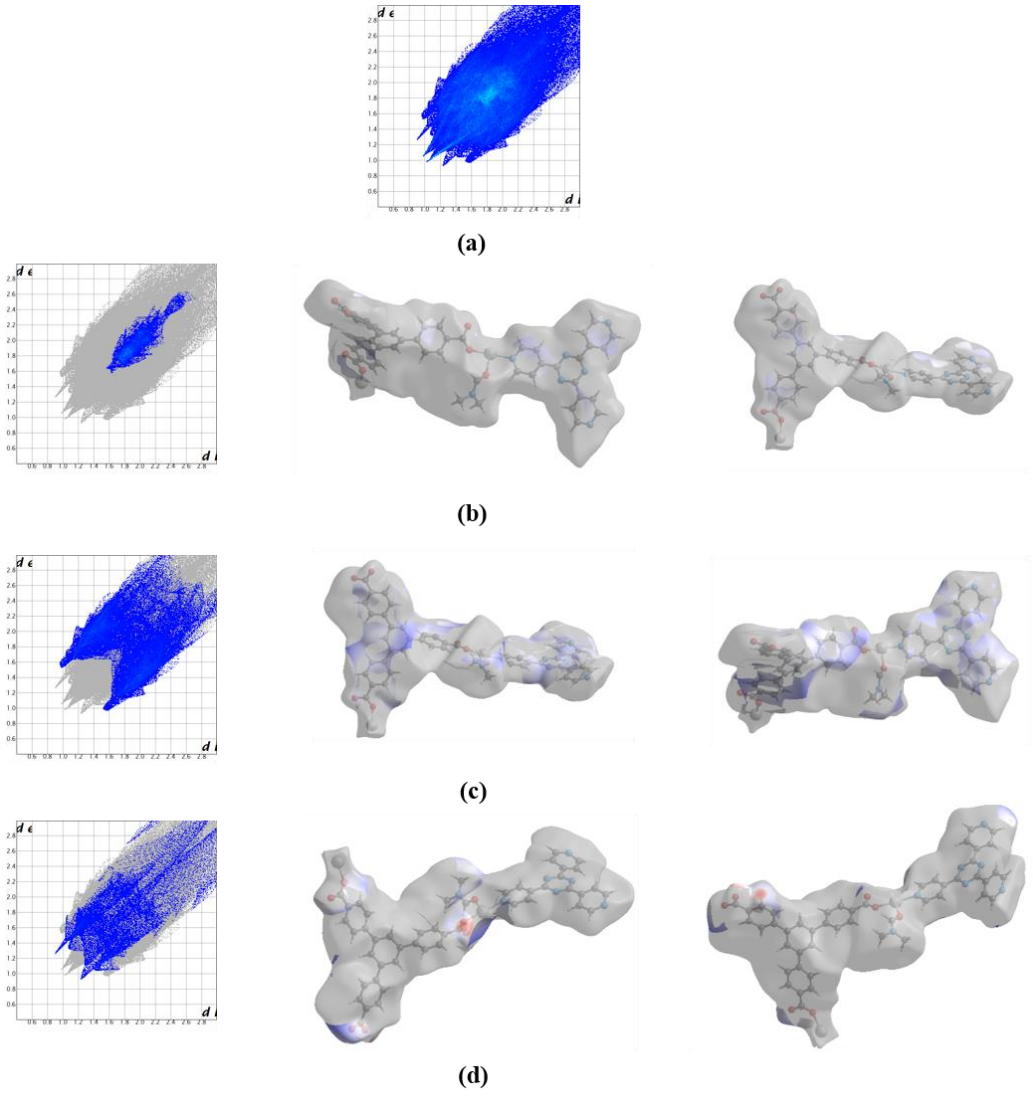

Figure 9.1.6 - Fingerprint plots and corresponding regions plotted on the Hirshfeld surface for 1: (a) Overall fingerprint plot, (b) C···C decomposed fingerprint and D_{norm} plots, (c) C···H decomposed fingerprint and D_{norm} plots (reciprocal contacts included), (d) O···H decomposed fingerprint and D_{norm} plots (reciprocal contacts included).

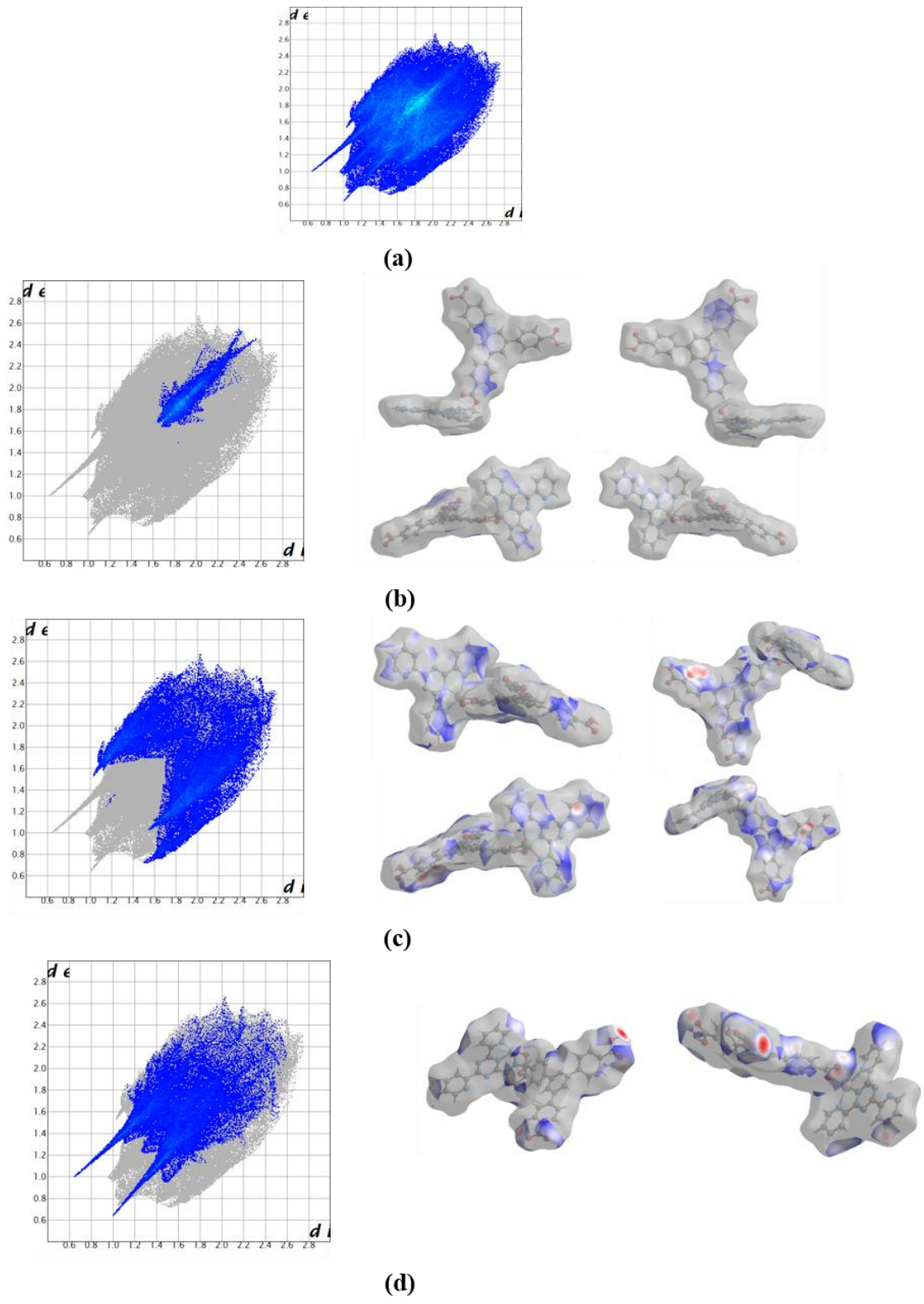

Figure 9.1.7 - Fingerprint plots and corresponding regions plotted on the Hirshfeld surface for 2: (a) Overall fingerprint plot, (b) C···C decomposed fingerprint and D_{norm} plots, (c) C···H decomposed fingerprint and D_{norm} plots (reciprocal contacts included), (d) O···H decomposed fingerprint and D_{norm} plots (reciprocal contacts included).

In Fig. 9.1.6, decomposed fingerprint plots show that π-π, C-H···π, and H-bonding interactions all play a role in the supramolecular ordering of 2D coordination polymer sheets relative to each other. The decomposed C···C plot corresponds to π-π interactions, which cover 6.1% of the total Hirshfeld surface. The plot locates these at $d_{ext} = d_{int} \cong 1.8$ Å, which agrees well with face-on π-π stacking. The coloured region of the decomposed D_{norm} surface correspond with aromatic stacking between 4-tpt ligand groups in adjacent sheets, and between btb ligands in the same sheet building the **kgd** type network as detailed in the main manuscript. The decomposed fingerprint for C···H and H···C short contacts is shown in Fig. 9.1.6 (c), and the contacts are located on the peripheries of the stacking phenyl rings (C-H···π interactions), accounting for 24.9% of the overall Hirshfeld surface. Hydrogen bonds are evaluated using the decomposed O···H and H···O fingerprint plot, which shows modest 'wings' at ca. $d_{ext} = 0.7$ Å, $d_{int} = 1.1$ Å and $d_{int} = 0.7$ Å, $d_{ext} = 1.1$ Å, and are localised over the surface at aryl positions, implying a degree of guest solvent molecule-framework interaction. These cover 9.3% of the Hirshfeld surface.

In Fig. 9.1.7, decomposed fingerprint plots show that π-π, C-H···π, and H-bonding interactions all play a major role in the supramolecular ordering of 1D chains relative to each other. The decomposed C···C plot corresponds to π-π interactions, which cover 6.8% of the total Hirshfeld surface. The plot locates these at $d_{ext} = d_{int} \cong 1.8$ Å, which agrees well with face-on π-π stacking. The coloured region of the decomposed D_{norm} surface correspond with A and B type stacking as detailed in the main manuscript. The decomposed fingerprint for C···H and H···C short contacts is shown in Fig. S14(c), and the contacts are located on the peripheries of the stacking phenyl rings (C-H···π interactions), accounting for 26.7% of the overall Hirshfeld surface. Hydrogen bonds are evaluated using the decomposed O···H and H···O fingerprint plot, which shows distinct 'wings' at ca. $d_{ext} = 0.7$ Å, $d_{int} = 1.1$ Å and $d_{int} = 0.7$ Å, $d_{ext} = 1.1$ Å, and are localised on the surface at distinct short contact regions around the pendant protonated carboxylate group and the oxygen atoms of the bound carboxylate. These cover 19.8% of the Hirshfeld surface.

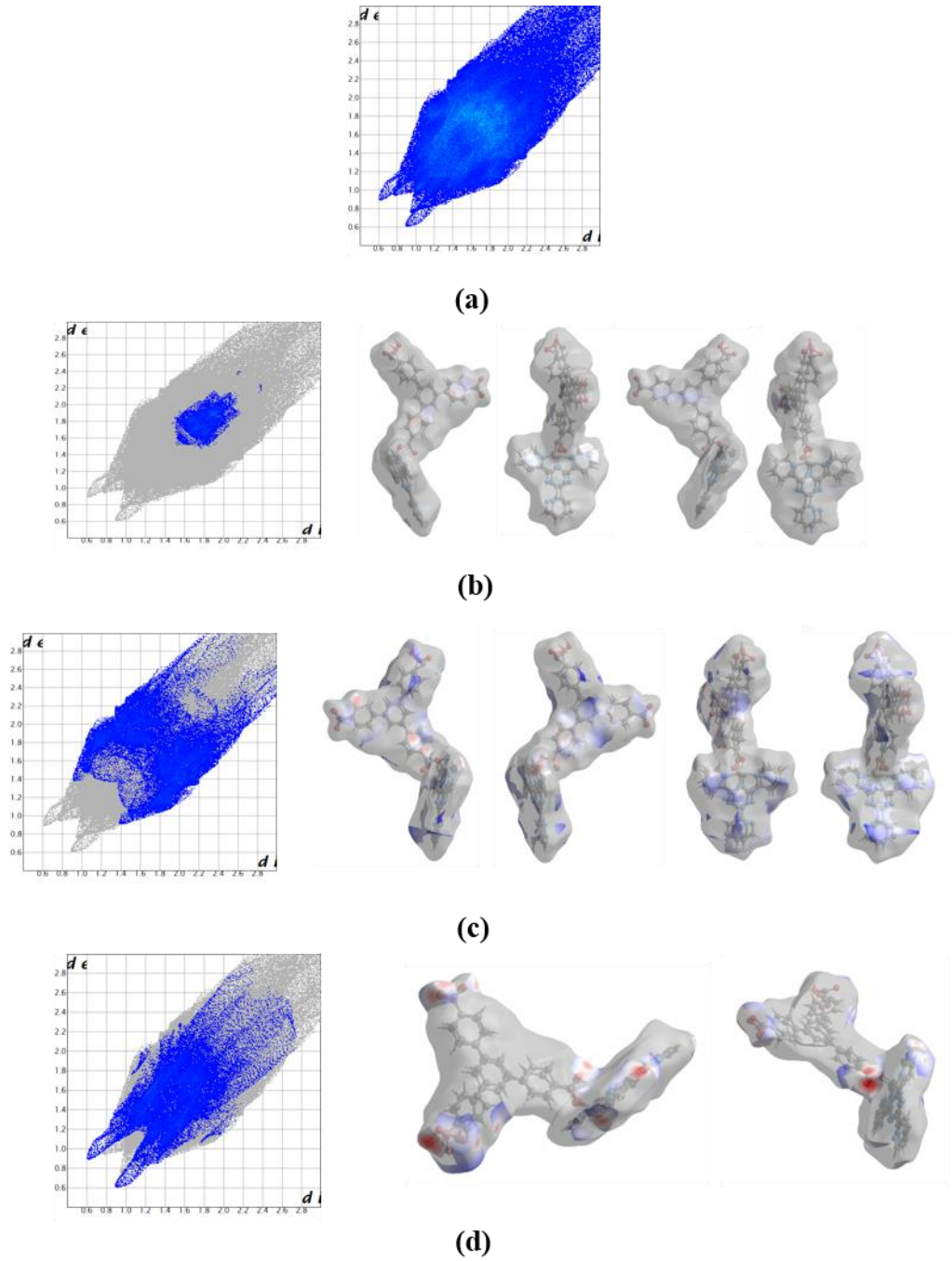

Figure 9.1.8 - Fingerprint plots and corresponding regions plotted on the Hirshfeld surface for 3: (a) Overall fingerprint plot, (b) C···C decomposed fingerprint and D_{norm} plots, (c) C···H decomposed fingerprint and D_{norm} plots (reciprocal contacts included), (d) O···H decomposed fingerprint and D_{norm} plots (reciprocal contacts included).

In Fig. 9.1.8, the decomposed C···C plot shows that π-π interactions cover 5.0% of the total Hirshfeld surface. As in 1, the coloured region of the decomposed D_{norm} surface correspond with A and B type stacking. The decomposed fingerprint for C···H and H···C short contacts accounts for 22.8% of the overall Hirshfeld surface. Hydrogen bonds are evaluated using

the decomposed O···H and H···O fingerprint plot, and are localised on the surface at short contact regions around the pendant protonated carboxylate group and the oxygen atoms of the bound carboxylate. These cover 17.7% of the Hirshfeld surface.

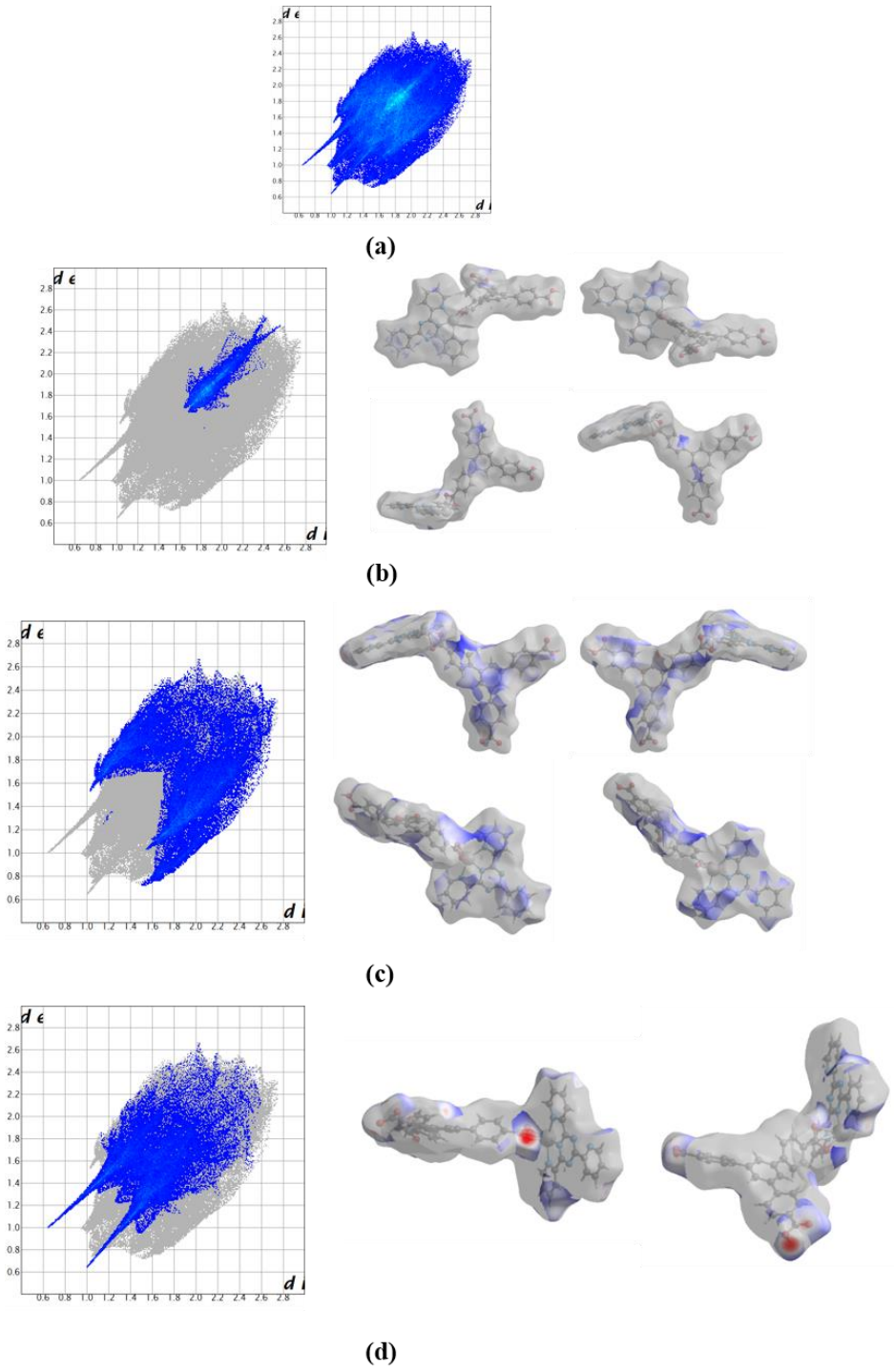

Figure 9.1.9 - Fingerprint plots and corresponding regions plotted on the Hirshfeld surface for 4: (a) Overall fingerprint plot, (b) C···C decomposed fingerprint and D_{norm} plots, (c) C···H decomposed fingerprint and D_{norm} plots (reciprocal contacts included), (d) O···H decomposed fingerprint and D_{norm} plots (reciprocal contacts included).

In Fig. 9.1.9, the decomposed C···C plot shows that π-π interactions cover 5.3% of the total Hirshfeld surface. Here, the decomposed C···C surface shows evidence of A, B, and C type stacking modes. The decomposed fingerprint for C···H and H···C short contacts accounts for 28.1% of the overall Hirshfeld surface. Hydrogen bonds are evaluated using the decomposed O···H and H···O fingerprint plot, and are localised on the surface at short contact regions around the pendant protonated carboxylate group and the oxygen atoms of the bound carboxylate despite the bidentate mode now adopted. These cover 18.4% of the Hirshfeld surface.

In Fig. 9.1.10, the decomposed C···C plot shows that π-π interactions cover 5.3% of the total Hirshfeld surface, and the decomposed C···C surface shows evidence of A, B, and C type stacking modes. The decomposed fingerprint for C···H and H···C short contacts accounts for 32.2% of the overall Hirshfeld surface. Hydrogen bonds are evaluated using the decomposed O···H and H···O fingerprint plot, and are localised on the surface at short contact regions around the pendant protonated carboxylate group and the oxygen atoms of the bound carboxylate despite the bidentate mode now adopted. These cover 18.7% of the Hirshfeld surface.

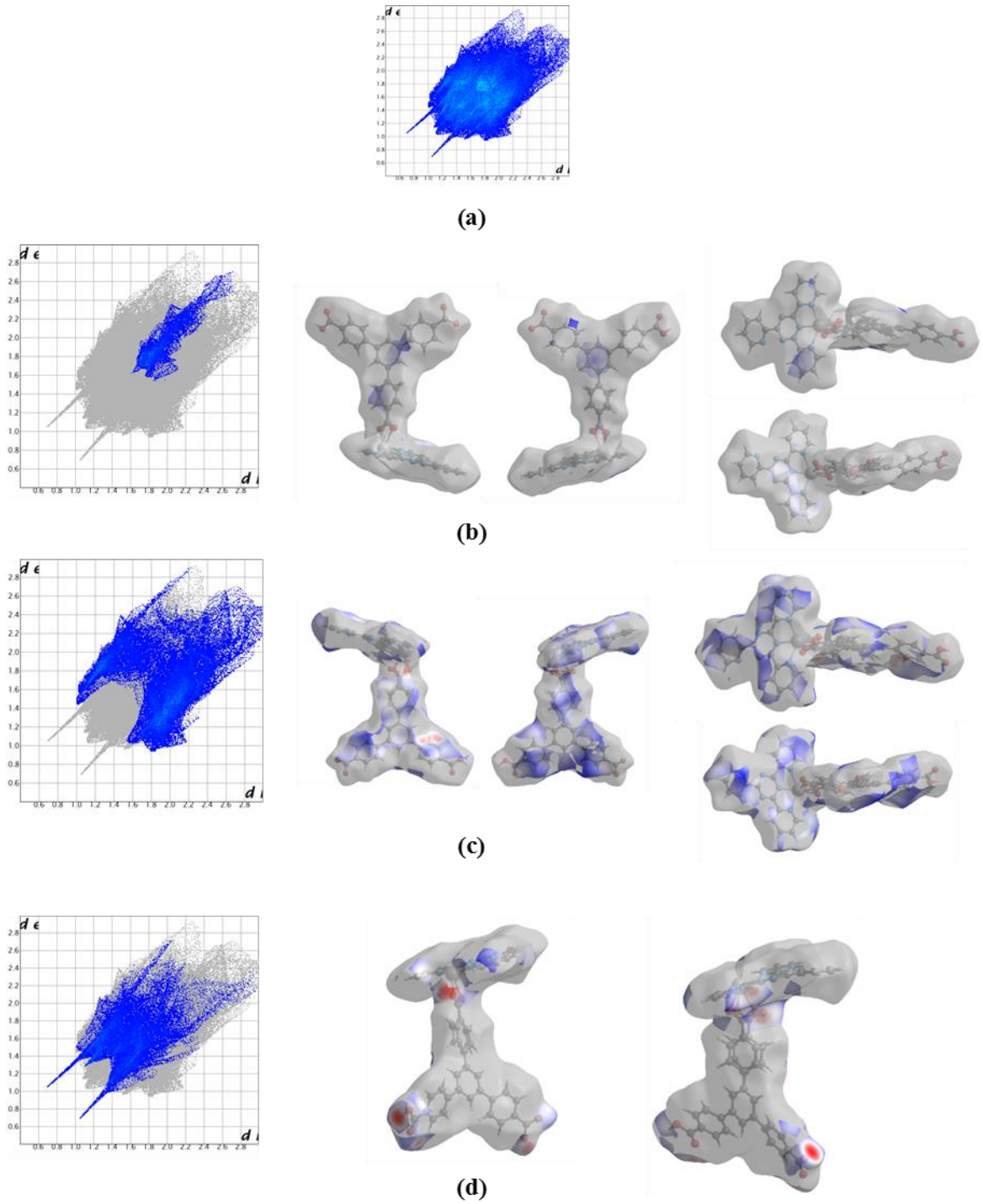

Figure 9.1.10 - Fingerprint plots and corresponding regions plotted on the Hirshfeld surface for 5: (a) Overall fingerprint plot, (b) C···C decomposed fingerprint and D_{norm} plots, (c) C···H decomposed fingerprint and D_{norm} plots (reciprocal contacts included), (d) O···H decomposed fingerprint and D_{norm} plots (reciprocal contacts included).

9.1.3: Linear Fit of C···H vs. C···C Ratios

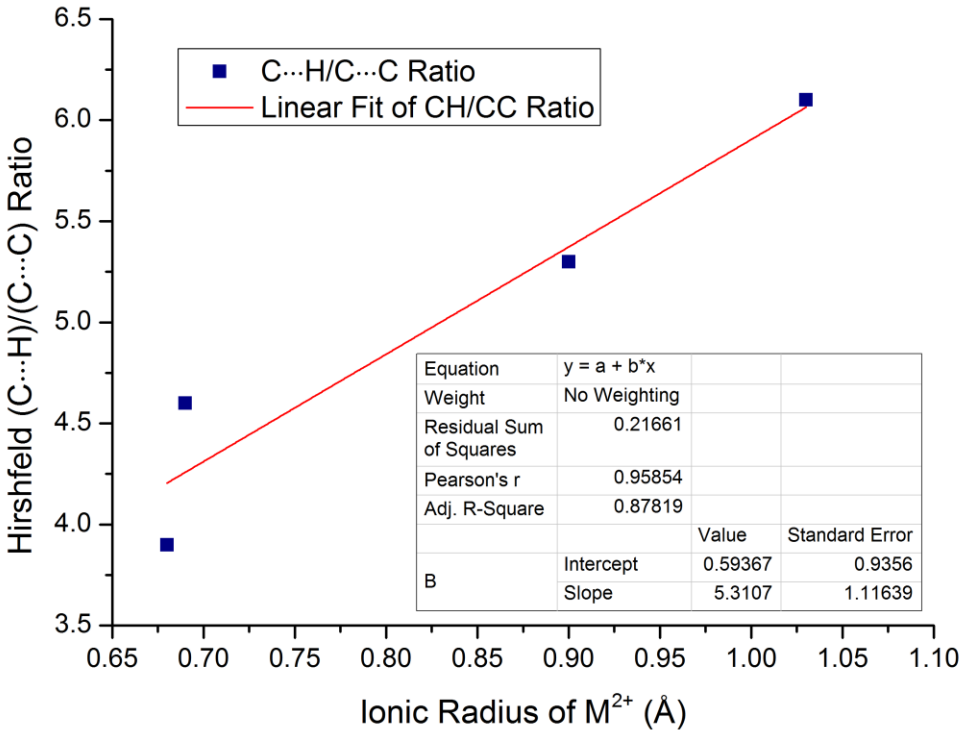

Figure 9.1.11 – Linear fit of the Hirshfeld surface-derived C···H/C···C ratio plotted against ionic radius of the corresponding metal ions.

9.2: CO_2 Adsorption Analyses

9.2.1: Modelling of the isotherms of the flexible MOF **10**

Each part of the isotherms, before (I) and after the step (II) are simulated using a classic Langmuir model:

$$q_I(p) = \frac{q_{I,sat} b_I p}{1 + b_I p} \quad - \quad (9.2.1)$$

$$q_{II}(p) = \frac{q_{II,sat} b_{II} p}{1 + b_{II} p} \quad - \quad (9.2.2)$$

Where q_{sat} is the adsorbed amount of CO_2 at saturation (mmol/g) and b is the energetic parameter (Pa^{-1}). These parameters are determined by curve-fitting using MATLAB.

In order to simulate the isotherm on the all range of the adsorption, we used a sigmoidal function to weight both isotherms on the all range of pressure using the following equation:

$$s(p) = \frac{1}{1 + e^{-\lambda(p - p_{trans})}} \quad - \quad (9.2.3)$$

Where λ is the sigmoidal parameter (-) and p_{trans} is the pressure where the phase transition happens and corresponds to the midpoint of the sigmoid curve. These parameters are determined by curve-fitting using MATLAB. Finally, the total CO_2 adsorption isotherm is expressed as:

$$q_{total}(p) = s(p) q_{II}(p) + \big(1 - s(p)\big) q_I(p) \quad - \quad (9.2.4)$$

Figure 9.2.1 presents the model with q_{II} (blue), q_I (orange) and q_{total} (black). The formula used for the calculations of the mean deviations is:

$$D(\%) = \frac{100}{N} \sum_{i=1}^{N} \frac{\left| q_{exp,i} - q_{model,i} \right|}{q_{exp,i}} \quad - \quad (9.2.5)$$

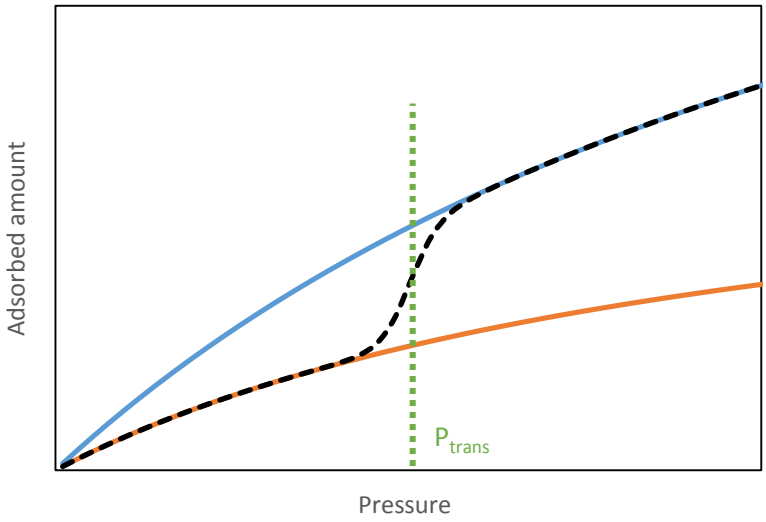

Figure 9.2.1 - Graphical representation of the applied model to account for the flexibility of 10 (q_{II} (blue), q_I (orange) and q_{total} (black)).

Table 9.2.1 - Parameters used in the modelling of adsorption isotherms for 10.

Parameter	CO_2						N_2
Temp. [K]	**278**	**293**	**298**	**308**	**323**	**338**	**293**
q_I [mmol g^{-1}]	4.7614	2.5195	3.3377	1.8349	3.9713	3.1134	0.07344
b_I [Pa^{-1}]	3.0410e-5	2.6136e-5	1.6741e-5	1.7100e-5	4.2857e-6	2.2659e-6	8.2746e-6
q_{II} [mmol g^{-1}]	6.2847	6.1404	6.0128	5.8263	5.3071	2.485	-
b_{II} [Pa^{-1}]	7.0953e-5	3.3124e-5	2.6771e-5	1.7097e-5	9.6267e-6	2.7822e-5	-
p_{trans} [Pa]	5215.4	11181	14780	22075	43559	80640	-
λ	1.295e-3	5.205e-4	5.852e-4	2.35e-4	1.8067e-4	8.1249e-5	-
Mean Deviation [%]	1.08	1.42	1.77	2.18	2.98	4.00	9.42

9.2.2: Estimation of the free energy difference between 'open' and 'closed' structures

Coudert *et al.*[10] provide a thermodynamic package to study the thermodynamics of structuratransitions induced by guest molecules. Studying this transition in the osmotic statistical ensemble, and considering the fluid as ideal, the osmotic potential is expressed, on a mass basis, as:

$$\Omega_{os}(T,p) = F_{host}(T) + pV - RT\int_0^p \frac{q(T,p)}{p}dp \qquad - \quad (9.2.6)$$

With F_{host}, the free energy of the host at zero pressure (J/kg).

At the transition pressure, the osmotic pressures of the two phases are equal and we can write that:

$$\Delta\Omega_{os}(T, p_{trans}) = 0 = \Delta F_{host}(T) + p_{trans}\Delta V - RT\Delta \int_0^{p_{trans}} \frac{q(p)}{p} dp \quad - \quad (9.2.7)$$

Considering the variation of volume equal to zero, and the phenomenon happening at relatively low pressure, the difference in the free energy can be expressed as:

$$\Delta F_{host}(T) = RT \left(\int_0^{p_{trans}} \frac{q_{II}(p)}{p} dp - \int_0^{p_{trans}} \frac{q_I(p)}{p} dp \right) \quad - \quad (9.2.8)$$

In the case of the Langmuir isotherm model, the integral can be expressed as:

$$\int_0^{p_{trans}} \frac{q(p)}{p} dp = q_{sat} \ln(1 + bp_{trans}) \quad - \quad (9.2.9)$$

Finally, the difference in the free energy is calculated as:

$$\Delta F_{host}(T) = RT\left(q_{II,sat} \ln(1 + b_{II}p_{trans}) - q_{I,sat} \ln(1 + b_I p_{trans})\right) \quad - \quad (9.2.10)$$

Figure 9.2.2 presents the free energy determination.

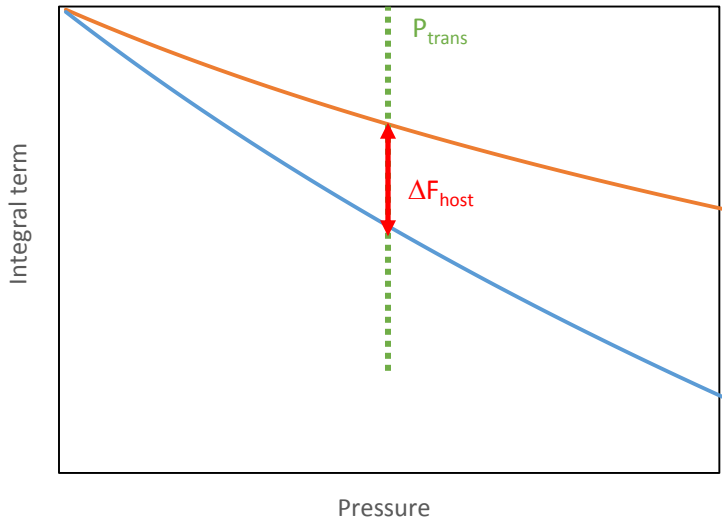

Figure 9.2.2 - Graphical representation of the free energy determination.

9.2.3: Determination of Adsorption Enthalpies

The isosteric heats of adsorption were determined using a classic Clausius-Clapeyron treatment on the fitted CO_2 isotherms at 278, 293 and 308 K:[11]

$$Q_{isos} = -R\left(\frac{\partial \ln p}{\partial(1/T)}\right)_{q_{ads}} \quad - \quad (9.2.11)$$

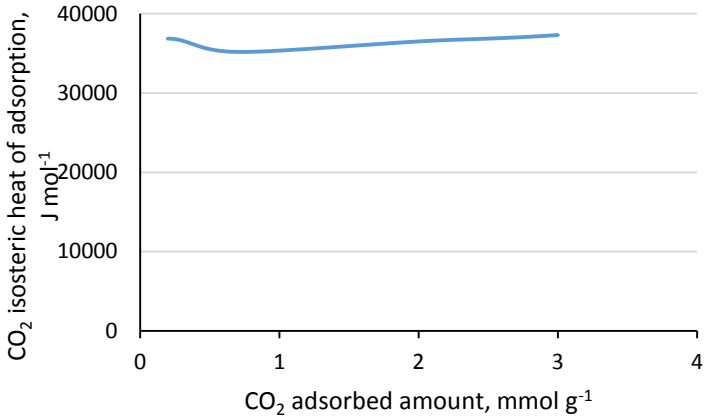

Figure 9.2.3 - CO_2 adsorption enthalpy plot calculated from 278, 293 and 308 K isotherms.

9.2.4: Adsorption Isotherms

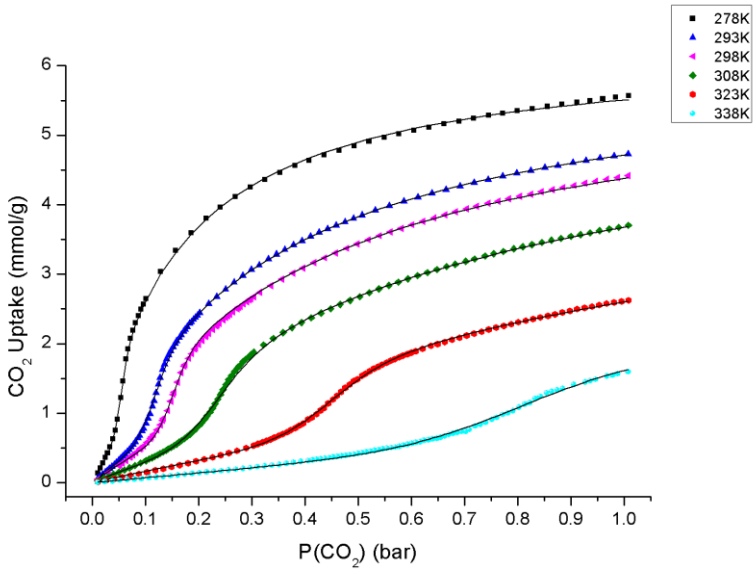

Figure 9.2.4 - CO_2 adsorption isotherms at various temperatures for 10 and mathematically generated fits (black curve).

9.3: Modelling the Excited State in **11** and **12**.

9.3.1: DFT calculations on **11** and **12**

Density functional theory (DFT) calculations were carried out using the Gaussian09 package[3]. The long range corrected CAM-B3LYP functional[4] was used in conjunction with SDDALL[5] basis set with an effective core potential for Cu (replacing the 10 core electrons with quasi relativistic pseudopotentials) as implemented in Gaussian09[3], the 6-31G(d) basis set for C, O and N, and 6-31G(p) basis set for H.[6] The model (Fig. 9.3.1) consists of two dinuclear Cu^{II} paddlewheel units joined together by 4,4'-azopyridine, in order to represent the azpy pillar in **11** and **12** and its immediate environment. To truncate the structure, the BTEB ligands were replaced with benzoic acids, and the last coordination site for the Cu^{II} centres further from the azpy ligand was fulfilled using water molecules. The ferromagnetic state of this model was optimized and this was followed by time dependent DFT calculations on the optimized structure.

Time dependent DFT calculations on our Cu model reveal a π- π* transition at 280 nm. Similar calculations were performed on the azpy ligand in isolation and the π- π* transition was found at 276 nm. Previous experimental work on 4,4'-azopyridine in the gas phase suggests that this transition occurs at 301 nm which implies that our methodology underestimates this transition by ~8%.[7] Other experimental works that involved looking at the UV spectrum in solvents found that this transition occurs at ~320 nm[8,9]. The environment specific nature of this transition is the possible reason for the large difference in the experimental and theoretical value for this transition.

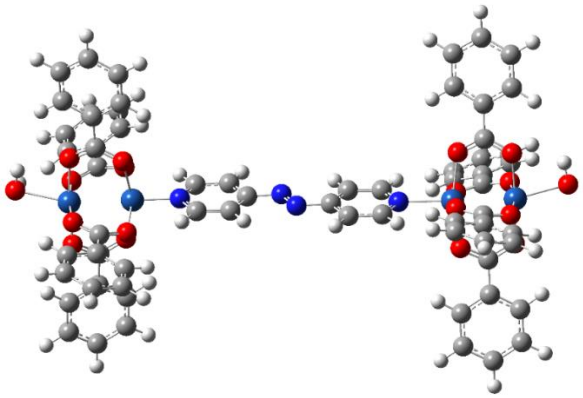

Figure 9.3.1 - Computational model employed for 11 and 12. Cu, C, N, O and H are shown in cyan, grey, blue, red and white respectively.

9.4: References

[1] *Crystal Explorer v. 3.1*, S. K. Wolff, D. J. Grimwood, J. J. McKinnon, M. J. Turner, D. Jayatilaka and M. A. Spackman, University of Western Australia, Perth, 2013.

[2] M. A. Spackman and D. Jayatilaka, *CrystEngComm*, 2009, **11**, 19–32.

[3] Gaussian 09, Revision D.01, M. J. Frisch, G. W. Trucks, H. B. Schlegel, G. E. Scuseria, M. A. Robb, J. R. Cheeseman, G. Scalmani, V. Barone, B. Mennucci, G. A. Petersson, H. Nakatsuji, M. Caricato, X. Li, H. P. Hratchian, A. F. Izmaylov, J. Bloino, G. Zheng, J. L. Sonnenberg, M. Hada, M. Ehara, K. Toyota, R. Fukuda, J. Hasegawa, M. Ishida, T. Nakajima, Y. Honda, O. Kitao, H. Nakai, T. Vreven, J. A. Montgomery Jr., J. E. Peralta, F. Ogliaro, M. Bearpark, J. J. Heyd, E. Brothers, K. N. Kudin, V. N. Staroverov, R. Kobayashi, J. Normand, K. Raghavachari, A. Rendell, J. C. Burant, S. S. Iyengar, J. Tomasi, M. Cossi, N. Rega, J. M. Millam, M. Klene, J. E. Knox, J. B. Cross, V. Bakken, C. Adamo, J. Jaramillo, R. Gomperts, R. E. Stratmann, O.Yazyev, A. J. Austin, R. Cammi, C. Pomelli, J. W. Ochterski, R. L. Martin, K. Morokuma, V. G. Zakrzewski, G. A. Voth, P. Salvador, J. J. Dannenberg, S. Dapprich, A. D. Daniels, Ö. Farkas, J. B. Foresman, J. V. Ortiz, J. Cioslowski, D. J. Fox, *Gaussian Inc.*, Wallingford CT, **2009**.

[4] T. Yanai, D. Tew, and N. Handy, *Chem. Phys. Lett.* **2004**, *393*, 51-57.

[5] M. Dolg, U. Wedig, H. Stoll, H. Preuss, *J. Chem. Phys.* **1987**, *86*, 866-872.

[6] M. Francl, W. Pietro, W. Hehre, J. Binkley, M. Gordon, D. DeFrees, J. Pople, *J. Chem. Phys.* **1982**, *77*, 3654-3665.

[7] J. Andersson, R. Petterson, L. Tegnér, *J. Photochem.* **1982**, *20*, 17-32.

[8] H. Jaffé, S. Yeh, R. Gardner, *J. Mol. Spectrosc.* **1958**, *2*, 120-136.

[9] P. Birnbaum, J. Linford, D. Style, *Trans. Faraday Soc.* **1953**, *49*, 735-744.

ChemPubSoc Europe

DOI: 10.1002/ejic.201501194

EurJIC European Journal of Inorganic Chemistry

Communication

Coordination Polymer Topology

CLUSTER ISSUE

Framework Isomerism: Highly Augmented Copper(II)-Paddlewheel-Based MOF with Unusual (3,4)-Net Topology

Nianyong Zhu,[a,b] Debobroto Sensharma,[a] Paul Wix,[a] Matthew J. Lennox,[c] Tina Düren,[d] Wai-Yeung Wong,[b,e] and Wolfgang Schmitt*[a]

Abstract: The synthesis and structure of a new, highly augmented $\{Cu_2\}$-"paddlewheel"-based metal–organic framework (MOF) that is stabilized by tritopic benzoate ligands is reported. The structure adopts an uncommon, less symmetrical, (3,4)-connected net topology and represents a rare framework isomer of the extensively studied $\{Cu_2\}$-based pto and tbo analogues related to the purely inorganic, solid-state structures of platinum oxide or the twisted boracite. The concomitant formation of three isomeric forms by using $\{Cu\}_2$-"paddlewheel" complexes and a single triangular, trifunctional ligand is unique and stems from the rotational flexibility of the benzoate moieties. Computational analyses support the structural studies and underline that this observed net topology can give rise to an exceptionally high surface area (greater than 3500 m^2/g) despite the triple-interpenetrated nature of the compound.

Introduction

Metal–organic frameworks (MOFs) represent a unique class of coordination compounds whose structural, chemical, and electronic characteristics promote applications in diverse areas of science.[1,2] MOFs are regarded as potentially applicable materials for gas storage, gas separation, fuel-gas conversion, or catalysis.[1,2a,2b] Their advantages include porosity, exceptionally high surface areas (up to 7000 m^2/g), high densities of active sites per volume, and high diffusion coefficients.[3] Also remarkable are their structural and constitutional diversities, the amenability to modification of both their organic and inorganic components, and the possibility to control their topology and cavity sizes.[1,2] This latter preparative control distinguishes MOFs from many other classes of coordination compounds. Their assembly processes can be rationalized by considering topological aspects of inorganic and organic nodes[4] to produce "default" nets that often relate to purely inorganic structure types (reticular synthesis concept).[4a] Attention has recently also been directed to polymorphism or framework isomerism of MOFs,[5] as compounds with identical framework composition give rise to distinctively different cavity geometries, thus influencing the performances of the MOFs in diverse applications (i.e. catalysis, whereby different pore geometries might give rise to shape-selectivity).[6] MOFs composed of square and triangular nodal topologies are well known to produce two edge-transitive topologies that can be described by the symbols tbo and pto according to the RCSR notation and relate to the purely inorganic, solid-state structures of platinum oxide or the twisted boracite.[7] Of particular interest in this context are $\{Cu\}_2$-"paddlewheel"-based secondary building units (SBUs), whose tbo/pto-type MOFs provide one of the largest family of MOFs represented in scientific publications.[8] Representative examples of MOFs with tbo topology are HKUST-1,[9] PCN-6/6',[10] and MOF-399.[7a] Networks of type pto occur, for instance, in MOF-14,[11] MOF-143/DUT-34,[7a,12] and MOF-388.[7a]

However, when considering the square and triangular geometries of organic and inorganic SBUs, one can expect that their assembly can lead to other "default" nets. A topological consideration to classify and enumerate the special class of A_3X_4-stoichiometric compounds in which each 3-connected node is connected to three 4-connected nodes and vice versa (each 4-connected node is connected to four 3-connected nodes) includes early approaches by Wells.[13] However, considering the reported MOFs and the current entries in the RCSR and EPINET databases, one can predict only a very limited number of augmented topological A_3X_4-type MOF isomers composed of 4-connected square/rectangular and triangular tritopic linkers.[12] Under this purview, Klein et al. predicted the synthesis of a MOF that is classified by the EPINET notation as the sqc5590 net.[12] However, paddlewheel-based MOFs of this topology have, to the best of our knowledge, not been observed or isolated.

[a] *School of Chemistry & CRANN Institute & AMBER Centre, Trinity College Dublin, University of Dublin, College Green, Dublin 2, Republic of Ireland*
E-mail: schmittw@tcd.ie
www.chemistry.tcd.ie/staff/academic/schmittw
[b] *Institute of Molecular Functional Materials & Department of Chemistry, Hong Kong Baptist University, Waterloo Road, Hong Kong, HK*
[c] *School of Chemistry, University of Nottingham, Nottingham NG7 2RD, UK*
[d] *Department of Chemical Engineering, University of Bath, Bath BA2 7AY, UK*
[e] *HKBU Institute of Research and Continuing Education, Shenzhen Virtual University Park, Shenzhen 518057, China*

Supporting information and ORCID(s) from the author(s) for this article are available on the WWW under http://dx.doi.org/10.1002/ejic.201501194.

Results and Discussion

We previously used the trifunctional ligand 4,4′,4″-[1,3,5-benzenetriyltris(ethyne-2,1-diyl)]tribenzoic acid (BTEB) to prepare pto- and tbo-type MOFs, TCM-**4** and TCM-**8**, whose topologies give rise to exceptionally high surface areas.[14] Here we demonstrate that the degree of rotational flexibility within the BTEB ligand results in the formation of a new third topological isomer $[Cu_3(BTEB)_2(H_2O)_2(DMF)]$, TCM-**10** (Figure 1). The concomitant formation of three topological isomeric MOFs by using a single tritopic, triangular ligand is unique for the $\{Cu\}_2$-"paddlewheel" reaction system.

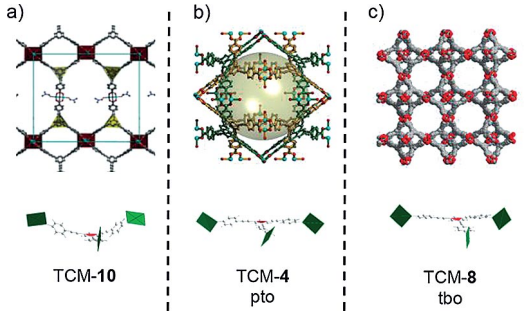

Figure 1. $\{Cu_2\}$/BTEB framework isomers and binding mode of the BTEB ligand; (a) TCM-**10** (representation of a single framework); (b) pto network in TCM-**4** (representation of the dual-interpenetrated structure); (c) tbo structure TCM-**8** (representation of a single framework).

TCM-**10** cocrystallizes reproducibly with TCM-**4** and TCM-**8** when BTEB and $Cu(NO_3)_2{\cdot}3H_2O$ are reacted in DMF in the presence of 4,4′-bipyridine at 85 °C. Whilst using lower concentrations of the reactants favor the formation of TCM-**4**, use of higher concentrations (and longer reaction times) seemed to promote the formation of TCM-**10**. TCM-**10** forms blue, agglomerated, block-shaped crystals that are distinctive from the green, polyhedron-type crystals of TCM-**4** and the individual, light-blue crystals of TCM-**8**. Crystals of TCM-**10** were separated manually, and single-crystal X-ray diffraction analysis demonstrates that the compound crystallizes in the monoclinic space group $P2_1/c$. The phase-purity of the sample of TCM-**10** was confirmed by powder X-ray diffraction (Supporting Information). The results of the single-crystal structure analysis reveal that TCM-**10** is composed of triple-interpenetrated frameworks, which contrasts the dual framework structures of TCM-**4/8**. The analysis clearly underlines that TCM-**10** represents an isomeric form of the pto and tbo nets in TCM-**4/8**; however, one may note that the topology differs from that of the initially predicted sqc5590 net.

The asymmetric unit of TCM-**10** contains two nonequivalent, fully deprotonated BTEB ligand molecules coordinated to three Cu^{II} ions. The structural parameters of the symmetry-generated dinuclear $\{Cu_2\}$ SBUs in TCM-**10** are closely related to those observed in TCM-**4/8**. O-Donor atoms of *syn,syn* bidentate carboxylate groups provide the bases of the square-pyramidal coordination polyhedra of each Cu^{II} center [Cu–O bond lengths: 1.939(4)–1.969(4) Å], and O donors of H_2O and DMF molecules bind in the apical positions [Cu–O bond lengths: 2.134(3)–2.142(3) Å]. The Cu–Cu distances in the dinuclear $\{Cu_2\}$ SBUs are about 2.6 Å. In agreement with the (3,4)-net topology, each $\{Cu_2\}$ SBU is coordinated by four tritopic BTEB ligands, and each BTEB moiety connects to three $\{Cu_2\}$ SBUs, which gives rise to a neutral network. It is observed that one of the squares defined by the $\{Cu_2\}$ SBUs is oriented perpendicular to the central benzene ring of the BTEB ligand, while the other two square SBUs adopt a conformation staggered by about 35° relative to the central benzene ring. Adopting the former 90° binding mode, the central phenyl and the outer benzoate ring systems are approximately coplanar, whilst the 35° binding mode results in a tilted conformation between central and outer phenyl rings. The two benzoate moieties that facilitate the 35° angles bridge in [010] parallel-aligned $\{Cu_2\}$ SBUs units, whereas the third benzoate group links orthogonally aligned $\{Cu_2\}$ SBUs in the direction of the crystallographic *c*-axis. In the corresponding pto and tbo structures that are formed by BTEB and $\{Cu_2\}$ SBUs, the angles between the central phenyl and the square $\{Cu_2\}$ SBUs are identical: about 55° for the pto structure and about 90° for the tbo structure (Figure 1). In both cases, the organic ligands adopt C_3 symmetry. Thus, the MOF presented here is not isoreticular to HKUST-1 or MOF-14 and may be regarded as an isomeric "intermediate" between the tbo and pto topologies.[8,11]

A more detailed topological consideration reflects the different binding arrangement of the benzoate groups of the BTEB ligands in TCM-**10** (Figure 2). The topological analysis suggests that the net can indeed be described as a (3,4,4)-connected, 3-nodal net with two topologically distinguishable 4-connected nodes. The overall point symbol is $\{4.8^2\}_4\{4^2.8^2.10^2\}_2\{8^4.12^2\}$. The 4-connected vertex with the point symbol $\{4^2.8^2.10^2\}$ represents the $\{Cu_2\}$ SBUs in which the four adjacent terminal phenyl rings of the ligand are all tilted against their respective central ring. The 4-connected vertex with the point symbol $\{8^4.12^2\}$ represents the Cu^{II} dimer in the structure where the terminal phenyl rings of the ligand are coplanar to the respective central ring. Thus, the network in TCM-**10** represents a less symmetrical (3,4)-connected net topology, which is represented only once in the TTD database (3,4,4T84)[15] and which distinctively differs

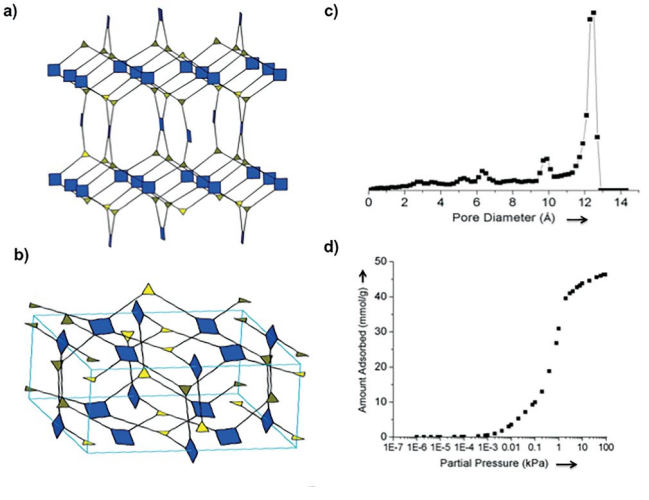

Figure 2. Augmented topological representation of a single net (a) and the triple interprenetration in TCM-**10** (b); (c) and (d) calculated poresize distribution and nitrogen adsorption isotherm for TCM-**10**.

from the nets in TCM-**4** and TCM-**8**. The corresponding augmented analogue can be represented by the point symbol $\{3.16^2\}\{3.8.9\}_2\{4.16^2\}\{4.8.10\}_2$ (see Supporting Information). The augmented topological representations that highlight the binding modes of the organic ligands are shown in Figures 2a and 2b.

The observed triple-interweaving of the nets in TCM-**10** (Figure 3) can also be attributed to the extended and flexible nature of the BTEB ligand. The π–π stacking that involves phenyl rings from different sub-nets and comprises bowing of the BTEB ligands stabilizes the interwoven structure (Figures 3, 4, and Supporting Information). The observed type of interpenetration and connectivity results in cylindrical/hexagonal channels that extend in the direction of the crystallographic *c*-axis. Significantly sized openings can also be observed in the [010] direction. Packing diagrams that highlight the channels and the interpenetration of the three symmetry-equivalent networks are displayed along the unit cell directions in Figures 3d–3f. Despite its interwoven nature, the unit cell of TCM-**10** has a solvent-accessible void volume of about 72 % (corresponding to 11925 Å^3). The significant solvent quantity in TCM-**10** is underlined by the thermogravimetric analysis carried out in a N_2 atmosphere. The thermogravimetric step associated with the loss of constitutional solvent molecules occurs up to 110 °C. The weight loss of about 5 % above 110 °C is caused by the removal of coordinated H_2O/DMF molecules before the oxidation of the BTEB moieties destroys the network structure above about 280 °C (Supporting Information).

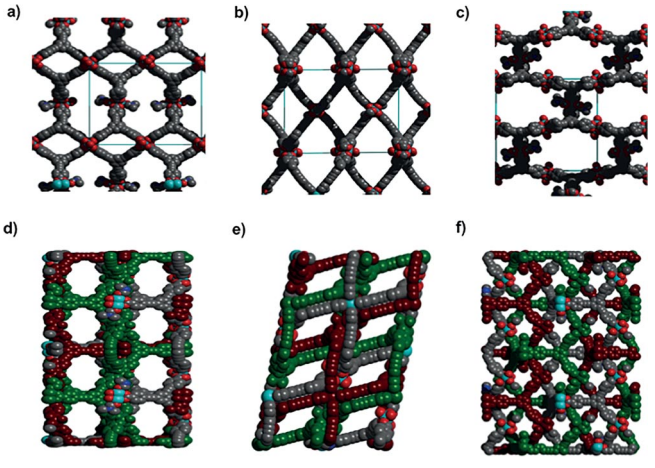

Figure 3. Space-filling representation of a single net in TCM-**10** with view in the [201] (a), [010] (b), and [101] directions (c). Triple interpenetration in TCM-**10** with view in the direction of the crystallographic *c*- (d), *b*- (e), and *a*- (f) axes.

Considering that TCM-**10** forms in a product mixture, theoretical calculations were conducted to evaluate the possible surface areas and gas-storage abilities of TCM-**10** and to compare these with the properties of TCM-**4**/**8**. A theoretical approach that calculates the largest solid sphere that can be inserted into the cavities whilst avoiding any overlap with framework atoms was used to determine the pore size distribution (PSD).[16] This analysis confirmed that TCM-**10** contains well-defined micropores with cross-sectional diameters of about 12.3 Å and

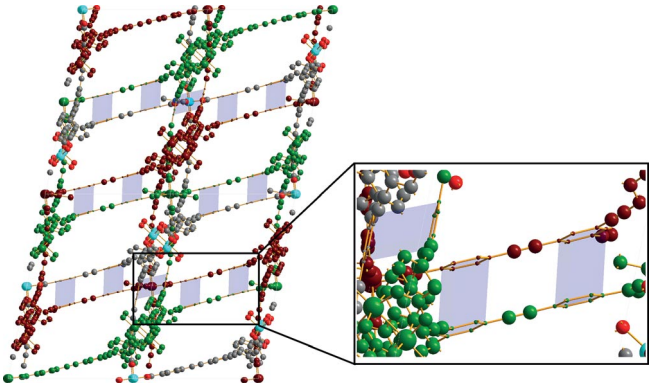

Figure 4. Stabilizing π–π interactions between nets in TCM-**10**; structure with view in the direction of the crystallographic *b*-axis. The highlighted interactions are characterized by interplane distances between the aromatic ring systems of about 3.8 Å.

smaller, narrow cavities of about 9.8 Å in diameter (Figure 2c). This pore-size characteristic is distinctively different from those of the corresponding dual-interpenetrated pto and tbo structures that contain either distinct micropores of 12.3, 14.5, and 18.5 Å in diameter (TCM-**8**) or larger defined pores with diameters larger than 20 Å (TCM-**4** or TCM-**4′**).[14a,14b] The accessible surface area for the fully desolvated structure of TCM-**10** of about 3850 m^2/g was calculated by "rolling" a nitrogen-sized sphere (diameter = 3.31 Å) along the surface of the framework atoms.[17] The value is noteworthy in view of the triple-interpenetrated nature of the compound. It is, in fact, closely comparable with that of the dual-interpenetrated pto structure but significantly lower than the surface area of the corresponding tbo structure. The BET surface area of the fully desolvated TCM-**10** was calculated to be 3904 m^2/g (see Supporting Information). In line with the calculated surface areas and He pore volume (1.65 cm^3/g), the maximum nitrogen uptake capacity of TCM-**10** is about 45 mmol/g (Figure 2d). The structure gives rise to a type-I adsorption isotherm whereby the low-pressure N_2 uptake is reduced in comparison to that of TCM-**4** or TCM-**8**.[18,14]

Table 1 compares the void volumes and calculated accessible theoretical surface areas of the three $\{Cu_2\}$/BTEB framework isomers. The variable BTEB connectivities result in closely related Cu/BTEB frameworks, each with its distinct pore size, surface area, and structural descriptor. One might remark that these Cu/BTEB framework isomers are not directly interconvertible. In the triple-interpenetrated TCM-**10** structure, each individual single net occupies about 10 % of the entire unit cell volume, indicating that the achievable void volumes of the as yet hypothetical dual-interpenetrated or single-network structures are very large. Similarly, considering that the individual nets in

Table 1. Comparison of the calculated surface areas and structural parameters of the isomeric $\{Cu_2\}$/BTEB frameworks.

	TCM-**4**	TCM-**8**	TCM-**10**
Interpenetration	dual	dual	triple
Cell volume (Å^3) /Z	80939/16	105620/16	16645/4
Void volume (%) per unit cell	78	84	72
Calcd. surface area (m^2/g)[17]	3820	5441	3848

TCM-**10**, TCM-**8**, and TCM-**4** occupy closely comparable volumes, one can conclude that the observed type of topology gives rise to an intermediate intrinsic surface area which is larger than that of the corresponding pto network but lower than that of the tbo network.

Conclusions

In summary, we describe the synthesis and structure of a new, highly augmented $\{Cu_2\}$ "paddlewheel"-based MOF that is stabilized by BTEB linkers. TCM-**10** reveals an uncommon, less symmetrical, (3,4)-connected net topology, thus representing a rare and new framework isomer to the extensively studied pto and tbo analogues.

The ethynyl moieties of the BTEB linkers not only result in an augmented structure, but they also impart the rotational flexibility of the benzoate groups through the separation of the phenyl rings. The topological and structural analysis of TCM-**10** demonstrates that this flexibility is key for the structural diversity of this system that enables the concomitant formation of three distinct framework isomers by using a single tritopic, triangular ligand. Thus, the BTEB linker is distinct from other smaller tritopic benzoates that have previously been used to prepare $\{Cu_2\}$-based MOFs. For instance, in the geometrically restrained benzenetribenzoate (BTB) linker, the planarity of the phenyl rings is hampered by the close contacts of H-atoms, thus stabilizing the pto topology in MOF-14.

Computational analyses suggest that the observed structure in TCM-**10** gives rise to a very high surface area, despite the triple-interpenetrated nature of the compound. The observed topology may be regarded as an "intermediate" between the tbo and pto topologies, resulting in higher intrinsic surface areas than the corresponding pto structures but lower surface areas than the tbo structures. TCM-**10** cocrystallizes with its isomers, and future studies will focus on the development of synthetic strategies to produce phase-pure samples of this MOF.

Experimental Section

4,4′,4′′-[1,3,5-Benzenetriyltris(ethyne-2,1-diyl)]tribenzoic acid (BTEB) was synthesized according to a literature method.[19] The topology of TCM-**10** was determined with help of the program package ToposPro 5.0.[20] Details of the computational and topological analyses are provided in the Supporting Information.

Preparation of $[Cu_3(BTEB)_2(H_2O)_2(DMF)]$ (TCM-10): To a solution of 0.065 g of $Cu(NO_3)_2{\cdot}3H_2O$ in DMF (2 mL), was added BTEB (0.094 g). The resulting mixture was sonicated for 10 min. Then, a solution of 4,4′-bipyridine (0.015 g) in DMF (0.25 mL) was added to this mixture. The resulting reaction mixture was kept in a closed vial at 85 °C in an oven for 48 h. A mixture containing light-blue, plate-like crystals (TCM-**8**), greenish-blue, polyhedron-type crystals (TCM-**4**), and aggregates of blue, block-like crystals (TCM-**10**) was obtained. The latter crystals of TCM-**10** are distinguishable from the other crystals by their color and morphology. TCM-**10** was isolated from the mixture manually. Yield: 5–10 %. Dried sample of TCM-**10** ($C_{69}H_{41}Cu_3NO_{15}$) with four constitutional H_2O molecules per formula unit: calcd. C 59.76, H 3.56, N 1.01; found C 59.76, H 3.39, N 1.40.

CCDC 1431313 (for TCM-**10**) contains the supplementary crystallographic data for this paper. These data can be obtained free of charge from The Cambridge Crystallographic Data Centre.

Acknowledgments

Science Foundation Ireland (SFI) (13/IA/1896 and 08/IN.1/I2047), the European Research Council (ERC) (consolidator grants for W. S. and T. D.), the Irish Research Council (P. W.), and Trinity College Dublin supported this work. W.-Y. W. thanks the Hong Kong Research Grants Council (HKBU 12302114), Areas of Excellence Scheme of the Hong Kong Special Administrative Region (HKSAR) (AoE/P-03/08), and the National Natural Science Foundation of China (Project No. 51573151) for financial support.

Keywords: Metal–organic frameworks · Copper · Topology · Polymorphism · Coordination chemistry

[1] L. R. McGillivray (Ed.), *Metal–Organic Frameworks – Design and Application*, John Wiley & Sons, Hoboken, **2010**.

[2] a) Special Issue: *Chem. Soc. Rev.*, **2014**, *43*, 5415–6176; b) A. K. Cheetham, C. N. R. Rao, *Science* **2007**, *318*, 58; c) P. Nugent, Y. Belmabkhout, S. D. Burd, A. J. Cairns, R. Luebke, K. Forrest, T. Pham, S. Ma, B. Space, L. Wojtas, M. Eddaoudi, M. J. Zaworotko, *Nature* **2013**, *495*, 80; d) H. Furukawa, K. E. Cordova, M. O'Keeffe, O. M. Yaghi, *Science* **2013**, *341*, 6149; e) D. J. Collins, H. C. Zhou, *J. Mater. Chem.* **2007**, *17*, 3154; f) J. Yang, A. Sudik, C. Wolverton, D. J. Siegel, *Chem. Soc. Rev.* **2010**, *39*, 656.

[3] a) O. K. Farha, I. Eryazici, N. C. Jeong, B. G. Hauser, A. A. Sarjeant, S. T. Nguyen, A. Ö. Yazaydın, J. T. Hupp, *J. Am. Chem. Soc.* **2012**, *134*, 15016; b) H. Furukawa, N. Ko, Y. B. Go, N. Aratani, S. B. Choi, E. Choi, A. Ö. Yazaydin, R. Q. Snurr, M. O'Keeffe, J. Kim, O. M. Yaghi, *Science* **2010**, *329*, 424; c) S. Han, T. M. Hermans, P. E. Fuller, Y. Wei, B. A. Grzybowski, *Angew. Chem. Int. Ed.* **2012**, *51*, 2662; *Angew. Chem.* **2012**, *124*, 2716; d) L. Alaerts, E. Seguin, H. Poelman, F. Thibault-Starzyk, P. A. Jacobs, D. E. De Vos, *Chem. Eur. J.* **2006**, *12*, 7353.

[4] a) O. M. Yaghi, M. O'Keeffe, N. W. Ockwig, H. K. Chae, M. Eddaoudi, J. Kim, *Nature* **2003**, *423*, 705; b) S. Natarajan, P. Mahataa, *Chem. Soc. Rev.* **2009**, *38*, 2304; c) S. R. Batten, *CrystEngComm* **2001**, *3*, 67; d) R. J. Hill, D.-L. Long, N. R. Champness, P. Hubberstey, M. Schröder, *Acc. Chem. Res.* **2005**, *38*, 335; e) B. F. Hoskins, R. Robson, *J. Am. Chem. Soc.* **1990**, *112*, 1546; f) J. J. Perry, J. A. Perman, M. J. Zaworotko, *Chem. Soc. Rev.* **2009**, *38*, 1400; g) M. O'Keeffe, M. Eddaoudi, H. Li, T. Reineke, O. M. Yaghi, *J. Solid State Chem.* **2000**, *152*, 3; h) M. Eddaoudi, D. B. Moler, H. Li, B. Chen, T. M. Reineke, M. O'Keeffe, O. M. Yaghi, *Acc. Chem. Res.* **2001**, *34*, 319.

[5] a) J. P. Zhang, X. C. Huang, X. M. Chen, *Chem. Soc. Rev.* **2009**, *38*, 2385; b) T. A. Makal, A. Yakovenko, H. C. Zhou, *J. Phys. Chem. Lett.* **2011**, *2*, 1682; c) M. R. Kishan, J. Tian, P. K. Thallapally, C. A. Fernandez, S. J. Dalgarno, J. E. Warren, B. P. McGrail, J. L. Atwood, *Chem. Commun.* **2010**, *46*, 538; d) D. Sun, S. Ma, J. M. Simmons, J.-R. Li, D. Yuana, H.-C. Zhou, *Chem. Commun.* **2010**, *46*, 1329; e) J.-P. Zhang, X.-C. Huang, X.-M. Chen, *Chem. Soc. Rev.* **2009**, *38*, 2385; f) B. Chen, F. R. Fronczeka, A. W. Maverick, *Chem. Commun.* **2003**, 2166; g) S. Masaoka, D. Tanaka, Y. Nakanishi, S. Kitagawa, *Angew. Chem. Int. Ed.* **2004**, *43*, 2530; *Angew. Chem.* **2004**, *116*, 2584; h) D. Frahm, F. Hoffmann, M. I. Fröba, *CrystEngComm* **2013**, *15*, 9429.

[6] a) Z.-Y. Gu, J. Park, A. Raiff, Z. Wei, H.-C. Zhou, *ChemCatChem* **2014**, *6*, 67 (and references cited therein.); b) S.-H. Cho, B. Ma, S. T. Nguyen, J. T. Hupp, T. E. Albrecht-Schmitt, *Chem. Commun.* **2006**, 2563; c) C. D. Wu, W. Lin, *Angew. Chem. Int. Ed.* **2007**, *46*, 1075; *Angew. Chem.* **2007**, *119*, 1093; *Angew. Chem.* **2007**, *119*, 1093; d) A. Phan, A. U. Czaja, F. Gándara, C. B. Knobler, O. M. Yaghi, *Inorg. Chem.* **2011**, *50*, 7388; e) M. Tonigold, Y. Lu, B. Bredenkötter, B. Rieger, S. Bahnmüller, J. Hitzbleck, G. Langstein, D. Volkmer, *Angew. Chem. Int. Ed.* **2009**, *48*, 7546; *Angew. Chem.* **2009**, *121*, 7682; *Angew. Chem.* **2009**, *121*, 7682; f) K. S. Suslick, P. Bhyrappa, J.-H. Chou, M. E. Kosal, S. Nakagaki, D. W. Smithenry, S. R. Wilson, *Acc. Chem. Res.* **2005**, *38*, 283; g) O. K. Farha, A. M. Shultz, A. A. Sarjeant, S. T.

Nguyen, J. T. Hupp, *J. Am. Chem. Soc.* **2011**, *133*, 5652; h) W.-Y. Gao, M. Chrzanowski, S. Ma, *Chem. Soc. Rev.* **2014**, *43*, 5841.
[7] a) H. Furukawa, Y. B. Go, N. Ko, Y. K. Park, F. J. Uribe-Romo, J. Kim, M. O'Keeffe, O. M. Yaghi, *Inorg. Chem.* **2011**, *50*, 9147; b) O. Delgado-Friedrichs, M. O'Keeffe, O. M. Yaghi, *Acta Crystallogr., Sect. A* **2006**, *62*, 350.
[8] M. Li, M. O'Keeffe, O. M. Yaghi, *Chem. Rev.* **2014**, *114*, 1343.
[9] S. S.-Y. Chui, S. M.-F. Lo, J. P. H. Charmant, A. G. Orpen, I. D. Williams, *Science* **1999**, *283*, 1148.
[10] a) D. Sun, S. Ma, Y. Ke, D. J. Collins, H.-C. Zhou, *J. Am. Chem. Soc.* **2006**, *128*, 3896; b) S. Ma, D. Sun, M. Ambrogio, J. A. Fillinger, S. Parkin, H.-C. Zhou, *J. Am. Chem. Soc.* **2007**, *129*, 1858.
[11] B. Chen, M. Eddaoudi, S. T. Hyde, M. O'Keeffe, O. M. Yaghi, *Science* **2001**, *291*, 1021.
[12] N. Klein, I. Senkovska, I. A. Baburin, R. Grünker, U. Stoeck, M. Schlichtenmayer, B. Streppel, U. Müller, S. Leoni, M. Hirscher, S. Kaskel, *Chem. Eur. J.* **2011**, *17*, 13007.
[13] A. F. Wells, *Acta Crystallogr., Sect. A* **1986**, *42*, 133.
[14] a) N. Zhu, M. J. Lennox, G. Tobin, L. Goodman, T. Düren, W. Schmitt, *Chem. Eur. J.* **2014**, *20*, 3595; b) N. Zhu, M. J. Lennox, T. Düren, W. Schmitt, *Chem. Commun.* **2014**, *50*, 4207.
[15] S. Xiang, J. Huang, L. Li, J. Zhang, L. Jiang, X. Kuang, C.-Y. Su, *Inorg. Chem.* **2011**, *50*, 1743.
[16] L. D. Gelb, K. E. Gubbins, *Langmuir* **1998**, *14*, 2097.
[17] T. Düren, F. Millange, G. Férey, K. S. Walton, R. Q. Snurr, *J. Phys. Chem. C* **2007**, *111*, 15350–15356.
[18] A. Gupta, S. Chempath, M. J. Sanborn, L. A. Clark, R. Q. Snurr, *Mol. Simul.* **2003**, *29*, 29.
[19] R. K. Castellano, J. Rebek Jr., *J. Am. Chem. Soc.* **1998**, *120*, 3657.
[20] V. A. Blatov, A. P. Shevchenko, D. M. Proserpio, *Cryst. Growth Des.* **2014**, *14*, 3576.

Received: October 16, 2015
Published Online: December 14, 2015

ChemPubSoc Europe

DOI: 10.1002/ejic.201800217

EurJIC European Journal of Inorganic Chemistry
Communication

Carbon Dioxide Sequestration

CO_2 Adsorption in SIFSIX-14-Cu-i: High Performance, Inflected Isotherms, and Water-Triggered Release via Reversible Structural Transformation

Debobroto Sensharma,[a] Sebastien Vaesen,[a] Colm Healy,[a] Jens Hartmann,[a] Amal Cherian Kathalikkattil,[a] Paul Wix,[a] Friedrich Steuber,[a] Nianyong Zhu,[a] and Wolfgang Schmitt*[a]

Abstract: **SIFSIX-14-Cu-i** belongs to a family of metal–organic materials (MOMs) with exciting gas-sorption properties and high technological impact. CO_2-adsorption isotherms are reported for **SIFSIX-14-Cu-i** revealing very high uptake combined with CO_2 selectivity. Importantly, the isotherms show distinct inflection points that result from CO_2-induced structural transformations and that can be modulated by the CO_2 uptake quantity. The observed behaviour directly relates to the unique structure of this azopyridine-stabilised compound and gives rise to the highest known working capacity for CO_2 uptake between 0.1 and 1 bar. Furthermore, the synthetic procedures for the reversible transformation of **SIFSIX-14-Cu-i** to a non-porous hydrated form are highlighted, and exploit the reversible porous to non-porous phase transition for instantaneous, moisture-mediated CO_2 release.

Introduction

The use of neutral, linear ditopic N-donor ligands, mononuclear metal centres, and charged inorganic anions, such as hexafluorosilicate ions (SiF_6^{2-}), provides a simple, rational and cheap method for the synthesis of microporous metal–organic materials such as the SIFSIX family.[1–6] SIFSIX materials are landmark compounds in the storage of CH_4 and CO_2.[3,7] They reveal exceptionally high selectivity for CO_2 over N_2, and can be used for separations of small-molecule hydrocarbons[8,9] and other gaseous adsorbates.[10] SIFSIX MOMs are generally based on "pillared sheet" **pcu**-type networks whereby ligand extensions can lead to isoreticular homologues and inter- or non-interpenetrated variants with tailored pore dimensions.[11]

CO_2 adsorption in such materials is particularly important in the context of pressing environmental concerns and critical future energy demands.[12] In microporous materials of this kind, ideal performance implies a strong selectivity for CO_2 over other gases, high volumetric uptake, and facile, low-energy recovery of the adsorbed CO_2. MOFs and other microporous materials with unsaturated metal centres (UMCs) or pendant amino functionalities often show high selectivities, but require elevated energies for CO_2 release and regeneration of the adsorbent.[13,14] SIFSIX MOMs do not have UMCs, but achieve exceptional selectivities through small, tailored pore diameters which optimise the degree of contact between the adsorbate and the adsorbent surface.[15] Some innovative approaches to tackle this problem have been reported, utilizing rational design to overcome these energetic difficulties.[16–18] With these considerations in mind, we identified the 4,4′-azopyridine (azpy) stabilised MOM $[Cu(azpy)_2(SiF_6)]$ (**SIFSIX-14-Cu-i**), as an optimal material for CO_2 adsorption as it possesses the following structural and electronic attributes: 1) an electron-rich N=N backbone associated with the 4,4′-azopyridine ligand to enhance CO_2-surface interaction, 2) a ligand sufficiently long enough to allow a high CO_2 uptake capacity, and 3) an interpenetrated framework structure to restrict the effective pore diameter.[19,20] Here, we report the first study focusing on the CO_2-adsorption behaviour in **SIFSIX-14-Cu-i**. The resulting isotherms are characteristic for a structural bi-stability giving rise to a CO_2 uptake–structure relationship that is mediated by the CO_2 uptake quantity. This structural effect results in inflected isotherms and leads to the highest known working capacity for CO_2 sorption between 0.1 and 1 bar. Further, it was found that **SIFSIX-14-Cu-i** shows a reversible porous to non-porous transition, which can be harnessed to release loaded CO_2 on demand on exposure to water as a stimulus.

Results and Discussion

During attempts to synthesise **SIFSIX-14-Cu-i** from MeOH/H_2O solvent mixtures, we noticed that previously established synthetic methods for other Cu-SIFSIX materials, only led to the

[a] *School of Chemistry & CRANN Institute, University of Dublin, Trinity College, Dublin 2, Ireland*
E-mail: schmittw@tcd.ie
http://chemistry.tcd.ie/staff/people/Schmitt/
Supporting information and ORCID(s) from the author(s) for this article are available on the WWW under https://doi.org/10.1002/ejic.201800217.

formation of the hydrated **sql** network in $[Cu(H_2O)_2(azpy)_2][SiF_6]\cdot H_2O$ (**H_2O-SIFSIX-14-Cu-i**).[21] However, phase-pure quantities of **SIFSIX-14-Cu-i** were synthesised by heating copper(II) hexafluorosilicate and 4,4′-azopyridine in dry methanol in a closed container, using a modified literature procedure (see the Supporting Information).[19] Appropriately sized crystals, suitable for single-crystal X-ray diffraction studies were grown by layering techniques using DMSO and MeOH solvents. The resulting crystal structure of **SIFSIX-14-Cu-i** (CCDC-1579765) contains constitutional MeOH guests, and the identified framework is consistent with previously reported SIFSIX-Cu homologues, and the reported network in **SIFSIX-14-Cu-i**.[15] It was found the isolated MOM crystallises in the tetragonal crystal system in the space group *I*4/*m* with unit cell axes lengths of 13.0690(3) and 8.3940(3) Å (see the Supporting Information). Structural analysis confirmed the doubly interpenetrated nature of the compound (Figure 1). The square-grid motif in the structure is characterised by Cu^{II}–N bond lengths of 2.0201(25) Å involving the equatorially binding azpy ligands. The pillaring hexafluorosilicate anions that bind in the apical positions of the Cu^{II} centres give rise to a Cu–F bond length of 2.4888(34) Å. Thus, the open-framework topology of **SIFSIX-14-Cu-i** differs significantly from the non-porous **sql** structure of **H_2O-SIFSIX-14-Cu-i**, which to some extent may be regarded as an ionisation isomer of the former structure. In **H_2O-SIFSIX-14-Cu-i** two axially coordinated H_2O ligands occupy the Jahn–Teller elongated positions on each Cu^{II} centre. Infinite, positively charged, square grid-like sheets with the composition $[Cu(H_2O)_2(4,4'\text{-azpy})_2]_n^{2n+}$ are charge-balanced by SiF_6^{2-} ions, which locate in the spaces between interpenetrating sheets (Figure 1c, Figure 1d). The hexafluorosilicate ions interact with the coordinated water molecules [F–O distance: 2.6826(17) Å] and constitutional pore water molecules [F–O distance: 2.7274(49) Å], forming an intricate H-bonded network and resulting in a stable, more dense, non-porous structure.

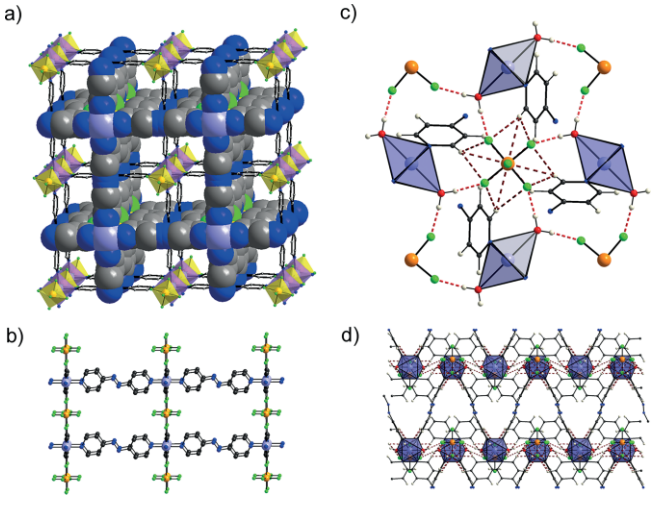

Figure 1. a) Two-fold interpenetrated structure of **SIFSIX-14-Cu-i**. b) Structure of a single net in **SIFSIX-14-Cu-i**; c) H···F interactions and binding environment of the SIF_6^{2-} ions in **H_2O-SIFSIX-14-Cu-i**. d) Dense network structure of **H_2O-SIFSIX-14-Cu-i**. Colour code: Cu blue/purple; Si orange/yellow; C grey, N blue; F green; O red; H white.

Gas-sorption experiments were carried out on **SIFSIX-14-Cu-i** and **H_2O-SIFSIX-14-Cu-i** after activation under high vacuum at 30 °C for 24 h (Figure 2 and the Supporting Information). N_2- and CO_2-sorption experiments on **H_2O-SIFSIX-14-Cu-i** confirmed that it is a non-porous material with negligible gas uptake (BET surface area of ca. 3 m^2/g). In contrast, the N_2-adsorption isotherm for **SIFSIX-14-Cu-i** at 77 K shows steep micropore adsorption at low partial pressure. The compound is characterised by a BET surface area of 435 m^2/g and a micropore volume of 0.16 cc/g as calculated by using the DFT method.[22] These values are lower but consistent with those reported for **SIFSIX-2-Cu-i** (735 m^2/g BET surface area and 0.26 cc/g micropore volume), a homologous MOM that is stabilised by bispyridylethyne linkers.[7] CO_2-sorption experiments on **SIFSIX-14-Cu-i** revealed high low-temperature uptake, with similar isotherms to the reported dipyridylethyne-based analogue, **SIFSIX-Cu-2-i**. Calculations on SIFSIX materials conclude that the adsorption mechanism is based on the relatively strong interactions between the partial positive charge on the CO_2 carbon atom and the partial negative charge on the electronegative equatorial fluorine atoms of the SiF_6^{2-} pillar.[7]

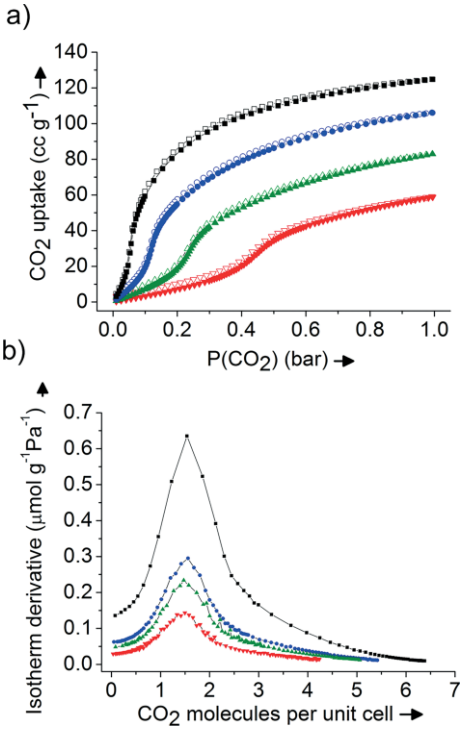

Figure 2. a) CO_2-sorption isotherms and b) first derivatives measured at 278 K (black), 293 K (blue), 308 K (green), 323 K (red); solid symbols: adsorption; open symbols: desorption.

However, a number of remarkable features that distinguish this compound from homologous materials in the SIFSIX series as well as other benchmark MOFs for CO_2 adsorption were observed. On measuring CO_2 isotherms across a range of temperatures, a distinct step in the isotherms was observed, becoming more pronounced at higher $P(CO_2)$ at higher temperatures. In terms of adsorption capacity, 1 cc of **SIFSIX-14-Cu-i** adsorbs

131.7 cc of CO_2 at 1 bar at 298 K. This value compares very well with other benchmark adsorbents for CO_2 capture, such as Zeolite 13X,[23] **SIFSIX-2-Cu-i**,[7] MIL-101,[24,25] and Mg-MOF-74[26] (Supporting Information). On the other hand, due to the inflection in the isotherm, the CO_2 quantity adsorbed at 0.1 bar is very low. In fact, of the listed benchmark materials only MOF-177[27] and MIL-101(Cr)[24] (Supporting Information), which are both mesoporous MOFs, adsorb less CO_2 in this pressure range. Thus, the observed change in the sign of the isotherm curvature results in an exceptionally high working capacity of 114.3 cc/cc between 0.1 and 1 bar. This is to the best of our knowledge the highest reported CO_2 working capacity in this pressure range and thus, renders **SIFSIX-14-Cu-i** an interesting material for use in pressure swing adsorption (PSA) technologies. **SIFSIX-14-Cu-i** shows no significant adsorption of N_2 at 293 K (Supporting Information). Using the Henry coefficients of the corresponding CO_2 isotherm, we calculate very high experimental CO_2/N_2 selectivities of 108 and 335 corresponding to fitted curves of the pre-inflection and post-inflection parts of the CO_2 isotherm (at 293 K), respectively.[28]

The inflection in the CO_2 isotherms implies a structural framework transition upon which a "closed framework" with low CO_2 uptake capacity opens up to form an "open framework" structure with a high CO_2 storage capacity. The transition occurs over a very small pressure range and is triggered by the adsorption of a specific amount of CO_2. The onset of the inflection is temperature dependent and occurs at higher pressures for isotherms that were recorded at higher temperatures. The reversibility of the uptake mechanism is assumed because the adsorption and desorption curves are superimposed and no differences are observed after 15 measurements without activation (Supporting Information). The reversibility is further consistent with the calculated isosteric heats of adsorption. Calculations using a Clausius–Clapeyron treatment based on the 278, 293, and 308 K isotherms, give moderate values that vary between 35–37 kJ/mol and which are expected to translate to reversible physisorption phenomena.[29] Through computation of the derivative of the experimental isotherms and expressing these as a function of the number of CO_2 molecules per the unit cell, it was determined that at the inflection point, 1.5 CO_2 molecules are accommodated per unit cell in the structure of **SIFSIX-14-Cu-i** (Figure 2b). From this we infer that initial adsorption of CO_2 stabilises a framework modification that is more amenable to CO_2 uptake than the empty framework. Gating,[30] breathing,[31] and swelling phenomena[32] can be ruled out on the basis of the absence of hysteretic desorption. The azpy ligand is a single aromatic system, and therefore the effect of rotation about the Cu–N bonds is reflected across the entire ligand. This, together with the characteristics of the desorption isotherms, and the similarity of powder X-ray diffraction (PXRD) patterns for the activated ("closed") and MeOH-included ("open") samples of **SIFSIX-14-Cu-i** (Supporting Information), lead to the conclusion that the relevant structural change is associated with a particular ordering of the azpy ligands defining the channel axis after guest adsorption and leading to more accessible voids. A crystallographic determination of the channel diameter (Supporting Information) indicates an effective pore diameter of ca. 3.6 Å in the structure, a value sufficiently close to the kinetic diameter of CO_2 (3.3–3.9 Å) for minor changes in ligand orientation to have marked effects.[33] On the basis of the evidence presented, we suggest a simple parallel ordering of ligands to the channel axis, or a stabilisation of suitable non-parallel ligand conformations (subject to the complication that there are no distinct "cages" in **SIFSIX-14-Cu-i**, because of the emergence of the channels from framework interpenetration).[34] The difference in the free energies between frameworks before and after the inflection was determined by using the method developed by Coudert et al. (Supporting Information).[35] The resulting ΔF_{host} value is equal to 2.7 kJ/mol and agrees well with the predicted energies of the encountered structural transition.

As with all Cu-SIFSIX structures, the title compound **SIFSIX-14-Cu-i** is susceptible to hydrolytic degradation in the presence of H_2O. However, here, this hydrolytic instability can be utilized to trigger a well-defined phase transition: a structural rearrangement that is more severe than the formerly outlined CO_2-mediated reordering. The H_2O-initiated transformation produces **H_2O-SIFSIX-14-Cu-i** upon which the entire quantity of the captured CO_2 is instantaneously released on demand. Importantly, the rearrangement is reversible, thus rendering **SIFSIX-14-Cu-i** as a stimulus-responsive material that can be recycled.

On exposure to air under ambient humidity, one notices a green colourisation of the original red/brown crystalline material, whereby **SIFSIX-14-Cu-i** converts quantitatively to **H_2O-SIFSIX-14-Cu-i** over a time period of few hours (Supporting Information). A more rapid structural transition forming the corresponding non-porous structure can be triggered through the addition of liquid H_2O and is associated with an instant release of the captured CO_2. The conversion can be monitored by PXRD measurements. The phase transition entails a large-scale structural reordering, involving a substitution of Cu–F bonds with Cu–O bonds, migration of SiF_6^{2-} ions into voids, and an overall change in the mode of interpenetration, and a total reorganisation of networks involving the breaking and reforming of Cu–N bonds. This observation agrees very well with previously conducted water vapour sorption studies.[19]

The important regenerative, reversible transformation from the non-porous **H_2O-SIFSIX-14-Cu-i** phase to **SIFSIX-14-Cu-i** was achieved by heating **H_2O-SIFSIX-14-Cu-i** in MeOH. Methanol effects a transformation by removing the kinetically labile, Jahn–Teller elongated, axial H_2O ligands from the Cu^{II} centres. This destabilises the H-bonding network that holds the SiF_6^{2-} ions in place in the square pore windows by removing the axially coordinated H_2O groups that participate in H···F interactions. As a consequence, the SiF_6^{2-} ions migrate to bridge adjacent Cu^{II} centres, and force a reconfiguration of the network into a porous 3D structure. The reverse conversion occurs when H_2O molecules bind to axial positions on the Cu^{II} centres in the dry 3D network: SiF_6^{2-} ions are displaced, occupy H-bonded positions in the pore windows, and the non-porous 2D framework is formed; this is the most stable arrangement in wet conditions. Hence the 2D to 3D transformation occurs reversibly with the introduction or removal of H_2O acting as a stimulus.

Unlike many of the paradigm-defining recyclable MOFs, the **SIFSIX-14-Cu-I** and **H_2O-SIFSIX-14-Cu-i** pair represents a system of two distinct structures, both of which contain identical (non-solvent) components; in the process of converting one to the other, no building blocks need to be re-added.[36–38] In preceding literature, MeOH has been shown to effect the removal of coordinated H_2O moieties from Cu^{II}–N-donor coordination polymers.[39,40] Coordination polymers of this kind are also known to undergo changes in structure and porosity on dehydration.[41] In agreement with the translational scale of the molecular rearrangements that facilitate the **SIFSIX-14-Cu-i** to **H_2O-SIFSIX-14-Cu-i** transition, we were unable to observe any evidence of the transformation proceeding in a single crystal–single crystal fashion under the applied conditions.[42] The samples obtained after one conversion–reconversion cycle are phase pure as characterized by PXRD, but the system is limited by some loss of yield due to leaching of ligand into MeOH (Supporting Information).

The very high CO_2 uptake capacity of **SIFSIX-14-Cu-i** and the contrasting non-porous nature of **H_2O-SIFSIX-14-Cu-i**, in combination with the facile reversible transition between the compounds, are properties that we combined to develop a stimulus-responsive system for the instantaneous release of large volumes of CO_2.[43,44] Thus, samples of **SIFSIX-14-Cu-i** were evacuated, saturated with CO_2, exposed to ambient air for a few seconds, and sealed in a flask. On contact with liquid H_2O, a large increase in CO_2 pressure was observed (Figure 3). Upon addition of a small quantity of MeOH and heating, **H_2O-SIFSIX-14-Cu-i** could be reconverted to **SIFSIX-14-Cu-i** and reused (Supporting Information). We note that moisture has been used as a stimulus for mechanical[45] and displacement-based[46] release of adsorbates from MOFs. However, moisture-triggered release from **H_2O-SIFSIX-14-Cu-i** represents a landmark in that CO_2 is forcibly excluded from the framework, leading to significantly faster release than would be seen by simple diffusion or displacement processes. Further, the large differences between the CO_2-sorption capacities of the porous and non-porous forms, lead to significantly larger gas uptake/release volumes in comparison to those of previously described materials.

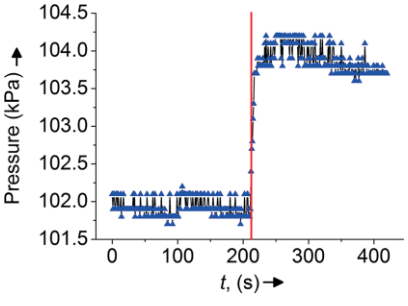

Figure 3. Pressure vs. time for the release of loaded CO_2 from **SIFSIX-14-Cu-i**. Excess liquid water was allowed to make contact with the sample at t = 210 s.

The key characteristics of the presented reaction system are summarized in Scheme 1.

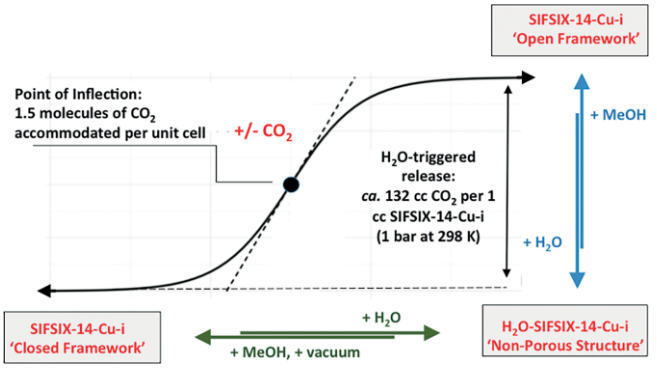

Scheme 1. Schematic representation of the CO_2- and H_2O-induced transformations.

Conclusions

In conclusion, we report excellent CO_2-adsorption and -desorption characteristics for **SIFSIX-14-Cu-i**. Uptakes at 1 bar and at room temperature are high, and a high selectivity for CO_2 over N_2 is observed. Importantly, the adsorption isotherms are inflected, providing evidence for framework-ordering mediated by the adsorbed CO_2 molecules. This effect results in the highest reported CO_2-sorption capacity between 0.1 and 1 bar. **SIFSIX-14-Cu-i** and the nonporous coordination polymer **H_2O-SIFSIX-14-Cu-i** are easily interconvertible. This reversible conversion can be used for the fast, moisture-triggered mechanical release of adsorbed CO_2.

CCDC 1579765 (for **SIFSIX-14-Cu-i**) contains the supplementary crystallographic data for this paper. These data can be obtained free of charge from The Cambridge Crystallographic Data Centre.

Acknowledgments

The authors thank the Science Foundation Ireland (13/IA/1896) and the European Research Council (CoG 2014-647719).

Keywords: CO_2 capture · Metal–organic frameworks · Porous materials · Coordination chemistry · Copper

[1] S. Kitagawa, *Angew. Chem. Int. Ed.* **2015**, *54*, 10686–10687; *Angew. Chem.* **2015**, *127*, 10834.
[2] S. Subramanian, M. J. Zaworotko, *Angew. Chem. Int. Ed. Engl.* **1995**, *34*, 2127–2129; *Angew. Chem.* **1995**, *107*, 2295.
[3] S. Noro, S. Kitagawa, M. Kondo, K. Seki, *Angew. Chem. Int. Ed.* **2000**, *39*, 2081–2084; *Angew. Chem.* **2000**, *112*, 2161.
[4] M.-J. Lin, A. Jouaiti, N. Kyritsakas, M. W. Hosseini, *CrystEngComm* **2009**, *11*, 189–191.
[5] M. Eddaoudi, O. Shekhah, Y. Belmabkhout, K. Adil, A. J. Cairns, P. Bhatt, *Chem. Commun.* **2015**, *4*, 1166–1169.
[6] P. Nugent, V. Rhodus, T. Pham, B. Tudor, K. Forrest, L. Wojtas, B. Space, M. Zaworotko, *Chem. Commun.* **2013**, *49*, 1606.
[7] P. Nugent, Y. Belmabkhout, S. D. Burd, A. J. Cairns, R. Luebke, K. Forrest, T. Pham, S. Ma, B. Space, L. Wojtas, B. Space, M. Zaworotko, *Nature* **2013**, *495*, 80–84.
[8] X. Cui, K. Chen, H. Xing, Q. Yang, R. Krishna, Z. Bao, H. Wu, W. Zhou, X. Dong, Y. Han, B. Li, Q. Ren, M. J. Zaworotko, B. Chen, *Science* **2016**, *353*, 141–144.
[9] Z. Zhang, Q. Yang, X. Cui, L. Yang, Z. Bao, Q. Ren, H. Xing, *Angew. Chem. Int. Ed.* **2017**, *56*, 16282–16287; *Angew. Chem.* **2017**, *129*, 000.

[10] S. K. Elsaidi, M. H. Mohamed, C. M. Simon, E. Braun, T. Pham, K. A. Forrest, W. Xu, D. Banerjee, B. Space, M. J. Zaworotko, P. K. Thallapally, *Chem. Sci.* **2017**, *8*, 2373–2380.
[11] A. Bajpai, M. Lusi, M. J. Zaworotko, *Chem. Commun.* **2017**, *53*, 3978–3981.
[12] A. Goeppert, M. Czaun, G. K. Surya Prakash, G. A. Olah, *Energy Environ. Sci.* **2012**, *5*, 7833.
[13] S. Ma, H. C. Zhou, *J. Am. Chem. Soc.* **2006**, *128*, 11734–11735.
[14] R. W. Flaig, T. M. Osborn Popp, A. M. Fracaroli, E. A. Kapustin, M. J. Kalmutzki, R. M. Altamimi, F. Fathieh, J. A. Reimer, O. M. Yaghi, *J. Am. Chem. Soc.* **2017**, *139*, 12125–12128.
[15] Y. Belmabkhout, V. Guillerm, M. Eddaoudi, *Chem. Eng. J.* **2016**, *296*, 386–397.
[16] P.-Q. Liao, H. Chen, D.-D. Zhou, S.-Y. Liu, C.-T. He, Z. Rui, H. Ji, J.-P. Zhang, X.-M. Chen, *Energy Environ. Sci.* **2015**, *8*, 1011–1016.
[17] P.-Q. Liao, X.-W. Chen, S.-Y. Liu, X.-Y. Li, Y.-T. Xu, M. Tang, Z. Rui, H. Ji, J.-P. Zhang, X.-M. Chen, *Chem. Sci.* **2016**, *7*, 6528–6533.
[18] P. Q. Liao, D. D. Zhou, A. X. Zhu, L. Jiang, R. B. Lin, J. P. Zhang, X. M. Chen, *J. Am. Chem. Soc.* **2012**, *134*, 17380–17383.
[19] D. O'Nolan, A. Kumar, M. J. Zaworotko, *J. Am. Chem. Soc.* **2017**, *139*, 8508–8513.
[20] B. Li, X. Cui, D. O'Nolan, H. M. Wen, M. Jiang, R. Krishna, H. Wu, R. B. Lin, Y. S. Chen, D. Yuan, H. Xing, W. Zhou, Q. Ren, G. Quian, M.J. Zaworotko, B. Chen, *Adv. Mater.* **2017**, *29*, 1–7.
[21] M. A. Withersby, A. J. Blake, N. R. Champness, P. A. Cooke, P. Hubberstey, A. L. Realf, S. J. Teat, M. Schröder, *J. Chem. Soc., Dalton Trans.* **2000**, *2*, 3261–3268.
[22] P. I. Ravikovitch, G. L. Haller, A. V. Neimark, *Adv. Colloid Interface Sci.* **1998**, *76*, 203–226.
[23] S. Cavenati, C. A. Grande, A. E. Rodrigues, *J. Chem. Eng. Data* **2004**, *49*, 1095–1101.
[24] P. L. Llewellyn, S. Bourrelly, C. Serre, A. Vimont, M. Daturi, L. Hamon, G. De Weireld, J. Chang, D. Hong, Y. K. Hwang, S. H. Jhung, G. Ferey, *Langmuir* **2008**, 7245–7250.
[25] Z. Zhou, L. Mei, C. Ma, F. Xu, J. Xiao, Q. Xia, Z. Li, *Chem. Eng. Sci.* **2016**, *147*, 109–117.
[26] D. Britt, H. Furukawa, B. Wang, T. G. Glover, O. M. Yaghi, *Proc. Natl. Acad. Sci. USA* **2009**, *106*, 20637–20640.
[27] D. Saha, Z. Bao, *Environ. Sci. Technol.* **2010**, *44*, 1820–1826.
[28] L. Hamon, P. L. Llewellyn, T. Devic, A. Ghoufi, G. Clet, V. Guillerm, G. D. Pirngruber, G. Maurin, C. Serre, G. Driver, W. van Beek, E. Jolimaître, A. Vimont, M. Daturi, G. Férey, *J. Am. Chem. Soc.* **2009**, *131*, 17490–17499.
[29] D. M. Ruthven, *Principles of Absorption and Absorption Processes*, Wiley-Interscience, New York, **1984**.
[30] R. Kitaura, K. Seki, G. Akiyama, S. Kitagawa, *Angew. Chem. Int. Ed.* **2003**, *42*, 428–431; *Angew. Chem.* **2003**, *115*, 444.
[31] C. Serre, F. Millange, C. Thouvenot, M. Noguès, G. Marsolier, D. Louër, G. Férey, *J. Am. Chem. Soc.* **2002**, *124*, 13519–13526.
[32] C. Serre, C. Mellot-Draznieks, S. Surblé, N. Audebrand, Y. Filinchuk, G. Férey, *Science* **2007**, *315-318*, 1828–1831.
[33] S. Sircar, *Ind. Eng. Chem. Res.* **2006**, *45*, 5435–5448.
[34] P. Kanoo, S. K. Reddy, G. Kumari, R. Haldar, C. Narayana, S. Balasubramanian, T. K. Maji, *Chem. Commun.* **2012**, *48*, 8487.
[35] F.-X. Coudert, M. Jeffroy, A. H. Fuchs, A. Boutin, C. Mellot-Draznieks, *J. Am. Chem. Soc.* **2008**, *130*, 14294–14302.
[36] L. Pan, H. Liu, X. Lei, X. Huang, D. H. Olson, N. J. Turro, J. Li, *Angew. Chem. Int. Ed.* **2003**, *42*, 542–546; *Angew. Chem.* **2003**, *115*, 560.
[37] A. Lan, K. Li, H. Wu, L. Kong, N. Nijem, D. H. Olson, T. J. Emge, Y. J. Chabal, D. C. Langreth, M. Hong, J. Li, *Inorg. Chem.* **2009**, *48*, 7165–7173.
[38] J. Li, D. J. Timmons, H. Zhou, *J. Am. Chem. Soc.* **2009**, 6368–6369.
[39] D. Jiang, A. Urakawa, M. Yulikov, T. Mallat, G. Jeschke, A. Baiker, *Chem. Eur. J.* **2009**, *15*, 12255–12262.
[40] D. Bradshaw, J. E. Warren, M. J. Rosseinsky, *Science* **2007**, *315*, 977–980.
[41] Y. Cheng, A. Rondo, H. Noguchi, H. Kajiro, K. Urita, T. Ohba, K. Kaneko, H. Kanoh, *Langmuir* **2009**, *25*, 4510–4513.
[42] I. Halasz, *Cryst. Growth Des.* **2010**, *10*, 2817–2823.
[43] S. Horike, S. Shimomura, S. Kitagawa, *Nat. Chem.* **2009**, *1*, 695–704.
[44] H. Li, M. R. Hill, *Acc. Chem. Res.* **2017**, *50*, 778–786.
[45] B. D. Chandler, G. D. Enright, K. A. Udachin, S. Pawsey, J. A. Ripmeester, D. T. Cramb, G. K. H. Shimizu, *Nat. Mater.* **2008**, *7*, 229–235.
[46] E. D. Bloch, W. L. Queen, S. Chavan, P. S. Wheatley, J. M. Zadrozny, R. Morris, C. M. Brown, C. Lamberti, S. Bordiga, J. R. Long, *J. Am. Chem. Soc.* **2015**, *137*, 3466–3469.

Received: February 13, 2018

CrystEngComm

COMMUNICATION

View Article Online
View Journal | View Issue

Cite this: *CrystEngComm*, 2018, **20**, 5127

Received 21st July 2018,
Accepted 15th August 2018

DOI: 10.1039/c8ce01211c

rsc.li/crystengcomm

Passing it up the ranks: hierarchical ion-size dependent supramolecular response in 1D coordination polymers†

Debobroto Sensharma, Paul Wix, Amal Cherian Kathalikkattil and Wolfgang Schmitt *

The synthesis and structural characterisations of four 1D coordination polymers based on the 1,3,5-tris(4-carboxyphenyl)benzene (H_3btb) and 2,4,6-tris(2-pyridyl)-1,3,5-triazine (2-tpt) ligands are reported: $[M^{II}(Hbtb)(2\text{-tpt})]\cdot x$DMF, M = Zn (**1**), Ni (**2**), Mn (**3**) and Cd (**4**). The tridentate chelating mode of the 2-tpt ligand hinders the formation of polynuclear assemblies, leading to the recurrence of structurally related 1D motifs in all four compounds. Two distinct packing arrangements are obtained for the 1D motifs demonstrating how variable radii and coordination environments influence supramolecular interactions throughout the structures. Further, the nature of the metal ion influences respective orientations of interacting groups in the structures, illustrating the importance of ligand flexibility in coordination polymer design.

After Bailar's analogy between organic polymers and coordination polymers in 1964, research activities encompassing the synthesis, characterisation, and use of coordination polymers have grown exponentially.[1,2] Extended metal–ligand assemblies such as coordination networks, coordination polymers and metal–organic frameworks have become desired synthetic targets as these materials have proven utility in catalysis, sensing, gas storage, and drug delivery, among other areas.[3–10] One-dimensional coordination polymers (1D CPs), which extend only lengthwise, are topologically the simplest class of these materials and are of interest due to their electronic, magnetic, optic and catalytic properties.[11–14] From a supramolecular point of view, 1D CPs offer a platform in which both, bonding and non-bonding interactions play a key role in influencing connectivity in their respective dimensions, and therefore the functions of the materials.[15,16] 1D chains may consist of straight, zigzag, or more intricate ladder or ribbon conformations.[12,17] The overall crystal structures are determined by the non-bonding interactions between individual chains, commonly involving H-bonding or π–π stacking interactions.[18–20] Various interwoven structural motifs and entanglements between chains can be promoted by these interactions, and dynamic changes in these arrangements can be engineered.[21]

1,3,5-Tris(4-carboxyphenyl)benzene (H_3btb) and 2,4,6-tris(2-pyridyl)-1,3,5-triazine (2-tpt) are examples of typical tritopic ligands used in coordination chemistry.[22,23] The H_3btb ligand has previously been combined with N-donors, and 2-tpt with carboxylate ligands, to yield a number of extended mixed-ligand materials.[24,25] The combination of these ligands presents attractive synthetic possibilities due to the availability of N- and O-donor functionalities, as well as extensive π-conjugation. These features confer stability and functionality to the resulting coordination polymers, and can result in synergistic structure directing effects.[26–29] The availability of the chelating 2,2′:6′,2″-terpyridine-type coordination mode by the 2-tpt ligand allows the conception of a polymer in which three coordinative positions on the metal centre are occupied by N-donor atoms. This impairs the formation of oligonuclear secondary building units (SBUs) and leads to structures based on mononuclear metal centres.[30] In this scenario, the variability between metal centres in terms of SBU formation becomes greatly reduced, potentially giving rise to systems in which a variety of metal centres could be applied for the formation of structurally related coordination polymers.

In this communication, we report the synthesis, X-ray crystal structures, and physicochemical characterisations of four one-dimensional coordination polymers based on M(II) centres with varying ionic radii, and the combination of H_3btb and 2-tpt ligands. The diversity of packing modes and differences in weak interactions are understood by examining essential changes in the coordination environments of each 1D polymer. We elucidate the underlying structural flexibility of

School of Chemistry & CRANN Institute, University of Dublin, Trinity College, Dublin 2, Ireland. E-mail: schmittw@tcd.ie; Fax: +353 1 6712826; Tel: +353 1 8963495

† Electronic supplementary information (ESI) available: Syntheses, physicochemical characterisations and structural analyses. CCDC 1852299, 1852474, 1852300 and 1852472. For ESI and crystallographic data in CIF or other electronic format see DOI: 10.1039/c8ce01211c

the polymer motif that allows various coordination geometries around the M(II) centres to result in the same 1D polymer, as well as the consequences of this accommodation for the organisation of 1D chains relative to each other in the 3D crystal structure, mediated by various π–π and H-bonding interactions between ligand moieties.

A variety of differently sized M(II) centres – Mn(II), Ni(II), Zn(II), and Cd(II) – were combined as chloride or nitrate salts with btb and 2-tpt in *N*,*N*-dimethylformamide. The initially formed slurry was clarified simply by agitation at room temperature. On heating the solutions for 4 days at 100 °C, single crystals of the four compounds were obtained. Single crystal X-ray diffraction studies were carried out on all four compounds: [Zn(Hbtb)(2-tpt)]·DMF (**1**), [Ni(Hbtb)(2-tpt)]·0.7DMF (**2**), [Mn(Hbtb)(2-tpt)]·1.25DMF (**3**) and [Cd(Hbtb)(2-tpt)]·DMF (**4**).

All four compounds consist of infinite one-dimensional coordination polymer chains (Fig. 1). Each metal centre is bound to two Hbtb ligands *via* the carboxylate groups, as well as one 2-tpt ligand. Two carboxylate groups of each Hbtb ligand bind to a metal centre, leaving one protonated carboxylic acid group unbound and pendant in the structure. The 2-tpt ligand, in which one pyridine ring remains uncoordinated, acts as a capping group for the metal centres. Together the two ligands give rise to 1D polymeric chains with both uncoordinated N- and O- donors. All structures build out honeycomb-like 2D networks which are facilitated by hydrogen bonds between the protonated carboxylic acid moiety of the Hbtb ligand and the carboxylate group of a deprotonated Hbtb arm (Fig. 2). Stabilised by numerous π–π interactions, these layers are stacked on top of each other adopting various accommodating stacking motifs, which we show to be determined by the size of the metal ion.

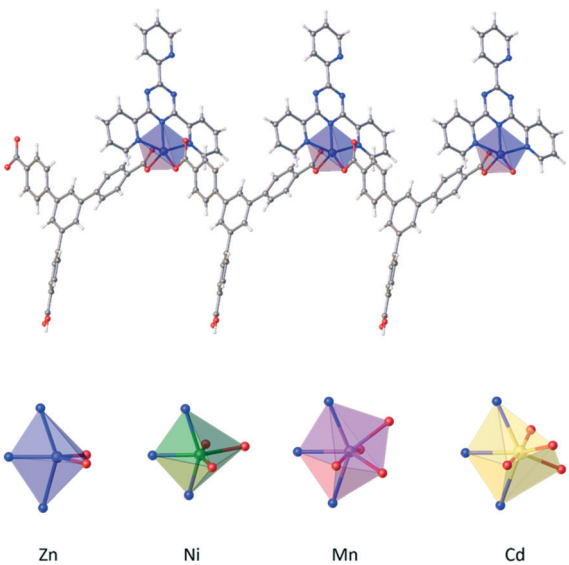

Fig. 1 The 1D polymer chain motif in **1** (above). Two Hbtb ligands are bound to each metal centre along with one 2-tpt ligand. Hydrogen atoms are omitted for clarity. Given below are the coordination environments observed in compounds **1**–**4** which adopt structurally similar 1-D chain motifs. Steric hindrance in **3** (Mn) and **4** (Cd) leads to the tilting of the carboxylate groups out of the horizontal plane present in **1** (Zn) and **2** (Ni).

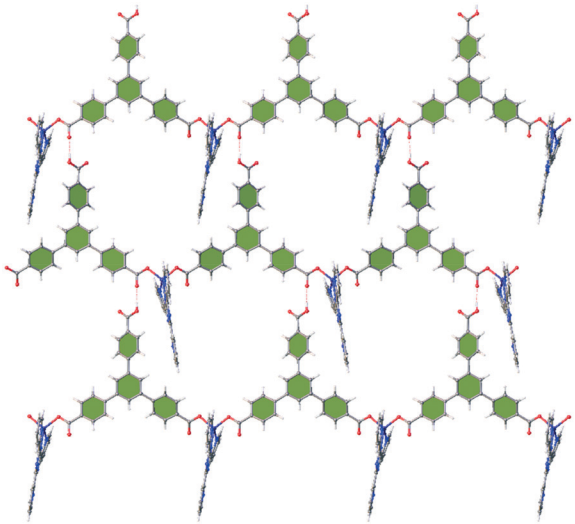

Fig. 2 The H-bonded 2D honeycomb structure present in all four compounds. Here shown for [Zn(Hbtb)(2-tpt)]·2DMF (**1**). View in the direction of the crystallographic *c*-axis.

In [Zn(Hbtb)(2-tpt)]·DMF (**1**) the carboxylate groups of the Hbtb ligands are bound to the Zn(II) centres in a *syn*-monodentate fashion. This creates a slightly distorted trigonal bipyramidal Zn(II) coordination environment in which two nitrogen donor atoms from the 2-tpt ligand are located in the axial positions. The M–O distances are the shortest in the reported series with 1.948(3) Å and 1.963(3) Å. With increasing ionic radii (Zn < Ni < Mn < Cd; see Table 1) the coordination number increases from 5 to 7 and the binding mode of the carboxylate functionality changes from monodentate to bidentate. Structural disorder leads to some variation in the denticity of **2**, **3**, and **4**. While the oxygen donors reside in the equatorial planes for **1** and **2**, steric effects lead to the rotation of the carboxylate functionalities relative to each other and hence, move out of the plane for **3** and **4** as shown in Fig. 1. This effect promotes a distorted octahedral Ni(II) coordination geometry in **2** and distorted capped octahedral Mn(II) or capped trigonal prismatic Cd(II) coordination environments in **3** and **4**, respectively, as determined by geometrical analysis with the program SHAPE V2.1. (Fig. 1 and Table S3†).[31]

The packing is stabilised by numerous π–π interactions between the Hbtb ligands. For the compounds containing the smaller metal ions, **1** (Zn(II)) and **2** (Ni(II)), two different stacking modes occur in the crystal structures, type 1 and type 2 (Fig. 4). Type 1 stacking is facilitated by two Hbtb ligands that are rotated 180° to each other and engage in π–π interactions with the central and the peripheral benzene rings. For type 2 stacking the Hbtb ligands are rotated 180° to each other and overlap with two peripheral benzene rings. Further, in **1** and **2**, the Hbtb ligands are stacked in a 1–2–1–2 fashion adopting adopting alternating type 1 and type 2 stacking sequences

Table 1 Comparison of different structural features in **1**–**4** (compare also ESI, Table S3 for further details)

	1 – Zn	2 – Ni	3 – Mn	4 – Cd
Coordination	5	5/6	6/7	6/7
Denticity	Mono/mono	Mono/bi	Mono/bi	Mono/bi
Ionic Radii (Å)	0.68	0.69	0.90	1.03
Stacking Pattern	1–2–1–2	1–2–1–2	1–2–1–3	1–2–1–3
M-O distances (Å)	1.94	1.95	2.17–2.41	2.14–2.56
Shape Analysis	Square pyramidal	Octahedral	Capped octahedral	Capped trigonal prismatic

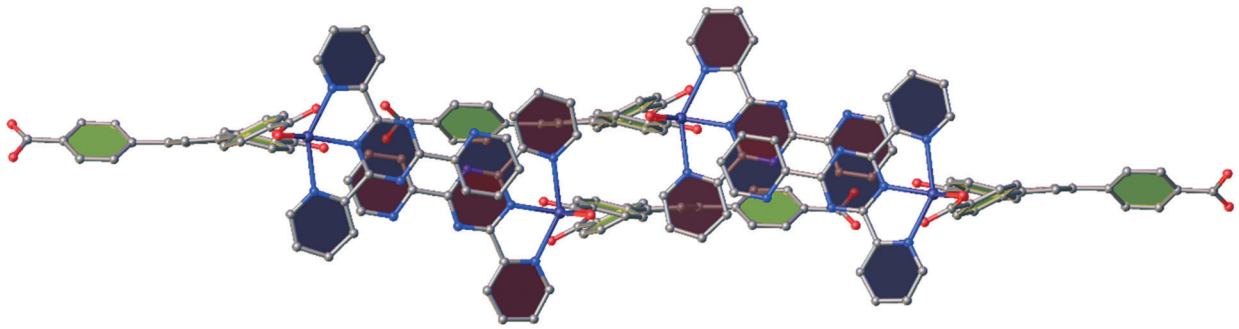

Fig. 3 Stacking of the 2-tpt ligand viewed in the direction of the crystallographic *b*-axis of compound **1**.

throughout the structure. Type 2 stacking is additionally stabilised through π–π interactions of the 2-tpt ligands which facilitate perpendicular arrangements to the Hbtb-based sheets (Fig. 3). The absence of crystalline products when 2,2′,6′,2″-terpyridine was used in place of 2-tpt under identical conditions indicates the importance of the pendant pyridyl aromatic system and consequent stacking interactions for the overall formation of the compounds. Contrarily, type 1 stacking does not involve such stabilising interactions of the 2-tpt ligands.

Generally, the strength of π–π interactions is perceived to be dependent on the angle between the two π-systems and correlates with the inter-plane distance.[32,33] Misalignments, tilting effects and consequent increased inter-plane distances hamper π–π interactions and thus they become less favourable within a supramolecular arrangement. Aromatic carboxylate ligands possess a conjugated π-system which aligns the aromatic rings with the carboxylate group. The benzene rings of the ligand itself are naturally non-coplanar with respect to each other because of the steric repulsion from hydrogen atoms on adjacent rings. Usually, angles of around 35–45° between benzene rings in biphenyl-type pairs are found in the literature.[34]

In **1** and **2**, in which the carboxylate ligand is bound in a monodentate fashion, this angle is consistent with the literature values as the free oxygen atom facilitates the facile rotation of the benzoate group to accommodate this preferred geometry. Only in the case of the larger M(II) ions, Mn (**3**) and Cd (**4**), the bidentate binding mode and subsequent steric repulsion of the oxygen atoms lead to an increase of the angle between the two carboxylate groups bound to the same metal ion from 41° up to 69° (Fig. 1). In this way the modified coordination environment of the metal ions extends to the aromatic system of the ligand and influences the relative orientations of the phenyl rings, leading to less favourable π–π interactions between the 2D sheets. Centroid-centroid distances and interplanar angles between phenyl rings in the case of type 2 stacking increase from 3.6 Å and 14.8° in **1** to 5.0 Å and 46.4° (outside the range of conventional π–π interactions) in **3** as a result of the steric repulsion from the coordination environment. While type 1 and type 2 stacking modes are observed in **3** and **4**, reduced favourability for stabilising π–π interactions forces the structures to accommodate a third, new stacking motif that governs the packing of the 2D sheets. This type 3 stacking motif is facilitated by two Hbtb ligands that are rotated 180° to each other around the perpendicular axis of the central benzene ring (Fig. 4). Consequently, the honeycomb type sheets in **3** and **4** stack in 1–2–1–3 fashion instead of 1–2–1–2. Thus, this flexibility in packing enables the system to accommodate various metal ions with large ionic radii difference (Fig. 5).

The challenge posed by unfavourable steric effects due to ion size in the 1D polymeric structure is overcome by rearrangements in the three dimensional packing illustrating

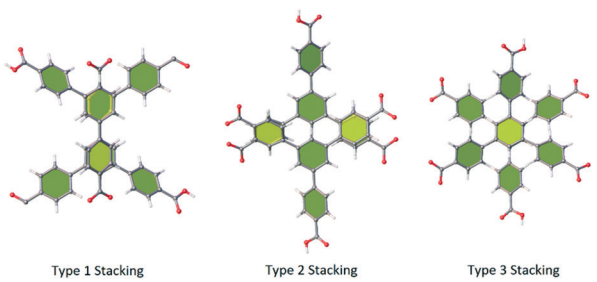

Fig. 4 Different stacking modes present in the crystal structures. Type 3 stacking only occurs in **3** and **4**.

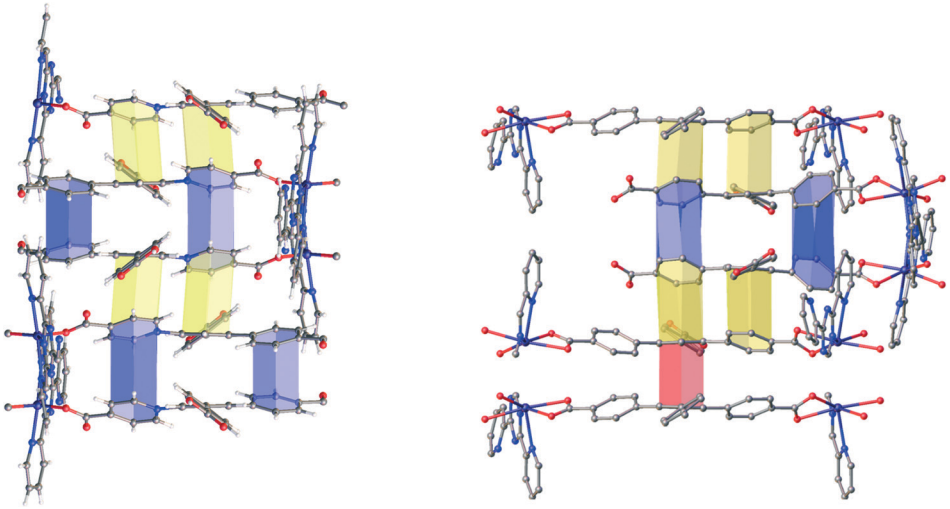

Fig. 5 Left: Packing representations in **1** with view in the [101]-direction showing the 1–2–1–2 stacking pattern; right: packing representations in **3** with view in the direction of the crystallographic *b*-axis showing the 1–2–1–3 stacking pattern.

a hierarchical supramolecular response to a local modification created at the metal centre.

Hirshfeld surface analyses were carried out in order to gain a better understanding of the nature of these interactions.[35,36] Decomposed fingerprints for percent values corresponding to C–C and C–H interactions were used as an indicator of the prevalence of the π–π interactions and the π-system overlap. Tilting of the benzene rings results in more C–H and less C–C contribution and therefore raises the C–H/C–C ratio, as stacking phenyl rings become more misaligned. The analysis highlights that this ratio correlates with the ion size of the transition metal. One notices a clear effect on the ratios, increasing from 3.9 for the smallest to 6.1 for the largest metal ion in the series (ESI,† Table S3).

In addition, Hirshfeld surface analysis also confirms the role of the pendant protonated carboxylic acid moiety in forming short H-bonding interactions with oxygen atoms from deprotonated carboxylate groups, resulting in 2D honeycomb-like motifs in all four compounds. The constitutional DMF solvent molecules do not play any apparent structural role in **1**–**4**, which is an explanation as to why they are heavily disordered.

Whilst **2** forms in low yield, bulk characterisations for **1**, **3**, and **4** were carried out. Phase-purity of the as-synthesised crystalline materials was ascertained by powder X-ray diffraction studies, elemental analysis (ESI) and FTIR spectroscopy. The thermal stability of the compounds was evaluated by thermogravimetric analysis, revealing stability up to 370 °C upon which the organic ligands undergo degradation. A preceding step corresponding to the loss of trapped DMF molecules at 120 °C is observed for all investigated compounds. The relative high temperature of solvent loss agrees well with the observation that in both kinds of packing arrangement, disordered DMF molecules are contained in inaccessible voids. Therefore, solvent loss can only occur with a related structural degradation.

In conclusion, we report the synthesis of a number of one-dimensional transition metal coordination polymers based on a mixed ligand strategy. The Hbtb ligand is used to provide linear extension, while the 2-tpt ligand chelates the metal centres, providing a valuable synthetic handle over SBU formation. The versatility of the synthetic strategy is demonstrated by the characterisation of four, structurally closely-related polymers formed by different metal centres, namely Cd(II), Zn(II), Mn(II), and Ni(II), and the analysis of their single crystal X-ray structures. These coordination polymers are formed despite large differences in the size and coordination environments of the metal centres used. We show how these differences are accommodated in the versatile 1D motif, but re-emerge in the 3D structure by re-organising the supramolecular interactions between individual 1D chains, resulting in divergent packing arrangements and exemplifying several key concepts in the engineering of crystalline coordination polymer frameworks. In future we aim to extend to our findings to structurally modified carboxylate and pyridyl ligands. The concept may provide a valuable a synthetic platform for the preparation of polymers that facilitate some control over optical, electronic or magnetic properties. Such advances towards the synthesis of 1-D polymers may impact on diverse areas of application, *e.g.* sensing or catalysis.

The authors thank the Science Foundation Ireland (SFI; 13/IA/1896), the European Research Council (SUPRAMOL CoG 2014–647719) and the Irish Research Council (fellowship GOIPG/2015/2713 for P.W.) for the financial support. Crystallographic data, CCDC 1852299, 1852474, 1852300 and 1852472.

Conflicts of interest

There are no conflicts to declare.

Notes and references

1 J. C. Bailar, in *Preparative Inorganic Reactions*, ed. W. L. Jolly, Interscience, New York, 1964, vol. 1, pp. 1–25.

2 P. Z. Moghadam, A. Li, S. B. Wiggin, A. Tao, A. G. P. Maloney, P. A. Wood, S. C. Ward and D. Fairen-Jimenez, *Chem. Mater.*, 2017, **29**, 2618–2625.
3 J. Lee, O. K. Farha, J. Roberts, K. A. Scheidt, S. T. Nguyen and J. T. Hupp, *Chem. Soc. Rev.*, 2009, **38**, 1450.
4 M. C. So, G. P. Wiederrecht, J. E. Mondloch, J. T. Hupp and O. K. Farha, *Chem. Commun.*, 2015, **51**, 3501–3510.
5 Z. Hu, B. J. Deibert and J. Li, *Chem. Soc. Rev.*, 2014, **43**, 5815–5840.
6 P. Nugent, Y. Belmabkhout, S. D. Burd, A. J. Cairns, R. Luebke, K. Forrest, T. Pham, S. Ma, B. Space, L. Wojtas, M. Eddaoudi and M. J. Zaworotko, *Nature*, 2013, **495**, 80–84.
7 D. Britt, H. Furukawa, B. Wang, T. G. Glover and O. M. Yaghi, *Proc. Natl. Acad. Sci. U. S. A.*, 2009, **106**, 20637–20640.
8 P. Horcajada, T. Chalati, C. Serre, B. Gillet, C. Sebrie, T. Baati, J. F. Eubank, D. Heurtaux, P. Clayette, C. Kreuz, J. S. Chang, Y. K. Hwang, V. Marsaud, P. N. Bories, L. Cynober, S. Gil, G. Férey, P. Couvreur and R. Gref, *Nat. Mater.*, 2010, **9**, 172–178.
9 D. Sensharma, S. Vaesen, C. Healy, J. Hartmann, A. C. Kathalikkattil, P. Wix, F. Steuber, N. Zhu and W. Schmitt, *Eur. J. Inorg. Chem.*, 2018, 1993–1997.
10 N. Zhu, G. Tobin and W. Schmitt, *Chem. Commun.*, 2012, **48**, 3638–3640.
11 C. T. Chen and K. S. Suslick, *Coord. Chem. Rev.*, 1993, **128**, 293–322.
12 W. L. Leong and J. J. Vittal, *Chem. Rev.*, 2011, **111**, 688–764.
13 C. Janiak, *Dalton Trans.*, 2003, 2781.
14 T. J. Prior and M. J. Rosseinsky, *CrystEngComm*, 2000, **2**, 128–133.
15 J. M. Lehn, *Polym. Int.*, 2002, **51**, 825–839.
16 A. M. Ako, C. S. Hawes, B. Twamley and W. Schmitt, *CrystEngComm*, 2017, **19**, 994–1000.
17 K. Biradha, C. Seward and M. J. Zaworotko, *Angew. Chem., Int. Ed.*, 1999, **38**, 492–495.
18 C.-B. Ma, C.-N. Chen and Q.-T. Liu, *CrystEngComm*, 2005, **7**, 650–655.
19 X.-M. Zhang, M.-L. Tong, M.-L. Gong and X.-M. Chen, *Eur. J. Inorg. Chem.*, 2003, **2003**, 138–142.
20 L. Carlucci, G. Ciani, A. Gramaccioli, D. M. Proserpio and S. Rizzato, *CrystEngComm*, 2000, **2**, 154–163.
21 J. J. Vittal, *Coord. Chem. Rev.*, 2007, **251**, 1781–1795.
22 H. Chae, J. Kim and Y. Go, *Nature*, 2004, **427**, 523–527.
23 P. Paul, B. Tyagi, A. K. Bilakhiya, P. Dastidar and E. Suresh, *Inorg. Chem.*, 2000, **39**, 14–22.
24 J. Wang, F. Yuan, H. M. Hu, B. Xu and G. L. Xue, *Inorg. Chem. Commun.*, 2016, **71**, 19–22.
25 N. Klein, I. Senkovska, I. A. Baburin, R. Grünker, U. Stoeck, M. Schlichtenmayer, B. Streppel, U. Mueller, S. Leoni, M. Hirscher and S. Kaskel, *Chem. – Eur. J.*, 2011, **17**, 13007–13016.
26 N. Zhu, M. J. Lennox, G. Tobin, L. Goodman, T. Düren and W. Schmitt, *Chem. – Eur. J.*, 2014, **20**, 3595–3599.
27 A. C. Kathalikkattil, D.-W. Kim, J. Tharun, H.-G. Soek, R. Roshan and D.-W. Park, *Green Chem.*, 2014, **16**, 1607.
28 N. Zhu, M. J. Lennox, T. Düren and W. Schmitt, *Chem. Commun.*, 2014, **50**, 4207–4210.
29 N. Zhu, D. Sensharma, P. Wix, M. J. Lennox, T. Düren, W.-Y. Wong and W. Schmitt, *Eur. J. Inorg. Chem.*, 2016, 1939–1943.
30 B. Therrien, *J. Organomet. Chem.*, 2011, **696**, 637–651.
31 M. Llunell, D. Casanova, J. Cirera, P. Alemany and S. Alvarez, *SHAPE, v2. 1*, Universitat de Barcelona, Barcelona, 2013.
32 C. A. Hunter and J. K. M. Sanders, *J. Am. Chem. Soc.*, 1990, **112**, 5525–5534.
33 G. R. Desiraju and A. Gavezzotti, *J. Chem. Soc., Chem. Commun.*, 1989, 621–623.
34 M. P. Johansson and J. Olsen, *J. Chem. Theory Comput.*, 2008, **4**, 1460–1471.
35 M. A. Spackman and D. Jayatilaka, *CrystEngComm*, 2009, **11**, 19–32.
36 S. K. Wolff, D. J. Grimwood, J. J. McKinnon, M. J. Turner, D. Jayatilaka and M. A. Spackman, *Crystal Explorer v. 3.1.*, University of Western Australia, Perth, 2013.